

Les Houches 2015: Physics at TeV Colliders Standard Model Working Group Report

Conveners

Higgs physics: SM issues

J. Bendavid (CMS), M. Grazzini (Theory), K. Tackmann (ATLAS), C. Williams (Theory)

SM: Loops and Multilegs

S. Badger (Theory), A. Denner (Theory), J. Huston (ATLAS), J. Thaler (Jets contact)

Tools and Monte Carlos

V. Ciulli (CMS), R. Frederix (Theory), M. Schönherr (Theory)

Abstract

This Report summarizes the proceedings of the 2015 Les Houches workshop on Physics at TeV Colliders. Session 1 dealt with (I) new developments relevant for high precision Standard Model calculations, (II) the new PDF4LHC parton distributions, (III) issues in the theoretical description of the production of Standard Model Higgs bosons and how to relate experimental measurements, (IV) a host of phenomenological studies essential for comparing LHC data from Run I with theoretical predictions and projections for future measurements in Run II, and (V) new developments in Monte Carlo event generators.

Acknowledgements

We would like to thank the organizers (G. Belanger, F. Boudjema, P. Gras, D. Guadagnoli, S. Gascon, J. P. Guillet, B. Herrmann, S. Kraml, G. H. de Monchenault, G. Moreau, E. Pilon, P. Slavich and D. Zerwas) and the Les Houches staff for the stimulating environment always present at Les Houches. We thank the Labex ENIGMASS for support.

Authors

J. R. Andersen¹, S. Badger², K. Becker³, M. Bell⁴, J. Bellm¹, J. Bendavid⁵, E. Bothmann⁶, R. Boughezal⁷, J. Butterworth⁴, S. Carrazza⁸, M. Chiesa⁹, L. Cieri¹⁰, V. Ciulli^{11,12}, A. Denner¹³, M. Duehrssen-Debling¹⁴, G. Falmagne¹⁵, S. Forte¹⁶, P. Francavilla¹⁷, R. Frederix¹⁸, M. Freytsis¹⁹, J. Gao⁷, P. Gras²⁰, M. Grazzini¹⁰, N. Greiner¹⁰, D. Grellscheid¹, G. Heinrich²¹, G. Hesketh⁴, S. Höche²², L. Hofer²³, T.-J. Hou²⁴, A. Huss²⁵, J. Huston²⁶, J. Isaacson²⁶, A. Jueid²⁷, S. Kallweit²⁸, D. Kar²⁹, Z. Kassabov^{16,30}, V. Konstantinides⁴, F. Krauss¹, S. Kuttimalai¹, A. Lazapoulos²⁵, P. Lenzi¹², Y. Li³¹, J.M. Lindert¹⁰, X. Liu³², G. Luisoni⁸, L. Lönnblad³³, P. Maierhöfer³⁴, D. Maître¹, A. C. Marini³⁵, G. Montagna^{9,36}, M. Moretti³⁷, P. M. Nadolsky²⁴, G. Nail^{38,39}, D. Napoletano¹, O. Nicrosini⁹, C. Oleari^{40,41}, D. Pagani⁴², C. Pandini⁴³, L. Perrozzi⁴⁴, F. Petriello^{7,45}, F. Piccinini⁹, S. Plätzer^{1,38}, I. Pogrebnyak²⁶, S. Pozzorini¹⁰, S. Prestel²², C. Reuschle⁴⁶, J. Rojo⁴⁷, L. Russo^{12,48}, P. Schichtel¹, M. Schönherr¹⁰, S. Schumann⁶, A. Siódmok⁸, P. Skands⁴⁹, D. Soper¹⁹, G. Soyez⁵⁰, P. Sun²⁶, F. J. Tackmann⁵¹, K. Tackmann⁵¹, E. Takasugi^{21,52}, J. Thaler³⁵, S. Uccirati³⁰, U. Utku⁴, L. Viliani^{11,12,14}, E. Vryonidou⁴², B. T. Wang²⁴, B. Waugh⁴, M. A. Weber^{8,52}, C. Williams⁵³, J. Winter²⁶, K. P. Xie²⁶, C.-P. Yuan²⁶, F. Yuan⁵⁴, K. Zapp⁸, M. Zaro^{55,56},

¹ Institute for Particle Physics Phenomenology, University of Durham, Durham DH1 3LE, UK

² Higgs Centre for Theoretical Physics, School of Physics and Astronomy, The University of Edinburgh, Edinburgh EH9 3JZ, Scotland, UK

³ Department of Physics, Oxford University, Denys Wilkinson Building, Keble Road, Oxford OX1 3RH, UK

⁴ Department of Physics and Astronomy, University College London, Gower Street, London WC1E 6BT, UK

⁵ California Institute of Technology, Pasadena, USA

⁶ II. Physikalisches Institut, Universität Göttingen, 37077 Göttingen, Germany

⁷ High Energy Physics Division, Argonne National Laboratory, Argonne, IL 60439, USA

⁸ CERN, TH Department, CH-1211 Geneva, Switzerland

⁹ INFN, Sezione di Pavia, Via A. Bassi 6, 27100 Pavia, Italy

¹⁰ Physik-Institut, Universität Zürich, Winterthurerstrasse 190, CH-8057 Zürich, Switzerland

¹¹ Dipartimento di Fisica e Astronomia, Università di Firenze, I-50019 Sesto Fiorentino, Florence, Italy

¹² INFN, Sezione di Firenze, Firenze, Italy

¹³ Universität Würzburg, Institut für Theoretische Physik und Astrophysik, D-97074 Würzburg, Germany

¹⁴ CERN, EP Department, CH-1211 Geneva, Switzerland

¹⁵ ENS Cachan, Université Paris-Saclay, 61 avenue du Président Wilson, Cachan, F-94230, France

- 16 TIF Lab, Dipartimento di Fisica, Università di Milano and INFN, Sezione di Milano, Via Celoria 16, I-20133 Milano, Italy
- 17 Laboratoire de Physique Nucléaire et de Hautes Energies, Institut Lagrange de Paris, CNRS, Paris, France
- 18 Physik Department T31, Technische Universität München, 85748 Garching, Germany
- 19 Institute of Theoretical Science, University of Oregon, Eugene, OR 97403-5203, USA
- 20 CEA/IRFU Saclay, France
- 21 Max Planck Institute for Physics, Föhringer Ring 6, 80805 München, Germany
- 22 SLAC National Accelerator Laboratory, Menlo Park, CA 94025, USA
- 23 Department de Física Quàntica i Astrofísica (FQA), Institut de Ciències del Cosmos (IC-CUB), Universitat de Barcelona (UB), Martí Franquès 1, E-08028 Barcelona, Spain
- 24 Department of Physics, Southern Methodist University, Dallas, TX 75275-0181, USA
- 25 Institute for Theoretical Physics, ETH, CH-8093 Zürich, Switzerland
- 26 Department of Physics and Astronomy, Michigan State University, East Lansing, MI 48824, USA
- 27 Département des Mathématiques, Université Abdelmalek Essaadi, Tanger, Morocco
- 28 PRISMA Cluster of Excellence, Institute of Physics, Johannes Gutenberg University, D-55099 Mainz, Germany
- 29 School of Physics, University of the Witwatersrand, Johannesburg, Wits 2050, South Africa
- 30 Dipartimento di Fisica, Università di Torino and INFN, Sezione di Torino, Via Pietro Giuria 1, I-10125 Torino, Italy
- 31 Fermilab, PO Box 500, Batavia, IL 60510, USA
- 32 Maryland Center for Fundamental Physics, University of Maryland, College Park, Maryland 20742, USA
- 33 Dept. of Astronomy and Theoretical Physics, Lund University, Sweden
- 34 Physikalisches Institut, Albert-Ludwigs-Universität Freiburg, 79104 Freiburg, Germany
- 35 Center for Theoretical Physics, Massachusetts Institute of Technology, Cambridge, MA 02139, USA
- 36 Dipartimento di Fisica, Università di Pavia, Pavia, Italy
- 37 Dipartimento di Fisica, Università di Ferrara and INFN, Sezione di Ferrara, Italy
- 38 Particle Physics Group, School of Physics and Astronomy, University of Manchester, Manchester M13 9PL, UK
- 39 Institut für Theoretische Physik, Karlsruhe Institute of Technology, 76131 Karlsruhe, Germany
- 40 Università di Milano-Bicocca, Milano, Italy

- ⁴¹ INFN, Sezione di Milano-Bicocca, Piazza della Scienza 3, 20126 Milano, Italy
- ⁴² Centre for Cosmology, Particle Physics and Phenomenology (CP3), Université catholique de Louvain, B-1348 Louvain-la-Neuve, Belgium
- ⁴³ Laboratoire de Physique Nucléaire et de Hautes Energies, UPMC and Université Paris-Diderot and CNRS/IN2P3, Paris, France
- ⁴⁴ Institute for Particle Physics, ETH, CH-8093 Zürich, Switzerland
- ⁴⁵ Department of Physics & Astronomy, Northwestern University, Evanston, IL 60208, USA
- ⁴⁶ HEP Theory Group, Department of Physics, Florida State University, Tallahassee, USA
- ⁴⁷ Rudolf Peierls Centre for Theoretical Physics, 1 Keble Road, University of Oxford, OX1 3NP Oxford, United Kingdom
- ⁴⁸ Università di Siena, Siena, Italy
- ⁴⁹ School of Physics and Astronomy, Monash University, VIC-3800, Australia
- ⁵⁰ IPhT, CEA Saclay, CNRS UMR 3681, F-91191 Gif-sur-Yvette, France
- ⁵¹ Deutsches Elektronen-Synchrotron (DESY), D-22607 Hamburg, Germany
- ⁵² University of California, Los Angeles, USA
- ⁵³ Department of Physics, University at Buffalo, The State University of New York, Buffalo 14260, USA
- ⁵⁴ Nuclear Science Division, Lawrence Berkeley National Laboratory, Berkeley, CA 94720, USA
- ⁵⁵ Sorbonne Universités, UPMC Univ. Paris 06, UMR 7589, LPTHE, F-75005, Paris, France
- ⁵⁶ CNRS, UMR 7589, LPTHE, F-75005, Paris, France

Contents

I	NLO automation and (N)NLO techniques	2
1	Update on the precision Standard Model wish list ¹	2
II	Parton distribution functions	13
1	Construction and phenomenological applications of PDF4LHC parton distributions ²	13
2	On the accuracy and Gaussianity of the PDF4LHC15 combined sets of parton distributions ³	20
III	SM Higgs working group report	33
1	Higgs boson production through gluon fusion at N3LO, and its theory uncertainty ⁴	33
2	Heavy quark mass effects in gluon fusion Higgs production ⁵	37
3	Simplified template cross sections ⁶	42
IV	Phenomenological studies	56
1	Electroweak corrections in Drell–Yan production ⁷	56
2	NLO EW technical and physics comparisons ⁸	61
3	A comparative study of Higgs boson plus jets production in gluon fusion ⁹	77
4	Photon isolation studies ¹⁰	122
5	Systematics of quark/gluon tagging ¹¹	132
6	Study of associated production of vector bosons and b-jets at the LHC ¹²	152
7	Irreducible backgrounds and measurement uncertainties ¹³	169
V	MC uncertainties and output formats	177
1	Towards parton shower variations ¹⁴	177
2	Reweighting the SHERPA parton shower ¹⁵	184
3	Ntuples for NNLO events produced by EERAD3 ¹⁶	188

¹ S. Badger, A. Denner, J. Huston

² J. Gao, T.-J. Hou, J. Huston, P. M. Nadolsky, B. T. Wang, K. P. Xie

³ S. Carrazza, S. Forte, Z. Kassabov, J. Rojo

⁴ A. Lazopoulos

⁵ S. Kuttimalai, F. Krauss, P. Maierhöfer, M. Schönherr

⁶ M. Duehrssen-Debling, P. Francavilla, F. J. Tackmann, K. Tackmann

⁷ A. Huss, M. Schönherr

⁸ A. Denner, V. Ciulli, M. Chiesa, R. Frederix, L. Hofer, S. Kallweit, J. M. Lindert, P. Maierhöfer, A. Marini, G. Montagna, M. Moretti, O. Nicrosini, D. Pagani, F. Piccinini, S. Pozzorini, M. Schönherr, E. Takasugi, S. Uccirati, M. A. Weber, M. Zaro

⁹ J. R. Andersen, S. Badger, K. Becker, J. Bellm, R. Boughezal, G. Falmagne, R. Frederix, M. Grazzini, N. Greiner, S. Höche, J. Huston, J. Isaacson, Y. Li, X. Liu, G. Luisoni, F. Petriello, S. Plätzer, S. Prestel, I. Pogrebnyak, P. Schichtel, M. Schönherr, P. Sun, F. J. Tackmann, E. Vryonidou, J. Winter, C.-P. Yuan, F. Yuan
¹⁰ L. Cieri, G. Heinrich

¹¹ G. Soyez, J. Thaler, M. Freytsis, P. Gras, D. Kar, L. Lönnblad, S. Plätzer, A. Siódmok, P. Skands, D. Soper

¹² V. Ciulli, M. Bell, J. Butterworth, G. Hesketh, D. Grellscheid, F. Krauss, G. Luisoni, G. Nail, D. Napoletano, C. Oleari, L. Perrozzi, S. Platzer, C. Reuschle, B. Waugh

¹³ J. Butterworth, F. Krauss, V. Ciulli, P. Francavilla, V. Konstantinides, P. Lenzi, C. Pandini, L. Perrozzi, L. Russo, M. Schönherr, U. Utku, L. Viliiani, B. Waugh

¹⁴ S. Höche, A. Jueid, G. Nail, S. Plätzer, M. Schönherr, A. Siódmok, P. Skands, D. Soper, K. Zapp

¹⁵ E. Bothmann, M. Schönherr, S. Schumann

¹⁶ G. Heinrich, D. Maître

The 2015 Les Houches workshop saw great progress, both in terms of the development of precision calculations as well as the analysis of high statistics 8 TeV LHC data. The term of the workshop also saw the first data at 13 TeV, and the calculation of inclusive Higgs boson production at N³LO in perturbative QCD. There has been considerable progress for differential predictions at N²LO in QCD and automated electroweak corrections at NLO.

In these proceedings, we report on the progress with the Les Houches high precision wish list, as well as the development of new tools, such as the PDF4LHC15 PDFs, and simplified cross sections for Higgs boson measurements. Detailed phenomenological studies, such as the comparison of predictions for Higgs boson + jets in gluon-gluon fusion were carried out. The 2015 workshop continued the emphasis on understanding electroweak corrections that started in the 2013 workshop. As the increased energy and luminosity allow more measurements to reach the TeV scale, greater attention must be paid to the impact of EW corrections. Finally, the systematics of quark/gluon tagging have been investigated, and, following a long tradition, a new Les Houches variable, the Les Houches Angularity, has been defined.

As the LHC turns back on, we eagerly await the high statistics data at 13 TeV that will dominate the work at Les Houches 2017.

Chapter I

NLO automation and (N)NLO techniques

1 Update on the precision Standard Model wish list ¹

Identifying key observables and processes that require improved theoretical input has been a key part of the Les Houches programme. In this contribution we summarise progress since the previous report in 2013 and explore the possibilities for further advancements during Run II.

1.1 Introduction

The 2013 Les Houches report introduced a new high precision wish list which was considered an “extremely ambitious” list of processes that could be used to fully exploit the Run II data [1]. In fact there has been remarkable theoretical advances in NNLO computations for QCD corrections and automated NLO electroweak corrections and many processes are now available in some form. Of course there still remains a number of outstanding items but the wish list certainly deserves to be updated to include recent progress.

An undoubted highlight in precision QCD predictions since the 2013 report has been the completion of the total inclusive Higgs production cross-section at N³LO [2]. There has also been remarkable progress for $2 \rightarrow 2$ predictions at NNLO in QCD where a large number of items from the 2013 wish list have now been completed. The focus here has been on producing fully differential predictions, and progress has largely been possible thanks to the perfection of infrared subtraction methods.

Automated tools for NLO QCD are now familiar in experimental analyses where parton-shower matching and matrix element improved multi-jet merging techniques are becoming a standard level of theoretical precision. The automation of full SM corrections including mixed electroweak predictions has also seen major improvements.

It is clear that computations at this level of complexity require careful verification. The importance of reproducing known results with alternative techniques and implementations cannot be stressed enough. Though there are still challenges ahead to make state-of-the-art $2 \rightarrow 2$ predictions publicly available to experimental analyses, the theoretical framework is in place to ensure this can be achieved during the course of Run II and keep theoretical uncertainties in line with the experiments.

Root Ntuples have been a useful tool for complicated final states at NLO and allow for extremely flexible re-weighting and analysis. The cost for this is the large disk space required to store the event information. A feasibility study using ROOT NTUPLES to store the much larger NNLO events in $e^+e^- \rightarrow 3$ jets is described in Sec. V.3. ApplGrid [3] and FastNLO [4] offer a simpler, but slightly less flexible, method to distribute NNLO predictions. The latter option is likely to be used heavily in precision PDF fits.

1.2 Developments in theoretical methods

Precision predictions require a long chain of different tools and methods all of which demand detailed and highly technical computations. In this section we attempt to summarise the current state of the art and point out some bottlenecks which will need to be overcome in order to complete the still unknown processes on the wish list.

¹ S. Badger, A. Denner, J. Huston

Computational methods for the amplitude level ingredients have seen substantial progress in the last few years. In order to be as pedagogical as possible we begin by defining the various components that are required to construct infrared finite observables at fixed order. Scattering amplitudes are generally decomposed into a basis of integrals together with rational coefficients,

$$A_{2 \rightarrow n}^{(L)} = \sum (\text{coefficients})_i (\text{integrals})_i, \quad (\text{I.1})$$

one must then remove infrared singularities to obtain a finite cross-section,

$$d\sigma_{2 \rightarrow n} \text{N}^k \text{LO} = \text{IR}_k(A_{2 \rightarrow n}^k, A_{2 \rightarrow n+1}^{k-1}, \dots, A_{2 \rightarrow n+k}^0). \quad (\text{I.2})$$

where the function IR_k represents an infrared subtraction technique. Ultra-violet renormalisation must also be performed but since it presents no technical difficulties we ignore it in our review. We briefly review the three main components – the computation of the loop integrals, the computation of their rational coefficients and methods for infrared subtraction.

1.2.1 Loop integrals

A major result since the last report has been the completion of the two-loop master integrals for vector boson pair production [5–8] employing Henn’s canonical differential equation technique [9]. The technique has also been used to obtain complete NLO QCD corrections the $H \rightarrow Z\gamma$ decay retaining the full top and Z mass dependence of the two-loop integrals [10]. Other notable examples include the off-shell integrals for ladder topologies at three loops [11] and two-loop master integrals for mixed QCD/electroweak corrections in Drell-Yan production [12].

Improvements in the understanding of the basis of multiple poly-logarithms through Symbol and Hopf algebra’s (see e.g. [13] for a review) has led to a high degree of automation for these integral computations. This is clearly a necessary step in order to apply such techniques to phenomenologically relevant cases, most notably in the case of $pp \rightarrow H$ at N^3LO .

There has also been developments for the direct evaluation of Feynman integrals. Panzer’s HyperInt [14] and Bogner’s MPL [15] packages have focused mainly on zero and one scale integrals with a high number of loops (see for example [16]) but the algorithms employed have potential applications to a wider class of two-loop integrals with more scales.

Direct numerical evaluation remains a powerful technique and the sector decomposition algorithm has seen a number of optimisations implemented into the publicly available codes [17–20]. Though performing a full integration over the phase space using numerical methods is extremely computationally intensive, very recently a complete computation of $pp \rightarrow HH$ via gluon fusion at NLO including the full top mass dependence has been completed [21].

Prospects for going beyond $2 \rightarrow 2$ scattering at two loops are also improving. Very recently an analytic basis of five-point master integrals for the planar sector massless QCD [22] and off-shell integrals needed for $pp \rightarrow H + 2j$ [23] have been completed. Extending these techniques to complete the non-planar sector definitely requires additional work but is now a realistic short term goal.

The most difficult processes on the wish list from the point of view of the loop integrals are those with many internal mass scales like $t\bar{t} + j$ and full m_t corrections to $H + j$ due to the potential appearance of elliptic functions. The mathematics of these special functions still remains to be fully understood and is an active area of research². Nevertheless, developments give hope that such processes will eventually be possible but for the time being remain out of reach for phenomenology. Numerical methods offer an alternative solution to this problem,

²For some recent studies of elliptic functions and elliptic multiple zeta values see [24–26]. A more complete set of references can be found in the recent review [27].

and presently have been the most successful for example in $pp \rightarrow t\bar{t}$ [28] and $pp \rightarrow HH$ [21]. Nevertheless, an analytic solution to the problem would allow for more flexible phenomenology.

1.2.2 Loop amplitudes and integrands

Following the completion of the two-loop integrals mentioned above, a complete set of helicity amplitudes has been obtained by two independent groups for $pp \rightarrow VV'$ [29–32]. A good deal of effort was spent to ensure stable numerical evaluation of these amplitudes requiring knowledge of the underlying basis of multiple poly-logarithms. This has resulted in a public code for numerical evaluation available from <http://vvamp.hepforge.org/>. Both approaches relied heavily on efficient implementations of integration-by-parts reduction identities [33–38].

The expressions, generated using Feynman diagrams, are quite lengthy and in many places contain spurious poles, but this has not hindered full NNLO predictions where the major computational effort is in the evaluations of double and single unresolved infrared divergent components.

1.2.3 Generalised unitarity and integrand reduction

Extending the current multi-loop methods to higher multiplicity still represents a serious challenge. The increased complexity in the kinematics, and large amount of gauge redundancy in the traditional Feynman diagram approach, has been solved numerically through on-shell and recursive off-shell methods at one-loop. This breakthrough has led to the development of the now commonly used automated one-loop codes [39–45].

The D -dimensional generalised unitarity cuts algorithm [46–50] has now been extended to multi-loop integrands using integrand reduction [51]³ and elements of computational algebraic geometry [53–61]. In contrast to the one-loop case, the basis of integrals obtained through this method is not currently known analytically and is much larger than the set of basis functions defined by standard integration-by-parts identities. Nevertheless, new results in non-supersymmetric theories have been obtained for five gluon scattering amplitudes with all positive helicities [60, 62]. The maximal unitarity method [63], which incorporates integration-by-parts (IBP) identities, has been applied to a variety of two-loop examples in four dimensions [64–68]. This approach can be seen as an extension of the generalised unitarity methods of Britto, Cachazo and Feng [48] and Forde [50]. Efficient algorithms to generate unitarity compatible IBP identities are a key ingredient in both approaches and have been the focus of on-going investigations [69–72].

Steady progress towards $2 \rightarrow 3$ processes on the wish list like $pp \rightarrow H+2j$, $pp \rightarrow 3j$ appears to be on course though there is clearly a long way to fully differential NNLO predictions.

1.2.4 Infrared subtraction methods for differential cross-sections

The construction of fully differential NNLO cross-sections for $2 \rightarrow 2$ processes has been a major theoretical challenge over the last years. This programme has been a major success with many different approaches now applied to LHC processes.

- Antenna subtraction [73, 74]:

Analytically integrated counter-terms for hadronic initial and final states. Almost completely local, requires averaging over azimuthal angles. Applied to $pp \rightarrow 2j$, $pp \rightarrow Z + j$ and $pp \rightarrow W + j$.

³We do not attempt a complete review of integrand reduction here. Further information can be found in the review article [52] and references therein.

- Sector Decomposition [75–77]:
Fully local counter-terms using extension of the FKS approach at NLO [78]. Numerically integrated counter-terms for hadronic initial and final states. Recently formulated in a four-dimensional setting [79]. Applied to $pp \rightarrow H + j$ [80,81] and $pp \rightarrow t\bar{t}$ [82] processes.
- q_T [83]:
Phase-space slicing approach for colour-less final states applied to many $pp \rightarrow VV'$ processes. An extension for $t\bar{t}$ final states has been recently proposed [84].
- N -jettiness [85–87]:
Extension of the q_T method to general hadronic final states matching to soft-collinear effective theory (SCET) below the N -jettiness cut-off parameter. Applied to $pp \rightarrow H + j$, $pp \rightarrow V + j$ and Drell-Yan including resummation and parton shower effects [88].
- ColorFull [89]:
Fully local counter-terms extending the Catani-Seymour dipole method [90]. Analytically integrated for infrared poles, numerical integration for finite parts. Currently developed for hadronic final states such as $H \rightarrow b\bar{b}$ [89] and $e^+e^- \rightarrow \text{jets}$ [91].

With the success of these methods for $2 \rightarrow 2$ applications it is an obvious question as to whether these techniques also apply to higher multiplicity. The extension to $2 \rightarrow 3$ for most methods is clear though the reality of dealing with an increasingly large number of counter-terms and a more complicated phase space is not to be underestimated. It is clear that in the near future such applications will be attempted based on the current technology.

The reverse unitarity method [92–95] is a powerful method for fully inclusive observables (and rapidity distributions). It has been utilised in the complete computation of the inclusive $pp \rightarrow H$ cross-section at $N^3\text{LO}_{\text{QCD}}$ [96] in the infinite top-mass limit. This computation has been carried out in many stages starting with expansions around the soft limit [97–99]. There are 5 main components: triple-virtual, squared real-virtual, double-virtual-real, double-real-virtual and triple-real, most of which have been verified by independent groups. The reverse unitarity method has then been used to obtain each component of the triple-virtual [100–102], squared real-virtual [103,104], double-virtual-real [105–108], double-real-virtual [109,110] and triple-real radiation [111] as an expansion in the dimensional regularisation parameter. The poles of these separate contributions cancel analytically when summed together and combined with the counter-terms for UV poles [112–115] and initial state infrared singularities [116–120]. A complete result for the $qq' \rightarrow H$ channel has also been obtained [121].

The analytic result for Higgs production at threshold [97] has given access to a number of additional predictions in the threshold limit for Drell-Yan [122,123], $H \rightarrow b\bar{b}$ [124], $V' \rightarrow VH$ [125].

1.3 The precision wish list

Following the 2013 report we break the list of precision observables into three sections: Higgs, vector bosons and top quarks.

Corrections are defined with respect to the leading order, and we organise the perturbative expansion into QCD corrections, electroweak (EW) corrections and mixed $\text{QCD} \times \text{EW}$,

$$d\sigma_X = d\sigma_X^{\text{LO}} \left(1 + \sum_{k=1} \alpha_s^k d\sigma_X^{\delta N^k \text{LO}_{\text{QCD}}} + \sum_{k=1} \alpha^k d\sigma_X^{\delta N^k \text{LO}_{\text{EW}}} + \sum_{k,l=1} \alpha_s^k \alpha^l d\sigma_X^{\delta N^{(k,l)} \text{LO}_{\text{QCD} \times \text{EW}}} \right). \quad (\text{I.3})$$

We explicitly separate the mixed QCD and EW corrections to distinguish between additive predictions QCD+EW and mixed predictions QCD×EW. The definition above only applies in the case where the leading order process contains only one unique power in each coupling constant. For example, in the case of $q\bar{q} \rightarrow q\bar{q}Z$ two leading order processes exist: via gluon exchange of $\mathcal{O}(\alpha_s^2\alpha)$, via electroweak boson exchange of $\mathcal{O}(\alpha^3)$ and the interference $\mathcal{O}(\alpha_s\alpha^2)$. In these cases it is customary to classify the Born process with highest power in α_s , and typically the largest cross section, as the leading order and label the others as subleading Born processes. The above classification is then, unless otherwise stated, understood with respect to the leading Born process.

In the following we attempt to give a current snap-shot of the state of perturbative computations at N²LO_{QCD} or higher and electroweak corrections at NLO_{EW}. The main aim is to summarise computations that appeared in the 2013 wish list and that have now been completed. There are obvious difficulties in compiling lists in this way which make it difficult to address every possible relevant computation. Specific approximations and extensions to fixed order are often necessary when comparing theory to data.

Following the 2013 wish list we clarify that it is desirable to have a prediction that combines all the known corrections. For example $d\sigma$ N²LO_{QCD}+NLO_{EW} refers to a single code that produced differential predictions including $\mathcal{O}(\alpha_s^2)$ and $\mathcal{O}(\alpha)$. In most cases this is a non-trivial task and when considered in combination with decays can lead to a large number of different sub-processes.

Electroweak corrections

Complete higher order corrections in the SM can quickly become technically complicated in comparison to the better known corrections in QCD. An introductory guide to the nomenclature and applications in which such corrections are important was presented in the last report so we do not repeat it here [1]. As a basic rule of thumb $\alpha_s^2 \sim \alpha$, so corrections at N²LO_{QCD} and NLO_{EW} are desirable together. Moreover, for energy scales that are large compared to the W-boson mass EW corrections are enhanced by large logarithms (often called Sudakov logarithms). There has been progress towards a complete automation of NLO_{EW} corrections within one-loop programs such as OPENLOOPS, GoSAM, RECOLA and MADGRAPH5_aMC@NLO which has led to the completion of many items from the 2013 list. A detailed comparison of these tools as well as comparisons with the Sudakov approximation for a variety of processes is presented in Sec. IV.2.

Heavy top effective Higgs interactions and finite mass effects

Many calculations of SM processes involving Higgs bosons use the effective gluon interaction in the $m_t \rightarrow \infty$ limit. At high energy hadron colliders this is by far the most dominant production process, yet at high transverse momentum the approximation will break down. The data collected during Run II will certainly probe the region where the approximation is invalid and finite mass effects are an important addition. Complete top mass corrections are extremely difficult since the occurring multi-loop integrals are thought to contain elliptic functions. As mentioned above, though there is active research in this area, phenomenological applications are only a realistic goal in a longer time frame. In the short term there are many approaches to approximate finite mass effects, either by re-weighting with a full leading order or including partial results where available. Expansions in m_t have also been successfully computed. It is clear that in all cases where the effective theory is used some approximate treatment of finite mass effects is desirable.

We list processes in the wish list as N^kLO_{HEFT} + N^lLO_{QCD} when re-weighting including the full top mass dependence up to order l has been performed. For example, consider the

differential cross section at NLO in the effective theory:

$$d\sigma_n^{\text{NLO}_{\text{HEFT}}} = d\sigma_n^{\text{LO}_{\text{HEFT}}} + d\sigma_n^{\text{V}_{\text{HEFT}}} + d\sigma_{n+1}^{\text{R}_{\text{HEFT}}}, \quad (\text{I.4})$$

where we have grouped together the different contributions to the NLO cross section: leading order (LO), virtual (V) and real radiation (R). The details of any infrared subtraction method will not affect the fact that there is an n particle and $n+1$ particle phase space. Including finite mass effects at LO can be simply achieved by replacing parts of the calculation with the those from the full theory where they are known:

$$d\sigma_n^{\text{NLO}_{\text{HEFT}}+\text{LO}_{\text{QCD}}} = d\sigma_n^{\text{LO}_{\text{QCD}}} + d\sigma_n^{\text{V}_{\text{HEFT}}} + d\sigma_{n+1}^{\text{R}_{\text{HEFT}}} \quad (\text{I.5})$$

or by re-weighting the NLO corrections,

$$d\sigma_n^{\text{NLO}_{\text{HEFT}}+\text{LO}_{\text{QCD}}} = \frac{d\sigma_n^{\text{LO}_{\text{QCD}}}}{d\sigma_n^{\text{LO}_{\text{HEFT}}}} \left(d\sigma_n^{\text{LO}_{\text{HEFT}}} + d\sigma_n^{\text{V}_{\text{HEFT}}} \right) + \frac{d\sigma_{n+1}^{\text{LO}_{\text{QCD}}}}{d\sigma_{n+1}^{\text{LO}_{\text{HEFT}}}} d\sigma_{n+1}^{\text{R}_{\text{HEFT}}}. \quad (\text{I.6})$$

Clearly more care is required in the latter case to ensure infrared finiteness is preserved. In either case the QCD correction will proceed through a heavy quark loop and can be taken in $N_f = 5$ (m_t only), $N_f = 4$ (m_t and m_b only) and so on. For totally inclusive quantities the distinction between the two approaches above is not important, the approach taken in the case of $pp \rightarrow H$ recently presents a good overview of this procedure [126]. While the above constructions to incorporate quark mass effects into NLO calculations of Higgs production in gluon fusion is expected to work well for top quarks, it fails for bottom quarks. The reason therefore lies in the smallness of the bottom quark mass and the invalidity of the HEFT expressions in this case. A more extensive discussion on this topic is presented in Sec. III.2.

Resummation

We do not attempt a complete classification of all possible resummation procedures that have been considered or applied to the processes in the list. In many cases precision measurements will require additional treatment beyond fixed order and since resummed predictions always match onto fixed order outside of the divergent region it would be desirable if all predictions were available this way. Since this is not feasible, some specific cases are highlighted in addition to the fixed order.

There are several important kinematic regions where perturbative predictions are expected to break down. Totally inclusive cross-sections often have large contributions from soft-gluon emission in which higher order logarithms can be computed analytically. The q_T and N -jettiness subtraction methods naturally match on to resummations of soft gluons, in the latter case through soft-collinear effective theory. A recent study using the q_T method has been applied in the case of $pp \rightarrow ZZ$ and $pp \rightarrow W^+W^-$ [127] where further details and references can be found. 0-jettiness resummations within SCET have been considered recently in Drell-Yan production [88] using the GENEVA Monte Carlo framework which also matches the results to a parton shower [128].

Observables with additional restrictions on jet transverse momenta can also introduce large logarithms and jet veto resummations have been studied extensively in the case of $pp \rightarrow H$ and $pp \rightarrow H + j$ [129].

With increasing precision of both experimental data and fixed order calculations other regions may also begin to play a role. A method for the resummation of logarithms from small jet radii has been developed and applied in the case of $pp \rightarrow H$ [129–131].

These represent only a tiny fraction of the currently available tools and predictions with resummed logarithms. For further information the interested reader may refer to [132] and references therein.

process	known	desired
$pp \rightarrow H$	σ $N^3\text{LO}_{\text{HEFT}}+N^2\text{LO}_{\text{QCD}}\left(\frac{1}{m_t^6}\right)$	
	$d\sigma$ NLO_{EW}	$d\sigma$ $N^3\text{LO}_{\text{HEFT}}+N^2\text{LO}_{\text{QCD}}$
	$d\sigma$ $N^2\text{LO}_{\text{HEFT}}+N\text{LO}_{\text{QCD}}+\text{PS}$	$+N\text{LO}_{\text{EW}}+N^{(1,1)}\text{LO}_{\text{QCD}}\times\text{EW}$
$pp \rightarrow H + j$	$d\sigma$ $N^2\text{LO}_{\text{HEFT}}$	$d\sigma$ $N^2\text{LO}_{\text{HEFT}}+N\text{LO}_{\text{QCD}}+N\text{LO}_{\text{EW}}$
	$d\sigma$ NLO_{EW}	
$pp \rightarrow H + 2j$	$d\sigma$ $\text{NLO}_{\text{HEFT}}+\text{LO}_{\text{QCD}}$	$d\sigma$ $N^2\text{LO}_{\text{HEFT}}+\text{LO}_{\text{QCD}}+N\text{LO}_{\text{EW}}$
	$d\sigma$ $N^2\text{LO}_{\text{QCD}}(\text{VBF}^*)$	$d\sigma$ $N^2\text{LO}_{\text{QCD}}(\text{VBF})+N\text{LO}_{\text{EW}}(\text{VBF})$
	$d\sigma$ $\text{NLO}_{\text{EW}}(\text{VBF})$	
$pp \rightarrow H + 3j$	$d\sigma$ NLO_{HEFT}	$d\sigma$ $\text{NLO}_{\text{QCD}}+\text{LO}_{\text{QCD}}+N\text{LO}_{\text{EW}}$
	$d\sigma$ NLO_{EW}	
$pp \rightarrow H + V$	$d\sigma$ $N^2\text{LO}_{\text{QCD}}$	$d\sigma$ $N^2\text{LO}_{\text{QCD}} + N\text{LO}_{gg\rightarrow HV} + N\text{LO}_{\text{EW}}$
$pp \rightarrow HH$	$d\sigma$ $N^2\text{LO}_{\text{HEFT}}$	$d\sigma$ $N^2\text{LO}_{\text{HEFT}}+N\text{LO}_{\text{QCD}}+N\text{LO}_{\text{EW}}$
	$d\sigma$ NLO_{QCD}	
$pp \rightarrow H + t\bar{t}$	$d\sigma$ NLO_{QCD}	$d\sigma$ $\text{NLO}_{\text{QCD}}+N\text{LO}_{\text{EW}}$
	$d\sigma$ NLO_{EW}	
$pp \rightarrow H + t$	$d\sigma$ NLO_{QCD}	$d\sigma$ $\text{NLO}_{\text{QCD}}+N\text{LO}_{\text{EW}}$
$pp \rightarrow H + \bar{t}$		

Table I.1: Precision wish list: Higgs boson final states. VBF* refers to the computation using the factorised 'projection-to-Born' approximation [136].

Parton showering

As in the case of resummation - we refrain from listing all processes in the wish list to be desired with matching to a parton shower (PS). $\text{NLO}_{\text{QCD}}+\text{PS}$ predictions can be considered fully automated within MADGRAPH5_aMC@NLO, SHERPA, POWHEG and HERWIG7. There have been many recent efforts in matching $N^2\text{LO}_{\text{QCD}}$ corrections to parton showers for singlet production processes. There are good prospects for extending these techniques to $2 \rightarrow 2$ processes in the short term - nevertheless we have refrained from adding these processes to the 2013 wish list.

Decay sub-processes

The description of decay sub-processes is incomplete though we do list a few notable cases. Ideally all on-shell (factorised) decays would be available up to the order of the core process. In some cases this is potentially an insufficient approximation and full off-shell decays including background interference would be desirable but are often prohibitive. The $t\bar{t}$ final state is an obvious example where the off-shell decay to $WWb\bar{b}$ at NNLO is beyond the scope of current theoretical methods.

Decays in the context of electroweak corrections are usually much more complicated. Full off-shell effects at NLO are expected to be small, but higher order corrections within factorisable contributions to the decay can be important. The case of vector boson pair production is particularly important given the completion of the $N^2\text{LO}_{\text{QCD}}$ computation, and corrections are known at NLO within the double pole approximation [133] and beyond [134, 135].

1.4 Higgs boson associated processes

H: Given the high importance of this process it has been investigated extensively in the literature. The calculation of the total inclusive cross section at $N^3\text{LO}_{\text{HEFT}}$ [2] reduces theoretical uncertainties to the 5% level, the remaining uncertainties being dominated by PDF and finite mass effects. Several resummation schemes have been considered and a comprehensive phenomenological study has been presented recently [126]. The most precise evaluation of the cross section combines the effective theory with:

- complete mass dependence at NLO including top, bottom and charm loops.
- m_H/m_t corrections at NNLO.
- electro-weak corrections at NLO.
- re-scaling of the $N^3\text{LO}_{\text{HEFT}}$ with the complete LO_{QCD} top loop.

The NNLO+PS computation [137] has been extended to include finite top and bottom mass corrections at NLO [138]. To match the data precisely it would be desirable to have fiducial predictions, requiring a fully differential computation.

H + j: Known through to $N^2\text{LO}_{\text{QCD}}$ in the infinite top mass limit [80, 81, 85, 139]. Finite top mass effects are expected to play an important role for $p_T > 150 - 200$ GeV.

H + $\geq 2j$: QCD corrections are an essential background to Higgs production in vector boson fusion (VBF). VBF production of a Higgs boson has recently been computed through to $N^2\text{LO}_{\text{QCD}}$ accuracy [136].

VH: Associated production of a Higgs boson with a vector boson is important for pinning down the EW couplings of the Higgs. First predictions at $N^2\text{LO}_{\text{QCD}}$ have been available for some time [140, 141]. Differential predictions at $N^2\text{LO}_{\text{QCD}}$ to *WH* [142] and *ZH* [143] have now been completed including effects from gluon initiated processes. These results have been studied more recently using the *N*-jettiness subtraction scheme within MCFM including a full set of decays [144]. A parton shower matched prediction using the MiNLO procedure in POWHEG has very recently been completed [145]. The total inclusive cross-section has been considered in the threshold limit at $N^3\text{LO}_{\text{QCD}}$, extracted from the inclusive Higgs cross-section [125].

HH: The $N^2\text{LO}_{\text{QCD}}$ corrections were originally computed in the infinite top mass limit [146] and have since been improved with threshold resummation to NNLL [147]. Finite top mass corrections are very important here and power corrections to $\mathcal{O}(1/m_t^8)$ have been computed [148, 149]. Though the convergence is seen to be relatively slow, improvements can be made by normalising to LO result in the full theory. A complete computation at NLO including all finite quark mass effects has very recently been achieved using numerical integration methods [21].

$t\bar{t}H$: NLO_{EW} corrections have been considered within the automated MADGRAPH5_aMC@NLO framework [150, 151]. Moreover, NLO QCD corrections have been calculated for the process including the top quark decays [152].

1.5 Vector boson associated processes

The numerous decay channels for vector bosons and the possible inclusion of full off-shell corrections versus factorised decays in the narrow width approximation make vector boson processes

process	known	desired
$pp \rightarrow V$	σ N ³ LO _{QCD} ($z \rightarrow 0$)	
	$d\sigma$ N ² LO _{QCD}	$d\sigma$ N ³ LO _{QCD} + N ² LO _{EW}
	$d\sigma$ NLO _{EW}	+ N ^(1,1) LO _{QCD×EW} + decays
	$d\sigma$ N ^(1,1) LO _{QCD×EW}	
$pp \rightarrow VV'$	$d\sigma$ N ² LO _{QCD} + decays	$d\sigma$ N ² LO _{QCD} + NLO _{EW} + decays
	$d\sigma$ NLO _{EW}	
$pp \rightarrow V + j$	$d\sigma$ N ² LO _{QCD}	$d\sigma$ N ² LO _{QCD} + NLO _{EW} + decays
$pp \rightarrow V + 2j$	$d\sigma$ NLO _{QCD} + decays	$d\sigma$ N ² LO _{QCD} + NLO _{EW} + decays
	$d\sigma$ NLO _{EW} + decays	
$pp \rightarrow VV' + 1, 2j$	$d\sigma$ NLO _{QCD} + decays	$d\sigma$ NLO _{QCD} + NLO _{EW} + decays
	$d\sigma$ NLO _{EW}	
$pp \rightarrow VV'V''$	$d\sigma$ NLO _{QCD}	$d\sigma$ NLO _{QCD} + NLO _{EW} + decays
	$d\sigma$ NLO _{EW}	
$pp \rightarrow \gamma\gamma$	$d\sigma$ N ² LO _{QCD}	$d\sigma$ N ² LO _{QCD} + NLO _{EW}
$pp \rightarrow \gamma\gamma + j$	$d\sigma$ NLO _{QCD}	$d\sigma$ N ² LO _{QCD} + NLO _{EW}

Table I.2: Precision wish list: vector boson final states. $V = W, Z$ and $V', V'' = W, Z, \gamma$.

complicated to classify. A full range of decays in the narrow width approximation would be a desirable minimum precision.

- V : Inclusive cross-sections and rapidity distributions in the threshold limit have been extracted from the $pp \rightarrow H$ results [122, 123]. Parton shower matched N²LO_{QCD} computations using both the MiNLO method [153], SCET resummation [88] and via the UN²LOPS technique [154]. Completing the inclusive N³LO_{QCD} computation beyond the threshold limit is an important step for phenomenological studies. The dominant factorisable corrections at $\mathcal{O}(\alpha_s\alpha)$ (N^(1,1)LO_{QCD×EW}) are also now available [155].
- $V + j$: Both $Z + j$ [156–159] and $W + j$ [159–161] have recently been completed through to N²LO_{QCD} including leptonic decays.
- $V + \geq 2j$: While fixed order NLO_{QCD} computations of $V + \geq 2$ jet final states have been known for many years recent progress has been made for NLO_{EW} corrections [162] including merging and showering [163, 164].
- $VV', V'\gamma$: Complete N²LO_{QCD} are now available for WW [165, 166], ZZ [167, 168], $Z\gamma$ [169], $W\gamma$ [169] using the q_T subtraction method. These results should become publicly available in the near future including all on-shell leptonic decays. There has been good progress in calculating NLO EW corrections for complete processes including decays [134, 135, 170, 171]. Thereby also the new automated approaches have been employed and a range of decays has been considered. Very recently the WZ final state has been computed at N²LO_{QCD} [172]. The remaining VV' processes, together with other colourless final states, will be available in the forthcoming MATRIX Monte Carlo program based on q_T subtraction.

process	known	desired
$pp \rightarrow t\bar{t}$	$d\sigma$ N ² LO _{QCD}	
	$d\sigma$ NLO _{QCD} + decays	$d\sigma$ N ² LO _{QCD} + NLO _{EW} + decays
	$d\sigma$ NLO _{EW}	
$pp \rightarrow t\bar{t} + j$	$d\sigma$ NLO _{QCD} + decays	$d\sigma$ N ² LO _{QCD} + NLO _{EW} + decays
	$d\sigma$ NLO _{EW}	
$pp \rightarrow t\bar{t} + 2j$	$d\sigma$ NLO _{QCD} + on-shell decays	$d\sigma$ NLO _{QCD} + NLO _{EW} + decays
$pp \rightarrow t\bar{t} + V$	$d\sigma$ NLO _{QCD}	$d\sigma$ NLO _{QCD} + NLO _{EW} + decays
	$d\sigma$ NLO _{EW}	
$pp \rightarrow t/\bar{t}$	$d\sigma$ N ² LO _{QCD} (t -channel)	$d\sigma$ N ² LO _{QCD} + NLO _{EW} + decays
$pp \rightarrow 2j$	$d\sigma$ N ² LO _{QCD} (gg,qq)	$d\sigma$ N ² LO _{QCD} + NLO _{EW}
	$d\sigma$ NLO _{EW}	
$pp \rightarrow j + \gamma$	$d\sigma$ NLO _{QCD}	$d\sigma$ N ² LO _{QCD} + NLO _{EW}
	$d\sigma$ NLO _{EW}	
$pp \rightarrow 3j$	$d\sigma$ NLO _{QCD}	$d\sigma$ N ² LO _{QCD} + NLO _{EW}

Table I.3: Precision wish list: top quark and jet final states

$\gamma\gamma, \gamma\gamma + j$: This process remains an important ingredient in Higgs measurements at Run II. Originally computed at N²LO_{QCD} with q_T subtraction [173], it has recently been re-computed [174] using the N -jettiness subtraction implemented within MCFM. The q_T resummation at NNLL requested on the 2013 wish list are also now available [173]. Given the recent excitement in di-photon production a detailed understanding of these processes at high q_T will be important in the coming years. Prospects for N³LO_{QCD} corrections remain closely connected with differential Higgs and Drell-Yan production at N³LO_{QCD}. At high transverse momentum it may also be interesting to have N²LO_{QCD} predictions for $\gamma\gamma + j$. Given that this is of equivalent complexity to $3j$ production we add this process to the wish list.

1.6 Top quark and jet associated processes

$t\bar{t}$: Another major achievement since the 2013 report has been the completion of fully differential predictions for $t\bar{t}$ production at N²LO_{QCD} [28, 82]. An on-shell description of the top quarks has been taken and it would be beneficial to extend these to studies including a full set of decays in the narrow width approximation in order to make fully fiducial predictions.

$t\bar{t}V$: NLO_{QCD} corrections to $t\bar{t}Z$ including a full range of decays have been considered recently [175, 176]. This will help to improve the constraints on anomalous EW couplings in the top quark sector during Run II. NLO_{EW} corrections have also been computed within the automated MADGRAPH5_aMC@NLO framework [151].

$2j$: This process is now almost fully complete at N²LO_{QCD}. The leading colour pure gluonic corrections known previously [177] have been expanded to include sub-leading colour $gg \rightarrow gg$ [178] and $q\bar{q} \rightarrow gg$ [179]. The qg initiated processes are expected in the near future.

t/\bar{t} : Fully differential N²LO_{QCD} corrections have been completed for the dominant t -

channel production process [180].

Chapter II

Parton distribution functions

1 Construction and phenomenological applications of PDF4LHC parton distributions ¹

We revisit the construction and application of combined PDF sets (PDF4LHC15) developed by the PDF4LHC group in 2015. Our focus is on the meta-analysis technique employed in the construction of the 30-member PDF4LHC15 sets, and especially on aspects that were not fully described in the main PDF4LHC recommendation document. These aspects include construction of the 30-member sets at NLO (in addition to NNLO), extension of the NLO and NNLO sets to low QCD scales, and construction of such sets for 4 active flavors. In addition, we clarify a point regarding the calculation of parton luminosity uncertainties at low mass. Finally, we present a website containing predictions based on PDF4LHC15 PDFs for some crucial LHC processes.

1.1 Introduction

To simplify applications of parton distribution functions (PDFs) in several categories of LHC experimental simulations, the 2015 recommendations [181] of the PDF4LHC working group introduce combinations of CT14 [182], MMHT2014 [183], and NNPDF3.0 [184] PDF ensembles, by utilizing the Monte Carlo (MC) replica technique [185]. The central PDF and the uncertainties of the combined set are derived from the 900 MC replicas of the error PDFs of the above three input ensembles. As the 900 error PDFs are often too many to be manageable, they are “compressed” into smaller PDF error sets using three reduction techniques [186–188]. Consequently, the final combined PDFs come in three versions, one with 30 error sets (PDF4LHC15_30), and the other two with 100 error sets (PDF4LHC15_100 and PDF4LHC15_MC). Two of these, PDF4LHC15_30 and PDF4LHC_100, are constructed in the form of Hessian eigenvector sets [189]. The PDF4LHC15_MC ensemble is constructed from MC replicas. The central sets are the same in the 900-replica prior as well as in the _100, _30, and _MC ensembles. They are equal to the average of central sets of CT14, MMHT2014, and NNPDF3.0 ensembles. The error sets of the three PDF4LHC15 ensembles are different, reflecting the specifics of each reduction technique. They are available in the LHAPDF library [190] at NLO and NNLO in QCD coupling strength α_s , with the central value of $\alpha_s(M_Z)$ equal to 0.118, and with additional sets corresponding to the α_s variations by 0.0015 around the central value.

The 30-member ensemble is constructed using the meta-parametrization technique introduced in [186]. This contribution describes additional developments in the 30-member ensemble that happened at the time, or immediately after, the release of the original PDF4LHC recommendation document. They include construction of the PDF4LHC15_30 ensemble at NLO, extension of PDF4LHC15_30 to scales below 8 GeV, and the specialized ensemble with 4 active quark flavors. These features are already incorporated in the LHAPDF distributions. We provide comparisons of PDFs and parton luminosities and introduce a website [191] illustrating essential LHC cross sections computed with the PDF4LHC15 and other ensembles, and using a variety of QCD programs.

When deciding on which of the three PDF4LHC sets to use, it is important to keep in mind that all of them reproduce well the uncertainties of the 900-replica “prior” PDF ensemble. This

¹ J. Gao, T.-J. Hou, J. Huston, P. M. Nadolsky, B. T. Wang, K. P. Xie

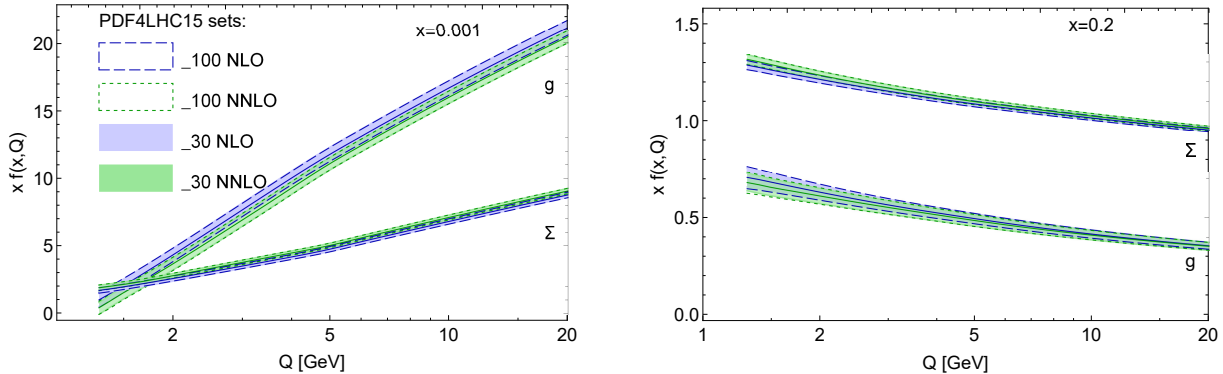


Fig. II.1: The singlet and gluon PDFs, $\Sigma(x, Q)$ and $g(x, Q)$, from 100- and 30-member PDF4LHC15 sets at NLO and NNLO, plotted vs. the QCD scale Q at $x = 10^{-3}$ (left) and 0.2 (right).

prior itself has some uncertainty both in its central value and especially in the size of the PDF uncertainty itself, reflecting differences between the central values and the uncertainty bands of CT14, MMHT2014 and NNPDF3.0, which become especially pronounced at very low x and high x . At moderate x values, contributing to the bulk of precision physics cross sections at the LHC, the agreement between the three input PDF sets is often quite better, meaning that the combined prior and the three reduced ensembles constructed from it are also known well. In general, the 30-member ensemble keeps the lowest, best-known eigenvector sets, and thus provides a slightly lower estimate for the uncertainty of the 900-replica prior, but one that is known with higher confidence than the exact uncertainty of the prior set. We will demonstrate that, across many practical applications, the 30-member error estimates are typically close both to those of the prior and of the Hessian 100 PDF error set.

1.2 QCD scale dependence of the 30-member NLO PDF4LHC ensemble

The NLO meta-parametrizations are constructed in a slightly different manner compared to the NNLO version. In Ref. [186], we have shown that the differences of the numerical implementation of DGLAP evolution at NNLO in CT10 [192], MSTW2008 [193], and NNPDF2.3 [194] PDFs are negligible compared to the intrinsic PDF uncertainties.² However, at NLO, the NNPDF2.3 group uses evolution that neglects some higher-order terms compared to HOPPET, which can result in deviations by up to 1 % in the small- and large- x regions, compared to the evolution used by CT10 and MSTW2008. These differences in NLO numerical DGLAP evolution, while formally allowed, also affect the most recent generation of NLO PDFs, i.e., CT14+MMHT2014 vs. NNPDF3.0. When the 900-replica prior ensemble at NLO is constructed by taking 300 replicas from each of the input CT14, MMHT14, and NNPDF3.0 ensembles, the implication is that Q -scale dependence of these replicas is not strictly Markovian. Probability regions at the low Q scale, as sampled by the MC replicas, are not exactly preserved by DGLAP evolution to a higher Q scale. This is in contrast to the consistent DGLAP evolution of a single input PDF set, which guarantees that the probability/confidence value associated with a given error set is independent of the Q scale.

Thus, the NLO prior ensemble is not inherently consistent, even though the deviations in DGLAP evolution of individual replicas are arguably small. One should apply a correction to restore the Markovian nature of the evolution. In the PDF4LHC15_30 NLO set we do this by first constructing the central PDF set at any Q by averaging the CT14, MMHT14, and

²CT10 PDFs use the x -space evolution provided by the program HOPPET [195].

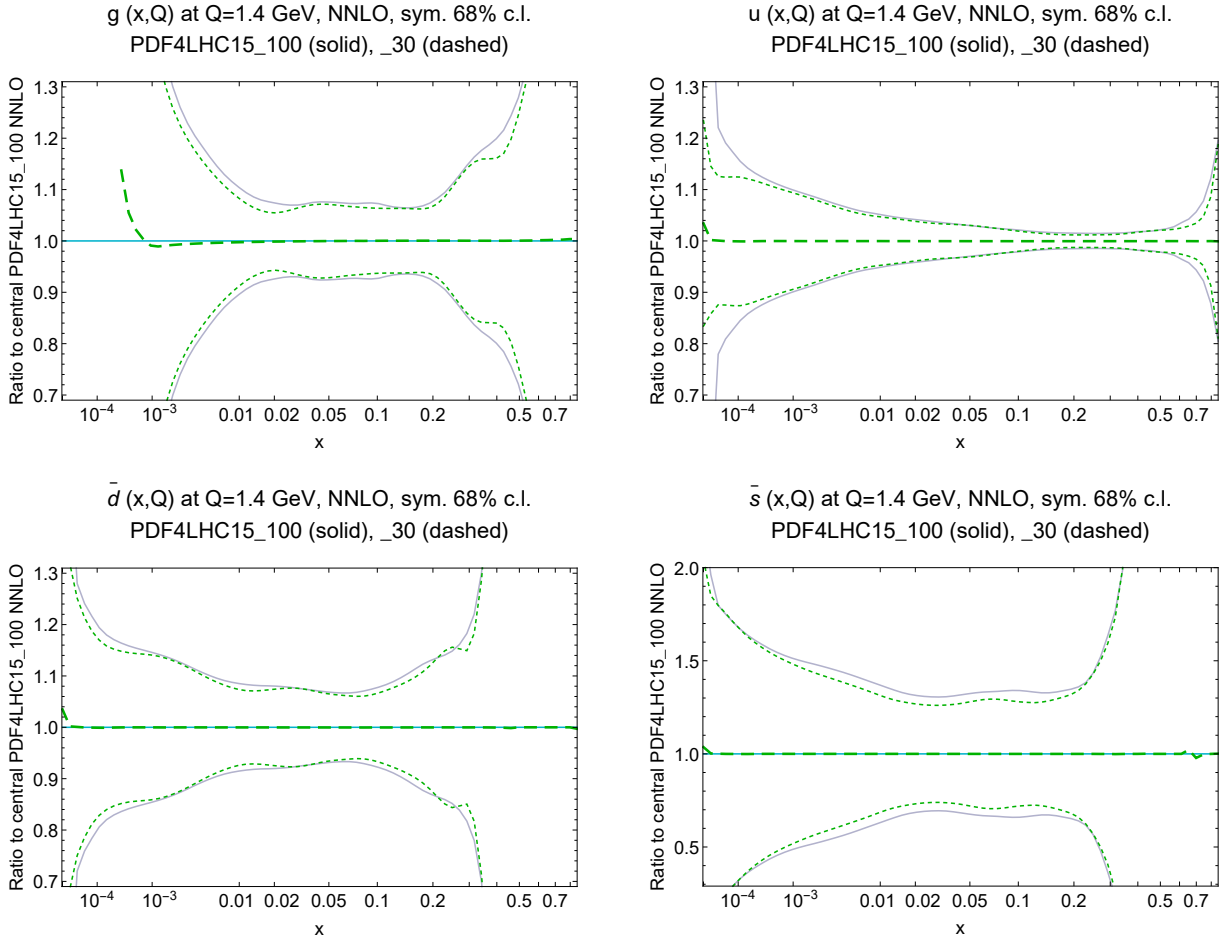


Fig. II.2: PDF central predictions and uncertainty bands for select parton flavors from the 100- and 30-member NNLO PDF4LHC15 ensembles, plotted versus x at a QCD scale $Q = 1.4$ GeV as ratios to the central PDF4LHC15_100 distributions.

NNPDF3.0 central sets that were evolved by their own native programs. Then, we reduce the 900-member into the 30-member set at scale $Q_0 = 8$ GeV and evolve all replicas to other Q values using HOPPET. Finally, we estimate the difference between the HOPPET evolution and native evolution of the central set, and subtract this difference at every Q from the HOPPET-evolved values of every error set. After such universal shift, the Q dependence of all error sets is practically the same as the native evolution of the central PDF. The probability regions are now independent of Q ; this preserves sum rules for momentum and quark quantum numbers.

1.3 PDF4LHC15_30 PDFs at low Q

The original formulation of the meta-PDFs had a minimum Q value of 8 GeV. The relatively high lower cutoff on Q was introduced to justify the combination of PDFs obtained in different heavy-quark schemes, and it is sufficient to describe all high- Q^2 physics at the LHC. However, the extension of the _30 PDFs down to lower Q values can be useful, too as for example in the simulation of parton showers and the underlying event in Monte-Carlo showering programs. The PDF4LHC15_30 version on LHAPDF includes such an extension down to a Q value of 1.4 GeV, obtained by backward evolution from 8 GeV using HOPPET. It should be remembered that the PDF4LHC15 combination is statistically consistent when the factorization scale in the PDFs is much higher than the bottom mass, as is typical in the bulk of LHC applications. The

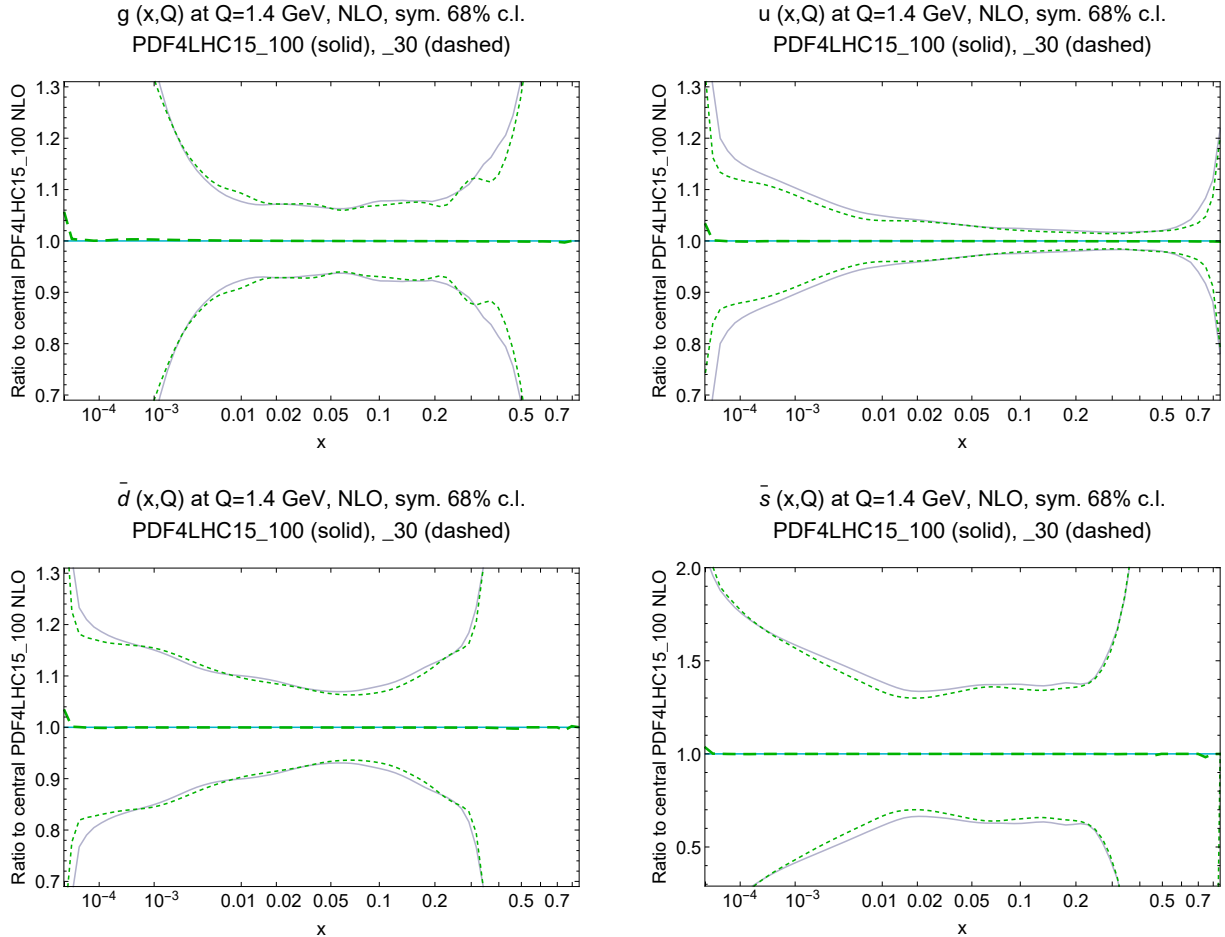


Fig. II.3: Same as Fig. II.2, for NLO PDF sets.

extension below $Q = 8$ GeV should be used in less accurate aspects of the calculation that are not sensitive to heavy-quark mass effects, such as inside the parton shower merged onto an (N)NLO fixed-order cross section.

Figure II.1 illustrates the Q dependence of singlet and gluon PDFs of the `_30` and `_100` ensembles at NLO and NNLO, for two select values of Bjorken x . Figs. II.2 and II.3 compare the uncertainty bands for the g, u, \bar{d} and \bar{s} distributions at a Q value of 1.4 GeV, at NNLO and NLO, respectively, for the PDF4LHC_30 and PDF4LHC_100 PDF sets. Good agreement between the two sets is found in all cases; the backward evolution is smooth and stable across the covered Q range, with only minor deviations observed below 2 GeV. [When examining the figures, recall that the `_30` error bands can be slightly narrower for unconstrained x regions and PDF flavors at any Q].

1.4 PDF4LHC15 parton luminosities at NLO and NNLO

Even more relevant for physics applications than the PDF error bands are the parton luminosities. We have calculated the luminosities as a function of the mass of the final state, for a center-of-mass energy of 13 TeV. Comparisons of the gg and $q\bar{q}$ PDF luminosities, at NLO and NNLO, and defined as in [196], are shown in Fig. II.4 for PDF4LHC15_100, `_30`, and `_MC` sets, and in Fig. II.4 for PDF4LHC15_100, CT14, MMHT14, and NNPDF3.0 sets. Note that the size of the uncertainties shown here, and the level of agreement among the error bands, are different at low mass from those shown in the PDF4LHC document [181]. That is because,

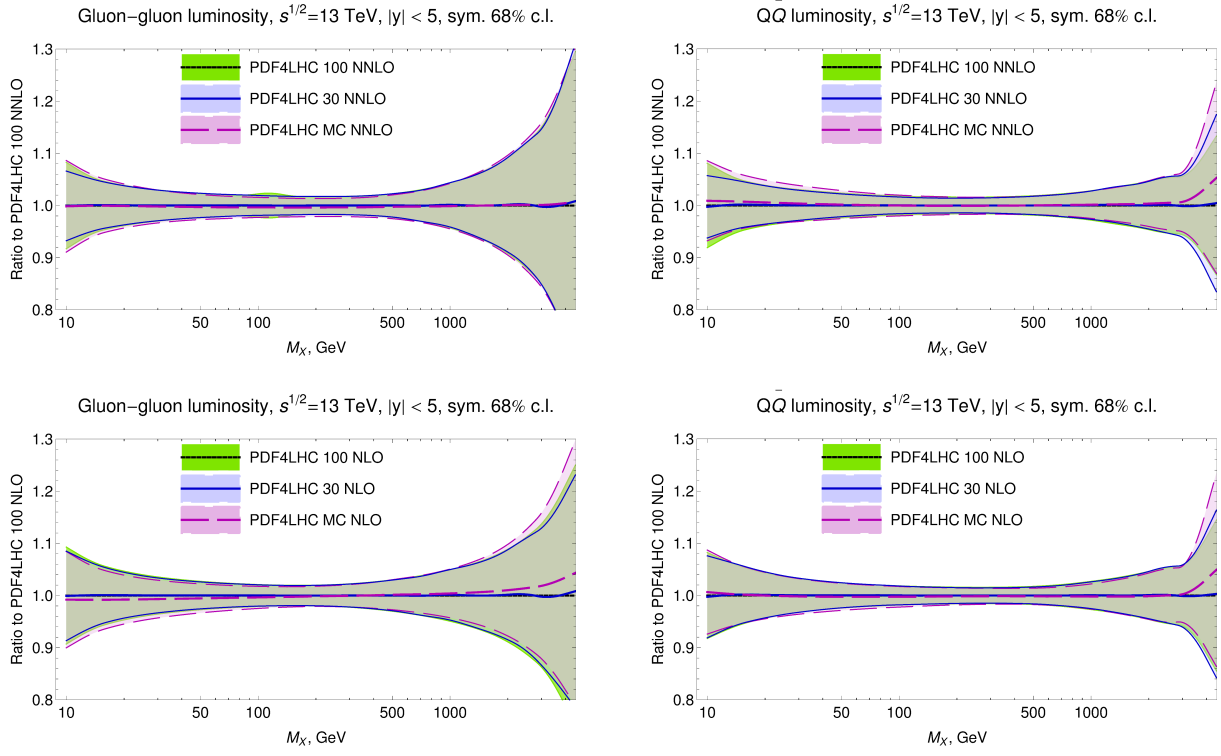


Fig. II.4: PDF4LHC15 NNLO and NLO parton luminosities at $\sqrt{s} = 13$ TeV in the experimentally accessible rapidity region $|y| < 5$.

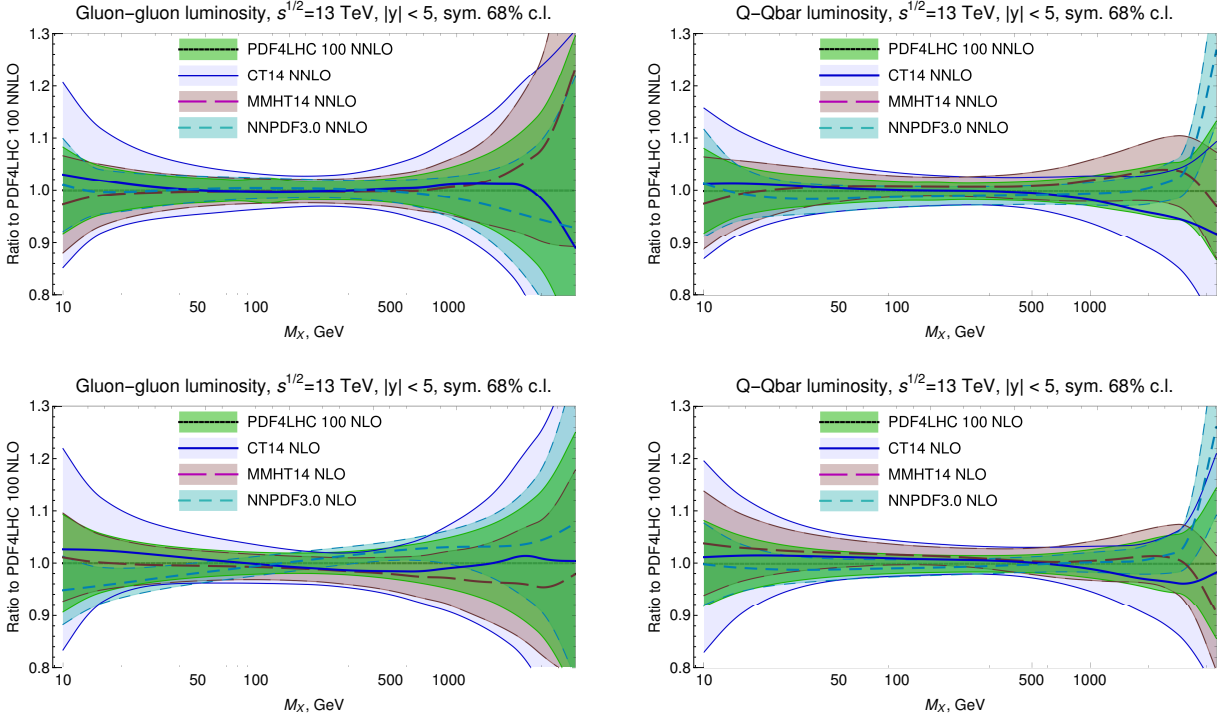


Fig. II.5: NNLO and NLO parton luminosities for PDF4LHC15_100, CT14, MMHT14, and NNPDF3.0 ensembles at $\sqrt{s} = 13$ TeV in the experimentally accessible rapidity region $|y| < 5$.

in our plots, a restriction has been applied on the x values of the PDFs to correspond to a

Process	Order	Type of calculation
$p + p \rightarrow Z + X$	NLO	AMCFAST/APPLGRID
$p + p \rightarrow W^+ + X$	NLO	AMCFAST/APPLGRID
$p + p \rightarrow W^- + X$	NLO	AMCFAST/APPLGRID
$p + p \rightarrow W + X, A_{ch,W}$	NLO	AMCFAST/APPLGRID
CMS $p + p \rightarrow W(l\nu) + X, A_{ch,l}$	NLO	AMCFAST/APPLGRID
$p + p \rightarrow W^+\bar{c} + X$	NLO	AMCFAST/APPLGRID
$p + p \rightarrow W^-c + X$	NLO	AMCFAST/APPLGRID
$p + p \rightarrow t\bar{t} + X$	NLO	AMCFAST/APPLGRID
$p + p \rightarrow t\bar{t}\gamma\gamma + X$	NLO	AMCFAST/APPLGRID
ATLAS inclusive jets	NLO	NLOJET++/APPLGRID
ATLAS inclusive dijets	NLO	NLOJET++/APPLGRID
$p + p \rightarrow H(\gamma\gamma) + X$	LO, NLO	MCFM
$p + p \rightarrow H(\gamma\gamma) + jet + X$	LO, NLO	MCFM

Table II.1: Processes, QCD orders, and computer codes employed for comparisons of PDFs in the online gallery [191].

rapidity cut of $|y| < 5$ on the produced state. Without such a cut, the luminosity integral at masses below 40 GeV receives contributions from extremely low x of less than 10^{-5} , where (a) the uncertainties are larger, (b) the LHAPDF grids provided for the 30 PDF sets are outside of their tabulated range, and (c) the final state is produced in the forward region outside of the experimental acceptance of the LHC detectors. Without the constraints on the x range, the comparisons of parton luminosities at low mass are less relevant to LHC measurements.

1.5 4-flavor PDF4LHC15_30 sets

The nominal _30 ensemble has been generated for a maximum number of quark flavors of up to $N_f = 5$. An alternative _30 ensemble have been now provided for a maximum quark flavors of $N_f = 4$ at NLO, based on the same prescription as for the $N_f = 5$ sets, except that they are combined at an initial scale of 1.4 GeV in order to avoid backward evolution. We choose $\alpha_S(M_Z, N_f = 4) = 0.1126$ based on matching to $\alpha_S(M_Z, N_f = 5) = 0.118$ with a pole mass of 4.56 GeV for the bottom quark (equal to the average of masses of 4.75 and 4.18 GeV from the CT14, MMHT14, and NNPDF3.0 ensembles, and consistent with the PDG pole mass value).

1.6 PDF4LHC15 predictions for QCD observables

The PDF4LHC recommendation document [181] contains detailed guidelines to help decide which individual or combined PDFs to use depending on the circumstances.

To assist in this decision, predictions for typical LHC QCD observables have been calculated for an assortment of PDF sets. In Ref. [197], PDF4LHC15 predictions were made with the APPLGRID fast interface [3] for published LHC measurements within the fiducial region. To provide a complementary perspective, at a gallery website [191], we present LHC cross sections for processes listed in Table II.1 at 7, 8, and 13 TeV, and computed with no or minimal experimental cuts. The three (N)NLO ensembles of the PDF4LHC15 family (_100, _30, _MC [181]) are compared to those of ABM12 [198], CT14 [182], HERA2.0 [199], MMHT14 [183], and NNPDF3.0 [184]. The cross sections are calculated using (N)LO hard matrix elements either by a fast convolution of the PDFs with the tabulated parton-level cross section in the APPLGRID format [3], or by direct Monte-Carlo integration in MCFM [200]. Default $\alpha_s(M_Z)$

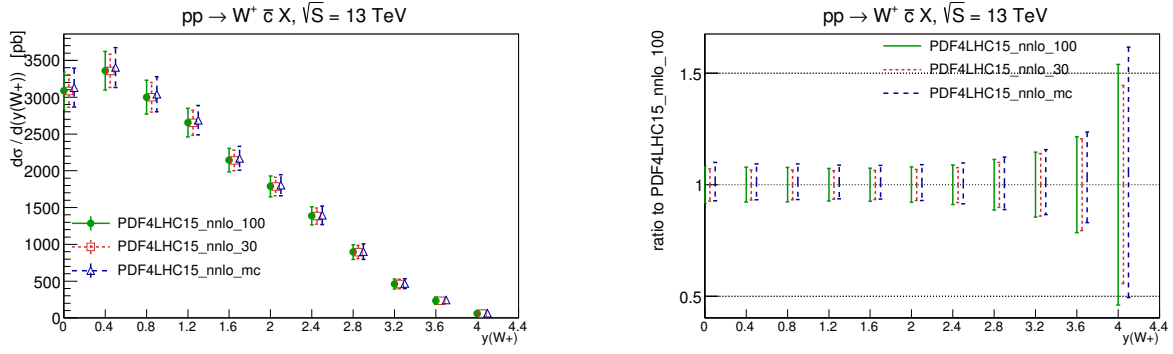


Fig. II.6: NLO predictions of $d\sigma/dy(W^+)$ in the process $pp \rightarrow W^+\bar{c} X$ at the LHC 13 TeV, computed with APPLGRID.

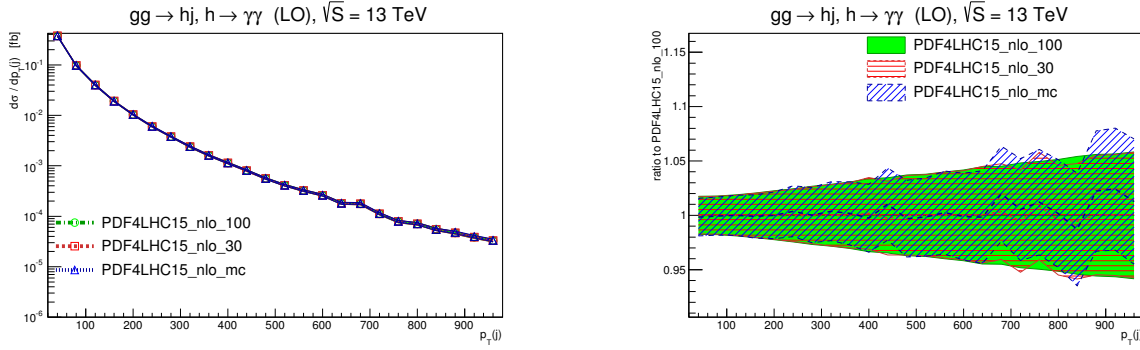


Fig. II.7: $d\sigma/dp_T(j)$ in the process $gg \rightarrow H(\gamma\gamma) + jet$ at the LHC 13 TeV, and its relative PDF uncertainties.

values are used with each PDF set. The APPLGRID files used in the computations are linked to the website. In the APPLGRID calculations, the hard cross sections are the same for all PDFs, while the MCFM-produced cross sections are sensitive to Monte-Carlo integration fluctuations that vary depending on the PDF ensemble, as will be discussed below.

The predictions were computed according to the following procedure. For production of W^\pm , Z^0 , $t\bar{t}$, $t\bar{t}\gamma\gamma$, $W^+\bar{c}(W^-c)$, we use MadGraph_aMC@NLO [45], combined with aMC-fast [201] to generate APPLGRID files for different rapidities of the final-state particle. The renormalization and factorization scales are $\mu_R = \mu_F = M_W$, M_Z , $H_T/2$, $H_T/2$, M_W , respectively. H_T is the scalar sum of transverse masses $\sqrt{p_T^2 + m^2}$ of final-state particles. For $W^+\bar{c}(W^-c)$ production, we neglect small contributions with initial-state c or b quarks. For NLO single-inclusive jet and dijet production, we use public APPLGRID files [202] in the bins of ATLAS measurements [203], created with the program NLOJET++ [204, 205]. Similarly, the W charge asymmetry in CMS experimental bins [206, 207] is computed with APPLGRID from [208].

For cross sections of the Standard Model Higgs boson and Higgs boson+jet production via gluon fusion, with subsequent decay to $\gamma\gamma$, we use MCFM in the heavy-top quark approximation. Minimal cuts are imposed on the photons; the QCD scales are $\mu_F = \mu_R = m_H$.

The PDF uncertainties shown are symmetric, computed according to the prescriptions provided with each PDF ensemble, except for the HERA2.0 predictions, which are shown with asymmetric uncertainties, including contributions from both the eigenvector sets and the variation sets.

For each scattering process, our gallery shows plots of differential cross sections and ratios of PDF uncertainties to the central prediction based on PDF4LHC15_100. Figs. II.6 and II.7 provide two examples of comparisons presented on the website. When computed with AP-PLGRID, the cross sections reflect genuine differences in the PDFs; the hard cross sections are the same with all PDF sets. Thus we observe, for instance, in $W^+\bar{c}$ production in Fig. II.6 that the uncertainties of _100, _30, and _MC ensembles are very close across the central-rapidity range for most processes, with the _30 uncertainty being only slightly smaller (as expected), and with the differences that can be nearly always eliminated by slightly scaling the _30 uncertainty up by a constant factor (e.g., by multiplying it by ≈ 1.05 in Fig. II.6). The differences between the PDF4LHC15 ensembles grow at rapidities above 2-3, where the cross sections also are rapidly decreasing. The PDF uncertainties fluctuate more in the forward regions, reflecting paucity of experimental constraints on the PDFs.

Another perspective is glanced from H and H +jet production cross sections calculated by MCFM, cf. Fig. II.7. [Additional comparisons can be viewed on the website.] These illustrate that often the differences between the PDF4LHC15 reduced ensembles will be washed out by Monte-Carlo integration errors, save exceptionally precise calculations. To start, although the LHAPDF grids for the _100, _30, and _MC *central* sets are just independent tabulations of the *same* prior central set (they are equivalent up to roundoff errors), they will produce different fluctuations during the Monte-Carlo integration in MCFM or alike program. This is exemplified in the right frame in Fig. II.7, where the Higgs boson production cross sections are slightly different for the three LHAPDF tabulations of the central set solely because of MC fluctuations. In this figure, the cross sections were evaluated with 10^6 Monte-Carlo samplings and with PDF reweighting of events turned on. The events are exactly the same for all PDF sets within a given ensemble, and the event sequences are not the same among the ensembles because of the different roundoffs of the central LHAPDF grids. Even when the event reweighting is on, the PDF error bands fluctuate together with their respective central predictions.

The MCFM example touches on broader questions. The MC fluctuations can be suppressed by increasing the number of events or by using coarser binning for the cross sections. These adjustments tend to either lengthen the calculations, especially with the _100-replica ensembles, or to wash out the already small differences between the three PDF4LHC15 ensembles. There are several ways for “averaging” the input central PDF sets, e.g., because they use different evolution codes or round-offs. Each of these will lead to a different pattern of MC fluctuations. Finally, if the MC integration is done without PDF event reweighting, MC fluctuations will vary independently replica-by-replica. Using the combined PDF4LHC ensemble with fewer members may turn out to be preferable in such situations.

Acknowledgements

Work at ANL is supported in part by the U.S. Department of Energy under Contract No. DE-AC02-06CH11357. Work at SMU was supported by the U.S. Department of Energy under Grant DE-SC0010129. Work at MSU was supported by the National Science Foundation under Grant PHY-1410972.

2 On the accuracy and Gaussianity of the PDF4LHC15 combined sets of parton distributions ³

We perform a systematic study of the combined PDF4LHC15 sets of parton distributions which have been recently presented as a means to implement the PDF4LHC prescriptions for the LHC Run II. These combined sets reproduce a prior large Monte Carlo (MC) sample in terms of

³ S. Carrazza, S. Forte, Z. Kassabov, J. Rojo

either a smaller MC replica sample, or a Gaussian (Hessian) representation with two different number of error sets, and obtained using two different methodologies. We study how well the three reduced sets reproduce the prior for all the $N_\sigma \simeq 600$ hadronic cross-sections used in the NNPDF3.0 fit. We then quantify deviations of the prior set from Gaussianity, and check that these deviations are well reproduced by the MC reduced set. Our results indicate that generally the three reduced sets perform reasonably well, and provide some guidance about which of these to use in specific applications.

2.1 Introduction

Recently, the PDF4LHC Working Group [209] has presented updated recommendations and guidelines [181] for the usage of Parton Distribution Functions (PDFs) for LHC calculations at Run II. These recommendations are specifically based on the usage of combined PDF sets, which are obtained using the Monte Carlo (MC) method [185,210], constructed from the combination of $N_{\text{rep}} = 300$ MC replicas from the NNPDF3.0 [184], MMHT2014 [183] and CT14 [182] PDF sets, for a total number of $N_{\text{rep}} = 900$ replicas. The combination has been performed both at NLO and at NNLO, and versions with $n_f = 4$ and $n_f = 5$ maximum number of active quark flavors are available. The impact of LHC measurements from Run I on PDF determinations has been discussed in a companion PDF4LHC report [211].

From this starting prior set, three reduced sets, two Hessian and one MC, are delivered for general usage. The reduced sets, constructed using different compression strategies, are supposed to reproduce as much as possible the information contained in the prior, but in terms of a substantially smaller number of error PDFs. The reduced Monte Carlo set, PDF4LHC15_mc, is constructed using the CMC-PDF method [187], and the two reduced Hessian sets, PDF4LHC15_100 and PDF4LHC15_30, are constructed using the MC2H [188] and META-PDF [186] techniques, respectively. The PDF4LHC15 combined sets are available from LHAPDF6 [190], and include additional PDF member sets to account for the uncertainty due to the value of the strong coupling constant, $\alpha_s(m_Z) = 0.1180 \pm 0.0015$.

The PDF4LHC 2015 report [181] presented general guidelines for the usage of the reduced sets, and some comparisons between them and the prior at the level of PDFs, parton luminosities, and LHC cross-sections, while referring to a repository of cross-sections on the PDF4LHC server [212] for a more detailed set of comparisons. It is the purpose of this contribution to make these comparisons more systematic and quantitative, in order to answer questions which have been frequently asked on the usage of the reduced sets. Specifically, we will perform a systematic study of the accuracy of the PDF4LHC15 reduced sets, by assessing the relative accuracy of uncertainties determined using each of them instead of the prior, for all hadronic observables included in the NNPDF3.0 PDF determination [184]. We will also compare the performance of the PDF4LHC15 reduced sets with that of the recently proposed SM-PDF sets [213]: specialized PDF sets which strive to minimize the number of PDF error sets which are needed for the description of a particular class of processes. We will then address the issue of the validity of the Gaussian approximation to PDF uncertainties by testing for gaussianity of the distribution of results obtained using the prior PDF set for a very wide variety of observables, and then assessing the performance and accuracy of both the Monte Carlo sets (which allows for non-Gaussian behaviour) and the Hessian compressed sets (which do not, by construction).

2.2 Validation of the PDF4LHC15 reduced PDF sets on a global dataset

We wish to compare the performance of the three reduced NLO sets, the two Hessian sets, PDF4LHC15_nlo_30 and PDF4LHC15_nlo_100, and the Monte Carlo set PDF4LHC15_nlo_mc, for all the hadronic cross-sections included in the NNPDF3.0 global analysis [184]. These cross-sections have computed at $\sqrt{s} = 7$ TeV using NLO theory with MCFM [214], NLOjet++ [204] and

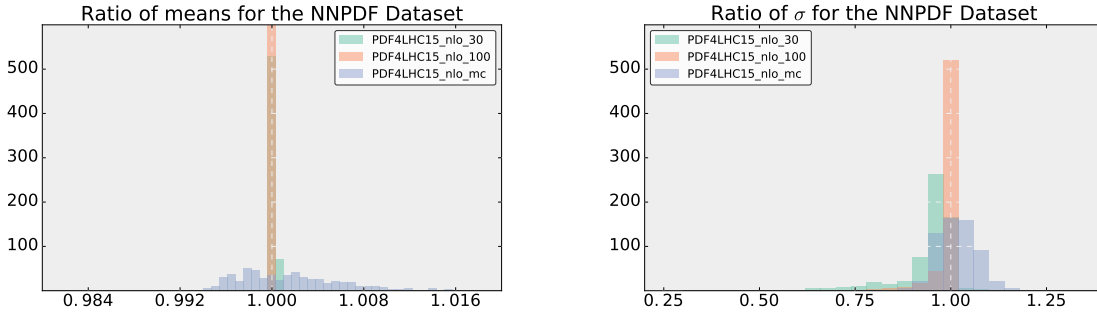


Fig. II.8: small Distribution of the ratio to the prior of means Eq. (II.1) (left) and of standard deviations Eq. (II.2) (right) computed for each of the $N_\sigma \simeq 600$ hadronic cross-sections included in the NNPDF3.0 global analysis, using each of the three reduced sets.

aMC@NLO [45, 201] interfaced to APPLgrid [3]. They include $N_\sigma \simeq 600$ independent observables for a variety of hadron collider processes such as electroweak gauge boson, jet production and top quark pair production, covering a wide region in the (x, Q) kinematical plane. In this calculation, the PDF4LHC15 combined sets are obtained from the LHAPDF6 interface.

In Fig. II.8 we show the distribution of the ratios

$$R_{\langle \sigma_i \rangle} \equiv \frac{\langle \sigma_i \rangle (\text{reduced})}{\langle \sigma_i \rangle (\text{prior})}, \quad i = 1 \dots, N_\sigma, \quad (\text{II.1})$$

$$R_{s_i} \equiv \frac{s_i(\text{reduced})}{s_i(\text{prior})}, \quad i = 1 \dots, N_\sigma. \quad (\text{II.2})$$

between respectively the means $\langle \sigma_i \rangle$, and the standard deviations s_i from each of the three reduced sets and the PDF4LHC15 prior, computed for all hadronic observables included in the NNPDF3.0 global analysis. For the Hessian sets the central value coincides with that of the prior, so the ratio of means is supposed to equal one by construction, with small deviations only due to rounding errors and interpolation in the construction of the LHAPDF grids, while for the MC set the mean is optimized by the CMC construction to fluctuate due to the finite size of the replica sample much less than expected on purely statistical grounds. Indeed, the histograms shows agreement of central values at the permille level. For standard deviations (i.e. PDF uncertainties) Fig. II.8 shows that using the PDF4LHC15_nlo_100 set they are reproduced typically with better than 5% accuracy. Differences are somewhat larger for the PDF4LHC15_nlo_mc and PDF4LHC15_nlo_30 sets.

In order to investigate the accuracy of PDF uncertainties in a more detailed quantitative way, we define the relative difference between the standard deviation, $s_i^{(\text{red})}$, of the cross-section σ_i computed with the reduced sets, and that of the prior, $s_i^{(\text{prior})}$:

$$\Delta_i \equiv \frac{|s_i^{(\text{prior})} - s_i^{(\text{red})}|}{s_i^{(\text{prior})}}, \quad i = 1, \dots, N_\sigma. \quad (\text{II.3})$$

In Figs. II.9 and II.10 the relative differences Δ_i are shown using NLO and NNLO PDFs for all hadronic observables which enter the NNPDF3.0 fit as a scatter plot in the (x, Q^2) kinematic plane, at the point corresponding to each observable using leading order kinematics [215], both for all observables, and for the 10% of observables exhibiting the largest relative differences. The x value corresponding to the the parton with highest x is always plotted, and for one-jet inclusive cross-sections, for which the x values of the two partons are not fixed even at leading

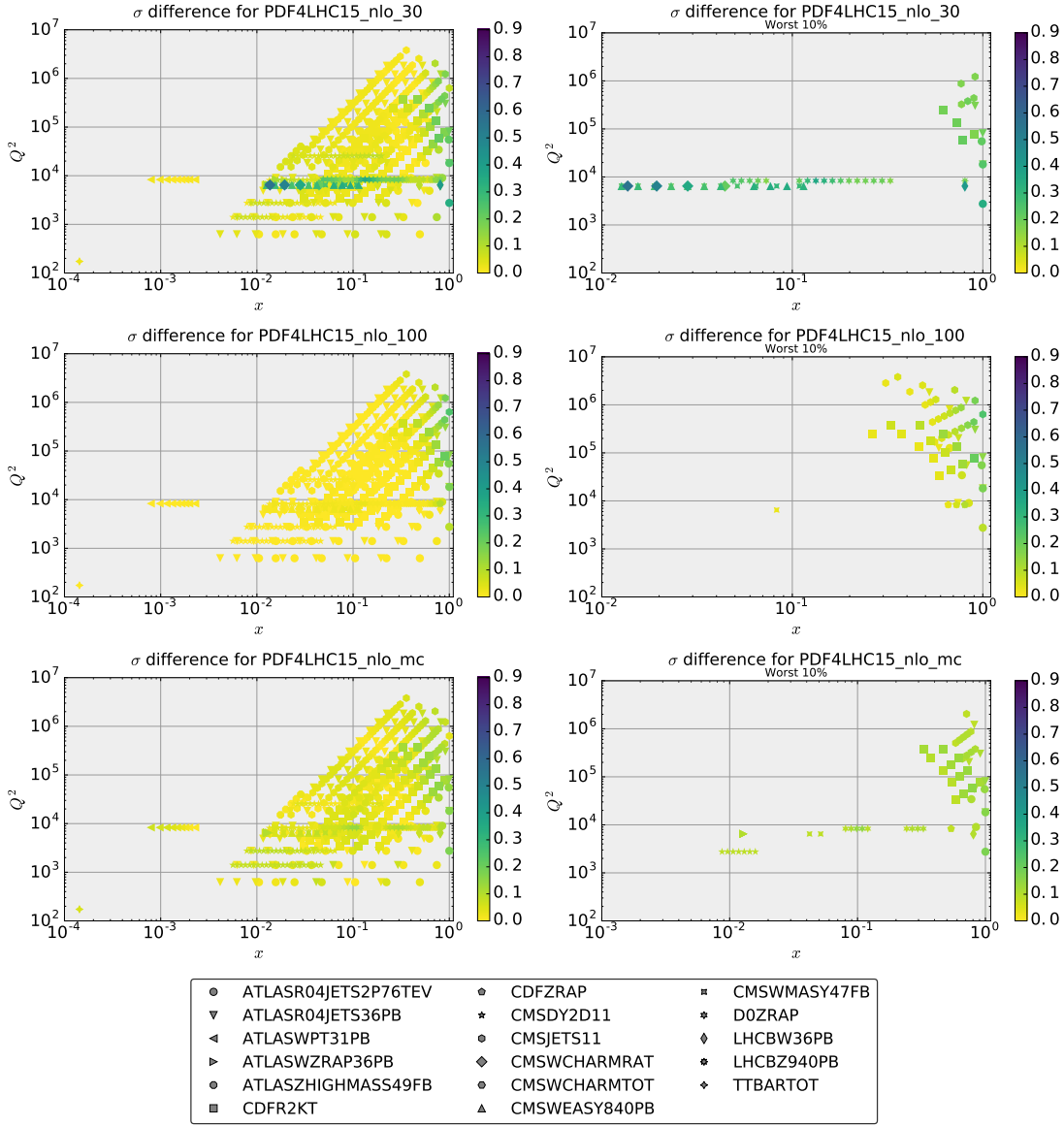


Fig. II.9: Relative difference Eq. (II.3), between the PDF uncertainties computed using the reduced set and the prior computed for all hadronic observables included in the NNPDF3.0 fit, shown as a scatter plot in the (x, Q^2) at the corresponding point, determined using leading-order kinematics. From top to bottom results for PDF4LHC_nlo_30, PDF4LHC_nlo_100 and PDF4LHC_nlo_mc are shown. In the left plots, all points are shown, in the right plots only the 10% of points with maximal deviation.

order, the largest accessible x which corresponds to the rapidity range of each data point is plotted. Of course, these x values should be only taken as indicative, and it should be born in mind that for most of the processes considered when one of the two partons involved is at large x , the other is at rather smaller x . In this comparison, NLO theory is used throughout.

From Figs. II.9 and II.10 we see that for PDF4LHC15_nlo_100 deviations are generally small, and concentrated in regions in which experimental information is scarce and PDF uncertainties are largest, such as the region of large x and large Q . For PDF4LHC15_nlo_mc and PDF4LHC15_nlo_30 the deviations are somewhat larger but still moderate in most cases, with a few outliers. No significant difference is observed between NLO and NNLO, consistent with the expectation that PDF uncertainties are driven by data, not by theory, and thus are very similar at NLO and NNLO.

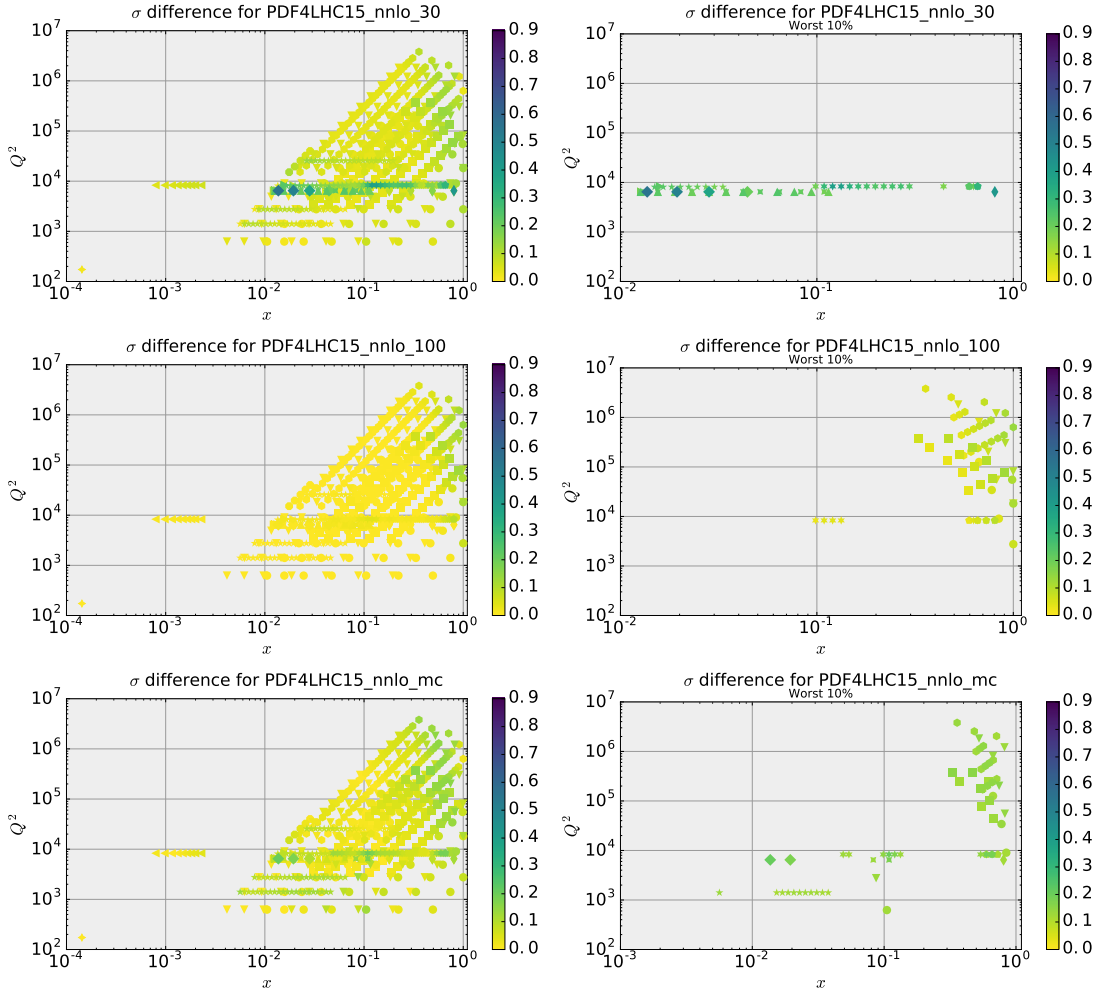


Fig. II.10: Same as Fig. II.9, but using the NNLO PDF sets.

This exercise shows that about $N_{\text{eig}} = 100$ Hessian eigenvectors are necessary for a good accuracy general-purpose PDF set. On the other hand, we have recently argued [213] that a much smaller set of Hessian eigenvectors is sufficient in order to accurately reproduce a subset of cross-sections, and presented a technique to construct such specialized minimal sets, dubbed SM-PDFs. In order to test and validate this claim, we have constructed two such SM-PDF sets, using the methodology of Ref. [213], and starting from the PDF4LHC15 NLO prior:

- **SM-PDF-ggh**: this SM-PDF set, with $N_{\text{eig}} = 4$ symmetric eigenvectors, reproduces the inclusive cross-section and the p_T and rapidity distributions of Higgs production in gluon fusion at $\sqrt{s} = 13$ TeV.
- **SM-PDF-Ladder**: this SM-PDF set, with has $N_{\text{eig}} = 17$ symmetric eigenvectors, reproduces all the observables listed in Table II.2, which include a wide variety of LHC processes at $\sqrt{s} = 13$ TeV.

The `APPLgrid` grids for the processes in Table II.2 have been computed using `aMC@NLO` interfaced to `aMCfast`.

In Fig. II.11 we show again the relative difference Δ_i Eq. (II.3), which was shown in Fig. II.9, but now comparing to the prior these two SM-PDF sets. In the case of the **SM-PDF-ggh** set, we find good agreement with the prior for all cross-sections on the region $x \simeq 0.01$ and $Q \simeq$

process	distribution	N_{bins}	range
$gg \rightarrow h$	$d\sigma/dp_t^h$	10	[0,200] GeV
	$d\sigma/dy^h$	10	[-2.5,2.5]
VBF hjj	$d\sigma/dp_t^h$	5	[0,200] GeV
	$d\sigma/dy^h$	5	[-2.5,2.5]
hW	$d\sigma/dp_t^h$	10	[0,200] GeV
	$d\sigma/dy^h$	10	[-2.5,2.5]
hZ	$d\sigma/dp_t^h$	10	[0,200] GeV
	$d\sigma/dy^h$	10	[-2.5,2.5]
$ht\bar{t}$	$d\sigma/dp_t^h$	10	[0,200] GeV
	$d\sigma/dy^h$	10	[-2.5,2.5]

process	distribution	N_{bins}	range
Z	$d\sigma/dp_t^{l-}$	10	[0,200] GeV
	$d\sigma/dy^{l-}$	10	[-2.5,2.5]
	$d\sigma/dp_t^{l+}$	10	[0,200] GeV
	$d\sigma/dy^{l+}$	10	[-2.5,2.5]
	$d\sigma/dp_t^Z$	10	[0,200] GeV
	$d\sigma/dy^Z$	5	[-4,4]
	$d\sigma/dm^{ll}$	10	[50,130] GeV
	$d\sigma/dp_t^{ll}$	10	[0,200] GeV

process	distribution	N_{bins}	range
$t\bar{t}$	$d\sigma/dp_t^t$	10	[40,400] GeV
	$d\sigma/dy^t$	10	[-2.5,2.5]
	$d\sigma/dp_t^{\bar{t}}$	10	[40,400] GeV
	$d\sigma/dy^{\bar{t}}$	10	[-2.5,2.5]
	$d\sigma/dm^{t\bar{t}}$	10	[300,1000]
	$d\sigma/dp_t^{t\bar{t}}$	10	[20,200]
	$d\sigma/dy^{t\bar{t}}$	12	[-3,3]

process	distribution	N_{bins}	range
W	$d\sigma/d\phi$	10	[0,200] GeV
	$d\sigma/dE_t^{\text{miss}}$	10	[-2.5,2.5]
	$d\sigma/dp_t^l$	10	[0,200] GeV
	$d\sigma/dy^l$	10	[-2.5,2.5]
	$d\sigma/dm_t$	10	[0,200] GeV
	$d\sigma/dp_T^W$	5	[-4,4]
	$d\sigma/y^W$	10	[50,130] GeV

Table II.2: LHC processes and the corresponding differential distributions used as input in the construction of the SM-PDF-Ladder set. In each case we indicate the range spanned by each distribution and the number of bins N_{bins} . All processes have been computed for $\sqrt{s} = 13$ TeV. Higgs bosons and top quarks are stable, while weak gauge bosons are assumed to decay leptonically. No acceptance cuts are imposed with the exception of the leptons from the gauge boson decay, for which we require $p_T^l \geq 10$ GeV and $|\eta^l| \leq 2.5$.

100 GeV, relevant for Higgs production in gluon fusion. On the other hand, as we move outside this region, the accuracy rapidly deteriorates. This exemplifies the virtues and limitations of the SM-PDF approach: a very small number of eigenvectors is sufficient to reproduce a reasonably small set of observables, but if one tries to stretch results to too many processes there is accuracy loss. The SM-PDF-Ladder set, on the other hand, exhibits a similar performance as the PDF4LHC15_nlo_30 set.

2.3 Non-Gaussianities in the PDF4LHC combination

As discussed in the PDF4LHC15 report [181], the Monte Carlo combination of individual PDF set in general is not Gaussian. This is both because one of the three sets entering the combination, NNPDF3.0, allows for non-Gaussian behaviour, and also because in general the combination of Gaussian sets is not necessarily Gaussian itself. We will now study in a more systematic way the degree of non-Gaussianity of the prior set, and specifically correlate the comparison of the reduced sets to the prior with the degree of non-Gaussianity of the prior. This has the threefold purpose of determining how much the accuracy of the Hessian set deteriorates in the presence of non-Gaussianities, of checking that the reduced MC set correctly reproduces the non-Gaussianity of the prior, and of providing guidance on when the MC set should be favored over the Hessian sets in order to reproduce the non-Gaussianity.

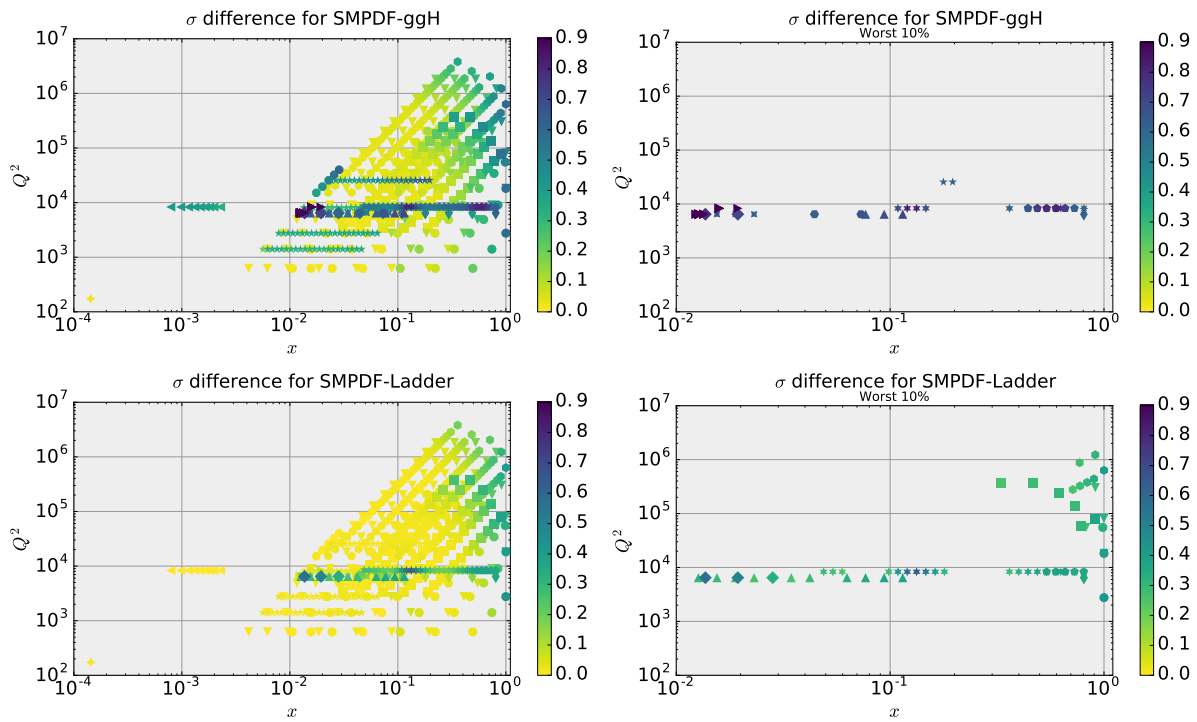


Fig. II.11: Same as Fig. II.9, this time for the two SM-PDF sets, SM-PDF-ggH (upper plots) and SM-PDF-Ladder (lower plots).

In order to study non-Gaussianity, we proceed in two steps. First, we turn the histogram, as obtained from a Monte Carlo representation, into a continuous probability distribution. Then, we compare this probability distribution to a Gaussian with the same mean and standard deviation. The first step is accomplished using the Kernel Density Estimate (KDE) method. The second, using the Kullback-Leibler (KL) divergence as a measure of the difference between two probability distributions (for a brief review of both methods see e.g. Ref. [216]).

The KDE method consists of constructing the probability distribution corresponding to a histogram as the average of kernel functions K centered at the data from which the histogram would be constructed. In our case, given $k = 1, \dots, N_{\text{rep}}$ replicas of the i -th cross-section $\{\sigma_i^{(k)}\}$, the probability distribution is

$$P(\sigma_i) = \frac{1}{N_{\text{rep}}} \sum_{k=1}^{N_{\text{rep}}} K\left(\sigma_i - \sigma_i^{(k)}\right), \quad i = 1, \dots, N_{\sigma}. \quad (\text{II.4})$$

We specifically choose

$$K(\sigma - \sigma_i) \equiv \frac{1}{h\sqrt{2\pi}} \exp\left(-\frac{(\sigma - \sigma_i)^2}{h}\right), \quad (\text{II.5})$$

where the parameter h , known as bandwidth, is

$$h = \hat{s}_i \left(\frac{4}{3N_{\text{rep}}}\right)^{\frac{1}{5}}, \quad (\text{II.6})$$

where \hat{s}_i is the standard deviation of the given sample of replicas. This choice is known as *Silverman rule*, and, if the underlying probability distribution is Gaussian, it minimizes the integral of the square difference between the ensuing distribution and this underlying Gaussian [217]. Once turned into continuous distributions via the KDE method, the prior and reduced Monte Carlo sets can be compared to each other, to a Gaussian, and to the Hessian sets. The comparison can be performed using the Kullback-Leibler (KL) divergence, which measures the information loss when using a probability distribution $Q(x)$ to approximate a prior $P(x)$, and is given by

$$D_{\text{KL}}^{(i)}(P|Q) = \int_{-\infty}^{+\infty} \left(P(x) \cdot \frac{\log P(x)}{\log Q(x)}\right) dx. \quad (\text{II.7})$$

As a first example, in Fig. II.12 we select a data bin in which the distribution of PDF replicas is clearly non-Gaussian, namely the most forward rapidity bin in the LHCb $Z \rightarrow \mu\mu$ 8 TeV measurement [218], and we compare the distribution obtained using the PDF4LHC15 prior to those found using the PDF4LHC15_nlo_mc and PDF4LHC15_nlo_100 reduced sets. The continuous distribution shown is obtained from the prior and reduced MC samples using the KDE method discussed above. For the PDF4LHC15_nlo_100 set the distribution shown is a Gaussian with with and central value using the standard procedure, based on linear error propagation, which is used to obtain predictions from Hessian sets: namely, the central set provides the mean, and the standard deviation is the sum in quadrature of the deviations obtained using each of the error sets.

The KL divergence between the prior and a Gaussian is equal to $D_{KL} = 0.153$, while the divergence between the prior and its reduced MC representation is $D_{KL} = 0.055$, and finally between the prior and Hessian set it is $D_{KL} = 0.19$. This shows that the reduced MC representation of the prior is much closer to it than the prior is to a Gaussian, while the Hessian representation differs from it even more. In order to facilitate the interpretation these values of the KL divergence, in Fig. II.13 we plot the value of the KL divergence between two Gaussian with different width, as a function of the ratio of their width: the plot shows that $D_{KL} \sim 0.05$

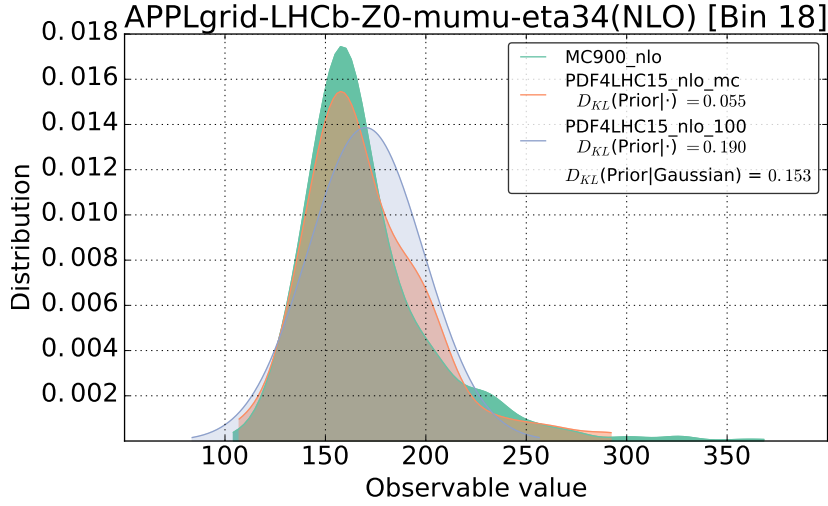


Fig. II.12: The probability distribution for the most forward bin in the LHCb $Z \rightarrow \mu\mu$ 8 TeV measurement obtained using the PDF4LHC15 prior and the PDF4LHC15_nlo_mc and PDF4LHC15_nlo_100 reduced sets. The value of the KL divergence D_{KL} Eq. (II.7) between the prior and a Gaussian, and between each of the two reduced sets and the prior for this distribution, are also given.

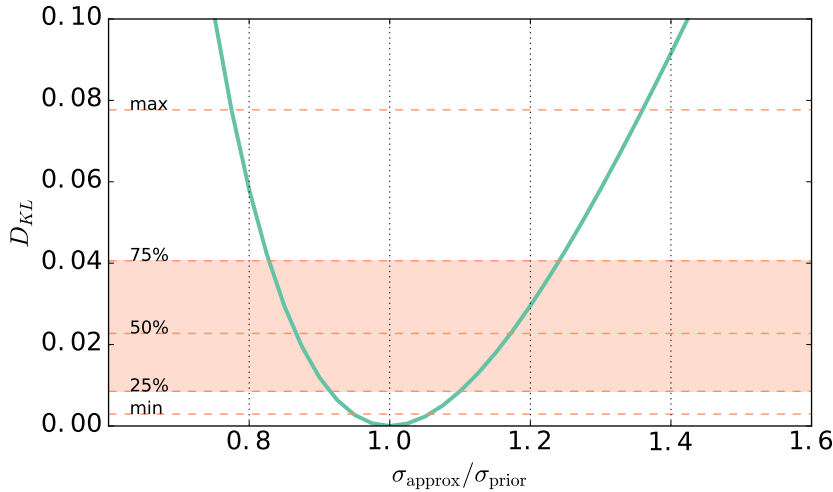


Fig. II.13: The KL divergence D_{KL} Eq. (II.7) between two Gaussian distributions with the same mean but different widths, as a function of the ratio of their standard deviations. We also show (horizontal lines) the highest value, lowest value, and the edges of the quartiles of the distribution of D_{KL} values between the prior and a Gaussian approximation to it, for all observables listed in Table II.2.

corresponds to distorting the width of a Gaussian by about 20%. In this figure we also show as horizontal lines the minimum and maximum values that we obtained, as well as the edges of the four quartiles of the distribution of results.

We have extended the type of comparisons shown in Fig. II.12 into a systematic study including all the cross-sections listed in Table II.2. As discussed in Sect. 2.2, this is a reasonably representative set of observables, since it is possible to construct a PDF set, the **SM-PDF-Ladder**, which is adequate to describe them and is also accurate to describe all the hadronic cross-section from the NNPDF3.0 fit (see Fig. II.11). Specifically, for each cross-section we have determined the probability distribution from the prior using the KDE method Eq. (II.4), and also a Gaussian

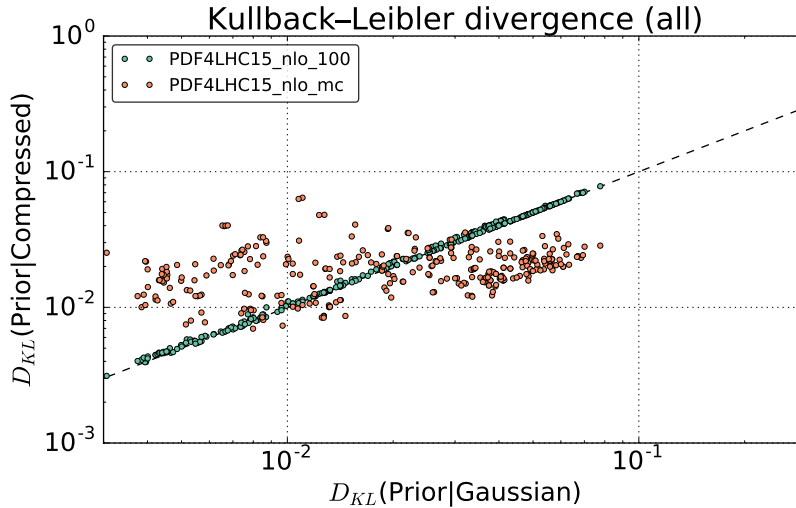


Fig. II.14: The KL divergence, Eq. (II.7) between the prior and each of its two reduced representations PDF4LHC15_nlo_prior (Monte Carlo) and PDF4LHC15_nlo_mc (Hessian) vs. the divergence between the prior and its Gaussian approximation, computed for all observables listed in Table II.2.

approximation to it, defined as the Gaussian with the same mean and standard deviation as the prior. We have computed the KL divergence between the prior distribution and this Gaussian approximation. It is clear that the vast majority of observables exhibits Gaussian behaviour to good approximation, with extreme cases such as shown in Fig. II.12 happening in a small fraction of the first quartile.

We have then computed for each observable the KL distance between the prior and the PDF4LHC15_nlo_mc and PDF4LHC15_nlo_100 combined sets. Results are collected in Fig. II.14 for all processes, while in Fig. II.15 we show a breakdown for the four classes of processes of Table II.2: Higgs, top, W and Z production. For each cross-section there are two points on the plot, one corresponding to PDF4LHC15_nlo_mc and the other to PDF4LHC15_nlo_100. The points are plotted with on the x axis the KL divergence between the prior and its gaussian approximation, and on the y axis the same quantity now evaluated between the prior and the compressed set. For the PDF4LHC15_nlo_100 all points cluster on the diagonal: this means that the reduced Hessian set only deviates from the prior inasmuch as the prior deviates from a Gaussian — only for a more extreme deviation from Gaussian such as shown in Fig. II.12 does the reduced Hessian deviate more. The PDF4LHC15_nlo_mc points instead approximately fall within a horizontal band: this means that the quality of the approximation to the prior of the reduced MC does not depend on the degree of non-Gaussianity of the prior itself.

Hence, the reduced MC set does reproduce well the non-Gaussian features of the prior, when they are present, and it will be advantageous to use it for points where the center of the band corresponding to PDF4LHC15_nlo_mc is below the diagonal. Figure II.15 shows that this happens for a significant fraction of the W and Z production cross-sections, but not for top and Higgs production. This is consistent with the expectation that non-Gaussian behaviour is mostly to be found in large x PDFs, which are probed by gauge boson production at high rapidity, but not by Higgs and top production which are mostly sensitive to the gluon PDF at medium and small x .

In order to further elucidate the dominant non-Gaussian features, we have performed a comparison of the mean and the standard deviation of each probability distribution with

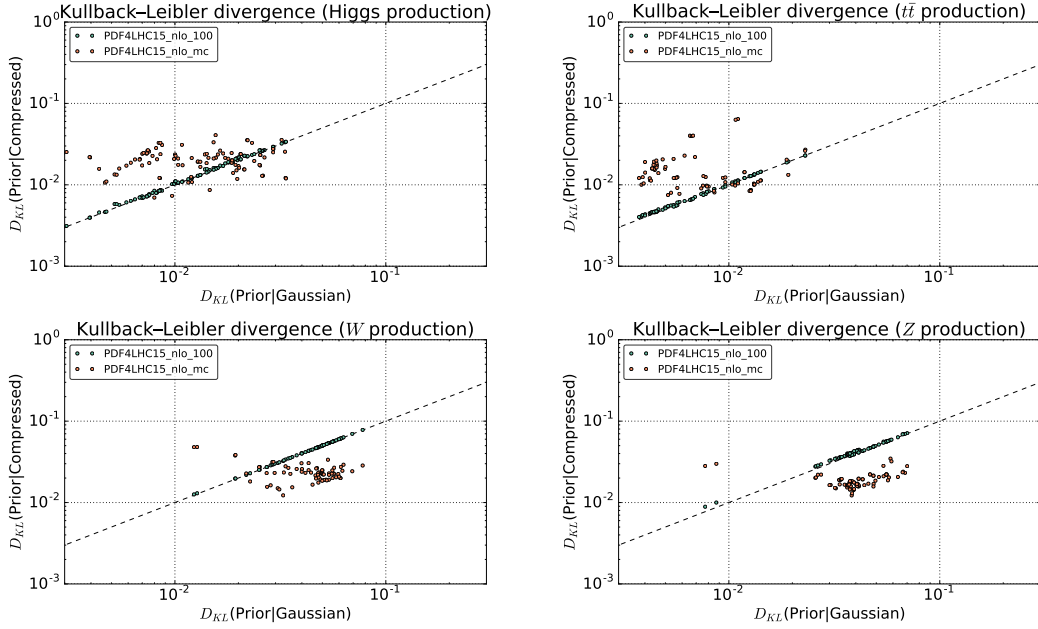


Fig. II.15: Same as Fig. II.14, now separating the contributions of the different classes of processes of Table II.2: Higgs production (top left), top quark pair production (top right), W production (bottom left) and Z production (bottom right).

respectively the median and the minimum 68% confidence interval R , defined as

$$R = \frac{1}{2} \min\{[x_{\min}, x_{\max}]; \int_{x_{\min}}^{x_{\max}} P(x) = 0.683\}. \quad (\text{II.8})$$

The deviation of the median from the mean is a measure of the asymmetry of the distribution, while the deviation R from the standard deviation is a measure of the presence of outliers. We then define two estimators, one for the deviation of the mean from the median and for the deviation of the standard deviation s from R :

$$\Delta_{\mu} = \frac{\text{median} - \mu}{s}, \quad (\text{II.9})$$

$$\Delta_s = \frac{R - s}{s}. \quad (\text{II.10})$$

Both Δ_{μ} and Δ_s would vanish for a Gaussian in the limit of infinite sample size.

In Fig. II.16 we represent these two estimators in a scatter plot, with Δ_{μ} and Δ_s respectively on the x and y axis, computed for all the cross-sections of Table II.2. In addition, we show a color code with the KL divergence between the prior and respectively its Gaussian approximation and its two reduced MC and Hessian representations. From this comparison, it is clear that the shift in the median is only weakly correlated to the degree of non-Gaussianity (top plot), and also weakly correlated to the shift in standard deviation, which instead is strongly correlated to non-Gaussianity.

In the presence of outliers, $R \leq s$, and indeed R is seen to be always negative. We expect asymmetries related to non-Gaussian behaviour to be due to the fact that in some cases PDFs are bounded from below by positivity, but not from above where outliers may be present. Indeed in the non-gaussian region Δ_{μ} tends to be negative, but with large fluctuations in its value. The same correlations are seen with the KL divergence between prior and Hessian, again

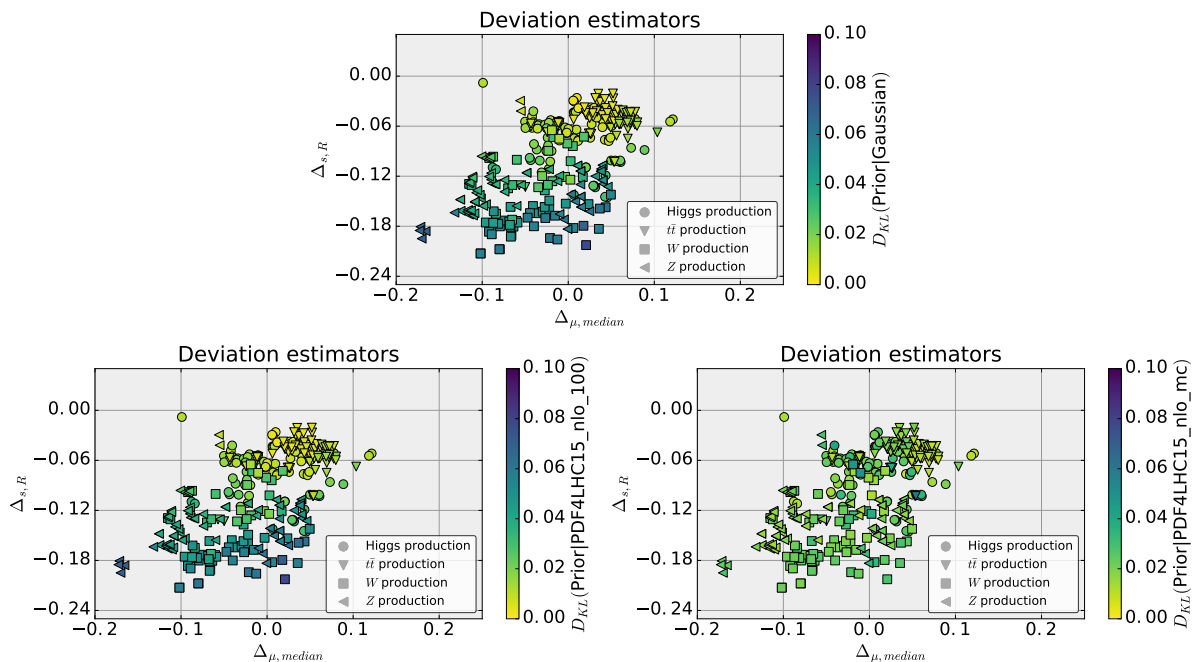


Fig. II.16: Scatter plot of indicators of deviation from gaussianity for all the cross-sections of Table II.2. For each observable, the shift between the median and the mean Eq. (II.9) is shown in the horizontal axis, while the shift between standard deviation and the 68% interval Eq. (II.10) is represented on the vertical axis. The color code shows the KL divergence between the prior and either a Gaussian (top) or the two reduced sets (bottom): Hessian (left) and MC (right).

showing that this is dominated by non-gaussian behaviour. On the other hand, no correlation is observed from the divergence between prior and reduced MC, consistent with our conclusion that the performance of the compressed MC set is independent of the degree of non-Gaussianity.

2.4 Summary and outlook

In this contribution we have performed a systematic comparison of the three reduced PDF4LHC15 PDF sets with the prior distribution they have been constructed from, with particular regard to non-Gaussian features, by comparing predictions for a wide variety of LHC cross-sections. Our general conclusion is that the three sets all perform as expected. We have specifically verified that the PDF4LHC15_n1o_100 Hessian set provides generally the most accurate representation of the mean and standard deviation of the probability distribution, while the PDF4LHC15_n1o_mc and PDF4LHC15_n1o_30 sets are less accurate though still quite good. We have also verified that specialized SM-PDF [213] sets can give an equally accurate representation, but with a smaller number of error-sets, at the price of not being suited for all possible processes, but with the option of combining them with other more accurate sets. We have then verified that in the presence of substantial deviations from Gaussianity, the PDF4LHC15_n1o_mc set is the most accurate. By providing a breakdown of our comparisons by type of process, we have verified that both deviations from Gaussianity and loss of accuracy of the smaller Hessian set are more marked in regions which are sensitive to poorly known PDFs, such as the anti-quarks at large x .

The results for the $N_\sigma \simeq 600$ cross-sections used for the calculations in Figs. II.9–II.11 are available from the link

<http://pcteserver.mi.infn.it/~nnpdf/PDF4LHC15/gall>

from where they can be accessed in HTML, CSV and ODS formats.

Acknowledgements

S. C. and S. F. are supported in part by an Italian PRIN2010 grant and by a European Investment Bank EIBURS grant. S. C. is supported by the HICCUP ERC Consolidator grant (614577). S. F. and Z. K. are supported by the Executive Research Agency (REA) of the European Commission under the Grant Agreement PITN-GA-2012-316704 (HiggsTools). J. R. is supported by an STFC Rutherford Fellowship and Grant ST/K005227/1 and ST/M003787/1 and by an European Research Council Starting Grant “*PDF4BSM*”.

Chapter III

SM Higgs working group report

A pillar of the physics program during the second Run of the LHC (Run II) is the detailed study of the Higgs boson. The Higgs discovery indeed represents the triumph of Run I, and now, in the second phase of exploration, the LHC will seek to constrain its properties in even greater detail. The Higgs boson is a special particle, both in the context of the Standard Model (SM) and in beyond the SM (BSM) scenarios. As the only fundamental scalar particle in the theory, the Higgs boson provides a unique window to extensions of the SM. For instance, the SM Higgs potential is uniquely determined once the Higgs mass is fixed. New scalars from BSM physics would alter the Higgs potential, resulting in modifications of the Higgs self couplings. Another possibility arises through direct modification of the Higgs coupling to other SM states. Theories such as Supersymmetry predict extended Higgs sectors which can naturally accommodate the SM-like properties of the Higgs boson observed in Run I.

Clearly, in order to constrain BSM scenarios, the Higgs boson must be studied in much greater detail than ever before. This section of the Les Houches proceedings details ongoing experimental and theoretical attempts to achieve this goal. The most obvious quantity for comparing data to the predictions of the SM is the inclusive Higgs cross section. Since the production of a Higgs boson through gluon fusion dominates this quantity, it is essential that accurate theoretical predictions are used to confront the LHC data, with a careful treatment of the uncertainties. This also allows for stringent constraints on Higgs coupling extractions. However, an additional advantage of the Run II program is the ability to study the Higgs in a differential setting. The limited amount of data in Run I resulted in rather crudely binned differential distributions for only the most accessible decay modes. The large data set anticipated in Run II, however, will allow for a much more varied set of observables and processes to be studied in ever greater detail. This will in turn allow us to constrain BSM contributions which may have a too small impact at the inclusive level, and thus may be only accessible through differential studies. At high values of the Higgs p_T the effective theory approach, which works extremely well for the inclusive cross section, begins to break down. If $p_T^H \sim m_t$ the top quark loop is resolved and theoretical predictions must be modified to take the loop structure into account. Addressing these various issues is the key goal of this report.

This report proceeds as follows, in section 1 recent calculations of the N3LO cross section are summarized, with particular emphasis on the recent attempts to estimate the remaining theoretical uncertainty. In section 2 the effects of the top quark mass on differential distributions are studied in the Sherpa framework. Section 3 presents a proposal to link the new experimental measurements of differential properties to theoretical predictions in the SM and beyond using simplified template cross sections.

1 Higgs boson production through gluon fusion at N3LO, and its theory uncertainty ¹

1.1 Motivation

Despite being a loop-induced process, Higgs production through gluon fusion is the dominant Higgs boson production mechanism at the LHC. The large leading-order cross-section, mainly due to the enhanced gluon luminosity at the LHC and the large value of the top Yukawa cou-

¹ A. Lazopoulos

pling, receives huge NLO corrections [219–227] the sheer magnitude of which have cast doubts on the perturbativity of this observable in the past. The NNLO corrections [92, 228, 229], computed in the heavy-top approximation, have been milder, and for the first time indications of reasonable perturbative behaviour appear. The N3LO corrections [2, 97–101, 105–111, 116–120], also computed in the heavy-top limit, have recently been completed, and show that we now have very good control at the per cent level of this all-important quantity. The uncertainty from pure initial state QCD effects is now at the 2 – 3% level. This brings to the foreground a number of other per-cent level uncertainties that have been hitherto ignored. An exhaustive phenomenological study of all these uncertainty sources is available in [126] where various approaches to assess these uncertainties to the best of our current knowledge is proposed. The purpose of this contribution is to clarify some salient features with respect to some of these estimates, which have been raised in discussions after the publication of [126]. The central value for the cross section, at 13TeV and values for input parameters as discussed in [126] is

$$\sigma = 48.58 \text{ pb}^{+2.22 \text{ pb} (+4.56\%)}_{-3.27 \text{ pb} (-6.72\%)} (\text{theory}) \pm 1.56 \text{ pb} (3.20\%) (\text{PDF} + \alpha_s). \quad (\text{III.1})$$

1.2 Uncertainty sources

There are currently three distinct sources of uncertainty on the best available estimate of the inclusive Higgs boson cross-section:

- The value of $a_s(m_Z)$: this is the largest source of uncertainty since the inclusive cross-section, starting at $\mathcal{O}(a_s^2)$ is very sensitive to the precise value of the strong coupling constant. To the best of the community’s current knowledge, a combination of various different extractions of α_s points to a value of $\alpha_s(m_Z) = 0.118 \pm 0.0015$, which in turn induces an uncertainty of 2.6% on the Higgs cross-section. We follow here the recommendation of the HXSWG [230], the PDF4LHC working group [181] and the upcoming PDG update. However it is worth pointing out there are approaches to α_s extraction that lead to values outside the quoted uncertainty range. If for example one adopts the best fit value for α_s from PDFs within the ABM collaboration, the Higgs cross section is 7.3% smaller, a value that is clearly outside the recommended uncertainty range. In conclusion, the total Higgs cross-section uncertainty strongly depends on the reliability of the uncertainty on α_s .
- The uncertainty due to the determination of PDFs from data: this is another intricate, global source of uncertainties. The recommendation of the PDF4LHC working group are followed here. This leads to an uncertainty of 1.86%. It is again worth noting that there are outlier PDFs, that have been excluded from the PDF4LHC combination for reasons explained in [181]. Moreover the PDF sets that are included in the combination currently agree remarkably well in the region of Bjorken x of the gluon density that affects the gluon fusion Higgs production, a situation that might change in the future, as more data are included in the individual fits.
- The total theory uncertainty due to missing higher order contributions to the total cross-section. These include uncertainties due to
 1. QCD corrections beyond N3LO in the heavy-top approximation
 2. EW corrections beyond $\mathcal{O}(a_s^2 a_{EW})$
 3. QCD corrections due to quark mass effects beyond $\mathcal{O}(a_s^3)$
 4. the truncation of the threshold expansion in which the N3LO result is derived
 5. missing higher orders in other processes used to extract the parton densities

6. parametric uncertainties of quark mass effects

The uncertainties for the Higgs cross-section through gluon fusion at the LHC with $\sqrt{S} = 13\text{TeV}$ are summarised in Table 1.2, from [126] that we reproduce here for convenience.

$\delta(\text{scale})$	$\delta(\text{trunc})$	$\delta(\text{PDF-TH})$	$\delta(\text{EW})$	$\delta(t, b, c)$	$\delta(1/m_t)$
+0.10 pb -1.15 pb	± 0.18 pb	± 0.56 pb	± 0.49 pb	± 0.40 pb	± 0.49 pb
+0.21% -2.37%	$\pm 0.37\%$	$\pm 1.16\%$	$\pm 1\%$	$\pm 0.83\%$	$\pm 1\%$

1.2.1 QCD corrections beyond N3LO in the EFT

The uncertainty from missing higher order corrections is estimated by a typical scale variation procedure, around a central scale of $m_H/2$. It is asymmetric and amounts to $+0.21\% - 2.37\%$. The asymmetry is typical of a scale variation that exhibits a maximum close to the central scale choice. In fact the only meaningful prediction from perturbation theory is the range in which the N3LO cross-section lies. The central value for the cross section is a reference point, but is not a priori preferred to any other value in the uncertainty interval. So if one prefers, one can symmetrise the uncertainty by moving the nominal central value at the middle of the uncertainty range.

A more interesting question is whether one should include resummation contributions beyond N3LO. The expected effect of resummation is to tame the renormalization scale dependence of the result and give an indication of the magnitude of missing higher order terms by probing its soft contributions. This relies on the validity of threshold dominance, as well as on cancelations due to sub-leading channels being negligible. It was shown in [126] that the effects of standard resummation approaches are actually negligible for the central choice of scale and within the range of the fixed order scale uncertainty.

Resummation results are defined up to formally sub-leading terms in the soft expansion. The numerical impact of such sub-leading terms can be non-negligible, however, especially when the contributions of the leading logarithmic terms is very small, as is the case in Higgs production at N3LO. Such is the situation when constants are exponentiated as in [231]. It is then impossible to maintain control, at the per cent level of precision, over the magnitude of the missing terms that might cancel, at N4LO, those that are arbitrarily included. We would therefore not consider such prescriptions as a probe of higher order corrections, and hence exclude them from the uncertainty estimate.

1.2.2 7-point scale variation

In [126], when estimating the scale uncertainty, we have kept the factorization and renormalization scales equal: the μ_F scale variation is remarkably flat, and it probes implicitly the parton density evolution, which, apart from being external to our computation, also interferes with our estimate of the PDF-TH uncertainty (due to the lack of N3LO parton densities).

However, one could attempt to probe the higher order missing terms using the 7-point scale variation method, where $\mu_R \neq \mu_F$ and $\mu_R, \mu_F \in [m_H/4, m_H]$ with $\mu_R/\mu_F \neq 4, 1/4$. In the present case this would fail to capture the maximum of the scale variation distribution, this maximum not being on one of the 7 points. We would need a scan over the μ_R - μ_F plane with the constraint $1/2 \leq \mu_R/\mu_F \leq 2$. Such a study will take place within the scope of the Higgs Cross Section Working Group's YR4, and we refer the reader to that document, currently in preparation, for further details.

1.3 Uncertainty due to light quark mass effects

The gluon fusion cross section with the full quark mass dependence is only known at NNLO for the top quark and at NLO for the light quarks. The effects due to the top quark mass are quite different than those of the light quarks: the former largely factorise (deviation from factorization of the leading order cross section are at the -0.6% level at NLO and at $+1\%$ level at NNLO), and, for all we know, we expect them to stay at the level of $+5 - 7\%$ at all orders in perturbation theory. For the light quark effects, including the top-light quark interference terms, on the contrary, there is no factorisation concept. The only available information, at LO and NLO, shows that the perturbative behaviour of the interference terms is actually quite good², while the perturbative behaviour of the light quarks contributions squared is quite bad. Fortunately, for the parameters of the Standard Model, the light quark contributions squared are negligible, while the interference terms dominate.

Note that we only want to assign an uncertainty to the missing interference effects at NNLO. It is therefore appropriate to look at the progression of the interference contributions per order, as opposed to the progression of the total interference contribution that includes a large LO correction. We assume that the missing NNLO light quark coefficient cannot induce a relative shift from the top only cross section that is larger than the one induced at NLO. We therefore estimate the uncertainty due to light quarks by

$$\delta(tbc)^{\overline{\text{MS}}} = \pm \left| \frac{\delta\sigma_{ex;t}^{NLO} - \delta\sigma_{ex;t+b+c}^{NLO}}{\delta\sigma_{ex;t}^{NLO}} \right| (R_{LO}\delta\sigma_{EFT}^{NNLO} + \delta_t\hat{\sigma}_{gg+qq,EFT}^{NNLO}) \simeq \pm 0.31 \text{ pb}, \quad (\text{III.2})$$

where

$$\delta\sigma_X^{NLO} \equiv \sigma_X^{NLO} - \sigma_X^{LO} \quad \text{and} \quad \delta\sigma_X^{NNLO} \equiv \sigma_X^{NNLO} - \sigma_X^{NLO}. \quad (\text{III.3})$$

In Table 7. of [126] the contributions due quark mass effects can be seen. The progression of the interference contributions per order is shown in the following table

$\overline{\text{MS}}$ scheme	LO	NLO	NNLO
$(\delta\sigma_{ex;t} - \delta\sigma_{ex;tbc})/\delta\sigma_{ex;t}$	0.073	0.032	X?

The assumption on which the uncertainty estimate is based is that X is not expected to be larger than the NLO value.

Also note that there is an apparent cancellation between top quark effects and light quark effects at LO and NLO. We remark that this cancellation is not particularly motivated theoretically and it is also a scheme dependent statement³ and a result of the particular ratios m_b/m_H and m_t/m_H in the Standard Model⁴. For the cancelation to persist at NNLO, the light quark interference terms themselves would have to induce a relative shift much larger than the one induced at NLO.

The same progression for the OS scheme is shown in the table below.

OS scheme	LO	NLO	NNLO
$(\delta\sigma_{ex;t} - \delta\sigma_{ex;tbc})/\delta\sigma_{ex;t}$	0.139	0.017	X?

²In the sense that interference terms do not follow the pattern of the EFT or the top only terms: they do not exhibit as large an NLO K-factor (1.56 vs 2.28)

³In the OS scheme at LO the light quark effects largely overwhelm the top mass corrections, while at NLO the level of the cancelation depends on whether the (sizeable) charm effects are included or not.

⁴For example the sign of the light quark effects would change for larger values of m_b .

The above estimated uncertainty accounts for the missing NNLO light quark effects but does not take into account the strong scheme dependence of the NLO cross section, as demonstrated in Table 8 of [126]. Although the OS scheme should be avoided in this context because of the bad convergence of the transition formula between the \overline{MS} and OS bottom and charm quark masses, it is nevertheless prudent to enlarge the uncertainty due to light quarks to account for the difference between the two schemes. We use the factor 1.3 which is the ratio of the OS to \overline{MS} contributions to the cross section from the top-bottom and top-charm interference terms, as explained in section 5 of [126].

1.3.1 Further theory uncertainties

Various other theory uncertainty sources have been considered. In particular uncertainties due to electroweak effects and the values of the quark masses as external parameters were discussed extensively in the Les Houches 2015 meeting. They were extensively studied in [126] where we refer the reader for further details.

1.4 Summary

With the completion of the computation of the Higgs cross section via gluon fusion at N3LO in the heavy-top effective theory, the scale uncertainty to the cross section has reached the 2 – 3% level. This is comparable with other theory uncertainty sources the impact of which can no longer be neglected. In [126] we have proposed a quantitative assessment of these uncertainties. In this contribution I attempted to clarify salient features with respect to some of these estimates, which have been raised in discussions after the publication of [126].

2 Heavy quark mass effects in gluon fusion Higgs production ⁵

2.1 Motivation

The Higgs Effective Field Theory (HEFT) framework for perturbative calculations of the gluon fusion Higgs production process is a well established tool that allows a significant reduction of complexity in higher-order QCD calculations. In this approach, the heavy-quark-loop induced Higgs-gluon coupling of the Standard Model (SM) is approximated by taking into account only the top quark contribution and by calculating production amplitudes in the limit of an infinite top quark mass. This is typically achieved by deriving the relevant amplitudes from the effective Lagrangian

$$\mathcal{L}_{\text{HEFT}} = -\frac{C_1}{4v} H G_{\mu\nu} G^{\mu\nu}, \quad (\text{III.4})$$

with the gluon field strength tensor $G_{\mu\nu}$, the Higgs field H , and a perturbatively calculable Wilson coefficient C_1 . This Lagrangian gives rise to tree-level couplings that replace the loop-induced SM couplings between gluons and the Higgs, effectively reducing the number of loops in any calculation by one.

When considering the total inclusive Higgs production cross section, finite top quark mass effects remain very moderate even at higher orders in QCD [232–237]. In the tail of the transverse momentum spectrum of the Higgs boson or for heavy Higgs boson (virtual) masses, however, the corrections can become very large, indicating a complete breakdown of the HEFT approximation [238, 239]. It has also been known for a long time that the bottom quark loops, which are entirely neglected in the HEFT, affect the spectrum in the small- p_{\perp}^H region [239, 240]. In this region, an all-order resummation of QCD corrections is required. Standard techniques need to

⁵ S. Kuttimalai, F. Krauss, P. Maierhöfer, M. Schönherr

be adapted in order to achieve this due to the bottom quark mass that introduces an additional scale into the calculation [241].

Several fully differential Monte Carlo codes have therefore been developed that take into account the full heavy quark mass dependence at NLO [227, 241–243]. NLO results for Higgs production in association with a jet are not available for finite heavy quark masses due to missing two-loop amplitudes for this process.

In this note, we present an approximate treatment of finite top mass effects at NLO based on one-loop amplitudes only. This allows us to calculate Higgs plus n -jet processes at NLO, while retaining finite top mass effects in an approximate way. Using this approximation, we employ multijet merging techniques [244] to merge higher-multiplicity NLO processes matched to a parton shower into one exclusive event sample, extending similar approaches [245–248] in terms of jet multiplicity and α_s accuracy. Based on leading order merging, we also suggest a method to address the issues raised in [241] concerning the inclusion of bottom quark contributions in the low- p_{\perp}^H region.

2.2 Implementation of Quark Mass Corrections

In order to take into account the full heavy quark mass effects in the hard scattering at leading order, we replace the approximate HEFT tree-level matrix elements provided by Sherpa’s matrix element generator Amegic++ [249] with the exact one-loop matrix elements provided by OpenLoops [40] in combination with Collier [250]. This allows the calculation of processes with up to three additional jets in the final state at leading order, with the full top and bottom quark mass dependency taken into account.

At NLO, the cross section for the production of a Higgs accompanied by a certain number $m - 1$ of jets receives contributions from two integrals of different phase space dimensionality.

$$\sigma = \int (B + V + I) d\phi_m + \int (R - S) d\phi_{m+1} \quad (\text{III.5})$$

The born term B and the real emission term R are present already at leading order for processes of the respective jet multiplicity and can be corrected as in the leading order calculation. $I(\phi_m)$ and $S(\phi_{m+1})$ denote the integrated and differential Catani-Seymour subtraction terms, respectively [90]. They render both integrals separately finite and are built up from leading-order m -particle matrix elements dressed with appropriate splitting kernels and can henceforth be corrected by using the full one-loop matrix elements instead of the tree-level HEFT approximation. Note that because we correct R and S with matrix elements of different final state multiplicity, the mere convergence of the corresponding integral already provides a crucial test for our implementation.

The IR-subtracted virtual correction V receives contributions from two-loop diagrams when taking into account the full heavy quark mass dependencies. Since these amplitudes are available only for the Higgs boson plus zero-jet final state, we employ an ad-hoc approximation that only involves one-loop matrix elements (even for the Higgs boson plus zero-jet final state). We assume a factorization of the α_s -corrections from the quark mass corrections and set

$$V = V_{\text{HEFT}} \frac{B}{B_{\text{HEFT}}} . \quad (\text{III.6})$$

In this approximation, we can straightforwardly apply finite top mass corrections in simulations employing CKKW multi jet merging at NLO in the MEPS@NLO scheme [244].

We expect the approximation (III.6) to give reasonable results only if the HEFT-approximation is valid. For any contribution involving the bottom Yukawa coupling y_b , it cannot be used due to the small bottom quark mass. This applies to the interference terms proportional

to $y_t y_b$ as well as the squared bottom contributions proportional to y_b^2 . We therefore calculate terms that involve y_b as separate processes at leading order. The NLO corrections to the total inclusive cross sections for the $y_t y_b$ contributions and the y_b^2 contributions are only of the order of 1% and 20%, respectively [251]. Furthermore, the y_b^2 contributions featuring the slightly larger NLO K-factor are significantly suppressed compared to the $y_t y_b$ terms [251]. We therefore consider a treatment at leading order sufficiently accurate. Any terms proportional to y_t^2 will however be calculated at NLO in the approximation described above.

2.3 Finite Top Mass Effects

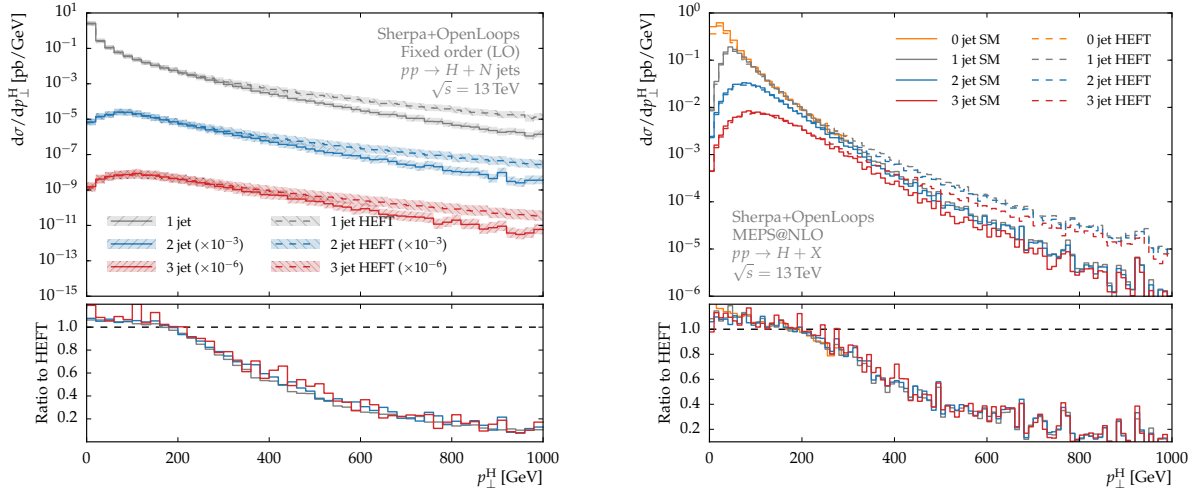
As mentioned in the introduction, the total inclusive cross section is only mildly affected by finite top mass effects. The low- p_\perp^H region, where the bulk of the cross section is located, can therefore be expected to exhibit only a moderate dependence on the top quark mass. In kinematic regimes where any invariant significantly exceeds m_t , however, we expect the HEFT approximation to break down. The p_\perp^H distributions in figure III.1a exemplify this picture. We show Higgs boson transverse momentum distributions for final states with one, two, and three jets calculated at fixed leading order. Jets are reconstructed using the anti- k_T algorithm with a radius parameter of $R = 0.4$ and a minimum jet p_\perp of 30 GeV except in the 1-jet case, where we apply only a small minimum p_\perp -cut of 1 GeV. The distributions for all three jet multiplicities exhibit a very similar pattern when comparing the full SM result to the HEFT approximation. Below $p_\perp^H \approx m_H$, we observe a flat excess of around 6% that recovers the correction factor to the total inclusive Higgs production cross section at leading order. The deviations become very large when p_\perp^H significantly exceeds m_t , as expected. The similarity of the top mass dependency of the p_\perp^H spectrum for all jet final multiplicities confirms similar findings for one- and two-jet configurations in [252].

In figure III.1b, we show analogous results obtained from the MEPS@NLO simulation. We included NLO matrix elements for the zero- and one-jet final states as well as leading order matrix elements for the two-jet final state in the merged setup and set Q_{cut} to 30 GeV. From the ratio plot in figure III.1b it is evident that in our approximation we recover the same suppression patterns as in the respective fixed leading order calculations for all jet multiplicities. This is a nontrivial observation as an m -jet configuration receives corrections from m -jet matrix elements as well as from $m + 1$ -jet matrix elements through the real emission corrections R in (III.6).

2.4 Nonzero Bottom Mass Effects

As pointed out already in [239, 240], the inclusion of the bottom quark in the loops affects the p_\perp^H distribution only at small values of p_\perp^H around m_b . In figure III.2 we reproduce these findings for the process $pp \rightarrow H + j$ at fixed order. In the p_\perp range around m_b where the bottom effects are large, a fixed order prediction is of course unreliable due to the large hierarchy of scales between m_H and the transverse momentum. This large separation of scales induces Sudakov logarithms $\ln(m_H/p_\perp)$ that spoil any fixed order expansion and require resummation.

It was argued in [241] that the resummation of these logarithms is complicated by the presence of the bottom quark in loops that couple to the Higgs boson. The bottom quark introduces m_b as an additional scale above which the matrix elements for additional QCD emissions do not factorize. Since a factorization is essential for the applicability of resummation techniques, it was proposed to use a separate resummation scale of the order of m_b for the contributions involving y_b , thereby restricting the range of transverse momenta where resummation is applied to the phase space where factorization is guaranteed. In this approach, the pure top quark contributions proportional to y_t^2 are treated as usual, with the resummation scale typically set to values of the order of m_H .



(a) LO fixed order calculation for up to three jets. The error bands indicate the uncertainties obtained from variations of the factorization and renormalization scales.

(b) Multijet merged calculation. We include the zero and one jet final states at NLO as well as the two jet final state at leading order. The individual curves show inclusive N -jet contributions.

Fig. III.1: The Higgs transverse momentum spectrum in gluon fusion. We show individual curves for the HEFT approximation (dashed) and the full SM result taking into account the mass dependence in the top quark loops. The lower panel shows the ratio of the SM results to the HEFT approximation.

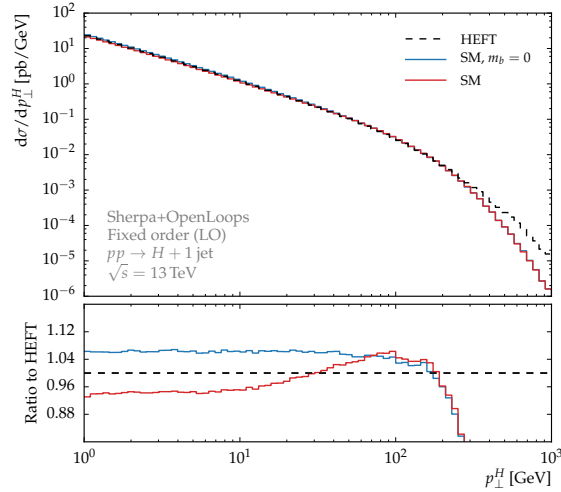
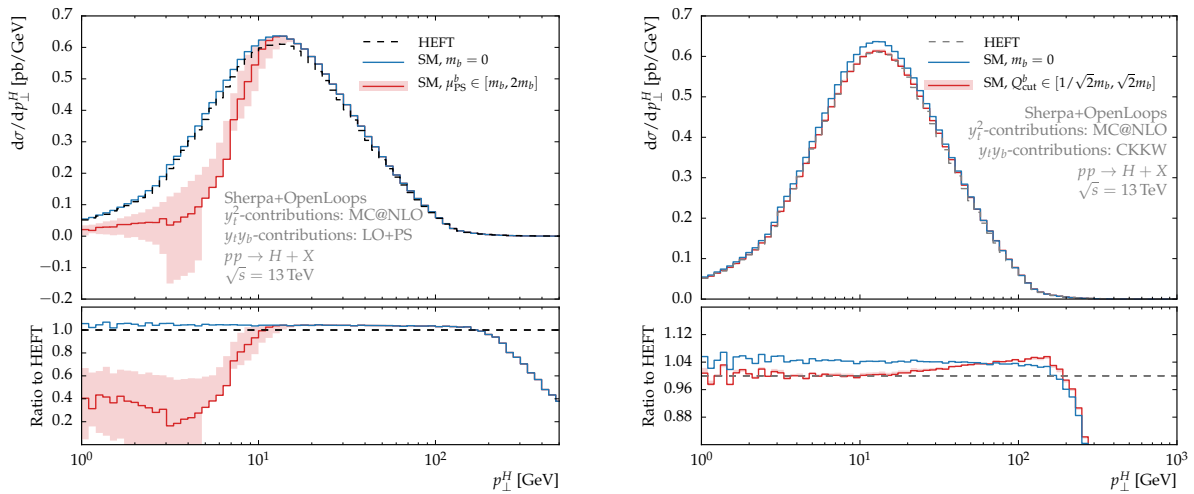


Fig. III.2: Bottom quark mass effects at fixed leading order. The minimum jet p_{\perp} is set to 1 GeV in order to display map out the low p_{\perp}^H region as well.

While reference [241] was concerned with analytical resummation techniques, similar approaches were studied in the context of NLO-matched parton shower Monte Carlos [251,253,254]. Our discussion will be restricted to the leading order as the approximation used for the NLO calculation of the top quark contributions (III.6) is invalid for the bottom quark terms. The equivalent of the resummation scale in analytic calculations is the parton shower starting scale μ_{PS} because it restricts parton shower emissions to the phase space below this scale and because this scale enters as the argument in the Sudakov form factors. Using separate parton shower starting scales for the top and the bottom contributions, respectively, requires to generate and shower them separately as well. A corresponding separation of terms in the one-loop matrix elements can be achieved with OpenLoops. By means of this separation into terms proportional to y_t^2 and the remainder, we can generate an MC@NLO sample for the top quark contributions while calculating the terms involving y_b at leading order. Figure III.3a shows the p_{\perp}^H spectrum obtained this way. We set the parton shower starting scale for the bottom contributions μ_{PS}^b to $\sqrt{2}m_b$ and show the error band obtained from variations of this scale by factors of $\sqrt{2}$ up and down. The parton shower starting scale for the top quark contributions will be $\mu_{\text{PS}}^t = m_H$ throughout. The suppression in the low p_{\perp} region below m_b is much more pronounced than in the fixed order result in figure III.2. This is because, pictorially speaking, without changing the cross section of the individual contributions, the parton shower simulation spreads the y_t^2 part over a much larger range, up to $\mathcal{O}(m_H)$, than for the negative $y_t y_b$, up to $\mathcal{O}(m_b)$ only. The spectrum in this region is therefore extremely sensitive to variations of μ_{PS}^b . When varying μ_{PS}^b to sufficiently low values, the differential cross section may even become negative, clearly an unphysical result. We stress, again, that this is not a physical effect but an artefact of the unitary nature of the parton shower. Setting the value of μ_{PS}^b to a small value, the entire leading order bottom cross section contributions will be distributed in a phase space with Higgs transverse momenta not significantly exceeding μ_{PS}^b . Since this cross section is negative, the spectrum must become negative at some point when lowering μ_{PS}^b .

We therefore suggest another approach at taking into account the bottom quark contributions in a parton shower Monte Carlo simulation. We account for the non-factorization of the real emission matrix elements above some scale Q_{cut}^b by correcting parton shower emissions harder than this scale with the appropriate fixed order matrix elements. This can be done consistently in the CKKW merging scheme [245,255]. Setting the merging scale for the bottom contributions Q_{cut}^b to m_b allows the correction of the parton shower in the regime where the matrix elements involving m_b do not factorize (without restricting all emissions to the phase space below). Above Q_{cut}^b , the fixed-order accuracy of the real emission matrix elements is thereby retained. Since any NLO prediction of the inclusive process describes the p_{\perp} spectrum only at leading order, our approach retains the same parametric fixed order accuracy when considering the p_{\perp}^H distribution. Beyond fixed order, the differences should be small since the NLO corrections to the inclusive cross section are at the percent level for the $y_t y_b$ interference terms.

In figure III.3b we show the bottom quark effects on the p_{\perp}^H spectrum in this approach. We include matrix elements with up to one jet in the merging such that a leading order accuracy in α_s is guaranteed for both the top and the bottom contributions to the p_{\perp}^H spectrum. This allows a comparison to figure III.2. The effects of the bottom quarks lead to a very similar suppression pattern over the entire displayed range of p_{\perp}^H . The large NLO K-factor that appears in the MC@NLO calculations of the top contributions however affects the overall relative normalization of the bottom quark effects. They are correspondingly smaller by roughly 50% in figure III.3b when compared to figure III.2. The sensitivity to variations of the scale in the calculation that effectively accounts for the presence of the bottom mass in the problem is drastically reduced. Figure III.3b includes an error band corresponding to variations of Q_{cut}^b by factors of $\sqrt{2}$ up and down. On the displayed scale, these variations are hardly visible.



(a) Bottom quark mass effects at LO+PS accuracy with a small parton shower starting scale of $\mu_{PS} = \sqrt{2}m_b$. The red error band shows variations of this scale by factors of $\sqrt{2}$ up and down.

(b) Bottom quark mass effects taken into account by means of CKKW merging with a small merging scale $Q_{cut}^b = m_b$. The red error band (hardly visible in this plot) shows variations of this scale by factors of $\sqrt{2}$ up and down.

Fig. III.3: The Higgs transverse momentum spectrum in gluon fusion. We show individual curves for the HEFT approximation (dashed) and the full SM result taking into account the mass dependency in the top quark loops neglecting (blue) and accounting for (red) bottom mass effects. Uncertainties in the treatment of finite bottom mass effects are shown as a red band.

2.5 Summary

We presented in this contribution an implementation of heavy quark mass effects in gluon fusion Higgs production that allows to systematically include finite top mass effects in an approximate way at NLO for in principle arbitrary jet multiplicities in the final state. Based on this approximation, we presented results for the Higgs boson transverse momentum distributions obtained from NLO matched and merged samples. When comparing the top quark mass dependence in one-, two-, and three-jet final states, we observed a universal suppression pattern that agrees very well with the corresponding leading order results.

Our treatment of contributions involving the bottom Yukawa coupling is based on m_b - and m_t -exact leading order matrix elements in combination with tree-level multijet merging techniques. We argued that this approximation is appropriate since it allows to retain leading order accuracy for the corresponding contributions in the p_T^H -spectrum and it also allows to account for the non-factorization of real emission amplitudes at scales above m_b .

3 Simplified template cross sections ⁶

3.1 Overview

After the successful Higgs coupling measurements during the LHC Run1, which had as their main results measured signal strength and multiplicative coupling modifiers, it is important to discuss in which way the experiments should present and perform Higgs coupling measurements in the future. Simplified template cross sections were developed to provide a natural way to evolve the signal strength measurements used during Run1. Compared to the Run1 measurements,

⁶ M. Duehrssen-Debling, P. Francavilla, F. J. Tackmann, K. Tackmann

the simplified template cross section framework allows one to reduce in a systematic fashion the theory dependences that must be directly folded into the measurements. This includes both the dependence on the theoretical uncertainties in the SM predictions as well as the dependence on the underlying physics model (i.e. the SM or BSM models). In addition, they provide more finely-grained measurements (and hence more information for theoretical interpretations), while at the same time allowing and benefitting from the global combination of the measurements in all decay channels.

The primary goals of the simplified template cross section framework are to maximize the sensitivity of the measurements while at the same time to minimize their theory dependence. This means in particular

- combination of all decay channels
- measurement of cross sections instead of signal strengths, in mutually exclusive regions of phase space
- cross sections are measured for specific production modes (with the SM production serving as kinematic template)
- measurements are performed in abstracted/simplified fiducial volumes
- allow the use of advanced analysis techniques such as event categorization, multivariate techniques, etc.

The measured exclusive regions of phase space, called “bins” for simplicity, are specific to the different production modes. Their definitions are motivated by

- minimizing the dependence on theoretical uncertainties that are directly folded into the measurements
- maximizing experimental sensitivity
- isolation of possible BSM effects
- minimizing the number of bins without loss of experimental sensitivity

These will of course be competing requirements in some cases and some compromise has to be achieved. The implementation of these basic design principles is discussed in more detail below.

A schematic overview of the simplified template cross section framework is shown in Fig. III.4. The experimental analyses shown on the left are very similar to the Run1 coupling measurements. For each decay channel, the events are categorized in the analyses, and there are several motivations for the precise form of the categorization. Typically, a subset of the experimental event categories is designed to enrich events of a given Higgs production mode, usually making use of specific event topologies. This is what eventually allows the splitting of the production modes in the global fit. Another subset of event categories is defined to increase the sensitivity of the analysis by splitting events according to their expected signal-to-background ratio and/or invariant-mass resolution. In other cases, the categories are motivated by the analysis itself, e.g. as a consequence of the backgrounds being estimated specifically for certain classes of events. While these are some of the primary motivations, in the future the details of the event categorization can also be optimized in order to give good sensitivity to the simplified template cross sections to be measured.

The center of Fig. III.4 shows a sketch of the simplified template cross sections, which are determined from the experimental categories by a global fit that combines all decay channels and

which represent the main results of the experimental measurements. They are cross sections per production mode, split into mutually exclusive kinematic bins for each of the main production modes. In addition, the different Higgs decays are treated by fitting the partial decay widths. Note that as usual, without additional assumptions on the total width, only ratios of partial widths and ratios of simplified template cross sections are experimentally accessible.

The measured simplified template cross sections together with the partial decay widths then serve as input for subsequent interpretations, as illustrated on the right of Fig. III.4. Such interpretations could for example be the determination of signal strength modifiers or coupling scale factors κ (providing compatibility with earlier results), EFT coefficients, tests of specific BSM models, and so forth. For this purpose, the experimental results should quote the full covariance among the different bins. By aiming to minimize the theory dependence that is folded into the first step of determining the simplified template cross sections from the event categories, this theory dependence is shifted into the second interpretation step, making the measurements more long-term useful. For example, the treatment of theoretical uncertainties can be decoupled from the measurements and can be dealt with at the interpretation stage. In this way, propagating improvements in theoretical predictions and their uncertainties into the measurements itself, which is a very time-consuming procedure and unlikely to be feasible for older datasets, becomes much less important. Propagating future theoretical advances into the interpretation, on the other hand, is generally much easier.

To increase the sensitivity to BSM effects, the simplified template cross sections can be interpreted together with e.g. POs in Higgs boson decays. To make this possible, the experimental and theoretical correlations between the simplified template cross sections and the decay POs would need to be evaluated and taken into account in the interpretation. This point will not be expanded on further in this section, but would be interesting to investigate in the future.

While the simplified template cross section bins have some similarity to a differential cross section measurement, they aim to combine the advantages of the signal strength measurements and fiducial and differential measurements. In particular, they are complementary to full-fledged fiducial and differential measurements and are neither designed nor meant to replace these. Fully fiducial differential measurements are of course essential but can only be carried out in a subset of decay channels in the foreseeable future. They are explicitly optimized for maximal theory independence. In practice, this means that in the measurements acceptance corrections are minimized, typically, simple selection cuts are used, and the measurements are unfolded to a fiducial volume that is as close as possible to the fiducial volume measured for a particular Higgs decay channel. In contrast, simplified template cross sections are optimized for sensitivity while reducing the dominant theory dependence in the measurement. In practice, this means that simplified fiducial volumes are used and larger acceptance corrections are allowed in order to maximally benefit from the use of event categories and multivariate techniques. They are also inclusive in the Higgs decay to allow for the combination of the different decay channels. The fiducial and differential measurements are designed to be agnostic to the production modes as much as possible. On the other hand, the separation into the production modes is an essential aspect of the simplified template cross sections to reduce their model dependence.

3.2 Guiding principles in the definition of simplified template cross section bins

As outlined above, several considerations have been taken into account in the definition of the simplified template cross section bins.

One important design goal is to reduce the dependence of the measurements on theoretical uncertainties in SM predictions. This has several aspects. First, this requires avoiding that the measurements have to extrapolate from a certain region in phase space to the full (or a larger region of) phase space whenever this extrapolation carries nontrivial or sizeable theoretical

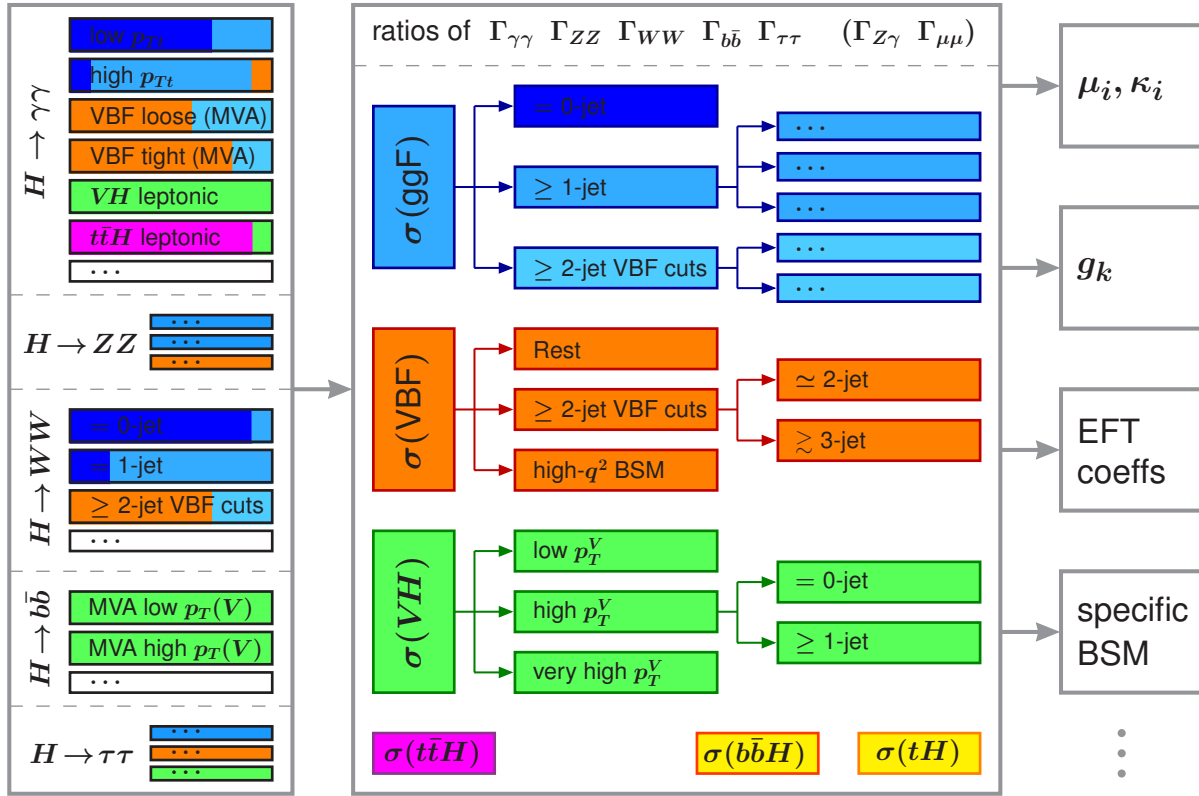


Fig. III.4: Schematic overview of the simplified template cross section framework.

uncertainties. An example is the case where an event category selects an exclusive region of phase space, such as an exclusive jet bin. In this case, the associated theoretical uncertainties can be largely avoided in the measurement by defining a corresponding truth jet bin. The definition of the bins is preferably in terms of quantities that are directly measured by the experiments to reduce the needed extrapolation.

There will of course always be residual theoretical uncertainties due to the experimental acceptances for each truth bin. Reducing the theory dependence thus also requires to avoid cases with large variation in the experimental acceptance within one truth bin, as this would introduce a direct dependence on the underlying theoretical distribution in the simulation. If this becomes an issue, the bin can be further split into two or more smaller bins, which reduces this dependence in the measurement and moves it to the interpretation step.

To maximize the experimental sensitivity, the analyses should continue to use event categories primarily optimized for sensitivity, while the definition of the truth bins should take into consideration the experimental requirements. However, in cases where multivariate analyses are used in the analyses, it has to be carefully checked and balanced against the requirement to not introduce theory dependence, e.g., by selecting specific regions of phase space.

Another design goal is to isolate regions of phase space, typically at large kinematic scales, where BSM effects could be potentially large and visible above the SM background. Explicitly separating these also reduces the dependence of the measurements on the assumed SM kinematic distribution.

In addition, the experimental sensitivity is maximized by allowing the combination of all decay channels, which requires the framework to be used by all analyses. To facilitate the experimental implementation, the bins should be mutually exclusive to avoid introducing

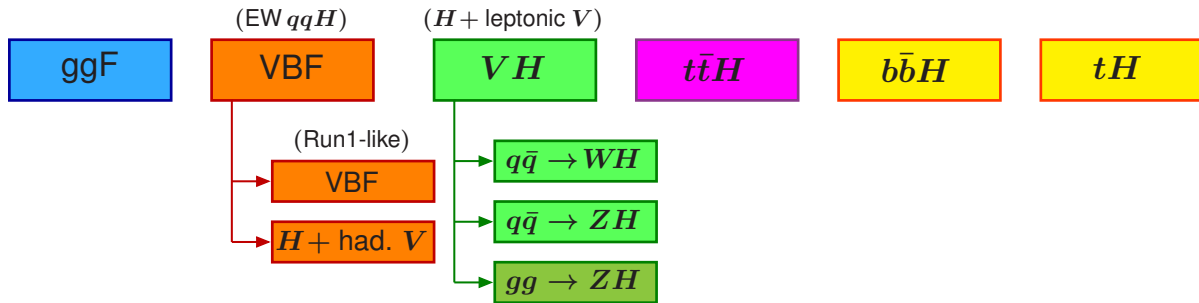


Fig. III.5: Stage 0 bins.

statistical correlations between different bins. In addition, the number of bins should be kept minimal to avoid technical complications in the individual analyses as well as the global fit, e.g. in the evaluation of the full covariance matrix. For example, each bin should typically have some sensitivity from at least one event category in order to avoid the need to statistically combine many poorly constrained or unconstrained measurements. On the other hand, in BSM sensitive bins experimental limits are already very useful for the theoretical interpretation.

3.2.1 Splitting of production modes

The definition of the production modes has some notable differences compared to Run1 to deal with the fact that the naive distinction between the $q\bar{q} \rightarrow VH$ and VBF processes, and similarly between $gg \rightarrow VH$ and gluon-fusion production, becomes ambiguous at higher order when the V decays hadronically. For this reason, the VH production mode is explicitly defined as Higgs production in association with a leptonically decaying V boson. The $q\bar{q} \rightarrow VH$ process with a hadronically decaying V boson is considered to be part of what is called “VBF production”, which is defined as electroweak qqH production. Similarly, the $gg \rightarrow ZH$ process with hadronically decaying Z boson is included in what is called “gluon-fusion production”.

In principle, also the separation of ZH production with a leptonic Z into $q\bar{q}$ or gg initial states becomes ambiguous at higher order. For present practical purposes, on the experimental side the split can be defined according to the separate MC samples for $q\bar{q} \rightarrow ZH$ and $gg \rightarrow ZH$ used in the analyses.

3.2.2 Staging

In practice, it will be impossible to define a set of bins that satisfies all of the above requirements for every analysis. Some analyses will only be able to constrain a subset of all bins or only constrain the sum of a set of bins. In addition, the number of bins that will be possible to measure increases with increasing amount of available data. For this reason, several stages with an increasing number of bins are defined. The evolution from one stage to the next can take place independently for each production mode.

3.2.2.1 Stage 0

Stage 0 is summarized in Fig. III.5 and corresponds most closely to the measurement of the production mode μ in Run1. At this stage, each main production mode has a single inclusive bin, with associated Higgs production separated into $q\bar{q} \rightarrow WH$, $q\bar{q} \rightarrow ZH$ and $gg \rightarrow ZH$ channels.

As discussed in Sec. 3.2.1, VBF production is defined as electroweak qqH production. For

better compatibility with Run1 measurements, the VBF production is split into a Run1-like VBF and Run1-like $V(\rightarrow jj)H$ bin, where the splitting is defined by the conventional Feynman diagrams included in the simulations. In practice, most decay channels will only provide a measurement for the Run1-like VBF bin.

3.2.2.2 Stage 1

Stage 1 defines a binning that is targeted to be used by all analyses on an intermediate time scale. In principle, all analyses should aim to eventually implement the full stage 1 binning. If necessary, intermediate stages to reach the full stage 1 binning can be implemented by a given analysis by merging bins that cannot be split. In this case, the analysis should ensure that the merged bins have similar acceptances, such that the individual bins can still be determined in an unbiased way in the global combination of all channels. In the diagrams presented below, the possibilities for merging bins are indicated by “(+)”.

3.2.2.3 Stage 2

Defining the stage 2 binning in full detail is very difficult before having gained experience with the practical implementation of the framework with the stage 1 binning. Therefore, instead of giving a detailed proposal for the stage 2 binning, we only give indications of interesting further separation of bins that should be considered for the stage 2 binning.

3.3 Definition of leptons and jets

The measured event categories in all decay channels are unfolded by the global fit to the simplified template cross sections bins. For this purpose, and for the comparison between the measured bins and theoretical predictions from either analytic calculations or MC simulations, the truth final state particles need to be defined unambiguously. The definition of the final state particles, leptons, jets, and in particular also the Higgs boson are explicitly kept simpler and more idealized than in the fiducial cross section measurements. Treating the Higgs boson as a final state particle is what allows the combination of the different decay channels.

For the moment, the definitions are adapted to the current scope of the measurements. Once a finer binning is introduced for $t\bar{t}H$ or processes such as VBF with the emission of a hard photon are added, some of the definitions below might have to be adapted or refined.

3.3.1 Higgs boson

The simplified template cross sections are defined for the production of an on-shell Higgs boson, and the unfolding should be done accordingly. A global cut on the Higgs rapidity at $|Y_H| < 2.5$ is included in all bins. As the current measurements have no sensitivity beyond this rapidity range, this part of phase space would only be extrapolated by the MC simulation. On the other hand, it is in principle possible to use forward electrons (up to $|\eta|$ of 4.9) in $H \rightarrow ZZ^* \rightarrow 4\ell$ and extend the accessible rapidity range. For this purpose, an additional otherwise inclusive bin for $|Y_H| > 2.5$ can be included.

3.3.2 Leptons

Electrons and muons from decays of signal vector bosons, e.g. from VH production, are defined as dressed, i.e. FSR photons should be added back to the electron or muon. τ leptons are defined from the sum of their decay products (for any τ decay mode). There should be no restriction on the transverse momentum or the rapidity of the leptons. That is, for a leptonically decaying vector boson the full decay phase space is included.

3.3.3 Jets

Truth jets are defined as anti- k_t jets with a jet radius of $R = 0.4$, and are built from all stable particles (exceptions are given below), including neutrinos, photons and leptons from hadron decays or produced in the shower. Stable particles here have the usual definition, having a lifetime greater than 10 ps, i.e. those particles that are passed to GEANT in the experimental simulation chain. All decay products from the Higgs boson decay are removed as they are accounted for by the truth Higgs boson. Similarly, leptons (as defined above) and neutrinos from decays of the signal V bosons are removed as they are treated separately, while decay products from hadronically decaying signal V bosons are included in the inputs to the truth jet building.

By default, truth jets are defined without restriction on their rapidity. A possible rapidity cut can be included in the bin definition. A common p_T threshold for jets should be used for all truth jets. A lower threshold would in principle have the advantage to split the events more evenly between the different jet bins. Experimentally, a higher threshold at 30 GeV is favored due to pile up and is therefore used for the jet definition to limit the amount of phase-space extrapolation in the measurements.

3.4 Bin definitions for the different production modes

In the following, the bin definitions for the different production modes in each stage are given. The bins are easily visualized through cut flow diagrams. In the diagrams, the bins on each branch are defined to be mutually exclusive and sum up to the preceding parent bin. For simplicity, sometimes not all cuts are explicitly written out in the diagrams, in which case the complete set of cuts are specified in the text. In case of ambiguities, a more specific bin is excluded from a more generic bin. As already mentioned, for the stage 1 binning the allowed possibilities for merging bins at intermediate stages are indicated by a “(+)” between two bins.

3.4.1 Bins for $gg \rightarrow H$ production

3.4.1.1 Stage 0

Inclusive gluon fusion cross section within $|Y_H| < 2.5$. Should the measurements start to have acceptance beyond 2.5, an additional bin for $|Y_H| > 2.5$ can be included.

3.4.1.2 Stage 1

Stage 1 refines the binning for $|Y_H| < 2.5$. The stage 1 binning is depicted in Fig. III.6 and summarized as follows:

- Split into jet bins: $N_j = 0$, $N_j = 1$, $N_j \geq 2$, $N_j \geq 2$ with VBF topology cuts (defined with the same cuts as the corresponding bin in VBF production). For the $N_j \geq 2$ with VBF topology cuts, $p_T^H < 200$ GeV is required, which gives priority to the $p_T^H > 200$ GeV bin for $N_j \geq 2$. Otherwise, the $N_j \geq 2$ with VBF topology cuts is excluded from the $N_j \geq 2$ bins. The jet bins are motivated by the use of jet bins in the experimental analyses. Introducing them also for the simplified template cross sections avoids folding the associated theoretical uncertainties into the measurement. The separation of the $N_j \geq 2$ with VBF topology cuts is motivated by the wish to separately measure the gluon fusion contamination in the VBF selection. If the fit has no sensitivity to determine the gluon fusion and the VBF contributions with this topology, the sum of the two contributions can be quoted as result.
- The $N_j \geq 2$ with VBF topology bin is split further into an exclusive 2-jet-like and inclusive 3-jet-like bin. The split is implemented by a cut on $p_T^{Hjj} = |\vec{p}_T^H + \vec{p}_T^{j1} + \vec{p}_T^{j2}|$ at 25 GeV. See the corresponding discussion for VBF for more details. This split is explicitly included here since it induces nontrivial theory uncertainties in the gluon-fusion contribution.

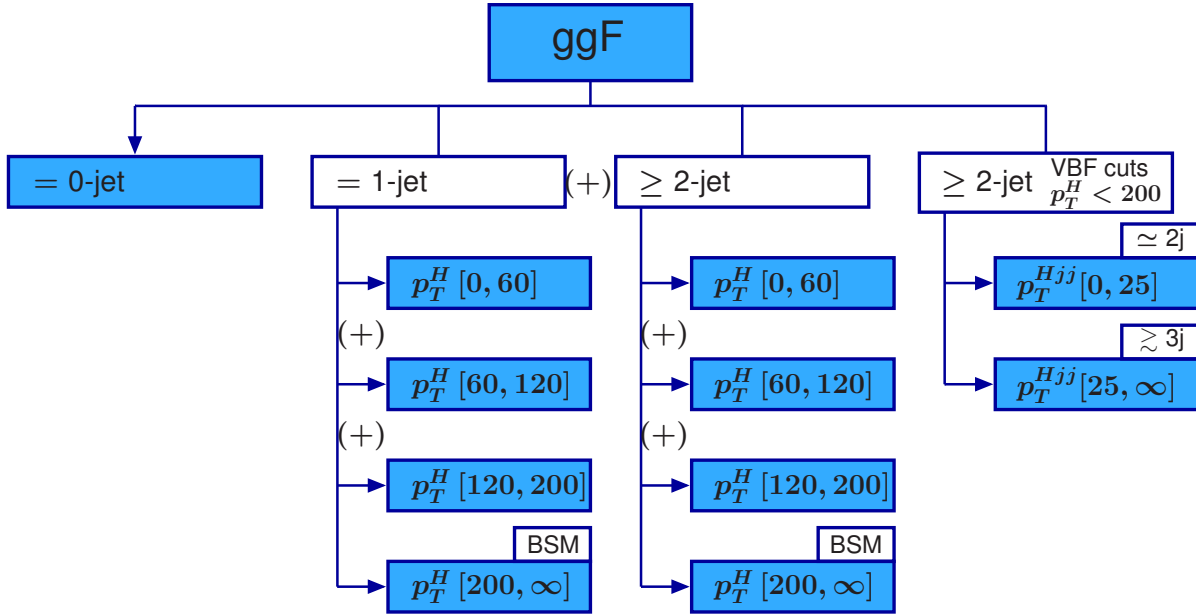


Fig. III.6: Stage 1 binning for gluon fusion production.

- The $N_j = 1$ and $N_j \geq 2$ bins are further split into p_T^H bins.
 - $0 \text{ GeV} < p_T^H < 60 \text{ GeV}$: The boson channels have most sensitivity in the low p_T^H region. The upper cut is chosen as low as possible to give a more even split of events but at the same time high enough that no resummation effects are expected. The cut should also be sufficiently high that the jet p_T cut introduces a negligible bias.
 - $60 \text{ GeV} < p_T^H < 120 \text{ GeV}$: This is the resulting intermediate bin between the low and high p_T^H regions. The lower cut here is high enough that this bin can be safely treated as a hard $H + j$ system in the theoretical description.
 - $120 \text{ GeV} < p_T^H < 200 \text{ GeV}$: The boosted selection in $H \rightarrow \tau\tau$ contributes to the high p_T^H region. Defining a separate bin avoids large extrapolations for the $H \rightarrow \tau\tau$ contribution. For $N_j = 2$, this bin likely provides a substantial part of the gluon-fusion contribution in the hadronic VH selection.
 - $p_T^H > 200 \text{ GeV}$: Beyond the top-quark mass, the top-quark loop gets resolved and top-quark mass effects become relevant. Splitting off the high- p_T^H region ensures the usability of the heavy-top expansion for the lower- p_T^H bins. At the same time, the high p_T^H bin in principle offers the possibility to distinguish a pointlike ggH vertex induced by heavier BSM particles in the loop from the resolved top-quark loop.

At intermediate stages, all lower three p_T^H bins, or any two adjacent bins, can be merged. Alternatively or in addition the $N_j = 1$ and $N_j \geq 2$ bins can be merged by individual analyses as needed, and potentially also when the combination is performed at an intermediate stage.

3.4.1.3 Stage 2

In stage 2, the high p_T^H bin should be split further, in particular if evidence for new heavy particles arises. In addition, the low p_T^H region can be split further to reduce any theory dependence there. If desired by the analyses, another possible option is to further split the $N_j \geq 2$ bin into $N_j = 2$ and $N_j \geq 3$.

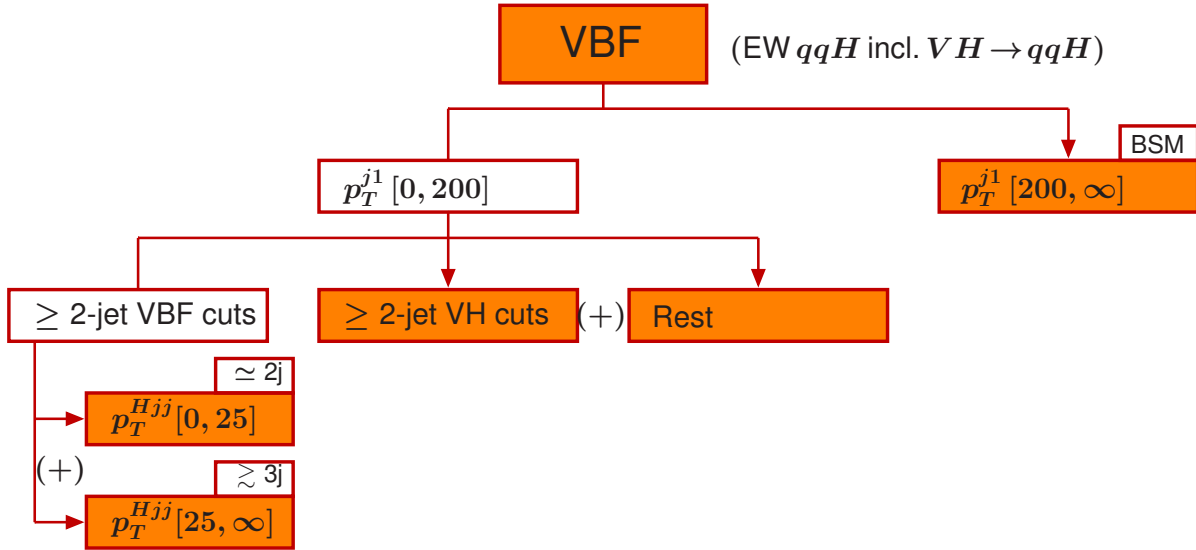


Fig. III.7: Stage 1 binning for vector boson fusion production.

3.4.2 Bins for VBF production

At higher order, VBF production and VH production with hadronically decaying V become ambiguous. Hence, what we refer to as VBF in this section, is defined as an electroweak $qq'H$ production, which includes both VBF and VH with hadronic V decays.

3.4.2.1 Stage 0

Inclusive vector boson fusion cross section within $|Y_H| < 2.5$. Should the measurements start to have acceptance beyond 2.5, an additional bin for $|Y_H| > 2.5$ can be included.

3.4.2.2 Stage 1

Stage 1 refines the binning for $|Y_H| < 2.5$. The stage 1 binning is depicted in Fig. III.7 and summarized as follows:

- VBF events are split by p_T^{j1} , the transverse momentum of the highest- p_T jet. The lower p_T^{j1} region is expected to be dominated by SM-like events, while the high- p_T^{j1} region is sensitive to potential BSM contributions, including events with typical VBF topology as well as boosted $V(\rightarrow jj)H$ events where the V is reconstructed as one jet. The suggested cut is at 200 GeV, to keep the fraction of SM events in the BSM bin small. Note that events with $N_j = 0$, corresponding to $p_T^{j1} < 30$ GeV, is included in the $p_T^{j1} < 200$ GeV bin.
- The $p_T^{j1} < 200$ GeV bin is split further:
 - Typical VBF topology: The adopted VBF topology cuts are $m_{jj} > 400$ GeV, $\Delta\eta_{jj} > 2.8$ (and without any additional rapidity cuts on the signal jets). This should provide a good intermediate compromise among the various VBF selection cuts employed by different channels.
 - * The bin with typical VBF topology is split into an exclusive 2-jet-like and inclusive 3-jet-like bin using a cut on p_T^{Hjj} at 25 GeV, where the cut value is a compromise between providing a good separation of gluon fusion and VBF and the selections used in the measurements. p_T^{Hjj} as quantity to define this split is

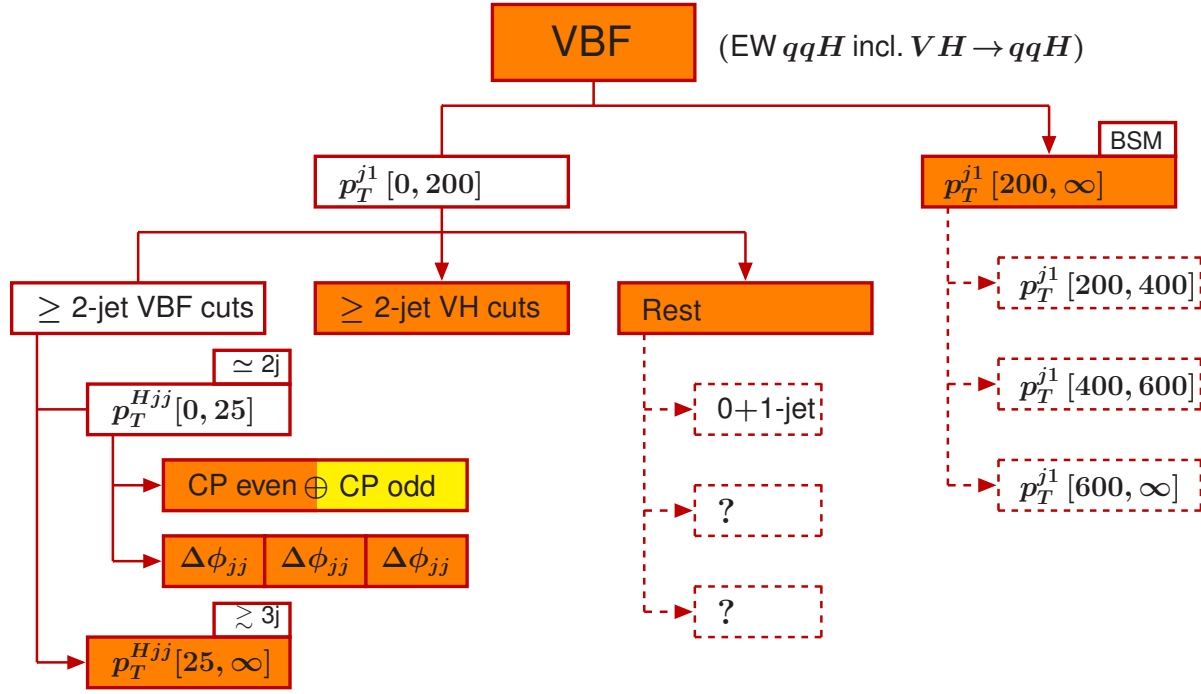


Fig. III.8: Possible stage 2 binning for vector boson fusion production.

chosen as a compromise between the different kinematic variables used by different channels to enrich VBF production. (In particular the kinematic variables $\Delta\phi_{H-jj}$ and p_T^{j3} are both correlated with p_T^{Hjj}).

- Typical $V(\rightarrow jj)H$ topology: events with at least two jets and $60 \text{ GeV} < m_{jj} < 120 \text{ GeV}$.
- Rest: all remaining events, including events with zero or one jet. The “rest” bin can be sensitive to certain BSM contributions that do not follow the typical SM VBF signature with two forward jets.

3.4.2.3 Stage 2

More splits are introduced at stage 2 as illustrated in Fig. III.8. While the details require more discussion and cannot be finalized at the present, this could include

- The high- p_T^{j1} bin can be split further by separating out very high- p_T^{j1} events for example with additional cuts at 400 GeV and 600 GeV.
- The “rest” bin can be split further, e.g., by explicitly separating out a looser VBF selection, and/or by separating out events with zero or one jets.
- The $N_j \simeq 2$ VBF topology bin can be split further to gain sensitivity to CP odd contributions, e.g. by splitting it into subbins of $\Delta\phi_{jj}$ or alternatively by measuring a continuous parameter.

3.4.3 Bins for VH production

In this section, VH is defined as Higgs production in association with a leptonically decaying V boson.

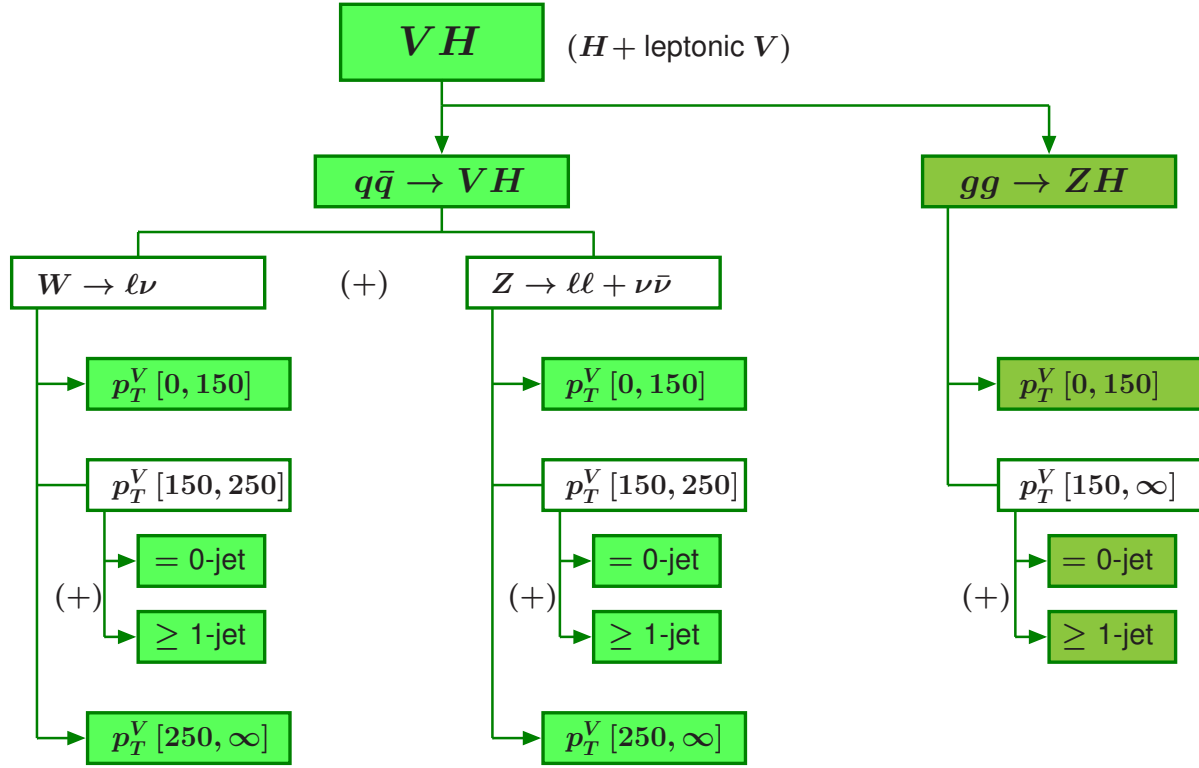


Fig. III.9: Stage 1 binning for associated production with vector bosons.

Note that $q\bar{q} \rightarrow VH$ production with a hadronically decaying V boson is considered part of VBF production. Similarly, $gg \rightarrow VH$ production with hadronically decaying V boson is considered part of gluon fusion production.

3.4.3.1 Stage 0

Inclusive associated production with vector bosons cross section within $|Y_H| < 2.5$. Should the measurements start to have acceptance beyond 2.5, an additional bin for $|Y_H| > 2.5$ can be included.

3.4.3.2 Stage 1

Stage 1 refines the binning for $|Y_H| < 2.5$. The stage 1 binning is depicted in Fig. III.9 and summarized as follows:

- VH production is first split into the production via a $q\bar{q}$ or gg initial state. This split becomes ambiguous at higher order. For practical purposes, on the experimental side the split can be defined according to the MC samples used in the analyses, which are split by $q\bar{q}$ and gg .
- The production via $q\bar{q} \rightarrow VH$ is split according to the vector boson: $W \rightarrow \ell\nu$ and $Z \rightarrow \ell\ell + \nu\bar{\nu}$.
- $W \rightarrow \ell\nu$ and $Z \rightarrow \ell\ell + \nu\bar{\nu}$ are split further into bins of p_T^V , aligned with the quantity used in the $H \rightarrow b\bar{b}$ analysis, which is one of the main contributors to the VH bins.
 - * $p_T^V < 150$ GeV receives contributions from the bosonic decay channels and from $H \rightarrow b\bar{b}$ with $W \rightarrow \ell\nu$ and $Z \rightarrow \ell\ell$, which do not rely on E_T^{miss} triggers.

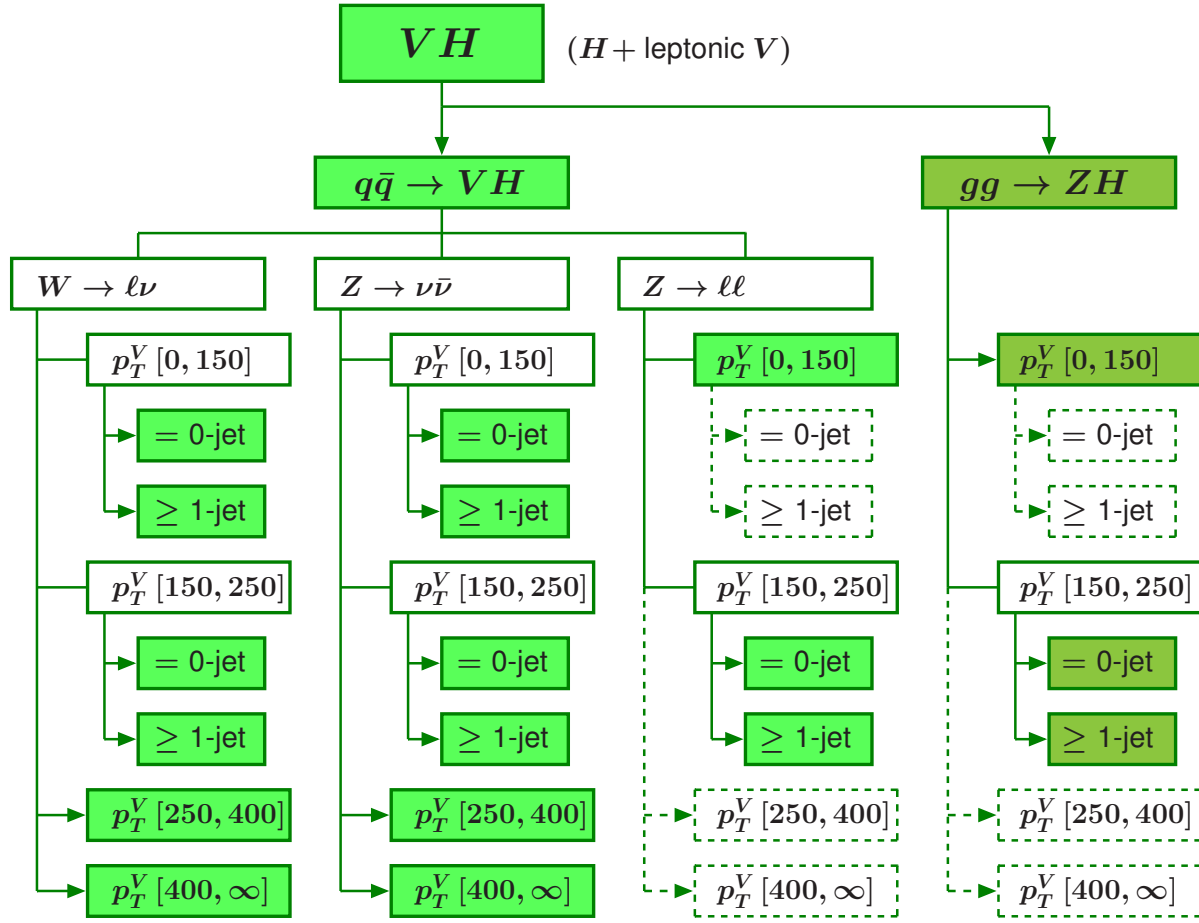


Fig. III.10: Possible Stage 2 binning for associated production with vector bosons.

- * $150 \text{ GeV} < p_T^V < 250 \text{ GeV}$ receives contributions from $H \rightarrow b\bar{b}$ with $Z \rightarrow \nu\bar{\nu}$ due to the high threshold of the E_T^{miss} trigger, as well as from $H \rightarrow b\bar{b}$ with $W \rightarrow \ell\nu$ and $Z \rightarrow \ell\ell$.
 - This bin is split further into a $N_j = 0$ and a $N_j \geq 1$ bin, reflecting the different experimental sensitivity and to avoid the corresponding theory dependence.
- * $p_T^V > 250 \text{ GeV}$ is sensitive to BSM contributions.
- The production via $gg \rightarrow ZH$ is split in analogy to production from the $q\bar{q}$ initial state, apart from the $p_T^V > 250 \text{ GeV}$ bin, which is not split out.

3.4.3.3 Stage 2

More splits are introduced at stage 2 as illustrated in Fig. III.8. While the details need more discussion, this could include

- Split of the $Z \rightarrow \ell\ell + \nu\bar{\nu}$ into $Z \rightarrow \ell\ell$ and $Z \rightarrow \nu\bar{\nu}$.
- Split of the $p_T^V < 150 \text{ GeV}$ into a $N_j = 0$ and a $N_j \geq 1$ bin, except maybe for the $Z \rightarrow \ell\ell$ channel, which will suffer from the low $Z \rightarrow \ell\ell$ branching ratio.
- Split of the $p_T^V > 250 \text{ GeV}$ bin into $p_T^V < 400 \text{ GeV}$ and $p_T^V > 400 \text{ GeV}$, to increase the sensitivity to BSM contributions with very high p_T^V , potentially apart from the $Z \rightarrow \ell\ell$.

- Potentially analogous splits for $gg \rightarrow ZH$ production.

3.4.4 Treatment of $t\bar{t}H$ production

3.4.4.1 Stage 0

Inclusive $t\bar{t}H$ production with $|Y_H| < 2.5$. Should the measurements start to have acceptance beyond 2.5, an additional bin for $|Y_H| > 2.5$ can be included.

3.4.4.2 Stage 1

Currently no additional splits beyond stage 0 are foreseen. One option might be to separate different top decay channels for $|Y_H| < 2.5$.

3.4.4.3 Stage 2

In the long term it could be useful to split into bins with 0 and ≥ 1 additional jets or one or more bins tailored for BSM sensitivity.

3.4.5 Treatment of $b\bar{b}H$ and tH production

In the foreseeable future, there will only be one inclusive bin for $b\bar{b}H$ production and only one inclusive bin for tH production for $|Y_H| < 2.5$. Should the measurements start to have acceptance beyond 2.5, an additional bin for $|Y_H| > 2.5$ can be included.

3.5 Practical considerations

To facilitate the combination of the results from ATLAS and CMS, the same bin definitions need to be used by the two collaborations. As for the Run1 Higgs coupling measurements, a combination of results from ATLAS and CMS will also require that the two collaborations estimate systematic and residual theoretical uncertainties in a compatible way. This might be facilitated for example by the use of the same Monte Carlo generators in the measurements.

After first experience with the measurement and interpretation has been collected, the stage 1 bin definitions should be reviewed. This should in particular include the definition of the VBF topology cuts as well as the p_T^{Hjj} split. In cases where the bin definitions are clearly inadequate, they should be improved for future measurements. The stage 2 bins will be defined in detail taking into account the experience gained during the measurements based on the stage 1 definitions.

An implementation of the bin definitions in Rivet is in development. This will ensure a consistent implementation used by both experiments as well as for theoretical studies.

3.6 Summary

Simplified template cross sections provide a way to evolve the signal strength measurements that were performed during LHC Run1, by reducing the theoretical uncertainties that are directly folded into the measurements and by providing more finely-grained measurements, while at the same time allowing and benefitting from the combination of measurements in many decay channels. Several stages are proposed: stage 0 essentially corresponds to the production mode measurements of Run1 and stage 1 defines a first complete setup, with indications for potential bin merging when a given channel cannot yet afford the full stage 1 granularity. A complete proposal for the stage 2 binning will need to be based on experience of using the simplified template cross section framework in real life, but some indications of what could be interesting are already given here.

Acknowledgements

We acknowledge discussions in Les Houches 2015 and WG2 of the LHC Higgs cross section working group, and contributions and feedback from Aaron Armbruster, Josh Bendavid, Fawzi Boudjema, André David, Marco Delmastro, Dag Gillberg, Admir Greljo, Thibault Guillemin, Chris Hays, Gino Isidori, Sabine Kraml, James Lacey, Kirtimaan Mohan, Carlo Pandini, Elisabetta Pianori, Michael Rauch, Chris White, and many others. The work of PF was partially supported by the ILP LABEX (under reference ANR-10-LABX-63 and ANR-11-IDEX-0004-02). The work of FT was supported by the DFG Emmy-Noether Grant No. TA 867/1-1. KT acknowledges partial support from the Collaborative Research Center SFB676 of the DFG "Particles, Strings and the early Universe".

Chapter IV

Phenomenological studies

1 Electroweak corrections in Drell–Yan production ¹

1.1 Introduction

The Drell–Yan-like production of electroweak gauge bosons represents one of the key Standard Model processes at hadron colliders whose detailed understanding is crucial in order to exploit the full potential of the measurements performed at the LHC. The neutral-current process $pp \rightarrow Z/\gamma \rightarrow \ell^+\ell^-$, in particular, has a very clean experimental signature owing to the two charged leptons in the final state which further allows for the full reconstruction of the kinematics of the intermediate gauge boson. Not only does this process constitute a powerful tool for detector calibration, but it also delivers important constraints in the fit of PDFs and allows for precision measurements such as the extraction of the weak mixing angle $\sin^2(\theta_{\text{eff}}^\ell)$.

On the theory side, Drell–Yan production belongs to one of the most precisely predicted processes: QCD corrections are known up to NNLO [95, 228, 256–261], the electroweak (EW) corrections up to NLO [262–273], and many further improvements beyond fixed-order predictions (see, e.g., references in Ref. [155]). Until recently, the largest missing piece in terms of fixed-order predictions were given by the NNLO mixed QCD–EW corrections. Different approaches of combining QCD and EW corrections revealed that the missing $\mathcal{O}(\alpha_s\alpha)$ corrections could have an impact of a few per cent in the resonance region, i.e. at the level that is relevant for precision phenomenology. In a series of papers [155, 274], the calculation of these corrections have been tackled using the so-called pole approximation (PA). This approach is suitable to describe observables that are dominated by resonances with sufficient accuracy.

In this work, we investigate how the $\mathcal{O}(\alpha_s\alpha)$ corrections generated through a universal process-independent resummation approach compares to the results of Ref. [155]. Section 1.2 gives a brief overview of the computation employing the PA and the implementation of the QED shower in the SHERPA Monte Carlo program [275]. In Sect. 1.3 we present our numerical results of the comparison before we conclude in Sect. 1.4.

1.2 Computational setup

The Pole approximation

The calculation of the $\mathcal{O}(\alpha_s\alpha)$ corrections presented in Refs. [155, 274] was performed in the framework of a pole expansion, which is based on a systematic expansion of the cross section around the gauge-boson resonance $p_V^2 \sim \mu_V^2$, with $\mu_V^2 = M_V^2 - iM_V\Gamma_V$ denoting the gauge-invariant location of the propagator pole in the complex plane. Only retaining the leading contributions that are enhanced by a resonant propagator, we obtain the so-called pole approximation (PA). As a result of applying the PA, the calculation is split into separate well-defined parts that can be classified into the non-factorizable and factorizable corrections: The non-factorizable corrections involve soft-photon exchange between the production and decay stages of the process and constitute the conceptually most difficult part of the calculation. They have been computed in Ref. [274] and were found to be negligible for all phenomenological purposes. The factorizable contributions, on the other hand, involve corrections where the production of the intermediate gauge boson and its decay proceed independently. Here, the factorizable correc-

¹ A. Huss, M. Schönherr

tions of “initial–final” type were identified as the numerically dominant contribution—combining the sizeable QCD corrections to the production sub-process with the large EW corrections of the gauge boson decay—and were computed in Ref. [155]. The remaining factorizable corrections are given by the “initial–initial” and “final–final” types. The latter were found to be numerically negligible [155], while the former are not expected to deliver a sizeable correction, in particular for observables that are less sensitive to initial-state radiation effects. In the remainder of this work, we will thus focus our attention to the initial–final factorizable corrections which we will often simply refer to as the $\mathcal{O}(\alpha_s\alpha)$ corrections in the PA. More details on this calculation can be found in Refs. [155, 274].

The QED resummation in Sherpa

Another approach to higher order QED or electroweak corrections is presented in the soft-photon resummation of Yennie, Frautschi and Suura (YFS) [276]. Therein the universal structure of real and virtual soft photon emissions is exploited to construct an all-order approximation to the process at hand which can be systematically supplemented with process-dependent finite hard real and virtual emission corrections. The implementation presented in Ref. [277] focusses on higher-order QED corrections to particle decays and is used since as the default mechanism for such corrections in SHERPA [275], both for elementary particle (e.g. W^\pm , Z , τ^\pm) as well as hadron decays.

In the present context of lepton pair production the higher-order QED corrections are effected in a factorised approach. The complete process $pp \rightarrow \ell^+\ell^-$ is calculated at LO or NLO in the strong coupling constant keeping all off-shell effects. Then, an intermediate resonance X is reconstructed from the lepton pair and assigned its invariant mass. Its decay width is then corrected for higher order QED corrections, including YFS resummation, to

$$\Gamma = \frac{1}{2m_X} \sum_{n_\gamma=0}^{\infty} \frac{1}{n_\gamma!} \int d\Phi e^{Y(\Omega)} \prod_{i=1}^{n_\gamma} d\Phi_i \tilde{S}(k_i) \Theta(k_i, \Omega) \left[\tilde{\beta}_0^0 + \tilde{\beta}_0^1 + \sum_{i=1}^{n_\gamma} \frac{\tilde{\beta}_1^1(k_i)}{\tilde{S}(k_i)} + \mathcal{O}(\alpha^2) \right]. \quad (\text{IV.1})$$

Therein, m_X is the mass of the decaying resonance and $d\Phi$ is the phase element of the leading order decay, and $\tilde{\beta}_0^0$ is the leading order decay squared matrix element. The $Y(\Omega)$ then is the sum of the eikonal approximations to virtual photon exchange and unresolved soft real photon emission, Ω denoting the region in which soft photons are not resolvable. The YFS form factor, $e^{Y(\Omega)}$, then resums these leading logarithmic universal corrections to all orders. Resolved photons are then described explicitly, emission by emission, by the eikonal \tilde{S} depending on the individual photon momentum k_i . $d\Phi_i$ is the corresponding phase space element. The eikonal approximations used in both the YFS form factor and for resolved real emissions can then, order-by-order, be corrected by supplementing the corresponding infrared-subtracted squared matrix elements $\tilde{\beta}_i^{i+j}$ of $\mathcal{O}(\alpha^{i+j})$ relative to the Born decay and containing i resolved photons. Since all charged particles are considered massive in the context of YFS resummation, all $\tilde{\beta}_i$ are free of any infrared singularity. Finally, it is interesting to note that in the case of multi-photon emission each emitted photon receives the hard emission correction $\tilde{\beta}_1^1$ in the respective one-photon emission projected phase space.

The implementation used here, as we restrict the γ^*/Z propagator virtuality to be near the Z mass, always identifies the resonance X with the Z boson. The calculation thus contains the $\mathcal{O}(\alpha)$ virtual corrections $\tilde{\beta}_0^1$ and real emission corrections $\tilde{\beta}_1^1$ resulting in an NLO QED accurate description. As NLO weak corrections are finite they can in principle be incorporated in the $\tilde{\beta}_0^1$. This is left to a future work.

1.3 Results

The numerical results presented in this section are obtained using the same input parameters and event selection cuts as in Ref. [155]. The electroweak coupling constant α is defined in the G_μ -scheme, with the exception of the photonic corrections which use $\alpha(0)$ as their coupling. For the parton distribution functions we use the NNPDF2.3QED NLO PDF set [194], in particular also the LO predictions shown in the following were evaluated using this choice. For the charged leptons in the final state we consider two different reconstruction strategies: In the case of “dressed” electrons, we apply a photon recombination procedure in order to treat all collinear lepton–photon configurations inclusively, whereas in the “bare” muon setup no such recombination is performed. Further details on the calculational setup and the event reconstruction are given in Ref. [155].

In order to establish the setup of the two computations, we first consider the relative $\mathcal{O}(\alpha)$ corrections by applying the YFS resummation in SHERPA to the LO prediction, $\sigma^{\text{LO}\otimes\text{YFS}}$, and compare it to the full EW corrections denoted as $\sigma^{\text{NLO}[\text{EW}]^2}$. The respective relative correction factors, normalised to the LO prediction, are then given by

$$\delta_\alpha^{\text{YFS}} = \frac{\sigma^{\text{LO}\otimes\text{YFS}} - \sigma^{\text{LO}}}{\sigma^{\text{LO}}}, \quad \delta_\alpha = \frac{\sigma^{\text{NLO}[\text{EW}]} - \sigma^{\text{LO}}}{\sigma^{\text{LO}}}. \quad (\text{IV.2})$$

Please note, the thus defined $\delta_\alpha^{\text{YFS}}$ retains also higher orders of α contrary to δ_α . For the mixed QCD–EW corrections, we generate terms of $\mathcal{O}(\alpha_s\alpha)$ by applying the YFS resummation on top of the fixed-order NLO QCD prediction, which we denote by $\sigma^{\text{NLO}[\text{QCD}]\otimes\text{YFS}}$. These results are compared to the best prediction of Ref. [155], $\sigma_{\text{PA}}^{\text{NNLO}[\text{QCD}\times\text{EW}]}$, which includes the full NLO QCD and EW corrections, supplemented by the dominant $\mathcal{O}(\alpha_s\alpha)$ corrections in the PA. In order to extract the genuine $\mathcal{O}(\alpha_s\alpha)$ contribution from the prediction based on the YFS resummation, we define the relative correction factor as follows,

$$\delta_{\alpha_s\alpha}^{\text{YFS}} = \frac{(\sigma^{\text{NLO}[\text{QCD}]\otimes\text{YFS}} - \sigma^{\text{NLO}[\text{QCD}]}) - (\sigma^{\text{LO}\otimes\text{YFS}} - \sigma^{\text{LO}})}{\sigma^{\text{LO}}}. \quad (\text{IV.3})$$

For the fixed-order prediction in the PA, the corresponding correction factor is given by

$$\delta_{\alpha_s\alpha}^{\text{PA}} = \frac{\sigma_{\text{PA}}^{\text{NNLO}[\text{QCD}\times\text{EW}]} - \sigma^{\text{NLO}[\text{QCD}+\text{EW}]}}{\sigma^{\text{LO}}}. \quad (\text{IV.4})$$

Again, as in Eq. IV.2, $\delta_{\alpha_s\alpha}^{\text{YFS}}$ also contains higher orders in α , contrary to $\delta_{\alpha_s\alpha}^{\text{PA}}$.

The numerical results comprise differential distributions in the lepton invariant mass $m_{\ell\ell}$, the transverse momentum of the positively charged lepton $p_T^{\ell^+}$, and the rapidity of the lepton pair $y_{\ell\ell}$, which are shown in Figs. IV.1–IV.3, respectively. The left plot in the figures shows a comparison of the $\mathcal{O}(\alpha)$ corrections, while the right-hand plot compares the corresponding $\mathcal{O}(\alpha_s\alpha)$ corrections. In each plot we show the absolute distributions in the top frame and the relative correction factors in the bottom panel as defined in Eq. (IV.2) for the $\mathcal{O}(\alpha)$ and Eqs. (IV.3) and (IV.4) for the mixed QCD–EW corrections.

For the invariant mass distribution shown in Fig. IV.1 we observe an overall good agreement between the YFS resummation and the fixed-order result. This reflects the property of this observable whose corrections are known to be dominated by final-state photon emission. Both at $\mathcal{O}(\alpha)$ and $\mathcal{O}(\alpha_s\alpha)$ we observe a small offset between the two predictions where the resummed approach leads to slightly smaller corrections below the Z resonance. This difference originates from multi-photon emissions, which is included in the YFS formalism, cf. Eq. (IV.1), whereas the fixed-order prediction is restricted to at most one photon emission. Figure IV.2

² A comparison of the PA at $\mathcal{O}(\alpha)$ against the full NLO EW corrections has been performed in Ref. [274].

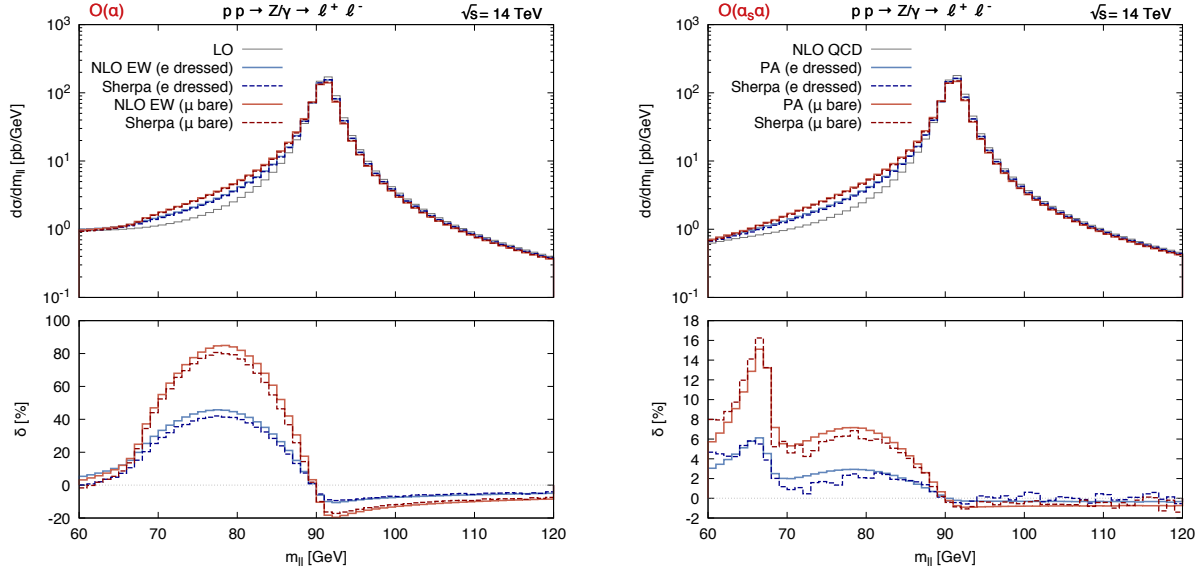


Fig. IV.1: Comparison of the $\mathcal{O}(\alpha)$ (left) and $\mathcal{O}(\alpha_s\alpha)$ (right) corrections to the invariant-mass distribution of the lepton pair $m_{\ell\ell}$ between Ref. [155] and Sherpa. The absolute distributions and the relative corrections at the respective order are shown in the top and bottom panels, respectively. Collinear lepton–photon configurations are treated both inclusively with a recombination procedure resulting in the “e dressed” setup (blue) or exclusively in the case of muons labelled as “ μ bare” (red).

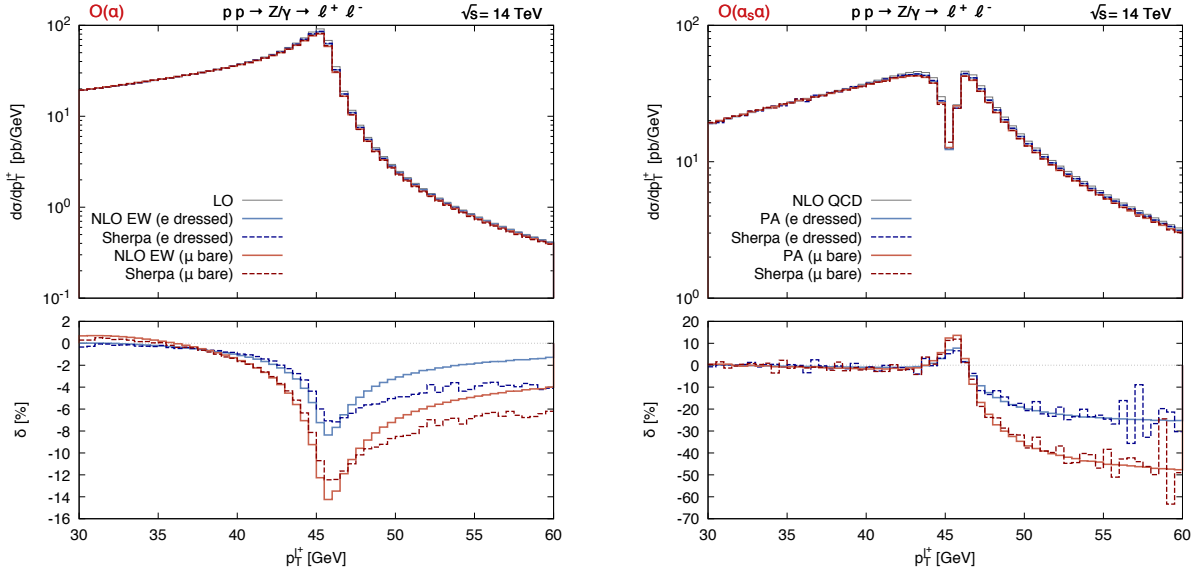


Fig. IV.2: Comparison of the $\mathcal{O}(\alpha)$ (left) and $\mathcal{O}(\alpha_s\alpha)$ (right) corrections to the transverse-momentum distribution of the positively charged lepton $p_T^{\ell^+}$ between Ref. [155] and Sherpa. The absolute distributions and the relative corrections at the respective order are shown in the top and bottom panels, respectively. Collinear lepton–photon configurations are treated both inclusively with a recombination procedure resulting in the “e dressed” setup (blue) or exclusively in the case of muons labelled as “ μ bare” (red).

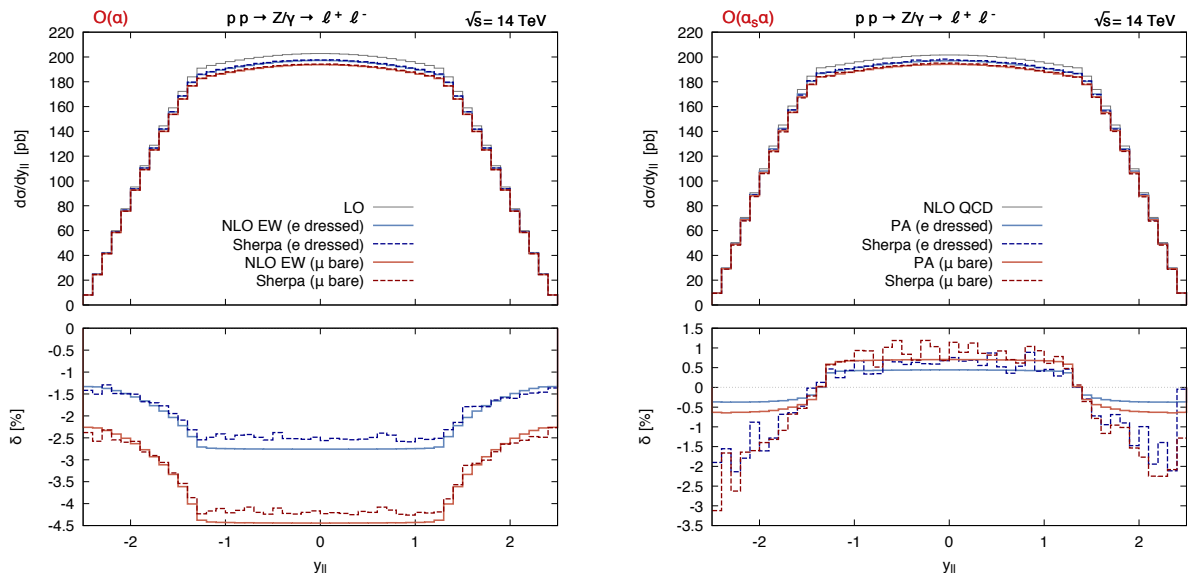


Fig. IV.3: Comparison of the $\mathcal{O}(\alpha)$ (left) and $\mathcal{O}(\alpha_s\alpha)$ (right) corrections to the rapidity distribution of the lepton pair $y_{\ell\ell}$ between Ref. [155] and Sherpa. The absolute distributions and the relative corrections at the respective order are shown in the top and bottom panels, respectively. Collinear lepton–photon configurations are treated both inclusively with a recombination procedure resulting in the “e dressed” setup (blue) or exclusively in the case of muons labelled as “ μ bare” (red).

shows the corrections to the transverse momentum distribution of the positively charged lepton, $p_T^{\ell^+}$. Although qualitatively displaying a similar shape in the $\mathcal{O}(\alpha)$ corrections, we observe larger differences between the two computations around the resonance and in the higher transverse momentum tails. This difference can be understood from the fact that this observable is sensitive to recoil effects from initial-state radiation which are not accounted for in the YFS approach as used here. Indeed, comparing the final-state factorizable $\mathcal{O}(\alpha)$ corrections in PA to the full NLO EW corrections, as it is done in Fig. 9 in Ref. [274], a very similar behaviour can be observed. For the mixed QCD–EW corrections, on the other hand, the EW corrections contained in the $\mathcal{O}(\alpha_s\alpha)$ PA prediction are confined to the decay sub-process similarly to the case of the YFS resummation. As a result, we see a much better agreement between the two computations here. Lastly, the numerical results for the rapidity distribution of the lepton pair, $y_{\ell\ell}$, are shown in Fig. IV.3. At $\mathcal{O}(\alpha)$, the resummed prediction is able to reproduce the exact fixed-order result to a large extent up to a small offset in the normalisation. This shift can be attributed to the finite weak corrections which are missing in the YFS resummed prediction here. The purely weak corrections amount to a flat correction of approximately -0.5% in this distribution as can be read off from Fig. 14 in Ref. [273] and matches well with the observed offset. For the mixed QCD–EW corrections we obtain corrections from the YFS resummation that are similar in shape to those of the fixed-order prediction in the PA, however, with larger negative corrections in the forward regime which possibly stem from multi-photon effects on the event acceptance in this region.

1.4 Conclusions and outlook

The Drell–Yan process is one of the most important “standard candle” processes at the LHC and, as such, has a wide range of applications. In this work, we have explored the possibility of generating mixed QCD–EW corrections of $\mathcal{O}(\alpha_s\alpha)$ to this process using the YFS resum-

mation available in the SHERPA Monte Carlo and performed a comparison to the fixed-order calculation of Ref. [155]. To this end, we have considered both $\mathcal{O}(\alpha)$ and $\mathcal{O}(\alpha_s\alpha)$ corrections to various differential distributions given by the invariant mass of the leptons, the lepton transverse momentum, and the rapidity of the lepton pair. We find that the QED resummation is able to capture the electroweak corrections to these observables remarkably well. Furthermore, we were able to identify various sources for the differences that were observed between the two predictions.

Building on the insights that were gained from this study, it will be interesting to investigate further observables and also repeating this comparison for the charged-current process. Potential improvements were identified in both computations which should be explored in order to gain further insights into the numerical impact of the various ingredients that enter the two predictions. Such improvements include the finite weak corrections that can be incorporated to the YFS approach through the $\hat{\beta}^1$ coefficient in Eq. (IV.1) on the one side, and supplementing the fixed-order calculation with multi-photon emission effects.

Acknowledgements

We would like to thank the Les Houches workshop for hospitality offered during which some of the work contained herein was performed. A.H. acknowledges support from the ERC Advanced Grant MC@NNLO (340983). MS acknowledges support by the Swiss National Science Foundation (SNF) under contract PP00P2-128552.

2 NLO EW technical and physics comparisons ³

Adequate predictions for scattering processes at particle colliders such as the LHC require the inclusion of next-to-leading order (NLO) perturbative corrections of the strong and electroweak (EW) interactions. For the calculation of NLO QCD corrections the automation has been established, and several tools exist [39–41, 278–283]. On the other hand, the automation of NLO EW corrections has just started, and only a few tools are available [150, 163, 284, 285]. In this section we review the status of the existing tools for the automated calculation of EW one-loop amplitudes and provide a comparison of some of them for specific processes. In addition, we also show a comparison of the Sudakov approximation for the EW corrections as implemented in ALPGEN [286] with complete NLO calculations. Finally, we present a comparison of theoretical predictions from various codes with experimental results from CMS for the ratio of the associated production of a Z/γ^* or an on-shell photon with additional jets as a function of the transverse momentum of the vector boson.

2.1 Codes for the automated calculation of electroweak NLO corrections

RECOLA

RECOLA is a Fortran95 computer program for the automated generation and numerical computation of scattering amplitudes in the full Standard Model (SM) (including QCD and the EW sector) at tree and one-loop level which has become publicly available very recently [43]. It is based on a one-loop generalization of Dyson–Schwinger recursion relations [287] and allows to generate one-loop amplitudes for (in principle) arbitrary decay and scattering processes in the SM with particular emphasis on high particle multiplicities. Counterterms [288] and rational terms [289] are included via dedicated tree-level Feynman rules. RECOLA was the first automated tool to calculate EW NLO corrections [284].

³ A. Denner, V. Ciulli, M. Chiesa, R. Frederix, L. Hofer, S. Kallweit, J. M. Lindert, P. Maierhöfer, A. Marini, G. Montagna, M. Moretti, O. Nicrosini, D. Pagani, F. Piccinini, S. Pozzorini, M. Schönherr, E. Takasugi, S. Uccirati, M. A. Weber, M. Zaro

RECOLA provides numerical results for scattering amplitudes in the 't Hooft–Feynman gauge. Dimensional regularization is used for ultraviolet singularities, while collinear and soft singularities can be treated either in dimensional or in mass regularization. RECOLA is interfaced to COLLIER [250, 290, 291], a recently published library for the fast and numerically stable calculation of one-loop tensor integrals. For renormalization, apart from the traditional on-shell scheme [288], RECOLA in particular features its generalization to the complex-mass scheme [292]. RECOLA further supports the G_μ , the $\alpha(0)$ and the $\alpha(M_Z)$ scheme for the renormalization of the electromagnetic coupling constant, and a dynamical N_f -flavour scheme for the strong coupling constant. Internal resonant particles can be treated in the complex-mass scheme. Moreover, resonant contributions can be consistently isolated such that matrix elements involving specific intermediate resonances can be calculated. The calculation of squared amplitudes, summed over spin and colour, is supported at leading order (LO), NLO, and for loop-induced processes. Besides the calculation of complete tree-level and one-loop results, RECOLA allows to select or discard specific orders of α_s (and thus also of α) in all computed objects, such as in the amplitudes, in the square of the Born amplitude or in the interference of the Born with the one-loop amplitude. Moreover, the code allows the computation of colour- and spin-correlated LO squared amplitudes required for dipole subtraction [90, 293].

For the calculation of physical cross sections RECOLA has to be interfaced to a Monte Carlo code or a multi-purpose event generator; such interfaces are presently being developed. Together with private Monte Carlo integrators, RECOLA has been used for the computation of EW corrections to $pp \rightarrow l^+l^-jj, \nu_l\bar{\nu}_ljj$ [162] and the QCD corrections to $pp \rightarrow e^+\nu_e\mu^-\bar{\nu}_\mu b\bar{b}H$ [152].

SHERPA/MUNICH+OPENLOOPS

The frameworks MUNICH + OPENLOOPS and SHERPA + OPENLOOPS automate the full chain of operations – from process definition to collider observables – that enter NLO QCD+EW simulations at parton level. The relevant scattering amplitudes at NLO QCD are publicly available in the form of an automatically generated library [294] that supports all interesting LHC processes (more than one hundred processes), can be easily extended upon user request and will be extended to NLO EW soon. The recently achieved automation of EW corrections [163, 164] is based on the well established QCD implementations and allows for NLO QCD+EW simulations for a vast range of SM processes, up to high particle multiplicity, at current and future colliders. To be precise, the new implementations allow for NLO calculations at any given order $\alpha_s^n\alpha^m$, including all relevant QCD–EW interference effects. Full NLO SM calculations that include all possible $\mathcal{O}(\alpha_s^{n+k}\alpha^{m-k})$ contributions to a certain process are also supported.

In these frameworks virtual amplitudes are provided by the OPENLOOPS program [294], which is based on the Open Loops algorithm [40] – a fast numerical recursion for the evaluation of one-loop scattering amplitudes. The extension to NLO EW corrections required the implementation of all $\mathcal{O}(\alpha)$ EW Feynman rules in the framework of the numerical Open Loops recursion including counterterms associated with so-called R_2 rational parts [289] and with the on-shell renormalization of UV singularities [288]. Additionally, for the treatment of heavy unstable particles the complex-mass scheme [292] has been implemented in a fully general way. Combined with the COLLIER tensor-reduction library [250], which implements the Denner–Dittmaier reduction techniques [295, 296] and the scalar integrals of Ref. [297], or with CUTTOOLS [298], which implements the OPP method [51], together with the ONELOOP library [299], the employed recursion permits to achieve very high CPU performance and a high degree of numerical stability.

All remaining tasks, i.e. the bookkeeping of partonic subprocesses, phase-space integration and the subtraction of QCD and QED bremsstrahlung are supported by the two independent

and fully automated Monte Carlo generators MUNICH [300] and SHERPA [275, 301]. The first one, MUNICH, is a fully generic and very fast parton-level Monte Carlo integrator. SHERPA is a particle-level Monte Carlo generator providing all stages of hadron-collider simulations, including parton showering, NLO matching, multi-jet merging, hadronization and underlying event simulations. For tree amplitudes, with all relevant colour and helicity correlations, MUNICH relies on OPENLOOPS, while SHERPA generates them internally with AMEGIC++ [249] and COMIX [302]. For the cancellation of infrared singularities both Monte Carlo tools, MUNICH and SHERPA, employ the dipole-subtraction scheme [90, 293] and its extension to EW corrections [303, 304]. Both codes were extensively checked against each other, and sub-permille level agreement was found. The implementation of parton-shower matching and multi-jet merging including NLO EW effects is available in an approximate way [164], while a fully consistent implementation is under way.

Employing the described frameworks in Ref. [163] the simulation of $W + 1, 2, 3$ jet production at NLO EW+QCD was presented. In order to make the calculation of the process with the highest jet multiplicity feasible, it was important to factorize these processes into a production part and into a decay part. At the NLO EW level this required a careful implementation of the narrow-width approximation in order to control numerical stability given the appearance of pseudo-resonances for two or more associated jets. It was found that $V +$ multijet final states feature genuinely different EW effects as compared to the case of $V + 1$ jet. Subsequently in Ref. [164] NLO QCD+EW simulations were presented for $Z +$ jets and $W^\pm +$ jets production including off-shell leptonic decays and multijet merging with up to two jets within the MEPS@NLO framework of the SHERPA Monte Carlo program.

MADGRAPH5_AMC@NLO

The results presented in Section 2.2 have been obtained via an extension of the public code MADGRAPH5_AMC@NLO [45] that allows to automatically calculate also NLO EW corrections. This version of the code is, at the moment, private and has already been used for the calculation of NLO QCD and EW corrections to the hadroproduction of a top-quark pair in association with a heavy boson [150, 151].

The automation of the NLO QCD and EW corrections for a generic SM process has required major improvements for all the building blocks of the MADGRAPH5_AMC@NLO code [282, 305]. The generation of the amplitudes and matrix elements at LO and NLO accuracy for the combined expansion in powers of α_s and α has been lengthly discussed in Refs. [45, 150]. The code at the moment is able to automatically calculate all the possible perturbative orders stemming from tree-level amplitudes and their interference with one-loop amplitudes, for any SM process. Moreover, it is possible to select any combination of perturbative orders. Thus, all the necessary R_2 and UV counterterms have been calculated both in the complex-mass scheme and with real masses and on-shell renormalization conditions for unstable particles. These counterterms are part of the so-called NLO UFO models [306], which is the general format used in MADGRAPH5_AMC@NLO for importing Feynman rules of a given Lagrangian. In the case of the SM at NLO, two different UFO models have been created in order to calculate EW corrections respectively in the $\alpha(m_Z)$ or G_μ scheme.

The subtraction of infrared divergences and the integration over the Born-like and real-emission phase space is automatically performed for any process by extending the framework described in Refs. [45, 305], taking into account all the EW-QCD IR divergences appearing at any perturbative order that enter into NLO predictions.

At the moment, NLO corrections for massive-only final states can be automatically calculated by running a code that can be generated in MADGRAPH5_AMC@NLO via few commands

of the form:⁴

```
import model QCDandEW_renormalization-scheme
generate process QCD=m QED=n [QCD QED]
output process_at_orders_m_n_with_QCD_and_QED_corrections
```

The indices m and n and the flags QCD and QED can be used to select the desired perturbative orders. In the case of massless final states, code-wise no additional improvement is required. However, with QCD and EW corrections a generic approach for the treatment of IR divergences and a IR-safe definition of final-state products is not straightforward. Thus, besides the generation of the code on the same line of the case of massive-only final states, with massless particle specific solutions are necessary to obtain IR-safe definition of the final state, as done, e.g. in Refs. [162,163], which are considered in these proceedings.

At the moment results can be obtained only at fixed order, without matching to shower effects. The matching with QED or in general EW shower will be also included in the future, by extending the matching procedure with QCD parton showers that is already available in the public version of the code.

2.2 Technical comparison of EW NLO cross sections

In order to assess the status of the automated tools for the calculation of EW corrections a technical comparison has been performed. Given the complexity of this enterprise, we have chosen the recent calculations of EW corrections to $pp \rightarrow l^+l^- + 2\text{jets}$, $pp \rightarrow l^+\nu + 2\text{jets}$, and $pp \rightarrow t\bar{t}H$ obtained with the automated tools RECOLA, SHERPA/MUNICH+OPENLOOPS, and MADGRAPH5_AMC@NLO, respectively and published in Refs. [151,162,164]. We invited all other groups to provide numbers for comparison with specific results in these publications and in addition some cumulative histograms using the setups of the respective publications. While the SHERPA/MUNICH+OPENLOOPS collaboration provided numbers for all three processes, none of the other groups delivered new results for comparison.

The input parameters and set-ups of the calculations in Refs. [151,162,164] are summarized in Table IV.1. The large number of parameters and settings that have to be adapted reflects the complexity of the calculations. Note that \hat{H}_T is calculated from the sum of transverse energies of all final-state particles, i.e.

$$\hat{H}_T = \sum_i E_{T,i} = \sum_i \sqrt{p_{T,i}^2 + m_i^2}, \quad (\text{IV.5})$$

while H_T from the sum of all transverse momenta,

$$H_T = \sum_i p_{T,i}. \quad (\text{IV.6})$$

The calculation of the factorization and renormalization scale for $pp \rightarrow l^+\nu + 2\text{jets}$, is performed using the transverse energy of the lepton–neutrino system,

$$\hat{H}'_T = p_{T,j_1} + p_{T,j_2} + p_{T,g} + p_{T,\gamma} + E_{T,l\nu}, \quad E_{T,l\nu} = \sqrt{p_{T,l\nu}^2 + m_{l\nu}^2}. \quad (\text{IV.7})$$

Radiated partons and photons are included at NLO. The cuts for the processes $pp \rightarrow l^+l^- + 2\text{jets}$ and $pp \rightarrow l^+\nu + 2\text{jets}$ are listed in Table IV.2, while no cuts have been applied for $pp \rightarrow t\bar{t}H$. The jet with highest transverse momentum is denoted j_1 in the following.

⁴These are representative commands, the future public version of the code may have to be used with different syntax.

parameter/setting	$pp \rightarrow l^+l^- + 2 \text{ jets}$	$pp \rightarrow l^+ \nu + 2 \text{ jets}$	$pp \rightarrow t\bar{t}H$
order of LO contribution	all	$\mathcal{O}(\alpha_s^2\alpha^2)$	$\mathcal{O}(\alpha_s^2\alpha)$
order of NLO corrections	$\mathcal{O}(\alpha_s^2\alpha^3)$	$\mathcal{O}(\alpha_s^3\alpha^2), \mathcal{O}(\alpha_s^2\alpha^3)$	$\mathcal{O}(\alpha_s^3\alpha), \mathcal{O}(\alpha_s^2\alpha^2)$
renormalization scheme	G_μ scheme	G_μ scheme	$\alpha(M_Z)$ scheme
complex/real masses	complex-mass scheme	complex-mass scheme	real masses
jet algorithm	anti- k_T , $R = 0.4$	anti- k_T , $R = 0.4$	–
partons clustered for	$ y < 5$	$ y < \infty$	–
photon/jet separation	democratic clustering + fragmentation	fermion–photon recombination and democratic clustering	–
$\max \frac{E_\gamma}{E_\gamma + E_j}$	0.7	0.5	–
PDF set	MSTW2008LO	NNPDF2.3QED	NNPDF2.3QED
factorization scale	$M_{Z,\text{pole}}$	$\hat{H}'_T/2$	$\hat{H}_T/2$
renormalization scale	$M_{Z,\text{pole}}$	$\hat{H}'_T/2$	$\hat{H}_T/2$
partons at LO	g,u,c,d,s,b	g,u,c,d,s,b	g,u,c,d,s,b, γ
partons at NLO	g,u,c,d,s	g,u,c,d,s,b	g,u,c,d,s,b, γ
γ -induced contributions	none	only at LO	all/none
collider energy	13 TeV	13 TeV	13 TeV
α_s (from PDF)	0.139395...	0.118	0.118
G_μ [GeV^{-2}]	$1.1663787 \cdot 10^{-5}$	$1.16637 \cdot 10^{-5}$	calculated from α
α	calculated from G_μ	calculated from G_μ	1/128.93
$M_{Z,\text{on-shell}}$	91.1876 GeV	91.1876 GeV	91.188 GeV
$\Gamma_{Z,\text{on-shell}}$	2.4952 GeV	2.4955 GeV	0 GeV
$M_{Z,\text{pole}}, \Gamma_{Z,\text{pole}}$	calculated	–	–
$M_{W,\text{on-shell}}$	80.385 GeV	80.385 GeV	80.385 GeV
$\Gamma_{W,\text{on-shell}}$	2.085 GeV	2.0897 GeV	0 GeV
$M_{W,\text{pole}}, \Gamma_{W,\text{pole}}$	calculated	–	–
complex masses	from pole masses	from on-shell masses	–
m_b	0 GeV	0 GeV	0 GeV
m_t	173.2 GeV	173.2 GeV	173.3 GeV
Γ_t	0 GeV	1.339 GeV	0 GeV
M_H	125 GeV	125 GeV	125 GeV
Γ_H	0 GeV	4.07 MeV	0 GeV

Table IV.1: Settings and input parameters used for technical comparisons.

pp $\rightarrow l^+l^- + 2$ jets	pp $\rightarrow l^+\nu + 2$ jets
$p_{T,j} > 30$ GeV	$p_{T,j} > 30$ GeV
$ y_j < 4.5$	$ \eta_j < 4.5$
$p_{T,l} > 20$ GeV	$p_{T,l} > 25$ GeV
$ y_l < 2.5$	$ \eta_l < 2.5$
$\Delta R_{ll} > 0.2$	$\Delta R_{j1} > 0.5$
$\Delta R_{j1} > 0.5$	$M_{T,W} > 40$ GeV
$66 \text{ GeV} < M_{ll} < 116 \text{ GeV}$	$E_{T,\text{miss}} > 25$ GeV

Table IV.2: Cuts used for technical comparisons.

In Table IV.3 we present a comparison of results from RECOLA and SHERPA/MUNICH+OPENLOOPS for the process $pp \rightarrow l^+l^- + 2$ jets in the setup defined in Tables IV.1 and IV.2. The results for the LO cross sections σ^{LO} including all SM tree-level contributions of order $\mathcal{O}(\alpha_s^2\alpha^2)$, $\mathcal{O}(\alpha_s\alpha^3)$, and $\mathcal{O}(\alpha^4)$, agree within 0.5% or better. The relative EW corrections $\delta_{\text{EW}}^{\text{NLO}} = \delta\sigma_{\text{EW}}^{\text{NLO}}/\sigma^{\text{LO}}$, where $\delta\sigma_{\text{EW}}^{\text{NLO}}$ contains the complete NLO corrections of order $\mathcal{O}(\alpha_s^2\alpha^3)$, agree at the level of $\mathcal{O}(1\%)$ or better. The difference in the NLO EW correction factors can be attributed to a different treatment of b-quark-initiated processes and of final-state photon radiation. While both calculations use democratic clustering for jets and photons, in Ref. [162] the quark–photon fragmentation function has been used for a consistent photon–jet separation; in the SHERPA/MUNICH+OPENLOOPS approach the cancellation of collinear singularities is enforced by recombining (anti)quark-photon pairs in a tiny cone around the singular region as described in Ref. [163]. While in the calculation of Ref. [162] the contributions of bottom quarks have been neglected at NLO, these are included in the calculation based on SHERPA/MUNICH+OPENLOOPS. Note that the agreement for $\delta_{\text{EW}}^{\text{NLO}}$ is better for large transverse momenta, where the contributions of b-quark-initiated processes are small.

In Table IV.4 we present results from SHERPA/MUNICH+OPENLOOPS for the process $pp \rightarrow l^+\nu + 2$ jets in the setup defined in Tables IV.1 and IV.2. The results for the LO cross sections $\sigma_{\text{QCD}}^{\text{LO}}$ include the tree-level contributions of order $\mathcal{O}(\alpha_s^2\alpha^2)$; the relative QCD corrections, $\delta_{\text{QCD}}^{\text{NLO}} = \delta\sigma_{\text{QCD}}^{\text{NLO}}/\sigma_{\text{QCD}}^{\text{LO}}$, and EW corrections, $\delta_{\text{EW}}^{\text{NLO}} = \delta\sigma_{\text{EW}}^{\text{NLO}}/\sigma_{\text{QCD}}^{\text{LO}}$, involve the complete NLO contributions of order $\mathcal{O}(\alpha_s^3\alpha^2)$ and $\mathcal{O}(\alpha_s^2\alpha^3)$, respectively. While none of the other groups provided results for this process, we nevertheless show these numbers as benchmarks for future comparisons. Moreover, in Section 2.3 these results are compared with a calculation in the Sudakov approximation for the EW corrections.

In Table IV.5 we present a comparison of results from MADGRAPH5_AMC@NLO and SHERPA/MUNICH+OPENLOOPS for the process $pp \rightarrow t\bar{t}H$ in the inclusive setup defined in Table IV.1. The relative corrections are normalized to the LO QCD cross section, $\delta_X^{\text{NLO}} = \delta\sigma_X^{\text{NLO}}/\sigma_{\text{QCD}}^{\text{LO}}$. The absolute QCD corrections, $\delta\sigma_{\text{QCD}}^{\text{NLO}}$ and EW corrections $\delta\sigma_{\text{EW}}^{\text{NLO}}$ comprise the complete NLO contributions of order $\mathcal{O}(\alpha_s^3\alpha)$ and $\mathcal{O}(\alpha_s^2\alpha^2)$, respectively. For the entries with “no γ ” the PDF of the photon has been artificially set to zero in order to gauge the impact of photons in the initial state. All the results are at per mille accuracy w.r.t. the corresponding LO QCD predictions. In the SHERPA/MUNICH+OPENLOOPS calculation, a six-flavour scheme is employed, consistently with the NNPDF2.3_QED PDF distribution. The gluon splitting into top-quark pairs in the PDF evolution as well as the six-flavour running and renormalization of α_s are taken into account. However, contributions from initial-state top quarks and top-quark bremsstrahlung are not included. This is justified by the fact that the former are formally

$pp \rightarrow l^+l^- + 2j$ G_μ scheme		RECOLA		SHERPA/MUNICH+OPENLOOPS	
		[arXiv:1411.0916]		σ^{LO}	$\delta_{\text{EW}}^{\text{NLO}}$
		σ^{LO}	$\delta_{\text{EW}}^{\text{NLO}}$		
		[fb]	[%]	[fb]	[%]
$p_{\text{T},j_1} >$	0.0 TeV	$5.120 \cdot 10^4$	-2.5	$5.122 \cdot 10^4$	-3.4
	0.25 TeV	$2.071 \cdot 10^3$	-7.6	$2.072 \cdot 10^3$	-8.5
	0.5 TeV	$2.060 \cdot 10^2$	-13.1	$2.061 \cdot 10^2$	-13.7
	0.75 TeV	$3.603 \cdot 10^1$	-17.5	$3.603 \cdot 10^1$	-17.4
	1.0 TeV	$7.806 \cdot 10^0$	-21.5	$7.801 \cdot 10^0$	-20.5
$M_{j_1j_2} >$	0.5 TeV	$4.203 \cdot 10^3$	-4.3	$4.202 \cdot 10^3$	-5.1
	1.0 TeV	$8.085 \cdot 10^2$	-5.8	$8.088 \cdot 10^2$	-6.5
	2.0 TeV	$8.377 \cdot 10^1$	-7.3	$8.368 \cdot 10^1$	-7.9
	4.0 TeV	$2.485 \cdot 10^0$	-8.2	$2.476 \cdot 10^0$	-8.4
$p_{\text{T},\ell^-} >$	0.25 TeV	$3.176 \cdot 10^2$	-12.9	$3.177 \cdot 10^2$	-14.4
	0.5 TeV	$2.099 \cdot 10^1$	-20.5	$2.097 \cdot 10^1$	-20.3
	0.75 TeV	$2.673 \cdot 10^0$	-26.3	$2.676 \cdot 10^0$	-27.3
	1 TeV	$4.552 \cdot 10^{-1}$	-30.9	$4.532 \cdot 10^{-1}$	-31.3
$p_{\text{T},\ell\ell} >$	0.25 TeV	$1.356 \cdot 10^3$	-9.3	$1.356 \cdot 10^3$	-10.9
	0.5 TeV	$1.094 \cdot 10^2$	-16.4	$1.093 \cdot 10^2$	-17.5
	0.75 TeV	$1.528 \cdot 10^1$	-22.0	$1.526 \cdot 10^1$	-21.1
	1.0 TeV	$1.879 \cdot 10^0$	-27.1	$1.873 \cdot 10^0$	-27.7
$H_{\text{T}} >$	0.5 TeV	$3.293 \cdot 10^3$	-7.1	$3.294 \cdot 10^3$	-8.0
	1.0 TeV	$3.012 \cdot 10^2$	-12.8	$3.012 \cdot 10^2$	-13.2
	1.5 TeV	$5.166 \cdot 10^1$	-17.6	$5.165 \cdot 10^1$	-16.8
	2.0 TeV	$1.087 \cdot 10^1$	-21.8	$1.087 \cdot 10^1$	-19.0

Table IV.3: Comparison of results from SHERPA/MUNICH+OPENLOOPS for $pp \rightarrow l^+l^- + 2\text{jets}$ in the setup defined in Tables IV.1 and IV.2.

$pp \rightarrow l^+ \nu + 2j$ G_μ scheme		SHERPA/MUNICH+OPENLOOPS [arXiv:1511.08692]		
		$\sigma_{\text{QCD}}^{\text{LO}}$	$\delta_{\text{QCD}}^{\text{NLO}}$	$\delta_{\text{EW}}^{\text{NLO}}$
		[pb]	[%]	[%]
$p_{\text{T},j_1} >$	0 TeV	$1.114 \cdot 10^2$	15.2	-2.7
	0.5 TeV	$1.551 \cdot 10^{-1}$	2.3	-12.5
	1 TeV	$4.092 \cdot 10^{-3}$	8.7	-19.5
$E_{\text{T,miss}} >$	0.5 TeV	$7.863 \cdot 10^{-3}$	-4.6	-22.4
	1 TeV	$7.863 \cdot 10^{-3}$	-2.9	-27.9
$p_{\text{T},l^+} >$	0.5 TeV	$1.647 \cdot 10^{-2}$	0.1	-21.1
	1 TeV	$2.912 \cdot 10^{-4}$	0.6	-30.4
$H_{\text{T}} >$	0.5 TeV	$1.2635 \cdot 10^0$	12.3	-8.0
	1 TeV	$2.304 \cdot 10^{-1}$	58.6	-12.3
	2 TeV	$5.749 \cdot 10^{-3}$	61.9	-18.0

Table IV.4: Results from SHERPA/MUNICH+OPENLOOPS for $pp \rightarrow l^+ \nu + 2\text{jets}$ in the setup defined in Tables IV.1 and IV.2.

$pp \rightarrow t\bar{t}H$ $\alpha(M_Z)$ scheme	MADGRAPH5_AMC@NLO [arXiv:1504.03446]				SHERPA/MUNICH+OPENLOOPS			
	$\sigma_{\text{QCD}}^{\text{LO}}$	$\delta_{\text{QCD}}^{\text{NLO}}$	$\delta_{\text{EW}}^{\text{NLO}}$	$\delta_{\text{EW, no } \gamma}^{\text{NLO}}$	$\sigma_{\text{QCD}}^{\text{LO}}$	$\delta_{\text{QCD}}^{\text{NLO}}$	$\delta_{\text{EW}}^{\text{NLO}}$	$\delta_{\text{EW, no } \gamma}^{\text{NLO}}$
	[pb]	[%]	[%]	[%]	[pb]	[%]	[%]	[%]
incl.	$3.617 \cdot 10^{-1}$	28.9	-1.2	-1.4	$3.617 \cdot 10^{-1}$	28.3	-1.3	-1.4
$p_{\text{T},H/t/\bar{t}} > 200$ GeV	$1.338 \cdot 10^{-2}$	23.4	-8.2	-8.5	$1.338 \cdot 10^{-2}$	22.5	-8.2	-8.4
$p_{\text{T},H/t/\bar{t}} > 400$ GeV	$3.977 \cdot 10^{-4}$	9.6	-13.8	-13.9	$3.995 \cdot 10^{-4}$	10.4	-13.9	-14.0
$p_{\text{T},H} > 500$ GeV	$2.013 \cdot 10^{-3}$	37.8	-10.6	-11.6	$2.014 \cdot 10^{-3}$	37.3	-10.8	-11.7
$ y_t > 2.5$	$4.961 \cdot 10^{-3}$	37.5	0.2	0.5	$5.006 \cdot 10^{-3}$	36.9	0.2	0.5

Table IV.5: Comparison of results from MADGRAPH5_AMC@NLO and SHERPA/MUNICH+OPENLOOPS for $pp \rightarrow t\bar{t}H$ in the setup defined in Table IV.1.

of order $\alpha_s^2 \log^2(\mu_R/m_t)$, while top-bremsstrahlung gives rise to Higgs+multi-top signatures. Conversely, the results from MADGRAPH5_AMC@NLO are obtained within the five-flavour scheme, renormalizing top-quark loops in the decoupling scheme. This means that top-quark contributions to the initial state and to the Bremsstrahlung should not be included in the hard cross section, and a running α_s with five active flavours should be employed. Therefore, one has to compensate the inputs from the NNPDF2.3_QED PDF distribution, i.e. the luminosities and α_s for given Bjorken x 's and scales, which are in the six-flavour scheme, to be consistent with the five-flavour scheme approach used in the matrix elements.⁵ In practice, both approaches are internally consistent, and the different treatments of the α_s evolution are exactly equivalent, as $\log(\mu_R/m_t)$ terms turn out to be accounted for to all orders in both calculations. However, the fact that top-quark contributions to the evolution of the gluon density are taken into account (through the NNPDF2.3_QED PDFs) in SHERPA/MUNICH+OPENLOOPS and are subtracted in MADGRAPH5_AMC@NLO gives rise to a difference of $\mathcal{O}(\alpha_s \log(\mu_F/m_t))$, which manifests itself as one-percent level deviations in the numerical predictions.

2.3 Comparison of Sudakov approximation with EW NLO corrections for distributions

In Refs. [308,309] a process-independent algorithm for the computation of one-loop EW corrections has been developed. According to the algorithm, the $\mathcal{O}(\alpha)$ corrections to a generic process involving N external particles of flavour i_1, \dots, i_N factorize in the high-energy limit as follows:

$$\delta \mathcal{M}_{i_1 \dots i_n}^{\text{NLL}} \Big|_{\text{Sudakov}} = \sum_{k=1}^N \sum_{l>k} \delta_{kl}^{\text{DL}} \mathcal{M}_{i_1 \dots j_k \dots j_l \dots i_n}^{\text{LO}} + \sum_{k=1}^N \delta_k^{\text{SL}} \mathcal{M}_{i_1 \dots j_k \dots i_n}^{\text{LO}} + \delta^{\text{PR}} \mathcal{M}_{i_1 \dots i_n}^{\text{NLL}}. \quad (\text{IV.8})$$

In Eq. (IV.8), the functions δ_{kl}^{DL} and δ_k^{SL} contain the Sudakov double and single logarithmic contributions, respectively. They depend only on the flavour and on the kinematics of the external particles. These terms multiply LO matrix elements that are obtained from the one of the original process $\mathcal{M}_{i_1 \dots i_n}^{\text{LO}}$ via SU(2) transformations of pairs or single external legs, j_k being in Eq. (IV.8) the SU(2) transformed of the particle i_k . The last term in Eq. (IV.8) comes from parameter renormalization:

$$\delta^{\text{PR}} \mathcal{M}_{i_1 \dots i_n}^{\text{NLL}} = \delta e \frac{\delta \mathcal{M}_{i_1 \dots i_n}^{\text{LO}}}{\delta e} + \delta c_w \frac{\delta \mathcal{M}_{i_1 \dots i_n}^{\text{LO}}}{\delta c_w} + \delta h_t \frac{\delta \mathcal{M}_{i_1 \dots i_n}^{\text{LO}}}{\delta h_t} + \delta h_H \frac{\delta \mathcal{M}_{i_1 \dots i_n}^{\text{LO}}}{\delta h_H}, \quad (\text{IV.9})$$

where $h_t = m_t/M_W$, $h_H = M_H^2/M_W^2$ and $c_w = M_W/M_Z$. In Ref. [310], the algorithm of Refs. [308,309] has been implemented in the ALPGEN v2.1.4 [286] event generator for the vector-boson + multi-jet production and applied to study the phenomenological impact of the one-loop weak corrections to New Physics searches in missing transverse energy plus multi-jets

⁵While NNPDF2.3_QED PDF distributions are in the variable-flavour scheme, with our choice of the scale, which is always larger than m_t , the variable-flavour scheme is equivalent to the six-flavour scheme. In order to remove the impact of the sixth flavour, one has to compensate its contribution to the running of α_s and to the DGLAP equation for the PDF evolution. At NLO QCD, this corresponds to

$$\sigma_{\text{QCD}}^{\text{NLO}} (\text{6f-PDFs}) = \sigma_{\text{QCD}}^{\text{NLO}} + \alpha_s \frac{2T_F}{3\pi} \left[\log \left(\frac{m_t^2}{\mu_R^2} \right) \sigma_{\text{QCD},q\bar{q}}^{\text{LO}} + \log \left(\frac{\mu_F^2}{\mu_R^2} \right) \sigma_{\text{QCD},gg}^{\text{LO}} \right]$$

as explained in Ref. [307], where the same issue has been addressed for the five- and the four-flavour scheme. The quantities $\sigma_{\text{QCD},q\bar{q}}^{\text{LO}}$ and $\sigma_{\text{QCD},gg}^{\text{LO}}$ correspond to the LO QCD cross sections from respectively only the $q\bar{q}$ and gg initial states. By setting $\mu_F = \mu_R$, as done here, the term proportional to $\sigma_{\text{QCD},gg}^{\text{LO}}$ in the r.h.s. of Eq. (5) is equal to zero. In Ref. [151] the $N_f = 5$ scheme was used in combination with NNPDF2.3_QED without including such a subtraction term.

pp \rightarrow W + 2j	SHERPA/MUNICH +OPENLOOPS	ALPGEN
$H_T > 0.5$ TeV	-8.09(2)%	-4.7(2)%
$H_T > 1$ TeV	-12.37(4)%	-9.6(2)%
$H_T > 2$ TeV	-17.8(2)%	-16.6(3)%
$p_{T,j_1} > 0.5$ TeV	-12.56(5)%	-9.4(2)%
$p_{T,j_1} > 1$ TeV	-19.1(2)%	-16.0(3)%
$p_{T,1} > 0.5$ TeV	-21.0(3)%	-20.1(2)%
$p_{T,1} > 1$ TeV	-31(1)%	-31.9(5)%
$E_T^{\text{miss}} > 0.5$ TeV	-22.0(3)%	-20.2(2)%
$E_T^{\text{miss}} > 1$ TeV	-30(1)%	-31.7(4)%

Table IV.6: Relative corrections $\frac{d\sigma^{\text{NLO}}}{d\sigma^{\text{LO}}} - 1$ to the combined $W^+ + 2$ jets and $W^- + 2$ jets production processes. Comparison between the full one-loop results (SHERPA/MUNICH+OPENLOOPS) and the predictions of the logarithmic approximation (ALPGEN).

pp \rightarrow $W^- + 2j$	SHERPA/MUNICH +OPENLOOPS	ALPGEN
$H_T > 0.5$ TeV	-8.12(2)%	-4.3(2)%
$H_T > 1$ TeV	-12.40(6)%	-9.4(2)%
$H_T > 2$ TeV	-17.7(2)%	-16.6(2)%
$p_{T,j_1} > 0.5$ TeV	-12.57(6)%	-9.3(2)%
$p_{T,j_1} > 1$ TeV	-18.9(2)%	-15.3(3)%
$p_{T,1^-} > 0.5$ TeV	-20.8(5)%	-20.0(2)%
$p_{T,1^-} > 1$ TeV	-32(2)%	-32.1(3)%
$E_T^{\text{miss}} > 0.5$ TeV	-21.9(4)%	-20.0(3)%
$E_T^{\text{miss}} > 1$ TeV	-31(1)%	-32.1(3)%

Table IV.7: Relative corrections $\frac{d\sigma^{\text{NLO}}}{d\sigma^{\text{LO}}} - 1$ to $W^- + 2$ jets production. Comparison between the full one-loop results (SHERPA/MUNICH+OPENLOOPS) and the predictions of the logarithmic approximation (ALPGEN).

production [310–313]. Following Eq. (IV.8), the analytic expressions of the process-independent corrections factors have been coded and all the required LO matrix elements are computed numerically by means of the ALPHA algorithm [314].

The ALPGEN results shown in Tables IV.6–IV.9 have been computed by using the `vbjet` package for the production of $nW + mZ + j\gamma + lH + k$ jets with $n + m + j + l + k \leq 8$ and $k \leq 3$. In order to compare the results of the different codes, it is worth recalling the following features of the `vbjet` package: it includes only the first two generations of quarks, the external massive vector bosons are produced on-shell and the matrix elements are computed including the

$pp \rightarrow W^+ + 2j$	SHERPA/MUNICH +OPENLOOPS	ALPGEN
$H_T > 0.5 \text{ TeV}$	-8.03(2)%	-4.5(3)%
$H_T > 1 \text{ TeV}$	-12.33(6)%	-9.9(2)%
$H_T > 2 \text{ TeV}$	-18.0(3)%	-17.3(2)%
$p_{T,j_1} > 0.5 \text{ TeV}$	-12.56(7)%	-9.5(3)%
$p_{T,j_1} > 1 \text{ TeV}$	-19.5(3)%	-15.9(4)%
$p_{T,1+} > 0.5 \text{ TeV}$	-21.1(3)%	-20.1(3)%
$p_{T,1+} > 1 \text{ TeV}$	-30(2)%	-31.9(3)%
$E_T^{\text{miss}} > 0.5 \text{ TeV}$	-22.4(6)%	-20.2(3)%
$E_T^{\text{miss}} > 1 \text{ TeV}$	-28(3)%	-31.7(4)%

Table IV.8: Relative corrections $\frac{d\sigma^{\text{NLO}}}{d\sigma^{\text{LO}}} - 1$ to $W^+ + 2$ jets production. Comparison between the full one-loop results (SHERPA/MUNICH+OPENLOOPS) and the predictions of the logarithmic approximation (ALPGEN).

effect of both QCD and EW interactions. Within the `vbj` package, the Sudakov corrections are computed using on-shell external vector bosons (the Z and W bosons are allowed to decay including spin-correlation effects only at the analyses level in order to apply the cuts listed in Table IV.2), they include the full logarithmic dependence in Eq. (IV.8) for the leading $\mathcal{O}(\alpha_s^2\alpha)$ LO contributions, while they only have double logarithmic accuracy for the subleading $\mathcal{O}(\alpha^3)$ Born processes. In Refs. [308,309] photonic contributions to virtual one-loop EW corrections are split into purely weak and purely electromagnetic terms by introducing a photon *mass* of the order of M_W : in Tables IV.6–IV.9 only the weak part of the photonic contribution has been included. No real corrections have been included in the results from ALPGEN. The input parameters used for the simulation are the ones defined in Table IV.1, with the following exceptions for $W + 2$ jets: as we are dealing with on-shell W bosons, the factorization and renormalization scale for QCD in Eq. (IV.7) depend on M_W^2 , rather than m_b^2 . As the NNPDF2.3 QED PDF set is not available in ALPGEN v2.1.4, we used the MSTW2008LO PDF set for both the $Z + 2$ jets and $W + 2$ jets calculations: even though this implies that a comparison at the level of cross sections is not possible for $W + 2$ jets, the PDF choice does not affect the relative corrections coming from virtual weak contributions.

In Tables IV.6–IV.9 we compare the results for the full relative EW corrections, $\delta_{\text{EW}}^{\text{NLO}}$, from Section 2.2 with the relative EW corrections calculated in the Sudakov approximation. Note that in the latter case no real corrections are included, and the virtual photonic corrections are regularized by a photon mass equal to M_W .

As reported in Tables IV.6–IV.8 the Sudakov approximation implemented in ALPGEN and the full one-loop results are in good agreement (at the percent level) for $W + 2$ jets production for the distributions in the lepton transverse momentum $p_{T,l}$ and the missing energy E_T^{miss} . For the distributions in the transverse momentum of the leading jet p_{T,j_1} and the variable $H_T = p_{T,j_1} + p_{T,j_2} + p_{T,l} + E_T^{\text{miss}}$, the Sudakov approximation tends to deviate by up to 4% from the exact fixed-order calculations in those regions of phase space where the vector boson p_T tends to be soft compared to the transverse momentum of the jets.

For the $Z + 2$ jets case shown in Table IV.9 this behaviour is emphasized. While the Sudakov

pp \rightarrow Z + 2j	RECOLA full	RECOLA*	ALPGEN
inclusive	-2.47(2)%	-2.69(2)%	-
$H_T > 0.5$ TeV	-7.05(3)%	-7.38(3)%	-5.2(3)%
$H_T > 1$ TeV	-12.79(4)%	-13.41(5)%	-10.4(1)%
$H_T > 1.5$ TeV	-17.59(8)%	-18.70(9)%	-13.7(1)%
$H_T > 2$ TeV	-21.7(2)%	-23.8(2)%	-14.9(2)%
$m_{jj} > 0.5$ TeV	-4.33(5)%	-4.56(5)%	-1.4(3)%
$m_{jj} > 1$ TeV	-5.76(8)%	-6.03(8)%	-2(1)%
$m_{jj} > 2$ TeV	-7.3(1)%	-7.6(1)%	-6(1)%
$m_{jj} > 4$ TeV	-8.2(2)%	-8.5(2)%	-15(2)%
$p_{T,j_1} > 0.25$ TeV	-7.64(3)%	-7.99(3)%	-5.8(1)%
$p_{T,j_1} > 0.5$ TeV	-13.09(6)%	-13.83(6)%	-10.4(1)%
$p_{T,j_1} > 0.75$ TeV	-17.5(1)%	-19.0(1)%	-13.0(1)%
$p_{T,j_1} > 1$ TeV	-21.4(2)%	-24.1(3)%	-14.0(2)%
$p_{T,l^-} > 0.25$ TeV	-12.93(8)%	-13.47(9)%	-11.0(1)%
$p_{T,l^-} > 0.5$ TeV	-20.5(2)%	-21.1(2)%	-18.7(1)%
$p_{T,l^-} > 0.75$ TeV	-26.3(4)%	-26.9(4)%	-23.9(1)%
$p_{T,l^-} > 1$ TeV	-30.9(8)%	-31.3(9)%	-28.4(2)%
$p_{T,Z} > 0.25$ TeV	-9.31(4)%	-9.77(4)%	-8.5(1)%
$p_{T,Z} > 0.5$ TeV	-16.37(8)%	-16.9(8)%	-16.3(1)%
$p_{T,Z} > 0.75$ TeV	-22.0(1)%	-22.5(1)%	-21.7(1)%
$p_{T,Z} > 1$ TeV	-27.1(4)%	-27.6(4)%	-26.8(2)%

Table IV.9: Relative corrections $\frac{d\sigma^{\text{NLO}}}{d\sigma^{\text{LO}}} - 1$ to Z + 2jets production. Comparison between the full one-loop results (RECOLA) and the predictions of the logarithmic approximation (ALPGEN, SHERPA). RECOLA* is the full one-loop result where the contribution of b -quarks has been removed from both LO and NLO and the contribution of gluon radiation has been removed from the NLO.

approximation works fine for the distribution in the transverse momentum of the Z boson, deviations between the Sudakov approximation and the exact fixed-order calculation amount to 3% for the distribution in the transverse momentum of the lepton, and reach even 10% for the distributions in the transverse momentum of the leading jet p_{T,j_1} and the variable $H_T = p_{T,j_1} + p_{T,j_2} + p_{T,l^+} + p_{T,l^-}$. It is worth noticing, however, that for Z + 2jets the difference between the ALPGEN predictions and the full one-loop results also originates from the on-shell approximation, as in this approximation the contribution of the diagrams containing a photon connecting the lepton pair to a quark line in the process $pp \rightarrow l^+l^- + 2\text{jets}$ is not included.

2.4 Ratio of the Z to gamma transverse momentum differential cross-section

The ratio of the associated production of a Z/γ^* or a γ with one or more jets has been recently measured in proton–proton collisions at 8 TeV center-of-mass energy by the CMS Collaboration at the CERN LHC [315]. In the limit of high transverse momentum of the vector boson p_T^V ($V = Z, \gamma$) and at LO in perturbative quantum chromodynamics (QCD), effects due to the mass of the Z boson (M_Z) are small, and the cross section ratio of Z + jets to γ + jets as a function of p_T^V is expected to become constant, reaching a plateau for $p_T^V \geq 300$ GeV [316]. (Hereafter, production of $Z/\gamma^* +$ jets is denoted by Z + jets.) A QCD calculation at NLO for $pp \rightarrow Z +$ jets and $pp \rightarrow \gamma +$ jets was provided by the BLACKHAT Collaboration [317]. The NLO QCD corrections tend to decrease the value of the cross section ratio. At higher energies, EW corrections can also introduce a dependence of the cross section on logarithmic terms of the form $\ln(p_T^Z/m_Z)$ that become large and pose a challenge for perturbative calculations.

Searches for new particles involving final states characterized by the presence of large missing transverse energy and hard jets, use the $\gamma +$ jets process to model the invisible Z decays, $Z \rightarrow \nu\bar{\nu}$, since the $\gamma +$ jets cross section is larger than the Z + jets process where the Z decays to leptons. A precise estimate of EW corrections on the cross section ratio for Z + jets and $\gamma +$ jets is therefore crucial to reduce uncertainties related to the $Z \rightarrow \nu\bar{\nu}$ background estimation in these searches.

In the CMS measurement [315], results are unfolded into a fiducial region defined at particle level. For Z + jets events, the leading leptons are required to have $p_T > 20$ GeV and $|\eta| < 2.4$, while jets are required to have $p_T > 30$ GeV within the region of $|\eta| < 2.4$. Electrons and muons have different energy losses due to final-state radiation at particle level. In order to compensate for these differences, a “dressed” level is defined to make the electron and muon channels compatible to within 1%. This is achieved by defining in simulation a particle momentum vector by adding the momentum of the stable lepton and the momenta of all photons with a radius of $\Delta R = 0.1$ around the stable lepton. All jets are required to be separated from each lepton by $\Delta R > 0.5$. At the particle level, a true isolated photon is defined as a prompt photon, around which the scalar sum of the p_T of all stable particles in a cone of radius $\Delta R = 0.4$ is less than 5 GeV. A true isolated photon is defined as a prompt photon (not generated by a hadron decay), around which the scalar sum of the p_T of all stable particles in a cone of radius $\Delta R = 0.4$ is less than 5 GeV. When comparing the cross sections for Z + jets and $\gamma +$ jets, the rapidity range of the bosons is restricted to $|y^V| < 1.4$ because this is the selected kinematic region for the photons. The ratio of the differential cross sections as a function of p_T is measured in the phase-space regions: $N_{\text{jets}} \geq 1, 2, 3$ and $H_T > 300$ GeV, $N_{\text{jets}} \geq 1$.

Figure IV.4 compares several predictions for the ratio within the fiducial regions as defined above⁶. The fixed-order partonic predictions computed with the ALPGEN generator are shown at LO and at approximated NLO accuracy [310], i.e. including the effect of virtual weak corrections in the Sudakov approximation obtained by means of the algorithm of Refs. [308,309], as described in Section 2.3. The predictions for Z+jets and γ +jets are computed in the G_μ and $\alpha(0)$ schemes, respectively, with the set of parameters listed above for the calculation of the $\mathcal{O}(\alpha)$ corrections to the process W+2 jets. The factorization scale is set to $\sum_j p_T^j + \sqrt{M_V^2 + p_{T,V}^2}$. CTEQ5L is used as PDF set: it is worth noticing, however, that PDFs largely cancel in the Z/ γ ratio as pointed out in Ref. [316]. More precisely, the predictions for $\gamma +$ jets and Z + jets are computed by using the `phjet` and `zjet` packages, respectively: at variance with the `vbjet` package, where the external vector bosons are produced on-shell, in `zjet` the Z boson decays in a fermion–antifermion pair including all the off-shell and spin-correlation effects. These packages include only the QCD

⁶We dropped the comparison for $H_T > 300$ GeV because fixed-order predictions are known to fail describing high jet activity with a comparatively low vector boson p_T .

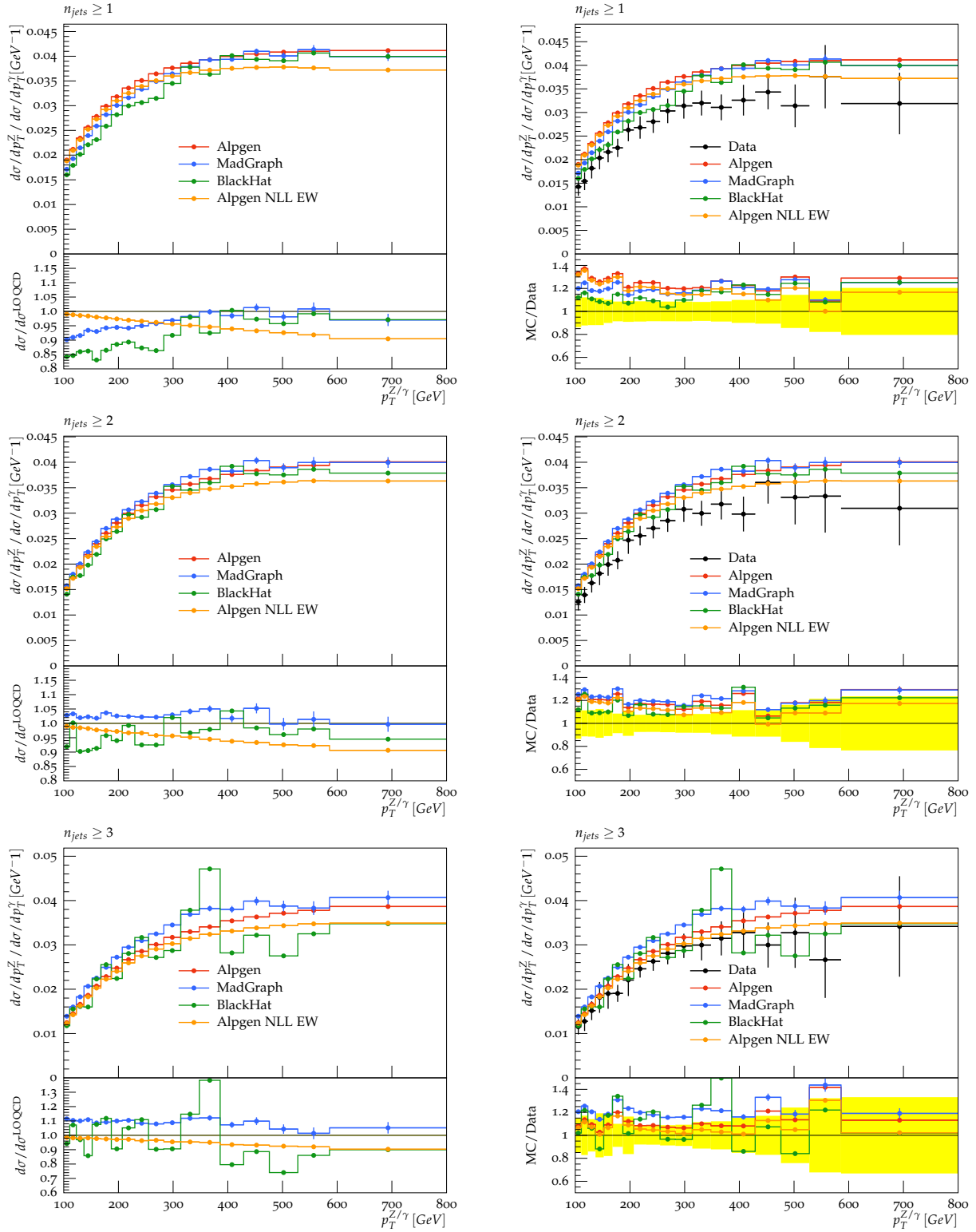


Fig. IV.4: Comparison of different predictions, among them (left) and to CMS data (right), for the ratio of Z + jets over γ + jets at 8 TeV pp center-of-mass energy. From top to bottom, results are shown for events with at least 1, 2 and 3 jets accompanying the boson. For fixed-order predictions this value corresponds to the number of partons in the final state at the lowest order.

contributions of order $\alpha_s^{n_{\text{jets}}}\alpha$ to the LO predictions. Though the LO results for $Z + \text{jets}$ include exactly off-shell and spin-correlation effects, the Sudakov corrections are obtained in the on-shell approximation by using the phase-space mapping described in Ref. [162].

The other predictions are also shown in the CMS paper, where a detailed description of the configuration used can be found. For $Z + \text{jets}$ and $\gamma + \text{jets}$ generated with the MADGRAPH5 [318] program, the LO multiparton matrix-element calculation includes up to four partons in the final state. The showering and hadronization, as well as the underlying event, are modelled by PYTHIA6 [319]. The events are generated with the CTEQ6L1 [189] parton distribution functions, and the ktMLM matching scheme [320] with a matching parameter of 20 GeV is applied. In addition to these Monte Carlo signal data sets, a NLO perturbative QCD calculation from the BLACKHAT Collaboration [317] is available for a boson accompanied by up to three jets. These calculations use MSTW2008nlo68cl [193] with $\alpha_s = 0.119$ as the PDF set, and the renormalization and factorization scales are set to $\mu_R = \mu_F = H_T + E_T^V$, where H_T is the scalar p_T sum of all outgoing partons with $p_T > 20$ GeV and E_T^V is defined as $\sqrt{m_Z^2 + (p_T^Z)^2}$ and p_T^γ , respectively, for $Z + \text{jets}$ and $\gamma + \text{jets}$. In addition, the photons must satisfy the Frixione cone isolation condition [321].

From the plot it is clear that both NLO QCD and EW corrections are negative with respect to the fixed-order LO predictions. The NLO QCD corrections are larger for lower transverse momentum of the bosons, reaching a 15% effect for $N_{\text{jets}} \geq 1$. A fraction of this effect seems to be included by MADGRAPH5 predictions, which include higher-order real-parton emissions in the matrix-element calculation. The EW corrections increase with the boson transverse momentum, up to about 10% for $p_T > 600$ GeV in events with at least one jet. Both QCD and EW corrections decrease for larger jet multiplicities. It can be also noticed that the Madgraph prediction overshoots the NLO QCD ones for larger multiplicities.

In Figure IV.4, these predictions are also compared to CMS results, showing that the agreement improves when NLO corrections are included, both in the case of QCD and EW ones. In particular, including the EW corrections, results are in better agreement in the region of high boson transverse-momenta, especially for larger jet multiplicities.

Finally, Figure IV.5 shows in addition, for events with a vector boson and at least one jet, fixed-order predictions from Sherpa+OpenLoops. The $Z + \text{jets}$ prediction is obtained from an off-shell calculation for $l^+l^- + \text{jets}$ including all Z/γ^* interference effects. The presented predictions are based on the recently achieved automation of NLO QCD+EW calculations [163, 164], as described in Section 2.2. Related predictions for the $Z + \text{jets}/\gamma + \text{jets}$ ratio (with an on-shell Z boson) from Munich+OpenLoops have already been presented in Ref. [322] and have for example been employed for background predictions in Ref. [323]. Here, we employ NNPDF2.3QED [324] parton distributions with $\alpha_s = 0.118$, and all input parameters and scale choices are as detailed in Ref. [164]. In particular, all unstable particles are treated in the complex-mass scheme [292], and renormalization and factorization scales are set to $\mu_{R,F} = \hat{H}'_T/2$, where \hat{H}'_T is the scalar sum of the transverse energy of all parton-level final-state objects, $\hat{H}'_T = \sum_{i \in \{\text{quarks, gluons}\}} p_{T,i} + p_{T,\gamma} + E_{T,V}$. QCD partons and photons that are radiated at NLO are included in \hat{H}'_T , and the vector-boson transverse energy, $E_{T,V}$, is computed using the total (off-shell) four-momentum of the corresponding (dressed) decay products, i.e. $E_{T,Z}^2 = p_{T,\parallel}^2 + m_{\parallel}^2$ and $E_{T,\gamma}^2 = p_{T,\gamma}^2$. The weak coupling constant α is renormalized in the G_μ scheme for the $l^+l^- + \text{jets}$ prediction, while the $\alpha(0)$ scheme is used for the $\gamma + \text{jets}$ prediction. Results are presented at the NLO QCD level and combining QCD and EW corrections via an additive prescription, i.e. $\sigma_{\text{QCD+EW}}^{\text{NLO}} = \sigma^{\text{LO}} + \delta\sigma_{\text{QCD}}^{\text{NLO}} + \delta\sigma_{\text{EW}}^{\text{NLO}}$. Isolated photons in the $\gamma + \text{jets}$ predictions are required to satisfy Frixione cone isolation [321] with parameters as specified in Ref. [315].

The agreement of the combined NLO QCD+EW prediction with the CMS data is re-

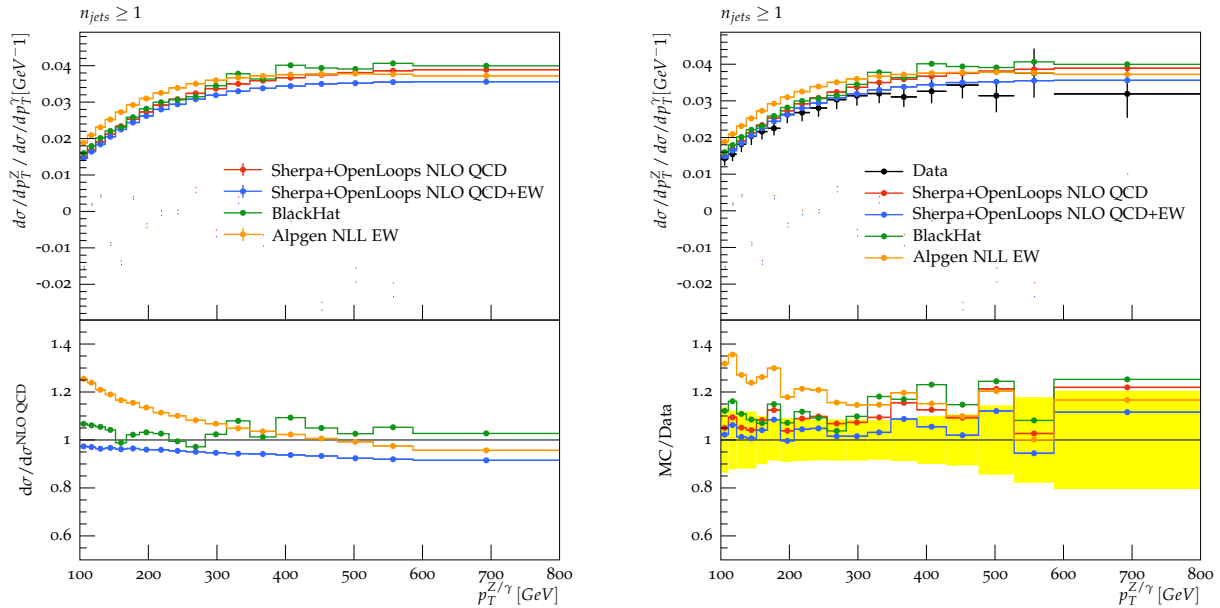


Fig. IV.5: Comparison of different predictions at NLO QCD, NLL EW and NLO QCD+EW order for the ratio of Z + jets over γ + jets at 8 TeV pp center-of-mass energy, in events with at least 1 jet accompanying the boson. For fixed-order predictions this value corresponds to the number of partons in the final state at the lowest order. The left plot shows a comparison among the predictions, the right plot a comparison to CMS data.

markable over the whole spectrum. As already noted, at low transverse momentum NLO QCD corrections to the ratio are relevant due to mass effects, but sizable EW corrections due to EW Sudakov logarithms (of different size for the two processes) alter the shape of the ratio prediction already much below 1 TeV. These results show the importance of combining NLO QCD and EW corrections in a unified framework.

2.5 Conclusions

In this contribution we have performed a comparison of calculations of EW corrections between different automated codes. While it is a non-trivial task to precisely adjust the settings of the different calculations such that they are consistent with each other, we found a typical agreement at the level of one per cent. We also compared the Sudakov approximation to exact NLO calculations. Depending on the considered process and the considered observable the Sudakov approximation can describe the complete EW NLO corrections at the level of one to ten per cent. When comparing CMS data for the ratio of the associated production of a Z/ γ^* or an on-shell photon with one or more jets to theoretical predictions, the inclusion of EW corrections results in a better agreement for high boson transverse momenta.

Acknowledgements

The work of A. Denner was supported by the Deutsche Forschungsgemeinschaft (DFG) under reference number DE 623/2-1. The work of D. Pagani is supported by the ERC grant 291377 “LHCtheory: Theoretical predictions and analyses of LHC physics: advancing the precision frontier”. M. Zaro is supported by the European Union’s Horizon 2020 research and innovation programme under the Marie Skłodowska-Curie grant agreement No 660171 and in part by the ILP LABEX (ANR-10-LABX-63), in turn supported by French state funds managed by the ANR within the “Investissements d’Avenir” programme under reference ANR-11-IDEX-0004-02.

3 A comparative study of Higgs boson plus jets production in gluon fusion ⁷

3.1 Introduction

There has been a great deal of progress in the attack on the Les Houches precision wish list. Such higher order calculations are needed for the full exploitation of precision LHC measurements. However, measurements by the ATLAS and CMS experiments are often compared to predictions involving parton shower Monte Carlos, often supplemented with matrix element information at leading order (LO) and next-to-leading order (NLO). Such frameworks allow for the generation of fully exclusive final states, often more amenable to comparisons with experimental data. There are a number of such matrix-element plus parton-shower (ME+PS) frameworks used by the LHC collider experiments, as can be seen from the predictions in this section. But the higher (fixed) order calculations often provide the highest precision. It is thus important to understand: (1) the degree to which the various ME+PS predictions agree with each other, (2) how well the ME+PS predictions agree with fixed-order predictions and (3) the impact of Sudakov regions⁸ and/or the imposition of jet vetoes/binning on both fixed-order and ME+PS predictions. We come to these comparisons with several expectations: outside of Sudakov regions, the influence of parton showering/resummation should be mild, and cross sections that are fairly inclusive should not be subject to large jet veto logs. This means that for observables like the leading jet's transverse momentum distribution for $h + \geq 1$ jet or the inclusive n -jet cross sections we do not expect any significant resummation correction, originating in either the parton showers or the dedicated resummed expressions. On the other hand, the more exclusive the cross section, the more different scales are involved, the larger the impact of such corrections should be, stabilizing the result. Besides the jet vetoed cross sections, exclusive p_{\perp} spectra, both of the Higgs and any jet, should be highly dependent on the type of resummation included.

The production of a Higgs boson through gluon–gluon fusion is an excellent testing ground for such comparisons, because of the importance of the process, and the enhanced rate for additional jet production associated with gluon–gluon fusion. First comparisons of Higgs production in gluon fusion were done in Les Houches 2013 [325], with comparisons of various predictions for $h + \geq 2$ jets from gluon–gluon fusion, a critical background for the measurement of vector boson fusion. In the present contribution to the Les Houches 2015 proceedings, we extend that study to more observables, for a variety of jet multiplicities, and with comparisons to fixed-order predictions as well as to ME+PS frameworks.

To allow for as standardized a comparison as possible, a group of generation parameters were agreed upon. MMHT2014 NLO PDFs (and the NNLO version for the NNLO calculations) were to be used, with a central value of $\alpha_s(m_Z) = 0.118$. Variations of scale choice are allowed; however, they should reproduce a scale of $\frac{1}{2}m_h$ in the zero-jet limit. All computations were done in the Higgs effective field theory approach in the strict $m_{\text{top}} \rightarrow \infty$ limit. Although this does not constitute a best-of setup for most contributions these common parameters do not alter their underlying methods' properties, capabilities and limits.

Alas, in some cases, there are deviations from these standards. These will be noted where present, and the impact on the comparisons will be discussed. The Higgs boson was left undecayed. Jets were reconstructed with the anti- k_T jet clustering algorithm [326] using $R = 0.4$, and a transverse momentum constraint of 30 GeV was imposed, along with a rapidity cut of $|\eta(j)| < 4.4$. To provide a common framework for the display of the results, a Rivet routine [327, 328] was created and distributed to each group providing a prediction.

⁷ J. R. Andersen, S. Badger, K. Becker, J. Bellm, R. Boughezal, G. Falmagne, R. Frederix, M. Grazzini, N. Greiner, S. Höche, J. Huston, J. Isaacson, Y. Li, X. Liu, G. Luisoni, F. Petriello, S. Plätzer, S. Prestel, I. Pogrebnyak, P. Schichtel, M. Schönherr, P. Sun, F. J. Tackmann, E. Vryonidou, J. Winter, C.-P. Yuan, F. Yuan

⁸By Sudakov region, we refer to kinematic situations where there is a severe restriction on phase space for gluon emission, such as the Higgs boson transverse momentum distribution at low p_{\perp} .

In this contribution, predictions have been made with fixed-order calculations at NLO for $pp \rightarrow h + 1, 2, 3j$ with standard scale choices and the MINLO approach including Sudakov factors (using GOSAM in combination with SHERPA, cf. Secs. 3.2.1-3.2.2), at approximate NNLO (using the LOOPSIM approach, cf. Sec. 3.2.3) and full NNLO for $pp \rightarrow h$ (using SHERPA, cf. Sec. 3.2.4) and $pp \rightarrow h + j$ (using the results of the BFGP group, cf. 3.2.5). These are compared to explicit high-precision resummation calculations for observables of interest, i.e. the inclusive Higgs boson transverse momentum (using HQT and RESBOS2, cf. Secs. 3.2.6 and 3.2.7), and the leading-jet p_\perp spectrum and jet-vetoed zero jet cross section (using the results of the STWZ group, cf. Sec. 3.2.8), as well as to the generic parton shower matched predictions of inclusive Higgs boson production at NNLO (using POWHEG and SHERPA, cf. Secs. 3.2.9 and 3.2.10) and the multijet merged predictions (provided by Madgraph5_aMC@NLO, Herwig 7.1 and SHERPA, cf. Secs. 3.2.11-3.2.13), using NLO matrix element information for up to two (three) jets (SHERPA). For observables requiring the presence of at least two jets, results obtained resumming BFKL-type logarithms (using HEJ, cf. Sec. 3.2.14) are added. Sec. 3.3 then presents the results in detail for a multitude of relevant observables.

3.2 Tools

3.2.1 NLO calculation of $pp \rightarrow h + 1, 2, 3$ jets

We compute $h + 1$ jet, $h + 2$ jets and $h + 3$ jets at NLO in QCD in the infinite top mass limit [329–331] using SHERPA [275] and GOSAM [44, 283], linked via the interface defined in the Binoth Les Houches Accord [332, 333]. The one-loop amplitudes are generated with GOSAM employing QGRAF [334], FORM [335, 336] and SPINNEY [337], The reduction of the loop integrals is performed using NINJA [338–340], GOLEM95 [341–343] and ONELOOP [299] for the evaluation of the scalar integrals. The calculation of tree-level matrix elements for the Born and the real emission contribution as well as the subtraction terms in the Catani-Seymour approach [90] have been done within SHERPA using the matrix element generator COMIX [302].

The computation is performed for a Higgs boson with mass $m_h = 125$ GeV, which is left undecayed. We used the MMHT2014nlo68clas118 PDF set. We present results obtained by processing events pre-generated and stored in form of ROOT Ntuples as described in [344]. Theoretical uncertainties are estimated by varying renormalization and factorization scales by factors of $\frac{1}{2}$ and 2 around the central scale

$$\mu_0 = \frac{1}{2} \sqrt{m_h^2 + \sum p_{T,j_i}^2}, \quad (\text{IV.10})$$

where i runs over all identified jets. This scale was chosen to facilitate comparison with the $h + 1$ jet NNLO calculation of Sec. 3.2.5.

3.2.2 MINLO calculation of $pp \rightarrow h + 1, 2, 3$ jets

Reprocessing the ROOT Ntuples of Sec. 3.2.1, we present fixed order NLO results evaluated with a MINLO [345] scale choice, as implemented in SHERPA, for $pp \rightarrow h + 1, 2$ jets and, for the first time, for $pp \rightarrow h + 3$ jets. Events are read-in by SHERPA, which applies the MINLO prescription event by event. As a MINLO core scale we choose

$$\mu_{\text{core}}^{\text{MINLO}} = \frac{1}{2} \hat{H}'_T = \frac{1}{2} \left(\sqrt{m_h^2 + p_{T,h}^2} + \sum_i p_{T,i} \right) \quad (\text{IV.11})$$

where i runs over all partons of the identified core.

3.2.3 *LOOPSIM merged nNLO calculation of $pp \rightarrow h + (1, 2)$ jets and $pp \rightarrow h + (2, 3)$ jets*

The fixed order Ntuples produced by GOSAM+SHERPA detailed in Sec. 3.2.1 can be combined using the LOOPSIM [346] procedure to make an approximate NNLO prediction, labelled nNLO in the following, which is missing the double virtual corrections but captures much of the double unresolved radiation contributions. There is a cut-off dependence on the additional real radiation since the fixed order Ntuples were generated with a jet $p_T > 25$ GeV. The LOOPSIM procedure uses a flavour sensitive k_T -algorithm where a jet radius of $R = 1$ was used. All other parameters and scales were chosen the same as in the fixed order case with the exception of the PDF where the NNLO PDF set `MMHT2014nnlo68c1` was used.

3.2.4 *NNLO calculation of $pp \rightarrow h$*

For the fully differential calculation of inclusive Higgs production at NNLO accuracy we use the implementation in the SHERPA Monte Carlo event generator presented in [275, 347], in this case without matching it to the parton shower. This calculation is performed using the q_T -slicing technique and was extensively checked against HNNLO [83]. For this study here we set $\mu_R = \mu_F = \frac{1}{2} m_h$ and use the `MMHT2014nnlo68c1` PDF set [183].

3.2.5 *NNLO calculation of $pp \rightarrow h + j$*

The NNLO calculation for Higgs production in association with one or more jets is obtained using the N -jettiness subtraction scheme [87, 160]. The application of this technique to obtain the full NNLO result for Higgs+jet, and its validation against another calculation using sector-improved residue subtraction [80], was described in [85]. In this study we adapt the dynamical scale choice

$$\mu_0 = \frac{1}{2} \sqrt{m_h^2 + \sum p_{T,j_i}^2} \quad (\text{IV.12})$$

for both the renormalization and factorization scales, where the sum runs over all reconstructed jets. This dynamical scale correctly captures the characteristic energy throughout the entire kinematic range. To estimate the theoretical uncertainties we equate μ_R and μ_F and vary them in the range $\frac{1}{2}\mu_0 \leq \mu_{R,F} \leq 2\mu_0$. We use `CT14nnlo` parton distribution functions [182]. The effects of the use of this PDF, as compared to the nominal PDF, should be minimal for most of the kinematic regions studied in this contribution. Jets are reconstructed using the anti- k_T algorithm with $R = 0.4$, subject to the requirements $p_T > 30$ GeV and $|\eta| < 4.4$.

3.2.6 *HQT*

HQT [348, 349] is a numerical program which combines the exact fixed order calculation of the transverse momentum spectrum valid at large q_T at $\mathcal{O}(\alpha_s^4)$ with the resummation of the logarithmically enhanced contributions at small transverse momenta at next-to-next-to-leading logarithmic accuracy. The calculation is performed according to the formalism of [348, 350] and it implements a unitarity constraint such that, upon integration over q_T , the inclusive NNLO cross section is recovered. The results are valid in the large m_{top} approximation. As any perturbative QCD computation in hadron collisions, the results depend on the factorization (μ_F) and renormalization (μ_R) scales. In addition, the resummation procedure introduces an additional scale, dubbed “resummation scale” (Q). The three scales must be chosen of the order of the hard scale of the process, m_h . The numerical results presented here are obtained by using HQT-2.0 with $\mu_F = \mu_R = Q = \frac{1}{2} m_h$ GeV as central scale choice. The procedure to estimate perturbative uncertainties is to perform independent variations of μ_F , μ_R and Q around the central value by a factor of 2 with the constraints $\frac{1}{2} < \mu_F/\mu_R < 2$ and $\frac{1}{2} < Q/\mu_R < 2$.

3.2.7 RESBOS2

RESBOS2 is the updated version of RESBOS [351], which resums the effect of multiple soft gluon radiation to all orders in the strong coupling via the q_T -resummation formalism proposed by Collins-Soper-Sterman [352]. The RESBOS2 prediction for inclusive Higgs boson production via the gluon fusion process includes the full NNLO QCD corrections in the total rate (similar to the setup of a HNNLO calculation) and the NLO contribution to the Higgs boson distribution at large transverse momentum (q_T) [353]. In this calculation, we include NNLL accuracy in the Sudakov factor and NNLO accuracy in the Wilson coefficient functions of the resummed piece, which is matched to the perturbative piece, evaluated at the NLO, in the high q_T region [354]. The renormalization and resummation scales have been varied by a factor of 2 around the central value of $\frac{1}{2}m_h$, with the non-perturbative parameters needed for the q_T resummation calculation taken to be the same values as those in [354]. The MMHT2014nnlo68c1 PDF set has been used.

The RESBOS2 prediction of inclusive Higgs plus jet production via gluon fusion is based on the transverse momentum dependent (TMD) resummation formalism, in the Collins 2011 scheme [355]. The prediction includes the NLL Sudakov factor and the NLO inclusive rate in the resummed piece which is matched to NLO QCD prediction in the large q_T region [356]. Here, q_T denotes the transverse momentum of the Higgs boson and jet system. Thus, the total inclusive rate of Higgs plus jet production, applying a minimum cut on the jet transverse momentum, will agree well with that given by the NLO calculation, such as produced by MCFM [357]. The resummation calculation provides a better description for kinematic distributions of Higgs boson and jet when they are almost back-to-back. In this calculation, we have fixed the resummation scale to be the jet transverse momentum ($p_\perp(j)$), as suggested in [356], and have varied the renormalization scale by a factor of 2 around its central value $\frac{1}{2}m_h$, with the non-perturbative parameters needed for the TMD resummation calculation taken to be the same values as those in [356]. The jets are defined based on the anti- k_T algorithm using $R = 0.4$; they furthermore have to obey the criteria that $p_\perp(j) > 30$ GeV and its rapidity $|\eta(j)| < 4.4$. The MMHT2014nnlo68c1 PDF set has been used.

3.2.8 Jet veto resummation

To resum the p_\perp spectrum of the leading jet as well as the exclusive 0-jet (jet-vetoed) cross section, the STWZ predictions [358] utilize the soft-collinear effective theory (SCET) formalism for jet-veto resummation at hadron colliders as developed in [358–361]. The results are obtained in the HEFT limit, taking $m_{\text{top}} \rightarrow \infty$. Jets are defined with a jet radius of $R = 0.4$ and without any cut on the jet rapidity. The MMHT2014nnlo68c1 PDFs are used. The calculation is carried out to NNLL'+NNLO order. The resummation is performed by renormalization group evolution in virtuality and rapidity space in SCET. The NNLL' resummation includes the RG evolution at next-to-next-to-leading logarithmic order together with the full NNLO singular matching correction, thus incorporating all two-loop virtual and singular real-emission contributions in the resummation. This allows to perform the matching to the full NNLO result by adding purely nonsingular corrections to the resummed contributions, and to achieve a smooth transition to the fixed-order result simply by turning off the RG evolution using profile scales [362, 363]. The perturbative uncertainties are estimated by varying the relevant virtuality and rapidity renormalization scales using profile scale variations, which has been established as a reliable method to assess perturbative uncertainties in resummed predictions. We evaluate separate fixed-order and resummation uncertainties which are added in quadrature [358, 360, 364]. The predictions use a complex value for the hard scale $\mu_H = -i\mu_{FO}$ where $\mu_{FO} = m_h$ is the fixed-order scale, which allows to resum large virtual corrections in the $gg \rightarrow h$ form factor in both the 0-jet limit and the inclusive cross section. This scale choice results in a similar inclusive cross section compared to a standard NNLO calculation with $\mu_R = \mu_F = \frac{1}{2}m_h$. The uncertainty

related to this resummation is estimated by varying the phase of μ_H and is also added in quadrature.

3.2.9 POWHEG NNLOPS

One of the generators under investigation is the NNLOPS prediction of Higgs boson production via gluon fusion [137]. To produce this sample, the Higgs-boson-plus-jet MINLO [345] predictions generated with POWHEG-BOX-v2 [365] are combined with an NNLO accurate analytical calculation by the program HNNLO (v.2.0) [83,241,366] following the instructions in [137]. Here, the rapidity spectrum of the Higgs boson of the POWHEG HJ MINLO prediction is reweighted with the spectrum from HNNLO, while ensuring that NLO precision is kept for the kinematic properties of the first additional jet. In the generation and the HNNLO calculation, the default parameters are set as follows, in particular the renormalization and factorization scales have been set to $\mu_R = \mu_F = \frac{1}{2} m_h$ and the MMHT2014nnlo68c1 [183] has been used. To evaluate the uncertainties in the choice of the renormalization and factorization scales, the 21-point scale variations described in detail in [137] are evaluated. The NNLOPS sample is showered with PYTHIA 8 (v.8.253) [367] using the NNPDF 2.3 leading-order PDF set [194] and the A14 tune [368]. The variation of the renormalization scale also varies consistently the resummation scale in the Sudakov form factor of the MINLO procedure [369]. Other resummation properties are not varied in this simulation.

3.2.10 SHERPA NNLOPS

A second NNLO prediction matched to a parton shower is investigated in this study. The computation is performed in the UN²LOPS method [154,347], which is based on the UNLOPS algorithm for merging inclusive NLO matched calculations of varying jet multiplicity, while leaving their total cross sections unchanged [370,371]. The event samples used in this comparison were generated with an implementation of the UN²LOPS matching scheme in the event generator SHERPA. The NNLO prediction needed for the matching is computed within SHERPA itself, using a q_T cutoff method [372], for details see [154,347]. We used a parton shower based on Catani-Seymour dipole factorization [373,374], which has been matched to the Higgs plus jet NLO calculation using the S-MC@NLO method [375,376]. Renormalization and factorization scales for the fixed-order calculation have been set to $\mu_R = \mu_F = \frac{1}{2} m_h$, and the the parton shower starting scale is set to the same value. The MMHT2014nnlo68c1 PDF set [183] has been used throughout.

3.2.11 Madgraph5_aMC@NLO

Higgs production in gluon fusion, in association with multiple jets, is generated with Madgraph5_aMC@NLO [45] at NLO accuracy using the following commands

```
import model HC_NLO_X0_UF0-heft
generate p p > x0 /t [QCD] @0
add process p p > x0 j /t [QCD] @1
add process p p > x0 j j /t [QCD] @2
output MG5aMC_FxFx_Hjets
```

The first command loads the model that includes the Higgs boson effective coupling to gluons in the $m_t \rightarrow \infty$ limit. This model can be found on the FeynRules [377] website⁹ and was originally created for the studies in [378]. In this model, the Standard Model Higgs boson is called ‘x0’, and therefore the second to fourth commands generate this boson in association with 0, 1 and 2 jets, respectively. The model, and therefore also the definitions of p and j, are in

⁹<http://feynrules.irmp.ucl.ac.be>

the 5 flavour scheme. The ‘/t’ syntax is needed to remove the explicit top quark contributions from the loops (they are already integrated out in the effective Higgs-gluon vertices). By setting the parameter `ickkw` to 3 in the `run_card.dat`, the FxFx merging [379] is turned on. The LHE events are matched to the PYTHIA 8 (v.210) parton shower [367], using the FxFx interface also used in [380]. As central choices for the factorisation and renormalisation scales we use the default value in the `Madgraph5_aMC@NLO` code, which, in the context of FxFx merging, is roughly given by the transverse energy of the Higgs boson, after the partons entering the matrix elements have been clustered to a $pp \rightarrow hj$ configuration. $pp \rightarrow h$ configurations thus are calculated using m_h as the scale. The central merging scale is taken to be 35 GeV, while the variations include 25 GeV and 50 GeV. These scales include values both below as well as above the default minimal jet transverse momentum used in the analysis and should therefore cover the complete range of uncertainties coming from the merging. The uncertainty band is computed by varying the factorisation and renormalisation scales by a factor of 2 up and down from the central value, using the reweighting technique as described in [381], for each of the three choices of merging scales. It is therefore obtained as the bin-by-bin envelope of $3 \times 3 \times 3 = 27$ individual values. This is similar to what is done in [380]—apart from the uncertainties coming from the parton distribution function, which are not taking into account here. Throughout the `MMHT2014nlo68c1` PDF set with $\alpha_s(m_Z) = 0.12$ has been used, as compared to the canonical choice of 0.118. There is a partial cancellation between the effects of the larger scale choice and the larger value of $\alpha_s(m_Z)$, but for most of the comparisons, when there are notable differences, they can be traced to the larger scale choice of `Madgraph5_aMC@NLO`.

3.2.12 *Herwig 7.1*

We provide predictions from NLO merging of $h + 0, 1, 2$ jets at NLO and $h + 3, 4$ jets at LO in the Higgs effective theory. The merging is carried out with the `Herwig 7.1` [382] dipole shower module based on [383, 384], in a modified version of the algorithms set out in [370, 385], and implemented in [386, 387]. The merging implementation will become publicly available in `Herwig 7.1`. We use `Madgraph5_aMC@NLO` [45] generated amplitudes together with `ColorFull` [388] for the point-by-point evaluation of tree-level type objects (tree level matrix elements squared, colour- and spin-correlated matrix elements), and `OpenLoops` [40] for the evaluation of Born/one-loop interferences. Subtraction terms and their integrated counter-parts, phase space generation, integration and process bookkeeping is handled by the `Matchbox` module as outlined in [382].

The algorithm we use is a modified, unitarized merging algorithm. We allow finite, higher-order cross section corrections in higher multiplicity jet bins, but still choose a unitarization procedure to remove potentially dangerous, logarithmic enhanced terms in inclusive quantities. Below the merging scale of 30 GeV, NLO accuracy of the first additional emission off each contribution is reached by the standard subtractive matching. Scales are determined through clustering and the core scale is defined as $\mu_R = \mu_F = \frac{1}{2} m_h$. The shower starting scale is set to the same value. The uncertainty band is obtained by variation of the renormalization and factorization scales of the hard input processes, and is covering all other uncertainties present in the algorithm (specifically, merging and shower scale variations). The `MMHT2014nlo68clas0118` PDF set [183] is used.

3.2.13 *SHERPA MEPS@NLO*

We provide a multijet merged sample of Higgs boson production in gluon fusion in association jets wherein the $h + 0, 1, 2, 3$ jet final states are calculated at NLO accuracy [244, 275, 389, 390]. Therein, NLO QCD computations are matched to the parton shower using a variant of the `S-MC@NLO` method [375, 376, 391]. The one-loop matrix elements are provided by `GOSAM` [283, 330, 331] and are interfaced using the `BLHA` [333] standard.

The individual jet multiplicity contributions are merged using a merging cut of $Q_{\text{cut}} = 20$ GeV. The n -parton matrix elements are then clustered in the scheme of [244,255,389] to find a suitable core configuration and defining $\mu_{\text{core}} = \frac{1}{2} m_h$ for the present study. The factorisation and parton shower starting scales are then set directly to μ_{core} while the renormalisation scale is determined by through CKKW scale setting using the identified emission scales and the above defined core scale. The uncertainties are assessed varying $Q_{\text{cut}} \in [15, 30]$ GeV, ensuring that the description of all analysis jets always proceeds at NLO accuracy. Renormalisation and factorisation scales are varied independently by a factor of two keeping $\frac{1}{2} < \mu_F/\mu_R < 2$. The shower starting scale is varied by a factor $\sqrt{2}$. The MMHT2014nlo68c1as0118 PDF set [183] is used throughout.

3.2.14 HEJ

High Energy Jets (HEJ) describes hard, wide angle (high energy-) emissions to all orders and to all multiplicities. The predictions are based on events generated according to an all-order resummation, merged with high-multiplicity full tree-level matrix-elements. The explicit all-order summation is built on an approximation to the n -parton hard scattering matrix element [392–394] which becomes exact in the limit of wide-angle emissions, ensuring leading logarithmic accuracy for both real and virtual corrections. A first set of sub-leading logarithmic terms are included by allowing one un-ordered gluon emission from quarks. All of these logarithmic terms are important when the partonic invariant mass is large compared to the typical transverse momentum in the event. This is precisely the situation which arises in typical “VBF” cuts, including those used in this study. Matching to the full tree level accuracy for up to three jets is obtained by supplementing the resummation with a merging procedure [395,396].

The implementation of this framework in a fully-flexible Monte Carlo event generator is available at <http://hej.web.cern.ch>, and produces exclusive samples for events with at least two jets. The predictions include resummation also for events with up to two un-ordered emissions, i.e. contributions from the first sub-leading configurations.

The factorisation and renormalisation scales can be chosen arbitrarily, just as in a standard fixed-order calculation. Here, we have chosen to evaluate two powers of the strong coupling at a scale given by the Higgs mass, and for the central predictions the remaining scales are evaluated at $\mu_R = \frac{1}{2} H_T$. Thus, for the n -jet tree-level evaluation,

$$\alpha_s^{n+2} = \alpha_s^2(m_h) \cdot \alpha_s^n(\mu_R). \quad (\text{IV.13})$$

The scale variation bands shown in the plots here correspond to varying $\mu_F, \mu_R \in \{\frac{1}{2}\mu_c, \frac{1}{\sqrt{2}}\mu_c, \mu_c, \sqrt{2}\mu_c, 2\mu_c\}$ with $\mu_c = \frac{1}{2} H_T$, but discarding evaluations where any ratio μ_F/μ_R or μ_R/μ_F is bigger than two (which results in a total of 18 variations around the central scale). The CT10nlo [192,397] parton distribution functions were used in the predictions.

3.3 Results

In the following comparisons, we show the central values of each prediction on the left (both as absolute predictions and in ratio to a reference prediction), and a similar comparison of the predictions with uncertainty bands on the right. The reason for the former is that with the overlapping uncertainty bands, it can be difficult to discriminate the behavior of the central predictions. But it is also useful to compare the uncertainty bands from each prediction given similar prescriptions for scale variation. Note that it is not enough to say that different predictions agree within their scale uncertainty bands. In most cases, the predictions should be held to a higher standard, as the scale logs are common to all of the calculations that are being compared.

In general, the POWHEG NNLOPS calculation has been chosen as the reference for the ratios presented. For some observables, other calculations have been chosen, especially if that reference calculation has the highest precision. Predictions of similar precision are typically grouped together to improve readability. The top ratio plot always compares the NNLOPS predictions to the reference. The second ratio plot then contains the multijet merged predictions, while the third ratio plot has the predictions at pure fixed order. Additional ratios are added as needed. The BFKL resummation of HEJ is inserted into the top ratio plot where applicable.

3.3.1 Inclusive observables

This section contains observables which characterize the h +jets phase space in the most inclusive way. Only the presence of a Higgs boson is required, with no restrictions on its momentum. Two important predictions in this category then are the rapidity and the transverse momentum distribution of the Higgs boson. The latter is differentiated into two cases: the inclusive spectrum of the Higgs boson and the exclusive spectrum, requiring zero accompanying jets. Also, to get an overview on the amount of QCD activity accompanying Higgs boson production, we examine the predictions for the inclusive as well as exclusive cross sections for various jet multiplicities as obtained by the different approaches.

We start by examining the inclusive Higgs boson rapidity distribution in Figure IV.6. While the absolute predictions are given in the top panel, the plots in the bottom panel depict the respective ratios to the NNLO prediction. For better visibility, we have divided the predictions into three groups based on their simulation type and/or claimed accuracy. The upper ratio plot contains the NNLO predictions, while the middle ratio plot shows predictions obtained from different strategies for merging matrix elements plus parton showers at NLO. The lower ratio plot displays the comparison between the pure NNLO prediction and the matched result from RESBOS2 that includes the effects from the q_T -resummation. Overall, we find very good agreement in the description of the shape of the Higgs boson rapidity distribution. The main source of deviations stems from the different normalizations given at NNLO or NLO and the different (core) scale choices. As expected, the SHERPA NNLOPS and POWHEG NNLOPS results agree well with the fixed-order NNLO prediction. The larger fluctuations found for SHERPA NNLOPS wrt. POWHEG NNLOPS stem from the fact that the former is computed directly rather than reweighted from an NLO computation for hj final states. RESBOS2 predicts a slightly smaller rate for $y(h) < 2$ and a slightly larger rate for $2 < y(h) < 3.5$ than the one given by the NNLO calculation. The `Madgraph5_aMC@NLO`, SHERPA MEPS@NLO and Herwig 7.1 have slightly lower (NLO) normalizations. Here, the `Madgraph5_aMC@NLO` scale choice reducing to m_h , rather than $\frac{1}{2}m_h$, is clearly noticeable. The upper edge of the `Madgraph5_aMC@NLO` uncertainty band (equal to a scale that reduces to $\frac{1}{2}m_h$) agrees with the central value of the other NLO ME+PS predictions. There are no major differences in the size of the uncertainty envelopes, although to some extent, the NNLO scale uncertainty bands (including RESBOS2) are smaller than those at NLO, as expected. Note that the NLO-based predictions fall off more rapidly at higher y than the NNLO-based predictions do. This is expected because of the influence of additional $\ln(1-x)$ corrections present in the determination of NNLO PDFs. Similar effects can be observed in going from LO to NLO.

In Figures IV.7 and IV.8, the inclusive and exclusive (i.e. vetoing events with jets above 30 GeV) Higgs boson transverse momentum distributions are shown, respectively. For the former, the ratios in the bottom panels are taken with respect to the HQT result, while POWHEG NNLOPS serves as the reference for the latter case. In general, good agreement is found, with differences being somewhat more pronounced in the exclusive case. For the inclusive version of the $p_\perp(h)$ observable, good agreement is observed with HQT, with some larger deviations evident at very low p_\perp . Here, the resummation properties of the different parton showers dominate the

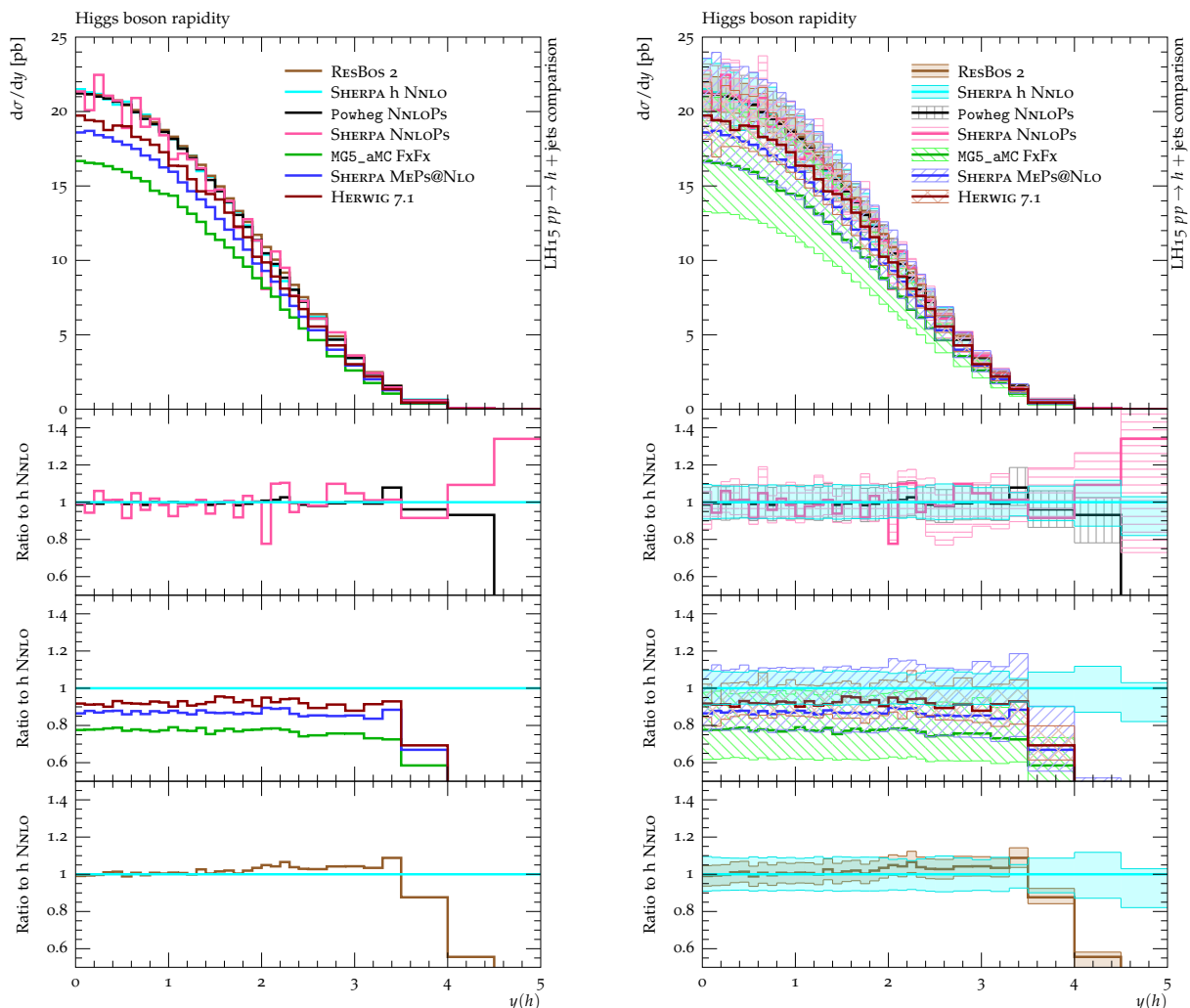


Fig. IV.6: The inclusive Higgs boson rapidity without (left) and with (right) uncertainties. To enhance visibility, the NNLOPs, multijet merged and analytic q_T -resummation predictions are grouped together and shown with respect to the same reference curve in the upper, lower and middle ratio plots, respectively. The reference prediction is taken from the NNLO-accurate description of inclusive h production.

spectra of the matched and merged predictions. While at low p_\perp the SHERPA NNLOPs curve starts about 15% higher than both HQT and POWHEG NNLOPs, it approaches the HQT results at higher p_\perp . The POWHEG NNLOPs prediction follows HQT closely up to p_\perp values of $\sim m_h$. The differences observed beyond that value are due to the dynamical scale choice employed by POWHEG NNLOPs. The multijet merged calculations, due to their similar scale choices, follow the pattern of the POWHEG NNLOPs prediction. Note that the differences in Madgraph5_aMC@NLO's central scale choice becomes less significant as the Higgs boson transverse momentum increases. Herwig 7.1 clearly provides the softest spectrum and SHERPA as well as Madgraph5_aMC@NLO predict a noticeably different shape for the Sudakov suppression at low p_\perp , which is not covered by the HQT uncertainty envelope. For SHERPA, the more significant suppression of the lowest p_\perp values can be traced back to the performance of the CSSHOWER which tends to radiate more strongly in this region. The third ratio plot finally presents the direct comparison between the two analytic resummation approaches, HQT and RESBOS2, which are in good agreement with each other. The leftover $\mathcal{O}(10\%)$ deviations between the two approaches can be attributed to

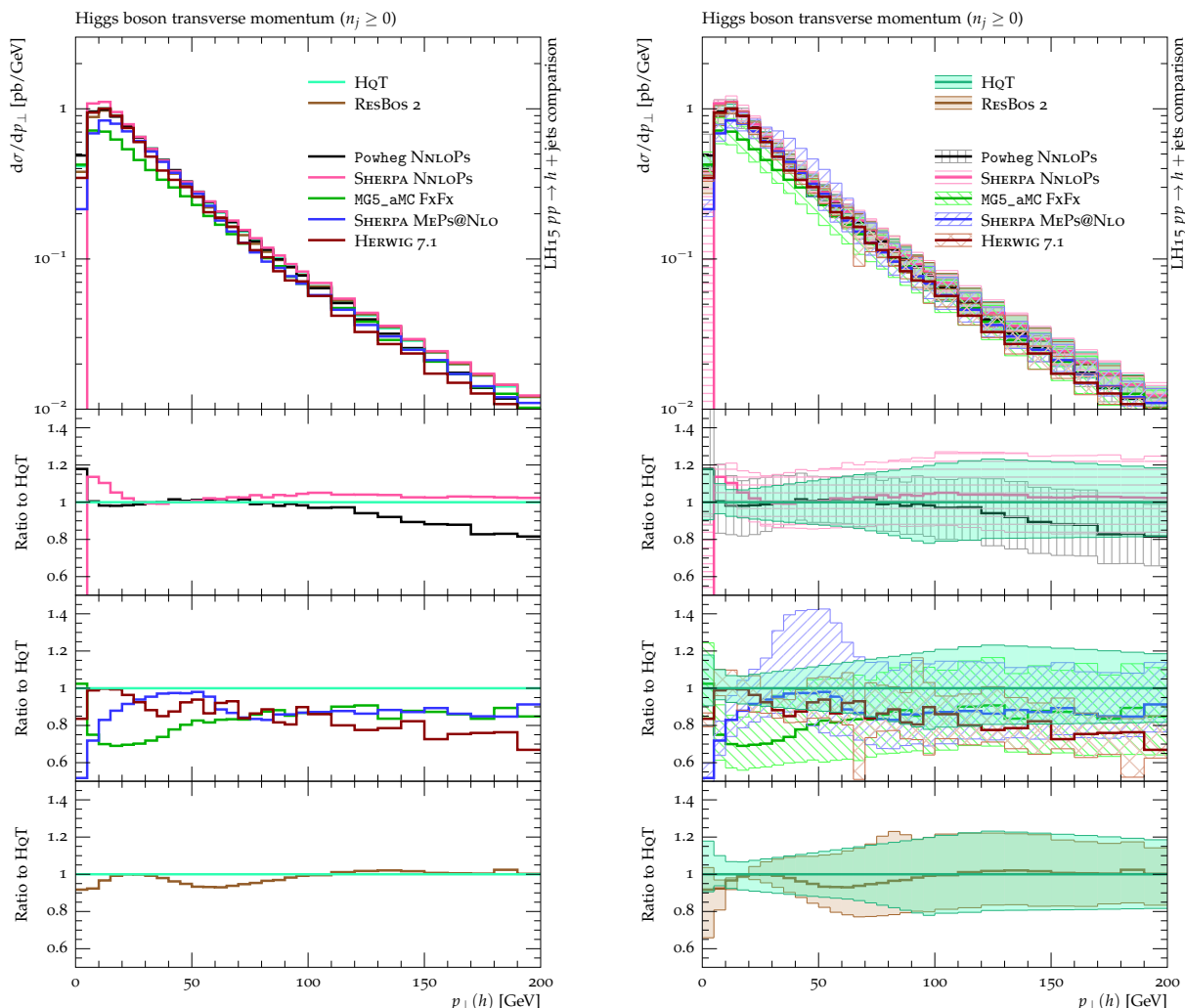


Fig. IV.7: The Higgs boson transverse momentum in the inclusive event selection without (left) and with (right) uncertainties. For the ratios in the bottom panel, the same grouping strategy has been used as in Figure IV.6, while the reference prediction has been changed from that of pure NNLO to the one as given by HQT.

non-perturbative effects, still included in the latter, and the different handling of the process-dependent pieces in the CFG and CSS schemes. The RESBOS2 scale variation band features a cross-over point at $p_{\perp}(h) \approx 20$ GeV but this does not indicate or imply a vanishing uncertainty at this point. Lastly, we refrain from showing any fixed-order prediction here because they are neither stable nor reliable at low p_{\perp} in the Sudakov region where resummation effects play a dominant role.

As shown in Figure IV.8, the exclusive version of the Higgs boson $p_{\perp}(h)$ distribution exhibits deviations among the predictions that are more sizable. The $p_{\perp}(h)$ distribution declines much faster, easily spanning three orders of magnitude between zero and 100 GeV. This observable is less straightforward than the inclusive p_{\perp} -spectrum, as not only do Sudakov effects dominate the low- p_{\perp} region, but resummation effects are also entering through the veto on any jet activity. A reliable description of the observable therefore necessitates both a proper understanding of the small $p_{\perp}(h)$ region and of jet production. Thus, this is a stringent test of all predictions combining matrix elements and parton showers (ME+PS), as the high transverse momentum of the Higgs boson is produced by a combination of soft jets (those that are below

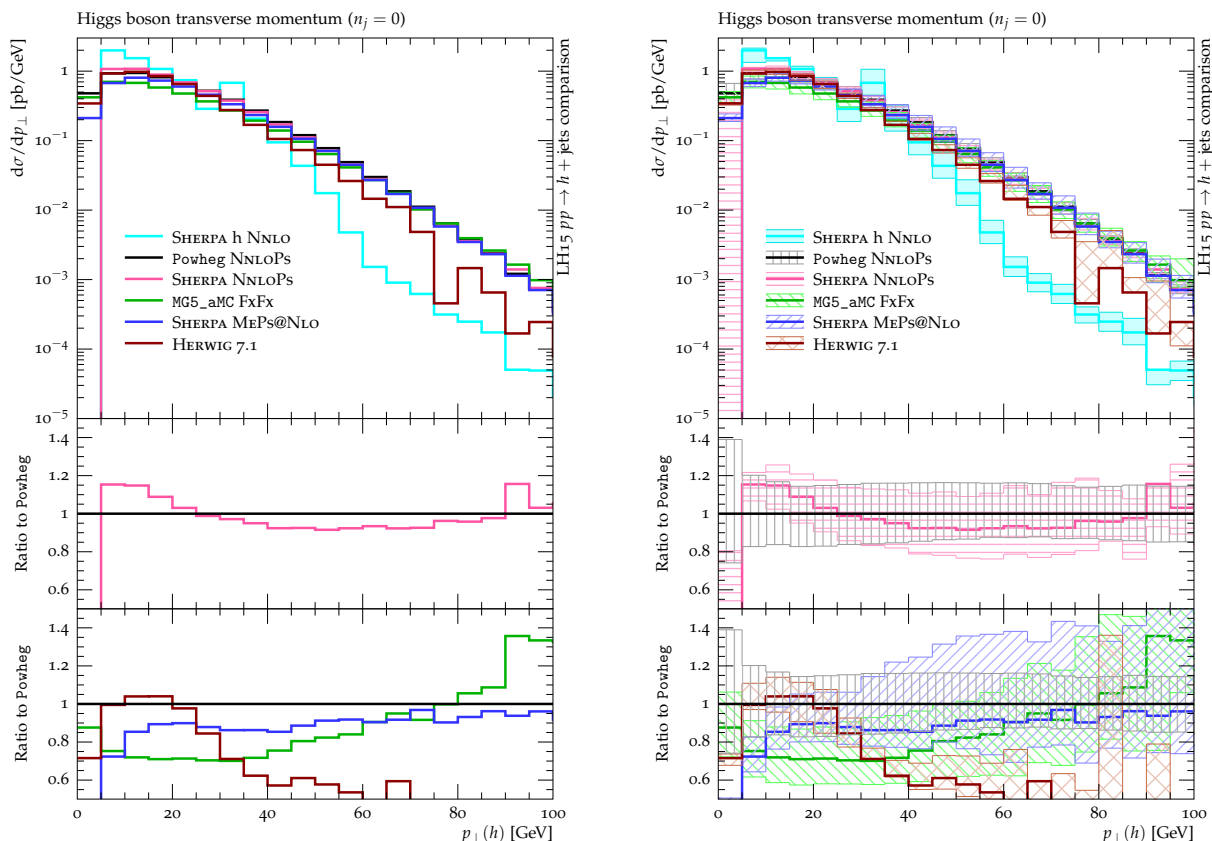


Fig. IV.8: The Higgs boson transverse momentum in the exclusive event selection (i.e. in the absence of any jet) without (left) and with (right) uncertainties. The panels have been arranged as in the previous figure, apart from dropping the last panel, and switching to a new reference curve obtained from POWHEG NNLOPS.

the 30 GeV threshold) and soft gluon radiation. Note that the comparison is now taken with respect to POWHEG NNLOPS. The inclusive NNLO calculation is shown for this case in order to demonstrate the failure of a fixed-order calculation on both accounts; thus, only the parton showered predictions are included in the study of the respective differences. Among them, apart from the differences already seen in the inclusive spectrum, both NNLOPS calculations agree well with one another, remaining within the 20% uncertainty bands throughout the spectrum. While the SHERPA MEPS@NLO prediction remains mostly flat with respect to the NNLOPS predictions, both `Madgraph5_aMC@NLO` and `Herwig 7.1` exhibit shape differences at larger transverse momenta. In the case of `Herwig 7.1`, the deviations grow larger than 40%. From the resummation (i.e. parton-shower) point-of-view, all predictions are at a similar level here, although formally the NNLOPS techniques should lead to a more accurate description of the exact zero-jet bin. The NLO merging approaches reduce to an NLOPS treatment in this zero-jet bin. It is however hard to infer this formal difference from the behavior of the scale variation bands as they are very comparable in size among all predictions. We conclude that the deviation of the predictions probably provides us with a better reflection of the true uncertainty.

To obtain a first impression of how the different predictions compare beyond the zero-jet bins ($n_j \geq 0$ and $n_j = 0$), we now examine the various inclusive and exclusive n_j cross sections. Accordingly, Figures IV.9 and IV.10, respectively, show the inclusive ($n_j \geq N$) and the exclusive ($n_j = N$) jet multiplicity distributions up to $N = 3$, requiring anti- k_T jets with $p_{\perp} > 30$ GeV. Two statements can be made before discussing the individual results in more detail: first of all,

Order	$\mu_R = \mu_F = \frac{1}{2} m_h$	$\mu_R = \mu_F = \frac{1}{2} \sqrt{\Sigma_T}$	$\mu_R = \mu_F = \frac{1}{2} \hat{H}'_T$
NLO	$17.0^{+3.0}_{-2.9}$ pb	$16.2^{+3.1}_{-2.8}$ pb	$13.5^{+2.0}_{-2.1}$ pb
NNLO	–	$16.4^{+0.0}_{-0.9}$ pb	–

Table IV.10: The total cross section for the inclusive production of a Higgs boson and one additional jet using different core scale choices. The two dynamical scales are $\Sigma_T = m_h^2 + \sum_{\text{jets}} p_T^2$, see also Eq. (IV.12), and $\hat{H}'_T = m_{T,h} + \sum_{\text{partons}} p_T$, see also Eq. (IV.11). We note that though the NNLO figures are not available for $\frac{1}{2} \hat{H}'_T$ or $\frac{1}{2} m_h$, the variations will be very small.

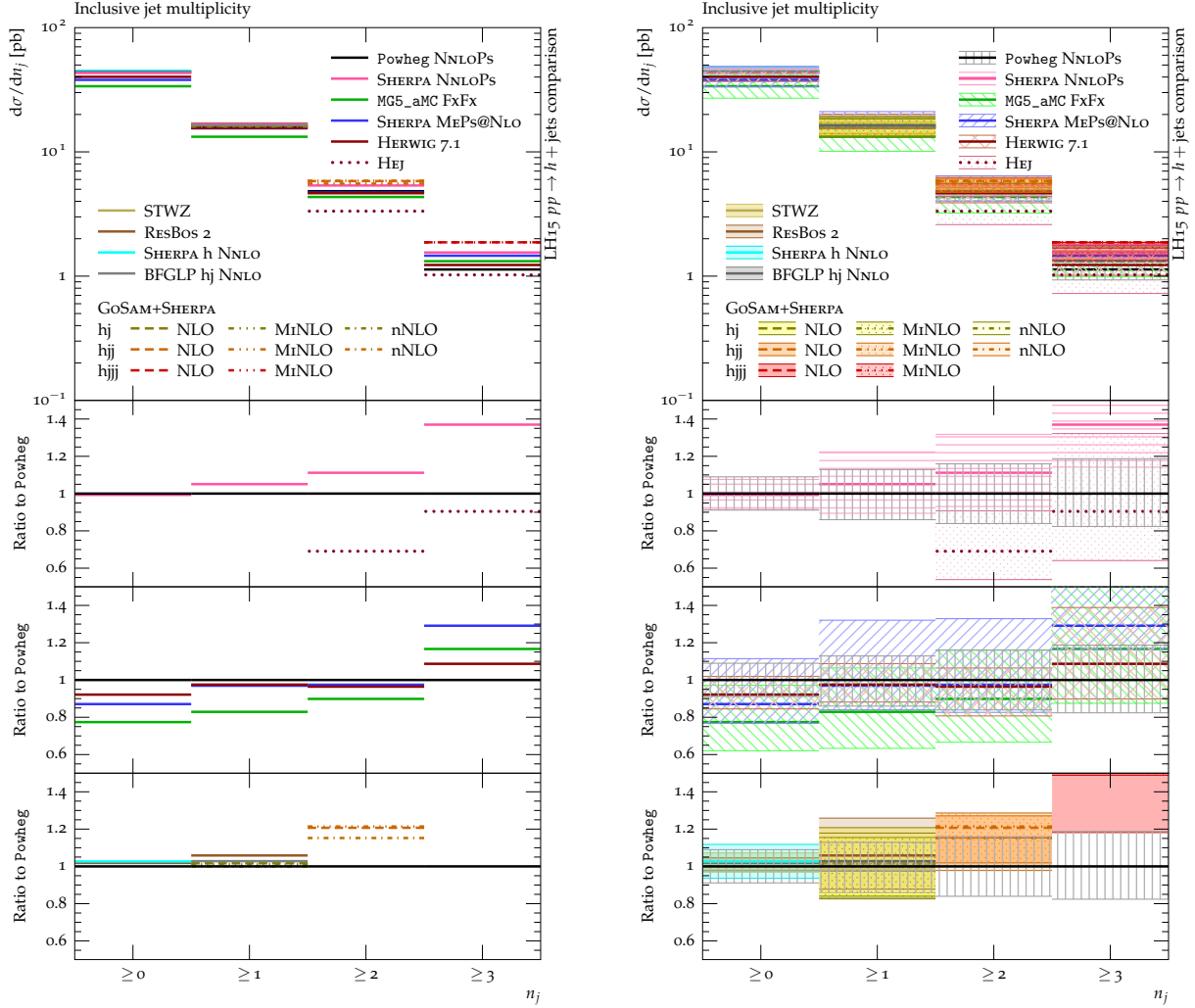


Fig. IV.9: The central predictions on their own (left panel) and including their theoretical uncertainties (right panel) for the inclusive jet multiplicities as predicted by fixed-order calculations, resummed calculations, NNLO and NLO Monte Carlos. The bottom panel is divided up into three subplots all showing the ratios with respect to the POWHEG NNLOPS prediction. The upper of these plots contains the HEJ and SHERPA NNLOPS ratios, while the middle one includes all NLO merged predictions (Madgraph5_aMC@NLO, Herwig 7.1 and SHERPA) and the lower one shows all those listed in the bottom left legend of the main panel.

the agreement between all results is basically very good, and second, the level of agreement is barely altered for exclusive jet predictions compared to the inclusive jet predictions. Although not shown here, when the minimum jet- p_{\perp} threshold is increased to 50 GeV the picture does not change significantly. Again, the bottom panels are split up into several ratio plots with the common reference provided by the POWHEG NNLOPS result. The upper ratio plot depicts the NNLOPS methods together with HEJ, which provides predictions only starting at $N = 2$. Due to the similar core scale choices in either NNLOPS calculation, they share a common fully inclusive cross section, with SHERPA being greater than POWHEG for higher jet multiplicities. Conversely, HEJ undershoots by 30% in the two-jet bin; however, this bin is described with an accuracy no higher than LO by all predictions in this upper panel. In the three-jet bin ($N = 3$), HEJ retains LO accuracy, while both NNLOPS calculations produce this cross section by their respective parton showers only. It is thus natural to find the largest differences between the NNLOPS predictions for $N = 3$. Please note that the respective parton shower uncertainties are partially incorporated in the SHERPA NNLOPS uncertainty estimate, while they are not assessed for POWHEG, resulting in a rather slowly increasing uncertainty band for rising $N \leq n_j$. And, more surprisingly, the POWHEG band remains very flat in the $N = n_j$ case. The central ratio plot compares the NLO matched and merged predictions with each other and against the common reference POWHEG NNLOPS. All these predictions claim NLO accuracy for $N = 0, 1, 2$, and thus overlap well within uncertainties, where the lower value for Madgraph5_aMC@NLO can again be attributed to the different scale choice. Again, with the same scale choice, all of the calculations should agree much better. For $N = 3$, only the SHERPA MEPS@NLO prediction retains NLO accuracy, while Madgraph5_aMC@NLO and Herwig 7.1 revert to LO accuracy, which is nicely reflected in the sizes of the uncertainty estimates. Unsurprisingly, in the $N = 3$ case, all three NLO merged calculations predict larger cross sections with respect to the reference whose rate is only given by the parton shower, i.e. PYTHIA.

Lastly, fixed-order predictions are shown for all jet multiplicities at NLO (provided by GOSAM+ SHERPA) for the 1-jet, 2-jet and 3-jet bins and at approximate NNLO (labeled nNLO, provided by LOOPSIM) for the 1-jet and 2-jet bins. Complete NNLO predictions are shown for the 0-jet inclusive and exclusive bins using SHERPA (without PS), and for the 1-jet inclusive bin using the prediction of Boughezal et al. (BFGLP). The zero-jet bin comparison also contains the resummation prediction of Stewart et al. (STWZ); the comparisons for the $n_j \geq 1, 2, 3$ jet bins also include the MINLO enhanced NLO calculations. Figure IV.9 also contains the RESBOS2 q_T -resummed predictions in the zero-jet bin (with precision corresponding to NNLO+NNLL) as well as in the one-jet bin (with precision corresponding to NLO+NLL). All of the above are grouped together in the lower ratio plot. For the zeroth bin, good agreement can be found between POWHEG and SHERPA h NNLO as well as with the STWZ approach and RESBOS2; the uncertainties also are of comparable size, except for the significantly wider $n_j = 0$ envelope of POWHEG. In the 1-jet case, POWHEG (being NLO-accurate in this bin) sits less than 3% below the pure NLO prediction, with the small difference being due to slightly different scale choices. Unlike the inclusive Higgs boson production case, the NNLO corrections for inclusive 1-jet production are small (cf. Table IV.10)– slightly positive for the central scale choice as given in Eq. (IV.12). There is a notable decrease in the scale uncertainty with respect to the NLO band given by GOSAM+SHERPA. As expected, the uncertainty envelope of the RESBOS2 prediction is of similar size while its central value is about 5% higher than the reference as a result of its scale choice being $\mu = \frac{1}{2}m_h$. The 2-jet bin shows the GOSAM+SHERPA NLO prediction 10-20% above POWHEG, which gives a LO prediction in this case. For the same reason, we assume that the POWHEG uncertainties in the higher jet multiplicities are probably underestimated. In the 3-jet bin (both inclusive and exclusive), the GOSAM+SHERPA and SHERPA MEPS@NLO predictions clearly indicate the presence of NLO corrections in the third jet bin. The LOOPSIM inclusive results for h_j and $h_j j$ are always somewhat below the respective GOSAM+SHERPA results, and in the

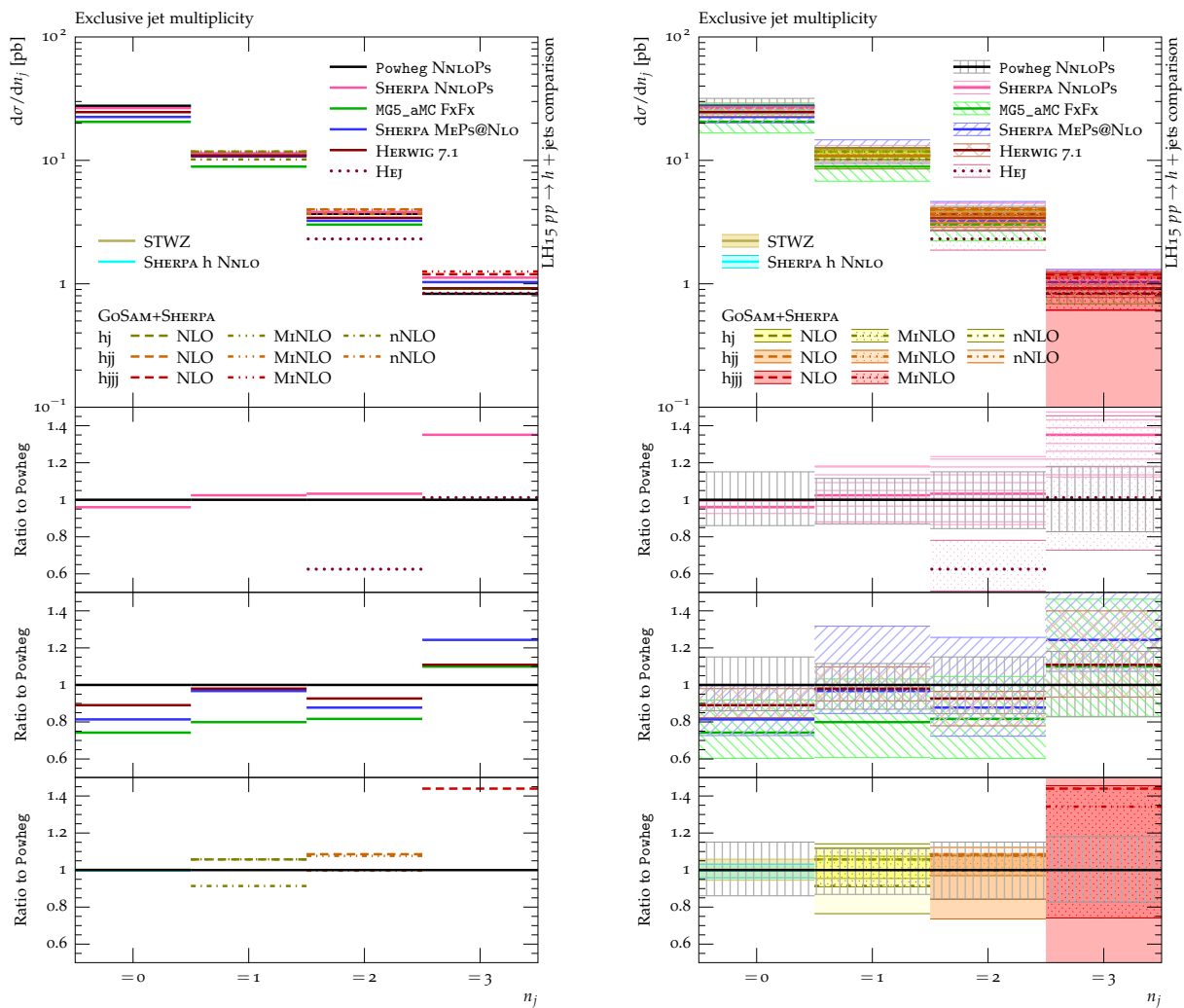


Fig. IV.10: The central predictions on their own (left panel) and including their theoretical uncertainties (right panel) for the exclusive jet multiplicities as predicted by fixed-order calculations, resummed calculations, NNLO and NLO Monte Carols. The bottom panel is divided up into three subplots all showing the ratios with respect to the POWHEG NNLOPs prediction. The upper of these plots contains the HEJ and SHERPA NNLOPs ratios, while the middle one includes all NLO merged predictions (Madgraph5_aMC@NLO, Herwig 7.1 and SHERPA) and the lower one shows all those listed in the bottom left legend of the main panel.

exclusive case this difference gets more pronounced. However, the relatively large Monte Carlo generation cut of 25 GeV means that the total rates predicted by LOOPSIM should be interpreted with care. Furthermore, compared to the NLO benchmark, the MINLO approach predicts 10-20% larger cross sections for all $n_j \geq 1, 2, 3$ jet bins. Note that the MINLO ratio for inclusive $hjjj$ turns out to be outside the plot range appearing at around 1.65, with the lower edge of the uncertainty band at a ratio value of 1.5. In the cases where NNLO precision is available, the reduction in scale uncertainty is clear. For $n_j \geq 1$ the variation around $\mu_R = \sqrt{\Sigma_T}/2$ is about 5.5% while for $n_j \geq 0$ it is about 10.0% around $\mu_R = \frac{1}{2}m_h$. The latter result can be improved to only a few percent using the N³LO prediction of Anastasiou et al. [2]. In order to compare more easily with results presented previously in the literature, we give numerical values at NLO and NNLO for different scale choices in Table IV.10. As observed previously [80], the convergence of the total cross section predictions is improved for scales that limit to $\frac{1}{2}m_h$. The dynamical

scale of $\sqrt{\Sigma_T}$ defined in Eq. (IV.12) is slightly harder than the fixed scale given the minimum jet $p_\perp(j) > 30$ GeV. On the other hand it is softer than \hat{H}'_T defined in Eq. (IV.11) which explains the differences observed at NLO.

3.3.2 One-jet observables

In this section, we move away from the fully inclusive picture and require the presence of at least one or exactly one jet associated with the Higgs boson. Recall that the jets are defined based on the anti- k_T algorithm using $R = 0.4$; they furthermore have to fulfil the selection criteria that $p_\perp(j) > 30$ GeV and $|\eta(j)| < 4.4$. The set of observables presented here includes the transverse momentum distributions of the Higgs boson h , the leading jet j_1 and the hj_1 two-body system as well as the rapidity spectrum of the leading jet.

The Higgs boson transverse momentum distribution in the presence of at least one jet is shown in Figure IV.11. The exclusive version of this plot, i.e. where one requires the Higgs boson and the jet to be the only resolved final state objects, is presented in Figure IV.12. As for the zero-jet cases discussed earlier in Figures IV.7 and IV.8, the one-jet $p_\perp(h)$ variables are prone to large Sudakov effects that arise at low p_\perp , but are also present beyond this region, in particular for the exclusive final states. Moreover, the Sudakov shoulder effect can be observed for all fixed-order predictions shown here. The jet- p_\perp threshold leads to a non-smooth behavior of the $p_\perp(h)$ observable at LO, and therefore to the existence of a critical point at 30 GeV, for which the cancellations between real and virtual soft-gluon singularities will be imperfect at any given fixed, higher order in perturbation theory [398]. For the BFGLP hj NNLO prediction, an averaging procedure has been used to dampen the effect around the jet threshold, while for the NLO predictions, the large oscillations are a clear indication of the instability emerging at the jet threshold. The NNLOPS, NLO ME+PS and RESBOS2 predictions do not suffer from the Sudakov shoulder effect since they include the necessary all-order resummation corrections.

Comparing the different fixed-order predictions, which are detailed in the third ratio plot, noticeable differences only occur between the NNLO prediction and the four NLO predictions as obtained from POWHEG and the three variations on GOSAM+SHERPA (pure NLO, MINLO and LOOPSIM). The NNLO tail is harder by about 15% which is expected since the p_\perp tail is affected by multijet contributions. The NNLO treatment includes these contributions to a larger extent, as it includes $h + 2$ -jet and $h + 3$ -jet contributions at NLO and LO, respectively. For $p_\perp(h) < 30$ GeV, the (N)NLO description is degraded to (N)LO. Here, the presence of the $\mathcal{O}(\alpha_s)$ term of the Sudakov resummation, also included in the NLL resummation of RESBOS2, affects the BFGLP hj NNLO calculation. However, it can also be noticed (see fourth ratio plot in Figure IV.11) that apart from the BFGLP hj NNLO calculation, RESBOS2 and also POWHEG, all other approaches predict a more steeply falling shoulder resulting in a significantly lower cross section as $p_\perp(h) \rightarrow 0$. For larger $p_\perp(h)$ values, $p_\perp(h) \gtrsim \frac{1}{2}m_h$, in general there is good agreement between POWHEG, Madgraph5_aMC@NLO, SHERPA MEPS@NLO and the NLO curves; this can be expected as these predictions are all NLO-accurate. As before, Herwig 7.1 tends to be softer, whereas Madgraph5_aMC@NLO, using the nominal $\frac{1}{2}m_h$ core scale, turns out to be harder by almost 40%, as indicated by the upper edge of its corresponding uncertainty band (see the second or last subplot to the right in Figure IV.11). SHERPA's NNLOPS prediction also features a harder tail than POWHEG owing to the different scale setting procedures employed by the two approaches. While in POWHEG the scale setting is accomplished through the MINLO procedure, SHERPA's NNLOPS uses the fixed scale choice of $\frac{1}{2}m_h$ and therefore enhances the p_\perp tail with respect to POWHEG's result. In this region, the RESBOS2 prediction closely resembles the one given by SHERPA NNLOPS, since it is dominated by the fixed-order contribution evaluated with the same scale choice as used in SHERPA.

We furthermore observe that apart from the BFGLP hj NNLO computation, all uncer-

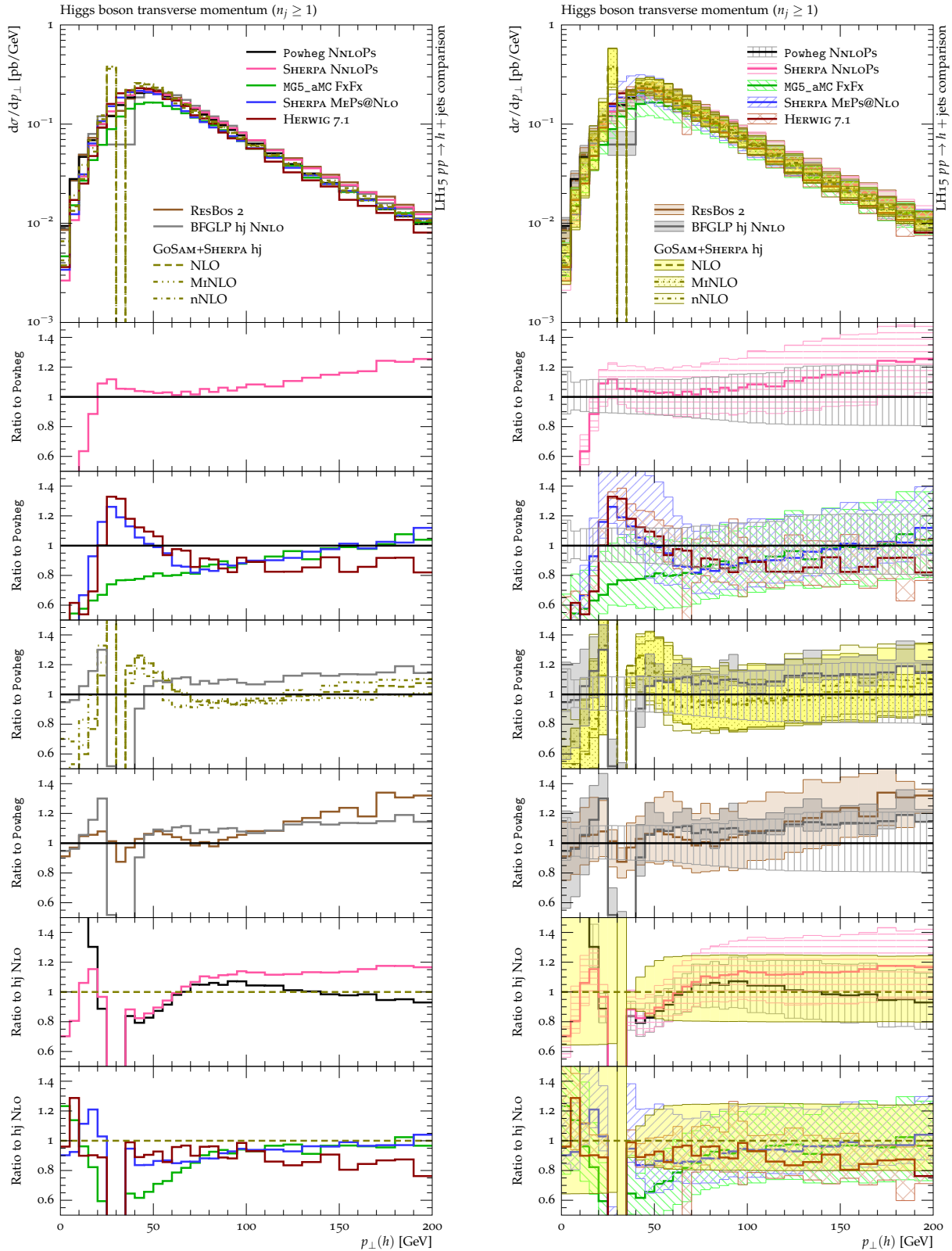


Fig. IV.11: The Higgs boson transverse momentum in the presence of at least one jet without (left) and with (right) uncertainty bands. The ratio plot panel is divided into six parts where the upper four exhibit the ratios wrt. the POWHEG NNLOs result while the lower two show them wrt. the NLO calculation for $h+1$ jet as provided by GOSAM+SHERPA. The grouping in the ratio plots has been arranged to separately compare with each other the NNLOs predictions (first and fifth subplot), the NLO merging predictions (second and last subplot) and the fixed-order predictions (third subplot in the middle).

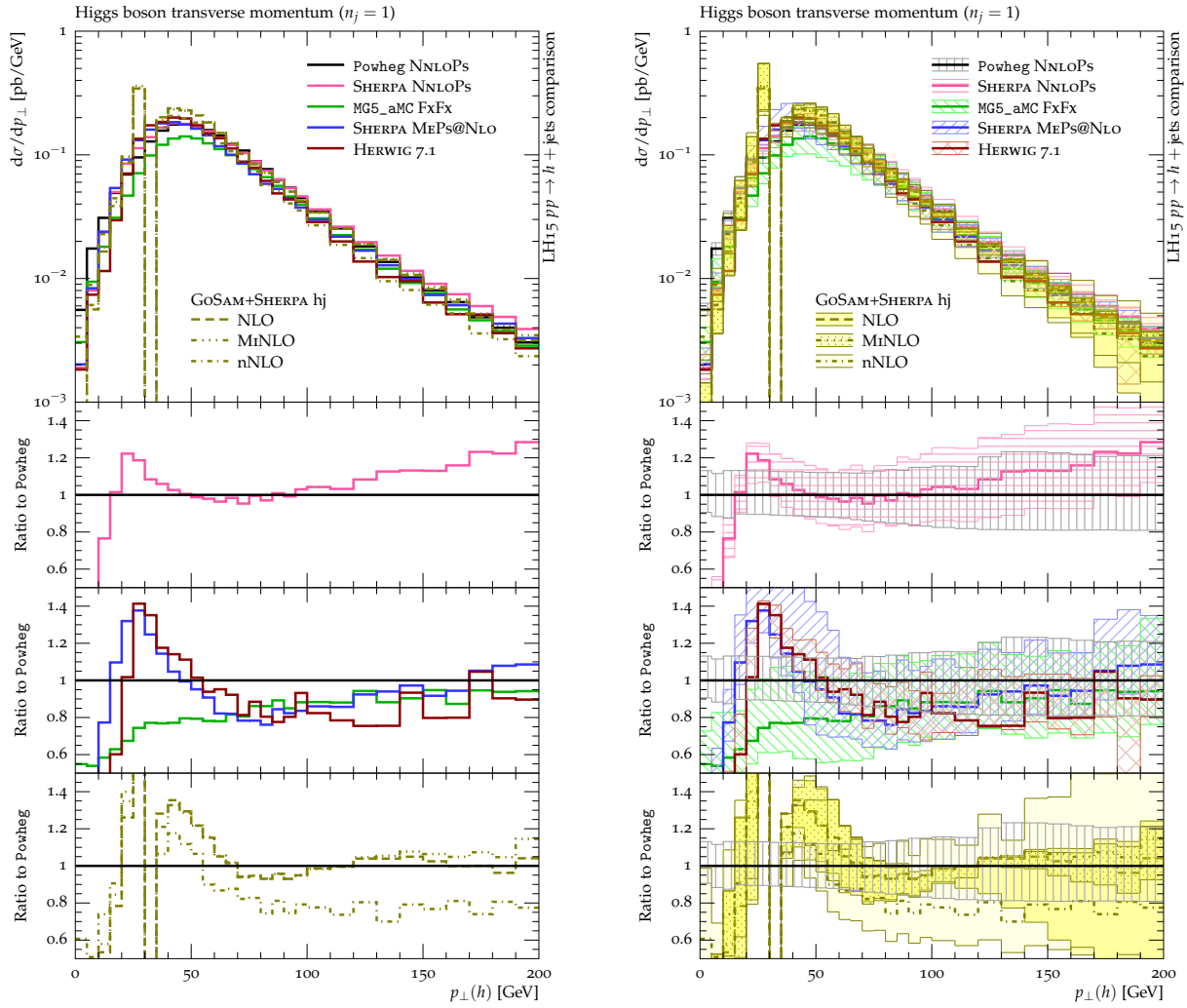


Fig. IV.12: The Higgs boson transverse momentum in the presence of exactly one jet without (left) and with (right) uncertainty bands. The ratio plot panel is divided into three parts all of which depict the corresponding ratios wrt. the POWHEG NNLOPs result. From top to bottom, the predictions are grouped such that the NNLOPs results, the ME+PS results at NLO and the fixed-order results are compared directly in the first, second and third ratio plot, respectively.

tainty envelopes are of similar size. This does not come as a surprise because all of these predictions are effectively given at NLO. The NNLO uncertainty band (shown in grey) is found to be significantly smaller. Comparing the second and last ratio plots with each other, we also notice that the ME+PS predictions are in better overall agreement with the pure NLO prediction given by GOSAM+SHERPA than they are in agreement with POWHEG, with the exception of Madgraph5_aMC@NLO below $p_{\perp}(h) \lesssim \frac{1}{2}m_h$. This is surprising since all parton shower matched calculations are of the same intrinsic accuracy (NLO), use similar local scale definitions along the lines of CKKW and include Sudakov factors of NLL accuracy. It may, however, be related to the way the resummation is controlled in POWHEG and the MC@NLO-type matchings used in Madgraph5_aMC@NLO, Herwig 7.1 and SHERPA. The different parton shower starting scales employed in Herwig 7.1 and SHERPA ($\sim \frac{1}{2}m_h$), Madgraph5_aMC@NLO ($\sim m_h$) and POWHEG (E_{cm}) do also play a role.

For the exclusive one-jet case, we reduce the number of ratio plots and show only those that display the ratios to POWHEG in the same way as before. Note that for the exclusive version

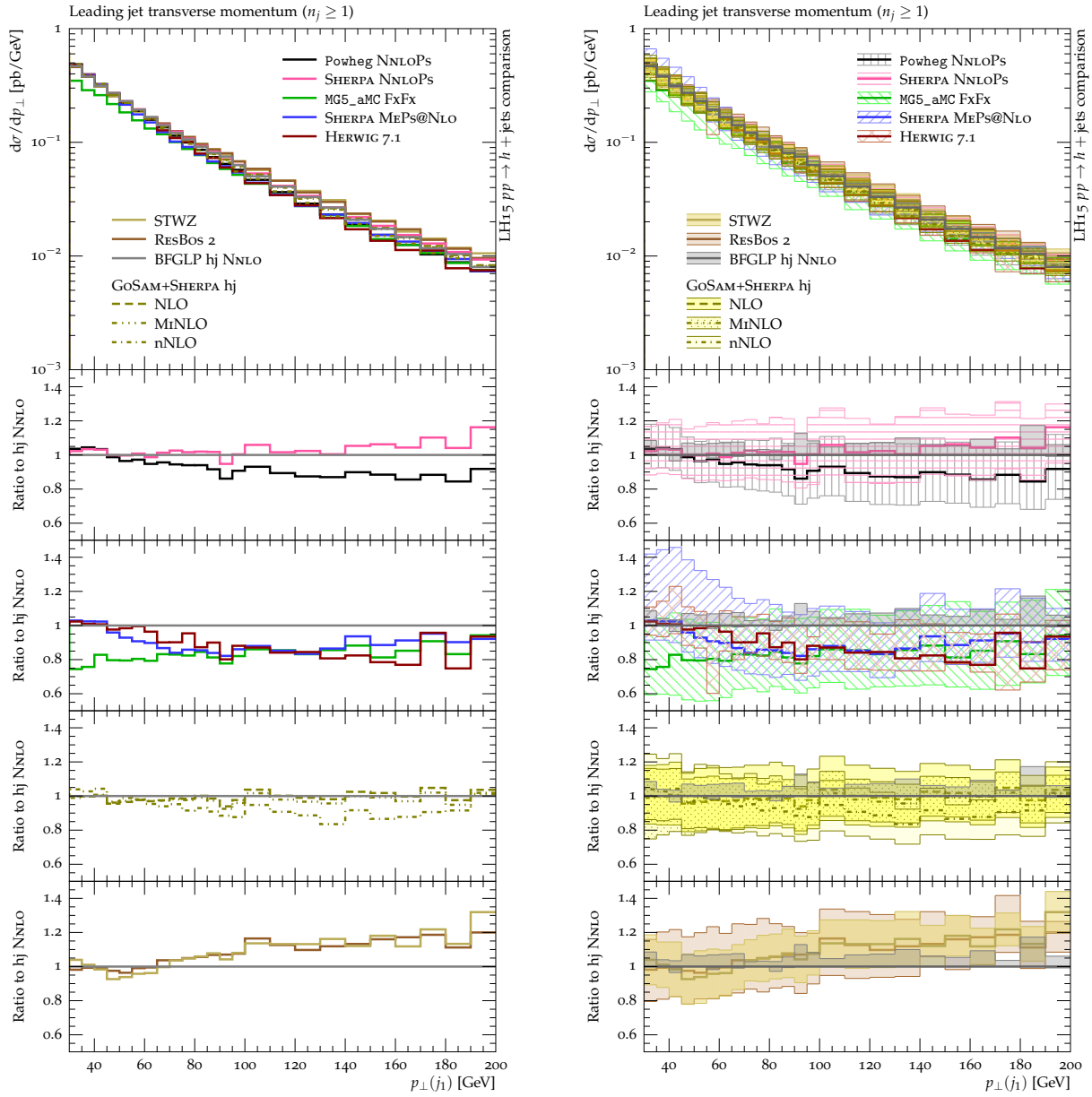


Fig. IV.13: The leading jet transverse momentum distribution for $h + \geq 1$ -jet production, to the right (left) shown with (without) the uncertainty bands provided by the various calculations. The part below the main plot contains four ratio plots taken wrt. the NNLO result of the BFGLP group following the same strategy for grouping the predictions as before (NNLOPs versus NLO ME+PS versus fixed-order and resummation results).

of the observable, the NNLO result is not available, turning this comparison into one between NLO-accurate predictions, except for the NNLO-approximate result given by LOOPSIM, labelled GO-SAM+SHERPA hj nNLO. Figure IV.12 clearly shows that the differences among the results are very similar to those discussed in the inclusive case; they are however pronounced such that the deviations wrt. the POWHEG NNLOPs prediction for h production become larger for the full transverse momentum range. There is one exception to this: LOOPSIM predicts a softer tail of the $p_{\perp}(h)$ distribution by about 20%, which in the end is a restatement of the fact that there is a 20% difference in the one-jet rate between the pure NLO and the LOOPSIM result, as already shown in Figure IV.10.

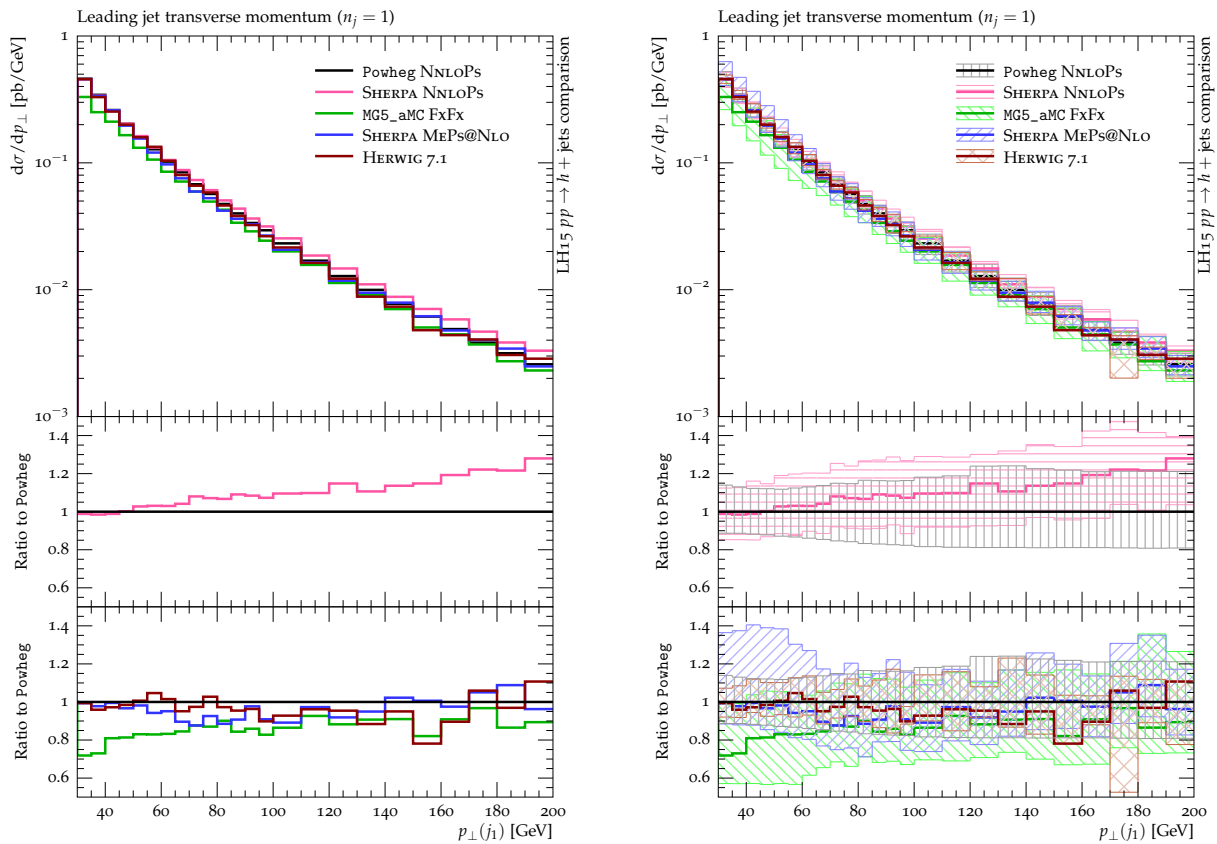


Fig. IV.14: The leading jet transverse momentum distribution for exclusive $h + 1$ -jet production, to the right (left) shown with (without) the uncertainty bands provided by the various calculations. Ratio plots are displayed in the lower part of the plot using the POWHEG NNLOPs result for Higgs boson production as their reference. Predictions are grouped in similar fashion to the previous plots.

Next we discuss the leading jet transverse momentum distribution for $h + \geq 1$ -jet final states. For this type of observable, we do not expect large Sudakov effects (i.e. shifts owing to parton showering/resummation). The impact of jet veto logarithms (owing to the restriction that all jets be greater than 30 GeV) has been examined and found to be reasonably small at NLO and NNLO [129, 399]. In the exclusive jet case, the $p_{\perp}(j_1)$ variable however is prone to larger resummation effects, and we note that the scale uncertainties shown will not reflect the true uncertainty. The inclusive jet results for all approaches are shown in Figure IV.13 including the NNLO prediction of the BFGLP group, the prediction of Stewart, Tackmann et al. and the prediction provided by RESBOS2. Figure IV.14 depicts the exclusive one-jet case presenting the results obtained by the Monte Carlo tools only; no fixed-order/resummation predictions are shown. Accordingly, different reference predictions (NNLO and POWHEG) are used in the ratio plots associated with Figures IV.13 and IV.14. Overall we find a rather remarkable agreement between all results where the largest deviations rarely exceed the 20% mark. For the exclusive lead-jet transverse momentum distribution of Figure IV.14, this means that all predictions are in reasonably good agreement with POWHEG. The Madgraph5_aMC@NLO prediction is lower than POWHEG for almost the entire transverse momentum range, again because of the central scale choice being higher than in the other approaches. For the inclusive lead-jet transverse momentum spectrum (see Figure IV.13), the remarkable agreement implies that all predictions indeed lie within each other's uncertainty bands (as they should). The quoted uncertainties are similar

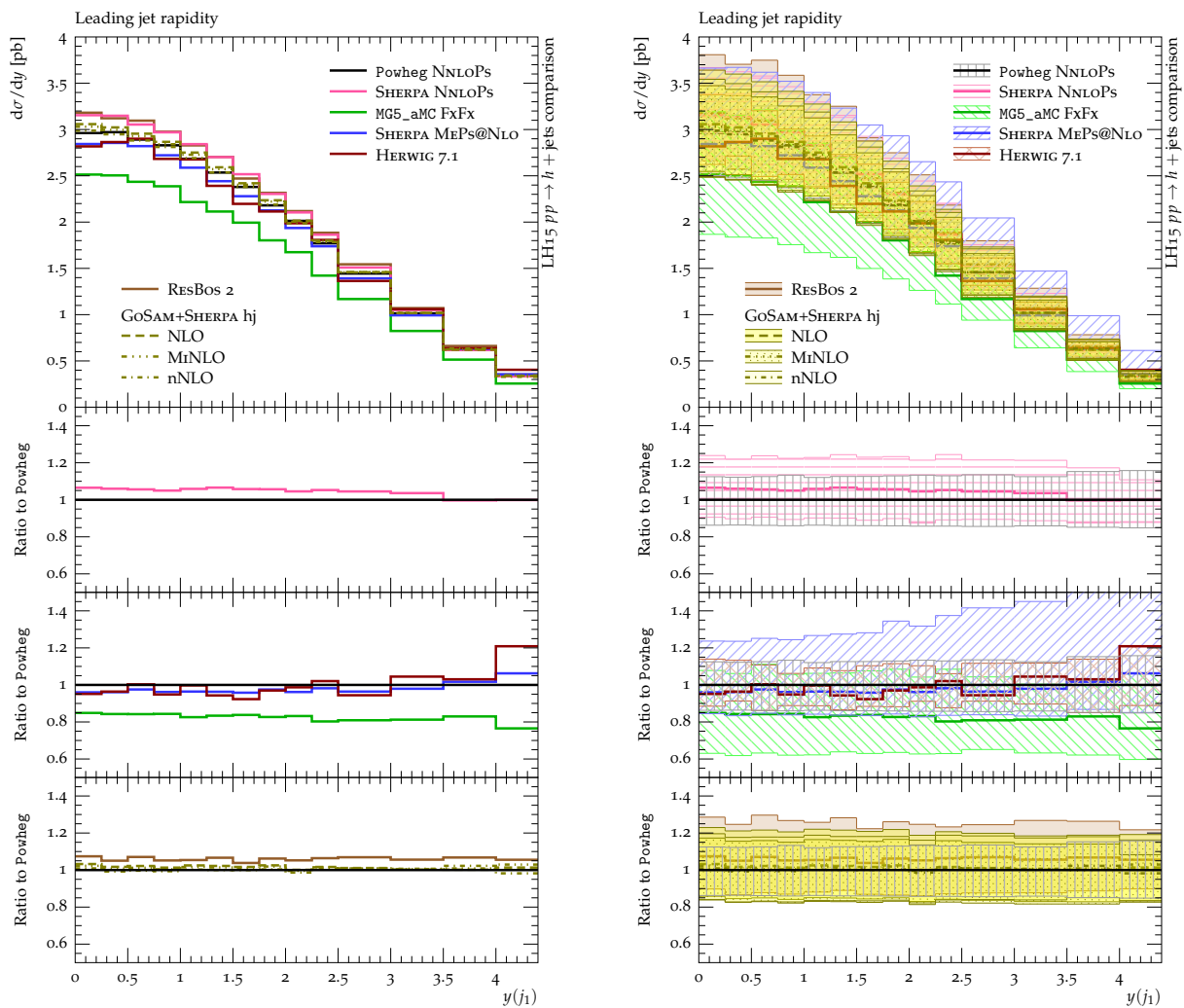


Fig. IV.15: The rapidity distribution for the leading jet in $h + \geq 1$ -jet production, shown without (left) and with (right) theoretical uncertainties. Ratio plots are displayed in the lower part of the plot using the POWHEG NNLOPS result for Higgs boson production as their reference. Predictions are grouped, from top to bottom, according to the categories NNLOPS, ME+PS at NLO and NLO fixed order as well as resummation.

in size, with values at and around the 20% level, and only those of the BFGLP hj NNLO calculation are significantly smaller.

Despite the good agreement seen among all predictions in Figure IV.13, it is worthwhile to go through the ratio plots and discuss some of the interesting features. In the top ratio panel, the two NNLOPS predictions are compared to the NNLO $h + \geq 1$ -jet prediction. The agreement among all three is good at low transverse momentum, but at higher $p_{\perp}(j_1)$ there is a tendency for SHERPA NNLOPS to move to the upper edge of the NNLO uncertainty band and POWHEG NNLOPS to move slightly below, resulting in a 20% net difference between the two. Again, this is a result of using $\mu = \frac{1}{2}m_h$ within SHERPA versus using MINLO/CKKW scales within the POWHEG approach. In the second ratio panel, Herwig 7.1, SHERPA and Madgraph5_aMC@NLO (taking into account its larger limit scale) agree reasonably well with each other over the entire transverse momentum range, but fall about 15% low wrt. the BFGLP prediction in the mid-range of the p_{\perp} distribution. The third ratio panel shows that there is almost no difference in normalization nor shape between the NNLO and the NLO $h + \geq 1$ -jet predictions

using the given scale choice, cf. Eq. (IV.12). This extends to the MINLO reweighted NLO result and the nNLO prediction provided by the LOOPSIM approach, although the latter is somewhat softer. Nevertheless we should bear in mind that if we were to include in this comparison a fixed-order calculation based on the scale choice $\frac{1}{2}\hat{H}'_T$, the resulting prediction would fall close to the multijet merged predictions, showcasing the still largish scale dependence of the hj NLO calculation. In the bottom ratio panel, the STWZ and RESBOS2 predictions agree very well with one another, partly because in their calculation they both rely on the same fixed-order piece dominating this observable and coincide in their use of fixed scale. Both approaches provide a resummation improved NLO calculation for this observable, agreeing with the NNLO prediction at low p_\perp . At the largest p_\perp values, where no resummation effects are present, deviations rise up to 30% owing to their fixed scale choice, which furthermore brings them into agreement with SHERPA's NNLOPS result. As a matter of fact, for sufficiently large values of $p_\perp(j_1)$, all three predictions converge to an NLO prediction employing a fixed scale of $\mu = \frac{1}{2}m_h$.

In summary, the fixed-order NNLO prediction of the BFGLP group, which has the best theoretical uncertainties available, is in good agreement with the SHERPA NNLOPS prediction, and to a somewhat lesser extent, with the POWHEG NNLOPS predictions. The level of moderate disagreements observed with the multijet merged calculations may be due to the different scale choices that are still important at NLO. The largest deviation seen with `Madgraph5_aMC@NLO` can mainly be traced back to its different choice of central scales. There is no sign of any serious impact of the merging of the fixed-order predictions with parton showers, as expected for such an inclusive cross section.

Even better agreement is observed for predictions for the rapidity distribution of the lead jet, $y(j_1)$, as demonstrated by Figure IV.15. This level of agreement seems to be even slightly better than the one found for $y(h)$ in Figure IV.6. We do not observe any shape differences, and the rate differences follow the already established pattern where most noticeably the `Madgraph5_aMC@NLO` cross section is reduced owing to their choice of using a higher central scale. Similarly, SHERPA NNLOPS and RESBOS2 are higher by about 6-7% as a result of using the fixed scale $\mu = \frac{1}{2}m_h$. Again, uncertainty envelopes are similar in size and do not point to any shape changes when varying the scales; Herwig 7.1's band is slightly narrower while SHERPA MEPS@NLO's and `Madgraph5_aMC@NLO`'s band are somewhat wider compared to all other NLO-accurate predictions.

We finish this section by examining the results for the transverse momentum of the Higgs-boson plus leading-jet system. In other words, we are interested in studying the different descriptions of the recoil of the hj_1 system. In the inclusive one-jet case depicted in Figure IV.16, the system may recoil against a second jet (or secondary jets) plus soft radiation, while for the exclusive jet scenario shown in Figure IV.17, it is only soft radiation that recoils against the hj_1 system. The latter case will therefore be strongly affected by the level at which resummation is taken into account. Formally, for the observable in question, the predictions of highest accuracy are facilitated by the NLO merging approaches as they provide an NLO description of the second jet; all other predictions are only LO accurate in the second jet, i.e. larger differences can be expected. In the exclusive (= 1-jet) case, all predictions that include parton showering operate at the same level of precision while the fixed-order calculations cannot do anything but fail in describing the $p_\perp(hj_1)$ distribution.

For the $h + \geq 1$ -jet events, differences of $\mathcal{O}(30\%)$ are observed among the ME+PS predictions below the jet threshold, while there is better agreement at higher p_\perp values, where again Herwig 7.1 turns out to be on the softer side. The POWHEG and SHERPA NNLOPS curves surprisingly fit right in with the ME+PS results throughout the spectrum. The mostly comparable behavior of the NNLOPS results to those obtained from NLO merging is not what one would expect a priori, however the NLO matching (POWHEG- and S-MC@NLO-type, respectively) of the

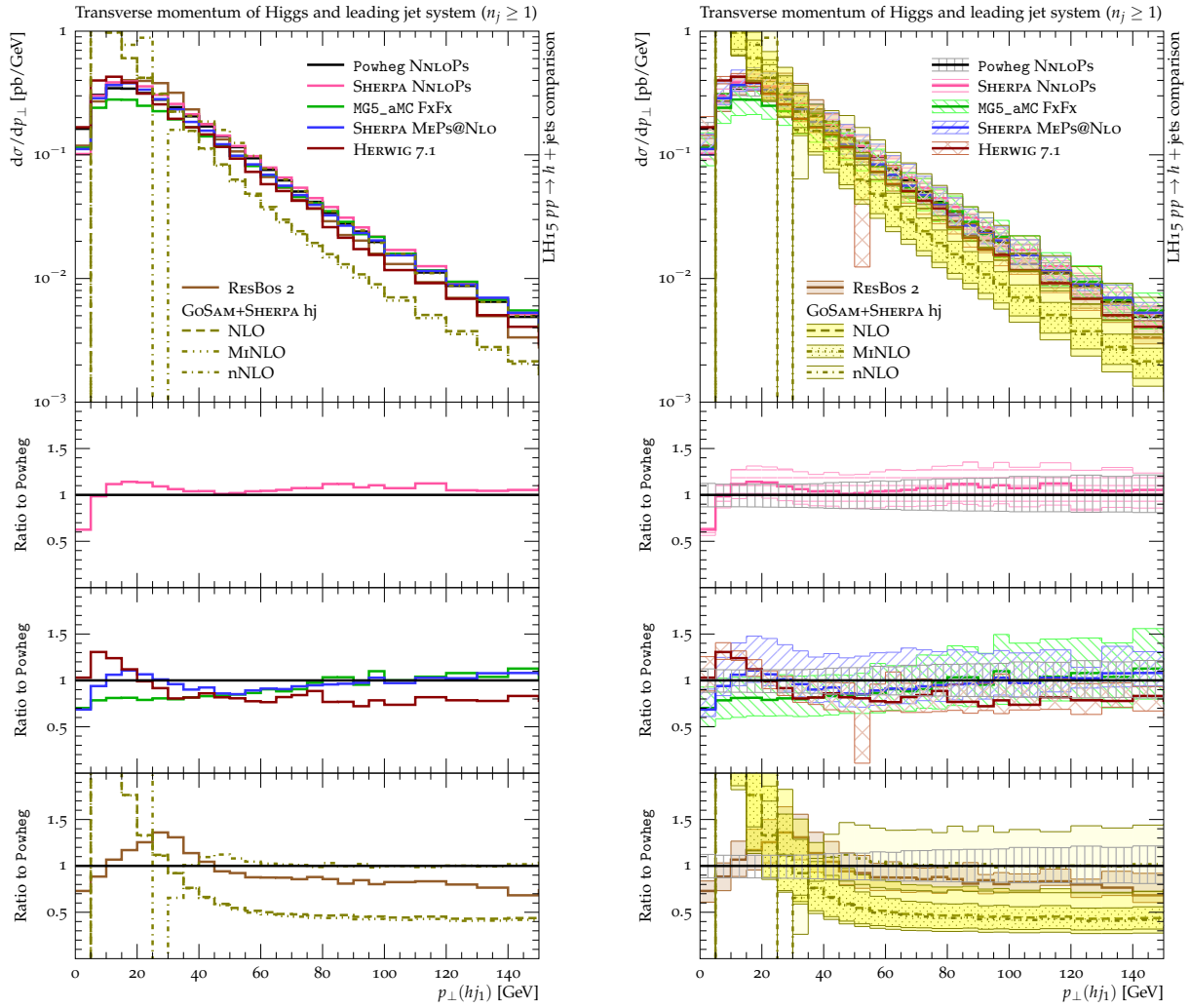


Fig. IV.16: The transverse momentum of the Higgs-boson-leading-jet system in the presence of at least one jet. For better visibility, results are shown without (left) and with (right) theoretical uncertainties. The plot layout exactly corresponds to that of Figure IV.15, except for the extended \hat{y} -axis range in the ratio plots.

hj configurations transfers a differential K -factor to their second parton emission such that the LOPs treatment of the $h + \geq 2$ -jet rate obtains a more appropriate normalization. The hj NLO calculations (i.e. the pure and MINLO reweighted GOSAM+SHERPA results) cannot compete with this performance since they miss an adequate description of the second jet giving recoil to the hj system. Correspondingly, the $p_{\perp}(hj_1)$ observable is described poorly with values clearly overshooting below the jet threshold due to the missing Sudakov suppression and undershooting by 60% beyond $p_{\perp} = 50$ GeV due to missing higher (than two-) jet multiplicity contributions. It is interesting to see that the LOOPSIM procedure lifts this large discrepancy in the p_{\perp} tail. This is evidence that an adequate description of a second and third jet is sufficient to describe this observable in this regime. Thus, the good agreement with the ME+PS results is largely driven by the hjj NLO component used to build the nNLO prediction for the $h + \geq 1$ -jet process. However, as a result of the cut-off dependence of the procedure nothing can be said about the $p_{\perp} < 25$ GeV region. On the contrary, RESBOS2 predicts this region with NLL precision but reverts to a LO description in the tail of the distribution leveling off about 30% above the GOSAM+SHERPA result as a consequence of employing a lower scale (that is $\mu = \frac{1}{2}m_h$). Note

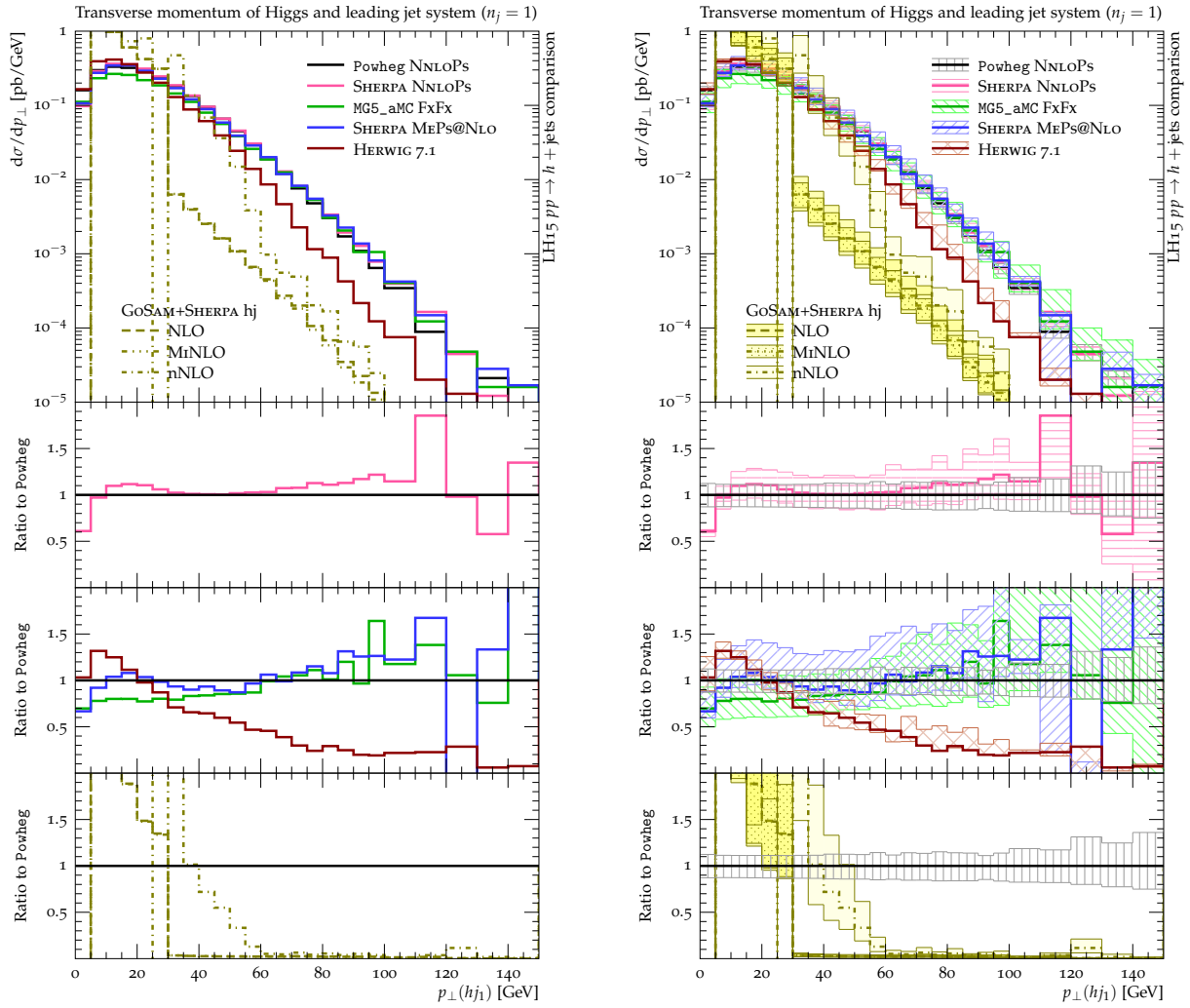


Fig. IV.17: The transverse momentum of the Higgs-boson-leading-jet system in the presence of exactly one jet. Again, results are shown without (left) and with (right) theoretical uncertainties as given by the different groups. Note that the plot layout corresponds exactly to that of Figure IV.12, except for the extended \hat{y} -axis range used in the ratio plots.

that for the jet associated Higgs boson production, the transverse momentum of the hj_1 system constitutes exactly the q_T quantity that is to be resummed by RESBOS2 imposing the constraint $p_\perp(hj_1) < p_\perp(j_1)$, which is to ensure that j_1 is indeed the leading jet (as any other jet is integrated out in the resummation formalism used by RESBOS2). In addition, terms of the form $\ln(1/R^2)$ are also taken into account by the resummation carried out in RESBOS2 and lead to a somewhat broader, upward shifted Sudakov peak.

Lastly, we comment on the uncertainties quoted by the different calculations: the RESBOS2, GOSAM+SHERPA NLO and MiNLO envelopes have an appropriate size reflecting the underlying LO nature of the $p_\perp(hj_1)$ prediction above the jet threshold. The LOOPSIM procedure leaves us with a somewhat wider band as it involves two real-emission (LO-like) contributions (hjj and $hjjj$), which impact the $p_\perp(hj_1)$ observable. Madgraph5_aMC@NLO and SHERPA MEPS@NLO on the one side and Herwig 7.1 on the other side produce NLO variations that are fairly different in size. However, the Herwig 7.1 as well as the POWHEG and SHERPA NNLOPS envelopes are most likely underestimated; in particular the POWHEG and SHERPA NNLOPS bands do not behave as expected from a LO variation for above-jet-threshold $p_\perp(hj)$.

The exclusive (exactly one jet) case for the $p_{\perp}(hj_1)$ observable is shown in Figure IV.17. Apart from the NNLOPS outcomes, there is a much greater divergence of the predictions for exactly one jet, especially at high p_{\perp} . Recall that for this situation, the recoil is generated only from soft emissions, and it is clear that a highly exclusive distribution such as the one in question serves as a stress test for the ME+PS as well as the NNLOPS predictions (in fact any parton shower or resummed prediction). For the same reason, caution has to be taken in interpreting the uncertainties. The current case is similar to the case for the Higgs boson p_{\perp} distribution with no jets and it is no surprise that different approaches can lead to different answers. Most notably, we observe NNLOPS predictions that are in slightly worse agreement as compared to the inclusive case, and the expected complete failure of the GOSAM+SHERPA results (including the LOOPSIM result where the one-jet requirement removes the effect that yielded the improvement in the inclusive case),¹⁰ and the severe decline of the Herwig 7.1 differential cross section dropping to about 25% wrt. the POWHEG result at $p_{\perp} \sim 100$ GeV.

3.3.3 Dijet observables

Moving to topologies with one more jet in the final state, we discuss a number of $h + 2$ -jet observables in this section. It is important to understand, in detail, the level of (dis-)agreement among the available predictions since the $h + 2$ -jet gluon fusion contribution constitutes the major irreducible background in any LHC Run-II analysis targeting the prominent vector boson fusion channel. Following the layout of the previous sections, we compare predictions from three different categories with each other: NNLOPS h production, MEPS@NLO $h +$ jets production and fixed-order (and related) hjj production at $\mathcal{O}(\alpha_s^5)$. As before we have provided one ratio plot for each category in order to enhance the readability of our plots; common to all figures is the use of POWHEG’s NNLOPS prediction to serve as the reference result. Note that for each category, the accuracy with which the $h + 2$ -jet events are described is different: the NNLOPS predictions are at the LOPS level while the multijet merged results incorporate the precision given by NLOPS matching. HEJ generates predictions derived from the behavior of QCD in the high-energy limit, starting from a LO accurate $h + 2$ -jet configuration. With two or more jets in the final state, HEJ can provide meaningful predictions for the first time. As for earlier cases, the last category contains NLO-accurate predictions solely, free of any parton showering.

The Higgs boson p_{\perp} spectrum, in the presence of at least two jets, is shown in Figure IV.18. Although all calculations agree on the position of the maximum of the distribution (situated at $p_{\perp} \gtrsim 60$ GeV, i.e. twice the jet threshold),¹¹ varying behavior is observed for both larger and smaller transverse momenta. Examining first the region where $p_{\perp} \gtrsim 60$ GeV, good agreement between all multijet merged calculations and POWHEG is found. Only Herwig 7.1 predicts a somewhat more rapidly falling distribution. SHERPA NNLOPS, due to its scale choice, exhibits a more or less constant $\mathcal{O}(+20\%)$ offset with respect to the POWHEG NNLOPS, but remains well within their respective uncertainties. In comparison to all the NLO uncertainty bands, the NNLOPS envelopes are expected to be larger reflecting the loss of one order in accuracy. A clear difference however is not found indicating that the NNLOPS estimates are too optimistic. From this point of view, the larger difference seen between the two NNLOPS predictions is no surprise at all – rather typical for comparisons at the LOPS level, and two different parton showers at work. The fixed-order predictions (NLO, MiNLO and LOOPSIM) agree well in this region with one another, but surpass the POWHEG reference and, more importantly, the multijet merged calculations with the same accuracy, by about 20%. This deviation is just covered by

¹⁰Owing to the kinematic constraints on the jets, harder radiation that goes forward does not get identified as a jet; these contributions actually form the (naively unexpected) $p_{\perp} > 30$ GeV tail of the GOSAM+SHERPA results though the mechanism is highly suppressed.

¹¹Note that around this two-jet threshold, we again find remnants of the Sudakov shoulder effect affecting the fixed-order predictions.

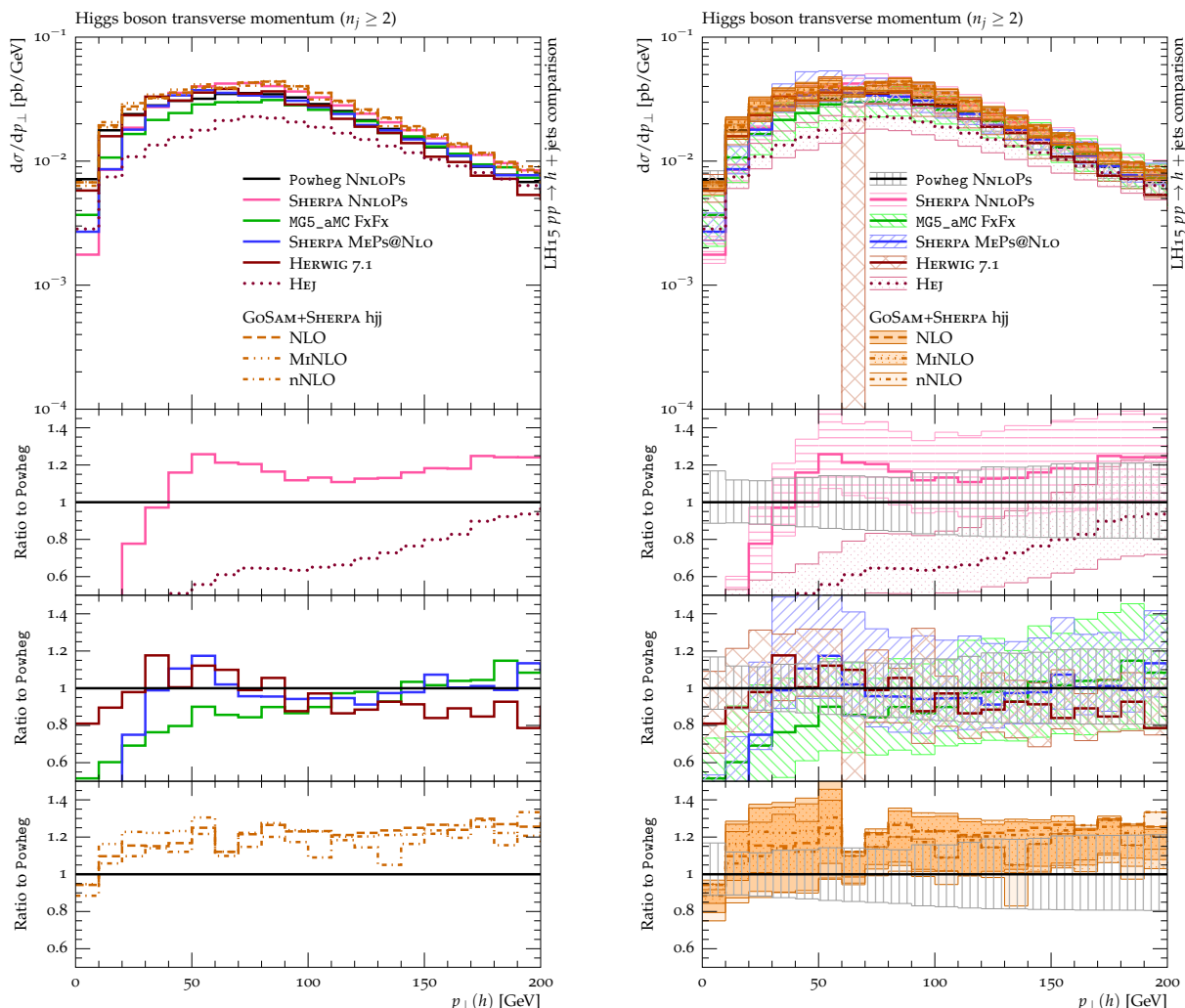


Fig. IV.18: The transverse momentum of the Higgs boson in the presence of at least two jets without (left) and with (right) uncertainties, supplemented by three ratio plots using the reference result as obtained from POWHEG’s NNLOPs calculation for h production. The predictions are grouped – from top to bottom – according to the categories NNLOPs h production, ME+PS merging at NLO (at least up to two jets) and NLO fixed-order hjj production. HEJ’s prediction is added to the first, the NNLOPs subpanel.

the edge of the uncertainty bands associated with either of the NLO calculations. Finally, HEJ clearly produces the hardest spectrum in this region, exhibiting a considerably different slope with respect to all other calculations, albeit it starts out from an approximately 40% lower cross section at $p_{\perp} \approx 60$ GeV.

In the region below the peak, $p_{\perp} \lesssim 60$ GeV, the various calculations are more widely spread. This is expected as effects from parton showering have a larger impact here, but none of the considered shower Monte Carlos in Figure IV.18 works at a higher level regarding the resummation precision. We can readily distinguish between two topologies if we assume the jets to be produced near their p_{\perp} threshold: while for $p_{\perp}(h) > 30$ GeV, both the leading and subleading jet have to be in the same hemisphere opposite the Higgs boson, for $p_{\perp}(h) < 30$ GeV, the subleading jet has to cross over into the Higgs boson’s hemisphere opposite the leading jet. Because of parton shower effects, deviations among the predictions are greater in the former region, but it is the latter region that receives the larger resummation corrections, as both

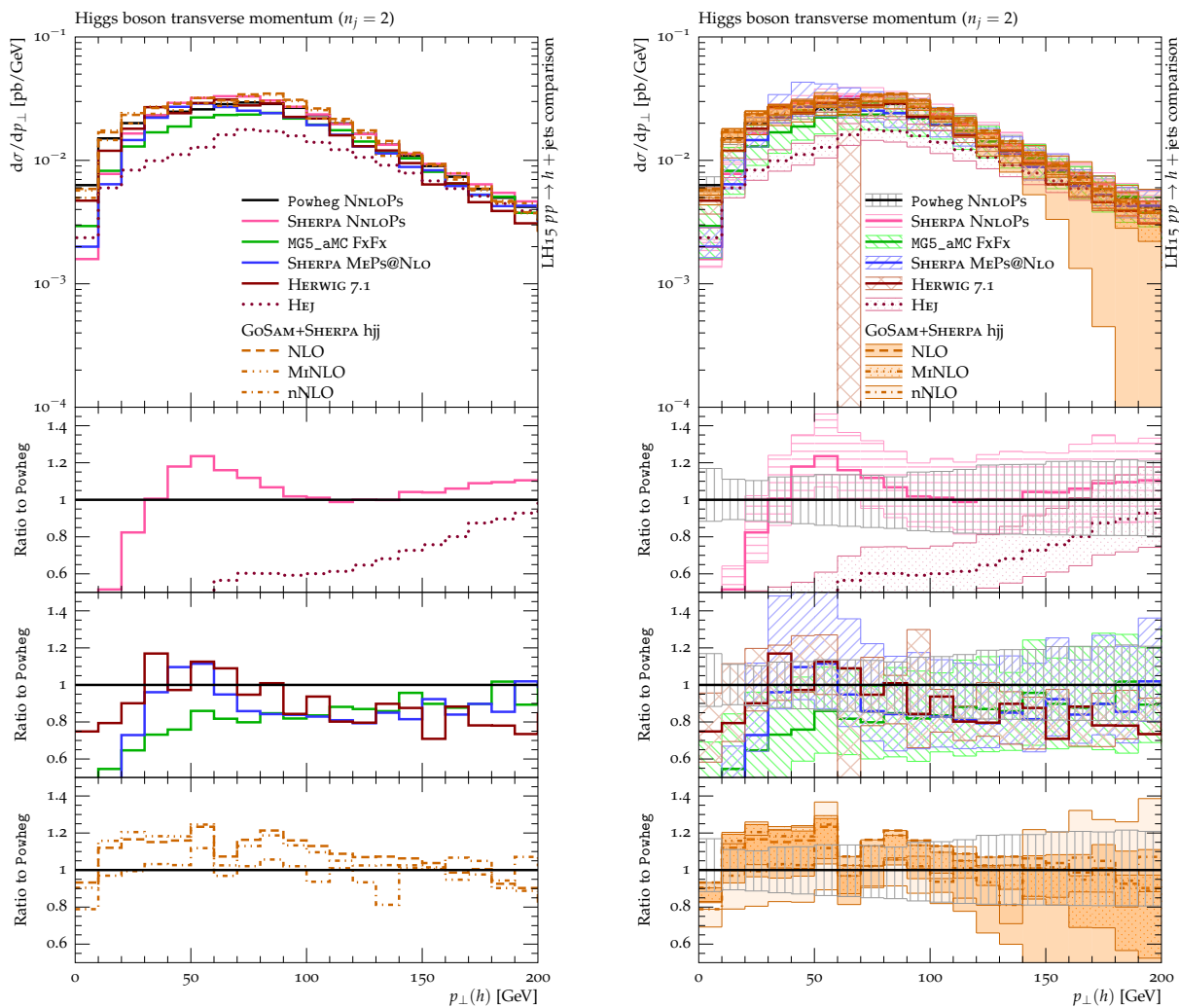


Fig. IV.19: The transverse momentum of the Higgs boson in the presence of exactly two jets without (left) and with (right) uncertainties, supplemented by three ratio plots using the reference result as obtained from POWHEG’s NNLOPS calculation for h production. The predictions are grouped – from top to bottom – according to the categories NNLOPS h production, ME+PS merging at NLO (at least up to two jets) and NLO fixed-order hjj production. HEJ’s prediction is added to the first, the NNLOPS subpanel.

jets recoil mainly against each other (to form a jet-balanced configuration) and soft radiation off them has a large influence on the small Higgs boson transverse momentum. An important role is also played by the assignment of scales in the context of multijet merging. To assign a meaningful history in this regime, in particular for sufficiently hard jets, the clustering algorithm that is needed to define the local CKKW or MINLO scales must allow for the possibility of Higgs boson radiation off a dijet process. In consequence, the value of the scales increases and the cross section is reduced, explaining the identical behavior of both the SHERPA MEPS@NLO and SHERPA NNLOPS predictions. The Herwig 7.1, Madgraph5_aMC@NLO and HEJ predictions are largely similar in shape, but offset as a result of the larger central scale choice in Madgraph5_aMC@NLO and the LO accuracy of the total cross section in HEJ. POWHEG NNLOPS gives the slowest decline of the differential cross section as $p_{\perp} \rightarrow 0$. The various fixed-order predictions are somewhat more widely spread than for large p_{\perp} (as indicated by the wider uncertainty bands), and start to exhibit a slope wrt. the POWHEG reference, retaining however a more or less

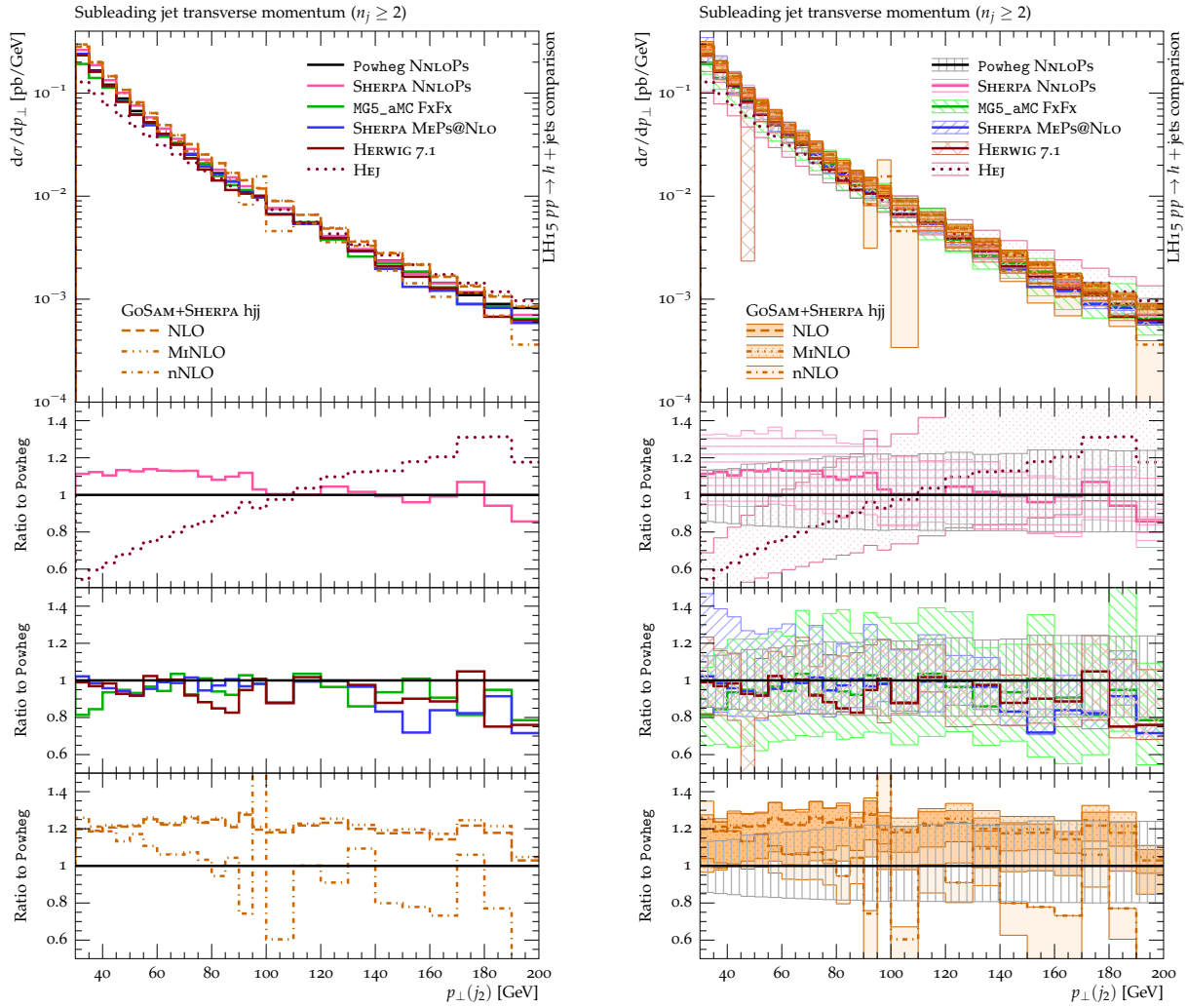


Fig. IV.20: The subleading jet p_{\perp} for $h + \geq 2$ -jets production shown without (left) and with (right) theoretical uncertainties. The plot layout is the same as in the previous figure.

constant ratio wrt. Herwig 7.1 and Madgraph5_aMC@NLO. In the $p_{\perp}(h)$ region below 30 GeV, the global scale setting of the fixed-order calculations is certainly not flexible enough to deal with the jet-balanced configurations in a similar way as done by SHERPA.

Figure IV.19 displays the Higgs boson's transverse momentum in the presence of exactly two jets. Apart from the overall reduction of the cross section, the general features as observed in Figure IV.18 for each generator are reproduced. There are, however, two notable exceptions. The decrease in the POWHEG NNLOPS prediction at large $p_{\perp}(h)$ is less, as compared to the other generators. On the one hand, it now overshoots the multijet merged predictions by about 10-20%, but on the other hand it achieves a much better agreement with SHERPA NNLOPS. This, however, is not very surprising given that the jet veto (on the third jet) in the NNLOPS calculations is only described at parton shower level, lacking any matrix element input. The latter is mandatory for a good description of the rejected 30 GeV emission. As seen before, the fixed-order predictions start to lose their perturbative stability when the p_{\perp} ratio between the observed Higgs boson and the rejected jet turns out to be large. This effect is more pronounced for the MiNLO procedure because it generates lower scale values on average. In the LOOPSIM approach, perturbative stability is improved as a result of the inclusion of $hjjj$ information.

The subleading jet p_{\perp} spectra for $h + \geq 2$ and h plus exactly two jets are shown in

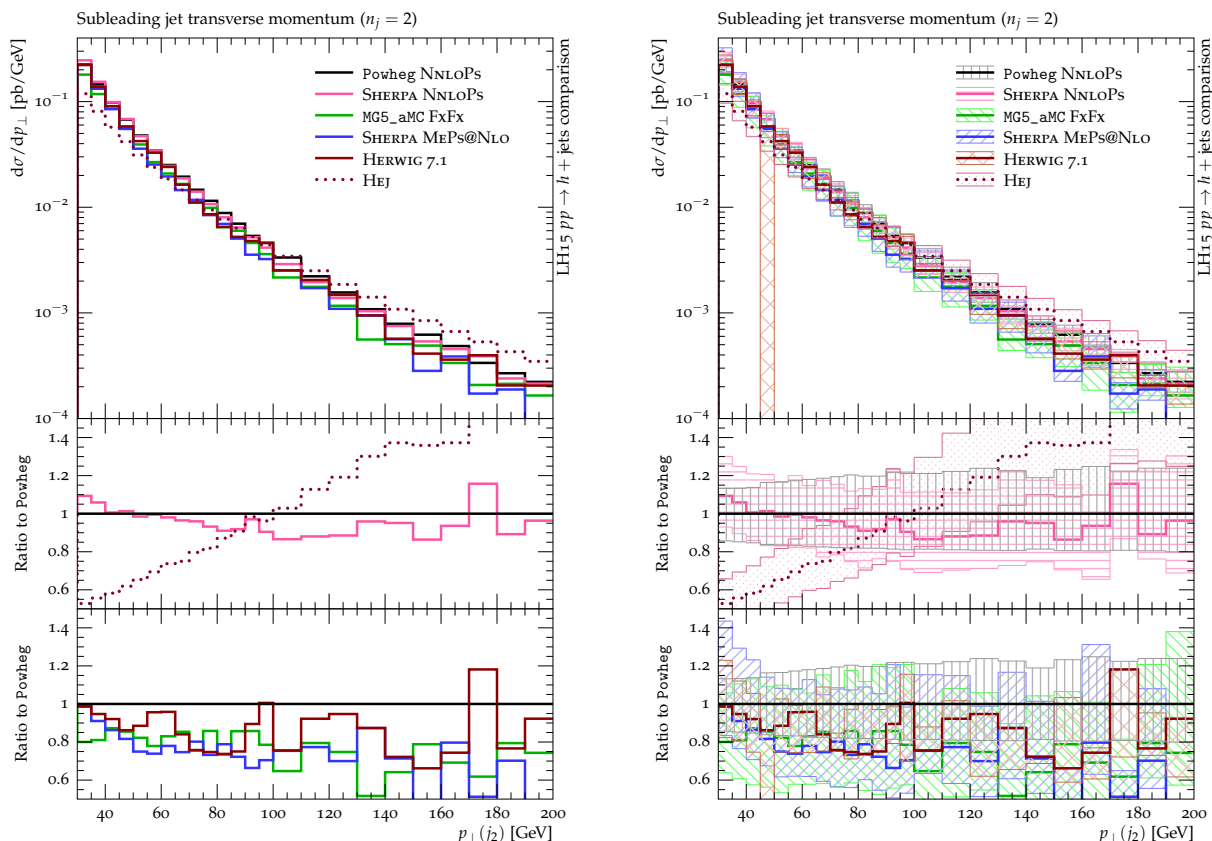


Fig. IV.21: The subleading jet p_{\perp} for exclusive $h + 2$ -jets production shown without (left) and with (right) theoretical uncertainties. Again, the layout is similar to that of Figure IV.18 except for dropping the results of the NLO fixed-order hjj production and the associated ratio subpanel.

Figures IV.20 and IV.21, respectively. A comparison between the second jet results (of the $n_j \geq 2$ and $n_j = 2$ case) with the first jet results (of the $n_j \geq 1$ and $n_j = 1$ case, depicted in Figures IV.13 and IV.14, respectively) reveals a rather consistent picture. The agreement among the ME+PS predictions, and between the ME+PS and the POWHEG predictions, is slightly better than in the case of the leading jet. For $n_j = 2$ (cf. Figure IV.21), POWHEG's NNLOPs approach predicts harder subleading jets than the others do, apart from HEJ. Madgraph5_aMC@NLO, SHERPA and Herwig 7.1 lie in reasonable agreement with each other, but systematically lower than POWHEG by about 10-20%. The agreement in the inclusive (i.e. $n_j \geq 2$) case eventually results from a compensating effect, since all the different methods for NLO merging give larger three-jet rates wrt. POWHEG. The GOSAM+SHERPA hjj NLO predictions do not have a different shape, but their rate is higher, which likely comes from choosing $\frac{1}{2} \sum_T^{1/2}$ as the central scale; recall that in the one-jet case this choice already produced large NLO cross sections, as large as the NNLO one, and larger than the ME+PS ones. With two jets in the final state, this effect is easily seen to be enhanced. The LOOPSIM NNLO estimate for the $p_{\perp}(j_2)$ spectrum gradually decreases wrt. the other GOSAM results, in a similar, slightly more pronounced way to what we found for $p_{\perp}(j_1)$ in the $n_j \geq 1$ case. LOOPSIM combines the NLO-accurate hjj and $hjjj$ bins, and in doing so seems closer to the NLO-merged results, and therefore reproduces some of their characteristics. The hardest spectrum is delivered by HEJ even though its total rate is significantly lower. In the plot range, HEJ's prediction is consistent with the others due to overlapping uncertainties (LO for HEJ), but this statement gets stretched for the exclusive two-jet scenario. Moreover, for $n_j = 2$, the uncertainties reported here have to be considered with caution, owing to the neglect of

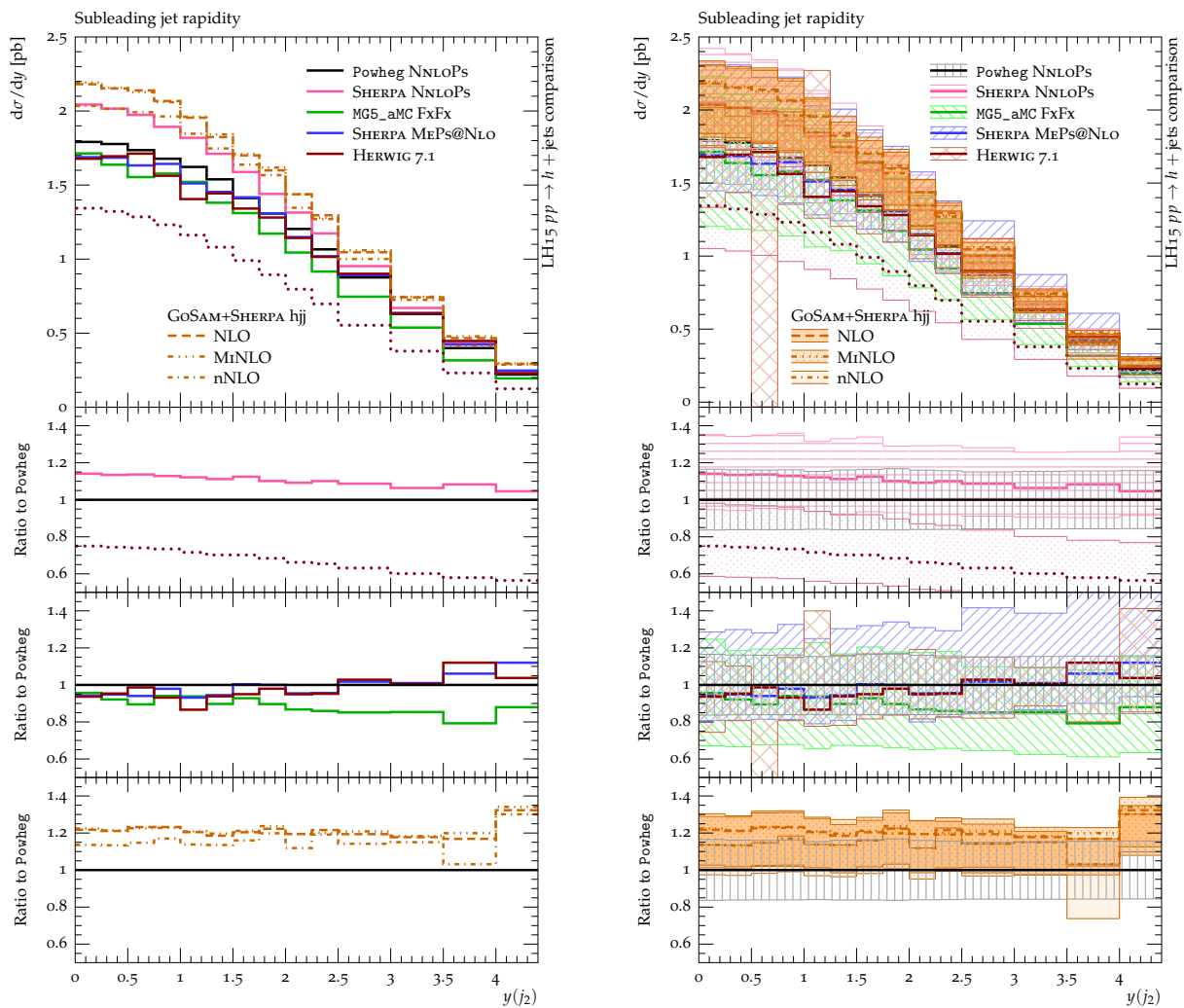


Fig. IV.22: The rapidity separation between the leading and subleading jets for $h + \geq 2$ -jets production, shown without (left) and with (right) theoretical uncertainties. The plot layout is the same as the one used in Figure IV.18.

important resummation effects. However, the statements made regarding error estimates when discussing $p_{\perp}(h)$ for $n_j \geq 2$, carry over to the current case, as well as for all other observables in this section.

Figure IV.22 depicts the rapidity distribution of the subleading jet. The conclusion of this comparison is more or less the same as for the leading jet, see Figure IV.15. Only minor differences between the computations are encountered, in particular concerning the shape of the rapidity spectrum – the larger effects are driven by the different rate predictions. While SHERPA NNLOPs and Madgraph5_aMC@NLO prefer a slightly more central production than the other calculations, the rate difference previously observed between POWHEG NNLOPs, Madgraph5_aMC@NLO, Herwig 7.1 and SHERPA MEPS@NLO on the one side, and SHERPA NNLOPs and the various GoSAM+SHERPA NLO calculations on the other side, is the feature that most stands out when plotting the subleading jet rapidity. The largest deviations are again delivered by HEJ; apart from the lower total rate, HEJ predicts fewer subleading jets at large rapidities than the other approaches. It again becomes apparent that the quoted uncertainties of the NNLOPs calculations are likely underestimated.

As before, we are also interested in multiparticle or system observables. As an example we

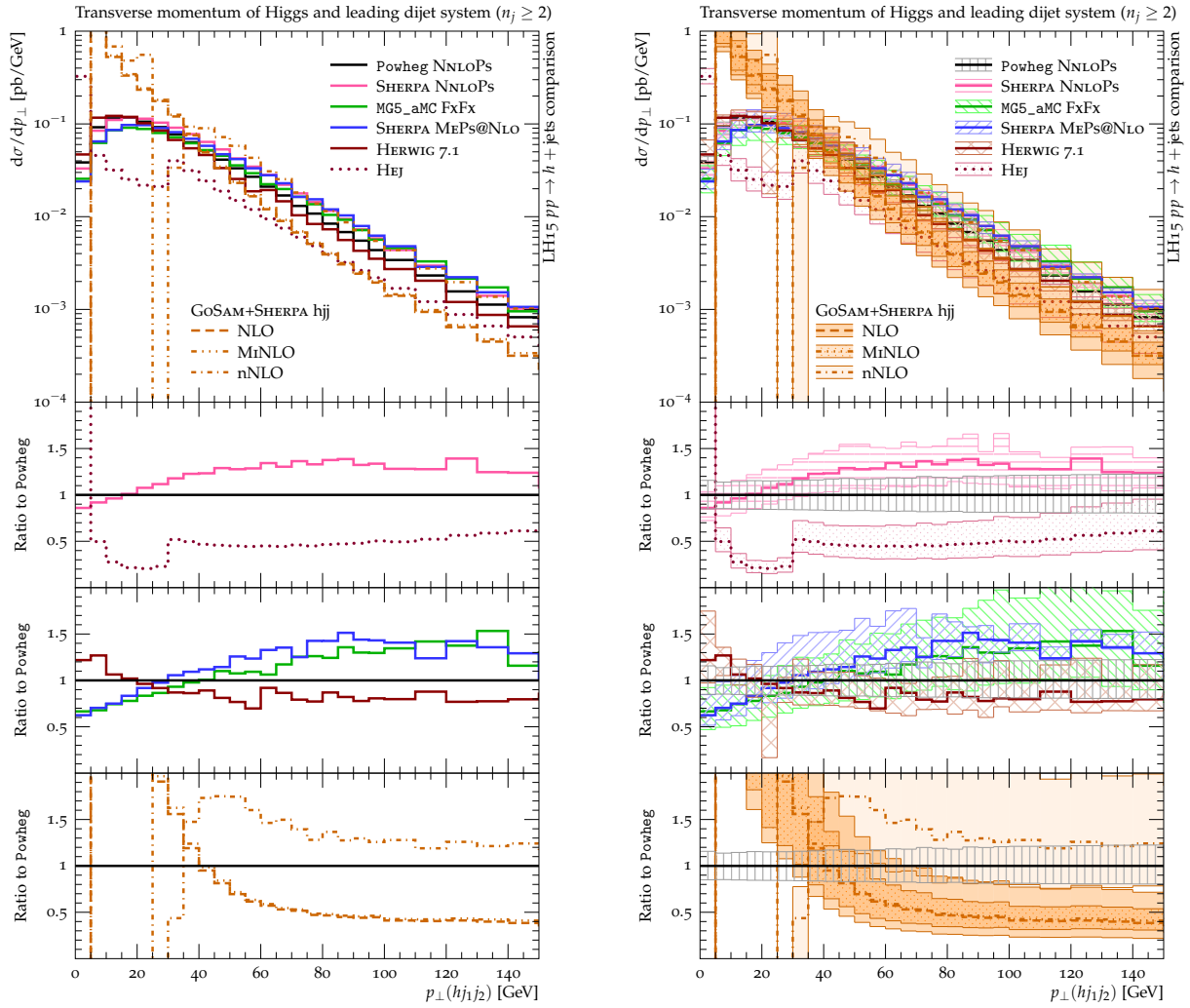


Fig. IV.23: The transverse momentum distribution of the Higgs boson plus two leading jet system, shown without (left) and with (right) uncertainties. The plot layout is the same as in Figure IV.18.

show the transverse momentum distribution of the Higgs boson plus two leading jet system in Figure IV.23. The $p_{\perp}(hj_1j_2)$ variable is the two-jet analog of the $p_{\perp}(hj_1)$ variable for inclusive one-jet events. The physics of this type of recoil observable has been already discussed in detail for Figure IV.16. The variations between the different approaches are qualitatively similar to those of $p_{\perp}(hj_1)$, cf. Figure IV.16, only their absolute size is increased. **Madgraph5_aMC@NLO** and SHERPA have a slope with respect to POWHEG at low p_{\perp} and overshoot by about 25% at higher p_{\perp} , while Herwig 7.1 is again somewhat lower than POWHEG at high p_{\perp} . In the soft domain, the SHERPA NNLOPS result resembles the corresponding ME+PS one as a result of using the same parton shower. While the latter prediction levels off above POWHEG (due to the ME description of a third jet at NLO), the former falls back to the same level slightly above the plotted range. Recall that for SHERPA NNLOPS a third, fourth and so forth jet is described by the parton shower only, the same as for POWHEG. The behavior of HEJ is again largely affected by the lower rate. The shape difference once more puts emphasis on the fact that HEJ generates harder transverse momentum spectra in general while possessing a discontinuity where the events start to possess a resolved third jet. In the GOSAM+SHERPA NLO predictions, the recoil is solely described by the real emission contribution, hence the divergent behavior in the soft domain and the

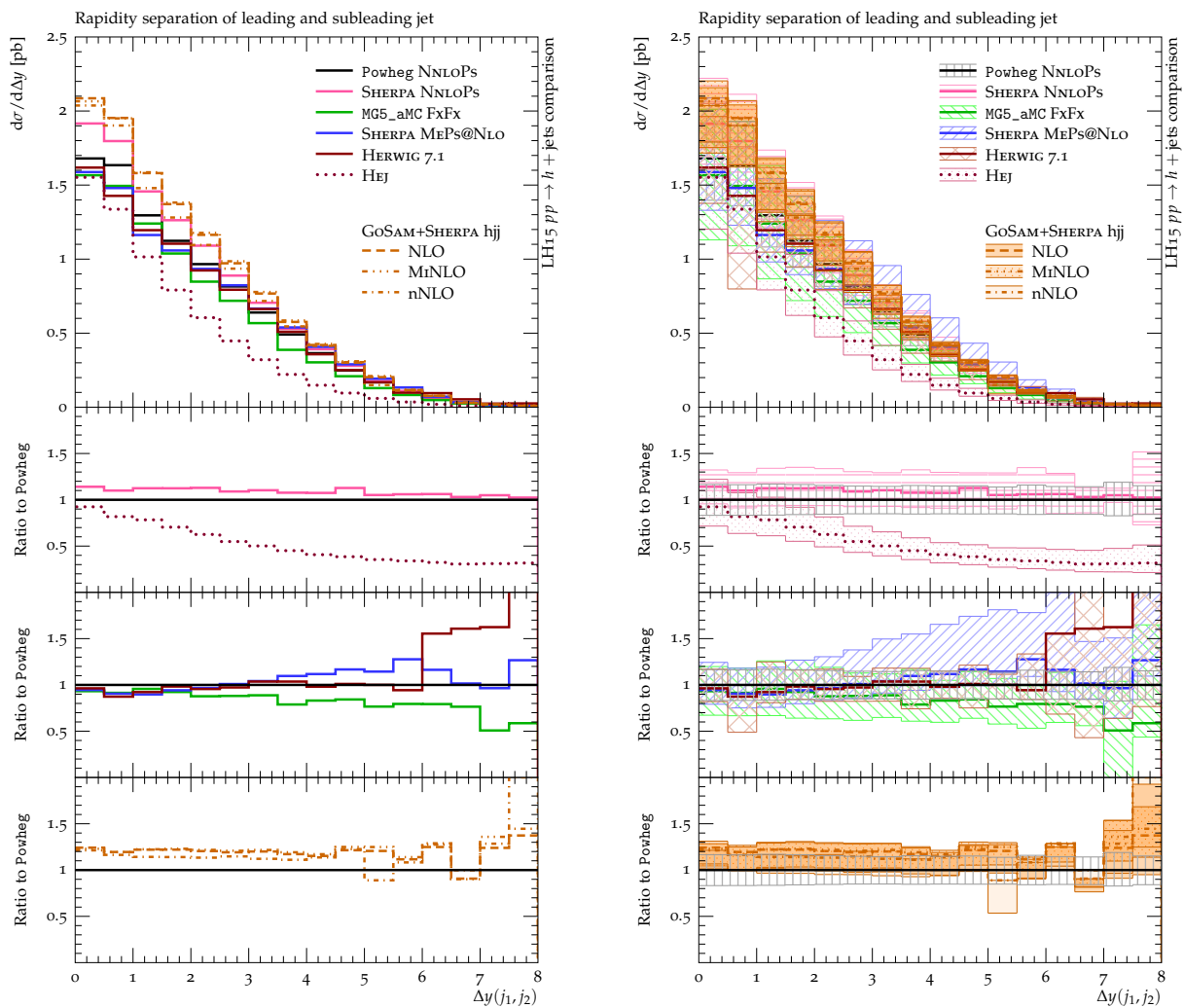


Fig. IV.24: The rapidity separation between the leading and subleading jets for $h + \geq 2$ -jets production, shown without (left) and with (right) theoretical uncertainties. The plot layout is the same as the one used in Figure IV.18.

significantly lower rate but constant LO shape wrt. POWHEG at higher p_{\perp} . For the same reason, the associated uncertainty bands are found to be larger as well. LOOPSIM, as before, benefits from the fact that the third jet enters at NLO accuracy, but cannot describe the soft region due to the procedure's cut-off dependence. Also, LOOPSIM's uncertainty band is relatively wide due to the strong impact of the four-jet contributions on the $p_{\perp}(hj_1j_2)$ distribution. On the positive side, these contributions are only included because of LOOPSIM's combination of jet bins, while on the negative side they are described with LO accuracy. Note that this peculiar behavior of the $p_{\perp}(hj_1j_2)$ observable has been already pointed out and discussed in more detail in Ref. [331].

We now turn to the discussion of jet–jet correlations. The rapidity separation between the leading and subleading jets is shown in Figure IV.24, considering $h + \geq 2$ -jet final states. Taking the findings regarding the individual jet rapidity spectra into account, cf. Figures IV.15 and IV.22, the $\Delta y(j_1, j_2)$ results are found to behave very similarly. While SHERPA NNLOPs and Madgraph5_aMC@NLO tend to be slightly more central than POWHEG, the SHERPA MEPS@NLO implementation predicts the leading jets to have a somewhat larger rapidity separation. Surprisingly, Herwig 7.1 shows a large increase beyond $\Delta y > 6$. However, it is not clear whether this is simply due to a lack of statistics. The various GOSAM+SHERPA NLO results are in good

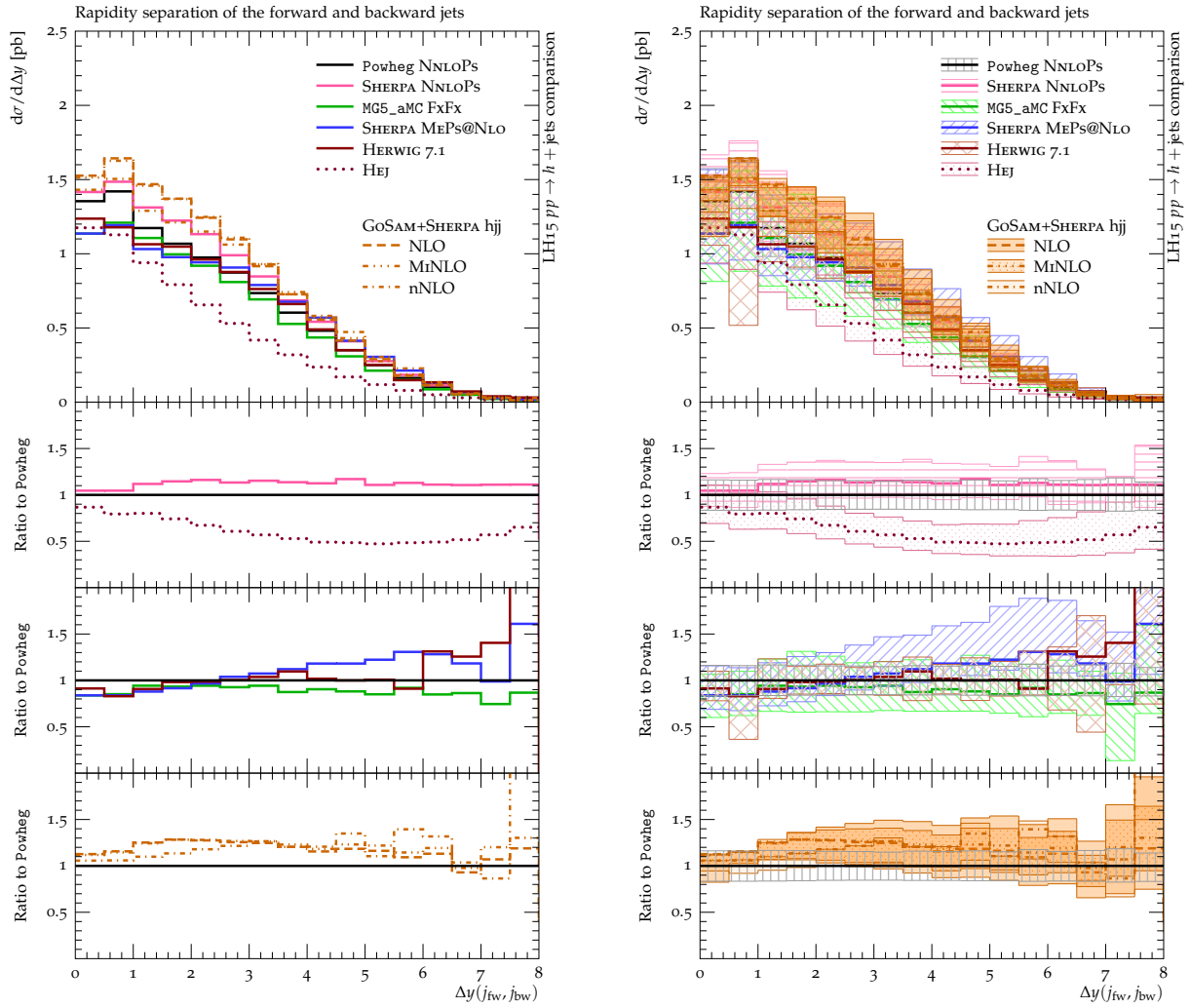


Fig. IV.25: The rapidity separation between the two jets most widely separated in rapidity, i.e. the two most forward/backward jets for $h + \geq 2$ -jets production, shown without (left) and with (right) uncertainties. The plot layout is the same as the one used in Figure IV.18.

agreement with each other and, as seen in the subleading jet's spectrum, larger than POWHEG by about 20%. For the NLO-based calculations, the uncertainties are as expected or observed previously, except for the fact that SHERPA's quoted uncertainties for the MEPS@NLO calculation rise at larger rapidity separation, likely due to identified scales of low value in that region. The NNLOPS predictions formally possess LO accuracy only, but as mentioned several times this is not reflected by the given uncertainty estimates. HEJ again predicts a more rapid decrease of the $\Delta y(j_1, j_2)$ distribution. As this observable is used to identify VBF topologies, it is clear that the cross section computed by HEJ after imposing VBF selection criteria will turn out to be substantially different.

As a short digression, it is interesting to consider the rapidity separation of the most forward and backward jets, instead of the two leading jets. Of course, only that fraction of dijet events which are accompanied by a third (or more) jet (i.e. three-jet events) result in a different value for this observable, as compared to $\Delta y(j_1, j_2)$ for the p_\perp ordered case. It is argued that additional jet production in such rapidity ordered states is well described by calculations incorporating BFKL effects. The overall pattern of results between the p_\perp and rapidity ordered case is the same; certainly, the latter selection leads to a wider Δy distribution.

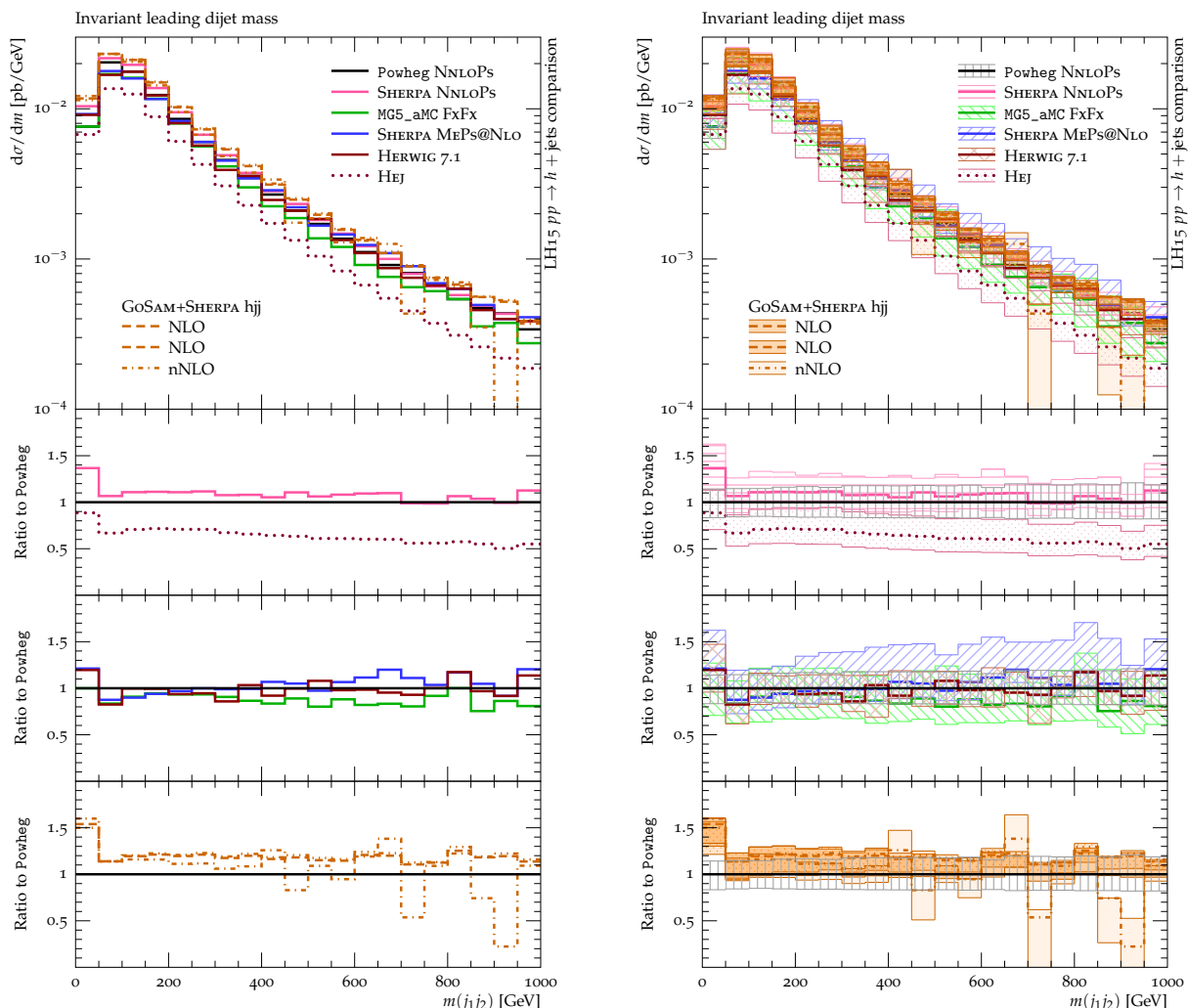


Fig. IV.26: The invariant mass distribution of the leading dijet system in $h + \geq 2$ -jets production, shown without (left) and with (right) theoretical uncertainties. The plot layout is the same as the one used in Figure IV.18.

In more detail, Figure IV.25 shows a somewhat different relative and absolute behavior of the various calculations. POWHEG NNLOs here tends to generate slightly more central jets than the other calculations, while the opposite is true for SHERPA MEPS@NLO, which exhibits a clear slope wrt. POWHEG. Again, for SHERPA MEPS@NLO, this behavior can be traced back to SHERPA MEPS@NLO using its parton shower in the scale setting procedure for forward jet production. The fixed order calculations of GOSAM+SHERPA now possess a small shape difference compared to the POWHEG reference, which was not present in the leading jets version of this observable. On the other hand, HEJ produces the same relative shape that it showed in the leading jets case, up to rapidity separations of around 4. For larger rapidity differences, it moves closer to the reference prediction, being 30% below the reference at $\Delta y = 8$. Taking the assumption that HEJ provides the best description in this kinematic regime at face value, all DGLAP based parton shower resummations, as well as fixed order calculations, predict cross sections that are too large at large rapidity intervals.

Similar conclusions as for Figure IV.24 hold for for the dijet invariant mass distribution formed by the leading jets, although the differences among predictions are smaller. In fact, Figure IV.26 shows that there are almost no shape deviations among the various predictions,

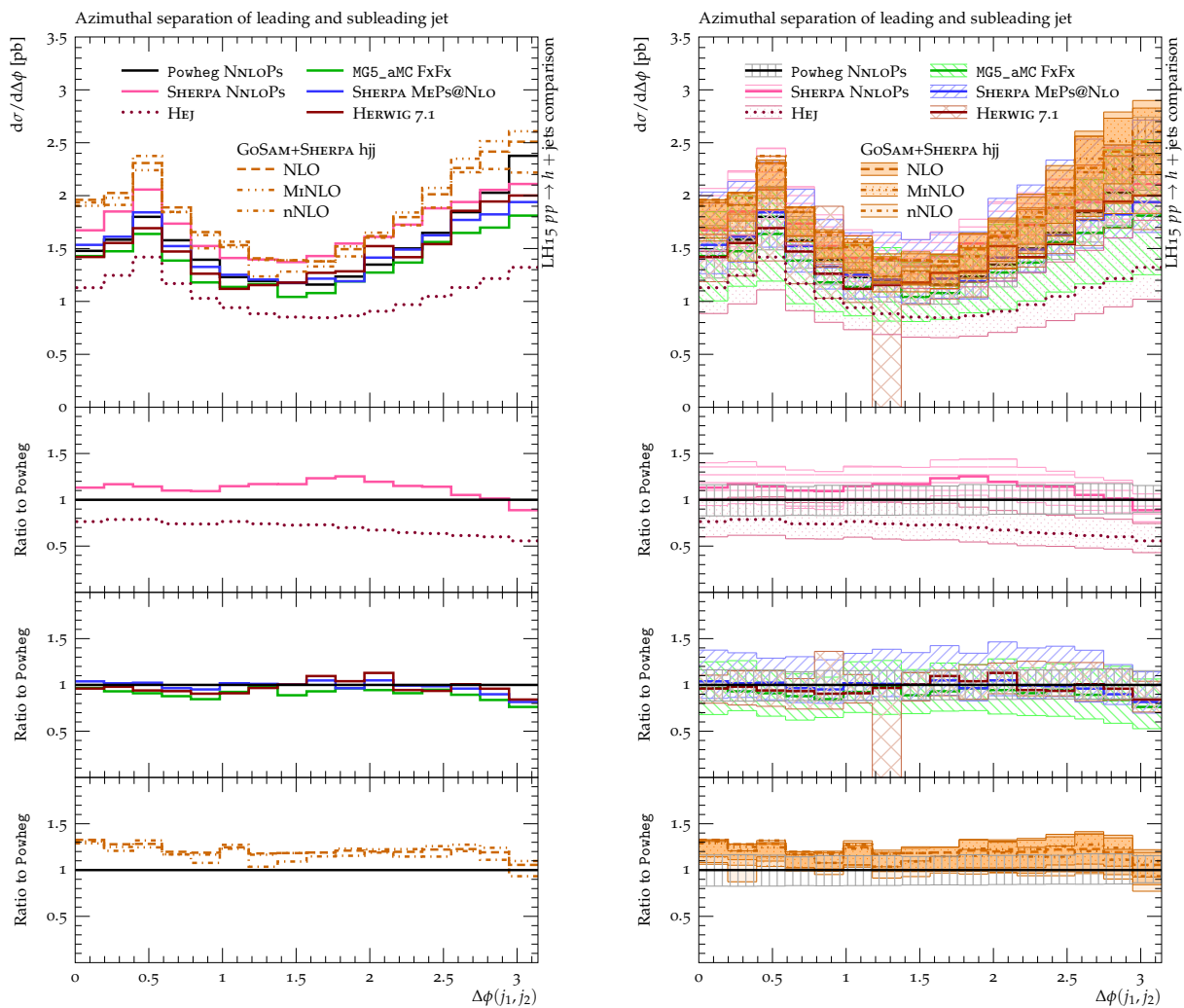


Fig. IV.27: The azimuthal angle separation, $\Delta\phi(j_1, j_2)$, between the two leading jets for $h + \geq 2$ -jets production, presented without (left) and with (right) the associated theoretical uncertainties. Again, the plot layout is the same as the one used in Figure IV.18.

except for the first-to-second bin transition, which POWHEG and Madgraph5_aMC@NLO predict to rise more strongly. All other deviations are mainly driven by rate differences. SHERPA NNLOPs is larger than POWHEG NNLOPs by about 10%, and maintains this excess almost throughout the whole range. The multijet merged calculations are also in good agreement with the POWHEG reference and, more importantly, with one another. Only Madgraph5_aMC@NLO falls below Herwig 7.1 and SHERPA MEPS@NLO, being about 20% lower at 1 TeV, but well within the uncertainties of the other calculations. The GOSAM+SHERPA NLO calculations display the same increase of the cross section wrt. the reference as seen before – a constant 20% increase. The scale variations in all three methods, pure NLO, MiNLO and LOOPSIM, are also in agreement for this observable. Only LOOPSIM suffers somewhat from the limited statistics of its NLO $hjjj$ component. Again, HEJ deviates more strongly, but this time mainly as a result of its LO normalization, being a near constant $\sim 40\%$ below the other predictions.

As a last multi-object observable, we examine the azimuthal separation of the leading dijet pair. Although this observable plays a crucial role only after VBF selection cuts are made, it is interesting to analyze this observable for the inclusive dijet selection in order to judge which features are impressed upon it by the VBF event selection. Inherent differences in the

description on the inclusive level will invariably feed through to the VBF analysis level, and will then be overlaid with the cut efficiency effects of the various calculations. The observable possesses two topologically distinct regions. In the first at $\Delta\phi \gtrsim 0$, both jets are in the same azimuthal hemisphere and recoil against the Higgs boson plus softer radiation (including further jets if present). For this configuration, larger parton shower effects are expected. Conversely, for $\Delta\phi \lesssim \pi$, both jets are back-to-back, recoiling against each other – but they do not necessarily have to be p_\perp balanced. In this situation, the Higgs boson will mostly have small-sized to medium-sized transverse momentum. While the Higgs boson’s transverse momentum is affected by parton showering off these topologies, the $\Delta\phi$ distribution is more robust regarding these corrections. The various predictions for the $\Delta\phi$ separation between the two leading jets are shown in Figure IV.27, and are found to be in reasonable agreement with each other, neglecting for a moment the lower rate of HEJ due to the LO normalization. HEJ features a roughly 20% smaller cross section for small $\Delta\phi$, which increases to about 40% in the dijet back-to-back region. SHERPA NNLOPS exhibits again a larger cross section, $\mathcal{O}(15\%)$ for $\Delta\phi \lesssim 2.5$, when compared to the POWHEG NNLOPS result. It agrees with POWHEG NNLOPS in the dijet back-to-back region. All multijet merged distributions agree very well with each other and the reference. The same applies to the various GOSAM+SHERPA NLO calculations; they agree very well among themselves, despite their different scales and inputs, but exhibit a 20% higher rate wrt. the reference for $\Delta\phi > 0.5$, which increases to 30% as $\Delta\phi \rightarrow 0$. There is one feature of the POWHEG reference that stands out from the crowd of other predictions, which is that it rises more strongly than the others towards the $\Delta\phi = \pi$ limit. The shape change wrt. HEJ is however fairly mild. Recalling that the second jet is only described at LO in POWHEG, it is more than plausible that any NLO treatment will depopulate this area to some extent. As for the case of SHERPA NNLOPS, it is more subtle, but the reason for the different behavior, as before, lies in the choice of scales. Again, the example of the p_\perp balanced jet topologies and their scale setting, which we discussed for the $p_\perp(h)$ distribution in the $n_j \geq 2$ -jet bin, can be used to understand why SHERPA’s NNLOPS generates this different behavior in this region.

3.3.4 VBF observables

A situation where Higgs boson production through gluon fusion primarily serves as a background is found in analyses intended to measure its couplings to weak vector bosons. To enhance the relative contribution of processes where the Higgs boson production proceeds through weak vector boson fusion (VBF), additional cuts are placed on the so-called tagging jets. The tagging jets themselves can now be defined in multiple ways. In the study performed during the Les Houches 2013 workshop [325], the standard leading (p_\perp -ordered) jet selection was supplemented with the forward-backward selection defining the pair of jets with the largest rapidity separation as tagging jets. Another strategy using the highest invariant mass jet pair was also studied more recently [331].

In this analysis, the leading and subleading jets are required to have a mass greater than 400 GeV and a rapidity separation greater than 2.8. This set of cuts is referred to as VBF cuts. An alternative set of cuts (VBF2) requires that any two jets satisfy the above requirements. For many observables, the distributions are similar for the two cases, and only the VBF cut scenario will be presented. Results for the alternative choice can be found at the project’s webpage [328].

The inclusive jet multiplicity distributions after the application of the VBF (VBF2) cuts are shown in Figure IV.28 (Figure IV.29). The hierarchy observed is essentially the same as for the inclusive jet multiplicity distribution without any cuts. The differences among the predictions are slightly smaller with the VBF2 cuts than with the VBF cuts. In both cases, the NNLOPS calculations are again in good agreement, with SHERPA NNLOPS predicting slightly larger cross sections. HEJ predicts only about 50% of the cross section of NNLOPS. For the

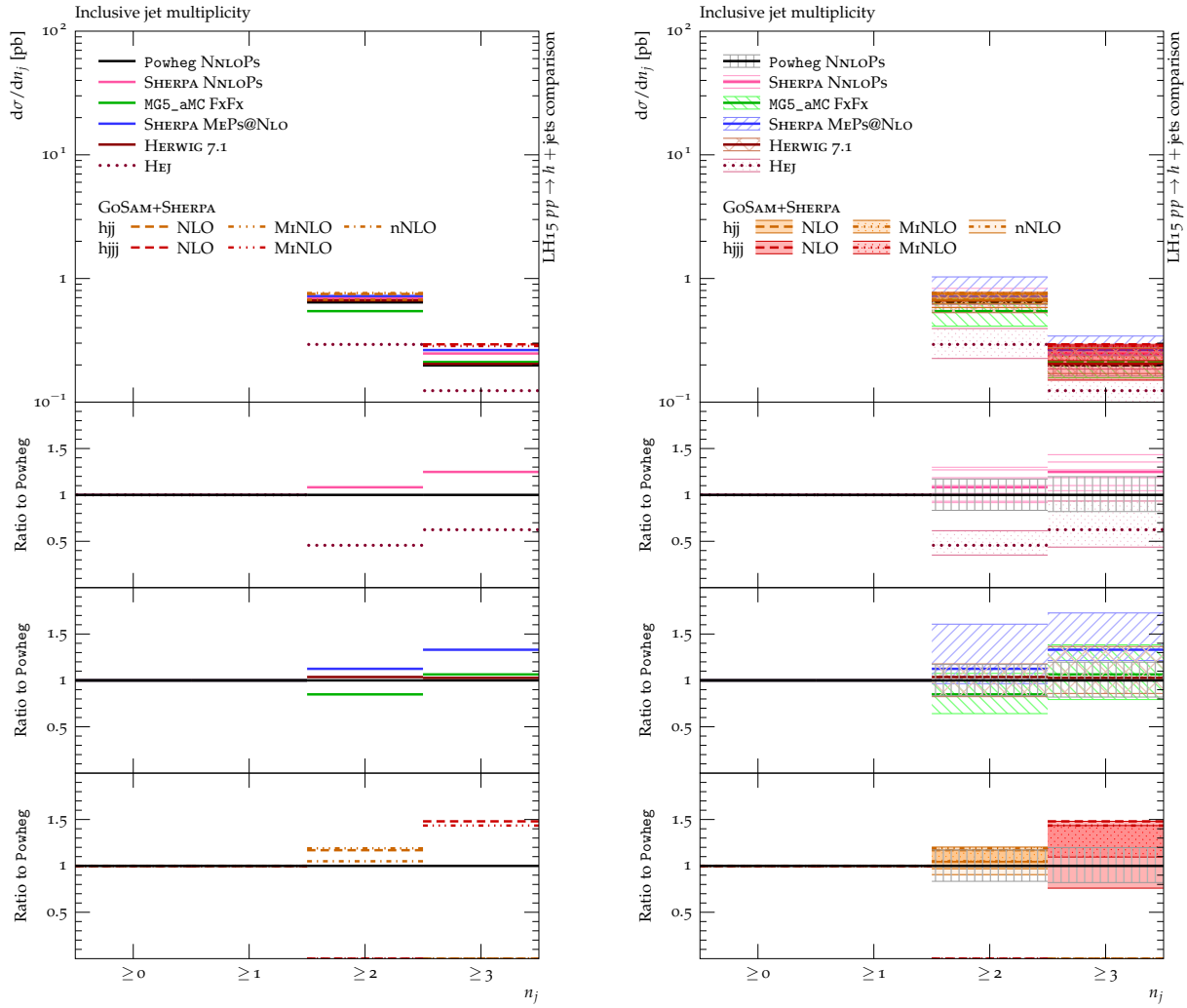


Fig. IV.28: The inclusive jet multiplicities after imposing the leading tag-jets definition (see text for the details of the ‘VBF’ selection), shown without (left) and with (right) uncertainties.

≥ 2 -jet bin, the NLO merged predictions vary from a 20% smaller cross section (**Madgraph5_aMC@NLO**) to a 20% larger cross section (**SHERPA MEPS@NLO**); both are at the edge of the NNLOPS uncertainty band. Interestingly, their uncertainty is of similar size as NNLOPS, $\sim 20\%$, despite being of NLO accuracy for these observables (only LO for NNLOPS). This hints at underestimated uncertainties of the NNLOPS calculations for this observable. The NLO and MiNLO GOSAM+SHERPA predictions are also 20% larger than the NNLOPS result in the ≥ 2 jet bin, close to the **SHERPA MEPS@NLO** prediction, while the **LOOPSIM** prediction is about 5% higher than the NNLOPS predictions. More differences are apparent after requiring a third jet. The NLO and MiNLO GOSAM+SHERPA predictions are substantially larger than the NNLOPS predictions and the prediction from **Madgraph5_aMC@NLO** and **Herwig 7.1**, but in better agreement with that from **SHERPA MEPS@NLO**. This is expected given the NLO normalization present in those calculations (NLO, MiNLO GOSAM+SHERPA, **SHERPA MEPS@NLO**). The third jet arises from parton showering in the NNLOPS calculations and from the parton shower matched leading order matrix elements in **Madgraph5_aMC@NLO** and **Herwig 7.1**. Owing to the matching techniques employed and the resummation uncertainties that have not been evaluated, the uncertainties are underestimated in both calculations. The same therefore holds for **POWHEG NNLOPS** and (partially) for **SHERPA NNLOPS**.

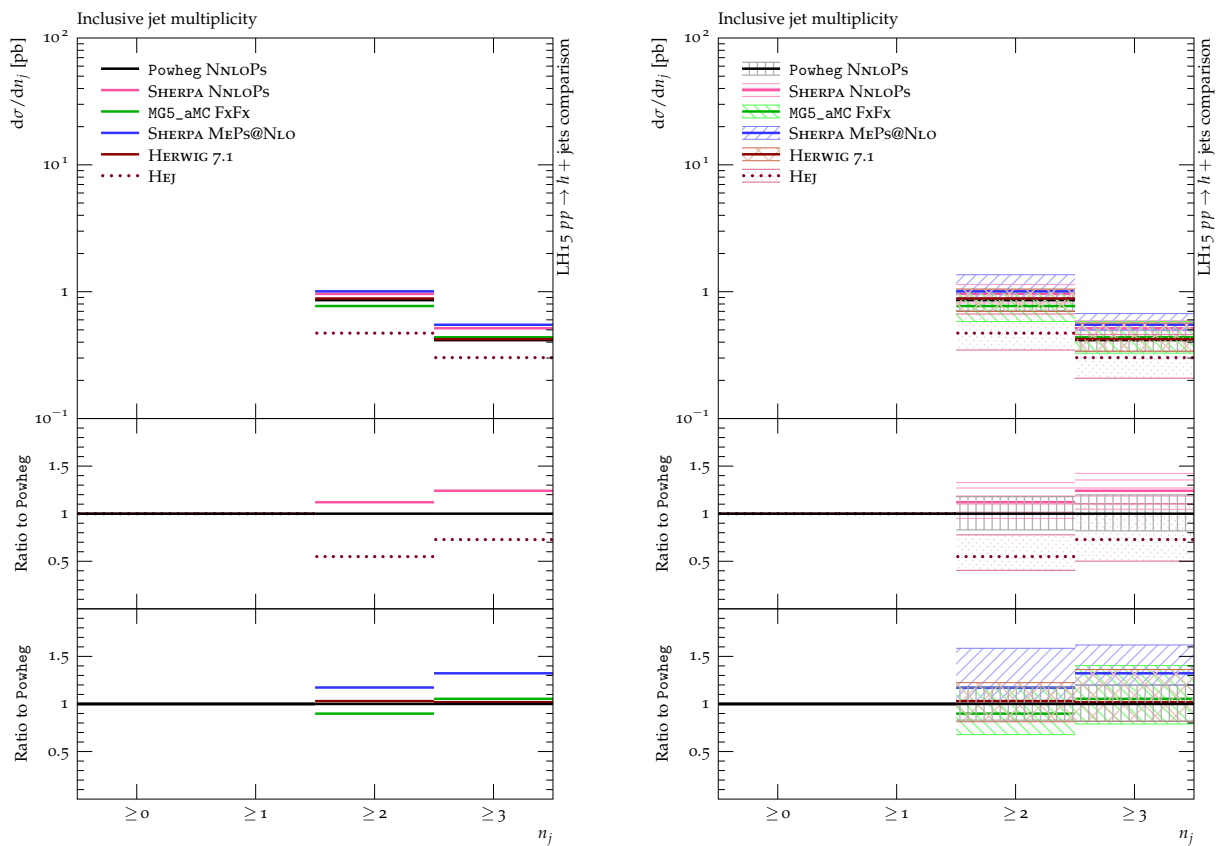


Fig. IV.29: The inclusive jet multiplicities after the application of the ‘VBF2’ tag-jets cuts (see text for the definition), shown without (left) and with (right) uncertainties.

The azimuthal separation between the two tagging jets is a crucial observable in VBF measurements. In general, there is good agreement among the various predictions for this observable, with the caveat that SHERPA, in both its NNLOs and its MEPS@NLO forms, predicts a shallower dip at $\Delta\phi(j_1, j_2) \approx \frac{\pi}{2}$, something that can be traced to its parton shower. Similar distributions (and agreement) are observed if the generalised tagging jet definition (VBF2) is used.

3.3.5 Multijet observables

In this section we consider observables sensitive to more than two jets. The most accurate predictions here come from the NLO computations of GOSAM+SHERPA and SHERPA MEPS@NLO both of which include the 3rd jet at NLO accuracy and the 4th jet at LO accuracy. Madgraph5_aMC@NLO and Herwig 7.1 both include the 3rd jet at LO while the 4th jet is LO in Herwig 7.1 but showered in Madgraph5_aMC@NLO. HEJ also includes LO matrix elements for the production of the thirf jet. The NNLOs codes only have parton shower accuracy throughout the observables of this section.

The Higgs boson transverse momentum distribution for $h + \geq 3$ jets is shown in Figure IV.31. In general we see larger results from predictions with at least LO accuracy over POWHEG, which includes the 3rd jet via the parton shower. The SHERPA NNLOs result is also significantly larger than POWHEG which shows that the SHERPA shower generates more radiation than PYTHIA 8. The HEJ prediction begins to increase over POWHEG at high p_T and is closer there to the NLO results of GOSAM+SHERPA and SHERPA MEPS@NLO. The multijet merged calculations on the whole agree well within scale uncertainties, though these are rather large for

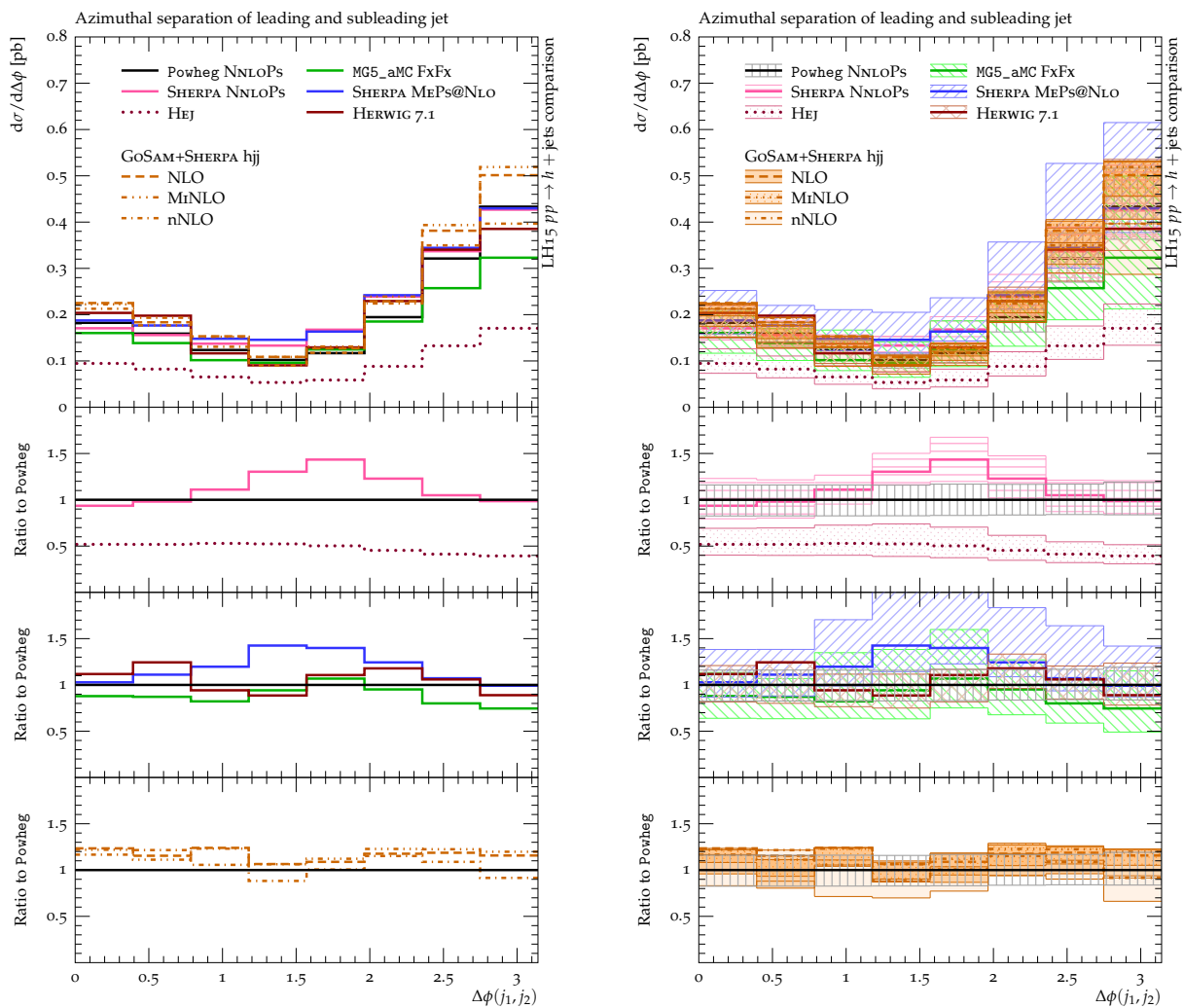


Fig. IV.30: The azimuthal separation of the leading jet pair (VBF cuts) shown without (left) and with (right) uncertainties in $h + \geq 2$ -jet production.

Madgraph5_aMC@NLO, and the central value for Herwig 7.1 shows a clear deviation below the jet p_T cut. The benefit of NLO accuracy is clearly seen in the GOSAM+SHERPA result, which has large corrections with respect to POWHEG. The MINLO scale choice used in the fixed order computation has a central value that is almost identical to the dynamical scale of $\frac{1}{2} \sqrt{m_h^2 + \sum p_{T,j_i}^2}$. The scale variations however are much smaller than the fixed order NLO.

The third jet p_T for $h + \geq 3$ jets is shown in Figure IV.32. Overall, a similar pattern to the previous Higgs boson transverse momentum distribution is followed. SHERPA MEPS@NLO has a much smaller scale uncertainty than Madgraph5_aMC@NLO, which mirrors the small scale uncertainty of the NLO GOSAM+SHERPA calculation. The fixed order GOSAM+SHERPA results show more than a 50% increase over POWHEG at large p_T . The close agreement between central values of GOSAM+SHERPA using the dynamical scale of $\frac{1}{2} \sqrt{m_h^2 + \sum p_{T,j_i}^2}$, and MINLO is somewhat surprising. The MINLO results again show a significant decrease in scale variations - particularly at high p_T . Care should be taken in interpreting the high p_T region since due to the complexity of the phase space, the MC statistical error is beginning to come into play.

The H_T^{jet} distribution, defined as sum scalar sum of all jet transverse momenta, is shown in Figure IV.33. Requiring $h + \geq 1$ -jet final states this observable is extremely sensitive to addi-

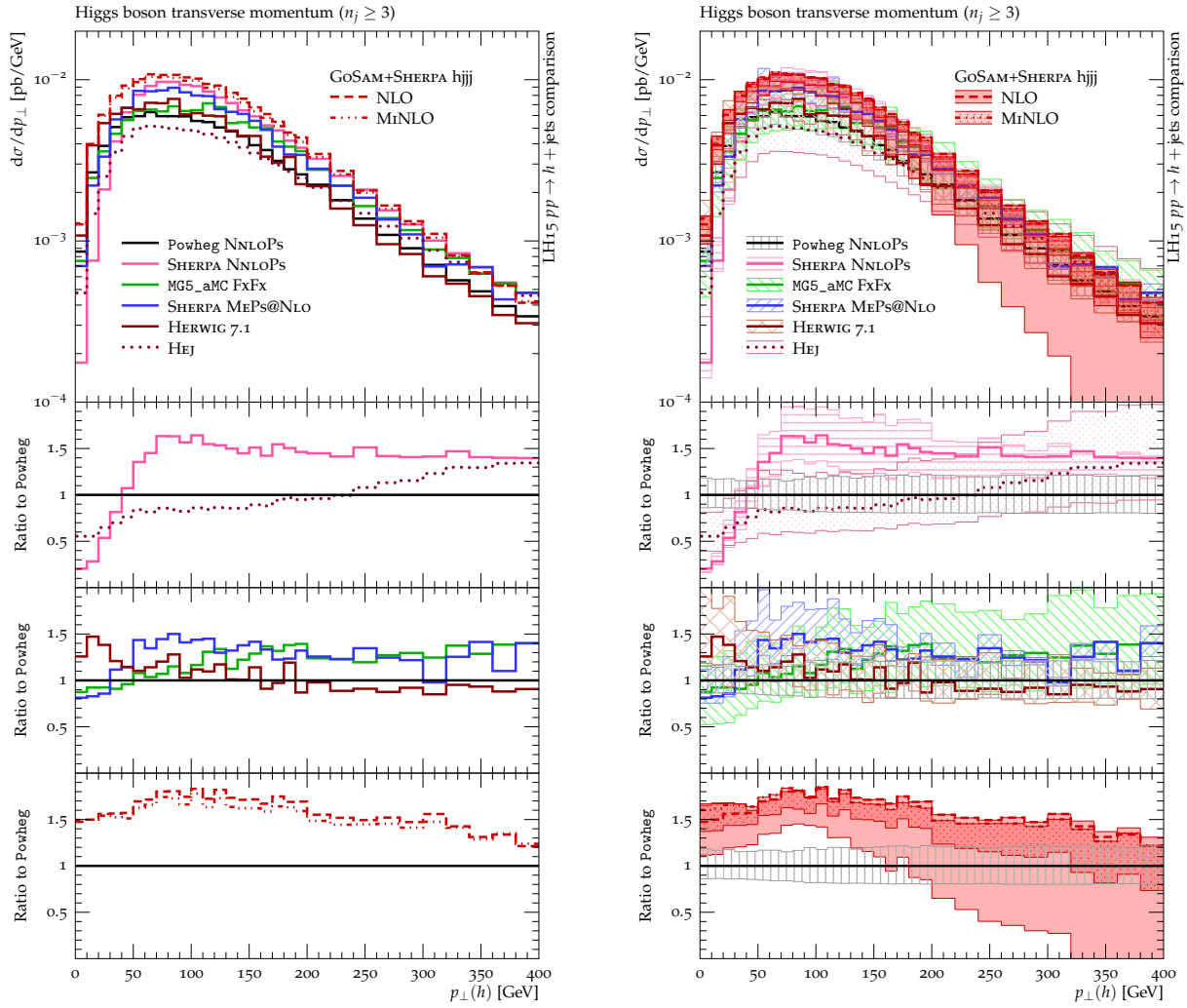


Fig. IV.31: The Higgs boson transverse momentum in the presence of at least three jets, shown without (left) and with (right) theoretical uncertainties.

tional radiation and is a useful case to observe the impact of different jet multiplicities. While the NNLOs computations of SHERPA and POWHEG deviate significantly for $150 \text{ GeV} < H_T^{\text{jet}} < 600 \text{ GeV}$, SHERPA NNLOs agrees better with the BFGLP h_j NNLO fixed order prediction and, to a certain extent, the SHERPA MEPS@NLO computation. Herwig 7.1 and Madgraph5_aMC@NLO give results consistent with POWHEG except for deviations at low energies but with relatively large errors.

For very high H_T^{jet} all tools including some approximation to the 3rd jet converge, while NLO predictions for $h+1$ jet quickly begin to fall away from the other predictions. The LOOPSIM $h+(1,2)$ jet prediction at nNLO does a good job of matching the complete NNLO result here, as it is designed to do. One also clearly sees the benefit of the 3rd jet at NLO accuracy. The scale variations for the NLO $h+3$ jet cross section, either at fixed order with LOOPSIM or with the MINLO procedure or with the fully merged prediction with SHERPA MEPS@NLO, have significantly smaller errors above 400 GeV than the other predictions.

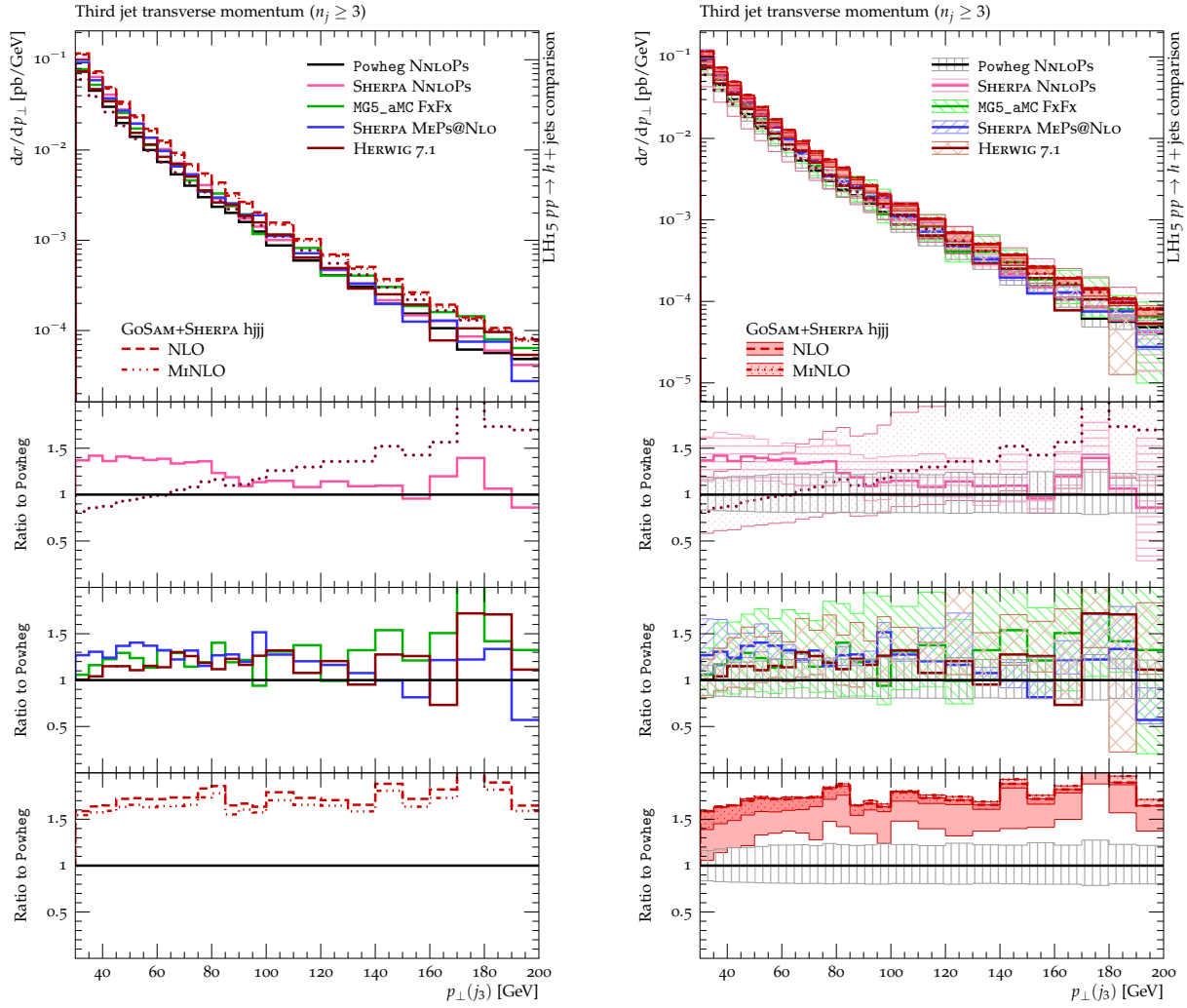


Fig. IV.32: The third jet transverse momentum distribution for $H + \geq 3$ jets shown without (left) and with (right) theoretical uncertainty bands.

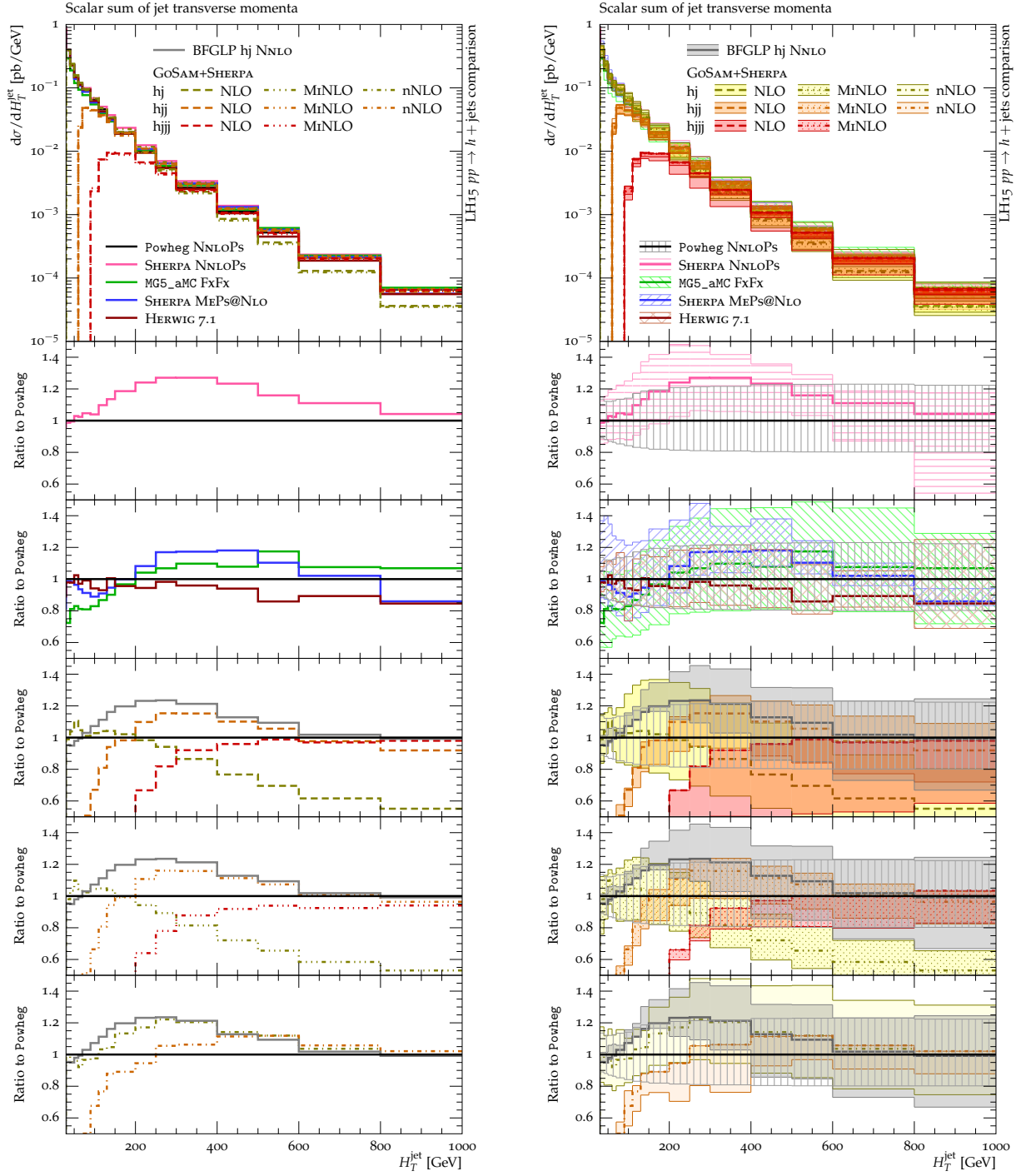


Fig. IV.33: The $H_{T,\text{jets}}$ distribution for $H + \geq 1$ jet final states, without (left) and with (right) uncertainties.

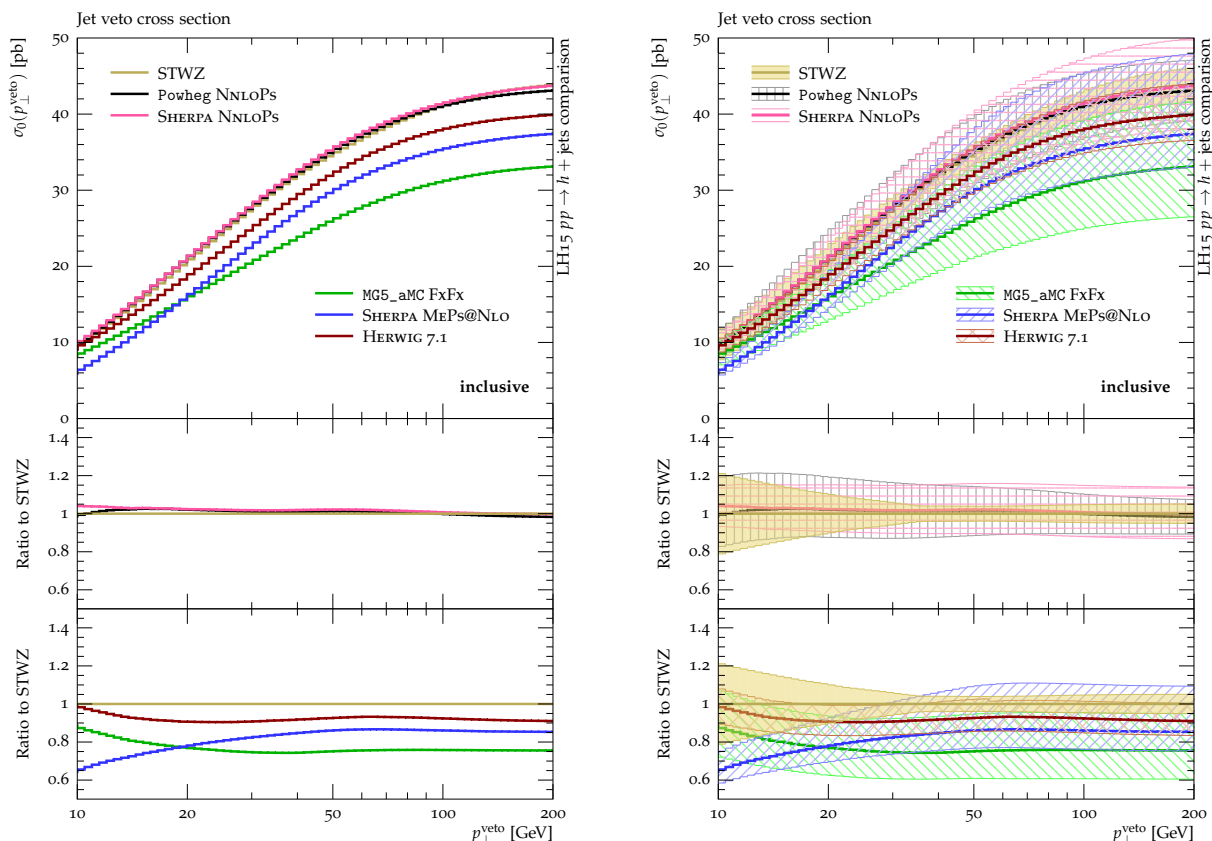


Fig. IV.34: The exclusive zero jet cross section as a function of the vetoed minimal leading jet transverse momentum, without (left) and with (right) uncertainties.

3.3.6 Jet veto cross sections

In this section, we investigate jet veto cross sections, where the phase space for additional gluon radiation is suppressed by means of a jet veto. In Figures IV.34-IV.36, additional radiation has been vetoed by the application of a maximal transverse momentum for the (sub)leading jet, p_{\perp}^{veto} . The observables plotted in the figures recover the respective inclusive cross sections as $p_{\perp}^{\text{veto}} \rightarrow \infty$. In this region, the fixed order part of the respective calculations dominates the cross section and associated uncertainties. The opposite regime, where $p_{\perp}^{\text{veto}} \rightarrow 0$, is a classic example of a resummation-dominated observable. Here, the properties of the respective parton showers come fully into play and differences are largely due to their separate characteristics.

We start by considering the cross section for the production of a Higgs boson and no additional jets, as a function of the minimum jet transverse momentum as shown in Figure IV.34. Remarkable, and possibly largely accidental, agreement between both NNLOPs simulations and the dedicated resummation calculation of STWZ is found, typically better than 5% within the considered range. However, as the resummation accuracy for both NNLOPs' implementations is limited by their parton shower's accuracy and they do not (POWHEG) or only partially (SHERPA) assess their intrinsic resummation uncertainties and the interplay with the hard process' scale variations, their uncertainties are less well-determined than those of STWZ. Consequently, while both NNLOPs' uncertainties are largely independent of p_{\perp}^{veto} , those of the dedicated STWZ calculation show the expected comparably large uncertainty in the resummation dominated region gradually easing into the near constant small fixed-order uncertainty at large p_{\perp}^{veto} as the influence of the resummation decreases. For $p_{\perp}^{\text{veto}} \rightarrow \infty$ all vetoed cross sections revert to their inclusive NNLO accuracy, showing the improved convergence of the STWZ calculation

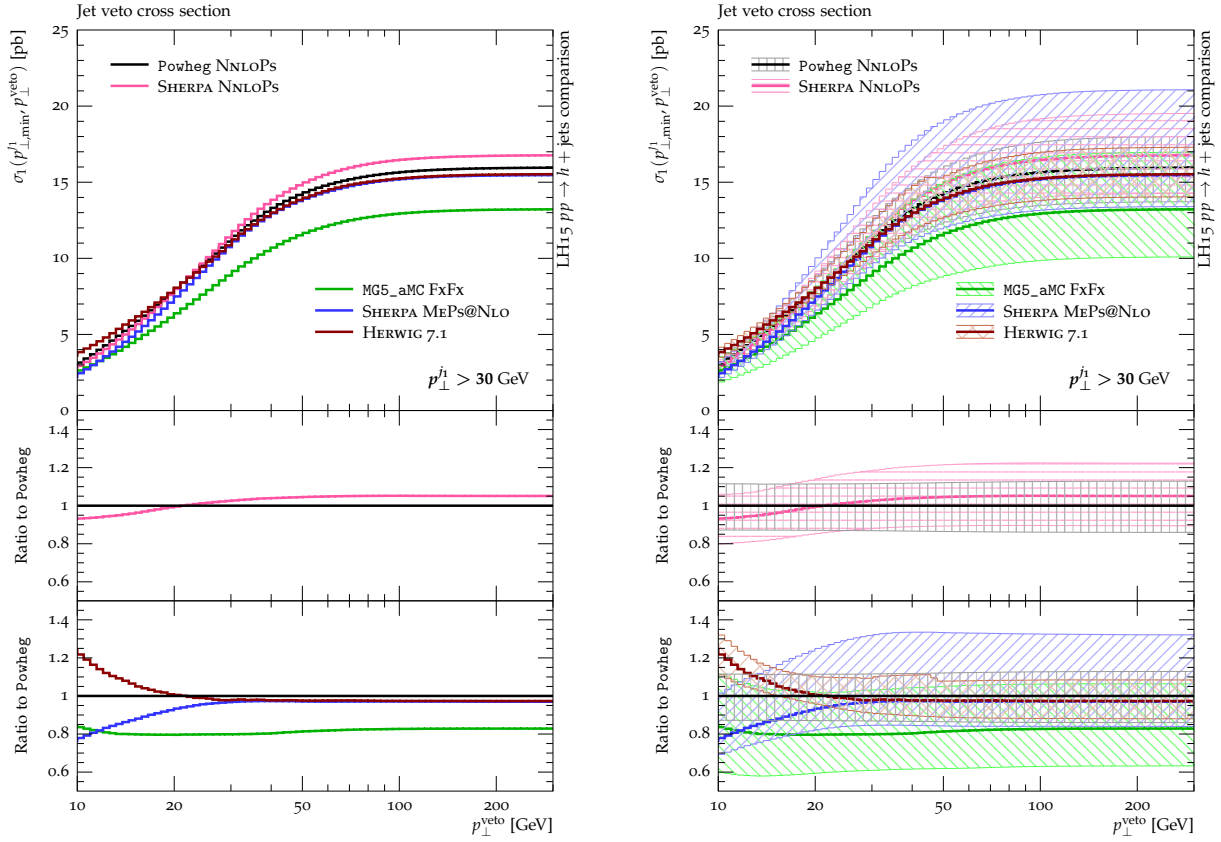


Fig. IV.35: The cross section for events containing a Higgs boson and one jet with $p_{\perp} > 30$ GeV as a function of the vetoed minimal second jet transverse momentum without (left) and with (right) uncertainties.

thanks to its included π^2 -resummation, cf. also Fig. IV.9. The multijet merged predictions have a wider variation, and have veto cross sections lower than those provided by the STWZ and the NNLOPS predictions. In addition to suffering from their NLO normalisation in the $p_{\perp}^{\text{veto}} \rightarrow \infty$ limit, they also show different behavior as $p_{\perp}^{\text{veto}} \rightarrow 0$. For example, SHERPA MEPS@NLO exhibits more QCD activity than the other computations.

Next, we require the presence of at least one jet with a minimal transverse momentum of either 30 or 200 GeV. The cross sections as a function of the subleading jets' maximal transverse momentum are displayed in Figure IV.35 and Figure IV.36 for the two lead jet cuts. Note that, although all parton shower matched or merged calculations have the same accuracy both as $p_{\perp}^{\text{veto}} \rightarrow \infty$ and in the resummation dominated region, the multijet merged calculations possess a better description of the second jet emission, and thus should lead to more accurate results throughout the spectrum, provided the merging systematics are under control. Currently employed uncertainty estimates, however, will not reflect this, as resummation uncertainties are not assessed or only incompletely assessed.

If we put no special requirements on the leading jet, cf. Figure IV.35, good agreement between all calculations is found. The NNLOPS predictions agree again within 5% of one another and have very similar uncertainties. This is noteworthy as, in comparison with the results of Figure IV.34, both calculations' accuracies have been degraded by one order. The multijet merged calculations show similar behavior as in the previous case: Madgraph5_aMC@NLO exhibits a smaller cross section due to its scale choice while SHERPA MEPS@NLO predicts more soft radiation. The relative lack of small p_{\perp} radiation is more pronounced in Herwig 7.1 for this

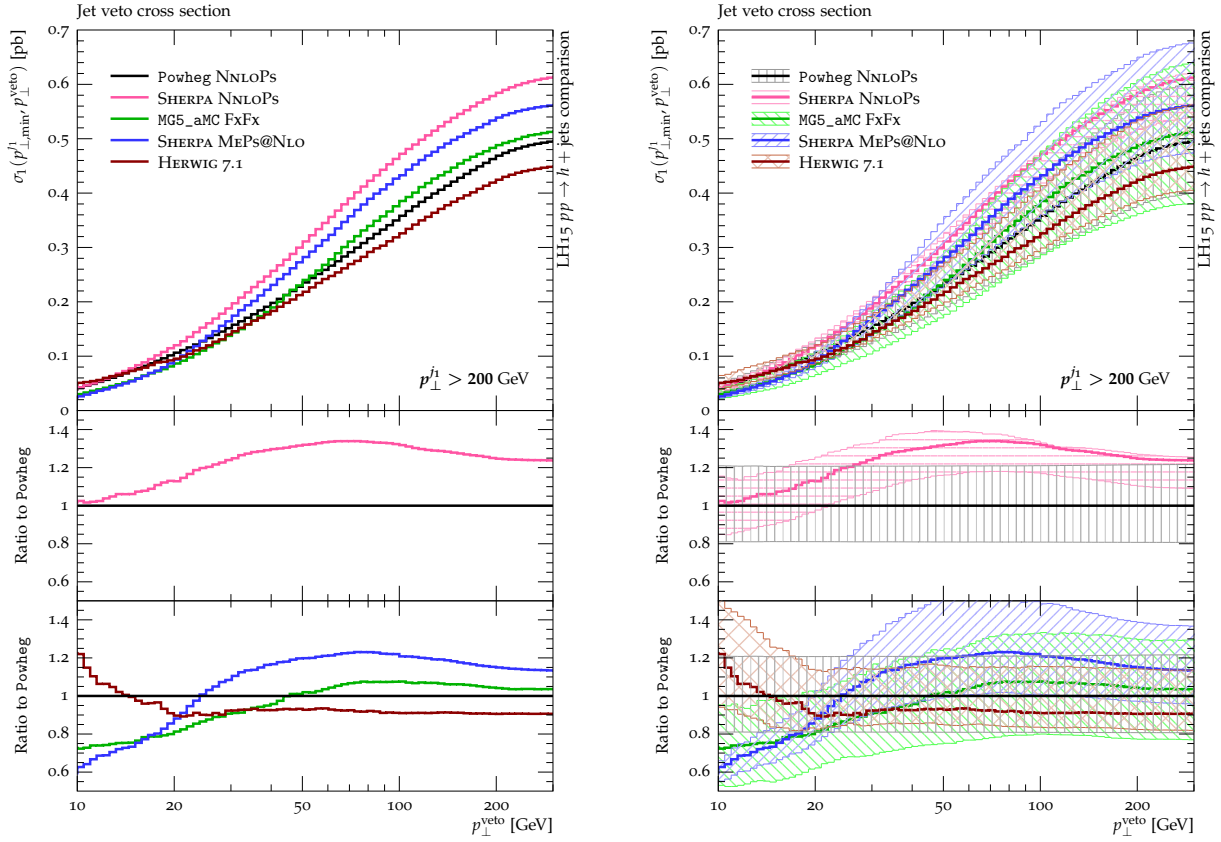


Fig. IV.36: The cross section for events containing a Higgs boson and one jet with $p_{\perp} > 200$ GeV as a function of the vetoed minimal second jet transverse momentum without (left) and with (right) uncertainties.

observable. Again, the uncertainties of `Madgraph5_aMC@NLO` and SHERPA are of similar size while those of `Herwig 7.1` are somewhat smaller than those of the NNLOPs predictions, especially in the resummation-dominated region $p_{\perp}^{\text{veto}} \rightarrow 0$.

Raising the requirements on the leading jet to 200 GeV, in Figure IV.36, displays clear distinctions between the different calculations. SHERPA NNLOPs and POWHEG NNLOPs have noticeably different shapes, with SHERPA having a much lower cross section for low values of the subleading jet veto requirement. The multijet merged calculations show `Herwig 7.1` largely agreeing with POWHEG with a constant offset of -10% , and the familiar lower probability of low- p_{\perp} jet emissions. The asymptotic cross section for SHERPA MEPS@NLO is similar to that from SHERPA NNLOPs and, unsurprisingly, due to the use of the same parton shower, shows a similar radiation pattern. As before, it exhibits a relative overabundance of soft jet radiation. Lastly, the asymptotic cross section from `Madgraph5_aMC@NLO` is the same level as POWHEG's, despite its higher scale choice. The pattern of the uncertainties, however, remains the same as before.

3.4 Conclusions

Precision Higgs boson measurements will soon be possible using the new 13 TeV data currently being collected during Run II of the LHC. The largest Higgs boson production process is gluon fusion. A variety of theoretical tools exist for predictions for Higgs boson (+jets) production in this channel. As higher order corrections are especially sizable for $gg \rightarrow h$, it is important to understand the accuracies and regions of applicability of the various predictions. Too often, the comment has been that since the predictions agree within the theoretical uncertainties, all is

well. However, a higher standard must be used, as the predictions have many of the theoretical uncertainties, such as scale uncertainties, in common.

We have compared fixed order predictions at NLO and NNLO (including approximate NNLO), resummed predictions, NNLO predictions matched to parton showers, multijet merged predictions at NLO accuracy, and resummations in the BFKL limit. This allows a better understanding of two main issues: firstly how consistent are calculations which should be consistent, and secondly the impact of soft gluon radiation and higher order corrections. All predictions have been carried out without non-perturbative corrections to allow for a one-to-one comparisons. A few observations follow.

NNLO effects can change not only the normalization of distributions, but also the shape. For example, NLO predictions of the Higgs rapidity distribution are all similar in normalization and shape; however, the NLO predictions fall off more rapidly at high rapidity than predictions at NNLO. The differences between NLO and NNLO, however, are only noticeable in regions beyond the kinematic cuts applied at the LHC. It is interesting that, for the scale choices used in this study, there is neither a shape nor normalization shift from the NNLO corrections for the inclusive lead jet p_{\perp} distribution while they are present for the Higgs boson p_{\perp} in the presence of at least one jet..

The highest precision for inclusive jet multiplicity distributions is present with fixed order predictions, either at NLO or NNLO; in general, predictions from resummed/parton shower programs agree well with the fixed order predictions within their expected accuracy. The most extensive comparisons in this study are with respect to the p_{\perp} distribution for the lead jet in $h + \geq 1$ jet events. With the recent NNLO calculation for this quantity, the uncertainties are less than 10%. As mentioned above, the NNLO corrections are small. The NNLOPS predictions for this variable are in good agreement with each other as well as with the NLO/NNLO predictions for $p_{\perp} \leq 100$ GeV/c, with some separation between the NNLOPS results at higher transverse momentum. The multijet jet merged predictions agree well with NLO/NNLO at low p_{\perp} , but fall below by about 15-20% at high p_{\perp} , an effect that can be attributed to the specific scale choices. The resummed prediction from STWZ and RESBOS2 agree well at low p_{\perp} , but rise above the fixed order results by about 20% at high p_{\perp} , again due to differences in the scale choice. One of the key take-home points is that the introduction of a parton shower or a resummation should not greatly affect the fixed order results, for observables that are suitably inclusive. These conclusions are largely true for comparisons for the sub-leading and third-leading jet as well. The situation is more complex for exclusive final states, where a jet veto is applied to any additional jet. Here, there are jet veto logs that have to be resummed. We note, though, in general that there is still good agreement among the predictions used here. Although, this is not explicitly part of this study, we note that the impact of jet veto logarithms (after resummation) on the NNLO prediction for $h + \geq 1$ jet are small, indicating again that the fixed order predictions for that quantity should be reliable [129, 399].

Resummed/parton shower predictions provide a better description for observables where Sudakov effects are important, such as the transverse momentum distribution for inclusive (exclusive) Higgs production. For the inclusive case, all predictions agree well with each other (and with the reference HQT), with some deviations observed at the lowest p_{\perp} values. Differences are more evident for the exclusive case, where the high transverse momentum for the Higgs boson must be supplied by a combination of jets lower than the 30 GeV cutoff and soft gluon radiation. Although the fixed order predictions are unstable at low p_{\perp} , there is good agreement with the resummed/parton shower predictions at high p_{\perp} , where the bulk of the transverse momentum for the resummed/parton shower prediction is provided by the hard matrix element.

In Sudakov regions involving multiple jets the situation gets more complex and discrepancies are often more evident, as for example for the Higgs boson p_{\perp} distribution in $h + \geq n$

jet production, or the system p_{\perp} for $h + n$ jets. It is interesting to note that the fixed order predictions are more stable at low transverse momentum when more jets are involved (as expected).

The rapidity interval between two jets for $h + \geq 2$ jets might be thought of as a fairly robust variable. However, differences can be observed among the various multijet merged predictions at high Δy . This is especially true if the two most forward-backward (rather than the two leading) jets are chosen, indicating perhaps that the differences in evidence are a result of the parton shower. It is interesting to note that the POWHEG NNLOPS and SHERPA NNLOPS predictions agree well with each other and with the fixed order predictions (taking into account the NLO corrections present in the latter). The $\Delta\phi$ distribution between the two leading jets is an observable where basically all predictions agree.

In order to measure the vector boson fusion process, additional kinematic cuts are necessary to reduce the gluon-gluon fusion background, requiring a dijet rapidity separation, and/or a dijet mass requirement, applied either to the leading jets (VBF) or to any pair of jets (VBF2). The cross sections for ≥ 2 and ≥ 3 jets from SHERPA MEPS@NLO and from GOSAM+SHERPA (with either of the VBF cuts) are larger than those from POWHEG NNLOPS, expected as the normalizations for the ≥ 2 and ≥ 3 jet cross section for the former are at NLO. In general, the predictions for the kinematic distributions are similar among the various programs for both VBF and VBF2 cuts, except that both SHERPA MEPS@NLO and SHERPA NNLOPS tend to predict a shallower dip that occurs in the $\Delta\phi$ distribution at values around 1.5. The effect is larger when the the second tagging definition is used, as might be expected if the effect was primarily due to the parton shower.

A multi-jet quantity such as $H_{T,\text{jets}}$ is sensitive to radiation/production of extra jets. Basically, all programs, with the exception of Herwig 7.1, predict larger cross section than POWHEG NNLOPS. The largest deviations are from the NNLO $h + \geq 1$ jet prediction, at $H_{T,\text{jets}}$ values roughly from 200 GeV to 400 GeV. It is interesting that the LOOPSIM (nNLO) prediction for the same quantity is in good agreement with the exact NNLO prediction, as expected from the LOOPSIM procedure.

Finally, we conclude with a brief review of the results from the jet veto cross section comparisons. For $h +$ no jets, the NNLOPS predictions are in remarkable agreement with those obtained from STWZ. There is a wider variation from the multijet merged programs, with all predicting a smaller jet veto cross section than STWZ and the NNLOPS programs. For h plus exactly one jet (≥ 30 GeV), the two NNLOPS predictions are still in agreement with each other, and with the multijet predictions, with some divergence as the jet veto threshold is reduced below 30 GeV. If the lead jet threshold is increased to 200 GeV, there is a wide divergence of predictions, indicating the difficulties of dealing with such multi-scale situations.

Acknowledgements

We thank the organisers. The work of SH, YL and SP was supported by the U.S. Department of Energy under contract DE-AC02-76SF00515. The work of FJT was supported by the German Science Foundation (DFG) through the Emmy-Noether Grant No. TA 867/1-1. MS acknowledges support by the Swiss National Science Foundation (SNF) under contract PP00P2-128552. KB would like to thank Keith Hamilton and Giulia Zanderighi for their advice and support.

4 Photon isolation studies ¹²

We study the effect of various photon isolation criteria in processes involving single photon plus jet and diphoton production.

¹² L. Cieri, G. Heinrich

4.1 Introduction

Final states involving isolated photons have played and still do play a very important role at the LHC. Due to the clean photon signal, the diphoton channel has been the discovery channel for the Higgs boson, and it keeps intriguing us by exhibiting structures that may hint to resonances existing around 750 GeV.

Even within the Standard Model, photons in the final state can have a number of different origins. They can either originate directly from the hard interaction (in this case they are called *direct*), or they can come from a fragmentation process of a QCD parton in the final state. Further there is a (large but reducible) background of secondary photons coming from the decay of pions, η -mesons, etc. In order to suppress the background, an *isolation criterion* is usually applied, which suppresses both the secondary photons and the fragmentation component.

Beyond the leading order, the distinction between the direct and the fragmentation contribution is not unique any more. For example, at NLO, the collinear splitting of a parent quark into a photon and quark leads to a singularity, which can be absorbed into fragmentation functions, analogous to the absorption of initial state QCD radiation into “bare PDFs”. The fragmentation functions have a perturbative component, involving the splitting function $P_{q\rightarrow\gamma+q}(x)$, and a non-perturbative component which has to be obtained from fits to data. As these fits have been done based on LEP data, and are less refined than the PDF fits which are based on a wealth of data and which are constantly improved, there is an inherent uncertainty in the fragmentation component which makes it desirable to suppress this contribution as much as possible. Another reason to suppress it, apart from the obvious experimental reasons, is given by the fact that higher orders for this part are much more difficult to calculate than for the direct photon contribution, as it requires the calculation of jet cross sections, which are then convoluted with the fragmentation functions.

In the following we will study the behaviour of the direct and fragmentation contributions with different isolation criteria and at different orders in perturbation theory, not only for diphotons, but also for photon plus jet final states. We will also study how the effects vary with the centre of mass energy by comparing results for $\sqrt{s} = 8, 14$ and 100 TeV.

4.2 Isolation criteria

The most commonly used isolation criterion at hadron collider experiments is a *cone-based isolation* prescription. In this procedure, the photon candidate is called isolated if in a cone of radius R in rapidity y and azimuthal angle ϕ around the photon direction, the amount of hadronic transverse energy $\sum E_T^{had}$ is smaller than some value E_T^{max} chosen by the experiment:

$$\sum E_T^{had} \leq E_T^{max}$$

inside a cone with $(y - y_\gamma)^2 + (\phi - \phi_\gamma)^2 \leq R^2$. (IV.14)

E_T^{max} can be defined either in absolute terms, or as fraction ϵ_c of p_T^γ (typically $\epsilon_c = 0.1$ or below).

In a theoretical calculation, the need for a fragmentation contribution can be eliminated by using a *smooth isolation* criterion [321], where the threshold on the hadronic energy inside the isolation cone decreases with the radial distance from the photon. It is described by the cone size R , a weight factor n and an isolation parameter ϵ_f . With this criterion, the photon is isolated if

$$\sum E_T^{had} \leq E_T^{max} \chi(r)$$

inside each cone with $r^2 = (y - y_\gamma)^2 + (\phi - \phi_\gamma)^2 \leq R^2$, (IV.15)

where the function $\chi(r)$ has to fulfill

$$\chi(r) \rightarrow 0 \text{ if } r \rightarrow 0 \text{ and } 0 < \chi(r) < 1 \text{ if } 0 < r < R. \quad (\text{IV.16})$$

One possible choice is

$$\chi(r) = \left(\frac{1 - \cos(r)}{1 - \cos R} \right)^n, \quad (\text{IV.17})$$

where usually $n = 1$ and $E_T^{max} = \epsilon_f p_T^\gamma$ are chosen.

However, due to finite detector resolution, an experimental realization of this criterion will only be possible to some minimal value of r , thereby leaving potentially a residual collinear contribution.

We would also like to point out that ϵ_f and ϵ_c are not directly comparable, because ϵ_f is still multiplied by $\chi(r)$ and therefore can be much larger than ϵ_c for comparable values of $\sum E_T^{had}$.

4.3 Results

4.3.1 Diphotons at NLO

We compare the standard and the smooth cone [321] isolation prescriptions using an acceptance criterion based on Higgs boson searches and studies [400]. We present numerical results at NLO requiring $p_T^{\text{harder}} \geq 40$ GeV and $p_T^{\text{softer}} \geq 30$ GeV, and restricting the rapidity of both photons to $|y_\gamma| < 2.37$. We use the NNPDF23_nlo_as_0119 [194] PDF set with densities and α_s evaluated at each corresponding order (i.e., we use $(n + 1)$ -loop α_s at NⁿLO, with $n = 0, 1$) and we consider $N_f = 5$ massless quarks/antiquarks as well as gluons in the initial state. The QED coupling constant α is fixed to $\alpha = 1/137$. We show results for three different values for the centre of mass energy: $\sqrt{s} = 8$ TeV, 14 TeV and 100 TeV, where we consider the standard cone isolation criterion implemented in the numerical code `DiPhox` [401], and we use two different sets of fragmentation functions: the Bourhis-Fontannaz-Guillet (BFG) [402] set¹³ and the LO fragmentation functions by Owens¹⁴ [403]. The smooth cone isolation prescription is implemented in the numerical code `2 γ NNLO` [404]. We compare both isolation criteria using the following isolation parameters: $\epsilon_c = \epsilon_f = 0.05, 0.1, \text{ and } 0.5$. We impose a size of the cone $R = 0.4$ and in the smooth cone isolation criterion we use $n = 1$.

In Fig. IV.37 we show the invariant mass distributions at the centre of mass energies $\sqrt{s} = 8$ TeV, 14 TeV and 100 TeV for two values of the isolation parameter: $\epsilon = 0.1$ (left panel) and $\epsilon = 0.5$ (right panel). In Fig. IV.37 we notice the different orders of magnitude of the cross-sections depending on the centre of mass energy. In the following we study in detail each centre of mass energy and whether it is possible to define a “*tight isolation prescription*” [1].

In the left panel of Fig. IV.38 we show the invariant mass distribution of the diphoton pair at NLO for a centre of mass energy of $\sqrt{s} = 8$ TeV. For tight isolation parameters ($\epsilon \leq 0.1$) we observe that the two criteria give essentially the same result (agreement at percent level) considering the BFG fragmentation functions. While for *loose* isolation parameters (in particular for $\epsilon = 0.5$) the result with the smooth cone is about 9% smaller than the standard cone result (with BFG). The cross-section obtained with the Owens set of fragmentation functions coincides (within 1%) with the standard cone (BFG) and smooth cone differential cross-sections for the tight isolation parameter $\epsilon = 0.05$. However, for $\epsilon = 0.1$, the cross section obtained with the Owens fragmentation functions starts to deviate (being about 2.3% larger) from the result with the BFG fragmentation functions and the cross section obtained with the smooth cone isolation

¹³The BFG set is obtained from an NLO fit to LEP data.

¹⁴The LO Owens fragmentation functions are used only in combination with the LO matrix elements.

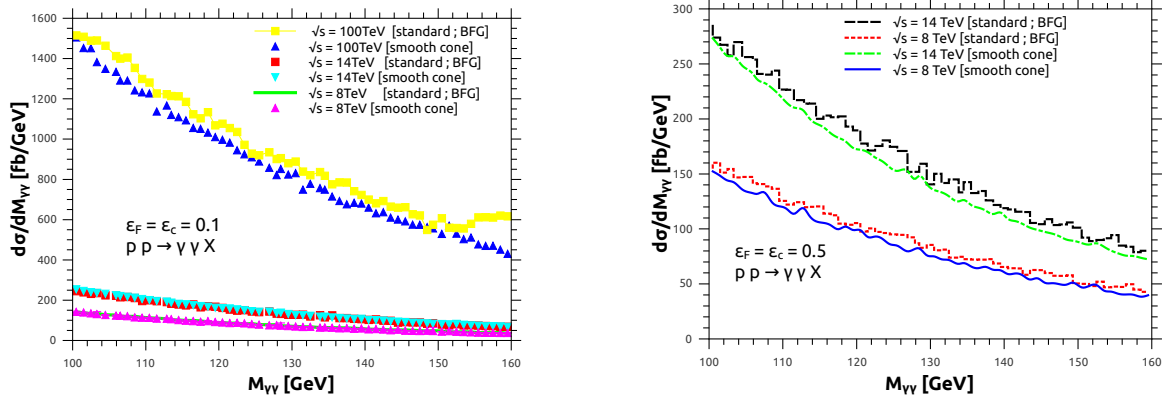


Fig. IV.37: Comparison of different isolation criteria at $\sqrt{s} = 8$ TeV, 14 TeV and 100 TeV. In the left panel we show the invariant mass distribution obtained with $\epsilon = 0.1$ and in the right panel the corresponding one for $\epsilon = 0.5$.

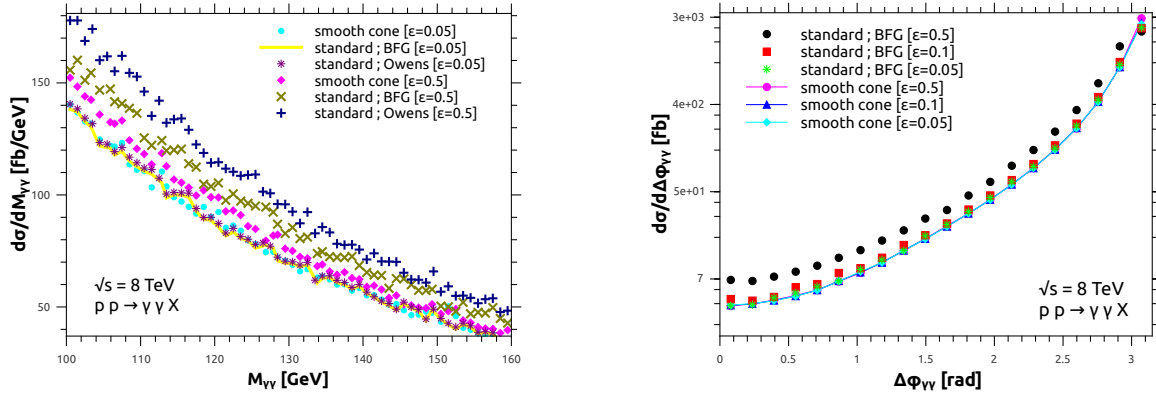


Fig. IV.38: Comparison of different isolation criteria at $\sqrt{s} = 8$ TeV. In the left panel we show the invariant mass distribution and in the right panel the $\Delta\Phi_{\gamma\gamma}$.

criterion. For $\epsilon = 0.5$ the Owens result exhibits large deviations from the BFG (10%) and smooth (19%) cross-sections.

In the right panel of Fig. IV.38 we present the results for the $\Delta\Phi_{\gamma\gamma}$ distribution. In this differential distribution, $\Delta\Phi_{\gamma\gamma} = \pi$ is the Born-like kinematical region in which the two photons are back-to-back. All the other kinematical regions are away from the back-to-back configuration. Kinematical regions with $\Delta\Phi_{\gamma\gamma} \neq \pi$ receive contributions from NLO real radiation configurations to the direct photon matrix element, or from the fragmentation part. The standard cone cross-section obtained with the BFG set of fragmentation functions is about 4% larger than the smooth cone cross-section ($\Delta\Phi_{\gamma\gamma} \neq \pi$) if tight isolation parameters are considered ($\epsilon \leq 0.1$).

For $\epsilon = 0.5$, the distribution obtained with the smooth cone isolation is about 37% smaller than the standard cone result with BFG fragmentation functions for $\Delta\Phi_{\gamma\gamma} \neq \pi$.

The ratio between the smooth cone results with $\epsilon = 0.05$ and $\epsilon = 0.5$ is close to 1 (within 0.1%) for all the kinematical ranges with the exception of the last bin¹⁵ $\Delta\Phi_{\gamma\gamma} \simeq \pi$, which contains the Born-like contributions. This fact can be explained noticing that all configurations

¹⁵Concerning the $\Delta\Phi_{\gamma\gamma}$ distribution in the last bin $\Delta\Phi_{\gamma\gamma} \simeq \pi$ the cross section with the smooth cone criterion using $\epsilon = 0.5$ is about 12.8% larger than the cross section obtained with $\epsilon = 0.05$.

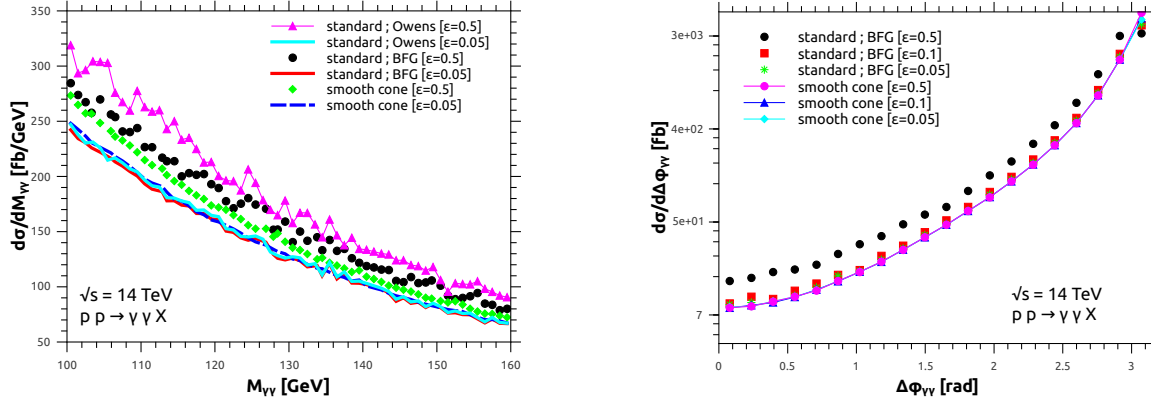


Fig. IV.39: Comparison of different isolation criteria at $\sqrt{s} = 14$ TeV. In the left panel we show the invariant mass distribution and in the right panel the $\Delta\Phi_{\gamma\gamma}$ distribution.

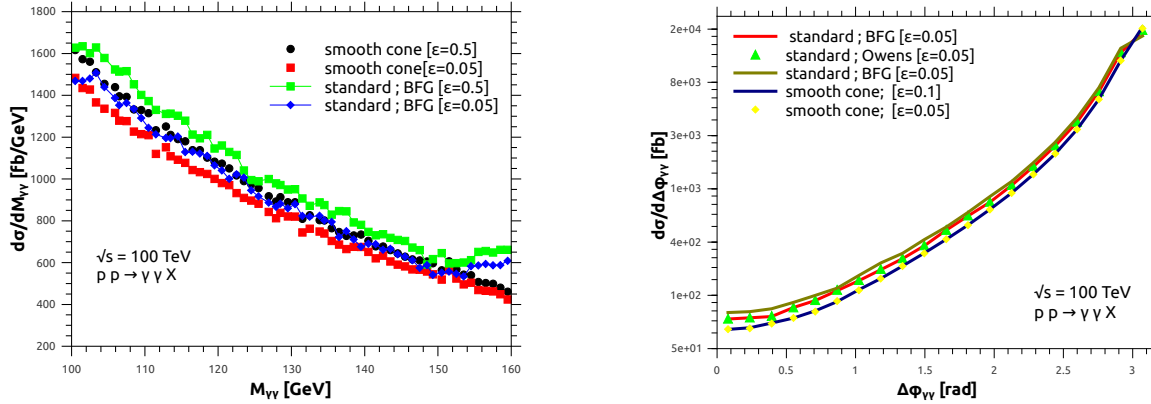


Fig. IV.40: Comparison of different isolation criteria at $\sqrt{s} = 100$ TeV. In the left panel we show the invariant mass distribution and in the right panel the $\Delta\Phi_{\gamma\gamma}$ distribution.

where the extra QCD parton (which is present at NLO in the real radiation part) lies outside the cone around each photon are independent of the value for ϵ or E_T^{max} , while the nearly collinear configurations are suppressed with smooth isolation, and the ones where the extra parton is soft or collinear to one of the photons contribute to the back-to-back situation $\Delta\Phi_{\gamma\gamma} \simeq \pi$.

At $\sqrt{s} = 14$ TeV (Fig. IV.39), concerning the invariant mass and the $\Delta\Phi_{\gamma\gamma}$ distributions, we have essentially the same considerations as at $\sqrt{s} = 8$ TeV.

In Fig IV.40 we present our results for $\sqrt{s} = 100$ TeV. In the left panel we show the invariant mass distribution in which we compare the results using the smooth and standard cone isolation criteria. The cross section obtained using the smooth isolation criterion is about 7.5% smaller than the standard cone result using BFG fragmentation functions for $\epsilon = 0.05$. For $\epsilon = 0.5$, the smooth cone result is about 8.4% smaller than the standard cone result with BFG fragmentation. The cross section obtained using the Owens set of fragmentation functions is about 18% larger than the BFG result with $\epsilon = 0.5$, which is almost twice the same ratio at 8 TeV. Regarding the smooth cone result with $\epsilon = 0.5$, the cross section obtained with the Owens set is about 26.4% larger.

In the right panel of Fig IV.40 we show the $\Delta\Phi_{\gamma\gamma}$ distribution for $\sqrt{s} = 100$ TeV. The cross sections obtained with the standard cone isolation criterion with BFG and Owens fragmentation

functions coincide (within 1%) if $\epsilon = 0.05$. The standard result (with BFG) obtained using $\epsilon = 0.1$ is about 23% larger than the cross section with the smooth cone isolation (if $\Delta\Phi_{\gamma\gamma} \neq \pi$).

Similar to the centre of mass energies already discussed, far away from $\Delta\Phi_{\gamma\gamma} \simeq \pi$ there is no difference between the smooth cone result with $\epsilon = 0.05$ and $\epsilon = 0.5$.

At $\sqrt{s} = 100$ TeV the fragmentation functions, extracted at lower energies (from LEP data), reach the limit of their validity range. Notice that the invariant mass distributions (left panel of Fig IV.40), obtained with the standard cone isolation criterion, show a rising slope in the last bins, which most likely comes from the fact that the range of validity of the fragmentation functions (BFG quote a range of $10 \text{ GeV} \leq Q \leq 100 \text{ TeV}$) is surpassed.

At $\sqrt{s} = 8$ TeV and 14 TeV it is possible to define a tight isolation prescription as done in the 2013 Les Houches proceedings [1].

If we require $\epsilon \leq 0.05$ the two isolation criteria give very similar cross sections, with agreement at the percent level, also at the level of distributions. For $0.05 \leq \epsilon \leq 0.1$ we have agreement at the percent level, for all the kinematical regions in which a LO Born cross-section is present. For kinematical regions far way from the back-to-back configuration, in which the direct LO contribution vanishes (i.e $\Delta\Phi_{\gamma\gamma} \neq \pi$ in the $\Delta\Phi_{\gamma\gamma}$ distribution), the discrepancies between cross-sections obtained using the standard and the smooth cone isolation criteria are at the 4% percent level. Given the size of the scale uncertainties at these energies and at this perturbative order ($\pm 6\%$ percent at the level of total cross-sections), a tight isolation prescription ($\epsilon < 0.1$) allows the comparison of cross sections obtained using these two different types of isolation criteria.

4.3.2 Photon + Jet at NLO

In this section we use the program `JetPhox` [405,406] to calculate cross sections for the production of a photon and a jet. As `JetPhox` allows to calculate the fragmentation component at NLO, it can be used to assess the importance of this contribution for various isolation parameters and centre of mass energies.

Unless stated otherwise, we use the Bourhis-Fontannaz-Guillet (BFG) [402] fragmentation functions (set II). For comparison, we also give results obtained with the (LO) fragmentation functions by Owens [403], which we use for consistency only in combination with the leading order matrix elements.

We use the following settings and cuts: the NNPDF23_nlo_as_0119 [194] PDF set with α_s taken from the PDFs. For the renormalisation, factorisation and fragmentation scales we use $\mu = \mu_f = \mu_F = p_T^\gamma$. The photon is required to be in the rapidity range $|y^\gamma| \leq 2.37$ and to have a minimum transverse momentum of $p_{T,min}^\gamma = 30 \text{ GeV}$. For the jet we use the k_T -algorithm with $R = 0.4$ and the rapidity and transverse momentum cuts $|y^{jet}| \leq 4.7$, $p_{T,min}^{jet} = 25 \text{ GeV}$.

We will compare three different isolation prescriptions:

- (a) smooth isolation (“Frixione isolation” [321]) as defined in eq. (IV.15), with $R = 0.4$, $n = 1$ and various values of ϵ_f ,
- (b) standard cone isolation as defined in eq. (IV.14) with $R = 0.4$ and $E_T^{max} = \epsilon_c p_T^\gamma$,
- (c) “hybrid” cone isolation with E_T^{max} composed of both, a fixed amount of energy and a fraction of the photon transverse momentum, as used e.g. in Ref. [407]: $E_T^{max} = \epsilon p_T^\gamma + 6 \text{ GeV}$ with $\epsilon = 0.05$.

In Table IV.11 we show results for the total NLO cross sections using criterion (a) at $\sqrt{s} = 8, 14$ and 100 TeV. Table IV.12 shows results for the standard cone isolation criterion (b), Table IV.13

\sqrt{s} [TeV]	smooth isol.	$\epsilon_f = 0.05$	$\epsilon_f = 0.1$	$\epsilon_f = 0.5$
8	LO	13.172	13.172	13.172
	NLO	25.418	25.757	27.501
14	LO	23.396	23.396	23.396
	NLO	46.793	47.409	50.719
100	LO	13.607	13.607	13.607
	NLO	300.70	305.09	327.76

Table IV.11: Total cross sections (in nanobarn) for the smooth isolation criterion [321] with different values of ϵ_f .

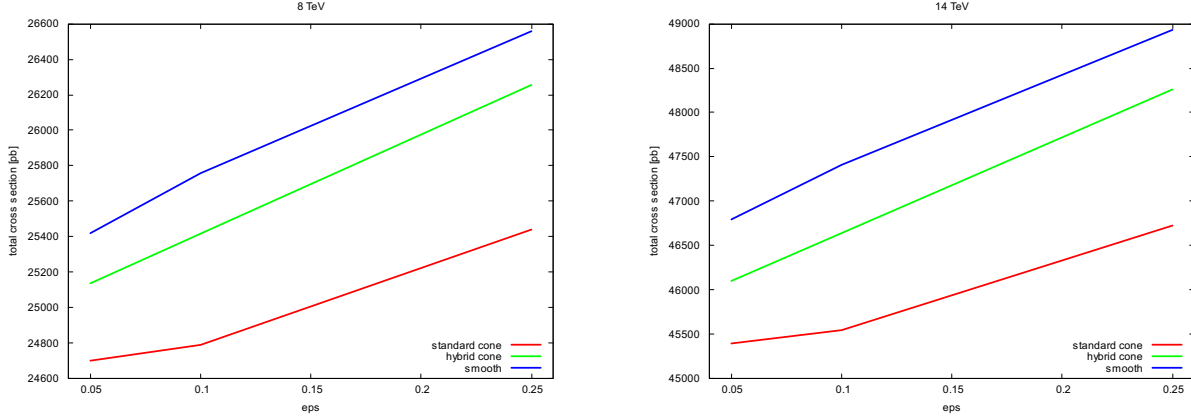


Fig. IV.41: Comparison of different isolation criteria at $\sqrt{s} = 8$ and 14 TeV.

for the hybrid cone isolation criterion (c). The results for the direct and fragmentation parts are shown separately. In particular, one can see that the NLO corrections to the fragmentation part are substantial, in particular for small values of ϵ_c , with K-factors (for the fragmentation component) of about 2.2 (8 TeV) to 2.4 (100 TeV) for standard cone isolation, and about 1.7 for hybrid cone isolation. With the hybrid isolation criterion, this K-factor does not increase as the centre of mass energy increases. However, as the fragmentation component is about one order of magnitude smaller than the direct component, the K-factor for the fragmentation part does not play a major role.

The results for the total cross sections at $\sqrt{s} = 8$ TeV obtained with the three criteria are compared to each other in Fig. IV.41. As to be expected, the hybrid isolation leads to larger values of the cross section than the standard cone isolation for the same value of ϵ_c , because it allows a larger fragmentation component. It is interesting to observe that, in contrast to the diphoton case, the cross sections obtained with the smooth isolation criterion are always larger than the ones obtained with standard or hybrid cone isolation. This means that the subtraction terms for collinear configurations in the direct photon component are more dominant in the photon plus jet case than in the diphoton case.

Fig. IV.42 shows various options for the fragmentation contribution separately, for $\sqrt{s} = 14$ TeV. In Figs. IV.43, IV.44, IV.45 we compare the standard and the hybrid cone isolation for the distributions of p_T^γ , $\Delta R^{\gamma-jet}$ and $\Delta\phi^{\gamma-jet}$, respectively.

\sqrt{s} [TeV]	standard cone isol.	$\epsilon_c = 0.05$	$\epsilon_c = 0.1$	$\epsilon_c = 0.25$
8	dir NLO	22.682	21.249	18.803
	frag LO (BFG)	0.824	1.738	3.956
	frag LO (Owens)	0.930	1.980	4.808
	frag NLO	2.017	3.539	6.636
	total NLO	24.699	24.788	25.439
14	dir NLO	41.577	38.861	34.145
	frag LO (BFG)	1.559	3.296	7.554
	frag LO (Owens)	1.772	3.788	9.296
	frag NLO	3.815	6.682	12.577
	total NLO	45.393	45.544	46.724
100	dir NLO	265.44	246.55	213.66
	frag LO	10.593	22.547	52.634
	frag NLO	25.688	45.321	86.586
	total NLO	291.13	291.87	300.25

Table IV.12: Total cross sections (in nanobarn) for the cone isolation criterion with $R = 0.4$ and different values of ϵ_c . Note that “frag LO” refers to the matrix element being calculated at leading order, while the BFG fragmentation functions are always NLO fits, the Owens fragmentation functions LO fits.

\sqrt{s} [TeV]	hybrid cone isol.	$\epsilon_c = 0.05$	$\epsilon_c = 0.1$	$\epsilon_c = 0.25$
8	dir NLO	19.392	18.769	17.504
	frag LO	3.324	3.987	5.625
	frag NLO	5.744	6.646	8.751
	total NLO	25.136	25.416	26.255
14	dir NLO	35.302	34.111	31.631
	frag LO	6.288	7.572	10.775
	frag NLO	10.797	12.527	16.627
	total NLO	46.099	46.638	48.259
100	dir NLO	223.201	214.327	195.901
	frag LO	42.409	51.708	75.429
	frag NLO	72.411	84.668	114.829
	total NLO	295.61	298.99	310.73

Table IV.13: Total cross sections (in nanobarn) for the cone isolation criterion which uses a “hybrid” isolation [407] considering both fixed energy in the cone and a fraction of the photon transverse momentum, with $R = 0.4$, $E_{T,fix}^{cone} = 6$ GeV and different values of ϵ_c .

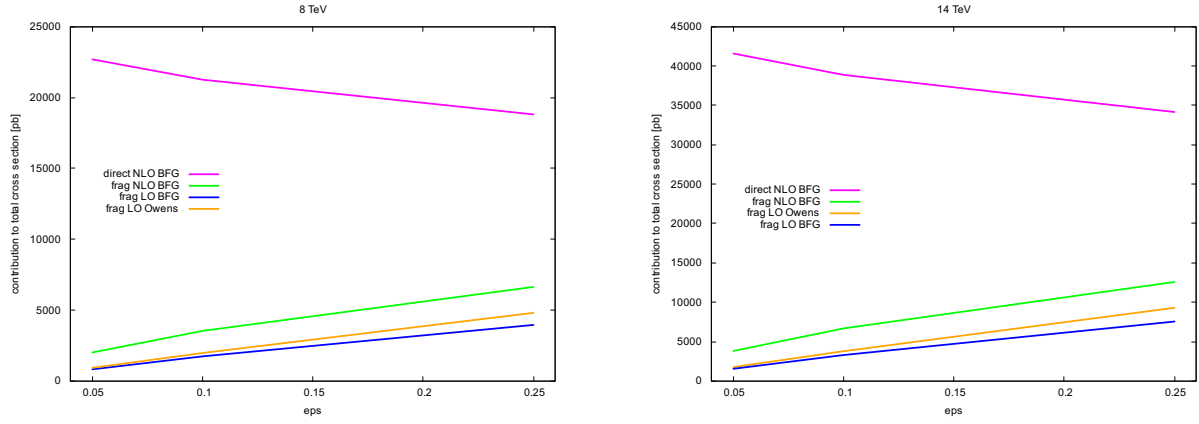


Fig. IV.42: Comparison of different fragmentation components at $\sqrt{s} = 8$ and 14 TeV.

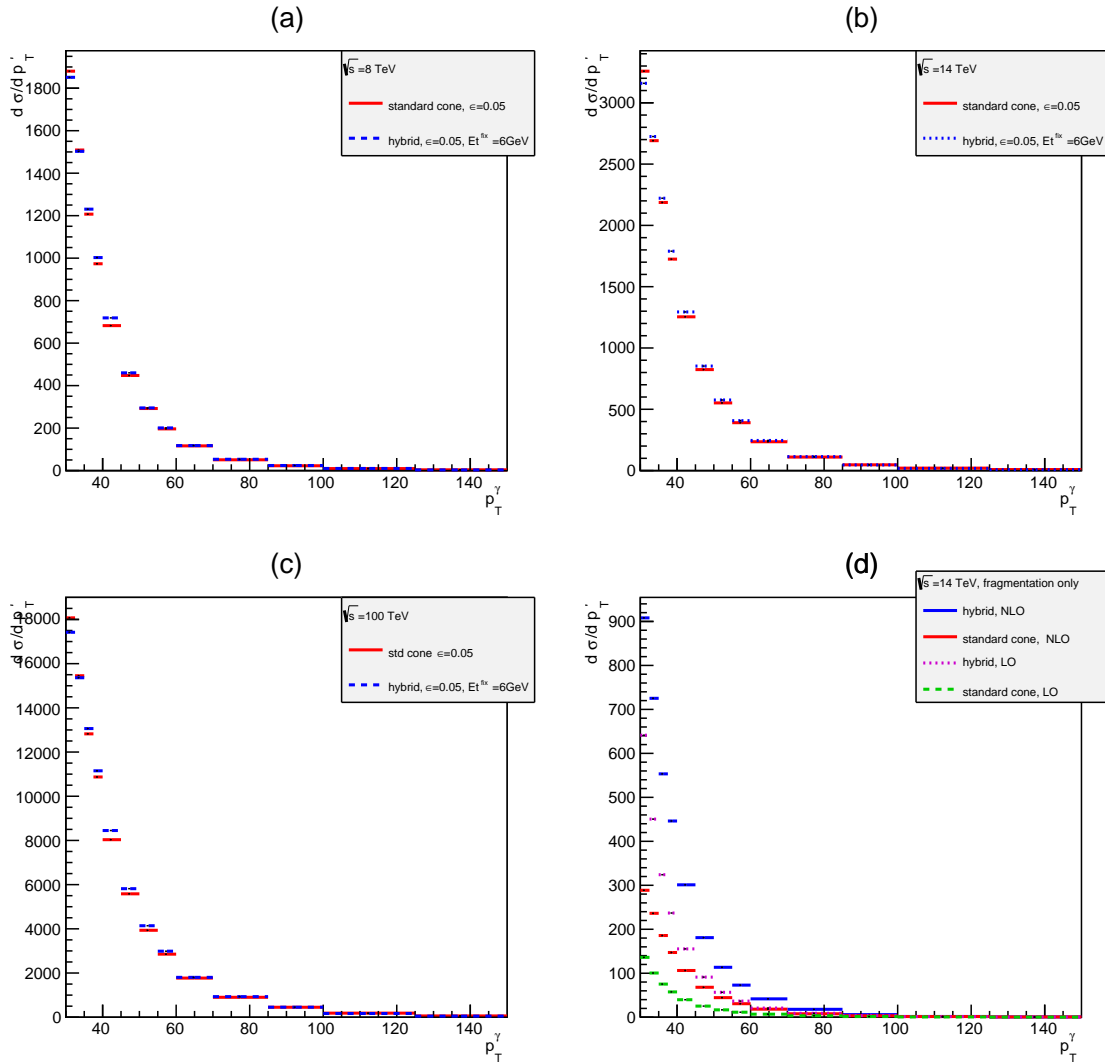


Fig. IV.43: Photon transverse momentum distribution for standard and hybrid cone isolation at (a) $\sqrt{s} = 8$ TeV, (b) $\sqrt{s} = 14$ TeV and (c) $\sqrt{s} = 100$ TeV. Panel (d) compares different fragmentation contributions at $\sqrt{s} = 14$ TeV, where the isolation parameters are the same as in the other panels.

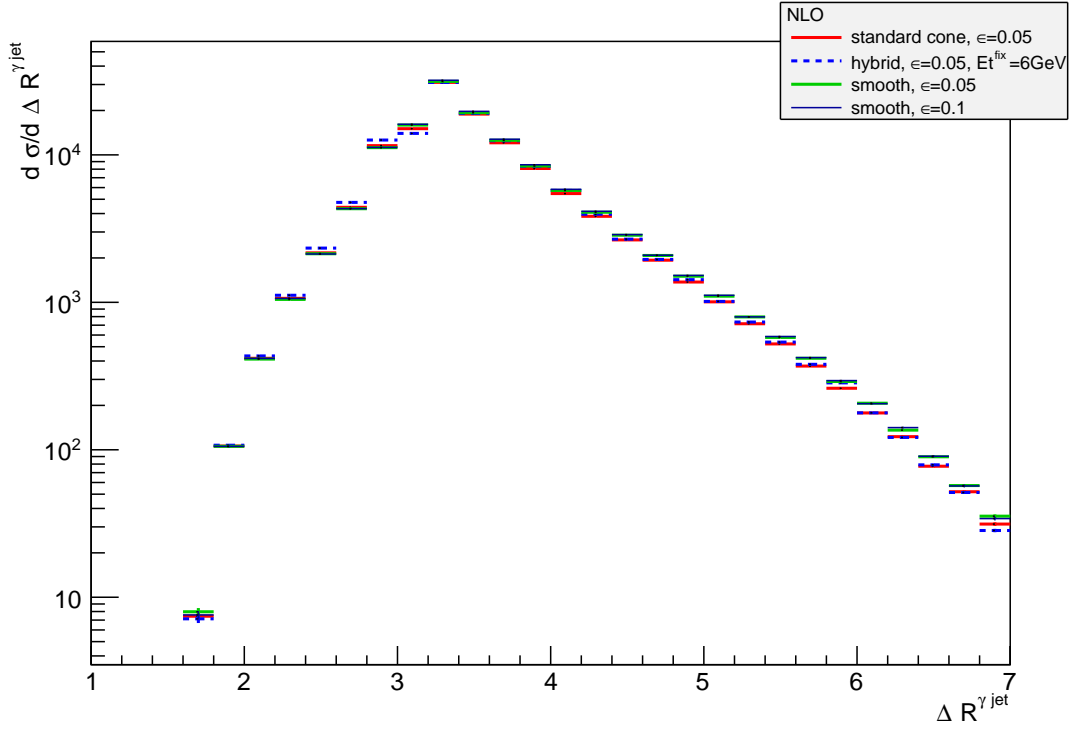


Fig. IV.44: Photon-jet R -separation for standard and hybrid cone isolation at $\sqrt{s} = 8$ TeV.

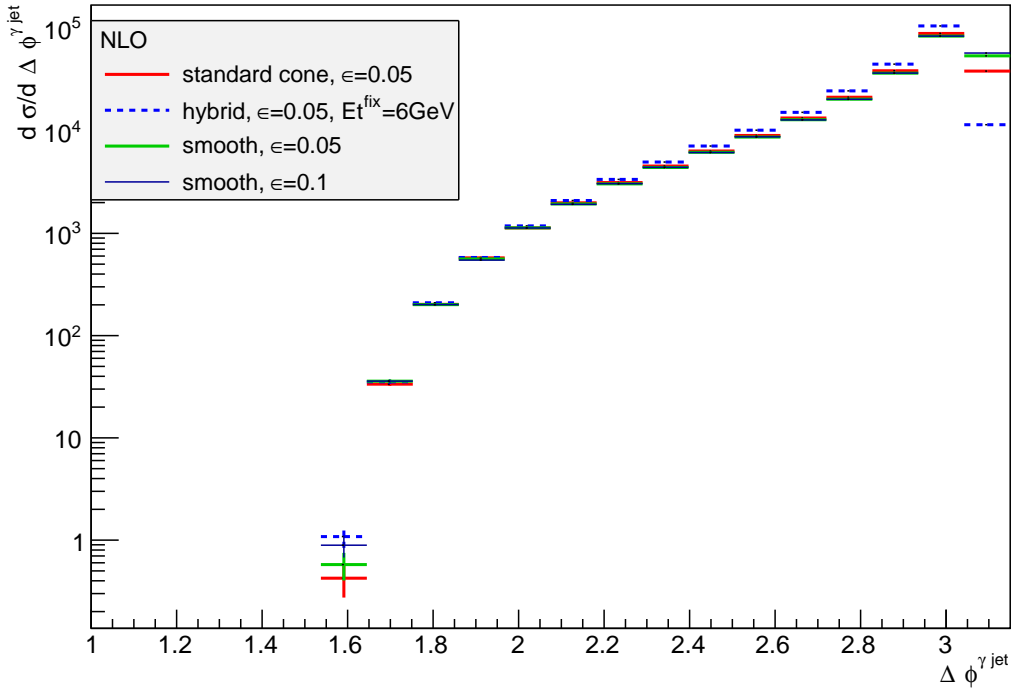


Fig. IV.45: Photon-jet azimuthal angle separation for standard and hybrid cone isolation at $\sqrt{s} = 8$ TeV.

4.4 Summary

We have studied various photon isolation criteria at $\sqrt{s} = 8, 14$ and 100 TeV for both diphoton production and photon plus jet production at NLO. In the diphoton case, we observe that, for tight isolation parameters ($\epsilon \leq 0.1$), the smooth and standard cone isolation criteria give results which agree at the percent level, where the standard cone isolation always gives a larger result. For looser isolation, the two criteria start to deviate, the differences being in the 10% range for $\epsilon = 0.5$ for the $m_{\gamma\gamma}$ distribution, and even larger for the $\Delta\Phi_{\gamma\gamma}$ distribution.

At 100 TeV, the fragmentation functions may be called at scales which are close to their limit of validity. Therefore a new fit of the photon fragmentation functions based on LHC data would be desirable.

The photon+jet case shows a different behaviour when comparing the smooth isolation with cone isolation including the fragmentation part, in the sense that the smooth cone result is larger than the “standard” cone result, which is the opposite behaviour as in the diphoton case. However, for tight isolation, the results with the two criteria also agree within a few percent. In addition, a new isolation criterion, used recently by ATLAS [407] has been implemented, where both a fixed energy in the cone and a fraction of the photon transverse momentum are used to determine the maximally allowed hadronic energy in the cone. This “hybrid” criterion leads to results which are very similar to the “standard” cone isolation where only a fraction of the photon momentum is used, except for low p_T^γ values, where the spectrum with hybrid isolation is slightly shifted towards larger p_T^γ values.

5 Systematics of quark/gluon tagging ¹⁶

By measuring the substructure of a jet, one can assign it a “quark” or “gluon” tag. In the eikonal (double-logarithmic) limit, quark/gluon discrimination is determined solely by the color factor of the initiating parton (C_F versus C_A). In this section, we confront the challenges faced when going beyond this leading-order understanding, using parton shower generators to assess the impact of higher-order perturbative and nonperturbative physics. Working in the idealized context of electron-positron collisions, where one can define a proxy for quark and gluon jets based on the Lorentz structure of the production vertex, we find a fascinating interplay between perturbative shower effects and nonperturbative hadronization effects.

5.1 Overview

Jets are a robust tool for studying short-distance collisions involving quarks and gluons. With a suitable jet definition, one can connect jet measurements made on clusters of hadrons to perturbative calculations made on clusters of partons. More ambitiously, one can try to tag jets with a suitably-defined flavor label, thereby enhancing the fraction of, say, quark-tagged jets over gluon-tagged jets. This is relevant for searches for physics beyond the standard model, where signals of interest are often dominated by quarks while the corresponding backgrounds are dominated by gluons. A wide variety of quark/gluon discriminants have been proposed [408–415], and there is a growing catalog of quark/gluon studies at the Large Hadron Collider (LHC) [416–421].¹⁷

In order to achieve robust quark/gluon tagging, though, one needs theoretical and experimental control over quark/gluon radiation patterns. At the level of eikonal partons, a quark radiates proportional to its $C_F = 4/3$ color factor while a gluon radiates proportional to $C_A = 3$. In this section, we demonstrate that quark/gluon discrimination performance is highly sensitive to subleading perturbative effects beyond the eikonal limit, such as $g \rightarrow q\bar{q}$ splittings and color

¹⁶ G. Soyez, J. Thaler, M. Freytsis, P. Gras, D. Kar, L. Lönnblad, S. Plätzer, A. Siódmok, P. Skands, D. Soper

¹⁷For an incomplete selection of earlier proposed discriminants, see Refs. [422–427].

coherence, as well as to nonperturbative effects such as color reconnection and hadronization. While these effects are modeled (to differing degrees) in parton shower generators, they are relatively unconstrained by existing collider measurements, especially in the gluon channel. The goal of this section is to highlight these uncertainties, which then suggests a set of future LHC measurements that will improve the modeling of jets in general and quark/gluon tagging in particular.

A common misconception about quark/gluon tagging is that it is an intrinsically ill-defined problem. Of course, quark and gluon partons carry color while jets are composed of color-singlet hadrons, so the labels “quark” and “gluon” are fundamentally ambiguous. But this is philosophically no different from the fact that a “jet” is fundamentally ambiguous and one must therefore always specify a concrete jet finding procedure. As discussed in Sec. 5.2, one can indeed create a well-defined quark/gluon tagging procedure based unambiguous hadron-level measurements. In this way, even if what one means by “quark” or “gluon” is based on a naive or ambiguous concept (like Born-level cross sections or eikonal limits), quark/gluon discrimination is still a well-defined technique for enhancing desired signals over unwanted backgrounds.

There are a wide range of possible quark/gluon discriminants and a similarly large range of ways to quantify discrimination power. As a concrete set of discriminants, we consider the generalized angularities λ_β^κ [414] (see also [428–431]),

$$\lambda_\beta^\kappa = \sum_{i \in \text{jet}} z_i^\kappa \theta_i^\beta, \quad (\text{IV.18})$$

with the notation to be explained in Sec. 5.3. We consider five different (κ, β) working points, which roughly map onto five variables in common use in the literature:

$$\begin{array}{ccccc} (0, 0) & (2, 0) & (1, 0.5) & (1, 1) & (1, 2) \\ \text{multiplicity} & p_T^D & \text{LHA} & \text{width} & \text{mass} \end{array} \quad (\text{IV.19})$$

Here, multiplicity is the hadron multiplicity within the jet, p_T^D was defined in Refs. [411, 412], LHA refers to the “Les Houches Angularity” (named after the venue of this workshop), width is closely related to jet broadening [432–434], and mass is closely related to jet thrust [435]. To quantify discrimination performance, we focus on classifier separation (a default output of TMVA [436]):

$$\Delta = \frac{1}{2} \int d\lambda \frac{(p_q(\lambda) - p_g(\lambda))^2}{p_q(\lambda) + p_g(\lambda)}, \quad (\text{IV.20})$$

where p_q (p_g) is the probability distribution for λ in a generated quark jet (gluon jet) sample. This and other potential performance metrics are discussed in Sec. 5.4.

We begin our parton shower generator predictions for quark/gluon discrimination in Sec. 5.5, using an idealized setup with e^+e^- collisions. Here, we can use the following processes as proxies for quark and gluon jets:

$$\text{“quark jets”} : e^+e^- \rightarrow (\gamma/Z)^* \rightarrow u\bar{u}, \quad (\text{IV.21})$$

$$\text{“gluon jets”} : e^+e^- \rightarrow h^* \rightarrow gg, \quad (\text{IV.22})$$

where h is the Higgs boson. These processes are physically distinguishable by the quantum numbers of the associated color singlet production operator, giving a way to define truth-level quarks and gluons labels without reference to the final state.¹⁸ We compare six different parton shower generators both before hadronization (“parton level”) and after hadronization (“hadron level”):

¹⁸Of course, the quantum numbers of the color singlet operator are not measurable event by event. The idea here is to have a fundamental definition of “quark” and “gluon” that does not reference QCD partons directly.

- PYTHIA 8.205 [319, 367],
- HERWIG++ 2.7.1 [437, 438],
- SHERPA 2.1.1 [275],
- VINCIA 1.201 [439],
- DEDUCTOR 1.0.2 [440] (with hadronization performed by PYTHIA 8.212),¹⁹
- ARIADNE 5.0. β [441].²⁰

In the future, we plan to make HERWIG 7 [382] and DIRE [443] predictions about quark/gluon discrimination as well as investigate predictions from analytic resummation [413, 414].

As we will see, the differences between these generators arise from physics at the interface between perturbative showering and nonperturbative fragmentation. One might think that the largest differences between generators would appear for infrared-and-collinear (IRC) unsafe observables like multiplicity and p_T^D , where nonperturbative hadronization plays an important role. Surprisingly, comparably-sized differences are also seen for the IRC safe angularities, indicating that these generators have different behavior even at the level of the perturbative final state shower. In Sec. 5.6, we study these differences as a function of collision energy Q , jet radius R , and strong coupling constant α_s , showing that the generators have somewhat different discrimination trends. In Sec. 5.7, we compare the default parton shower configurations to physically-motivated changes, showing that modest changes to the shower/hadronization parameters can give rather large differences in quark/gluon separation power.

At the end of the day, most of the disagreement between generators is due to gluon radiation patterns. This is not so surprising, since most of these generators have been tuned to reproduce distributions from e^+e^- colliders, and quark (but less so gluon) radiation patterns are highly constrained by event shape measurements at LEP [444–447]. In Sec. 5.8, we suggest a possible analysis strategy at the LHC to specifically constrain gluon radiation patterns. At a hadron collider, the distinction between quark jets and gluon jets is rather subtle, since radiation patterns depend on color connections between the measured final state jets and the unmeasured initial state partons. That said, we suspect that much can be learned from hadron-level measurements, even without isolating “pure” quark or gluon samples.

We present our final recommendations and conclusions in Sec. 5.9. The main take home message from this study is that, contrary to the standard lore, existing measurements at e^+e^- colliders are insufficient to constrain uncertainties in the final state shower. Therefore, gluon-enriched measurements at the LHC will be crucial to achieve robust quark/gluon discrimination.

5.2 What is a quark/gluon jet?

As part of the 2015 Les Houches workshop, an attempt was made to define exactly what is meant by a “quark jet” or “gluon jet” (see Fig. IV.46). Here are some suggested options for defining a quark jet, in (approximate) order from most ill-defined to most well-defined. Related statement can be made for gluon jets.

A quark jet is...

- **A quark parton.** This definition (incorrectly) assumes that there is a one-to-one map between a jet and its initiating parton. Because it neglects the important role of additional radiation in determining the structure of a jet, we immediately dismiss this definition.

¹⁹Note that this DEDUCTOR plus PYTHIA combination has not yet been tuned to data.

²⁰This version of ARIADNE is not yet public, but available from the author on request. For e^+e^- collisions, the physics is the same as in ARIADNE 4 [442].

What is a Quark Jet?

From lunch/dinner discussions

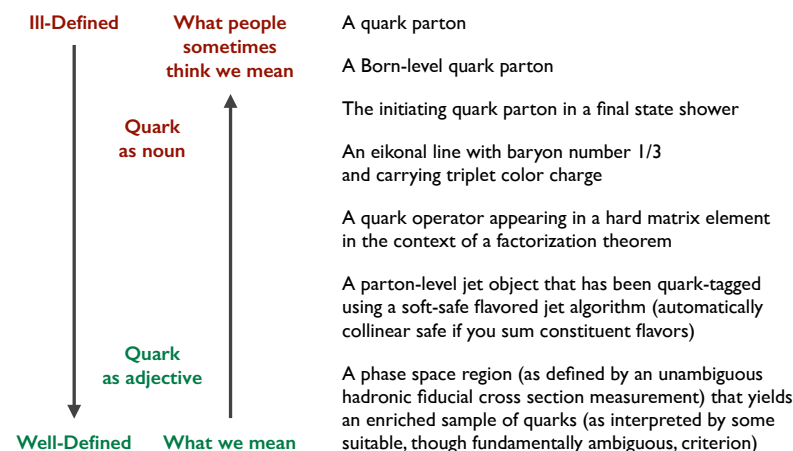


Fig. IV.46: Original slide from the June 10, 2015 summary report of the quark/gluon Les Houches subgroup.

- **A Born-level quark parton.** This definition at least acknowledges the importance of radiative corrections to jet production, but it leaves open the question of how exactly to define the underlying Born-level process from an observed final state. (For one answer valid at the parton level, see flavored jet algorithms below.)
- **An initiating quark parton in a final state parton shower.** We suspect that this is the definition most LHC experimentalists have in mind. This definition assumes that the parton shower history is meaningful, though, which may not be the case beyond the strongly-ordered or leading-logarithmic approximations. Because the parton shower is semi-classical, this definition neglects the impact of genuinely quantum radiative corrections as well as nonperturbative hadronization.
- **A maximum- p_T quark parton within a jet in a final state parton shower.** This “max- p_T ” prescription is a variant on the initiating parton prescription above (see further discussion in [448]). It differs from the initiating parton by a calculable amount in a leading logarithmic shower [130] and is based on the same (naive) assumption that the parton shower history is meaningful.
- **An eikonal line with baryon number 1/3 and carrying triplet color charge.** This is another semi-classical definition that attempts to use a well-defined limit of QCD to define quarks in terms of light-like Wilson lines. Philosophically, this is similar to the parton shower picture, with a similar concern about how to extrapolate this definition away from the strict eikonal limit.
- **A parton-level jet object that has been quark-tagged using an IRC safe flavored jet algorithm.** This is the strategy adopted in [449]. While this definition neglects the impact of hadronization, it does allow for the calculation of quark jet cross sections at all perturbative orders, including quantum corrections.

The unifying theme in the above definitions is that they try to identify a quark as an object unto itself, without reference to the specific final state of interest. However, it is well-known that a

“quark” in one process may not look like a “quark” in other process, due to color correlations with the rest of the event, especially the initial state in pp collisions. The next definition attempts to deal with the process dependence in defining quarks.

- **A quark operator appearing in a hard matrix element in the context of a factorization theorem.** This is similar to the attitude taken in [450]. In the context of a well-defined cross section measurement, one can (sometimes) go to a limit of phase space where the hard production of short-distance quarks and gluons factorizes from the subsequent long-distance fragmentation. This yields a nice (gauge-covariant) operator definition of a quark jet. That said, even if a factorization theorem does exist for the measurement of interest, this definition is potentially ambiguous beyond leading power.

The definition we adopt for this study is inspired by the idea that one should think about quark/gluon tagging in the context of a specific measurement, but it tries to avoid relying on the presence of a factorization theorem.

- **A phase space region (as defined by an unambiguous hadronic fiducial cross section measurement) that yields an enriched sample of quarks (as interpreted by some suitable, though fundamentally ambiguous, criterion).** Here, the goal is to *tag* a phase space region as being quark-like, rather than try to determine a truth definition of a quark. This definition has the advantage of being explicitly tied to hadronic final states and to the discriminant variables of interest. *The main challenge with this definition is how to determine the criterion that corresponds to successful quark enrichment.* For that, we will have to rely to some degree on the other less well-defined notions of what a quark jet is.

To better understand this last definition, consider a quark/gluon discriminant λ . Since λ can be measured on any jet, one can unambiguously determine the cross section $d\sigma/d\lambda$ for any jet sample of interest. But measuring λ does not directly lead to the probability that the jet is a quark jet, nor to the probability distribution $p_q(\lambda)$ for λ within a quark jet sample. Rather, the process of measuring λ must be followed by a separate process of interpreting how the value of λ should be used as part of an analysis.

For example, the user could choose that small λ jets should be tagged as “quark-like” while large λ jets should be tagged as “gluon-like”. Alternatively, the user might combine λ with other discriminant variables as part of a more sophisticated classification scheme. The key point is that one first measures hadron-level discriminant variables on a final state of interest, and only later does one interpret exactly what those discriminants accomplish (which could be different depending on this physics goals of a specific analysis). Typically, one might use a Born-level or eikonal analysis to define which regions of phase space should be associated with “quarks” or “gluons”, but even if these phase space regions are based on naive or ambiguous logic, λ itself is a well-defined discriminant variable.

In Sec. 5.5, we will consider the generalized angularities λ_β^κ as our discriminant variables and we will assess the degree to which the measured values of λ_β^κ agree with a quark/gluon interpretation based on Born-level production modes. This is clearly an idealization, though one that makes some sense in the context of e^+e^- collisions, since the truth-level “quark” and “gluon” labels are defined by the Lorentz structure of the production vertex. In Sec. 5.9, we will recommend that the LHC experiments perform measurements of λ_β^κ in well-defined hadron-level final states, without necessarily attempting to determine separate $p_q(\lambda_\beta^\kappa)$ and $p_g(\lambda_\beta^\kappa)$ distributions. Eventually, one would want to use these hadron-level measurements to infer something about parton-level quark/gluon radiation patterns. Even without that interpretation step, though, direct measurements of $d\sigma/d\lambda_\beta^\kappa$ would provide valuable information for parton

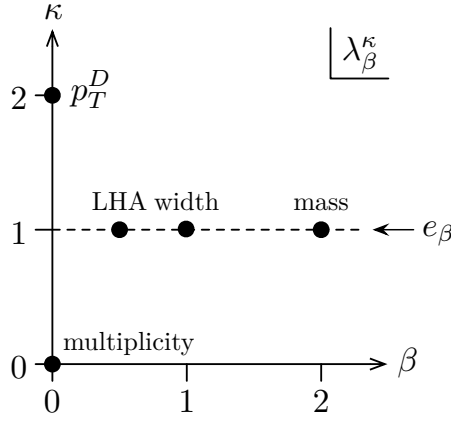


Fig. IV.47: Two-parameter family of generalized angularities, adapted from [414]. The dots correspond to the five benchmark angularities used in this study. The horizontal line at $\kappa = 1$ corresponds to the IRC safe angularities, $e_\beta = \lambda_\beta^1$.

shower tuning. This in turn would help λ_β^κ become a more robust and powerful discriminant in searches for new physics beyond the standard model.

5.3 Generalized angularities

A wide variety of quark/gluon discriminants have been proposed (see [409] for an extensive catalog), but here we limit ourselves to a two-parameter family of generalized angularities [414], shown in Fig. IV.47. These are defined as (repeating Eq. (IV.18) for convenience)

$$\lambda_\beta^\kappa = \sum_{i \in \text{jet}} z_i^\kappa \theta_i^\beta, \quad (\text{IV.23})$$

where i runs over the jet constituents, $z_i \in [0, 1]$ is a momentum fraction, and $\theta_i \in [0, 1]$ is a (normalized) angle to the jet axis. The parameters $\kappa \geq 0$ and $\beta \geq 0$ determine the momentum and angle weighting, respectively. For $\kappa = 1$, the generalized angularities are IRC safe and hence calculable in perturbation theory [431] (see also [430, 451–454]). For general $\kappa \neq 1$, there are quasi-perturbative techniques based on generalized fragmentation functions [414] (see also [410, 455–457]). In our parton shower studies, we determine λ_β^κ using all constituents of a jet, though one could also consider using charged-particle-only angularities to improve robustness to pileup (at the expense of losing some particle-level information).

For our e^+e^- study, we cluster jets with FASTJET 3.1.3 [458] using the ee -variant of the anti- k_t algorithm [326], with $|\vec{p}|$ -ordered winner-take-all recombination [431, 459, 460] to determine the jet axis \hat{n} . Unlike standard E -scheme recombination [461], the winner-take-all scheme yields a jet axis \hat{n} that does not necessarily align with the jet three-momentum \vec{p} ; this turns out to be a desirable feature for avoiding soft recoil effects [413, 431, 432, 462, 463]. We define

$$z_i \equiv \frac{E_i}{E_{\text{jet}}}, \quad \theta_i \equiv \frac{\Omega_{i\hat{n}}}{R}, \quad (\text{IV.24})$$

where E_i is the particle energy, $\Omega_{i\hat{n}}$ is the opening angle to the jet axis, and R is the jet radius (taken to be $R = 0.6$ by default). To translate our ee study to an eventual pp study (left to future work), one would use the standard pp version of anti- k_t with p_T -ordered winner-take-all recombination, defining

$$z_i \equiv \frac{p_{Ti}}{\sum_{j \in \text{jet}} p_{Tj}}, \quad \theta_i \equiv \frac{R_{i\hat{n}}}{R}, \quad (\text{IV.25})$$

where p_{Ti} is the particle transverse momentum and $R_{i\hat{n}}$ is the rapidity-azimuth distance to the jet axis.

By adjusting κ and β , one can probe different aspects of the jet fragmentation. We consider five benchmark values for (κ, β) indicated by the black dots in Fig. IV.47:

$$\begin{aligned}
(0, 0) &= \text{hadron multiplicity,} \\
(2, 0) &\Rightarrow p_T^D [411, 412] \text{ (specifically } \lambda_0^2 = (p_T^D)^2), \\
(1, 0.5) &= \text{Les Houches Angularity (LHA),} \\
(1, 1) &= \text{width or broadening [432–434],} \\
(1, 2) &\Rightarrow \text{mass or thrust [435] (specifically } \lambda_2^1 \simeq m_{\text{jet}}^2/E_{\text{jet}}^2).
\end{aligned}
\tag{IV.26}$$

Except for the LHA, these angularities (or their close cousins) have already been used in quark/gluon discrimination studies. The LHA has been included to have an IRC safe angularity that weights energies more heavily than angles, similar in spirit to the $\beta = 0.2$ value advocated in Ref. [413].

For the IRC safe case of $\kappa = 1$, there is an alternative version of the angularities based on energy correlation functions [413] (see also [463, 464]),

$$\text{ecf}_\beta = \sum_{i < j \in \text{jet}} z_i z_j \theta_{ij}^\beta \simeq \lambda_\beta^1,
\tag{IV.27}$$

where equality holds in the extreme eikonal limit.²¹ For the e^+e^- case, the pairwise angle θ_{ij} is typically normalized to the jet radius as $\theta_{ij} \equiv \Omega_{ij}/R$. To avoid a proliferation of curves, we will not show any results for ecf_β . We will also neglect quark/gluon discriminants that take into account azimuthal asymmetries within the jet, though observables like the covariance tensor [409] and 2-subjettiness [465, 466] can improve quark/gluon discrimination.

5.4 Classifier separation

Since we will be testing many parton shower variants, we need a way to quantify quark/gluon separation power in a robust way that can easily be summarized by a single number. For that purpose we use classifier separation (repeating Eq. (IV.20) for convenience),

$$\Delta = \frac{1}{2} \int d\lambda \frac{(p_q(\lambda) - p_g(\lambda))^2}{p_q(\lambda) + p_g(\lambda)},
\tag{IV.28}$$

where p_q (p_g) is the probability distribution for the quark jet (gluon jet) sample as a function of the classifier λ . Here, $\Delta = 0$ corresponds to no discrimination power and $\Delta = 1$ corresponds to perfect discrimination power.

A more common way to talk about discrimination power is in terms of receiver operating characteristic (ROC) curves. At a point (q, g) on the ROC curve, where $q, g \in [0, 1]$, one can define a selection that yields q efficiency for quarks and g mistag rate for gluons, or equivalently, a $(1 - g)$ efficiency for gluons for a $(1 - q)$ mistag rate for quarks. To turn the ROC curve into a single number, it is common to report the gluon rejection rate at, say, 50% quark efficiency. Since we are more interested in understanding the relative performance between parton showers rather than the absolute performance, we will not show ROC curves here, though they can be easily derived from the p_q and p_g distributions. If one observable has an everywhere better ROC curve

²¹This equality also relies on using a recoil-free axis choice \hat{n} to define θ_i . Amusingly, $\lim_{\beta \rightarrow 0} \text{ecf}_\beta = (1 - \lambda_0^2)/2$ (i.e. $\kappa = 2, \beta = 0$), such that the $\beta \rightarrow 0$ limit of the IRC safe energy correlation functions corresponds to the IRC unsafe p_T^D .

than another (i.e. it is Pareto optimal), then it will also have a larger Δ value. The converse is not true, however, since depending on the desired working point, a “bad” discriminant as measured by Δ might still be “good” by another metric. In that sense, Δ contains less information than the full ROC curve.

An alternative way to quantify discrimination power is through mutual information, which counts the number of “bits” of information gained from measuring a discriminant variable (see [414]). Given a sample with quark fraction $f \in [0, 1]$ and gluon fraction $(1 - f)$, the mutual information with the truth (a.k.a. the truth overlap) is

$$I(T; \Lambda) = \int d\lambda \left(f p_q(\lambda) \log_2 \frac{p_q(\lambda)}{p_{\text{tot}}(\lambda)} + (1 - f) p_g(\lambda) \log_2 \frac{p_g(\lambda)}{p_{\text{tot}}(\lambda)} \right), \quad (\text{IV.29})$$

where $T = \{q, g\}$ is the set of truth labels, $\Lambda = \{\lambda\}$ is the (continuous) set of discriminant values, and

$$p_{\text{tot}}(\lambda) = f p_q(\lambda) + (1 - f) p_g(\lambda). \quad (\text{IV.30})$$

The choice $f = 1/2$ was used in Ref. [414], though other f choices are plausible. Though we will not use mutual information in this study, it is amusing to note that the second derivative of $I(T; \Lambda)$ with respect to f is related to classifier separation as

$$-\frac{\log 2}{4} \frac{\partial^2 I(T; \Lambda)}{\partial f^2} \Big|_{f=\frac{1}{2}} = \Delta. \quad (\text{IV.31})$$

One advantage of Δ over $I(T; \Lambda)$ is that the integrand in Eq. (IV.28) is easier to interpret, since it tracks the fractional difference between the signal and background at a given value of λ .²² Specifically, by plotting

$$\frac{d\Delta}{d\lambda} = \frac{1}{2} \frac{(p_q(\lambda) - p_g(\lambda))^2}{p_q(\lambda) + p_g(\lambda)}, \quad (\text{IV.32})$$

one can easily identify which regions of phase space contribute the most to quark/gluon discrimination. One can then ask whether or not the regions exhibiting the most separation power are under sufficient theoretical control, including both the size of perturbative uncertainties and the impact of nonperturbative corrections.

5.5 Idealized quark/gluon discrimination

Our parton shower studies are based on the idealized case of discriminating quark and gluon jets in e^+e^- collisions. As we will see, this example demonstrates the importance of final state evolution for quark/gluon discrimination, separate from initial state complications arising in pp collisions. The analysis code used for this study is available as a RIVET routine [327], which can be downloaded from <https://github.com/gsoyez/lh2015-qg> under `MC_LHQQ_EE.cc`.

To define the truth-level jet flavor, we use a simple definition: a quark jet is a jet produced by a parton shower event generator in $e^+e^- \rightarrow (\gamma/Z)^* \rightarrow u\bar{u}$ hard scattering, while a gluon jet is a jet produced in $e^+e^- \rightarrow h^* \rightarrow gg$. Of course, an $e^+e^- \rightarrow u\bar{u}$ event can become a $e^+e^- \rightarrow u\bar{u}g$ event after one step of shower evolution, just as $e^+e^- \rightarrow gg$ can become $e^+e^- \rightarrow gu\bar{u}$. This illustrates the inescapable ambiguity in defining jet flavor.²³ To partially mitigate the effect of

²²Another advantage of Δ over $I(T; \Lambda)$ arises when trying to assign statistical uncertainties to finite Monte Carlo samples. Since Δ is defined as a simple integral, one can use standard error propagation to assign uncertainties to Δ . By contrast, because of the logarithms in the $I(T; \Lambda)$ integrand, one has to be careful about a potential binning bias [414].

²³In an e^+e^- context, our definition at least respects the Lorentz structure of the production vertex, so in that sense it is a fundamental definition that does not reference (ambiguous) quark or gluon partons directly.

wide-angle emissions, we restrict our analysis to jets that satisfy

$$\frac{E_{\text{jet}}}{Q/2} > 0.8, \quad (\text{IV.33})$$

with up to two jets studied per event. There is also the ambiguity of which parton shower to use, and we investigate this ambiguity by looking at results from several event generators: PYTHIA 8.205 [319,367], HERWIG++ 2.7.1 [437,438], SHERPA 2.1.1 [275], VINCIA 1.201 [439], DEDUCTOR 1.0.2 [440] (with hadronization performed by PYTHIA), and ARIADNE 5.0. β [441].

In Fig. IV.48, we show hadron-level distributions of the LHA (i.e. $\lambda_{0.5}^1$) in the quark sample (p_q) and gluon sample (p_g), comparing the baseline settings of six different parton shower generators with a center-of-mass collision energy of $Q = 200$ GeV and jet radius $R = 0.6$. In the quark sample in Fig. IV.48a, there is relatively little variation between the generators, which is not surprising since most of these programs have been tuned to match LEP data (though LEP never measured the LHA itself). Turning to the gluon sample in Fig. IV.48b, we see somewhat larger variations between the generators; this is expected since there is no data to directly constrain $e^+e^- \rightarrow gg$. In Fig. IV.48c, we plot the integrand of classifier separation, $d\Delta/d\lambda$ from Eq. (IV.32). This shows where in the LHA phase space the actual discrimination power lies, with large values of the integrand corresponding to places where the quark and gluon distributions are most dissimilar. Now we see considerable differences between the generators, reproducing the well-known fact that PYTHIA is more optimistic about quark/gluon separation compared to HERWIG [416]. The predicted discrimination power from the other four generators are intermediate between these extremes.

One might expect that the differences between generators are due simply to their having different hadronization models. It seems, however, that the differences already appear at the parton level prior to hadronization. We should say at the outset that it is nearly impossible to do a true apples-to-apples comparison of parton-level results, since these generators are interfaced to different hadronization models, and only the hadron-level comparison is physically meaningful. In particular, the crossover between the perturbative and nonperturbative regions is ambiguous and each of these showers has a different effective shower cutoff scale, resulting in different amounts of radiation being generated in the showering versus hadronization steps.²⁴

With that caveat in mind, we show parton-level results in Fig. IV.49. One immediately notices that three of the generators—HERWIG, SHERPA, and DEDUCTOR—yield a large population of events where the perturbative shower generates no emissions. This gives $\lambda_{0.5}^1 = 0$ such that non-zero values of the LHA are generated only by the hadronization model. By contrast, PYTHIA and VINCIA give overall larger values of the LHA from the perturbative shower alone. As mentioned above, some of this difference can be explained simply by the different shower cutoff scales used in each generator, but it probably also reflects a difference in how semi-perturbative gluon splittings are treated. Since Fig. IV.48a shows that all generators give similar distributions for quark jets after hadronization, we conclude that understanding quark/gluon discrimination is a challenge at the interface between perturbative showering and nonperturbative hadronization.

To summarize the overall discrimination power, we integrate Eq. (IV.32) to obtain the value of classifier separation Δ for the LHA. This is shown in Fig. IV.50, which also includes the four other benchmark angularities from Eq. (IV.26). There is a rather large spread in predicted discrimination power between the generators, especially at hadron level in Fig. IV.50a. While such differences might be expected for IRC unsafe angularities (multiplicity and p_T^D) which depend on nonperturbative modeling, these differences persist even for the IRC safe angularities

²⁴In general, generators based on string hadronization tend to use a lower shower cutoff scale (~ 0.5 MeV) compared to those based on cluster hadronization (~ 1 GeV).

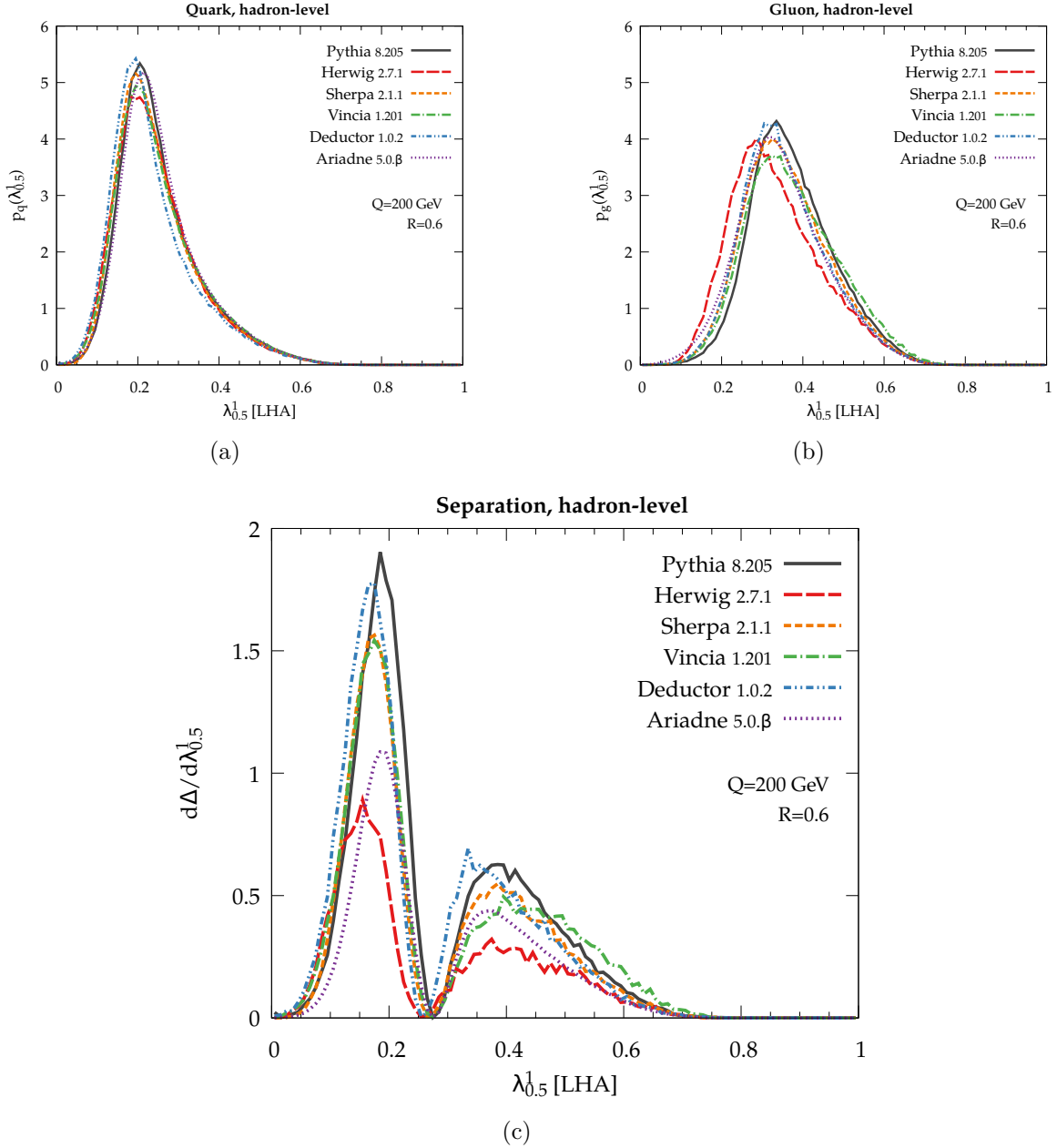


Fig. IV.48: Hadron-level distributions of the LHA for (a) the $e^+e^- \rightarrow u\bar{u}$ (“quark jet”) sample, (b) the $e^+e^- \rightarrow gg$ (“gluon jet”) sample, and (c) the classifier separation integrand in Eq. (IV.32). Six parton shower generators—PYTHIA 8.205, HERWIG++ 2.7.1, SHERPA 2.1.1, VINCIA 1.201, DEDUCTOR 1.0.2, and ARIADNE 5.0.β—are run at their baseline settings with center-of-mass energy $Q = 200$ GeV and jet radius $R = 0.6$.

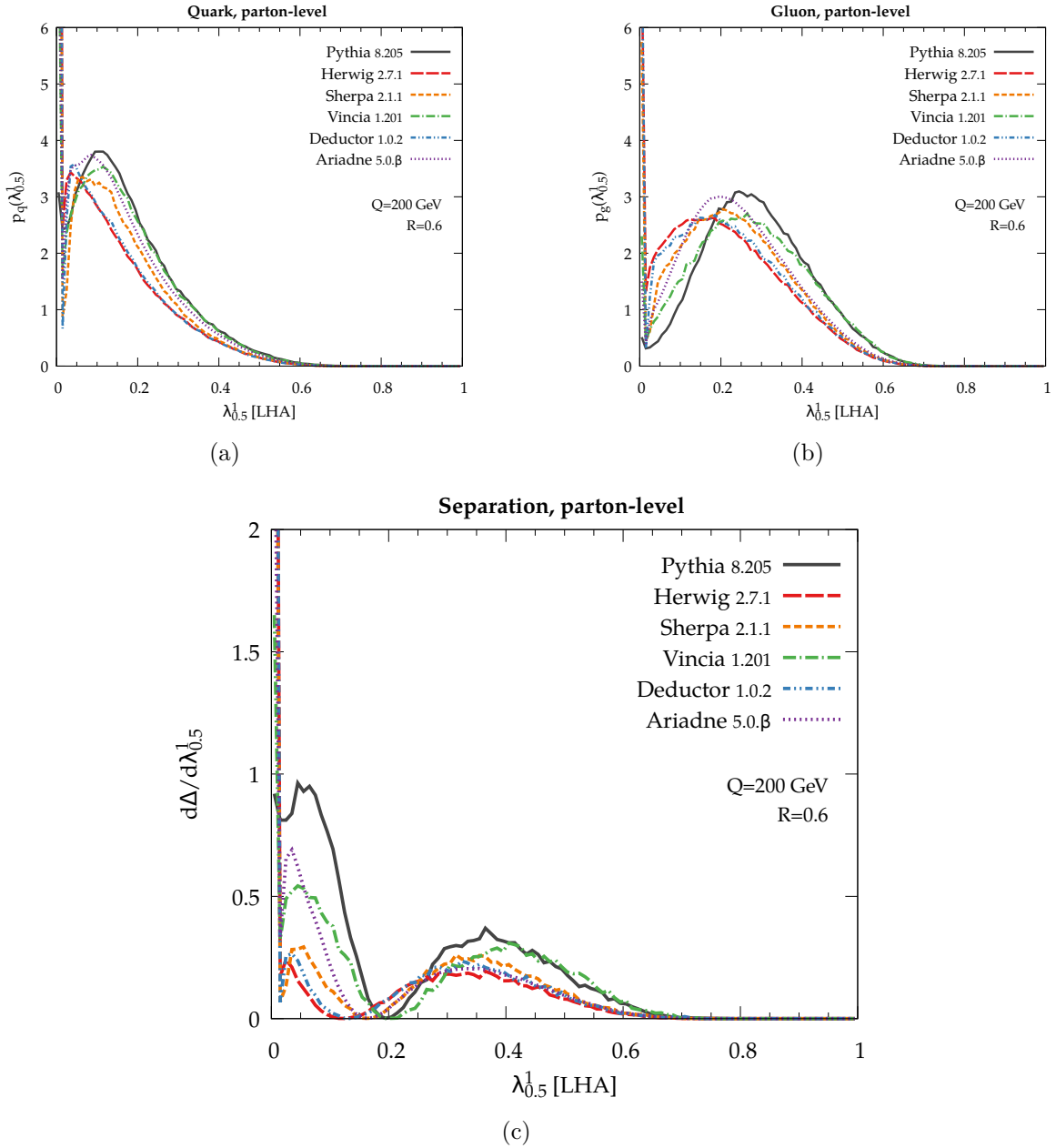


Fig. IV.49: Same as Fig. IV.48, but at the parton level. Note that HERWIG, SHERPA, and DEDUCTOR all have cross section spikes at $\lambda_{0.5}^1 = 0$ that extend above the plotted range.

at parton level (see Fig. IV.50b).²⁵ This suggests a more fundamental difference between the generators that is already present in the perturbative shower

For the IRC safe angularities with $\kappa = 1$, there is a generic trend seen by all of the hadron-level generators that discrimination power decreases as β increases. This trend agrees with the study performed in Ref. [413], but disagrees with the ATLAS study in Ref. [416], which found flat (or even increasing) discrimination power with increasing β . Understanding this β trend will therefore be crucial for understanding quark/gluon radiation patterns.

²⁵It is interesting that four of the generators—HERWIG, SHERPA, DEDUCTOR, and ARIADNE—have a comparatively narrow spread in predicted discrimination power at parton level, though this spread increases dramatically at hadron level.

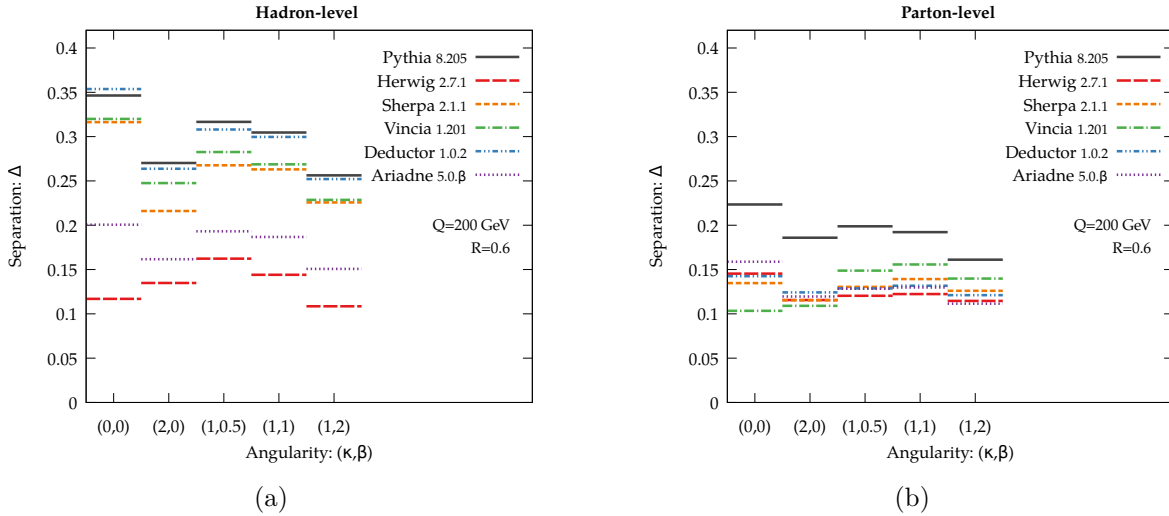


Fig. IV.50: Classifier separation Δ for the five benchmark angularities in Eq. (IV.26), determined from the various generators at (a) hadron level and (b) parton level. The first two columns correspond to IRC unsafe distributions (multiplicity and p_T^D), while the last three columns are the IRC safe angularities. The LHA (i.e. $\kappa = 1$, $\beta = 1/2$) is shown in the middle column.

5.6 Parameter dependence

Given the large absolute differences in discrimination power seen above, we next want to check if the parton shower generators exhibit similar or dissimilar trends as parameters are varied. We perform three parameter sweeps, using the boldface values below as defaults:

$$\begin{aligned}
 \text{Collision Energy : } Q &= \{50, 100, \mathbf{200}, 400, 800\} \text{ GeV}, \\
 \text{Jet Radius : } R &= \{0.2, 0.4, \mathbf{0.6}, 0.8, 1.0\}, \\
 \text{Strong Coupling : } \alpha_s/\alpha_{s0} &= \{0.8, 0.9, \mathbf{1.0}, 1.1, 1.2\},
 \end{aligned}
 \tag{IV.34}$$

where α_{s0} is the default value of the strong coupling, which is different between the generators (and sometimes different between different aspects of the same generator).

The resulting values of Δ for the LHA are shown in Fig. IV.51, at both the hadron level and parton level. There are number of surprising features in these plots. Perhaps the most obvious (and seen already in Fig. IV.50) is that even for the IRC safe angularities, the effect of hadronization is rather large, both on the absolute scale of discrimination and the trends. The main exception to this is HERWIG, which does not exhibit as much of an effect from hadronization, though an effect is still present.

The next surprising feature is that the parton-level trends for sweeping α_s do not necessarily correspond to those for sweeping Q and R . According to the perturbative next-to-leading-logarithmic (NLL) logic in Ref. [413], quark/gluon discrimination should depend on α_s evaluated at the scale $QR/2$, with larger values of $\alpha_s(QR/2)$ leading to improved discrimination power. Indeed, PYTHIA, HERWIG, and ARIADNE do show improved performance with larger α_s . However, larger values of Q and R correspond to smaller values of α_s , so the NLL logic would predict that increasing Q or R should lead to worse discrimination power. Instead, all of the generators show the opposite trend.

One reason to expect quark/gluon discrimination to improve as higher energies is that that phase space available for shower evolution increases as Q increases. The scale μ of the shower splitting is $\mu_0^2 < \mu^2 < Q^2$, where $\mu_0 = \mathcal{O}(\text{GeV})$ is the shower cutoff scale. With more range for shower evolution at higher Q , there is a greater possibility to see that a quark jet is

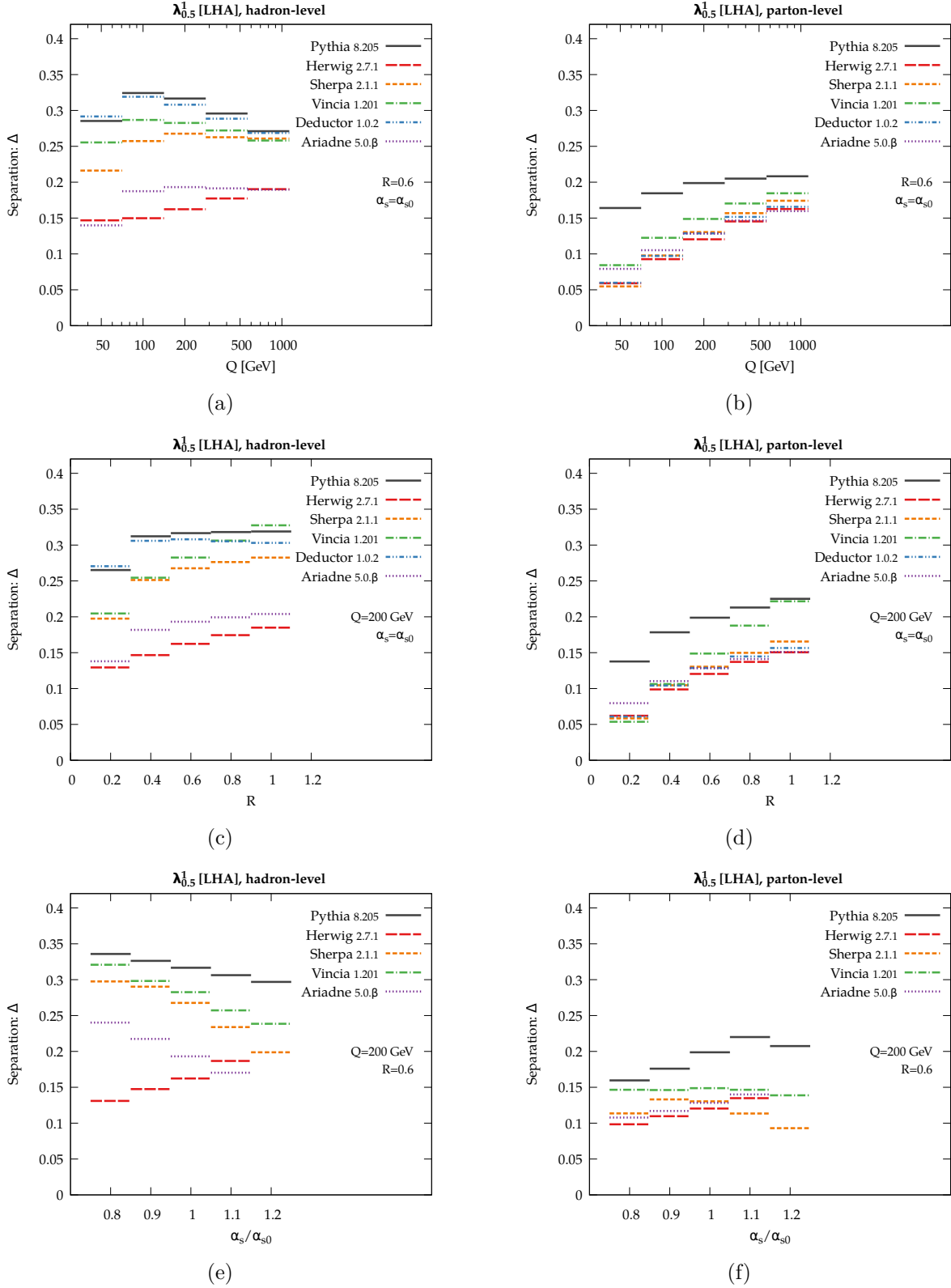


Fig. IV.51: Classifier separation Δ for the LHA, sweeping the collision energy Q (top row), jet radius R (middle row), and coupling constant α_s/α_{s0} (bottom row). Results are shown at hadron level (left column) and parton level (right column).

different from a gluon jet. Similarly, larger values of R allow for more emissions within a jet, and from scaling symmetry, one expects that parton-level discrimination power should depend on the combination QR .²⁶ By contrast, the NLL logic says that quark/gluon discrimination should be dominated by the leading emission(s) in a jet, and since α_s is smaller at higher values of QR , those leading emissions are more similar between quarks and gluons. Given these two different but equally plausible logics, both of which probably play some role in the complete story, this motivates experimental tests of quark/gluon separation as a function of Q and R .

For many of the generators, going from parton-level to hadron-level reverses or flattens the Q and α_s trends, though the R trends are more stable. The study in Ref. [413] did not include nonperturbative hadronization corrections, so we do not yet have a theoretical expectation for the impact of hadronization. In future work, we plan to follow Ref. [451] and include nonperturbative hadronization corrections via shape functions [467–473] as well as test the impact of imposing a hard IR cutoff scale. With confusions already at parton level, though, further perturbative calculations beyond NLL accuracy are also needed. For example, at NLL accuracy, one does account for the fact that a jet can contain multiple perturbative emissions, but those emissions are treated as if they themselves do not radiate. By contrast, parton showers (while formally only LL accurate) allow every emission to reradiate, which might be driving the Q and R discrimination trends.

5.7 Impact of generator settings

Formally, parton shower generators are only accurate to modified leading-logarithmic (MLL) accuracy, though they include physically important effects like energy/momentum conservation and matrix element corrections that go beyond MLL. We can assess the impact of these higher-order effects by changing the baseline parameter settings in each parton shower generator.

Because each generator is different, we cannot always make the same changes for each generator. Similarly, the spread in discrimination power shown below should *not* be seen as representing the intrinsic uncertainties in the shower, since many of these changes we explore are not physically motivated. The goal of these plots is to demonstrate possible areas where small parameter changes could have a large impact on quark/gluon discrimination. Ultimately, collider data and higher-order calculations will be essential for understanding the origin of quark/gluon differences. In all cases, we show both hadron-level and parton-level results, even if a setting is only expected to have an impact at the hadron level.

Our PYTHIA baseline is based on the Monash 2013 tune, with parameters described in Ref. [474]. In Fig. IV.52, we consider the following PYTHIA variations:

- PYTHIA: NO $g \rightarrow q\bar{q}$. While the dominant gluon splitting in the parton shower is $g \rightarrow gg$, PYTHIA—and every other shower in this study—also generates the subleading $g \rightarrow q\bar{q}$ splittings by default. This variation turns off $g \rightarrow q\bar{q}$, which makes gluon jets look more gluon-like, thereby increasing the separation power.
- PYTHIA: NO ME. The first emission in PYTHIA is improved by applying a matrix element correction [475], but this variation turns those corrections off, showing the impact of non-singular terms. No matrix element correction is available for $h^* \rightarrow gg$, though, so the true impact of these corrections might be larger than the relatively small effect seen for this variation.

²⁶At small values of R , one has to worry about the flavor purity of a jet sample, since scale evolution can change the leading parton flavor [130, 131]. Similarly, the restriction in Eq. (IV.33) can impose a non-trivial bias on the jet flavor at small R .

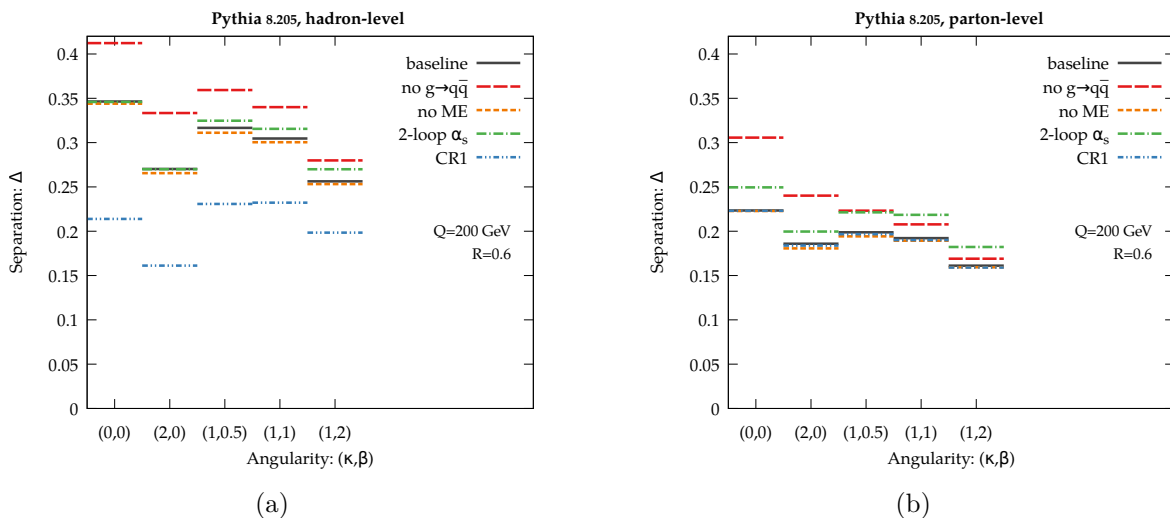


Fig. IV.52: Settings variations for PYTHIA 8.205. Shown are (a) hadron-level and (b) parton-level results for the classifier separation Δ derived from the five benchmark angularities.

- PYTHIA: 2-LOOP α_s . The default PYTHIA setting is to use 1-loop running for α_s . This variation turns on 2-loop running for α_s , which has a small (beneficial) effect at parton level which is washed out at hadron level.
- PYTHIA: CR1. Often, one thinks of color reconnection as being primarily important for hadron colliders, but even at a lepton collider, color reconnection will change the Lund strings used for hadronization. Compared to the baseline, this variation uses an alternative “SU(3)”-based color reconnection model [476] (i.e. `ColourReconnection:mode = 1`). No attempts were made to retune any of the other hadronization parameters (as would normally be mandated in a tuning context), so this change simply illustrates the effect of switching on this reconnection model with default parameters, leaving all other parameters unchanged. At parton level, this variation has no effect as expected. At hadron level, this variation considerably decreases quark/gluon separation compared to the baseline.

The most surprising PYTHIA effect is the large potential impact of the color reconnection model, which is also important for the HERWIG generator described next.

Our HERWIG++ baseline uses version 2.7.1, with improved modeling of underlying event [477] and the most recent UE-EE-5-MRST tune [478], which is able to describe the double-parton scattering cross section [479] and underlying event data from $\sqrt{s} = 300$ GeV to $\sqrt{s} = 7$ TeV. In Fig. IV.53, we consider the following HERWIG variations:

- HERWIG: NO $g \rightarrow q\bar{q}$. Turning off $g \rightarrow q\bar{q}$ splittings in HERWIG has the reverse behavior as seen in PYTHIA, leading to slightly worse discrimination power, though the effect is modest.
- HERWIG: NO CR. The variation turns off color reconnections in HERWIG. This has no effect at parton level, as expected. At hadron level, this variation for HERWIG gives a rather dramatic improvement in quark/gluon discrimination power. We think this arises since color reconnection in HERWIG allows any color-anticolor pair to reconnect, even if they arose from an initially color octet configuration. By turning off color reconnection, the gluons look more octet-like, explaining the improvement seen.

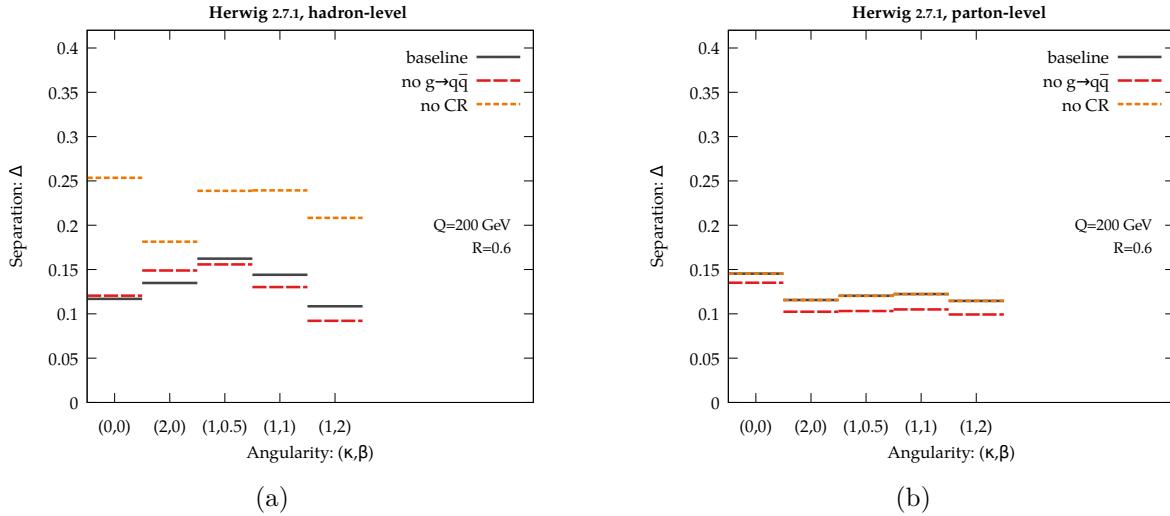


Fig. IV.53: Same as Fig. IV.52, but for HERWIG 2.7.1.

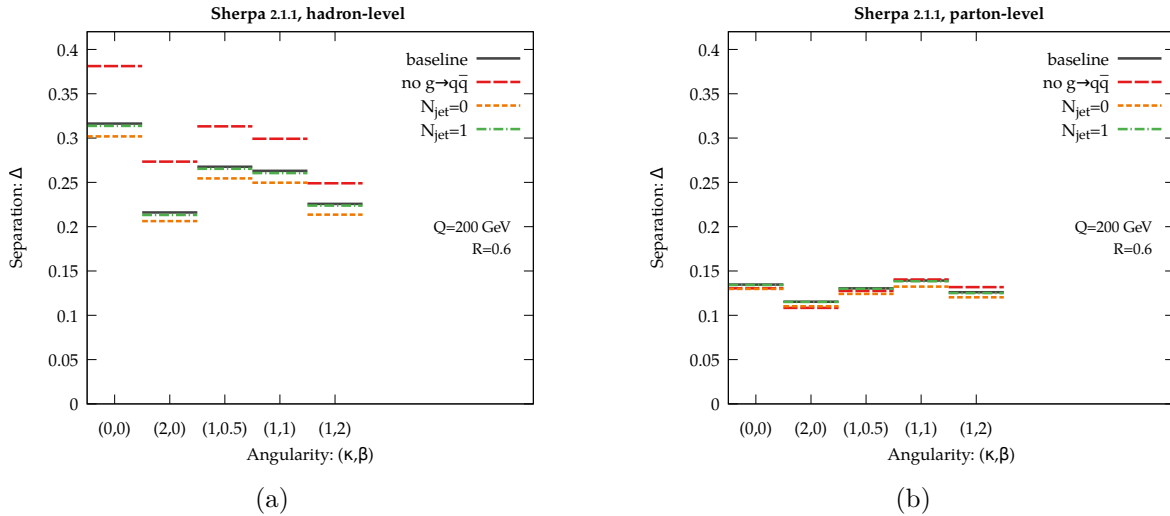


Fig. IV.54: Same as Fig. IV.52, but for SHERPA 2.1.1.

The importance of color reconnections in HERWIG is a big surprise from this study, motivating future detailed studies into which color reconnection models are most realistic when compared to data. In the future, we also plan to test the default angular-ordered HERWIG shower against an alternative dipole shower [384].

Our SHERPA baseline uses matrix element corrections for the first two emissions ($N_{\text{jet}} = 2$) with CKKW-style matching [245]. In Fig. IV.54, we consider the following SHERPA variations:

- SHERPA: No $g \rightarrow q\bar{q}$. Turning off $g \rightarrow q\bar{q}$ splittings in SHERPA has a negligible effect at parton level, but it leads to a large jump in discrimination power at hadron level, again due to an interplay between the perturbative shower and nonperturbative hadronization.
- SHERPA: $N_{\text{jet}} = 1$. This variation only performs CKKW matching for the first emission, leading to negligible changes in the discrimination performance.
- SHERPA: $N_{\text{jet}} = 0$. Turning off all matrix element corrections in SHERPA slightly decreases the predicted quark/gluon discrimination power, in agreement with the behavior

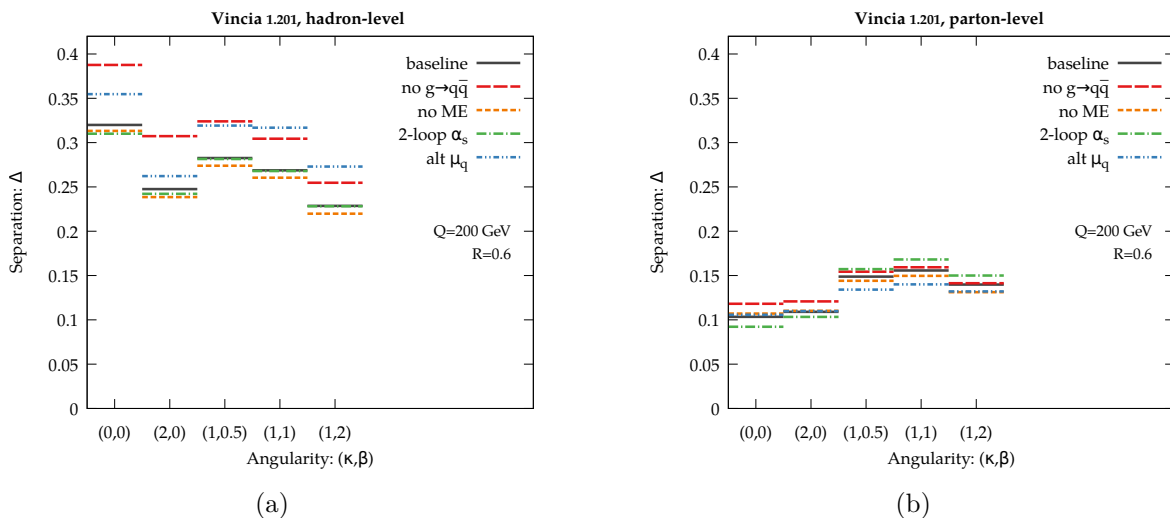


Fig. IV.55: Same as Fig. IV.52, but for VINCIA 1.201.

of PYTHIA.

Within SHERPA, matrix element corrections appear to have a very small effect at parton level. The large changes seen at hadron level from turning off $g \rightarrow q\bar{q}$ splittings motivates further investigations into the shower/hadronization interface.

Our VINCIA baseline is based on the “jeppsson5” tune. While VINCIA has NLO matrix elements for $e^+e^- \rightarrow q\bar{q}$, it does not have them for $e^+e^- \rightarrow gg$, so we will use LO VINCIA throughout. In Fig. IV.55, we consider the following VINCIA variations:

- VINCIA: NO $g \rightarrow q\bar{q}$. This variation turns off $g \rightarrow q\bar{q}$, leading to the expected increase in separation power as seen in PYTHIA.
- VINCIA: NO ME. By default, each $2 \rightarrow 3$ antenna in VINCIA has an associated matrix element correction factor. Since the antenna are already rather close to the true matrix elements, turning off these matrix elements has a modest effect on quark/gluon discrimination power.
- VINCIA: 2-LOOP α_s . Like for PYTHIA, this variation switches from 1-loop to 2-loop α_s running, yielding a modest parton-level difference and almost no hadron-level difference.
- VINCIA: ALT μ_q . By default, the α_s scale used in VINCIA is determined by the transverse momentum of the corresponding antenna. In this variation, the α_s scale is set to half the invariant mass of the mother antenna. This slightly decreases the discrimination power at hadron level, but increases the discrimination power at parton level, again showing the complicated interplay of perturbative and nonperturbative effects.

Since VINCIA and PYTHIA share the same underlying engine, it is not surprising that they exhibit similar behaviors as parameters are changed. The biggest surprise is the way that changing the α_s scale for the antenna can lead to different trends at parton and hadron level.

Our DEDUCTOR baseline uses leading color plus (LC+) showering, which includes some subleading color structures. We find that switching from LC+ to LC showering at parton level has a negligible impact on quark/gluon discrimination power. When DEDUCTOR interfaces with the default tune of PYTHIA 8.212 for hadronization, only leading color is used in the showering,

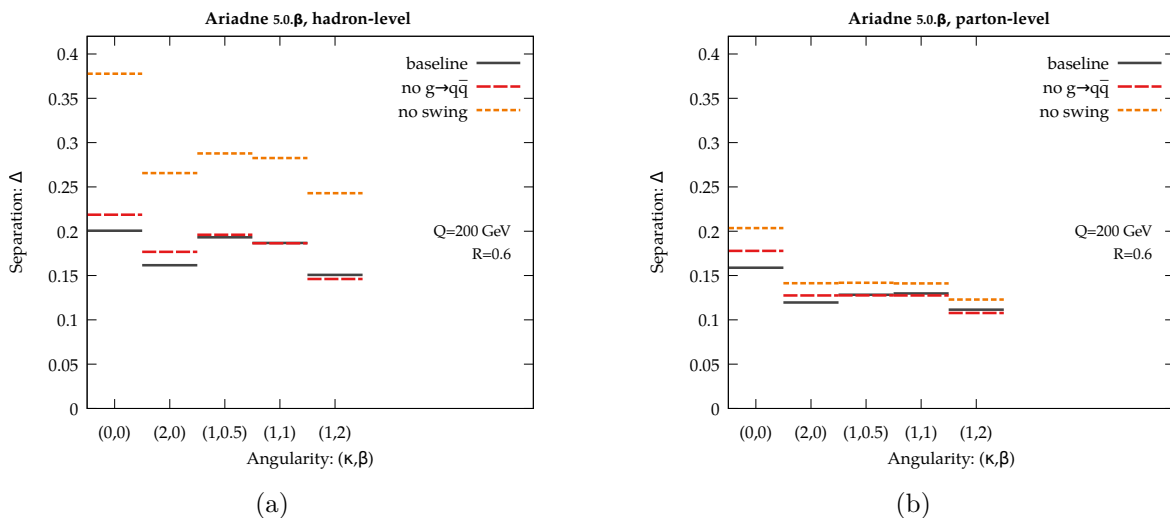


Fig. IV.56: Same as Fig. IV.52, but for ARIADNE 5.0.β.

such that partons with their LC color information can be directly passed to the Lund string model. No DEDUCTOR variations are shown here, but we anticipate studying the effect of $g \rightarrow q\bar{q}$ splitting in future work.

Finally, our ARIADNE baseline is based on a beta release of version 5. In Fig. IV.56, we consider the following ARIADNE variation:

- ARIADNE: NO $g \rightarrow q\bar{q}$. This variation turns off $g \rightarrow q\bar{q}$, leading to modest change in separation power, similar in magnitude to HERWIG.
- ARIADNE: NO SWING. Swing refers to color reconnections performed during the perturbative cascade, where dipoles in the same color state are allowed to reconnect in a way which prefers low-mass dipoles [441, 480]. Turning off swing has an effect already at parton level, which is amplified at hadron level, leading to improved quark/gluon separation.

Like for PYTHIA and HERWIG, color reconnections play a surprisingly important role in ARIADNE.

5.8 Looking towards the LHC

It is clear from our e^+e^- study that quark/gluon radiation patterns face considerable theoretical uncertainties, as seen from the differing behaviors of parton shower generators. This is true even accounting only for final state physics effects, so additional initial state complications can only increase the uncertainties faced in pp collisions. Beyond just the application to quark/gluon tagging, this is an important challenge for any analysis that uses jets. For example, a proper experimental determination of jet energy scale corrections requires robust parton shower tools that correctly model effects like out-of-cone radiation. Eventually, one would like to perform improved analytic calculations to address these radiation pattern uncertainties. In the near term, though, measurements from the LHC will be essential for improving the parton shower modeling of jets.

At the LHC, there is no way to isolate pure samples of quark or gluon jets, but one can isolate quark/gluon-enriched samples, as defined by the flavor label of the jet in the corresponding Born-level partonic process. As shown in Fig. IV.57, the Born-level jet in $W/Z/\gamma + \text{jet}$ is more than 70% quark enriched over the entire jet p_T range of interest. For jets softer than around 200

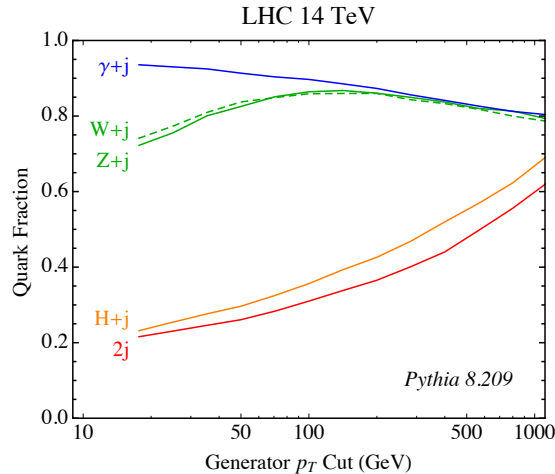


Fig. IV.57: Quark fraction of jets at parton level, as defined by the Born-level parton flavor.

GeV, the Born-level jet in dijets or $H + \text{jet}$ is more than 60% gluon enriched, with that fraction decreasing as the jet p_T increases. More sophisticated enrichment procedures are described in Ref. [450].

In principle, one could try to “diagonalize” some combination of vector boson plus jet and dijet samples in order to define separate quark or gluon samples (see e.g. [416]). In the spirit of Sec. 5.2, though, we think it is more beneficial for the LHC experiments to perform process-specific measurements without trying to directly determine their quark and gluon composition. For example, instead of quark/gluon separation, one can ask the more well-defined question about whether one can tell “the jet in Z plus jets” (quark-enriched) apart from “the jet in dijets” (gluon-enriched). Similarly, one could test for differences within a jet sample, such as comparing central jets versus forward jets in dijet production. This process-based strategy is also helpful for sidestepping the known process dependence of defining quarks and gluons at the LHC, where color correlations to the rest of the event impede a universal definition of quark and gluon jets.

Already, one would learn a lot from unfolded measurements at the LHC of the generalized angularities in a variety of quark/gluon enriched samples. Even detector-level measurement comparing a wide range of generators (and generator modifications) would help in understanding how to improve quark/gluon modeling. The five benchmark angularities in Eq. (IV.26) probe both the perturbative and nonperturbative structure of jets and are therefore a good starting point for a more comprehensive quark/gluon jet shape analysis. In this spirit, we are encouraged by the track multiplicity study of Ref. [421], though for parton shower tuning it is important to have measurements not only of jet shape averages but also of the full jet shape probability distributions.

Finally, we think it would be useful to perform LHC jet shape measurements after jet grooming (see e.g. [481–484]). Often jet grooming is described as a pileup mitigation strategy, but even independent of pileup, grooming modifies the observed jet radiation patterns in ways that are interesting from the quark/gluon perspective. Using techniques from Refs. [485, 486], one can calculate the quark/gluon discrimination power for angularities after jet grooming. Those calculations generically predict that groomed jet shapes should have reduced quark/gluon discrimination power compared to ungroomed jet shapes. That said, because techniques like soft drop [486] remove soft radiation from jets, they tend to reduce the process dependence in quark/gluon radiation patterns, and may therefore yield a more robust theoretical definition for quark and gluon jets.

5.9 Summary and recommendations

By measuring the substructure of jets, one can gain valuable information about the quark/gluon composition of a jet sample. The challenge we have identified in this study is that the precise radiation patterns of quark and gluon jets is poorly understood, in the sense that parton shower generators give rather different predictions for absolute quark/gluon discrimination power as well as relative trends as a function of the jet kinematics. At the moment, analytic calculations are not at a level of accuracy where they can offer a useful guide. Therefore, LHC measurements are the best near-term strategy to constrain quark/gluon radiation patterns and enable quark/gluon discrimination to become a robust experimental tool.

In terms of specific measurements that should be highest priority for ATLAS and CMS, our study has not revealed a silver bullet. Rather, all of the generalized angularities studied here showed similar levels of disagreement between generators, so a systematic LHC study of even one observable is likely to offer crucial new information. What is essential is to make measurements at multiple jet p_T scales with multiple jet radii R in multiple different jet samples. Unfolded distributions would be most useful for parton shower tuning, but even detector-level measurements compared to detector-simulated parton showers would help spot troubling trends. For the IRC safe angularities in particular, studying the β dependence would help separate information about collinear and soft radiation patterns, especially given the fact that the β trends seen in the parton shower generators here disagree with those seen in Ref. [416].

If possible, it would be interesting to study the LHA ($\beta = 1/2$) on archival LEP data, since this angularity probes the core of jets in a new way, distinct from broadening-like ($\beta = 1$) or thrust-like ($\beta = 2$) observables. Among the IRC safe angularities studied here, LHA has the best predicted discrimination power, making it (and other $0 < \beta < 1$ angularities) a well-motivated target for future lepton collider measurements. Similarly, it would be worthwhile to improve our analytic understanding of the LHA. From Fig. IV.48c, we see that the LHA has discrimination power both at small values of $\lambda_{0.5}^1$ (where non-perturbative corrections play an important role) as well as at larger values of $\lambda_{0.5}^1$ (where fixed-order corrections are important), so one must go beyond an NLL understanding to understand the quark/gluon performance of the LHA.

The key lesson to parton shower authors is that, contrary to some standard lore, existing LEP measurements *do not* constrain all of the relevant aspects of the final state parton shower. While we have extensive information about quark jet radiation patterns from LEP event shapes, gluon jet radiation patterns are largely unconstrained. This has important implications for parton shower tuning strategies, since LHC data can and should be used to adjust final state shower parameters. For example, the ATLAS A14 tune of PYTHIA has a 10% lower value of α_s in the final state shower compared to the Monash tune, which yields better agreement with charge particle multiplicity distributions [421]. However, A14 has not been tested on LEP event shapes, suggesting that a global tuning strategy is needed. In addition, it is worth mentioning that similar quark/gluon studies have been carried out in deep inelastic electron-proton scattering [487], which offer an intermediate step between pp and e^+e^- collisions, and this ep data could also be valuable for parton shower tuning.

Based on this study, we have identified three aspects of the final state parton shower that deserve closer scrutiny.

- *Gluon splitting to quarks.* Some of the largest differences between generators came from turning on and off the $g \rightarrow q\bar{q}$ splitting process. While PYTHIA, SHERPA, VINCIA, and ARIADNE suggest that (unphysically) turning off $g \rightarrow q\bar{q}$ would improve quark/gluon separation, HERWIG (and the analytic calculation in Ref. [413]) suggests the opposite conclusion. Beyond quark/gluon discrimination, it would be helpful to identify other contexts where $g \rightarrow q\bar{q}$ might play an important role.

- *Color reconnection in the final state.* Color reconnection is often thought of as an issue mainly at hadron colliders, but we have seen that it can have an impact in e^+e^- collisions as well. This is particularly the case with the default color reconnection model in HERWIG, since it allows the reconnection of color/anticolor lines even if they originally came from an octet configuration. We also saw large changes from PYTHIA: CR1 and ARIADNE: NO SWING, suggesting that one should revisit color reconnection physics when tuning to LEP data.
- *Reconsidering α_s defaults:* In the context of parton shower tuning, the value of α_s used internally within a code need not match the world average value, since higher-order effects not captured by the shower can often be mimicked by adjusting α_s . That said, one has to be careful whether a value of α_s tuned for one process is really appropriate for another. For example, PYTHIA uses a relatively large value of α_s in its final state shower, which allows it to match LEP event shape data. The same value of α_s , though, probably also leads to too much radiation within gluon jets.

Finally, we want to emphasize that despite the uncertainties currently present in parton shower generators, parton showers in particular (and QCD resummation techniques more generally) will be essential for understanding quark/gluon discrimination. Fixed-order QCD calculations cannot reliably probe the very soft and very collinear structure of jets, which is precisely where valuable information about quark/gluon radiation patterns reside. Given the ubiquity and value of parton shower generators, improving the understanding of quark/gluon discrimination will assist every jet study at the LHC.

Acknowledgments

We thank Samuel Bein, Andy Buckley, Jon Butterworth, Mario Campanelli, Andrew Larkoski, Peter Loch, Ben Nachman, Zoltan Nagy, Chris Pollard, Salvatore Rappoccio, Gavin Salam, Alexander Schmidt, Frank Tackmann, and Wouter Waalewijn for helpful discussions and feedback. DK acknowledges support from the Science Faculty Research Council, University of Witwatersrand. The work of LL, SP, and AS is supported in part by the MCnetITN FP7 Marie Curie Initial Training Network, contract PITN-GA-2012-315877. LL is also supported by the Swedish Research Council (contracts 621-2012-2283 and 621-2013-4287). SP acknowledges support from a FP7 Marie Curie Intra European Fellowship under Grant Agreement PIEF-GA-2013-628739. The work of DS is supported by the U.S. Department of Energy (DOE) under Grant DE-SC-0011640. The work of GS is supported by the Paris-Saclay IDEX under the IDEOPTIMALJE grant. The work of JT is supported by the DOE under cooperative research agreement DE-SC-00012567, by the DOE Early Career research program DE-SC-0006389, and by a Sloan Research Fellowship from the Alfred P. Sloan Foundation.

6 Study of associated production of vector bosons and b-jets at the LHC ²⁷

6.1 Introduction

The vector boson production in association with one and two b jets at the CERN Large Hadron Collider is important for many different experimental and theoretical reasons. Bottom quarks have a peculiar signature which allows one to easily identify them thanks to a displaced decay vertex. The associated production with vector bosons is an important background to VH production with the Higgs boson decaying to b quarks, and many new physics searches. Theoretically, it offers an interesting testing ground for predictions involving heavy quarks.

²⁷ V. Ciulli, M. Bell, J. Butterworth, G. Hesketh, D. Grellscheid, F. Krauss, G. Luisoni, G. Nail, D. Napoletano, C. Oleari, L. Perrozzi, S. Platzer, C. Reuschle, B. Waugh

There are two possible options for the calculation of processes with b-quarks in the final state at hadron colliders. In the four-flavour scheme (4F) b-quarks are not present in the parton density of the incident protons. They can only be generated in the final state and they are usually massive. In the five-flavour scheme (5F) the b-quark mass is considered small with respect to the scale of the process Q and powers of logarithms of the type $\log(Q^2/m_b^2)$ are resummed into a b parton density function. The b-quark is therefore massless in this approach, though higher order mass effects can be included in the calculation. A critical review of the different flavour number schemes and of the status of theoretical calculations is available in Ref. [488]. To all orders in perturbation theory the two approaches give identical results up to power suppressed mass terms. At finite order, however, they may give different results. In the 4F scheme the computation is more complicated, but the full kinematics of the heavy quarks is taken into account. Furthermore it can be easily interfaced to parton showers, even at NLO using the MC@NLO [489] or the POWHEG [490] formalisms. On the other hand logarithms in the initial state are not resummed and could lead to large discrepancies in the inclusive quantities like the total cross-section. In the 5F approach, on the opposite, calculations for the inclusive quantities are highly simplified and generally more accurate, but differential distributions and exclusive observables are technically more involved.

The goal of this study is to compare the most recent measurements with the predictions of the state of the art generators using 4F and 5F scheme. The report is organised as follows. In Section 6.2 we provide a short description of the ATLAS and CMS measurements, available in the Rivet framework, for $V + b + X$ and $V + b\bar{b} + X$, where V is a Z or a W boson. In Section 6.3 we describe the generator setups used to obtain the predictions, which are compared to the measurements in Section 6.4 for the Z and 6.5 for the W , before conclusions are drawn in Section 6.6.

6.2 Rivet Routines

Results in this study were produced using three Rivet routines to compare to published ATLAS and CMS data.

ATLAS $Z+b(b)$ Measurement of differential production cross-sections for a Z boson in association with b-jets in proton-proton collisions at $\sqrt{s} = 7$ TeV with the ATLAS detector [491] (Rivet routine ATLAS_2014_I1306294). A pair of opposite-sign charge dressed leptons²⁸ (i.e. electrons or muons) with $p_T > 20$ GeV and $|\eta| < 2.5$ are required, with a dilepton mass between 76 and 106 GeV. Anti- k_t 0.4 jets are reconstructed from all final state particles, and required to have $p_T > 20$ GeV, $|y| < 2.4$ and not overlap with the leptons used to make the Z candidate ($\Delta R(jet, l) > 0.5$). Jets are labelled as b -jets based on matching with $\Delta R < 0.3$ to a weakly decaying b -hadron with $p_T > 5$ GeV.

Distributions include the p_T and rapidity of b -jets and of the Z -boson, and for each b -jet, the y_{boost} of the b -jet and Z . For events with $Z p_T > 20$ GeV, the ΔR , $\Delta\phi$, and Δy between the Z and all b -jets are plotted. For events with at least two b -jets, the ΔR and di- b -jets mass for the two leading b -jets, along with the $Z p_T$ and rapidity are plotted.

CMS $Z+BB$ Cross-section and angular correlations in Z boson with b-hadrons events at $\sqrt{s} = 7$ TeV [492] (Rivet routine CMS_2013_I1256943). A pair of opposite-sign charge dressed lepton with $p_T > 20$ GeV and $|\eta| < 2.4$ are required, with dilepton mass between 81 and 101 GeV. Exactly two weakly decaying b-hadrons with $p_T > 15$ GeV and $|\eta| < 2$ are then required.

²⁸Leptons are dressed by adding the four-vectors of all photons within $\Delta R < 0.1$ to the lepton 4-vector

Distributions include the Z p_T , the ΔR and $\Delta\phi$ between b -hadrons, ΔR between the Z and closest b -hadron, and the asymmetry of the ΔR between the Z and closest b -hadron, and the Z and the furthest b -hadron. The angular distributions are repeated with a requirement of Z $p_T > 50$ GeV.

ATLAS W+b Measurement of the cross-section for W boson production in association with b -jets in pp collisions at $\sqrt{s} = 7$ TeV with the ATLAS detector [493] (Rivet routine ATLAS_2013_I1219109). A dressed lepton with $p_T > 25$ GeV and $|\eta| < 2.5$ and a same-flavour neutrino with $p_T > 25$ GeV are used to form a W candidate, which is required to have a transverse mass greater than 60 GeV. Anti- k_t 0.4 jets are reconstructed from all final state particles, and required to have $p_T > 25$ GeV, $|y| < 2.1$ and not overlap with the charged lepton used to make the W candidate ($\Delta R(jet, l) > 0.5$). Events with more than two selected jets are vetoed, and the at least one of the selected jets is required to be labelled as b -jet, based on matching with $\Delta R < 0.3$ to a weakly decaying b -hadron with $p_T > 5$ GeV.

Distributions include the number of jets, and the b -jet p_T in events containing exactly one or two selected jets.

6.3 Event generators

SHERPA

In this section we present the setups that are used in this study for the SHERPA event generator [275]. In particular for $Z+b(b)$ we consider three different classes of samples: 4F MC@NLO, 5F MEPS and a 5F MEPS@NLO one.

4F MC@NLO: This first set of results is obtained in the four-flavour scheme, and based on the MC@NLO technique [489], as implemented in SHERPA [375]. In a four-flavour scheme calculation, b -quarks can only be produced as final state massive particles. They are, therefore, completely decoupled from the evolution of the strong coupling, α_S and that of the PDFs. In this scheme the associated production at tree-level starts from processes such as $jj \rightarrow b\bar{b}Z$ where j can be either a light quark or a gluon. No specific cuts are applied on the b -quarks, their finite mass regulates collinear divergences that would appear in the massless case. In most cases, therefore, a b -jet actually originates from the parton shower evolution and hadronization of a b -quark produced by the matrix element.

5F MEPS: In a 5F scheme b -quarks are treated as massless partons. Collinear logs are resummed into a b -PDF and they can appear as initial state particles as well as final state ones. In order to account for 0 and 1 b -jets bins as well as to cure the collinear singularity that would arise with a massless final state parton, we use multi-jet merging. In SHERPA, the well-established mechanism for combining into one inclusive sample towers of matrix elements with increasing jet multiplicity at tree-level is the CKKW [245]. For this sample we merge together LO samples of $jj \rightarrow Z$, $jj \rightarrow Z + j$, $jj \rightarrow Z + jj$, $jj \rightarrow Z + jjj$ where now j can be a light quark, a b -quark or a gluon, and all these samples are further matched to the SHERPA parton shower CSS [373]. Merging rests on a jet-criterion, applied to the matrix elements. As a result, jets are being produced by the fixed-order matrix elements and further evolved by the parton shower. As a consequence, the jet criterion separating the two regimes is typically chosen such that the jets produced by the shower are softer than the jets entering the analysis. This is realised here by a cut-off of $\mu_{jet} = 10$ GeV.

5F MEPS@NLO: In this scheme we use the extension to next-to leading order matrix elements, in a technique dubbed MEPS@NLO [244]. In particular, we merge $jj \rightarrow Z$,

$jj \rightarrow Z + j$, $jj \rightarrow Z + jj$ calculated with NLO accuracy and we further merge this sample with $jj \rightarrow Z + jjj$ at the LO. As in the previous case matching criterion has to be chosen, and this is realised by a cut-off of $\mu_{\text{jet}} = 10 \text{ GeV}$.

In SHERPA, tree-level cross sections are provided by two matrix element generators, AMEGIC++ [249] and COMIX [302], which also implement the automated infrared subtraction [301] through the Catani–Seymour scheme [90, 293]. For parton showering, the implementation of [373] is employed with the difference that for $g \rightarrow b\bar{b}$ splittings the invariant mass of the $b\bar{b}$ pair, instead of their transverse momentum, is being used as scale. NLO matrix elements are instead obtained from OPENLOOPS [40, 494].

The SHERPA W+b sample is the same one used for the study presented in Section 7. It is generated with AMEGIC at LO in the 5F scheme, using NNPDF [184] library. The b -quark is massive, with the mass value set to 4.75 GeV, and the W boson is treated through the narrow width approximation. The order of the electroweak couplings is fixed to 2, therefore removing single-top contribution. Multi-parton interactions (MPI) are switched on/off to estimate this contribution.

HERWIG7

In this section we present the setup for those results obtained with the HERWIG7 event generator [382, 437].

Based on extensions of the previously developed MATCHBOX module [384], HERWIG7 facilitates the automated setup of all ingredients necessary for a full NLO QCD calculation in the subtraction formalism: an implementation of the Catani–Seymour dipole subtraction method [90, 293], as well as interfaces to a list of external matrix-element providers – either at the level of squared matrix elements, based on extensions of the BLHA standard [1, 332, 333], or at the level of color-ordered subamplitudes, where the color bases are provided by an interface to the COLORFULL [388] and CVOLVER [495] libraries.

For this study the relevant tree-level matrix elements are taken from MADGRAPH5_aMC@NLO [45, 318] (via a matrix-element interface at the level of color-ordered subamplitudes), whereas the relevant tree-level/one-loop interference terms are provided by OPENLOOPS [40, 494] (at the level of squared matrix elements).

Fully automated NLO matching algorithms are available, henceforth referred to as subtractive ($NLO\oplus$) and multiplicative ($NLO\otimes$) matching – based on the MC@NLO [489] and POWHEG [490] formalism respectively – for the systematic and consistent combination of NLO QCD calculations with both shower variants (the angular-ordered $QTilde$ shower [496] and the *Dipole* shower [383]) in HERWIG7.

We consider four different classes of samples, for varying combinations of matching and shower algorithms (a selection of plots can be found in sections 6.4 and 6.5):

4F, Zbb For this set we consider the subtractive and multiplicative matching together with the $QTilde$ shower. The tree-level process of the underlying hard sub-process in this case is $pp \rightarrow e^+e^-b\bar{b}$. For this sample the b quark is considered massive and p only consists of light quarks or a gluon, not a b quark.

5F, Zbb For this set we consider the subtractive and multiplicative matching together with the $QTilde$ and *Dipole* shower. The tree-level process of the underlying hard sub-process in this case is $pp \rightarrow e^+e^-b\bar{b}$. For this sample the b quark is treated as massless, and p may also include a b quark. Generator-level cuts on the b quarks have thus been applied. Only in the shower evolution of the $QTilde$ shower is the b quark assumed massive.

5F, Zb For this set we consider the subtractive and multiplicative matching together with the *QTilde* and *Dipole* shower. The tree-level process of the underlying hard sub-process in this case is $pp \rightarrow e^+e^-j_b$, where $j_b \ni \{b, \bar{b}\}$. For this sample the b quark is treated as massless, and p may also include a b quark. Generator-level cuts on the b quark have thus been applied. Only in the shower evolution of the *QTilde* shower is the b quark assumed massive. For single b -quark production only one p must contribute a b quark at a time, at the level of the hard sub-process at hand.

4F, Wbb For this set we consider the subtractive and multiplicative matching together with the *QTilde* shower. The tree-level process of the underlying hard sub-process in this case is $pp' \rightarrow Wb\bar{b} \rightarrow l\nu_l b\bar{b}$, where $l \in \{e^+, e^-, \mu^+, \mu^-\}$ and ν_l the associated (anti-)neutrino. For this sample the b quark is considered massive and p, p' only consist of light quarks or a gluon, not a b quark; p' simply denotes the contribution of pair-wise different quark flavours in the initial state, as a result from the Wdu or Wsc vertex.

In all samples the uncertainty bands are purely from scale variations by simultaneously varying all scales in the hard sub-process and in the shower by factors of two up and down, i.e. factorization and renormalization scale in the hard sub-process, as well as scales related to α_s and the PDFs in the shower, as well as the hard shower scale. The central scale choice is always a fixed scale (the Z mass in associated Z production; the W mass in associated W production).

The PDF sets being used are MMHT2014lo68cl and MMHT2014nlo68cl [183], i.e. the default PDF sets to which the showers are currently tuned. An internal study showed that using different PDF sets (a different $n_f=5$ PDF set for the 5F runs or $n_f=4$ PDF sets for the 4F runs) results in only minor differences, within the scale variation uncertainties.

In case the b quark is assumed massive, its mass is set to the default value in HERWIG7. All other relevant parameters, like W and Z mass and width, etc., are set to their respective default values in HERWIG7 as well.

For the 5F, Zbb sample we cut on the final state b quarks by including them into the jet definition and requiring at least two jets, with a min. p^\perp of 18 GeV and 15 GeV for the first and second jet respectively. The statistics for this sample are 100k unweighted events.

For the 5F, Zb sample we cut on the final state b quark (similarly to above) by requiring at least one jet, with a min. p^\perp of 18 GeV for the first jet. The statistics for this sample are 100k unweighted events.

For both 5F samples we apply generator level cuts on the invariant mass of the charged-lepton pair, with a min. invariant mass of 60 GeV and a max. invariant mass of 120 GeV.

For the 4F, Zbb sample we apply no cuts on the b quarks. However, we require the same generator level cuts as for the 5F, Zbb and Zb samples on the invariant mass of the charged-lepton pair again. In addition we cut slightly on the charged leptons, with a min. p^\perp of 5 GeV and a rapidity range between -4 and 4. The statistics for this sample are 100k unweighted events.

For the 4F, Wbb sample we also apply no cuts on the b quarks. However, we require a slight generator level cut on the transverse mass of the W , with a min. transverse mass of 20 GeV. We also cut slightly on the charged lepton, with a min. p^\perp of 5 GeV and a rapidity range between -4 and 4. The statistics for this sample are 100k unweighted events.

POWHEG BOX

The results obtained with the POWHEG BOX framework are based on the generators presented in ref. [497]. The tree-level amplitudes, which include Born, real, spin- and colour-correlated Born amplitudes, were automatically generated using an interface [365] to MADGRAPH4 [498, 499],

whereas the one-loop amplitudes were generated with GOSAM [44, 283] via the Binoth-Les-Houches (BLHA) interface [332, 333], presented for the POWHEG BOX and GOSAM in [500]. The version of GOSAM is the 2.0: it uses QGRAF [334], FORM [336] and SPINNEY [337] for the generation of the Feynman diagrams. These diagrams are then computed at running time with NINJA [339, 340], which is a reduction program based on the Laurent expansion of the integrand [338], and using ONELOOP [299] for the evaluation of the scalar one-loop integrals. For unstable phase-space points, the reduction automatically switches to GOLEM [343], that allows to compute the same one-loop amplitude evaluating tensor integrals.

Further details can be found in ref. [497]. Here we briefly summarize the most important features.

1. We have used a mixed renormalization scheme [501], generally known as decoupling scheme, in which the n_{lf} light flavours are subtracted in the usual $\overline{\text{MS}}$ scheme, while the heavy-flavour loop is subtracted at zero momentum. In this scheme, the heavy flavour decouples at low energies. To make contact with other results expressed in terms of the $\overline{\text{MS}}$ strong coupling constant, running with 5 light flavours, and with pdfs with 5 flavours, we have switched our scheme using the procedure discussed in ref. [307].
2. We have generated $Wb\bar{b}j$ events using the MiNLO [345] prescription, that attaches a suitable Sudakov form factor to the $Wb\bar{b}j$ cross section at NLO, and subtracts its expansion (not to have double counting of the Sudakov logarithms), in order to get a finite cross section down to small transverse momentum of the hardest jet. The scales of the primary process (i.e. the process obtained by the attempt to cluster a $Wb\bar{b}j$ event with a procedure similar to CKKW [245]) have been chosen as follows:

- (a) if there has been a clusterization, then the scales are set to

$$\mu_{\text{R}} = \mu_{\text{F}} = \mu \equiv \frac{\sqrt{\hat{s}}}{4}, \quad \hat{s} = (p_{\text{W}} + p_{\text{b}} + p_{\bar{\text{b}}})^2, \quad (\text{IV.35})$$

where p_{W} , p_{b} and $p_{\bar{\text{b}}}$ are the momenta of the W , b and \bar{b} in the primary process

- (b) If the event has not been clustered by the MiNLO procedure, i.e. if the underlying Born $Wb\bar{b}j$ process is not clustered by MiNLO, we take as scale the partonic center-of-mass energy of the event.

The bands in the plots of Figures IV.70 and IV.71 of this section are the envelope of the distributions obtained by varying the renormalization and factorization scales by a factor of 2 around the reference scale μ of eq. (IV.35), i.e. by multiplying the factorization and the renormalization scale by the scale factors K_{F} and K_{R} , respectively, where

$$(K_{\text{R}}, K_{\text{F}}) = (0.5, 0.5), (0.5, 1), (1, 0.5), (1, 1), (2, 1), (1, 2), (2, 2). \quad (\text{IV.36})$$

These variations have been computed using the POWHEG BOX reweighting procedure, that recomputes the weight associated with an event in a fast way.

6.4 $Z+b(b)$ production

$Z+b(b)$ with *SHERPA*

Figures IV.58 and IV.59 show a selection of the plots comparing Sherpa predictions to data. There is overall a good agreement, but for the normalization. The 5F LO order predictions are generally below the data, though compatible within the large scale uncertainty. For NLO predictions this uncertainty is smaller and some patterns can be observed. Both the 5F and the 4F NLO are in good agreement with distributions for events with two b-tagged jets. But when a single b-jet is tagged, the 5F and 4F results have an opposite behaviour: the 5F is 20% above the data (except for high Z p_T), while 4F is 20% below.

It is nevertheless remarkable that the ratio of 4F NLO predictions to data is flat for all the observables. This is particularly interesting, since it is more efficient to generate a sample of $Z + b\bar{b}$ events with the 4F scheme than with the 5F. The reason why an overall normalization factor is needed could lie in the large logarithms, that in the 5F scheme are resummed in the b parton distribution function. However they might not affect the shape of the distributions. To check this hypothesis the 4F NLO predictions have been rescaled to the integrated cross-sections calculated with MCFM [357]. Depending on the observable and the applied selection, four different cross-sections are defined, as explained in [491]. The value is corrected for QED final-state radiation, hadronisation, underlying event and multi-parton interactions. The uncertainty is given by the envelope of the results obtained with several PDFs, taking for each the sum in quadrature of all theory uncertainties. A selection of the plots is shown in Figure IV.60. The results are very encouraging but further studies are needed to understand if this approach fails for other observables, e.g. those related to the presence of additional light-quark jets.

$Z+b(b)$ with *HERWIG7*

A selection of results obtained with HERWIG7 is shown in Figures IV.61, IV.62 and IV.63 for the 5F, Zbb setup, in Figures IV.64, IV.65 and IV.66 for the 5F, Zb setup, and in Figures IV.67, IV.68 and IV.69 for the 4F, Zbb setup. We refer to section 6.3 for the process setups of the 5F, Zb and Zbb samples, as well as for the 4F, Zbb sample.

Regarding the 5F, Zbb setup we note that we should expect somewhat large uncertainties in observables which are also sensitive to events with 1 b jet, since at the level of the hard sub-process events with only 1 b jet are only described by the real emission in this sample. Within those uncertainties, the prediction describes the data, with the exception of the $\Delta\phi(Z, b)$ and $\Delta R(Z, b)$ observables in Figure IV.62, where the prediction shows a slight tendency to be systematically above the data towards the lower values of $\Delta\phi(Z, b)$ and $\Delta R(Z, b)$. Looking at the CMS data comparisons the *Dipole* shower together with the subtractive matching seems to undershoot the data in the ΔR_{BB} and $\Delta\phi_{BB}$ observables, which, however, seems not to be the case in the corresponding observables (for $Z + \geq 2b$ -jets) in the ATLAS data comparisons (not shown here); however, here the combinations with the multiplicative matching seem to overshoot the data.

A brief internal study with the $NLO \oplus QTilde$ combination showed that a 5F, Zbj setup (where at the level of the hard sub-process events with only 1 b jet are already produced at the Born level) yields the expected reduction in the uncertainty bands.

The predictions from the 5F, Zb setup describes the data overall well. There seems to be a slight tendency, though, to systematically overshoot the data in the b -jet $|y|$ and $y_{\text{boost}}(Z, b)$ observables for $Z + \geq 1b$ -jet in Figure IV.65 (the same holds for the $\Delta y(Z, B)$ observable, not shown here).

With the 4F, Zbb setup we see that the predictions are generally below the data. However, also here we notice a similar behaviour as already pointed out for the SHERPA results, in that

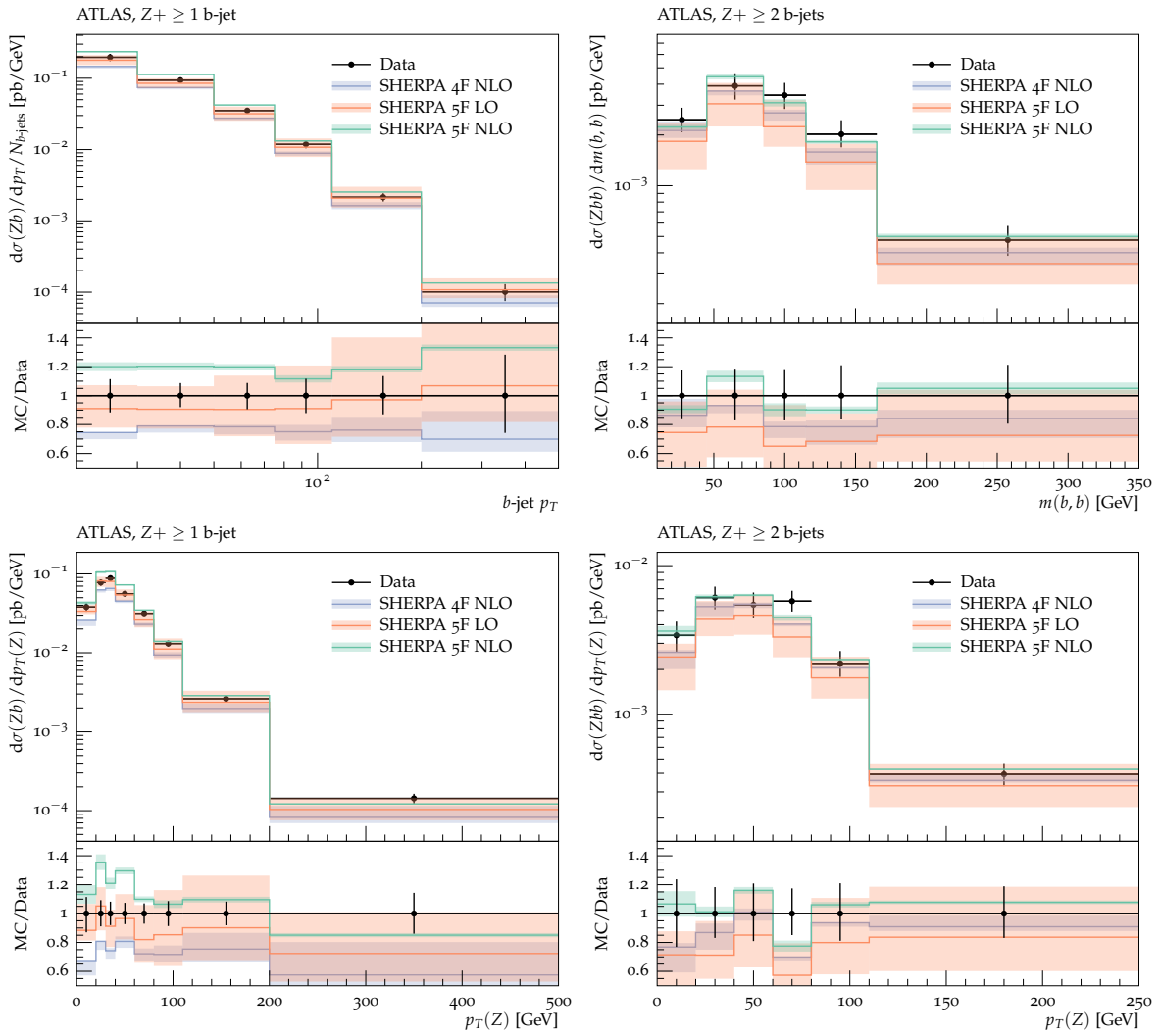


Fig. IV.58: A selection of the plots comparing Sherpa predictions to ATLAS results.

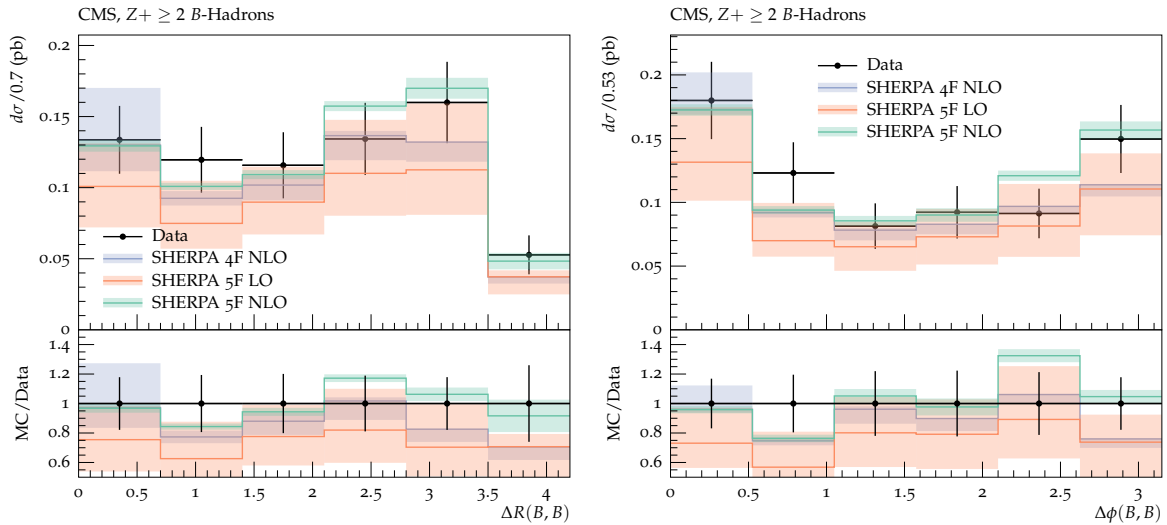


Fig. IV.59: A selection of the plots comparing Sherpa predictions to CMS results.

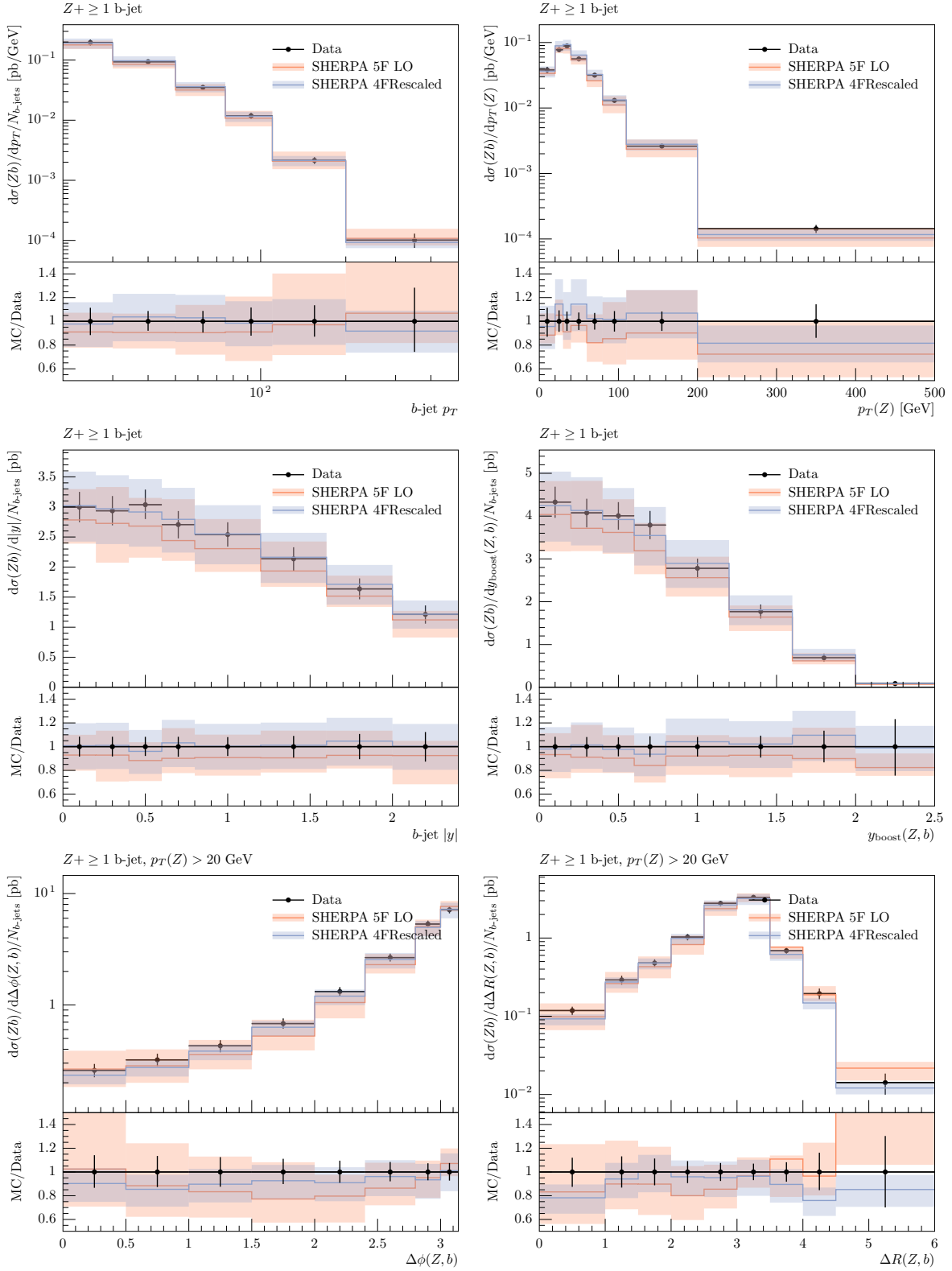


Fig. IV.60: A selection of the plots comparing rescaled Sherpa 4F NLO predictions to ATLAS results.

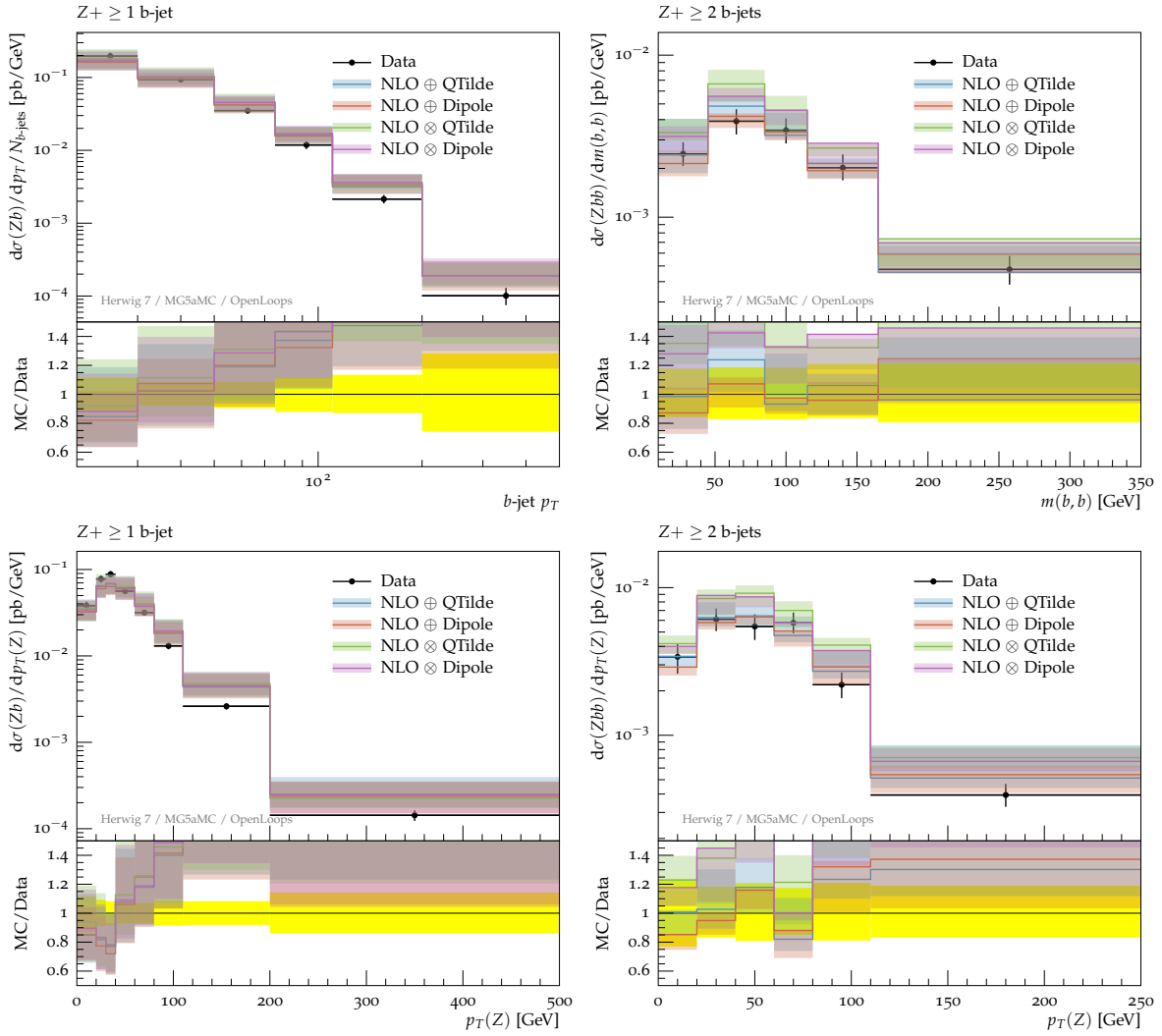


Fig. IV.61: A selection of the plots comparing HERWIG7 5F, Zbb predictions to ATLAS results.

the ratio of this 4F NLO prediction to data is flat – except for the ΔR_{BB} and $\Delta\phi_{BB}$ observables in Figure IV.69, where we notice that the predictions fall below the data at the lowest end of the distributions.

6.5 W+b production

Figures IV.70 and IV.71 present a comparison between the data of the ATLAS $W+b$ measurement and 4F NLO predictions obtained with the POWHEG BOX generator for $Wb\bar{b}j$ presented in sec. 6.3 and the HERWIG7 generator for $Wb\bar{b}$ discussed in sec. 6.3. Figures IV.72 and IV.73 present the same comparison but with 5F LO predictions obtained with the SHERPA generator as explained in sec. 6.3.

The first Figure present results for the total cross section in the case of only one b-tagged jet (“1 jet”), one b-tagged and at least an additional jet (“2 jet”), or both (“1+2 jet”). Despite the underlying generators consider two different underlying partonic processes, $Wb\bar{b}j$ in the POWHEG BOX and $Wb\bar{b}$ in the case of HERWIG7, the agreement between the two 4F NLO theoretical predictions is very good and the uncertainties due to scale variations are very similar. The general good agreement between the $Wb\bar{b}$ and the $Wb\bar{b}j$ predictions is not trivial a priori

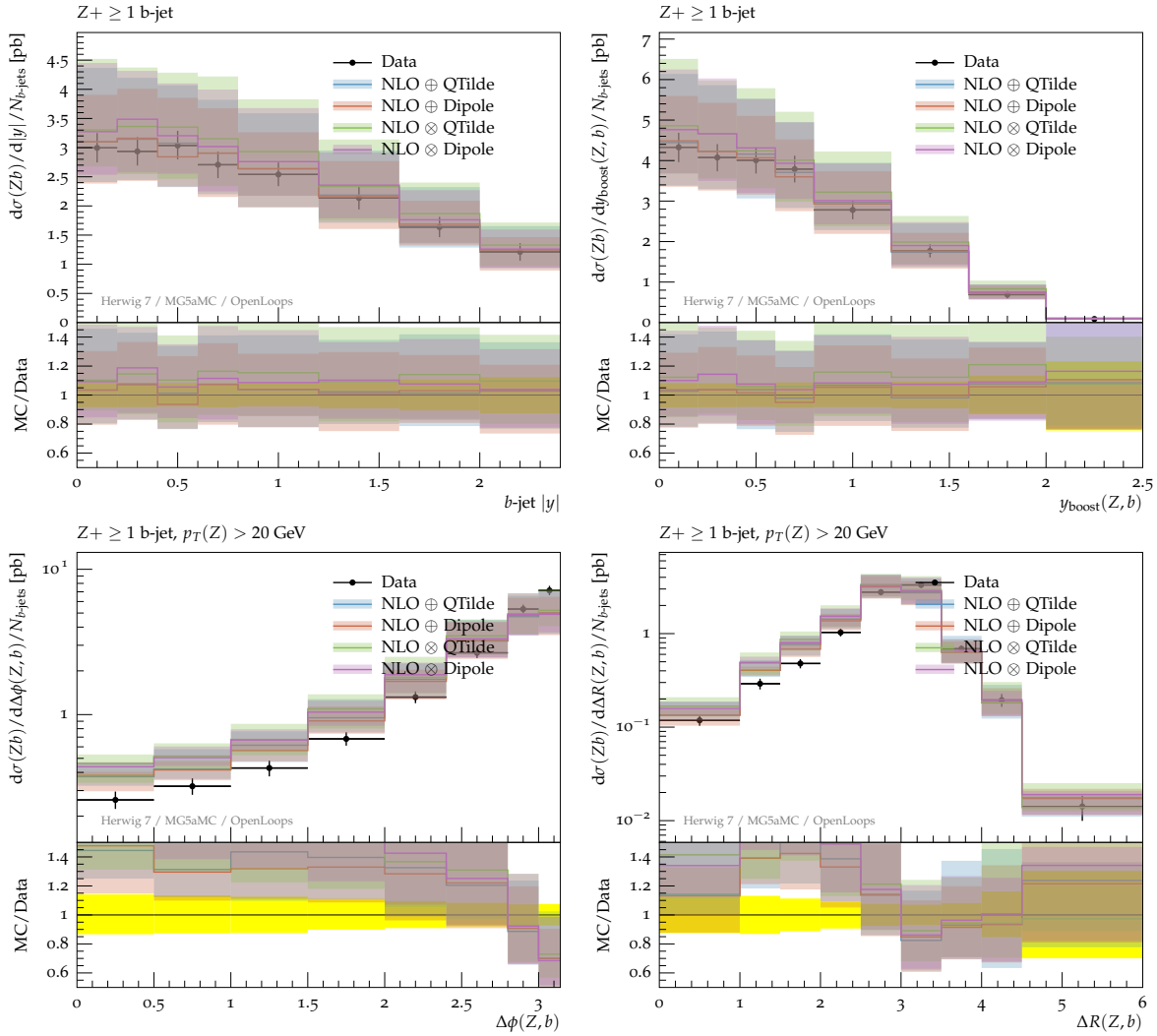


Fig. IV.62: A selection of the plots comparing HERWIG7 5F, $Zb\bar{b}$ predictions to ATLAS results; together with the plots in figure IV.61 a comparison to the rescaled SHERPA 4F NLO predictions in Figure IV.60 can be made.

due to the different choices of scales in the two codes, and the fact that in the $Wb\bar{b}j$ code the transverse momentum of the jet goes to zero and the divergent behavior is regulated by the MinLO prescription [497]

The agreement of these 4F NLO predictions with the experimental data is however not so good. As shown in [497] this can only partially be compensated by the missing double-parton interaction (DPI) corrections, which are estimated and applied as an additive correction factor in the original ATLAS publication [493]. This is confirmed by the results obtained with SHERPA with and without MPI. Compared to the estimate of DPI corrections given in the paper, the MPI contribution determined by SHERPA is smaller for the “1 jet” case, but not incompatible given the large uncertainty: 0.2 pb vs $1.0^{+0.4}_{-0.3} \text{ pb}$; while a similar result is obtained for the “2 jet” case: 0.4 vs 0.3 ± 0.1 .

The 5F LO prediction for the cross section agrees very well with data for the “2-jet” final state, while overshoot the data for “1 jet” by more than one standard deviation (taking into account the experimental uncertainty only). Previous studies [502] have shown that the

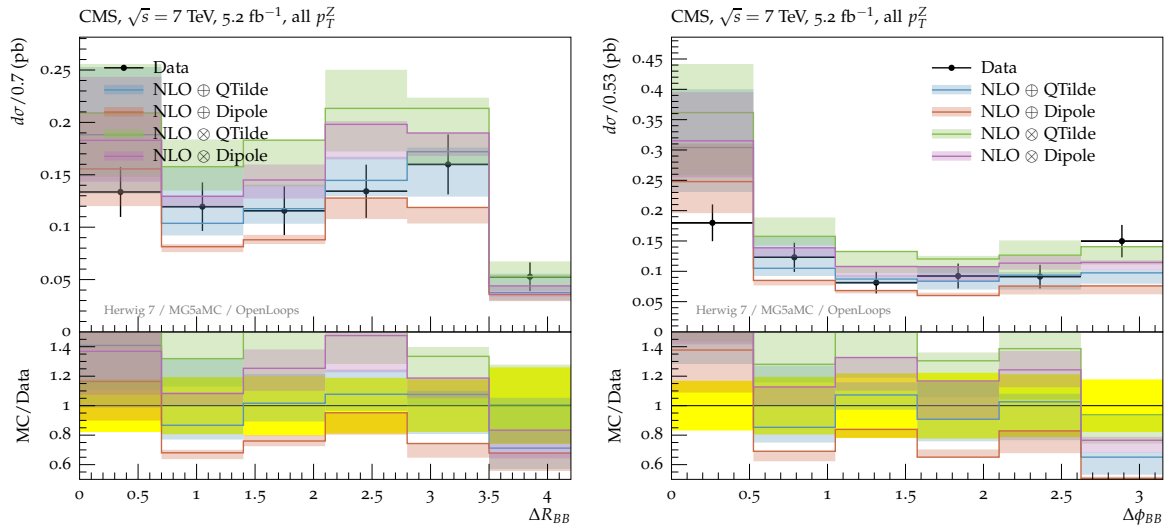


Fig. IV.63: A selection of the plots comparing HERWIG7 5F, Zbb predictions to CMS results.

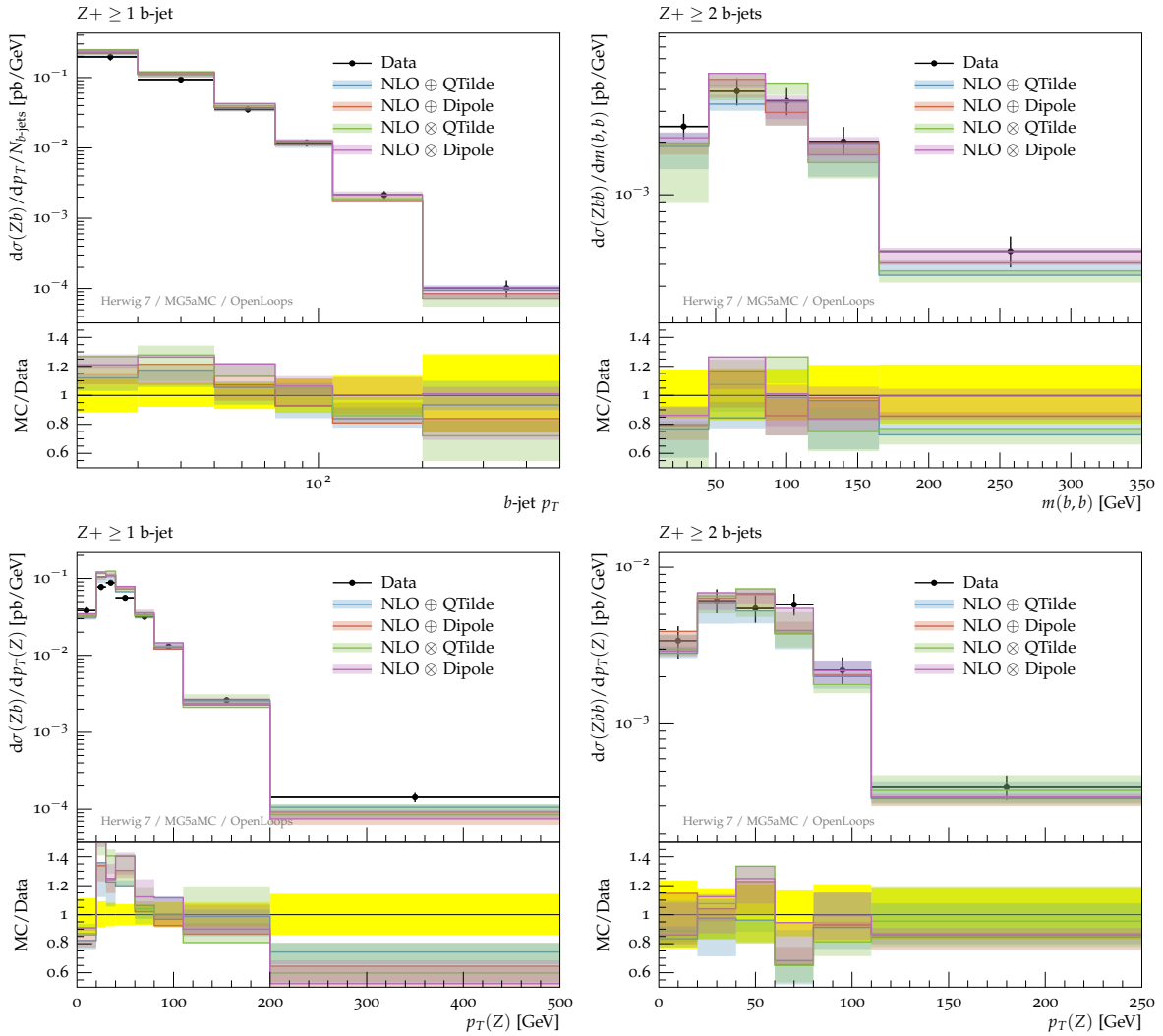


Fig. IV.64: A selection of the plots comparing HERWIG7 5F, Zb predictions to ATLAS results.

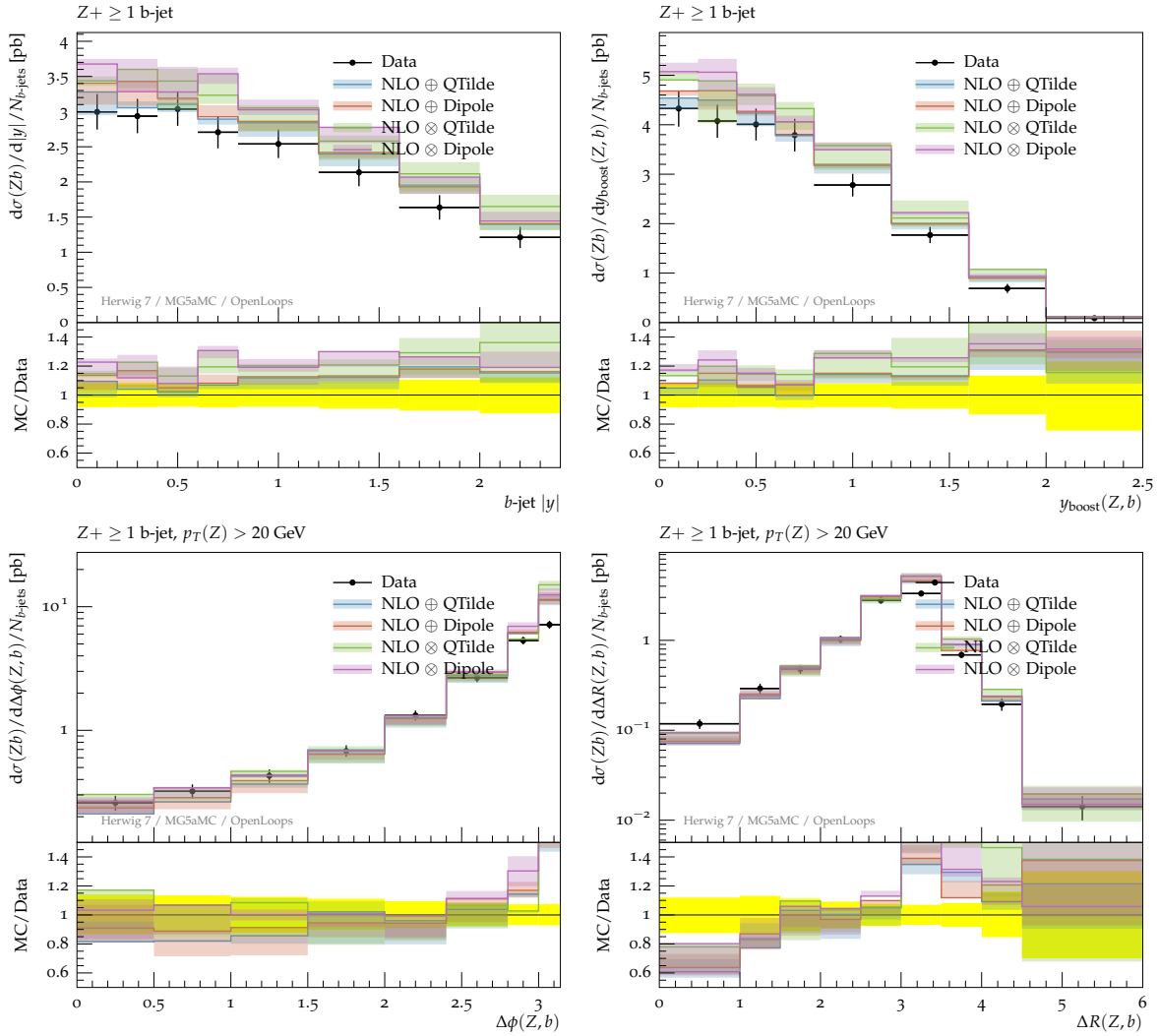


Fig. IV.65: A selection of the plots comparing HERWIG7 5F, Zb predictions to ATLAS results; together with the plots in Figure IV.64 a comparison to the rescaled SHERPA 4F NLO predictions in Figure IV.60 can be made.

contribution from $qb \rightarrow Wbq'$ can be sizeable in the 5F scheme, while in the 4F scheme it appears at tree level only in the NLO corrections to $qq' \rightarrow Wb\bar{b}$. Nevertheless it is quite surprising that the 5F predictions at LO are in better agreement with the data with respect to 4F at NLO. As pointed out in the introduction, this might arise from the presence of large logarithms in the initial state, which can be properly resummed in the b -quark PDF.

Turning to less inclusive distributions, the ATLAS analysis presented above also contains measurements for the transverse momentum spectrum of the b -tagged jet in the “1 jet” and “2 jet” samples. A comparison of the data with the POWHEG BOX and HERWIG7 predictions for these observables is shown in the plots of Figure IV.71. Similarly to the inclusive case, also for these distribution the different theoretical predictions are in very good agreement among each other, but roughly a factor of two smaller than the measurements. It is likely that also in this case, only part of the difference can be explained with missing DPI corrections (not given in the paper for these differential distributions). It is interesting to note that, as for the $Zb(b)$, the results are off by a constant factor, i.e. the shape is correct and only the normalization seems

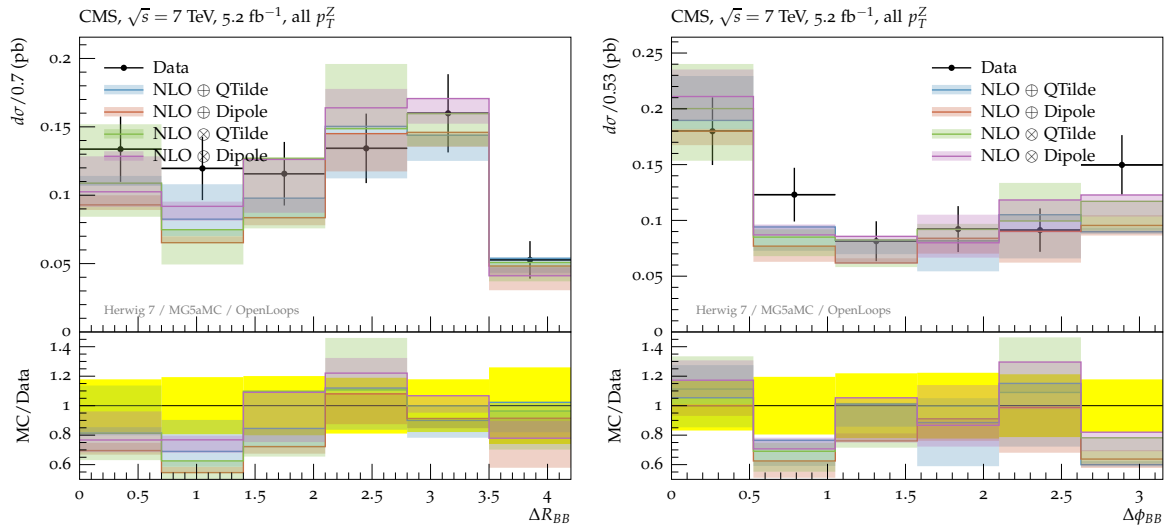


Fig. IV.66: A selection of the plots comparing HERWIG7 5F, Zb predictions to CMS results.

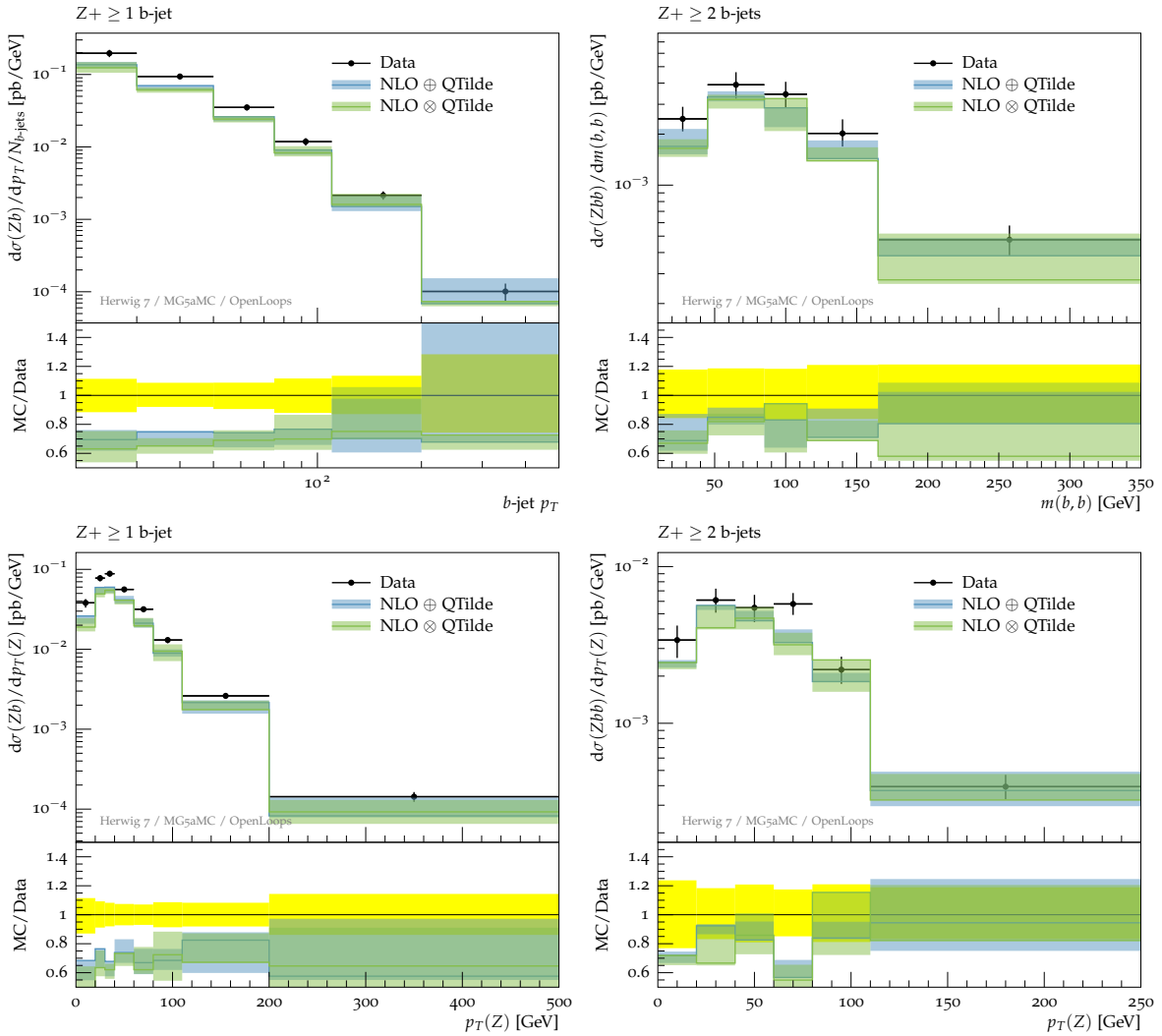


Fig. IV.67: A selection of the plots comparing HERWIG7 4F, Zbb predictions to ATLAS results.

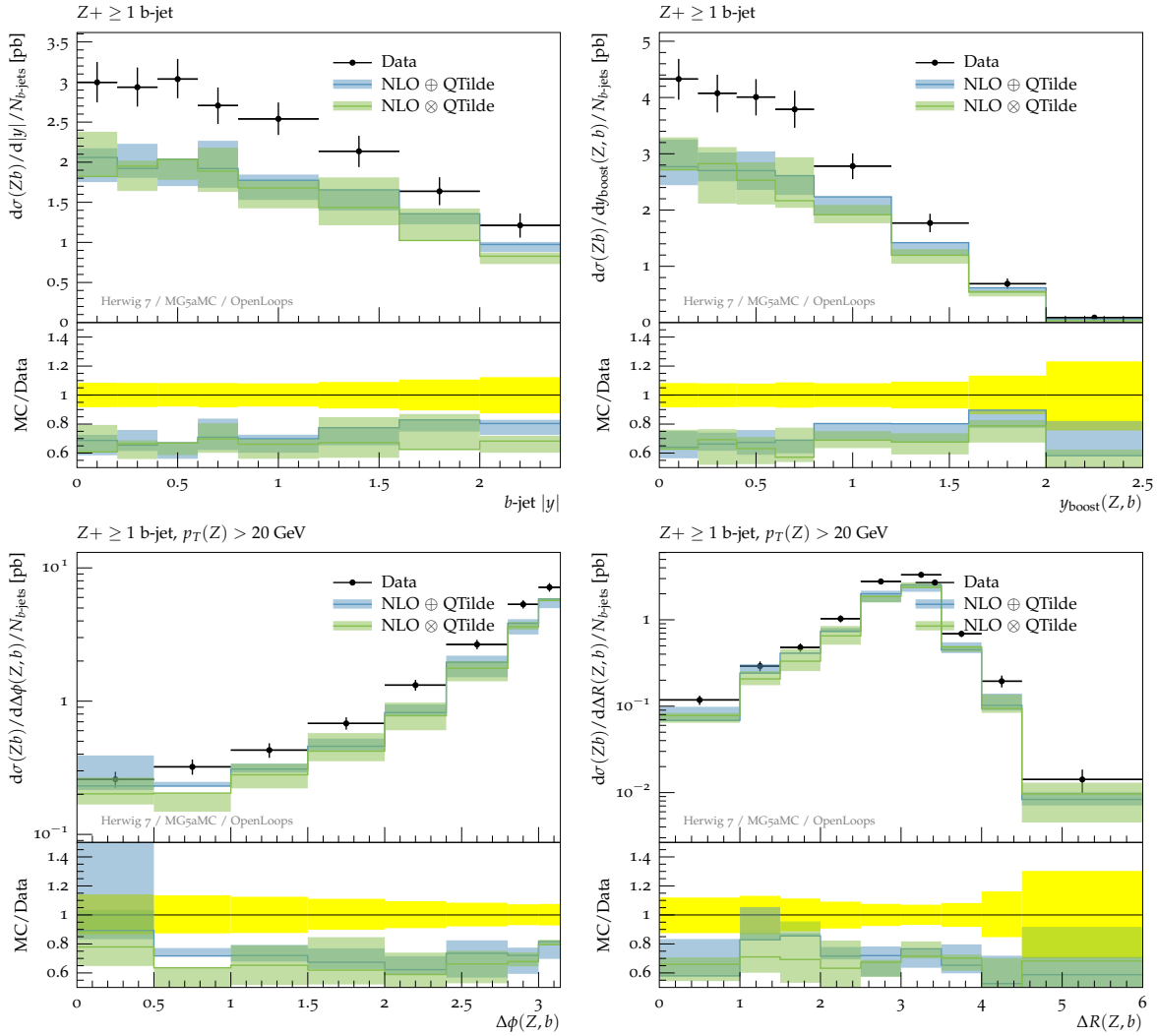


Fig. IV.68: A selection of the plots comparing HERWIG7 4F, Zbb predictions to ATLAS results; together with the plots in Figure IV.67 a comparison to the rescaled SHERPA 4F NLO predictions in Figure IV.60 can be made.

to be wrong.

The b-jet p_T spectrum predicted by the 5F LO calculation is in very good agreement with data in the “2 jet” case, but it is steeply falling in the “1 jet” sample, substantially overshooting the data for low p_T values.

6.6 Conclusions

We presented a comparison of generators predictions using 4F and 5F scheme to most recent measurements of vector boson production in association with b-jets at the LHC. In the 4F scheme a good agreement is found among the different generators at NLO accuracy, and among different matrix-element to parton-shower matching algorithms. The agreement with data however is good only when two b-jets are tagged in the final state or, when one b-jet only is required, if a rescaling to the 5F integrated cross-section is applied. For Wbb , even taking into account the contribution from MPI, predictions seem to significantly undershoot the data. The $Zb(b)$ production has been compared with predictions obtained in the 5F scheme with different setups,

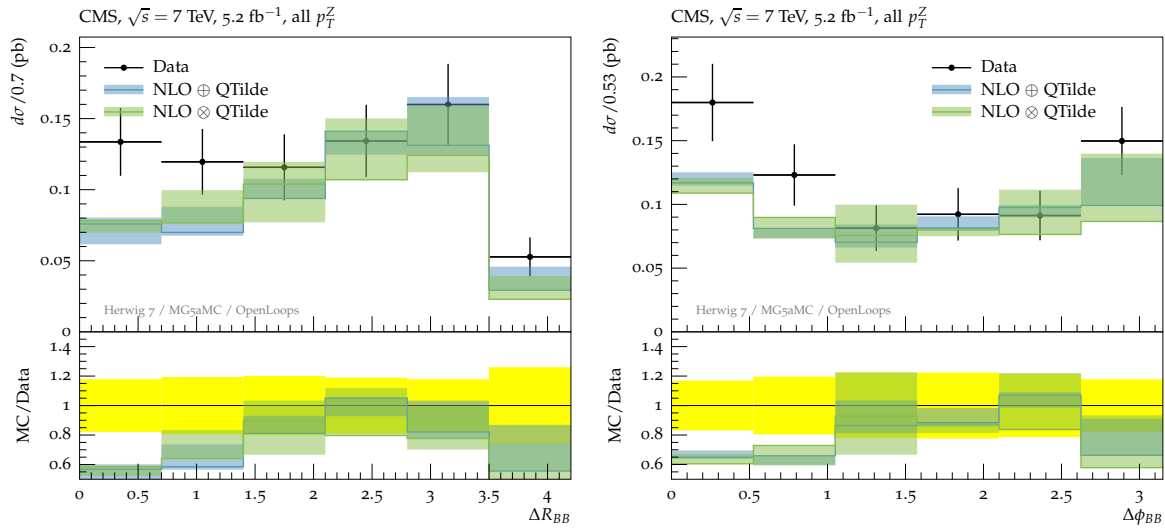


Fig. IV.69: A selection of the plots comparing HERWIG7 4F, Z_{bb} predictions to CMS results.

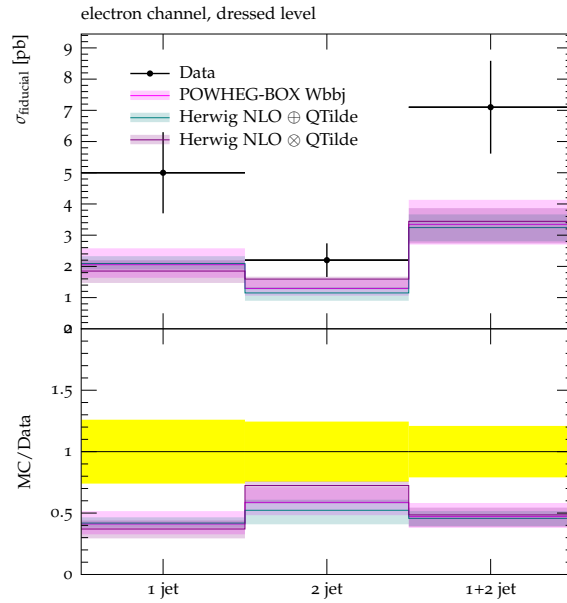


Fig. IV.70: ATLAS measured cross sections for Wb production with only a b-tagged jet (“1 jet”), one b-tagged and at least an additional jet (“2 jet”), or both (“1+2 jet”). The theoretical results are at the full shower+hadron level. No DPI corrections are included.

i.e. explicitly requiring one or two b-jets in the final state or a b-quark in the incoming proton when calculating the matrix element; or with no requirements on b-jets (treating them as light quarks) and combining final states with additional jets with a merging technique at LO and, where possible, also at NLO. Pro and cons of the different approaches are more difficult to pin down. In some case the scale uncertainty is quite large and not all distributions shows a nice agreement with data, especially if two b-tagged jets are present in the final state. For the Wb final state results have been also compared to a 5F calculation at LO: even if the precision is limited, because higher order corrections are missing, the cross section agrees better with data than for the 4F NLO calculation, as observed for the $Zb(b)$ process and as previous NLO studies

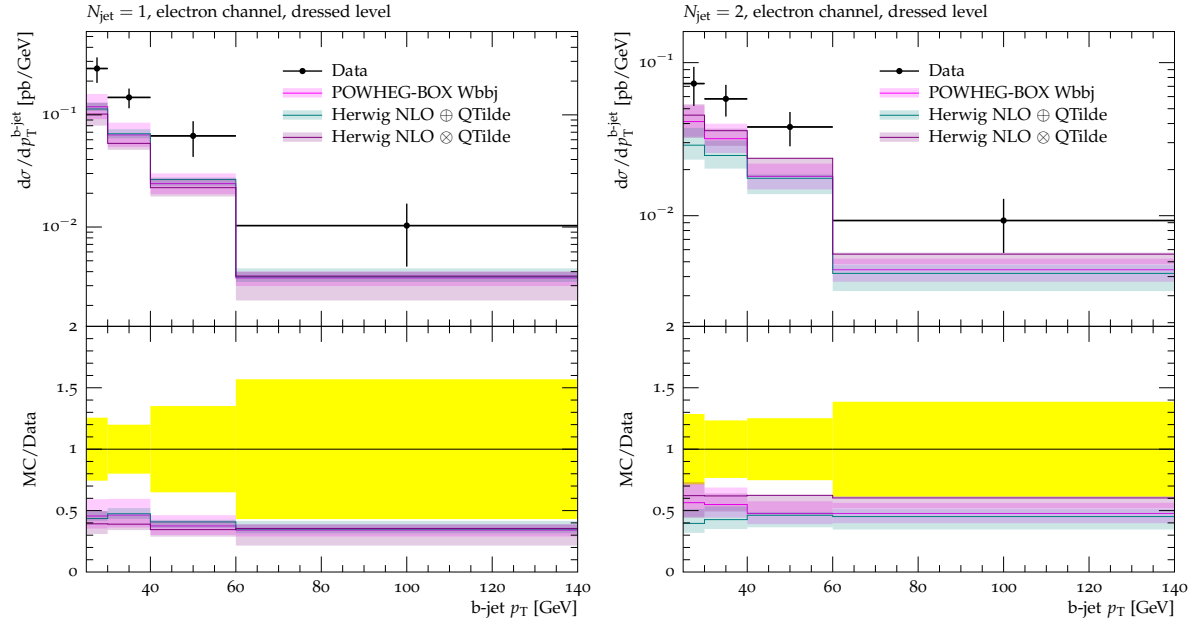


Fig. IV.71: ATLAS measured differential p_T distribution of the b -tagged jet in $W + b$ events with a single jet (left) or with at least one additional jet (right). The theoretical results are at the shower+hadron level. No DPI corrections are included.

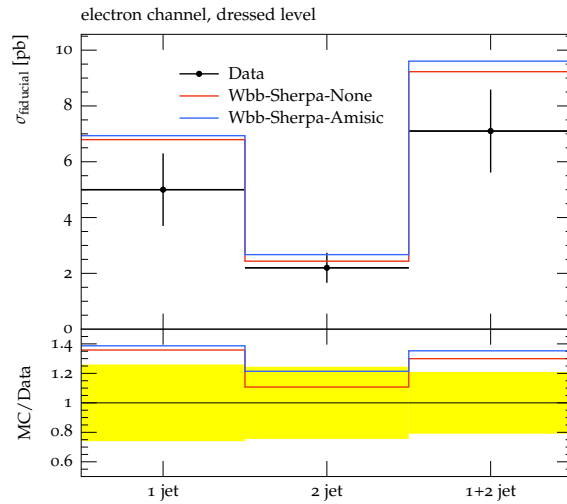


Fig. IV.72: ATLAS measured cross sections for Wb production with only a b -tagged jet (“1 jet”), one b -tagged and at least an additional jet (“2 jet”), or both (“1+2 jet”). Superimposed are shown the theoretical results obtained with SHERPA at LO in the 5F scheme, both with and without MPI.

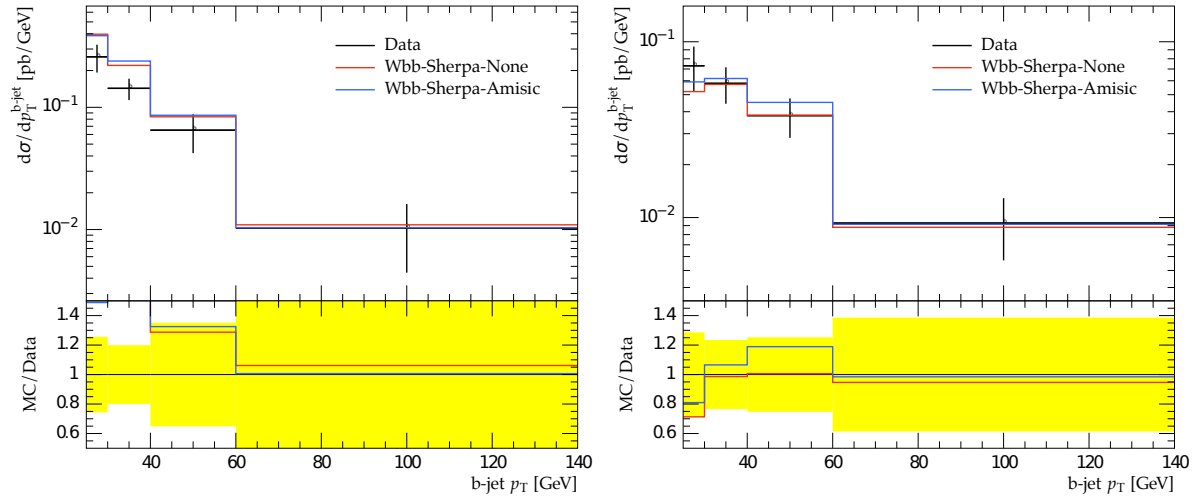


Fig. IV.73: ATLAS measured differential p_T distribution of the b -tagged jet in $W + b$ events with a single jet (left) or with at least one additional jet (right). Superimposed are shown the theoretical results obtained with SHERPA at LO in the 5F scheme, both with and without MPI.

at parton level suggested.

Overall these results show that the associated production of vector bosons and b -jets is still an important benchmark for perturbative QCD at hadron colliders. More measurements and additional theoretical studies are definitely needed.

Acknowledgements

S. Platzer acknowledges support by a FP7 Marie Curie Intra European Fellowship under Grant Agreement PIEF-GA-2013-628739. The work of C. Reuschle is supported in part by the U.S. Department of Energy under grant DE-FG02-13ER41942.

7 Irreducible backgrounds and measurement uncertainties ²⁹

7.1 Introduction

The general principle of minimising the model-dependence of results from particle colliders by making measurements of well-defined final states in fiducial regions is by now widely accepted, and implemented by the LHC collaborations. The fiducial regions are designed to reflect the acceptance of the detectors and data-selection. The final states are defined in terms of stable, or quasi-stable, particles. Increasingly impressive theoretical calculations are able to implement the appropriate kinematic cuts, and modulo some uncertainty associated with soft physics (for example hadronisation), can predict precisely what is actually being measured, without the need for additional assumptions or extrapolations into unmeasured regions of phase space.

This represents great progress. One area, however, where the principle of defining a measurement in terms of the final state is not so widely implemented, is in the consideration of background processes and their subtraction. Often backgrounds are subtracted using a mixture of theoretical and data-driven techniques, even though in some cases the backgrounds are strictly speaking “irreducible”, in that they produce final states identical to the “signal” final state (even

²⁹ J. Butterworth, F. Krauss, V. Ciulli, P. Francavilla, V. Konstantinides, P. Lenzi, C. Pandini, L. Perrozzi, L. Russo, M. Schönherr, U. Utku, L. Viliani, B. Waugh

in a perfect detector) and thus should be added to the signal at the amplitude, rather than cross-section, level. These subtractions are also often carried out before, or intermingled with, the unfolding and correction for detector effects such as efficiency and resolution, and thus are impossible to revert or reproduce once applied.

In practice, the uncertainty introduced by such subtractions is often insignificant compared to other uncertainties in the measurements, for example because the kinematic overlap is in fact small and interference terms are negligible. Nevertheless, as precision of both experiment and theory increase, such considerations can become important in some processes. In this contribution we highlight some such cases in an attempt to raise awareness of the issues for future studies.

7.2 Single top and $W + b$ -jet production

An example of a final state in which two contributions are often treated as distinct processes is the measurement of a leptonically-decaying W boson (that is, charged lepton plus missing transverse energy) in association with a b -tagged hadronic jet. The publication of the ATLAS analysis of 7 TeV LHC collision data [493] contains a measurement of the fiducial $W + b$ -jet cross section, presented as a function of jet multiplicity and of the transverse momentum of the leading b -jet. The $W + b$ -jet cross-section, corrected for all known detector effects, is quoted in a limited kinematic range, using jets reconstructed with the anti- k_t clustering algorithm with transverse momentum above 25 GeV and absolute rapidity within 2.1. The measurement is presented before and after the subtraction of the single-top contribution to the identical final state. Both versions are available in HEPDATA [503] and Rivet [327]³⁰. The unsubtracted version is shown in Fig. IV.74, and the subtracted version in Fig. IV.75, in the case where the b -jet is the only jet in the fiducial region (1-jet bin) and when there is an additional jet (2-jet bin).

Several things may be noted:

- In neither case does the theory describe the data especially well. This is a challenging final state to predict and the theory is likely to be superseded by more sophisticated and accurate predictions in future (indeed, NLO implementations of this process in MC are already available, as discussed in Section IV.6 of these proceedings). This strongly mitigates against embedding in a dependency on the theory in the experimental analysis - as is the case if the background is subtracted at detector-level - and is a strong motivation for the unsubtracted version of the measurement.
- The contributions from diagrams with and without top are comparable (as can be noted from the cross section in the highest p_T bin).
- The data uncertainties on the unsubtracted version are smaller.

Integrated over p_T , the unsubtracted fiducial cross section is $9.6 \pm 0.2(stat) \pm 1.7(syst)$ pb, a relative systematic uncertainty of 18%. The corresponding subtracted measurement is $7.1 \pm 0.5(stat) \pm 1.4(syst)$ pb, a relative systematic uncertainty of 20% - a small but noticeable decrease in precision. Looking in more detail, the main contributions to the systematic errors are:

- Jet energy scale: 10-50%
- Modelling of initial and final state QCD radiation (Wb , single top, $t\bar{t}$): 2-30%

³⁰The Rivet analysis was modified to add the histograms for the unsubtracted data.

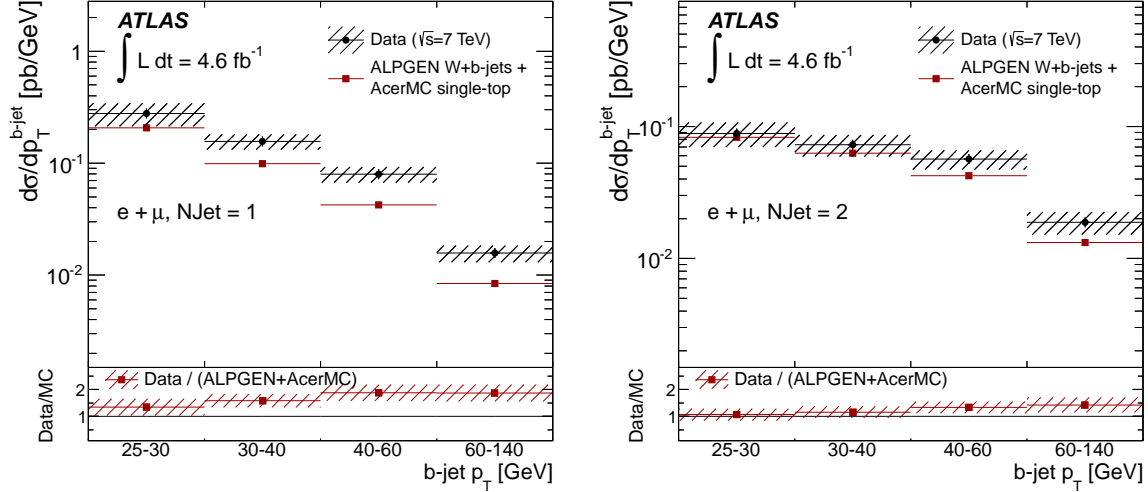


Fig. IV.74: Measured differential $W + b$ -jet cross-section before single-top subtraction as a function of the transverse momentum of the b -jet, in the 1-jet bin (left) and 2-jet bin (right). The measurements are compared to the sum of separate $W + b$ -jet and single-top predictions obtained using ALPGEN interfaced to HERWIG and JIMMY and scaled by a NNLO inclusive W normalization factor, and ACERMC interfaced to PYTHIA and scaled to a NLO single-top cross-section. The ratios between measured and predicted cross-sections are also shown. From [493].

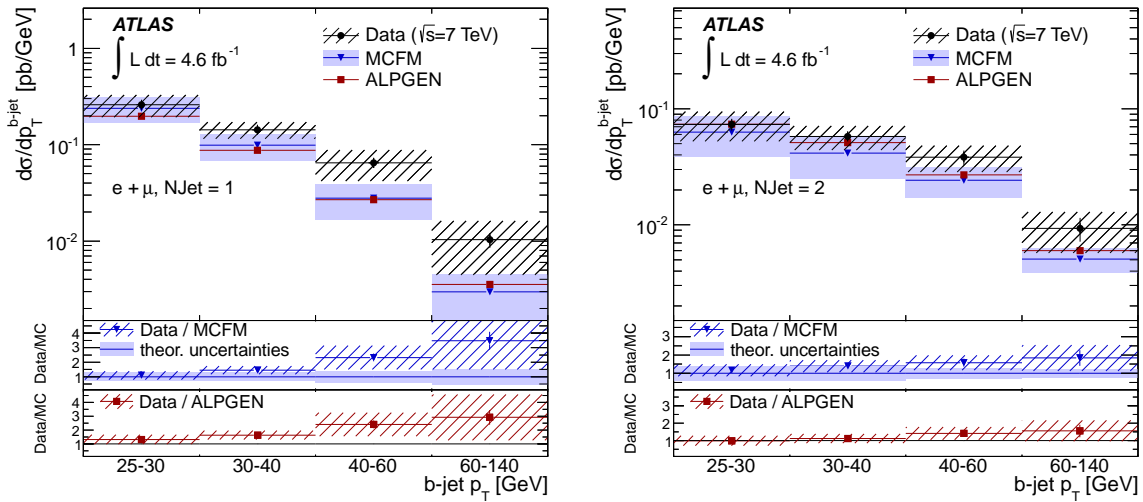


Fig. IV.75: Measured differential $W + b$ -jet cross-section after single-top subtraction as a function of the transverse momentum of the b -jet, in the 1-jet bin (left) and 2-jet bin (right). The measurements are compared to the a calculation of $W + b$ -jet production in the absence of top quark propagators obtained using ALPGEN interfaced to HERWIG and JIMMY and scaled by a NNLO inclusive W normalization factor, and ACERMC interfaced to PYTHIA and scaled to a NLO single-top cross-section. The ratios between measured and predicted cross-sections are also shown. From [493].

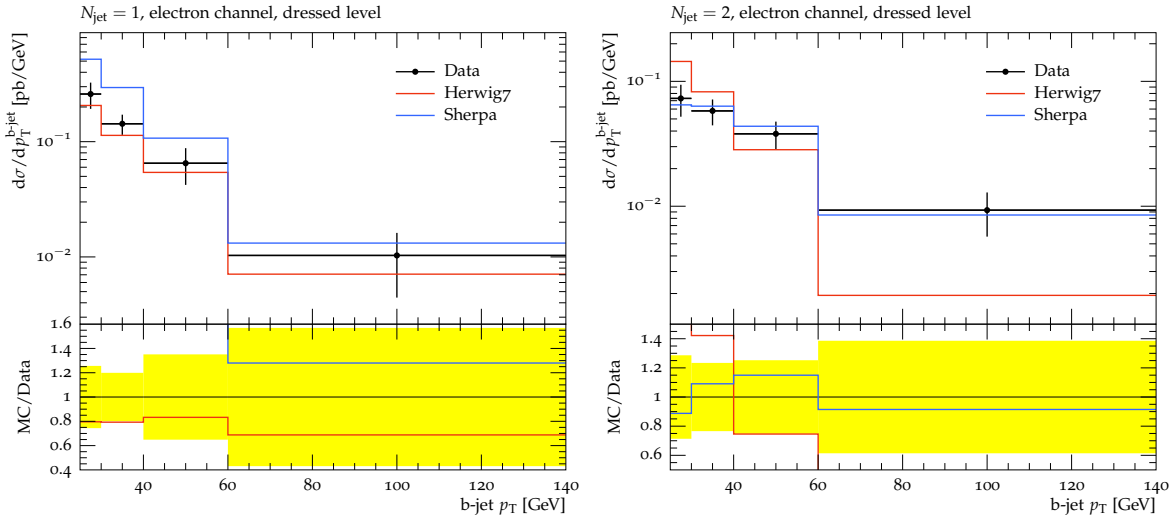


Fig. IV.76: Measured differential $W+b$ -jet cross-section after single-top subtraction as a function of the transverse momentum of the b -jet, in the 1-jet bin (left) and 2-jet bin (right). The measurements are compared to the expectations of Sherpa and Herwig, for Wb production processes excluding diagrams containing top quarks.

- b -tagging: 1-8%
- MC modelling of the Wb process: 2-8%

The fact that jet energy scale dominates masks, to a large extent, the effect of the modelling uncertainties introduced by the background subtraction. The uncertainty due to the modelling of QCD radiation varies strongly with jet p_T . This is exactly the kind of model dependence which one would expect to increase if a theory-based background subtraction is made, and indeed, in the highest p_T bin the systematic uncertainty goes from 16% before subtraction to 54% after it (compare Table 4 with Table 9 of Ref. [493]).

The comparisons were repeated using Sherpa 2.2 [275] and Herwig7 [382]. For Sherpa, all intermediate particles in the matrix element are kept on-shell and the AMEGIC ME generator is used for LO calculations [249]. Only decays of the W boson to the electron channel are allowed. Multi-parton interactions are switched off. The Sherpa default 5-flavour pdf library (NNPDF [184]) is used. In Wb production without tops, the b -quark is treated as massive with a mass of 4.75 GeV and the W boson is treated through the narrow width approximation. The order of the electroweak couplings is fixed to 2. For single top production, the b -quark is treated as massless in the matrix element calculation but retains its mass settings in the rest of the simulation. QCD and EW order couplings are not fixed. Production modes include all channels: s -channel, t -channel and tW single-top channels.

For Herwig, the built-in matrix elements for W +jet and single top were used. All leptonic decays were generated, but the electron only channel was selected in Rivet, with a normalisation factor of three applied post-hoc. Production includes s -channel, t -channel and tW single-top channels. The pdf MMHT2014 LO [183] is used.

The comparison of the non-top diagrams only to the subtracted data is shown in Fig IV.76. With these settings, Herwig agrees with the data normalisation both in the 1-jet and 2-jet bins. It correctly models the shape of the b -jet p_T in the 1-jet bin, but fails to describe it in the 2-jet bin. Sherpa models well the p_T dependence in both jet bins, but overestimates the normalisation of the 1-jet bin by nearly a factor of 2.

In Fig. IV.77 the unsubtracted measurement is shown, compared to Herwig and Sherpa.

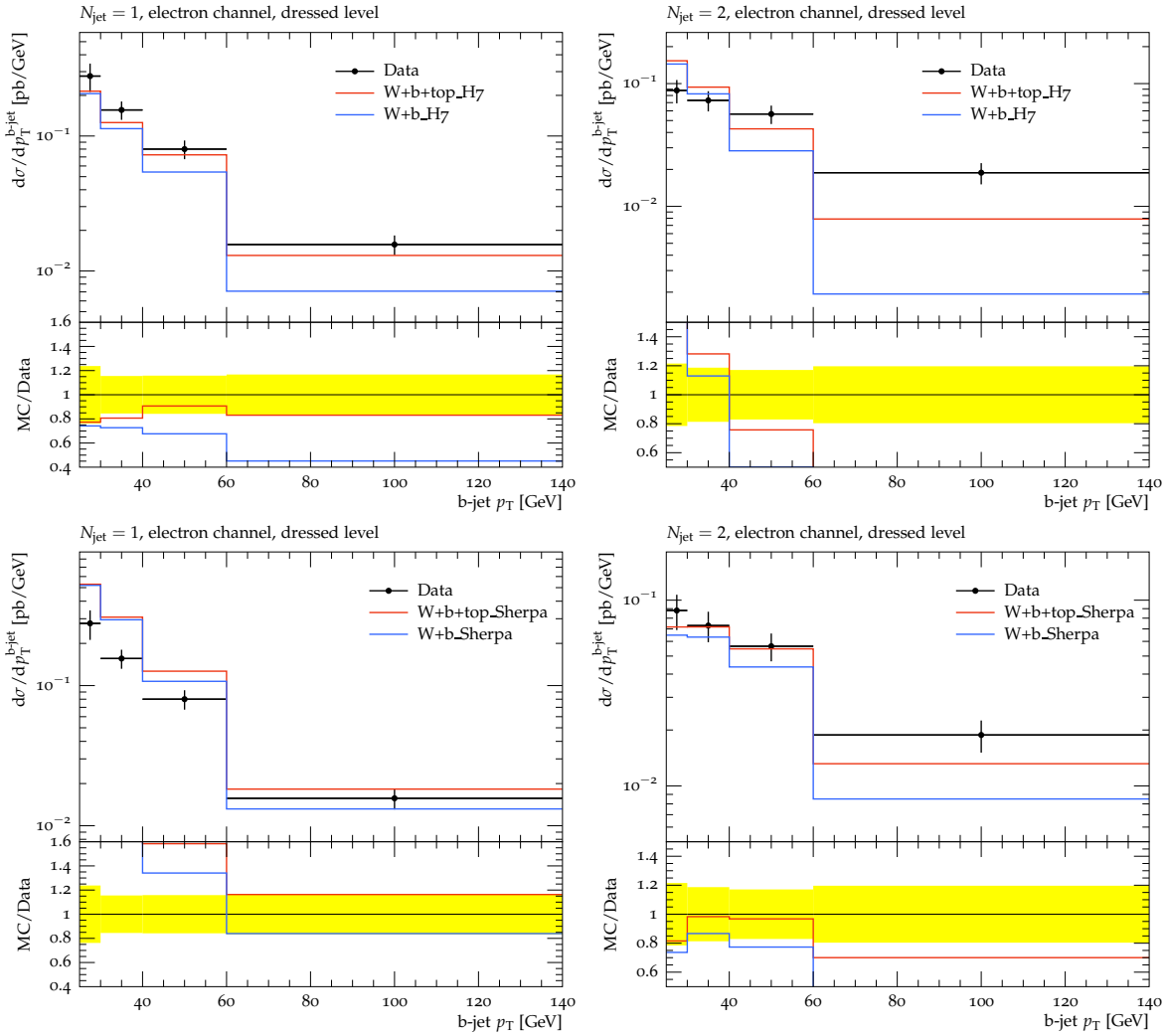


Fig. IV.77: Measured differential $W + b$ -jet cross-section, including single-top contributions, as a function of the transverse momentum of the b -jet, in the 1-jet bin (left) and 2-jet bin (right). The measurements are compared to the Sherpa (top) and Herwig (bottom) calculations of $W + b$ -jet production including resonant top contributions, but excluding finite width effects and interference terms between top and non-top diagrams. The contribution from non-top diagrams alone is also shown.

The predicted distributions from $W + b$ -jet diagrams are shown without and with top contribution (in the latter case the interference terms are neglected). Once more, Herwig agrees quite well with the data normalisation, and models well the b -jet p_T distribution in the 1-jet bin, while struggling with this dependence in the 2-jet bin. Also in this case Sherpa overestimates the normalisation of the 1-jet bin (this time by about 65%), but correctly models the normalisation of the 2-jet bin and the p_T dependence in both jet bins, within the data uncertainties.

In Fig. IV.78 we show the MC predictions for 13 TeV collisions. These measurements have yet to be performed, but the main point to be made here is that the total top contribution rises from 15% (32%) to 23% (42%) according to Sherpa (Herwig), with greater effects in some regions. This shows that any problems and uncertainties associated with the subtraction of irreducible backgrounds are likely to become more severe at higher energies. The differences between the generators themselves is another indication of the challenges associated with predicting these cross sections, and thus the need to minimise the theory dependence of the measurement.

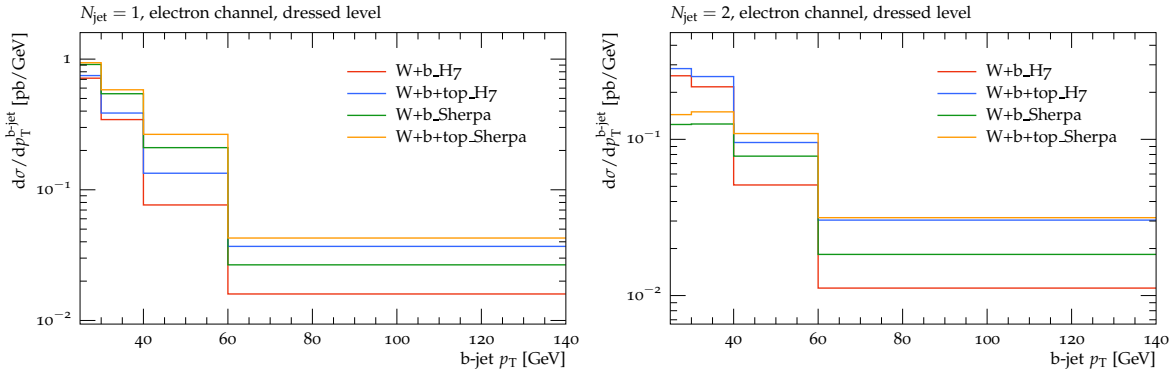


Fig. IV.78: Differential $W + b$ -jet cross-section at 13 TeV as a function of the transverse momentum of the b -jet, in the 1-jet bin (left) and 2-jet bin (right). In both Sherpa and Herwig calculations of $W + b$ -jet production including resonant top contributions, finite width effects and interference terms between top and non-top diagrams are not taken into account. The contributions from non-top diagrams alone are also shown.

7.3 Diboson plus jet production

Processes in which two W -bosons and two jets (including possibly b -jets) are produced are of great interest at the LHC. Contributing amplitudes include:

- $t\bar{t}$ (with on- or off-shell top quarks),
- genuine QCD processes with b quarks already entering from the initial state or being pair-produced in the final state through gluon splitting amplitudes,

and, to a lesser extent,

- electroweak processes such as vector-boson fusion diagrams including the Higgs boson as a propagator and b -associated Higgs boson production.

In Sherpa, the leading order processes for $t\bar{t}$ and tWb (both with on-shell tops), and $WWb\bar{b}$ (excluding all top contributions) were generated separately, and the full leading order $WWb\bar{b}$ process, including all top contributions was also generated for comparison. All processes were generated for centre-of-mass energies of 13 TeV.

An initial set of basic selection cut was applied, requiring two isolated leptons with $|\eta| < 2.5$, $p_T > 25$ GeV and missing $E_T > 25$ GeV, typical of an experimental analysis. The multiplicity of jets (identified with the anti- k_T algorithm, $R = 0.4$, $p_T > 25$ GeV, $|\eta| < 4.5$) in events passing these cuts is shown in Fig. IV.79. It can be seen that the diagrams involving at least one top quark dominate, though the contribution of non-top diagrams is significant at low jet multiplicities. Fig. IV.79 also compares the incoherent sum of the different contributions with the coherently generated $WWb\bar{b}$ process. It can be seen that the interference terms are largely positive.

Further cuts were applied to mimic a vector-boson-fusion like analysis, requiring that there are at least two jets in opposite hemispheres of rapidity, with a rapidity difference between them $\Delta y_{jj} > 2.4$ and a dijet invariant mass $m_{jj} > 500$ GeV, and after additional cuts on the transverse mass of the dilepton $m_{\ell\ell} > 20$ GeV and missing $E_T > 40$ GeV. Fig. IV.80 shows that the same general features persist, with the interference terms being large and positive for jet multiplicities below five.

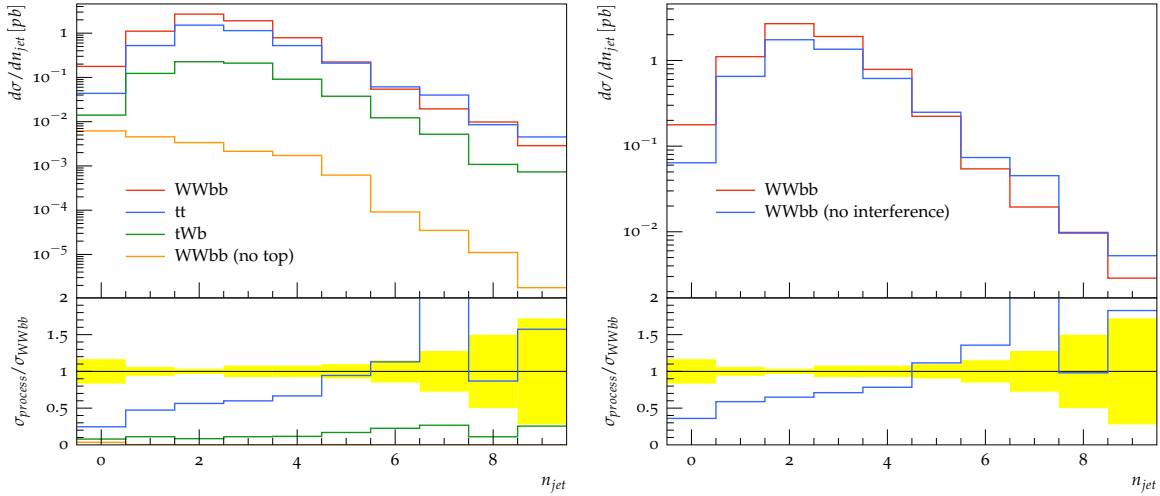


Fig. IV.79: Simulated $WWb\bar{b}$ events at 13 TeV using Sherpa. Individual contributions (left) and the comparison between incoherent and coherent sums (right) are shown.

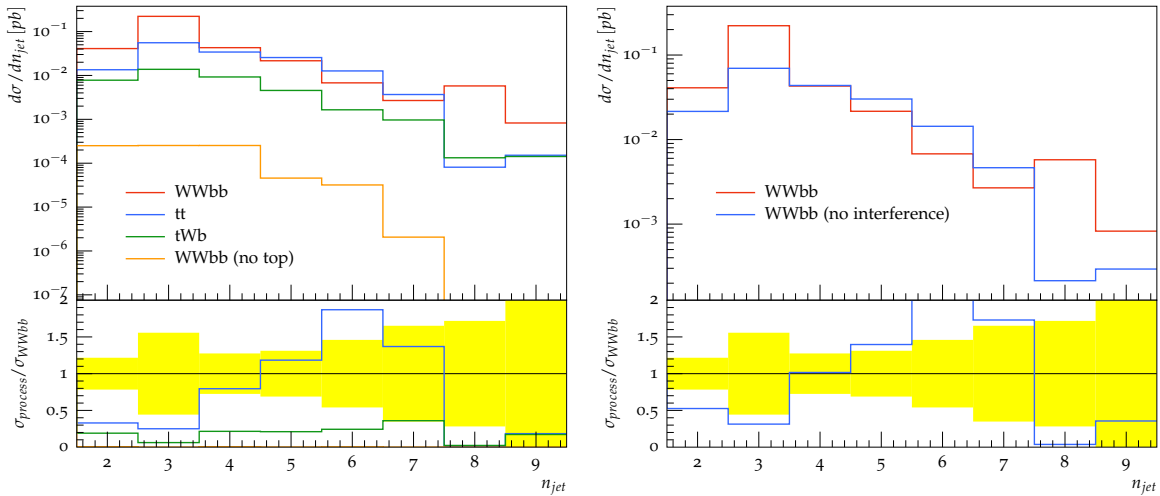


Fig. IV.80: Simulated $WWb\bar{b}$ events at 13 TeV using Sherpa, after vector-boson-fusion selection cuts. Individual contributions (left) and the comparison between incoherent and coherent sums (right) are shown.

7.4 Conclusions

This brief study exploits the Wb measurement made by ATLAS at 7 TeV, and the multi-process capabilities of Sherpa, to illustrate how distinct processes and their interference contribute to the same measurable $W + b$ -jet final state. The discussion draws the attention on the subtraction of irreducible backgrounds which, although commonly used, can increase the model-dependence of systematic uncertainties and lead to unphysical results, since the interference terms are not treated correctly. The ATLAS measurement shows increased systematic uncertainties in the region of high b -jet p_T when single top background contributions are subtracted. The simulation shows that the background will become more significant at 13 TeV, therefore expecting further increase of uncertainties. Furthermore, the studies performed with Sherpa indicate that, even after realistic selection of vector-boson-fusion-like topologies, interference terms are significant in $WWbb$ production. In conclusion, a careful treatment of the irreducible background in future

measurements at the LHC will become more and more relevant when presenting the results.

Acknowledgements

V. Ciulli and L. Russo acknowledge support by MIUR Italy under Grant Agreement 2012Z23ERZ of PRIN 2012.

Chapter V

MC uncertainties and output formats

1 Towards parton shower variations ¹

1.1 Introduction

Parton showers are the back-bone of Monte-Carlo event generation and particle level theory predictions for collider experiments for decades [504–513], their exclusive and fully-differential resummation being indispensable for the experimental collaborations. With the recent advances in high precision perturbative calculations finding their way into such particle level predictions through parton shower matchings [137, 154, 375, 489, 490, 514–516] the question regarding not only the well understood central value of the parton showers’ prediction but its uncertainties arises. However, such uncertainty estimates are not yet generally available and no systematic treatment on resummation properties is thus commonly evaluated for LHC physics predictions.²

In this contribution we will summarise the status and methods available in different parton shower programs. No attempt is made to harmonise the respective settings of each parton shower to produce comparable results. Due to the different evolution parameters and, thus, resummation variables, such a common parameter set would not produce an identical baseline. In the following we shortly describe the systematic variations available in each parton shower algorithm considered before discussing selected results on idealised observables in different kinematic regimes.

1.2 Tools

1.2.1 *Deductor*

Deductor [440, 519–521] is a dipole shower with virtuality based ordering. It uses a color approximation that goes beyond leading color (LC), namely the LC+ approximation. This includes some – but certainly not all – corrections to order $1/N_c^4$. For e^+e^- collisions at 500 GeV no substantial difference for the observables considered between LC and LC+ has been found. *Deductor* uses a two-loop running of α_s with $\alpha_s(M_Z) = 0.118$ and a parton shower cutoff of 1 GeV, and implements the CMW prescription [522] through a scaling of the argument of α_s .

1.2.2 *Herwig*

The *Herwig 7* event generator [382] is currently offering two shower modules: the traditional, angular ordered parton shower as set out in [496], as well as a dipole-type shower based on the work presented in [383, 384]. Though very different in their nature, both showers guarantee coherent evolution and reach a similar level of description of data when interfaced to the cluster hadronization model. The CMW prescription [522] is not implemented directly, but the relevant change in Λ is considered to be absorbed into using a tuned value of $\alpha_s(M_Z)$ throughout the simulation.

We do not include terms which modify the splitting kernels in the presence of variations of the argument of the strong coupling. For the parton level comparison at hand, which will have to be related to the cross-feed with non-perturbative models, we chose to use shower settings which put the *Herwig 7* showers onto a similar-as-possible level using the same two-loop running

¹ S. Höche, A. Jueid, G. Nail, S. Plätzer, M. Schönherr, A. Siódmok, P. Skands, D. Soper, K. Zapp

²With the notable exception of the *VINCIA* shower [517, 518].

of α_s , with $\alpha_s(M_Z) = 0.118$, a similar cutoff prescription and cutoff value ($p_{\perp, \min} = 1$ GeV) and not intrinsic p_{\perp} generated. The difference to the tuned settings may serve as a first indicator of the impact of non-perturbative corrections.

1.2.3 *Pythia*

The parton showers in *Pythia*-8 are based on the dipole type p_{\perp} -ordered evolution which has been available since *Pythia*-6.3 [523]. This is used for both ISR and FSR algorithms. Furthermore, *Pythia*-8 [367, 524] contains an implementation of $\gamma \rightarrow f\bar{f}$, $f = l, q$ splittings as a part of the parton-shower machinery, as well as weak gauge boson emissions [525] (The latter are however not included in this study.)

The evolution of parton showers is based on the DGLAP splitting kernels. For the case of one flavour, they are given by :

$$P_{q \rightarrow qg}(z) = C_F \frac{1+z^2}{1-z} \quad (\text{V.1})$$

$$P_{g \rightarrow gg}(z) = C_A \frac{(1-(1-z)z)^2}{z(1-z)} \quad (\text{V.2})$$

$$P_{g \rightarrow q\bar{q}} = T_R(z^2 + (1-z)^2) \quad (\text{V.3})$$

where z is the energy fraction and $C_F = 4/3$, $C_A = 3$ and $T_R = 1/2$ are the QCD factors. For QED radiation, there are only two splitting functions, $P_{f \rightarrow f\gamma}$ and $P_{\gamma \rightarrow f\bar{f}}$ which are given by :

$$P_{f \rightarrow f\gamma}(z) = Q_f^2 \frac{1+z^2}{1-z} \quad (\text{V.4})$$

$$P_{\gamma \rightarrow f\bar{f}} = Q_f^2 N_C (z^2 + (1-z)^2) \quad (\text{V.5})$$

Where Q_f is the electric charge of the fermion involved in the shower and $N_C = 3$ for quarks and $N_C = 1$ for leptons is the number of color degrees of freedom.

The ISR and FSR algorithms are cast as integro-differential equations whose solution is the probability of showering as one goes from one (shower-evolution) scale to a lower scale. The differential equations driving the shower evolution in *Pythia* are given by :

$$\frac{d\mathcal{P}_{\text{FSR}}}{dp_{\perp}^2} = \frac{1}{p_{\perp}^2} \int dz \frac{\alpha_s}{2\pi} P(z) \quad (\text{V.6})$$

$$\frac{d\mathcal{P}_{\text{ISR}}}{dp_{\perp}^2} = \frac{1}{p_{\perp}^2} \int dz \frac{\alpha_s}{2\pi} P(z) \frac{f(x/z, p_{\perp}^2)}{zf(x, p_{\perp}^2)} \quad (\text{V.7})$$

For ISR, $z = x/x'$ and $f(x/z, p_{\perp}^2)$ is the PDF of the new parent parton carrying a fraction x/z of the parent hadron at factorisation scale p_{\perp}^2 . The evolution variable p_{\perp} is defined in *Pythia* as:

$$p_{\perp, \text{evol}}^2 = p_{\perp}^2 = \begin{cases} (1-z)Q^2 & \text{for ISR} \\ z(1-z)Q^2 & \text{for FSR} \end{cases} \quad (\text{V.8})$$

where $Q^2 > 0$ is the virtuality of the branching parton.

The strength of the radiation is controlled by the effective value of the strong coupling constant $\alpha_s(M_Z)$. In *Pythia*, α_s can be set separately for ISR and FSR. The shower evolution scale ($p_{\perp, \text{evol}}$) is used as the default renormalization scale for the evaluation of α_s . Furthermore, in order to make uncertainty variations of the parton showers in *Pythia*, a multiplicative prefactor can be applied $\mu_R^2 = k_{\mu_R} p_{\perp, \text{evol}}^2$. The default value is $k_{\mu_R} = 1$.

We should note that in *Pythia*, the value of $\alpha_s(M_Z)$ is not comparable to the $\alpha_s^{\overline{\text{MS}}} = 0.118$ value. This is due to two reasons:

- In the limit of soft-gluon emission, the dominant splitting function term, can be absorbed into the LO splitting kernel by a translation to the Catani-Marchesini-Webber (CMW) scheme [522]:

$$\alpha_s^{\text{CMW}} = \alpha_s^{\overline{\text{MS}}} \left(1 + K \frac{\alpha_s}{2\pi} \right) \quad (\text{V.9})$$

$$\text{where } K = C_A \left(\frac{67}{18} - \frac{1}{6} \pi^2 \right) - \frac{5}{9} n_f$$

- The effective value of $\alpha_s(M_Z)$ tends to be a 10% larger when tuned to the experimental data, i.e. $\alpha_s(M_Z)^{\text{Pythia}} \sim 0.139$ which is chosen as the default value.

The translation from the $\overline{\text{MS}}$ to the CMW scheme is equivalent to a specific shift of the renormalization scale, $\mu_R \rightarrow \mu_R \exp(-K/4\pi\beta_0)$.

Finally, we note that corrections for parton masses are also available for ISR [523] and FSR [526].

1.2.4 Sherpa

The SHERPA Monte Carlo event generator [275] in its latest release, SHERPA-2.2.0, comprises two parton shower algorithms: CSSHOWER [373] and DIRE [443]. While the CSSHOWER is based on Catani-Seymour [90, 293] dipole splitting functions, DIRE combines the standard treatment of collinear configurations in parton showers with the resummation of soft logarithms in color dipole cascades. A third parton shower, ANTS [527], is under development. ANTS is based on dipole splitting functions in the spirit of [442, 528].

In general the splitting functions of all three algorithms take the form

$$D_{ijk}(t, z, \phi) = \frac{\alpha_s(k_{\text{tune}} b t)}{2\pi t} P_{ijk}(z) \quad (\text{V.10})$$

where $b = 1$ for DIRE. For CSSHOWER and ANTS, $b = k_{\text{CMW}}$, where

$$k_{\text{CMW}} = \exp \left[-\frac{67 - 3\pi^2 - \frac{1}{3} n_f(t)}{33 - 2n_f(t)} \right] \quad (\text{V.11})$$

is the Catani-Marchesini-Webber scale factor [522] to incorporate dominating higher-logarithmic contributions and $n_f(t)$ is the number of active flavours at scale t . The correction originating from k_{CMW} is included in DIRE by multiplying the soft enhanced term of the splitting functions with $1 + \alpha_s/(2\pi)\beta_0 k_{\text{CMW}}$. The k_{tune} are manually inserted scale factors to accommodate one more degree-of-freedom in a tuning context. However, in all current versions of the programs k_{tune} is fixed to 1 for final state splittings and $\frac{1}{2}$ for initial state splittings in the CSSHOWER, while ANTS and DIRE employ $k_{\text{tune}} = 1$ throughout. The $P_{ijk}(z)$ are the shower dependent splitting functions. Since PDF uncertainties are not addressed here, cf. Sec. V.2, ratios of PDFs are absorbed into the $P_{ijk}(z)$.

For the present study the showers run in their default setting. When now varying the argument of the strong coupling constant, i.e. replacing $t \rightarrow ct$ the higher-logarithmic structure induced by the running of the coupling constant in the presence of the CMW scale factor needs to be preserved in order not to upset the resummation quality of the parton shower. Thus, the following counter term is introduced

$$\alpha_s(k_{\text{tune}} k_{\text{CMW}} t) \rightarrow \alpha_s(k_{\text{tune}} k_{\text{CMW}} c \cdot t) \cdot f(c, t) \quad (\text{V.12})$$

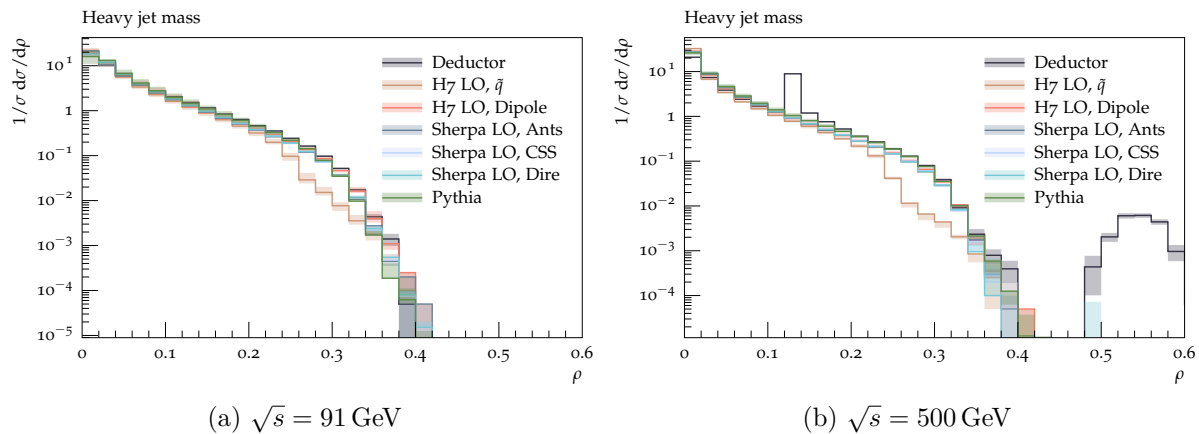


Fig. V.1: Comparison of Heavy Jet mass at two different energies.

where two forms for the counter term $f(c, t)$ are implemented,

$$f(c, t) = \begin{cases} 1 - \sum_{i=0}^{n_{\text{th}}+1} \frac{\alpha_s}{2\pi} \beta_0(n_f(t)) \log \frac{t_i}{t_{i-1}} & \text{additive threshold treatment} \\ \prod_{i=0}^{n_{\text{th}}+1} \left(1 - \frac{\alpha_s}{2\pi} \beta_0(n_f(t)) \log \frac{t_i}{t_{i-1}}\right) & \text{multiplicative threshold treatment.} \end{cases} \quad (\text{V.13})$$

Therein, the sum and product run over the number n_{th} of parton mass thresholds in the interval $[t, c \cdot t]$ with $t_0 = t$, $t_{n_{\text{th}}+1} = c \cdot t$ and t_i are the encompassed parton mass thresholds. If $c < 1$, then the ordering is reversed recovering the correct sign. $\beta(n_f)$ is the QCD beta function. Obviously, both forms coincide if the interval $[t, c \cdot t]$ contains zero or one parton mass thresholds. For this study the additive threshold treatment was used. We vary the renormalization scale by a factor two, i.e. $c = 4$ and $c = 1/4$ in Eq. (V.12).

1.3 Results

The events generated by the tools of Sec. 1.2 were analysed with RIVET [327] using three custom analyses. The analysis for e^+e^- , is closely derived from ALEPH_2004_S5765862 [444] which contains descriptions of the observables studied. The pp results were produced using analyses that closely follow content of MC_HINC/MC_HJETS. The jets definitions used in all of these analyses are implemented in FASTJET [458].

We investigate three separate processes at leading order with two different scenarios. In sections 1.3.1-1.3.3 we display a selection of plots for discussion. The content of the uncertainty bands for each generator are described in Sec. 1.2

1.3.1 $e^+e^- \rightarrow \text{jets}$

This process is a natural starting point to explore shower uncertainties as we only encounter final state radiation. For this process, the two scenarios correspond to CoM energies of $\sqrt{s} = 91 \text{ GeV}$ and $\sqrt{s} = 500 \text{ GeV}$. The jets are defined by the Durham jet algorithm with $y_{\text{cut}} = 0.7$. From the analysis we present a subset of the event shape observables and jet fractions. The results of both scenarios yielded similar conclusions and we will omit the 500 GeV results with one exception.

The predictions for the heavy jet mass, Fig. V.1, show consistency over the majority of the distribution as well as consistent predictions for the size of the uncertainty bands. The Deductor curve for ρ at 500 GeV has two features of interest; these stem from the $t\bar{t}$ contribution without the top decay. The new features emerge from the heavy jet containing 1 or 2 of the un-decayed top quarks.

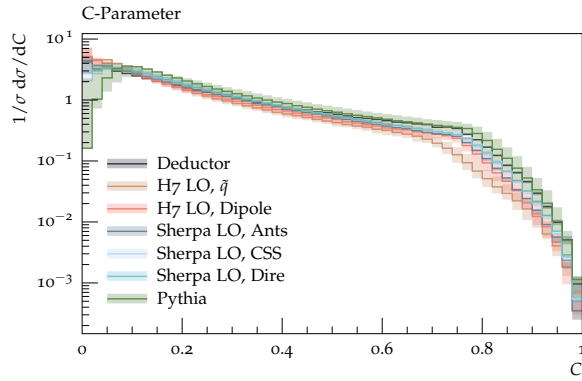


Fig. V.2: C-parameter at $\sqrt{s} = 91$ GeV.

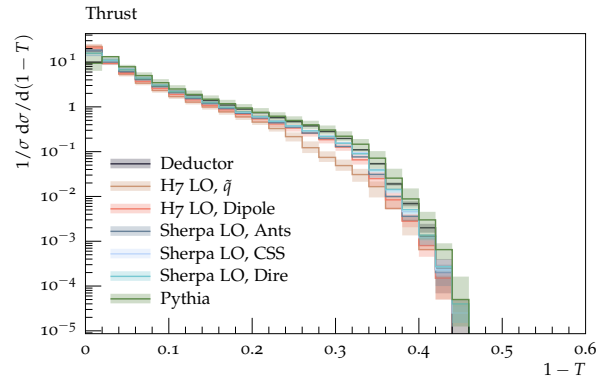
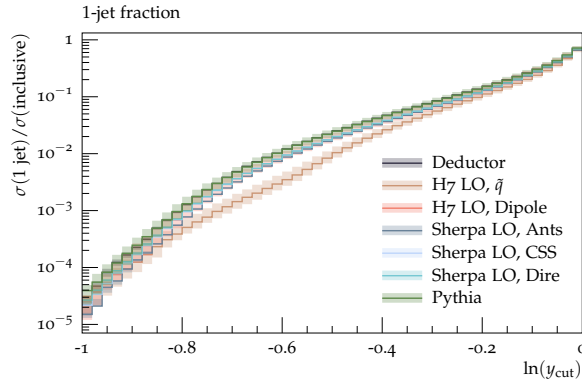
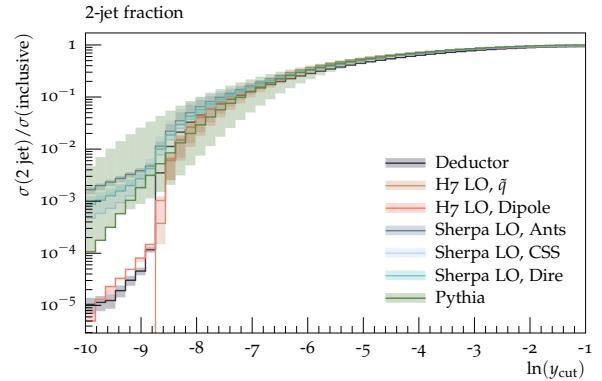


Fig. V.3: Thrust at $\sqrt{s} = 91$ GeV.



(a) 1-jet fraction



(b) 2-jet fraction

Fig. V.4: Jet fractions at $\sqrt{s} = 91$ GeV.

The Herwig QTilde Shower “dead-zone” can be seen in Fig. V.1-V.3 and Fig. V.4a. The C-parameter, Fig. V.2, has reasonable agreement over the majority of the distribution but differences are evident in its behaviour near $C = 0$, and in the region $C > 3/4$. As the region $C > 3/4$ is driven by non-planar events, which contain multiple emissions, it is sensitive to the shower implementation and differences should be expected. This same is true for Thrust, Fig. V.3, which again shows good agreement over the majority of the distribution, and differences that do emerge are in regions that are sensitive to multiple emissions, or as we approach the dijet configuration. Aside from Herwig QTilde Shower, the results for the 1-jet fraction are in good agreement within uncertainty bands. For the 2-jet fraction we see the differences that come from the implementation of the shower cutoff. There is also a large disagreement on the size of the uncertainty bands reported; here the choice of evolution variable can cause the shower to probe much smaller values of p_{\perp} . In this region we should expect some interplay with hadronization and, though beyond the aim of this study, this merits further investigation.

1.3.2 $pp \rightarrow h$

Higgs production (via HEFT) presents two new aspects: initial-state radiation, and the gluon PDF. The simulations take place at $\sqrt{s} = 13$ TeV, and the analysis considers anti- k_T jets with $p_{\perp} \geq 40$ GeV. We explore two scenarios $m_H = 125$ GeV and $m_H = 500$ GeV to quantify the impact of the hard scale. However, we neglect to show the heavy Higgs results, as they offer no new insight.

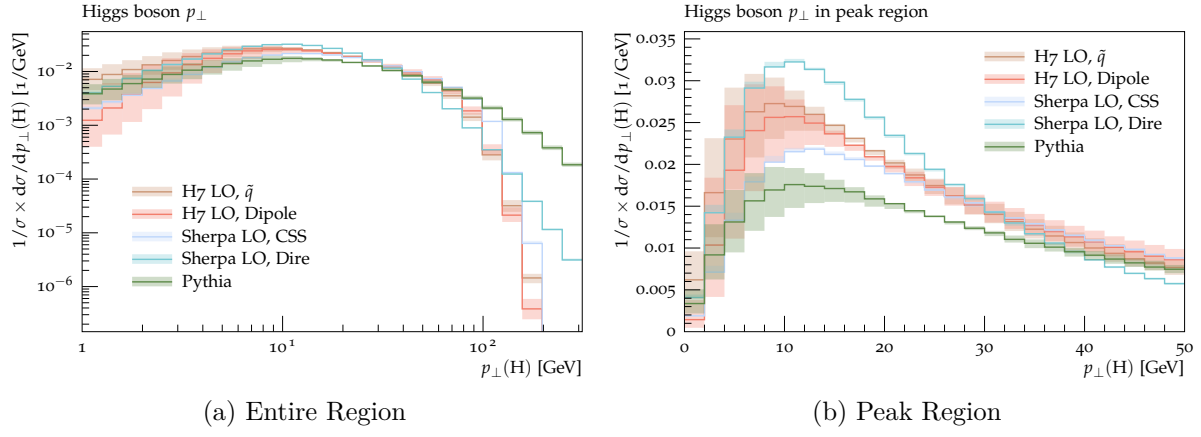


Fig. V.5: Generator comparison of the H p_{\perp} showing the overall behaviour V.5a as well as the behaviour in the peak region V.5b

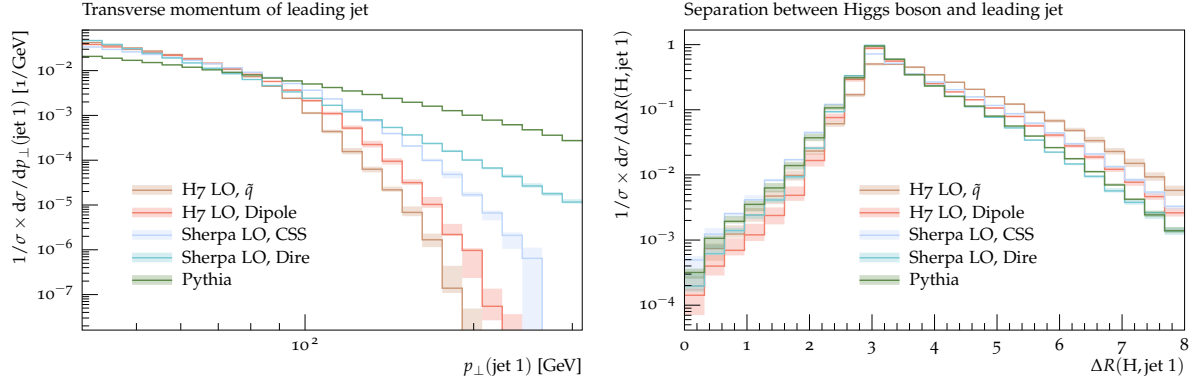


Fig. V.6: p_{\perp} of the leading jet

Fig. V.7: Comparison for the lego-plot distance between the Higgs and the leading jet

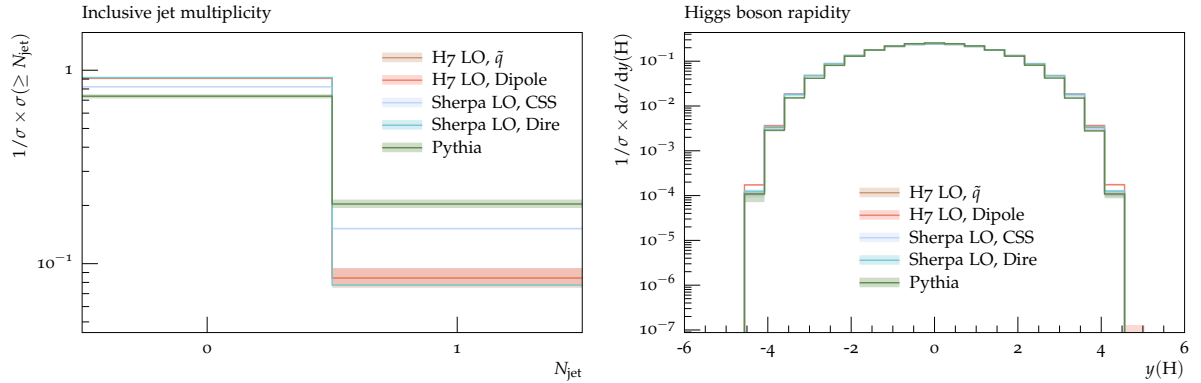


Fig. V.8: Comparison for inclusive jet multiplicity

Fig. V.9: Higgs rapidity

The p_{\perp} distributions for the Higgs, Fig. V.5, have good agreement at low p_{\perp} and expectedly disagree at high p_{\perp} , where the differences are not reflected in the uncertainty bands. In the peak region further differences are also apparent, and can be attributed to different shower implementations: evolution variable, α_s and intrinsic k_T , and recoil. The high p_{\perp} behaviour

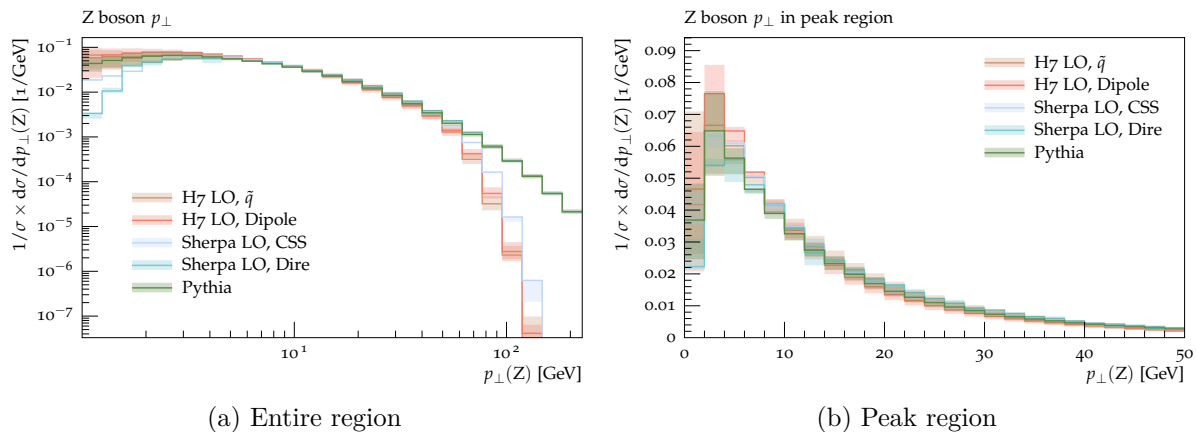


Fig. V.10: Generator comparison of the $Z p_{\perp}$ showing the overall behaviour V.10a as well as the behaviour in the peak region V.10b.

of Herwig and SHERPA CSSHOWER are closer to the scale m_H , while Pythia and SHERPA DIRE extend further and probe the phase space of a power-shower setup. The agreement displayed between the different Herwig showers is expected from the setup, nevertheless it is a satisfying result given their different implementations. The leading jet p_{\perp} , Fig. V.6, is consistent at low p_{\perp} with the exception of Pythia, which has a notably harder distribution. Though the high p_{\perp} predictions are markedly different, Herwig and SHERPA CSSHOWER do again show the same suppression near the scale m_H ; the harder jets produced by a power-shower can clearly be seen here. The lego-distance, Fig. V.7, has two notable regions $\Delta R \geq \pi$ and $\Delta R < \pi$. For the first region, we see that the generators give differing predictions with small uncertainty bands, this region is typically driven by few hard-emissions. The second region, driven by multiple emissions, displays better agreement and, expectedly, has larger uncertainty bands. The inclusive jet multiplicity shows some agreement between generators, but notably SHERPA CSSHOWER and Pythia produce a smaller fraction of 0-jet events. Finally, we show the resilience of an inclusive observable to the shower, and its uncertainties. This can be seen in the Higgs rapidity, Fig. V.9.

1.3.3 $pp \rightarrow Z$

To complement the previous process a quark-initiated setup is presented, again using two different hard scales of 91 GeV and 500 GeV. The analysis and findings of this section are similar to that of Sec. 1.3.2. The predictions for the inclusive jet multiplicity, Fig. V.13, are much less consistent Fig. V.8.

1.4 Conclusions

Clearly there is a need to find a robust prescription to produce variations that we can definitively call ‘shower-uncertainties’. Such a prescription should not only be theoretically grounded, but also practical in its use. This will require further studies with more detailed appraisals of the different shower components and their interplay with rest of the event generation machinery. All of the multi-purpose event generators are able to assign uncertainties to their prescription and so will enable more detailed studies in the future.

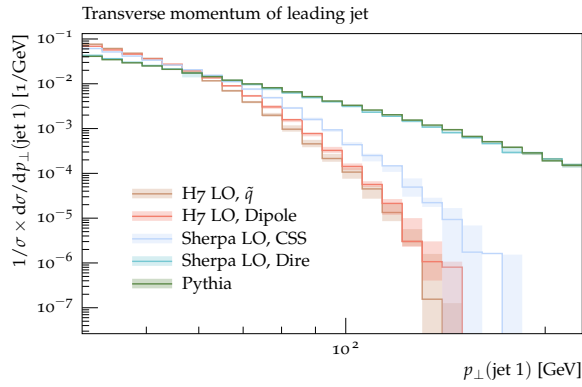


Fig. V.11: p_{\perp} of the leading jet

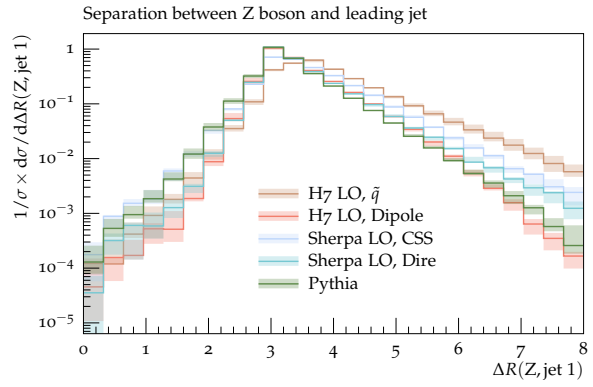


Fig. V.12: Lego-plot distance between the Z and the leading jet

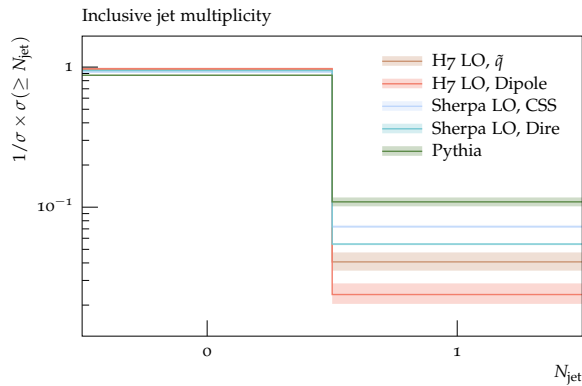


Fig. V.13: Inclusive jet multiplicity

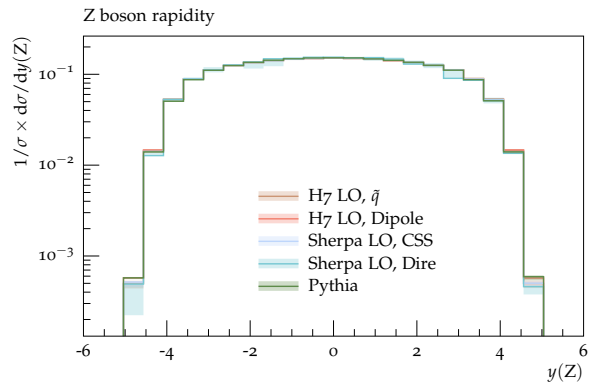


Fig. V.14: Z rapidity

Acknowledgments

We thank the organisers. The work of DS is been supported by the U.S. Department of Energy under Grant DE-SC0011640. SP acknowledges support by a FP7 Marie Curie Intra European Fellowship under Grant Agreement PIEF-GA-2013-628739. MS acknowledges support by the Swiss National Science Foundation (SNF) under contract PP00P2-128552. The work of SH was supported by the U.S. Department of Energy under contract DE-AC02-76SF00515.

2 Reweighting the SHERPA parton shower ³

2.1 Introduction

The last ten years of improving Monte-Carlo event generators (MCEG) enabled quantitative predictions at an unprecedented accuracy. These developments led to a considerable growth in computational cost per event. This can become limiting, as calculations must often be performed repeatedly, e.g. to assess theory uncertainties. For QCD calculations such re-calculations are necessary for each combination of QCD input parameters. Those include parton density functions (PDF), the strong coupling (α_s) or the renormalisation/factorisation scale. This adds up to $\mathcal{O}(10^3)$ re-calculations quickly. For PDF fits, the demand for re-calculations is even higher.

This issue is addressed by *not doing the whole calculation again*. Instead, parameter-independent bits of the calculation are stored as weights and can then be recombined with different parameter values. This can either be done directly for each event, or after projecting

³ E. Bothmann, M. Schönherr, S. Schumann

weights to interpolation grids first, with one grid per observable bin and dependence structure [3, 4]. PDF fitters use such interpolation grids for cross section predictions, as the time needed for a recombination is of the order of milliseconds only.

For leading-order (LO) events, getting the *parameter-independent weight* is easy: divide the event weight by the PDFs $f_a f_b$ of the incoming partons and by α_S^p , with p being the perturbative order of the process. Then multiply with $f'_a f'_b \alpha_S'^p$ to get the new event weights for a different set of input PDFs f' and a different value of the strong coupling α_S' . For the proper evaluation of these *variational weights* the partonic momentum fractions x_1 and x_2 as well as the factorisation and renormalisation scale need to be book-kept. At next-to-leading order (NLO) the procedure is more complicated, because of the additional scale-dependence of the virtual corrections and the different kinematics and initial states of the subtraction parts [344].

The newly added internal reweighting of SHERPA [275] as of version 2.2.0 performs *on-the-fly* during event generation [529]. The result for each combination is inserted into the `HepMC::WeightContainer` object and thus can be either saved to disk, programmatically accessed or directly passed via the internal interface to the Rivet analysis framework [327]. The supported event generation modes are (N)LO, (N)LO+PS (i.e. matched to a parton shower) and MEPS@LO (i.e. merged LO matrix elements with a shower). The recently introduced interfaces `MCgrid` [530] and `aMCfast` [201] on the other hand allow for the automated creation of interpolation grids using general MCEGs. (N)LO and (N)LO+PS are supported.

For both reweighting approaches, event generations involving a parton shower come with a caveat: The shower takes no part in the reweighting procedure, and is kept as-is. Its dependences on PDF, scale and α_S are thus not taken into account. Therefore the reweighting leads to an *inconsistent result*, where dependences in the hard process have been updated, but not in the shower. There are indications that this does not affect major parts of phase space [531, 532]. A more thorough study is however still missing. We address this by presenting ongoing work to extend the internal SHERPA reweighting to include all dependences of the parton shower emissions, using a property of the veto algorithm that allows for a simple multiplicative reweighting.

2.2 Reweighting the veto algorithm

The default shower of SHERPA, CSSHOWER [373], uses the veto algorithm to numerically integrate the Sudakov form factors

$$\Delta(t_0, t_c) = e^{-\int_{t_c}^{t_0} \Gamma(t) dt}, \quad (\text{V.14})$$

which give the no-branching probabilities between the starting scale t_0 and the cut-off scale t_c . In the veto algorithm the splitting kernels Γ are replaced with integrable overestimates $\hat{\Gamma}$. This is balanced by only accepting a proposed emission with the probability $P_{\text{acc}} = \Gamma/\hat{\Gamma}$. A multiplicative factor in Γ is therefore equivalent to a multiplicative factor in P_{acc} [374]. This observation is for example used to apply matrix element corrections [375], where the splitting kernels are replaced with a real-emission-like kernel R/B . This is done a-posteriori, i.e. the event weight is multiplied by $(R/B)/\Gamma$. The emission itself is unchanged. The same method is also used in the Vincia parton shower to calculate uncertainty variations for different scales, finite terms of the antenna functions, ordering parameters and sub-leading colour corrections [518].

The emission kernels Γ depend linearly on α_S and on a ratio of PDF values $f_a(x/z)/f_b(x)$ ⁴. A change of PDFs $f \rightarrow f'$ and the strong coupling $\alpha_S \rightarrow \alpha_S'$ is equivalent to modifying the

⁴The exact definition of the flavours a, b and the momentum fractions $x, x/z$ depend on the dipole configuration of the emission. There is no PDF dependence in the case of dipoles that consist only of final-state partons.

emission probability accordingly⁵:

$$P_{\text{acc}} \rightarrow q P_{\text{acc}}, \quad q \equiv \frac{\alpha'_S}{\alpha_S} \cdot \frac{f'_a(x/z)/f'_b(x)}{f_a(x/z)/f_b(x)}, \quad (\text{V.15})$$

i.e. we need to multiply the event weight for each accepted emission by the corresponding q in order to reweight the event with a new choice of PDFs. For the rejected emissions we obtain

$$P_{\text{rej}} = 1 - P_{\text{acc}} \rightarrow 1 - q P_{\text{acc}} = \left[1 + (1 - q) \frac{P_{\text{acc}}}{1 - P_{\text{acc}}} \right] P_{\text{rej}}, \quad (\text{V.16})$$

so for each of those we need to multiply the event weight with the expression in square brackets.

Our current implementation supports PDF and α_S reweighting of parton shower emissions for both LO+PS and NLO+PS events. One can choose a maximum number of reweighted emissions per event. This is useful because some observables are sensitive only to the first few emissions. The reduced amount of reweighting per event then allows for faster event generations.

2.3 Validation

We present a selection of plots to validate our implementation. All contain comparisons between “dedicated” and “reweighted” results. The “dedicated” results are produced through normal runs for the varied input parameters, whereas the “reweighted” ones are obtained by reweightings from a run with a central parameter choice. The reweighting is done for the matrix element exclusively (“ME”), including all parton shower emissions (“ME+PS”) or just the first emission (“ME+PS(1st em.)”).

In Fig. V.15, we present uncertainty bands for PDF and α_S variations. The left-hand plot features a CT14n1o [182] PDF error band for the W -boson transverse momentum distribution in W production at the LHC at NLO+PS. The band is a combination of the central member and 56 Hessian eigenvector members. So for the “dedicated” band, 57 independent event generation runs had to be performed, whereas each of the reweighting bands is generated by a single run.⁶

A few observations can be made for the W p_{\perp} plot: (i) For $p_{\perp} < 10$ GeV, solely reweighting the ME underestimates the error found with the dedicated calculation by about 4% in both directions. The ME+PS reweighting is able to reproduce the error. (ii) For p_{\perp} values between 20 GeV and the W mass, the ME reweighting *overestimates* the positive error slightly, by about 1%. Again, the ME+PS reweighting correctly reproduces the error. (iii) The reweighted bands are much smoother because the prediction for each PDF member shares the statistics of the central run. Unfortunately there is no way to guarantee this for the dedicated runs when varying input parameters of the parton shower, which makes closure tests between reweighting and dedicated runs a statistical exercise.

The right-hand plot in Fig. V.15 contains a band for an α_S variation for the thrust observable for $e^+e^- \rightarrow q\bar{q}$ at LEP at LO+PS. The variations considered around the central values of $\alpha_S(m_Z) = 0.120$ include $\alpha_S(m_Z) = 0.108$ and $\alpha_S(m_Z) = 0.128$. The running of α_S is evaluated at the one-loop order. The plot shows the envelope for the three values. The reweighted band is obtained by reweighting all emissions in the run with the central α_S value. It reproduces the dedicated band within statistical errors. For this we note that the variance of the reweighted

⁵Both α_S and f depend on the emission scale. Although the emission scales can not be reweighted themselves using the presented method, the functional form of these dependences can be changed.

⁶We are yet to do a detailed timing study (and to optimise the code), but for the case of doing 57 variations and reweighting the ME and up to one parton shower emission, the run took about a factor of 6 longer than a run without any reweighting. Comparing the time needed to generate the entire error band, the reweighting run thus needed one order of magnitude less than the combination of dedicated runs.

prediction increases. In some bins, the sum of squared weights is a factor of 100 higher compared to the dedicated result.

Jet resolutions are sensitive to the specifics of parton shower emissions, which is why we have in Fig. V.16 a series of closure tests for this observable for W -boson production at the LHC at LO+PS. The reweightings are done from the central CT14 to the central MMHT2014 set [183]. The maximum number of shower emissions being reweighted is varied between 0, 1 and ∞ . The corresponding reweighted predictions are compared to the dedicated MMHT2014 result. This is done for the $0 \rightarrow 1$ and for the $3 \rightarrow 4$ jet resolution. We observe deviations for the ME-only reweighting prediction of about $\pm 2\%$. The 1-emission-reweighting fixes the deviation for $d_{01} > 10$ GeV, but can not fix the deviations elsewhere. The all-emissions-reweighting is perfect within statistics for all bins of both jet resolutions.

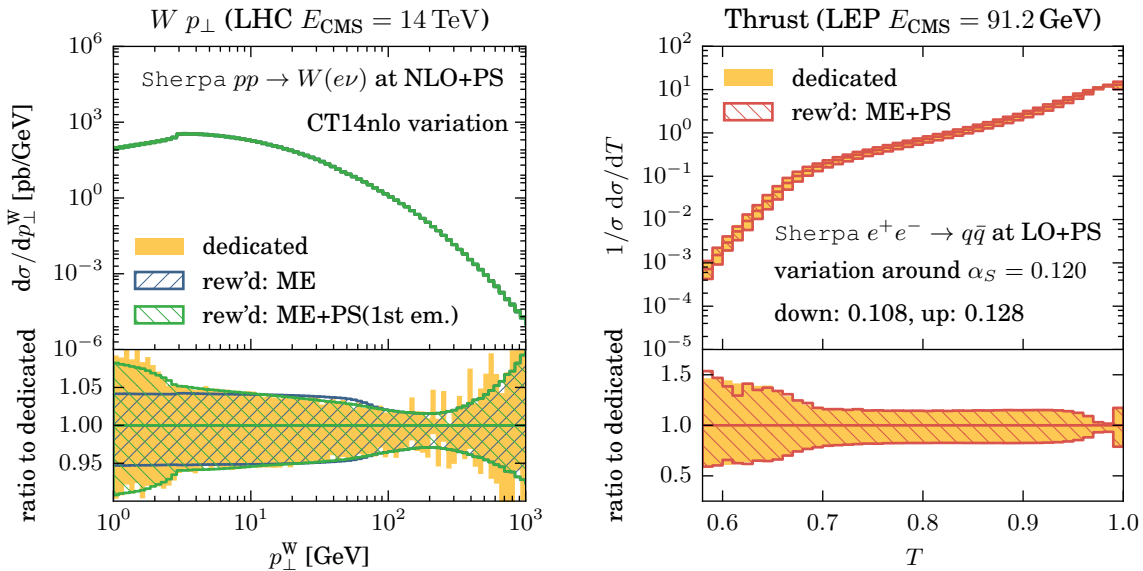


Fig. V.15: A PDF variation for the W -boson p_{\perp} distribution at the LHC at NLO+PS (left) and an α_S variation for the Thrust for $q\bar{q}$ production at LEP at LO+PS (right). Predictions generated by single reweighting runs (“rew’d”) are compared to predictions from dedicated runs.

2.4 Conclusions

We have presented the extension of the internal reweighting of SHERPA to include the α_S and PDF dependences of parton shower emissions. It has been shown that the ME-only reweighting has shortcomings compared to the newly implemented full reweighting. We did this by comparing theory uncertainty bands generated by reweighting runs with dedicated calculations for α_S and PDF variations at LO+PS and (N)LO+PS. Now with the support for these input parameters in place, the next step is to allow for varying the scales at which α_S and the PDFs are evaluated for a given emission. This is different from varying the actual emission scale (e.g. indirectly by choosing a new starting scale), which is not covered by the presented reweighting method.

The full direct reweighting for parton showers will leave us with a complete picture of how to reweight when all information is still available. This will help us when bringing parton shower reweighting also to grids, where individual event information is *not* available. For this we are considering an approximate approach. Such shower-aware grids would allow for including more data in PDF fits, namely data that is currently omitted because its theoretical prediction is sensitive to higher-order corrections.

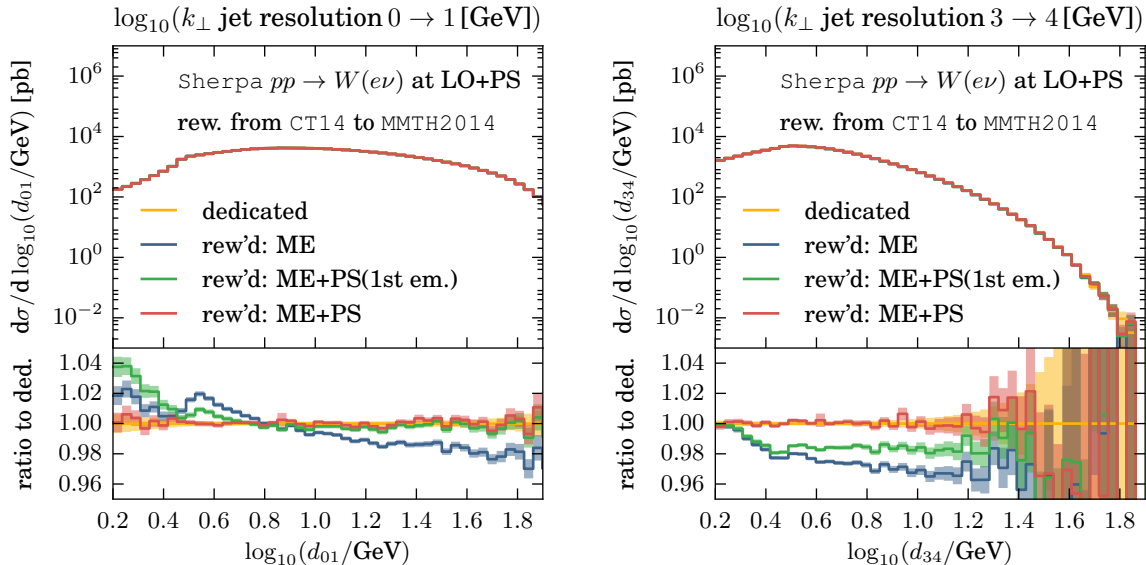


Fig. V.16: Predictions for jet resolutions for W -boson productions at the LHC at LO+PS. Results from reweighting runs CT14 \rightarrow MMHT2014 PDF are compared to the dedicated result for direct use of the MMHT2014 PDF.

Acknowledgements

We acknowledge financial support from BMBF under contract 05H15MGCAA, the Swiss National Foundation (SNF) under contract PP00P2-128552 and from the EU MCnetITN research network funded under Framework Programme 7 contract PITN-GA-2012-315877.

3 Ntuples for NNLO events produced by EERAD3 ⁷

We study the production of Ntuples based on the program EERAD3 which produces parton-level QCD events to calculate event shapes and jet rates in electron-positron annihilation through to order α_s^3 . The aim of this study is to assess the viability of Ntuples as a general way to have NNLO results stored and made available to the experimental community.

3.1 Introduction

High precision calculations will be vital in the next phase(s) of the LHC in order to be able profit from the high quality data being collected. In order to further explore the Higgs sector and distinguish BSM effects from higher order effects within the Standard model, next-to-next-to leading order (NNLO) predictions are necessary for a number of processes. However, such predictions are the results of complex calculations, which may take a considerable amount of time and computing resources. Running such programs for various scale choices, parton distribution functions and sets of cuts is a tedious, time consuming task.

For processes with multi-particle final states at NLO, one is faced with similar problems. A possible solution, described in detail in Ref. [344], is to store the phase space points and the corresponding matrix element weights, together with other relevant information, in Root Ntuple files. This has the following advantages:

1. the results are flexible for (tighter) cuts to be applied at a later stage,

⁷ G. Heinrich, D. Maître

2. scale and PDF variations can be performed without lengthy runs of the original program,
3. it allows to make the results readily available to experimentalists.

The Ntuple format for NLO results already has been used successfully for various high-multiplicity processes, e.g. W+4 jets [533], W+5 jets [534], or H+3 jets [330, 331].

In this note we investigate whether the Ntuple format is also a viable option to store NNLO results. The limitation here can come only from the size of the files containing the Ntuples. Total sizes of the order of a TeraByte have proven practical for NLO calculations.

To get a first idea of the file sizes needed to store events which allow to produce reasonably smooth histograms for observables calculated at NNLO, we take the program `EERAD3` [535] as an example. `EERAD3` is a parton level event generator which computes the QCD corrections to event shape observables and jet rates in electron-positron annihilation to order α_s^3 [536, 537]. As this example does not require any parton distribution functions, and therefore does not contain any factorization scale dependence, it lends itself for a first study, which can be extended to the case of hadronic collisions later.

3.2 Ntuples at NNLO

3.2.1 Brief description of the `EERAD3` program

The perturbative expansion for the distribution of an event shape observable O up to NNLO at the centre-of-mass energy \sqrt{s} and renormalisation scale $\mu^2 = s$, with $\alpha_s \equiv \alpha_s(\sqrt{s})$, is given by

$$\frac{1}{\sigma_{\text{had}}} \frac{d\sigma}{dO} = \left(\frac{\alpha_s}{2\pi}\right) \frac{d\bar{A}}{dO} + \left(\frac{\alpha_s}{2\pi}\right)^2 \frac{d\bar{B}}{dO} + \left(\frac{\alpha_s}{2\pi}\right)^3 \frac{d\bar{C}}{dO} + \mathcal{O}(\alpha_s^4). \quad (\text{V.17})$$

In Eq. (V.17) the event shape distribution is normalised to the total hadronic cross section σ_{had} . The latter can be expanded as

$$\sigma_{\text{had}} = \sigma_0 \left(1 + \frac{3}{2} C_F \left(\frac{\alpha_s}{2\pi}\right) + K_2 \left(\frac{\alpha_s}{2\pi}\right)^2 + \mathcal{O}(\alpha_s^3) \right), \quad (\text{V.18})$$

where the Born cross section for $e^+e^- \rightarrow q\bar{q}$ is $\sigma_0 = \frac{4\pi\alpha}{3s} N e_q^2$, assuming massless quarks. The constant K_2 is given by [538]

$$K_2 = \frac{1}{4} \left[-\frac{3}{2} C_F^2 + C_F C_A \left(\frac{123}{2} - 44\zeta_3 \right) + C_F T_R N_F (-22 + 16\zeta_3) \right], \quad (\text{V.19})$$

with $C_A = N$, $C_F = (N^2 - 1)/(2N)$, $T_R = 1/2$, and N_F light quark flavours. The program `EERAD3` computes the perturbative coefficients A , B and C , which are normalised to σ_0 :

$$\frac{1}{\sigma_0} \frac{d\sigma}{dO} = \left(\frac{\alpha_s}{2\pi}\right) \frac{dA}{dO} + \left(\frac{\alpha_s}{2\pi}\right)^2 \frac{dB}{dO} + \left(\frac{\alpha_s}{2\pi}\right)^3 \frac{dC}{dO} + \mathcal{O}(\alpha_s^4). \quad (\text{V.20})$$

A , B and C are straightforwardly related to \bar{A} , \bar{B} and \bar{C} :

$$\bar{A} = A, \quad \bar{B} = B - \frac{3}{2} C_F A, \quad \bar{C} = C - \frac{3}{2} C_F B + \left(\frac{9}{4} C_F^2 - K_2\right) A. \quad (\text{V.21})$$

As these coefficients are computed at a renormalisation scale fixed to the centre-of-mass energy, they depend only on the value of the observable O .

The QCD coupling constant evolves according to the renormalisation group equation, which reads to NNLO:

$$\mu^2 \frac{d\alpha_s(\mu)}{d\mu^2} = -\alpha_s(\mu) \left[\beta_0 \left(\frac{\alpha_s(\mu)}{2\pi} \right) + \beta_1 \left(\frac{\alpha_s(\mu)}{2\pi} \right)^2 + \beta_2 \left(\frac{\alpha_s(\mu)}{2\pi} \right)^3 + \mathcal{O}(\alpha_s^4) \right] \quad (\text{V.22})$$

The coefficients β_i can be found e.g. in [535]. Eq. (V.22) is solved by introducing Λ as integration constant with $L = \log(\mu^2/\Lambda^2)$, yielding the running coupling constant:

$$\alpha_s(\mu) = \frac{2\pi}{\beta_0 L} \left(1 - \frac{\beta_1}{\beta_0^2} \frac{\log L}{L} + \frac{1}{\beta_0^2 L^2} \left(\frac{\beta_1^2}{\beta_0^2} (\log^2 L - \log L - 1) + \frac{\beta_2}{\beta_0} \right) \right). \quad (\text{V.23})$$

In terms of the running coupling $\alpha_s(\mu)$, the NNLO (non-singlet) expression for event shape distributions therefore becomes

$$\begin{aligned} \frac{1}{\sigma_{\text{had}}} \frac{d\sigma}{dO}(s, \mu^2, O) &= \left(\frac{\alpha_s(\mu)}{2\pi} \right) \frac{dA}{dO} + \left(\frac{\alpha_s(\mu)}{2\pi} \right)^2 \left(\frac{dB}{dO} + \frac{dA}{dO} \left[\beta_0 \log \frac{\mu^2}{s} - \frac{3}{2} C_F \right] \right) \\ &+ \left(\frac{\alpha_s(\mu)}{2\pi} \right)^3 \left(\frac{dC}{dO} + \frac{dB}{dO} \left[2\beta_0 \log \frac{\mu^2}{s} - \frac{3}{2} C_F \right] \right. \\ &+ \left. \frac{dA}{dO} \left[\beta_0^2 \log^2 \frac{\mu^2}{s} + \beta_1 \log \frac{\mu^2}{s} - 3\beta_0 C_F \log \frac{\mu^2}{s} - K_2 + \frac{9}{4} C_F^2 \right] \right) \\ &+ \mathcal{O}(\alpha_s^4). \end{aligned} \quad (\text{V.24})$$

The program `EERAD3` computes the perturbative coefficients A , B and C defined in eq. (V.20), where the renormalisation scale has been fixed to the centre-of-mass energy. In order to be able to perform variations of the renormalization scale, it is therefore sufficient to store the coefficients A , B and C in the `Ntuples` and apply Eq. (V.24) at the level of the `Ntuple` analysis.

3.2.2 Details about the `EERAD3 Ntuples`

The input file `eerad3.input` contains the field `nshot3 nshot4 nshot5`. They denote the numbers of sampling points per iteration to be used by the Monte Carlo integrator `Vegas` for the 3-parton, 4-parton, 5-parton channels, respectively. The field `itmax1 itmax2` contains the number of iterations for the “warm up run” (grid construction, `itmax1` iterations) and the “production run” (event generation and integration, `itmax2` iterations). The total number of events in each channel is then roughly given by `nshot × itmax2`, modulo events which do not pass the cuts.

For the implementation of this experimentation we used the same format as for the `BlackHat+Sherpa NLO Ntuples` [344], removing however the unnecessary information about the partonic initial states. Figure V.17 shows the size of the `Ntuple` file as a function of the number of events. In Table V.1, we list the size of the `Ntuple` files for a million events. The `Ntuples` contain the NNLO results for the sum of all colour factors, i.e. `icol=0`. Further, we used `y0=1d-7`, `iaver=0`, `cutvar=1d-5`. The event numbers given in Table V.1 are summed over all partonic channels.

The first column of Table V.1 shows the size of the `Ntuple` file if all phase-space information is recorded in the `Ntuple`. An alternative strategy is to use the fact that there is a clear relationship between the kinematical information of a real phase-space point (“real” refers to the phase-space with the largest final state multiplicity) and its subtractions. Starting from one

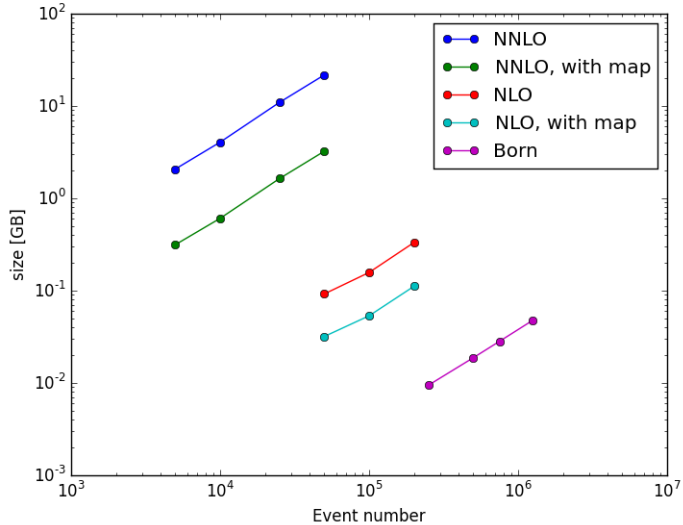


Fig. V.17: File size as a function of the number of events.

run	size/Mevents [GB]	size/Mevents [GB] with mapping
LO	0.038	0.038
NLO	1.66	0.56
NNLO	433.9	64.7

Table V.1: Sizes of the Ntuple files for various choices of the total number of events.

phase-space configuration for the real radiation one can get to all the kinematical configurations for the subtractions using a fixed number of phase-space mappings. If we can enumerate these mappings and record the mapping label instead of the actual mapped momenta we can save a significant amount of storage, at the cost of having to perform the mappings when the Ntuple file is analysed. The second column of Table V.1 shows the size of an Ntuple file if the mapping label is recorded instead of the momenta for the subtractions. However, apart from the increased CPU time to read an Ntuple file produced in this way there is another disadvantage: the Ntuple is more tightly bound to the program that produced it, as the implementation of the mappings has to be provided along with the Ntuple file.

We should mention that the reconstruction of observables from the information contained in the Ntuples is only applicable to observables which are rotation-invariant. This is due to the fact that the phase space in EERAD3 is constructed assuming rotational invariance.

3.3 Summary and outlook

We have produced Root Ntuple files based on the program EERAD3, a partonic Monte Carl program to calculate event shapes and jet rates in electron-positron annihilation up to NNLO. We have found that the size of the Ntuple files needed to produce reasonably smooth histograms is of the order of 2-3 TeraBytes. Therefore it seems that Ntuples can be a convenient way to store NNLO results in hadronic collisions as well.

Apart from the obvious advantages of Ntuples to be able to perform scale and PDF variations without having to run the full program, there are a number of other aspects which

make the use of Ntuples for NNLO results additionally appealing:

- the results can be made available to experimentalists, where they can apply different sets of cuts, PDFs, etc. without having to deal with the NNLO code
- it is easy to change value of $\alpha_s(M_Z)$, such that fits of α_s could be readily performed.

The file sizes presented here are obtained using the EERAD3 phase-space generator that was designed to optimize the CPU time. One can easily imagine that, if the focus was shifted to optimise the storage space, improvements for the file size could be achieved.

We are looking forward to the first NNLO results in hadronic collisions being available in the form of Ntuples.

References

- [1] J. R. Andersen et al., *Les Houches 2013: Physics at TeV Colliders: Standard Model Working Group Report*, arXiv:1405.1067 [hep-ph].
- [2] C. Anastasiou, C. Duhr, F. Dulat, F. Herzog, and B. Mistlberger, *Higgs Boson Gluon-Fusion Production in QCD at Three Loops*, Phys. Rev. Lett. **114** (2015) 212001, arXiv:1503.06056 [hep-ph].
- [3] T. Carli, D. Clements, A. Cooper-Sarkar, C. Gwenlan, G. P. Salam, F. Siegert, P. Starovoitov, and M. Sutton, *A posteriori inclusion of parton density functions in NLO QCD final-state calculations at hadron colliders: The APPLGRID Project*, Eur. Phys. J. **C66** (2010) 503–524, arXiv:0911.2985 [hep-ph].
- [4] T. Kluge, K. Rabbertz, and M. Wobisch, *FastNLO: Fast pQCD calculations for PDF fits*, in *Deep inelastic scattering. Proceedings, 14th International Workshop, DIS 2006, Tsukuba, Japan, April 20-24, 2006*, pp. 483–486. 2006. arXiv:hep-ph/0609285 [hep-ph]. http://lss.fnal.gov/cgi-bin/find_paper.pl?conf-06-352.
- [5] J. M. Henn, K. Melnikov, and V. A. Smirnov, *Two-loop planar master integrals for the production of off-shell vector bosons in hadron collisions*, JHEP **05** (2014) 090, arXiv:1402.7078 [hep-ph].
- [6] F. Caola, J. M. Henn, K. Melnikov, and V. A. Smirnov, *Non-planar master integrals for the production of two off-shell vector bosons in collisions of massless partons*, JHEP **09** (2014) 043, arXiv:1404.5590 [hep-ph].
- [7] T. Gehrmann, A. von Manteuffel, L. Tancredi, and E. Weihs, *The two-loop master integrals for $q\bar{q} \rightarrow VV$* , JHEP **06** (2014) 032, arXiv:1404.4853 [hep-ph].
- [8] C. G. Papadopoulos, D. Tommasini, and C. Wever, *Two-loop Master Integrals with the Simplified Differential Equations approach*, JHEP **01** (2015) 072, arXiv:1409.6114 [hep-ph].
- [9] J. M. Henn, *Multiloop integrals in dimensional regularization made simple*, Phys. Rev. Lett. **110** (2013) 251601, arXiv:1304.1806 [hep-th].
- [10] R. Bonciani, V. Del Duca, H. Frellesvig, J. M. Henn, F. Moriello, and V. A. Smirnov, *Next-to-leading order QCD corrections to the decay width $H \rightarrow Z\gamma Z$* , JHEP **08** (2015) 108, arXiv:1505.00567 [hep-ph].
- [11] S. Di Vita, P. Mastrolia, U. Schubert, and V. Yundin, *Three-loop master integrals for ladder-box diagrams with one massive leg*, JHEP **09** (2014) 148, arXiv:1408.3107 [hep-ph].
- [12] R. Bonciani, S. Di Vita, P. Mastrolia, and U. Schubert, *Two-Loop Master Integrals for the mixed EW-QCD virtual corrections to Drell-Yan scattering*, arXiv:1604.08581 [hep-ph].
- [13] C. Duhr, *Mathematical aspects of scattering amplitudes*, in *Theoretical Advanced Study Institute in Elementary Particle Physics: Journeys Through the Precision Frontier: Amplitudes for Colliders (TASI 2014) Boulder, Colorado, June 2-27, 2014*. 2014. arXiv:1411.7538 [hep-ph]. <http://inspirehep.net/record/1331430/files/arXiv:1411.7538.pdf>.
- [14] E. Panzer, *Algorithms for the symbolic integration of hyperlogarithms with applications to Feynman integrals*, Comput. Phys. Commun. **188** (2014) 148–166, arXiv:1403.3385 [hep-th].
- [15] C. Bogner, *MPL - a program for computations with iterated integrals on moduli spaces of curves of genus zero*, arXiv:1510.04562 [physics.comp-ph].
- [16] A. von Manteuffel, E. Panzer, and R. M. Schabinger, *On the Computation of Form*

- Factors in Massless QCD with Finite Master Integrals*, arXiv:1510.06758 [hep-ph].
- [17] A. V. Smirnov, *FIESTA 4: optimized Feynman integral calculations with GPU support*, arXiv:1511.03614 [hep-ph].
- [18] A. V. Smirnov, *FIESTA 3: cluster-parallelizable multiloop numerical calculations in physical regions*, Comput. Phys. Commun. **185** (2014) 2090–2100, arXiv:1312.3186 [hep-ph].
- [19] S. Borowka, G. Heinrich, S. P. Jones, M. Kerner, J. Schlenk, and T. Zirke, *SecDec-3.0: numerical evaluation of multi-scale integrals beyond one loop*, Comput. Phys. Commun. **196** (2015) 470–491, arXiv:1502.06595 [hep-ph].
- [20] S. Borowka, J. Carter, and G. Heinrich, *Numerical Evaluation of Multi-Loop Integrals for Arbitrary Kinematics with SecDec 2.0*, Comput. Phys. Commun. **184** (2013) 396–408, arXiv:1204.4152 [hep-ph].
- [21] S. Borowka, N. Greiner, G. Heinrich, S. P. Jones, M. Kerner, J. Schlenk, U. Schubert, and T. Zirke, *Higgs boson pair production in gluon fusion at NLO with full top-quark mass dependence*, arXiv:1604.06447 [hep-ph].
- [22] T. Gehrmann, J. M. Henn, and N. A. Lo Presti, *Analytic form of the two-loop planar five-gluon all-plus-helicity amplitude in QCD*, Phys. Rev. Lett. **116** (2016) no. 6, 062001, arXiv:1511.05409 [hep-ph].
- [23] C. G. Papadopoulos, D. Tommasini, and C. Wever, *The Pentabox Master Integrals with the Simplified Differential Equations approach*, arXiv:1511.09404 [hep-ph].
- [24] J. Broedel, C. R. Mafra, N. Matthes, and O. Schlotterer, *Elliptic multiple zeta values and one-loop superstring amplitudes*, JHEP **07** (2015) 112, arXiv:1412.5535 [hep-th].
- [25] L. Adams, C. Bogner, and S. Weinzierl, *The two-loop sunrise integral around four space-time dimensions and generalisations of the Clausen and Glaisher functions towards the elliptic case*, J. Math. Phys. **56** (2015) no. 7, 072303, arXiv:1504.03255 [hep-ph].
- [26] S. Bloch and P. Vanhove, *The elliptic dilogarithm for the sunset graph*, arXiv:1309.5865 [hep-th].
- [27] C. Bogner, *Generalizations of polylogarithms for Feynman integrals*, in *17th International workshop on Advanced Computing and Analysis Techniques in physics research (ACAT 2016) Valparaiso, Chile, January 18-22, 2016*. 2016. arXiv:1603.00420 [hep-ph]. <http://inspirehep.net/record/1425563/files/arXiv:1603.00420.pdf>.
- [28] M. Czakon, D. Heymes, and A. Mitov, *High-precision differential predictions for top-quark pairs at the LHC*, Phys. Rev. Lett. **116** (2016) no. 8, 082003, arXiv:1511.00549 [hep-ph].
- [29] F. Caola, J. M. Henn, K. Melnikov, A. V. Smirnov, and V. A. Smirnov, *Two-loop helicity amplitudes for the production of two off-shell electroweak bosons in quark-antiquark collisions*, JHEP **11** (2014) 041, arXiv:1408.6409 [hep-ph].
- [30] F. Caola, J. M. Henn, K. Melnikov, A. V. Smirnov, and V. A. Smirnov, *Two-loop helicity amplitudes for the production of two off-shell electroweak bosons in gluon fusion*, JHEP **06** (2015) 129, arXiv:1503.08759 [hep-ph].
- [31] A. von Manteuffel and L. Tancredi, *The two-loop helicity amplitudes for $gg \rightarrow V_1 V_2 \rightarrow 4$ leptons*, JHEP **06** (2015) 197, arXiv:1503.08835 [hep-ph].
- [32] T. Gehrmann, A. von Manteuffel, and L. Tancredi, *The two-loop helicity amplitudes for $q\bar{q}' \rightarrow V_1 V_2 \rightarrow 4$ leptons*, JHEP **09** (2015) 128, arXiv:1503.04812 [hep-ph].
- [33] A. V. Smirnov, *Algorithm FIRE – Feynman Integral REduction*, JHEP **10** (2008) 107, arXiv:0807.3243 [hep-ph].
- [34] A. V. Smirnov and V. A. Smirnov, *FIRE4, LiteRed and accompanying tools to solve*

- integration by parts relations*, Comput. Phys. Commun. **184** (2013) 2820–2827, [arXiv:1302.5885 \[hep-ph\]](#).
- [35] A. V. Smirnov, *FIRE5: a C++ implementation of Feynman Integral REDuction*, Comput. Phys. Commun. **189** (2014) 182–191, [arXiv:1408.2372 \[hep-ph\]](#).
- [36] R. N. Lee, *Presenting LiteRed: a tool for the Loop InTEgrals REDuction*, [arXiv:1212.2685 \[hep-ph\]](#).
- [37] C. Studerus, *Reduze-Feynman Integral Reduction in C++*, Comput. Phys. Commun. **181** (2010) 1293–1300, [arXiv:0912.2546 \[physics.comp-ph\]](#).
- [38] A. von Manteuffel and C. Studerus, *Reduze 2 - Distributed Feynman Integral Reduction*, [arXiv:1201.4330 \[hep-ph\]](#).
- [39] C. F. Berger, Z. Bern, L. J. Dixon, F. Febres Cordero, D. Forde, H. Ita, D. A. Kosower, and D. Maitre, *An Automated Implementation of On-Shell Methods for One-Loop Amplitudes*, Phys. Rev. **D78** (2008) 036003, [arXiv:0803.4180 \[hep-ph\]](#).
- [40] F. Cascioli, P. Maierhofer, and S. Pozzorini, *Scattering Amplitudes with Open Loops*, Phys. Rev. Lett. **108** (2012) 111601, [arXiv:1111.5206 \[hep-ph\]](#).
- [41] G. Bevilacqua, M. Czakon, M. V. Garzelli, A. van Hameren, A. Kardos, C. G. Papadopoulos, R. Pittau, and M. Worek, *HELAC-NLO*, Comput. Phys. Commun. **184** (2013) 986–997, [arXiv:1110.1499 \[hep-ph\]](#).
- [42] S. Badger, B. Biedermann, P. Uwer, and V. Yundin, *Numerical evaluation of virtual corrections to multi-jet production in massless QCD*, Comput. Phys. Commun. **184** (2013) 1981–1998, [arXiv:1209.0100 \[hep-ph\]](#).
- [43] S. Actis, A. Denner, L. Hofer, J.-N. Lang, A. Scharf, and S. Uccirati, *RECOLA: REcursive Computation of One-Loop Amplitudes*, [arXiv:1605.01090 \[hep-ph\]](#).
- [44] G. Cullen et al., *GOSAM-2.0: a tool for automated one-loop calculations within the Standard Model and beyond*, Eur. Phys. J. **C74** (2014) no. 8, 3001, [arXiv:1404.7096 \[hep-ph\]](#).
- [45] J. Alwall, R. Frederix, S. Frixione, V. Hirschi, F. Maltoni, O. Mattelaer, H. S. Shao, T. Stelzer, P. Torrielli, and M. Zaro, *The automated computation of tree-level and next-to-leading order differential cross sections, and their matching to parton shower simulations*, JHEP **07** (2014) 079, [arXiv:1405.0301 \[hep-ph\]](#).
- [46] Z. Bern, L. J. Dixon, D. C. Dunbar, and D. A. Kosower, *One-loop n-point gauge theory amplitudes, unitarity and collinear limits*, Nucl.Phys. **B425** (1994) 217–260, [arXiv:hep-ph/9403226 \[hep-ph\]](#).
- [47] Z. Bern, L. J. Dixon, D. C. Dunbar, and D. A. Kosower, *Fusing gauge theory tree amplitudes into loop amplitudes*, Nucl.Phys. **B435** (1995) 59–101, [arXiv:hep-ph/9409265 \[hep-ph\]](#).
- [48] R. Britto, F. Cachazo, and B. Feng, *Generalized unitarity and one-loop amplitudes in N=4 super-Yang-Mills*, Nucl.Phys. **B725** (2005) 275–305, [arXiv:hep-th/0412103 \[hep-th\]](#).
- [49] W. T. Giele, Z. Kunszt, and K. Melnikov, *Full one-loop amplitudes from tree amplitudes*, JHEP **0804** (2008) 049, [arXiv:0801.2237 \[hep-ph\]](#).
- [50] D. Forde, *Direct extraction of one-loop integral coefficients*, Phys. Rev. **D75** (2007) 125019, [arXiv:0704.1835 \[hep-ph\]](#).
- [51] G. Ossola, C. G. Papadopoulos, and R. Pittau, *Reducing full one-loop amplitudes to scalar integrals at the integrand level*, Nucl. Phys. **B763** (2007) 147–169, [hep-ph/0609007](#).
- [52] R. K. Ellis, Z. Kunszt, K. Melnikov, and G. Zanderighi, *One-loop calculations in*

- quantum field theory: from Feynman diagrams to unitarity cuts*, Phys. Rept. **518** (2012) 141–250, arXiv:1105.4319 [hep-ph].
- [53] P. Mastrolia and G. Ossola, *On the Integrand-Reduction Method for Two-Loop Scattering Amplitudes*, JHEP **11** (2011) 014, arXiv:1107.6041 [hep-ph].
- [54] S. Badger, H. Frellesvig, and Y. Zhang, *Hepta-Cuts of Two-Loop Scattering Amplitudes*, JHEP **04** (2012) 055, arXiv:1202.2019 [hep-ph].
- [55] Y. Zhang, *Integrand-Level Reduction of Loop Amplitudes by Computational Algebraic Geometry Methods*, JHEP **09** (2012) 042, arXiv:1205.5707 [hep-ph].
- [56] R. H. P. Kleiss, I. Malamos, C. G. Papadopoulos, and R. Verheyen, *Counting to One: Reducibility of One- and Two-Loop Amplitudes at the Integrand Level*, JHEP **12** (2012) 038, arXiv:1206.4180 [hep-ph].
- [57] B. Feng and R. Huang, *The classification of two-loop integrand basis in pure four-dimension*, JHEP **02** (2013) 117, arXiv:1209.3747 [hep-ph].
- [58] P. Mastrolia, E. Mirabella, G. Ossola, and T. Peraro, *Scattering Amplitudes from Multivariate Polynomial Division*, Phys. Lett. **B718** (2012) 173–177, arXiv:1205.7087 [hep-ph].
- [59] P. Mastrolia, E. Mirabella, G. Ossola, and T. Peraro, *Multiloop Integrand Reduction for Dimensionally Regulated Amplitudes*, Phys. Lett. **B727** (2013) 532–535, arXiv:1307.5832 [hep-ph].
- [60] S. Badger, H. Frellesvig, and Y. Zhang, *A Two-Loop Five-Gluon Helicity Amplitude in QCD*, JHEP **12** (2013) 045, arXiv:1310.1051 [hep-ph].
- [61] P. Mastrolia, T. Peraro, and A. Primo, *Adaptive Integrand Decomposition in parallel and orthogonal space*, arXiv:1605.03157 [hep-ph].
- [62] S. Badger, G. Mogull, A. Ochirov, and D. O’Connell, *A Complete Two-Loop, Five-Gluon Helicity Amplitude in Yang-Mills Theory*, JHEP **10** (2015) 064, arXiv:1507.08797 [hep-ph].
- [63] D. A. Kosower and K. J. Larsen, *Maximal Unitarity at Two Loops*, Phys. Rev. **D85** (2012) 045017, arXiv:1108.1180 [hep-th].
- [64] K. J. Larsen, *Global Poles of the Two-Loop Six-Point $N=4$ SYM integrand*, Phys. Rev. **D86** (2012) 085032, arXiv:1205.0297 [hep-th].
- [65] S. Caron-Huot and K. J. Larsen, *Uniqueness of two-loop master contours*, JHEP **10** (2012) 026, arXiv:1205.0801 [hep-ph].
- [66] H. Johansson, D. A. Kosower, and K. J. Larsen, *Two-Loop Maximal Unitarity with External Masses*, Phys. Rev. **D87** (2013) no. 2, 025030, arXiv:1208.1754 [hep-th].
- [67] H. Johansson, D. A. Kosower, and K. J. Larsen, *Maximal Unitarity for the Four-Mass Double Box*, Phys. Rev. **D89** (2014) no. 12, 125010, arXiv:1308.4632 [hep-th].
- [68] H. Johansson, D. A. Kosower, K. J. Larsen, and M. S  ygaard, *Cross-Order Integral Relations from Maximal Cuts*, Phys. Rev. **D92** (2015) no. 2, 025015, arXiv:1503.06711 [hep-th].
- [69] J. Gluza, K. Kajda, and D. A. Kosower, *Towards a Basis for Planar Two-Loop Integrals*, Phys. Rev. **D83** (2011) 045012, arXiv:1009.0472 [hep-th].
- [70] R. M. Schabinger, *A New Algorithm For The Generation Of Unitarity-Compatible Integration By Parts Relations*, JHEP **01** (2012) 077, arXiv:1111.4220 [hep-ph].
- [71] H. Ita, *Two-loop Integrand Decomposition into Master Integrals and Surface Terms*, arXiv:1510.05626 [hep-th].
- [72] K. J. Larsen and Y. Zhang, *Integration-by-parts reductions from unitarity cuts and algebraic geometry*, Phys. Rev. **D93** (2016) no. 4, 041701, arXiv:1511.01071 [hep-th].

- [73] A. Gehrmann-De Ridder, T. Gehrmann, and E. W. N. Glover, *Antenna subtraction at NNLO*, JHEP **09** (2005) 056, arXiv:hep-ph/0505111 [hep-ph].
- [74] J. Currie, E. W. N. Glover, and S. Wells, *Infrared Structure at NNLO Using Antenna Subtraction*, JHEP **04** (2013) 066, arXiv:1301.4693 [hep-ph].
- [75] M. Czakon, *A novel subtraction scheme for double-real radiation at NNLO*, Phys. Lett. **B693** (2010) 259–268, arXiv:1005.0274 [hep-ph].
- [76] M. Czakon, *Double-real radiation in hadronic top quark pair production as a proof of a certain concept*, Nucl. Phys. **B849** (2011) 250–295, arXiv:1101.0642 [hep-ph].
- [77] R. Boughezal, K. Melnikov, and F. Petriello, *A subtraction scheme for NNLO computations*, Phys.Rev. **D85** (2012) 034025, arXiv:1111.7041 [hep-ph].
- [78] S. Frixione, Z. Kunszt, and A. Signer, *Three jet cross-sections to next-to-leading order*, Nucl. Phys. **B467** (1996) 399–442, arXiv:hep-ph/9512328 [hep-ph].
- [79] M. Czakon and D. Heymes, *Four-dimensional formulation of the sector-improved residue subtraction scheme*, Nucl. Phys. **B890** (2014) 152–227, arXiv:1408.2500 [hep-ph].
- [80] R. Boughezal, F. Caola, K. Melnikov, F. Petriello, and M. Schulze, *Higgs boson production in association with a jet at next-to-next-to-leading order*, Phys. Rev. Lett. **115** (2015) no. 8, 082003, arXiv:1504.07922 [hep-ph].
- [81] F. Caola, K. Melnikov, and M. Schulze, *Fiducial cross sections for Higgs boson production in association with a jet at next-to-next-to-leading order in QCD*, Phys. Rev. **D92** (2015) no. 7, 074032, arXiv:1508.02684 [hep-ph].
- [82] M. Czakon, P. Fiedler, D. Heymes, and A. Mitov, *NNLO QCD predictions for fully-differential top-quark pair production at the Tevatron*, arXiv:1601.05375 [hep-ph].
- [83] S. Catani and M. Grazzini, *An NNLO subtraction formalism in hadron collisions and its application to Higgs boson production at the LHC*, Phys. Rev. Lett. **98** (2007) 222002, arXiv:hep-ph/0703012 [hep-ph].
- [84] R. Bonciani, S. Catani, M. Grazzini, H. Sargsyan, and A. Torre, *The q_T subtraction method for top quark production at hadron colliders*, Eur. Phys. J. **C75** (2015) no. 12, 581, arXiv:1508.03585 [hep-ph].
- [85] R. Boughezal, C. Focke, W. Giele, X. Liu, and F. Petriello, *Higgs boson production in association with a jet at NNLO using jettiness subtraction*, Phys. Lett. **B748** (2015) 5–8, arXiv:1505.03893 [hep-ph].
- [86] R. Boughezal, X. Liu, and F. Petriello, *N -jettiness soft function at next-to-next-to-leading order*, Phys. Rev. **D91** (2015) no. 9, 094035, arXiv:1504.02540 [hep-ph].
- [87] J. Gaunt, M. Stahlhofen, F. J. Tackmann, and J. R. Walsh, *N -jettiness Subtractions for NNLO QCD Calculations*, JHEP **09** (2015) 058, arXiv:1505.04794 [hep-ph].
- [88] S. Alioli, C. W. Bauer, C. Berggren, F. J. Tackmann, and J. R. Walsh, *Drell-Yan production at NNLL+NNLO matched to parton showers*, Phys. Rev. **D92** (2015) no. 9, 094020, arXiv:1508.01475 [hep-ph].
- [89] V. Del Duca, C. Duhr, G. Somogyi, F. Tramontano, and Z. Trnıcsanyi, *Higgs boson decay into b -quarks at NNLO accuracy*, JHEP **04** (2015) 036, arXiv:1501.07226 [hep-ph].
- [90] S. Catani and M. H. Seymour, *A General algorithm for calculating jet cross-sections in NLO QCD*, Nucl. Phys. **B485** (1997) 291–419, arXiv:hep-ph/9605323 [hep-ph]. [Erratum: Nucl. Phys. **B510**, 503 (1998)].
- [91] V. Del Duca, C. Duhr, A. Kardos, G. Somogyi, and Z. Trnıcsanyi, *Three-jet production in electron-positron collisions using the CoLoRFulNNLO method*,

- arXiv:1603.08927 [hep-ph].
- [92] C. Anastasiou and K. Melnikov, *Higgs boson production at hadron colliders in NNLO QCD*, Nucl. Phys. **B646** (2002) 220–256, arXiv:hep-ph/0207004 [hep-ph].
 - [93] C. Anastasiou, L. J. Dixon, and K. Melnikov, *NLO Higgs boson rapidity distributions at hadron colliders*, Nucl. Phys. Proc. Suppl. **116** (2003) 193–197, arXiv:hep-ph/0211141 [hep-ph]. [,193(2002)].
 - [94] C. Anastasiou, L. J. Dixon, K. Melnikov, and F. Petriello, *Dilepton rapidity distribution in the Drell-Yan process at NNLO in QCD*, Phys. Rev. Lett. **91** (2003) 182002, arXiv:hep-ph/0306192.
 - [95] C. Anastasiou, L. J. Dixon, K. Melnikov, and F. Petriello, *High precision QCD at hadron colliders: Electroweak gauge boson rapidity distributions at NNLO*, Phys. Rev. **D69** (2004) 094008, arXiv:hep-ph/0312266.
 - [96] C. Anastasiou, C. Duhr, F. Dulat, F. Herzog, and B. Mistlberger, *Higgs Boson Gluon-Fusion Production in QCD at Three Loops*, Phys.Rev.Lett. **114** (2015) no. 21, 212001, arXiv:1503.06056 [hep-ph].
 - [97] C. Anastasiou, C. Duhr, F. Dulat, E. Furlan, T. Gehrmann, F. Herzog, and B. Mistlberger, *Higgs boson gluon-fusion production at threshold in N^3LO QCD*, Phys. Lett. **B737** (2014) 325–328, arXiv:1403.4616 [hep-ph].
 - [98] C. Anastasiou, C. Duhr, F. Dulat, E. Furlan, T. Gehrmann, F. Herzog, and B. Mistlberger, *Higgs boson gluon-fusion production beyond threshold in N^3LO QCD*, JHEP **03** (2015) 091, arXiv:1411.3584 [hep-ph].
 - [99] Y. Li, A. von Manteuffel, R. M. Schabinger, and H. X. Zhu, *Soft-virtual corrections to Higgs production at N^3LO* , Phys. Rev. **D91** (2015) no. 3, 036008, arXiv:1412.2771 [hep-ph].
 - [100] P. A. Baikov, K. G. Chetyrkin, A. V. Smirnov, V. A. Smirnov, and M. Steinhauser, *Quark and gluon form factors to three loops*, Phys. Rev. Lett. **102** (2009) 212002, arXiv:0902.3519 [hep-ph].
 - [101] T. Gehrmann, E. W. N. Glover, T. Huber, N. Ikizlerli, and C. Studerus, *Calculation of the quark and gluon form factors to three loops in QCD*, JHEP **06** (2010) 094, arXiv:1004.3653 [hep-ph].
 - [102] T. Gehrmann, E. Glover, T. Huber, N. Ikizlerli, and C. Studerus, *The quark and gluon form factors to three loops in QCD through to $O(\epsilon^2)$* , JHEP **1011** (2010) 102, arXiv:1010.4478 [hep-ph].
 - [103] C. Anastasiou, C. Duhr, F. Dulat, F. Herzog, and B. Mistlberger, *Real-virtual contributions to the inclusive Higgs cross-section at N^3LO* , JHEP **1312** (2013) 088, arXiv:1311.1425 [hep-ph].
 - [104] W. B. Kilgore, *One-loop single-real-emission contributions to $pp \rightarrow H + X$ at next-to-next-to-next-to-leading order*, Phys.Rev. **D89** (2014) no. 7, 073008, arXiv:1312.1296 [hep-ph].
 - [105] C. Duhr and T. Gehrmann, *The two-loop soft current in dimensional regularization*, Phys. Lett. **B727** (2013) 452–455, arXiv:1309.4393 [hep-ph].
 - [106] Y. Li and H. X. Zhu, *Single soft gluon emission at two loops*, JHEP **11** (2013) 080, arXiv:1309.4391 [hep-ph].
 - [107] C. Duhr, T. Gehrmann, and M. Jaquier, *Two-loop splitting amplitudes and the single-real contribution to inclusive Higgs production at N^3LO* , JHEP **02** (2015) 077, arXiv:1411.3587 [hep-ph].
 - [108] F. Dulat and B. Mistlberger, *Real-Virtual-Virtual contributions to the inclusive Higgs*

- cross section at N³LO*, arXiv:1411.3586 [hep-ph].
- [109] Y. Li, A. von Manteuffel, R. M. Schabinger, and H. X. Zhu, *N³LO Higgs boson and Drell-Yan production at threshold: The one-loop two-emission contribution*, Phys. Rev. **D90** (2014) no. 5, 053006, arXiv:1404.5839 [hep-ph].
- [110] C. Anastasiou, C. Duhr, F. Dulat, E. Furlan, F. Herzog, and B. Mistlberger, *Soft expansion of double-real-virtual corrections to Higgs production at N³LO*, JHEP **08** (2015) 051, arXiv:1505.04110 [hep-ph].
- [111] C. Anastasiou, C. Duhr, F. Dulat, and B. Mistlberger, *Soft triple-real radiation for Higgs production at N³LO*, JHEP **1307** (2013) 003, arXiv:1302.4379 [hep-ph].
- [112] O. V. Tarasov, A. A. Vladimirov, and A. Yu. Zharkov, *The Gell-Mann-Low Function of QCD in the Three Loop Approximation*, Phys. Lett. **B93** (1980) 429–432.
- [113] S. A. Larin and J. A. M. Vermaseren, *The Three loop QCD Beta function and anomalous dimensions*, Phys. Lett. **B303** (1993) 334–336, arXiv:hep-ph/9302208 [hep-ph].
- [114] T. van Ritbergen, J. A. M. Vermaseren, and S. A. Larin, *The Four loop beta function in quantum chromodynamics*, Phys. Lett. **B400** (1997) 379–384, arXiv:hep-ph/9701390 [hep-ph].
- [115] M. Czakon, *The Four-loop QCD beta-function and anomalous dimensions*, Nucl. Phys. **B710** (2005) 485–498, arXiv:hep-ph/0411261 [hep-ph].
- [116] A. Vogt, S. Moch, and J. A. M. Vermaseren, *The Three-loop splitting functions in QCD: The Singlet case*, Nucl. Phys. **B691** (2004) 129–181, arXiv:hep-ph/0404111 [hep-ph].
- [117] S. Moch, J. A. M. Vermaseren, and A. Vogt, *The Three loop splitting functions in QCD: The Nonsinglet case*, Nucl. Phys. **B688** (2004) 101–134, arXiv:hep-ph/0403192 [hep-ph].
- [118] C. Anastasiou, S. Buehler, C. Duhr, and F. Herzog, *NNLO phase space master integrals for two-to-one inclusive cross sections in dimensional regularization*, JHEP **11** (2012) 062, arXiv:1208.3130 [hep-ph].
- [119] M. Höschele, J. Hoff, A. Pak, M. Steinhauser, and T. Ueda, *Higgs boson production at the LHC: NNLO partonic cross sections through order ϵ and convolutions with splitting functions to N³LO*, Phys. Lett. **B721** (2013) 244–251, arXiv:1211.6559 [hep-ph].
- [120] S. Buehler and A. Lazopoulos, *Scale dependence and collinear subtraction terms for Higgs production in gluon fusion at N³LO*, JHEP **10** (2013) 096, arXiv:1306.2223 [hep-ph].
- [121] C. Anzai, A. Hasselhuhn, M. Höschele, J. Hoff, W. Kilgore, et al., *Exact N³LO results for $qq' \rightarrow H + X$* , arXiv:1506.02674 [hep-ph].
- [122] T. Ahmed, M. Mahakhud, N. Rana, and V. Ravindran, *Drell-Yan Production at Threshold to Third Order in QCD*, Phys. Rev. Lett. **113** (2014) no. 11, 112002, arXiv:1404.0366 [hep-ph].
- [123] T. Ahmed, M. Mandal, N. Rana, and V. Ravindran, *Rapidity Distributions in Drell-Yan and Higgs Productions at Threshold to Third Order in QCD*, Phys. Rev. Lett. **113** (2014) 212003, arXiv:1404.6504 [hep-ph].
- [124] T. Ahmed, N. Rana, and V. Ravindran, *Higgs boson production through $b\bar{b}$ annihilation at threshold in N³LO QCD*, JHEP **10** (2014) 139, arXiv:1408.0787 [hep-ph].
- [125] M. C. Kumar, M. K. Mandal, and V. Ravindran, *Associated production of Higgs boson with vector boson at threshold N³LO in QCD*, JHEP **03** (2015) 037, arXiv:1412.3357 [hep-ph].
- [126] C. Anastasiou, C. Duhr, F. Dulat, E. Furlan, T. Gehrmann, F. Herzog, A. Lazopoulos, and B. Mistlberger, *High precision determination of the gluon fusion Higgs boson cross-section at the LHC*, arXiv:1602.00695 [hep-ph].

- [127] M. Grazzini, S. Kallweit, D. Rathlev, and M. Wiesemann, *Transverse-momentum resummation for vector-boson pair production at NNLL+NNLO*, JHEP **08** (2015) 154, [arXiv:1507.02565 \[hep-ph\]](#).
- [128] S. Alioli, C. W. Bauer, C. J. Berggren, A. Hornig, F. J. Tackmann, C. K. Vermilion, J. R. Walsh, and S. Zuberi, *Combining Higher-Order Resummation with Multiple NLO Calculations and Parton Showers in GENEVA*, JHEP **09** (2013) 120, [arXiv:1211.7049 \[hep-ph\]](#).
- [129] A. Banfi, F. Caola, F. A. Dreyer, P. F. Monni, G. P. Salam, G. Zanderighi, and F. Dulat, *Jet-vetoed Higgs cross section in gluon fusion at N³LO+NNLL with small-R resummation*, [arXiv:1511.02886 \[hep-ph\]](#).
- [130] M. Dasgupta, F. Dreyer, G. P. Salam, and G. Soyez, *Small-radius jets to all orders in QCD*, JHEP **04** (2015) 039, [arXiv:1411.5182 \[hep-ph\]](#).
- [131] M. Dasgupta, F. A. Dreyer, G. P. Salam, and G. Soyez, *Inclusive jet spectrum for small-radius jets*, [arXiv:1602.01110 \[hep-ph\]](#).
- [132] G. Luisoni and S. Marzani, *QCD resummation for hadronic final states*, J. Phys. **G42** (2015) no. 10, 103101, [arXiv:1505.04084 \[hep-ph\]](#).
- [133] M. Billoni, S. Dittmaier, B. Jäger, and C. Speckner, *Next-to-leading-order electroweak corrections to $pp \rightarrow W^+W^- \rightarrow 4$ leptons at the LHC in double-pole approximation*, JHEP **1312** (2013) 043, [arXiv:1310.1564 \[hep-ph\]](#).
- [134] B. Biedermann, A. Denner, S. Dittmaier, L. Hofer, and B. Jäger, *Electroweak corrections to $pp \rightarrow \mu^+\mu^-e^+e^- + X$ at the LHC – a Higgs background study*, [arXiv:1601.07787 \[hep-ph\]](#).
- [135] B. Biedermann, M. Billoni, A. Denner, S. Dittmaier, L. Hofer, B. Jager, and L. Salfelder, *Next-to-leading-order electroweak corrections to $pp \rightarrow W^+W^- \rightarrow 4$ leptons at the LHC*, [arXiv:1605.03419 \[hep-ph\]](#).
- [136] M. Cacciari, F. A. Dreyer, A. Karlberg, G. P. Salam, and G. Zanderighi, *Fully Differential Vector-Boson-Fusion Higgs Production at Next-to-Next-to-Leading Order*, Phys. Rev. Lett. **115** (2015) no. 8, 082002, [arXiv:1506.02660 \[hep-ph\]](#).
- [137] K. Hamilton, P. Nason, E. Re, and G. Zanderighi, *NNLOPS simulation of Higgs boson production*, JHEP **10** (2013) 222, [arXiv:1309.0017 \[hep-ph\]](#).
- [138] K. Hamilton, P. Nason, and G. Zanderighi, *Finite quark-mass effects in the NNLOPS POWHEG+MiNLO Higgs generator*, JHEP **05** (2015) 140, [arXiv:1501.04637 \[hep-ph\]](#).
- [139] X. Chen, T. Gehrmann, E. W. N. Glover, and M. Jaquier, *Precise QCD predictions for the production of Higgs + jet final states*, Phys. Lett. **B740** (2015) 147–150, [arXiv:1408.5325 \[hep-ph\]](#).
- [140] O. Brein, A. Djouadi, and R. Harlander, *NNLO QCD corrections to the Higgs-strahlung processes a hadron collider*, Phys.Lett. **B579** (2004) 149–156, [arXiv:hep-ph/0307206 \[hep-ph\]](#).
- [141] O. Brein, R. Harlander, M. Wiesemann, and T. Zirke, *Top-Quark Mediated Effects in Hadronic Higgs-Strahlung*, Eur. Phys. J. **C72** (2012) 1868, [arXiv:1111.0761 \[hep-ph\]](#).
- [142] G. Ferrera, M. Grazzini, and F. Tramontano, *Associated WH production at hadron colliders: a fully exclusive QCD calculation at NNLO*, Phys.Rev.Lett. **107** (2011) 152003, [arXiv:1107.1164 \[hep-ph\]](#).
- [143] G. Ferrera, M. Grazzini, and F. Tramontano, *Associated ZH production at hadron colliders: the fully differential NNLO QCD calculation*, Phys.Lett. **B740** (2015) 51–55, [arXiv:1407.4747 \[hep-ph\]](#).

- [144] J. M. Campbell, R. K. Ellis, and C. Williams, *Associated production of a Higgs boson at NNLO*, arXiv:1601.00658 [hep-ph].
- [145] W. Astill, W. Bizon, E. Re, and G. Zanderighi, *NNLOPS accurate associated HW production*, arXiv:1603.01620 [hep-ph].
- [146] D. de Florian and J. Mazzitelli, *Higgs Boson Pair Production at Next-to-Next-to-Leading Order in QCD*, Phys. Rev. Lett. **111** (2013) 201801, arXiv:1309.6594 [hep-ph].
- [147] D. de Florian and J. Mazzitelli, *Higgs pair production at next-to-next-to-leading logarithmic accuracy at the LHC*, JHEP **09** (2015) 053, arXiv:1505.07122 [hep-ph].
- [148] J. Grigo, J. Hoff, K. Melnikov, and M. Steinhauser, *On the Higgs boson pair production at the LHC*, Nucl. Phys. **B875** (2013) 1–17, arXiv:1305.7340 [hep-ph].
- [149] J. Grigo, J. Hoff, and M. Steinhauser, *Higgs boson pair production: top quark mass effects at NLO and NNLO*, Nucl. Phys. **B900** (2015) 412–430, arXiv:1508.00909 [hep-ph].
- [150] S. Frixione, V. Hirschi, D. Pagani, H. S. Shao, and M. Zaro, *Weak corrections to Higgs hadroproduction in association with a top-quark pair*, JHEP **09** (2014) 065, arXiv:1407.0823 [hep-ph].
- [151] S. Frixione, V. Hirschi, D. Pagani, H. S. Shao, and M. Zaro, *Electroweak and QCD corrections to top-pair hadroproduction in association with heavy bosons*, JHEP **06** (2015) 184, arXiv:1504.03446 [hep-ph].
- [152] A. Denner and R. Feger, *NLO QCD corrections to off-shell top-antitop production with leptonic decays in association with a Higgs boson at the LHC*, arXiv:1506.07448 [hep-ph].
- [153] A. Karlberg, E. Re, and G. Zanderighi, *NNLOPS accurate Drell-Yan production*, JHEP **09** (2014) 134, arXiv:1407.2940 [hep-ph].
- [154] S. Höche, Y. Li, and S. Prestel, *Drell-Yan lepton pair production at NNLO QCD with parton showers*, Phys. Rev. **D91** (2015) no. 7, 074015, arXiv:1405.3607 [hep-ph].
- [155] S. Dittmaier, A. Huss, and C. Schwinn, *Dominant mixed QCD-electroweak $O(\hat{s}_s\hat{s})$ corrections to Drell-Yan processes in the resonance region*, Nucl. Phys. **B904** (2016) 216–252, arXiv:1511.08016 [hep-ph].
- [156] A. Gehrmann-De Ridder, T. Gehrmann, E. W. N. Glover, A. Huss, and T. A. Morgan, *Precise QCD predictions for the production of a Z boson in association with a hadronic jet*, arXiv:1507.02850 [hep-ph].
- [157] R. Boughezal, J. M. Campbell, R. K. Ellis, C. Focke, W. T. Giele, X. Liu, and F. Petriello, *Z-boson production in association with a jet at next-to-next-to-leading order in perturbative QCD*, arXiv:1512.01291 [hep-ph].
- [158] R. Boughezal, X. Liu, and F. Petriello, *Phenomenology of the Z-boson plus jet process at NNLO*, arXiv:1602.08140 [hep-ph].
- [159] R. Boughezal, X. Liu, and F. Petriello, *A comparison of NNLO QCD predictions with 7 TeV ATLAS and CMS data for V+jet processes*, arXiv:1602.05612 [hep-ph].
- [160] R. Boughezal, C. Focke, X. Liu, and F. Petriello, *W-boson production in association with a jet at next-to-next-to-leading order in perturbative QCD*, Phys. Rev. Lett. **115** (2015) no. 6, 062002, arXiv:1504.02131 [hep-ph].
- [161] R. Boughezal, X. Liu, and F. Petriello, *W-boson plus jet differential distributions at NNLO in QCD*, arXiv:1602.06965 [hep-ph].
- [162] A. Denner, L. Hofer, A. Scharf, and S. Uccirati, *Electroweak corrections to lepton pair production in association with two hard jets at the LHC*, JHEP **01** (2015) 094, arXiv:1411.0916 [hep-ph].
- [163] S. Kallweit, J. M. Lindert, P. Maierhöfer, S. Pozzorini, and M. Schönherr, *NLO*

- electroweak automation and precise predictions for W +multijet production at the LHC*, JHEP **04** (2015) 012, [arXiv:1412.5157](#) [hep-ph].
- [164] S. Kallweit, J. M. Lindert, S. Pozzorini, M. Schönherr, and P. Maierhöfer, *NLO QCD+EW predictions for V +jets including off-shell vector-boson decays and multijet merging*, [arXiv:1511.08692](#) [hep-ph].
- [165] T. Gehrmann, M. Grazzini, S. Kallweit, P. Maierhöfer, A. von Manteuffel, S. Pozzorini, D. Rathlev, and L. Tancredi, *W^+W^- Production at Hadron Colliders in Next to Next to Leading Order QCD*, Phys. Rev. Lett. **113** (2014) no. 21, 212001, [arXiv:1408.5243](#) [hep-ph].
- [166] M. Grazzini, S. Kallweit, S. Pozzorini, D. Rathlev, and M. Wiesemann, *W^+W^- production at the LHC: fiducial cross sections and distributions in NNLO QCD*, [arXiv:1605.02716](#) [hep-ph].
- [167] F. Cascioli, T. Gehrmann, M. Grazzini, S. Kallweit, P. Maierhöfer, A. von Manteuffel, S. Pozzorini, D. Rathlev, L. Tancredi, and E. Weihs, *ZZ production at hadron colliders in NNLO QCD*, Phys. Lett. **B735** (2014) 311–313, [arXiv:1405.2219](#) [hep-ph].
- [168] M. Grazzini, S. Kallweit, and D. Rathlev, *ZZ production at the LHC: fiducial cross sections and distributions in NNLO QCD*, Phys. Lett. **B750** (2015) 407–410, [arXiv:1507.06257](#) [hep-ph].
- [169] M. Grazzini, S. Kallweit, and D. Rathlev, *$W\tilde{\chi}$ and $Z\tilde{\chi}$ production at the LHC in NNLO QCD*, JHEP **07** (2015) 085, [arXiv:1504.01330](#) [hep-ph].
- [170] A. Denner, S. Dittmaier, M. Hecht, and C. Pasold, *NLO QCD and electroweak corrections to $W + \gamma$ production with leptonic W -boson decays*, JHEP **04** (2015) 018, [arXiv:1412.7421](#) [hep-ph].
- [171] A. Denner, S. Dittmaier, M. Hecht, and C. Pasold, *NLO QCD and electroweak corrections to $Z + \gamma$ production with leptonic Z -boson decays*, JHEP **02** (2016) 057, [arXiv:1510.08742](#) [hep-ph].
- [172] M. Grazzini, S. Kallweit, D. Rathlev, and M. Wiesemann, *$W^\pm Z$ production at hadron colliders in NNLO QCD*, [arXiv:1604.08576](#) [hep-ph].
- [173] L. Cieri, F. Coradeschi, and D. de Florian, *Diphoton production at hadron colliders: transverse-momentum resummation at next-to-next-to-leading logarithmic accuracy*, JHEP **06** (2015) 185, [arXiv:1505.03162](#) [hep-ph].
- [174] J. M. Campbell, R. K. Ellis, Y. Li, and C. Williams, *Predictions for diphoton production at the LHC through NNLO in QCD*, [arXiv:1603.02663](#) [hep-ph].
- [175] R. Röntschi and M. Schulze, *Constraining couplings of top quarks to the Z boson in $t\bar{t} + Z$ production at the LHC*, JHEP **07** (2014) 091, [arXiv:1404.1005](#) [hep-ph]. [Erratum: JHEP09,132(2015)].
- [176] R. Röntschi and M. Schulze, *Probing top- Z dipole moments at the LHC and ILC*, JHEP **08** (2015) 044, [arXiv:1501.05939](#) [hep-ph].
- [177] A. Gehrmann-De Ridder, T. Gehrmann, E. Glover, and J. Pires, *Second order QCD corrections to jet production at hadron colliders: the all-gluon contribution*, Phys.Rev.Lett. **110** (2013) 162003, [arXiv:1301.7310](#) [hep-ph].
- [178] J. Currie, A. Gehrmann-De Ridder, E. Glover, and J. Pires, *NNLO QCD corrections to jet production at hadron colliders from gluon scattering*, JHEP **1401** (2014) 110, [arXiv:1310.3993](#) [hep-ph].
- [179] J. Currie, A. Gehrmann-De Ridder, T. Gehrmann, N. Glover, J. Pires, and S. Wells, *Second order QCD corrections to gluonic jet production at hadron colliders*, PoS **LL2014** (2014) 001, [arXiv:1407.5558](#) [hep-ph].

- [180] M. Brucherseifer, F. Caola, and K. Melnikov, *On the NNLO QCD corrections to single-top production at the LHC*, Phys. Lett. **B736** (2014) 58–63, [arXiv:1404.7116 \[hep-ph\]](#).
- [181] J. Butterworth et al., *PDF4LHC recommendations for LHC Run II*, [arXiv:1510.03865 \[hep-ph\]](#).
- [182] S. Dulat, T.-J. Hou, J. Gao, M. Guzzi, J. Huston, P. Nadolsky, J. Pumplin, C. Schmidt, D. Stump, and C. P. Yuan, *New parton distribution functions from a global analysis of quantum chromodynamics*, Phys. Rev. **D93** (2016) 033006, [arXiv:1506.07443 \[hep-ph\]](#).
- [183] L. A. Harland-Lang, A. D. Martin, P. Motylinski, and R. S. Thorne, *Parton distributions in the LHC era: MMHT 2014 PDFs*, Eur. Phys. J. **C75** (2015) 204, [arXiv:1412.3989 \[hep-ph\]](#).
- [184] NNPDF Collaboration, R. D. Ball et al., *Parton distributions for the LHC Run II*, JHEP **04** (2015) 040, [arXiv:1410.8849 \[hep-ph\]](#).
- [185] G. Watt and R. Thorne, *Study of Monte Carlo approach to experimental uncertainty propagation with MSTW 2008 PDFs*, JHEP **1208** (2012) 052, [arXiv:1205.4024 \[hep-ph\]](#).
- [186] J. Gao and P. Nadolsky, *A meta-analysis of parton distribution functions*, JHEP **1407** (2014) 035, [arXiv:1401.0013 \[hep-ph\]](#).
- [187] S. Carrazza, J. I. Latorre, J. Rojo, and G. Watt, *A compression algorithm for the combination of PDF sets*, Eur. Phys. J. **C75** (2015) 474, [arXiv:1504.06469 \[hep-ph\]](#).
- [188] S. Carrazza, S. Forte, Z. Kassabov, J. I. Latorre, and J. Rojo, *An Unbiased Hessian Representation for Monte Carlo PDFs*, Eur. Phys. J. **C75** (2015) 369, [arXiv:1505.06736 \[hep-ph\]](#).
- [189] J. Pumplin, D. R. Stump, J. Huston, H. L. Lai, P. M. Nadolsky, and W. K. Tung, *New generation of parton distributions with uncertainties from global QCD analysis*, JHEP **07** (2002) 012, [arXiv:hep-ph/0201195 \[hep-ph\]](#).
- [190] A. Buckley, J. Ferrando, S. Lloyd, K. Nordström, B. Page, M. Rüfenacht, M. Schönherr, and G. Watt, *LHAPDF6: parton density access in the LHC precision era*, Eur. Phys. J. **C75** (2015) 132, [arXiv:1412.7420 \[hep-ph\]](#).
- [191] http://metapdf.hepforge.org/2016_pdf4lh/.
- [192] J. Gao, M. Guzzi, J. Huston, H.-L. Lai, Z. Li, et al., *CT10 next-to-next-to-leading order global analysis of QCD*, Phys.Rev. **D89** (2014) no. 3, 033009, [arXiv:1302.6246 \[hep-ph\]](#).
- [193] A. Martin, W. Stirling, R. Thorne, and G. Watt, *Parton distributions for the LHC*, Eur.Phys.J. **C63** (2009) 189–285, [arXiv:0901.0002 \[hep-ph\]](#).
- [194] NNPDF Collaboration, R. D. Ball, V. Bertone, S. Carrazza, C. S. Deans, L. Del Debbio, et al., *Parton distributions with LHC data*, Nucl.Phys. **B867** (2013) 244–289, [arXiv:1207.1303 \[hep-ph\]](#).
- [195] G. P. Salam and J. Rojo, *A Higher Order Perturbative Parton Evolution Toolkit (HOPPET)*, Comput. Phys. Commun. **180** (2009) 120–156, [arXiv:0804.3755 \[hep-ph\]](#).
- [196] J. M. Campbell, J. W. Huston, and W. J. Stirling, *Hard interactions of quarks and gluons: A primer for LHC physics*, Rept. Prog. Phys. **70** (2007) 89, [arXiv:hep-ph/0611148](#).
- [197] <https://www.hep.ucl.ac.uk/pdf4lh/mc2h-gallery/website/>.
- [198] S. Alekhin, J. Blumlein, and S. Moch, *The ABM parton distributions tuned to LHC data*,

- Phys. Rev. **D89** (2014) 054028, [arXiv:1310.3059](#) [hep-ph].
- [199] ZEUS, H1 Collaboration, H. Abramowicz et al., *Combination of measurements of inclusive deep inelastic $e^\pm p$ scattering cross sections and QCD analysis of HERA data*, Eur. Phys. J. **C75** (2015) 580, [arXiv:1506.06042](#) [hep-ex].
- [200] J. M. Campbell, R. K. Ellis, and G. Zanderighi, *Next-to-Leading order Higgs + 2 jet production via gluon fusion*, JHEP **10** (2006) 028, [arXiv:hep-ph/0608194](#) [hep-ph].
- [201] V. Bertone, R. Frederix, S. Frixione, J. Rojo, and M. Sutton, *aMCfast: automation of fast NLO computations for PDF fits*, JHEP **08** (2014) 166, [arXiv:1406.7693](#) [hep-ph].
- [202] <https://applgrid.hepforge.org>.
- [203] ATLAS Collaboration, G. Aad et al., *Measurement of inclusive jet and dijet production in pp collisions at $\sqrt{s} = 7$ TeV using the ATLAS detector*, Phys. Rev. **D86** (2012) 014022, [arXiv:1112.6297](#) [hep-ex].
- [204] Z. Nagy, *Three jet cross-sections in hadron hadron collisions at next-to-leading order*, Phys.Rev.Lett. **88** (2002) 122003, [arXiv:hep-ph/0110315](#) [hep-ph].
- [205] Z. Nagy, *Next-to-leading order calculation of three jet observables in hadron hadron collision*, Phys. Rev. **D68** (2003) 094002, [arXiv:hep-ph/0307268](#) [hep-ph].
- [206] CMS Collaboration, S. Chatrchyan et al., *Measurement of the electron charge asymmetry in inclusive W production in pp collisions at $\sqrt{s} = 7$ TeV*, Phys.Rev.Lett. **109** (2012) 111806, [arXiv:1206.2598](#) [hep-ex].
- [207] CMS Collaboration, S. Chatrchyan et al., *Measurement of the muon charge asymmetry in inclusive pp to WX production at $\sqrt{s} = 7$ TeV and an improved determination of light parton distribution functions*, Phys.Rev. **D90** (2014) 032004, [arXiv:1312.6283](#) [hep-ex].
- [208] S. Alekhin et al., *HERAFitter*, Eur. Phys. J. **C75** (2015) 304, [arXiv:1410.4412](#) [hep-ph].
- [209] <http://www.hep.ucl.ac.uk/pdf4lhc/>, .
- [210] S. Forte and G. Watt, *Progress in the Determination of the Partonic Structure of the Proton*, Ann.Rev.Nucl.Part.Sci. **63** (2013) 291–328, [arXiv:1301.6754](#) [hep-ph].
- [211] J. Rojo et al., *The PDF4LHC report on PDFs and LHC data: Results from Run I and preparation for Run II*, J. Phys. **G42** (2015) 103103, [arXiv:1507.00556](#) [hep-ph].
- [212] <http://www.hep.ucl.ac.uk/pdf4lhc/mc2h-gallery/website/>, .
- [213] S. Carrazza, S. Forte, Z. Kassabov, and J. Rojo, *Specialized minimal PDFs for optimized LHC calculations*, [arXiv:1602.00005](#) [hep-ph].
- [214] J. Campbell, R. K. Ellis, and F. Tramontano, *Single top production and decay at next-to-leading order*, Phys. Rev. **D70** (2004) 094012, [arXiv:hep-ph/0408158](#).
- [215] The NNPDF Collaboration, R. D. Ball et al., *A first unbiased global NLO determination of parton distributions and their uncertainties*, Nucl. Phys. **B838** (2010) 136–206, [arXiv:1002.4407](#) [hep-ph].
- [216] C. M. Bishop, *Neural Networks for Pattern Recognition*. Oxford University Press, November, 1995.
- [217] B. W. Silverman, *Density Estimation for Statistics and Data Analysis*. Chapman and Hall, November, 1986.
- [218] LHCb Collaboration, R. Aaij et al., *Measurement of forward $Z \rightarrow e^+e^-$ production at $\sqrt{s} = 8$ TeV*, JHEP **05** (2015) 109, [arXiv:1503.00963](#) [hep-ex].
- [219] S. Dawson, *Radiative corrections to Higgs boson production*, Nucl. Phys. **B359** (1991) 283–300.
- [220] D. Graudenz, M. Spira, and P. M. Zerwas, *QCD corrections to Higgs boson production at*

- proton proton colliders*, Phys. Rev. Lett. **70** (1993) 1372–1375.
- [221] A. Djouadi, M. Spira, and P. M. Zerwas, *Production of Higgs bosons in proton colliders: QCD corrections*, Phys. Lett. **B264** (1991) 440–446.
- [222] M. Spira, A. Djouadi, D. Graudenz, and P. M. Zerwas, *Higgs boson production at the LHC*, Nucl. Phys. **B453** (1995) 17–82, [arXiv:hep-ph/9504378](#) [hep-ph].
- [223] R. Harlander and P. Kant, *Higgs production and decay: Analytic results at next-to-leading order QCD*, JHEP **12** (2005) 015, [arXiv:hep-ph/0509189](#) [hep-ph].
- [224] U. Aglietti, R. Bonciani, G. Degrossi, and A. Vicini, *Analytic Results for Virtual QCD Corrections to Higgs Production and Decay*, JHEP **01** (2007) 021, [arXiv:hep-ph/0611266](#) [hep-ph].
- [225] R. Bonciani, G. Degrossi, and A. Vicini, *Scalar particle contribution to Higgs production via gluon fusion at NLO*, JHEP **11** (2007) 095, [arXiv:0709.4227](#) [hep-ph].
- [226] C. Anastasiou, S. Beerli, S. Bucherer, A. Daleo, and Z. Kunszt, *Two-loop amplitudes and master integrals for the production of a Higgs boson via a massive quark and a scalar-quark loop*, JHEP **01** (2007) 082, [arXiv:hep-ph/0611236](#) [hep-ph].
- [227] C. Anastasiou, S. Bucherer, and Z. Kunszt, *HPro: A NLO Monte-Carlo for Higgs Production via Gluon Fusion with Finite Heavy Quark Masses*, JHEP **10** (2009) 068, [arXiv:0907.2362](#) [hep-ph].
- [228] R. V. Harlander and W. B. Kilgore, *Next-to-next-to-leading order Higgs production at hadron colliders*, Phys. Rev. Lett. **88** (2002) 201801, [arXiv:hep-ph/0201206](#) [hep-ph].
- [229] V. Ravindran, J. Smith, and W. L. van Neerven, *NNLO corrections to the total cross-section for Higgs boson production in hadron hadron collisions*, Nucl. Phys. **B665** (2003) 325–366, [arXiv:hep-ph/0302135](#) [hep-ph].
- [230] A. Denner, S. Dittmaier, M. Grazzini, R. V. Harlander, R. S. Thorne, M. Spira, and M. Steinhauser, *Standard Model input parameters for Higgs physics*, . <https://cds.cern.ch/record/2047636>.
- [231] M. Bonvini and S. Marzani, *Resummed Higgs cross section at N^3LL* , JHEP **09** (2014) 007, [arXiv:1405.3654](#) [hep-ph].
- [232] S. Marzani, R. D. Ball, V. Del Duca, S. Forte, and A. Vicini, *Higgs production via gluon-gluon fusion with finite top mass beyond next-to-leading order*, Nucl. Phys. **B800** (2008) 127–145, [arXiv:0801.2544](#) [hep-ph].
- [233] A. Pak, M. Rogal, and M. Steinhauser, *Virtual three-loop corrections to Higgs boson production in gluon fusion for finite top quark mass*, Phys. Lett. **B679** (2009) 473–477, [arXiv:0907.2998](#) [hep-ph].
- [234] A. Pak, M. Rogal, and M. Steinhauser, *Finite top quark mass effects in NNLO Higgs boson production at LHC*, JHEP **02** (2010) 025, [arXiv:0911.4662](#) [hep-ph].
- [235] R. V. Harlander, H. Mantler, S. Marzani, and K. J. Ozeren, *Higgs Production in Gluon Fusion at Next-to-Next-to-Leading Order QCD for Finite Top Mass*, Eur. Phys. J. **C66** (2010) 359–372, [arXiv:0912.2104](#) [hep-ph].
- [236] R. V. Harlander and K. J. Ozeren, *Finite top mass effects for hadronic Higgs production at next-to-next-to-leading order*, JHEP **11** (2009) 088, [arXiv:0909.3420](#) [hep-ph].
- [237] R. V. Harlander and K. J. Ozeren, *Top mass effects in Higgs production at next-to-next-to-leading order QCD: Virtual corrections*, Phys. Lett. **B679** (2009) 467–472, [arXiv:0907.2997](#) [hep-ph].
- [238] U. Baur and E. Glover, *Higgs Boson Production at Large Transverse Momentum in Hadronic Collisions*, Nuclear Physics B **339** (1990) no. 1, 38 – 66. <http://www.sciencedirect.com/science/article/pii/055032139090532I>.

- [239] R. Ellis, I. Hinchliffe, M. Soldate, and J. V. D. Bj Nuclear Physics B **297** (1988) no. 2, 221 – 243.
<http://www.sciencedirect.com/science/article/pii/0550321388900193>.
- [240] W.-Y. Keung and F. J. Petriello, *Electroweak and finite quark-mass effects on the Higgs boson transverse momentum distribution*, Phys. Rev. **D80** (2009) 013007, arXiv:0905.2775 [hep-ph].
- [241] M. Grazzini and H. Sargsyan, *Heavy-quark mass effects in Higgs boson production at the LHC*, JHEP **09** (2013) 129, arXiv:1306.4581 [hep-ph].
- [242] U. Langenegger, M. Spira, A. Starodumov, and P. Trub, *SM and MSSM Higgs Boson Production: Spectra at Large Transverse Momentum*, JHEP **06** (2006) 035, arXiv:hep-ph/0604156 [hep-ph].
- [243] E. Bagnaschi, G. Degrassi, P. Slavich, and A. Vicini, *Higgs Production via Gluon Fusion in the POWHEG Approach in the SM and in the MSSM*, Journal of High Energy Physics **1202** (2012) 088, arXiv:1111.2854 [hep-ph].
- [244] S. Höche, F. Krauss, M. Schönherr, and F. Siegert, *QCD matrix elements + parton showers: The NLO case*, JHEP **04** (2013) 027, arXiv:1207.5030 [hep-ph].
- [245] S. Catani, F. Krauss, R. Kuhn, and B. R. Webber, *QCD matrix elements + parton showers*, JHEP **11** (2001) 063, arXiv:hep-ph/0109231 [hep-ph].
- [246] F. Krauss, *Matrix elements and parton showers in hadronic interactions*, JHEP **08** (2002) 015, arXiv:hep-ph/0205283 [hep-ph].
- [247] L. Lönnblad, *Correcting the color dipole cascade model with fixed order matrix elements*, JHEP **05** (2002) 046, arXiv:hep-ph/0112284 [hep-ph].
- [248] J. Alwall, Q. Li, and F. Maltoni, *Matched predictions for Higgs production via heavy-quark loops in the SM and beyond*, Phys. Rev. **D85** (2012) 014031, arXiv:1110.1728 [hep-ph].
- [249] F. Krauss, R. Kuhn, and G. Soff, *AMEGIC++ 1.0: A Matrix element generator in C++*, JHEP **02** (2002) 044, arXiv:hep-ph/0109036 [hep-ph].
- [250] A. Denner, S. Dittmaier, and L. Hofer, *COLLIER - A fortran-library for one-loop integrals*, PoS **LL2014** (2014) 071, arXiv:1407.0087 [hep-ph].
- [251] E. Bagnaschi, R. V. Harlander, H. Mantler, A. Vicini, and M. Wiesemann, *Resummation Ambiguities in the Higgs Transverse Momentum Spectrum in the Standard Model and Beyond*, JHEP **01** (2016) 090, arXiv:1510.08850 [hep-ph].
- [252] M. Buschmann, C. Englert, D. Goncalves, T. Plehn, and M. Spannowsky, *Resolving the Higgs-Gluon Coupling with Jets*, Phys. Rev. **D90** (2014) no. 1, 013010, arXiv:1405.7651 [hep-ph].
- [253] E. Bagnaschi and A. Vicini, *The Higgs Transverse Momentum Distribution in Gluon Fusion as a Multiscale Problem*, JHEP **01** (2016) 056, arXiv:1505.00735 [hep-ph]. [JHEP01,056(2016)].
- [254] R. V. Harlander, H. Mantler, and M. Wiesemann, *Transverse Momentum Resummation for Higgs Production via Gluon Fusion in the MSSM*, JHEP **11** (2014) 116, arXiv:1409.0531 [hep-ph].
- [255] S. Höche, F. Krauss, S. Schumann, and F. Siegert, *QCD matrix elements and truncated showers*, JHEP **05** (2009) 053, arXiv:0903.1219 [hep-ph].
- [256] R. Hamberg, W. van Neerven, and T. Matsuura, *A Complete calculation of the order α_s^2 correction to the Drell-Yan K factor*, Nucl.Phys. **B359** (1991) 343–405. [Erratum-ibid. B **644** (2002) 403].
- [257] K. Melnikov and F. Petriello, *The W boson production cross section at the LHC through*

- $O(\alpha_s^2)$, Phys.Rev.Lett. **96** (2006) 231803, arXiv:hep-ph/0603182 [hep-ph].
- [258] K. Melnikov and F. Petriello, *Electroweak gauge boson production at hadron colliders through $O(\alpha(s)^{**2})$* , Phys.Rev. **D74** (2006) 114017, arXiv:hep-ph/0609070 [hep-ph].
- [259] S. Catani, L. Cieri, G. Ferrera, D. de Florian, and M. Grazzini, *Vector boson production at hadron colliders: A Fully exclusive QCD calculation at NNLO*, Phys.Rev.Lett. **103** (2009) 082001, arXiv:0903.2120 [hep-ph].
- [260] R. Gavin, Y. Li, F. Petriello, and S. Quackenbush, *FEWZ 2.0: A code for hadronic Z production at next-to-next-to-leading order*, Comput.Phys.Commun. **182** (2011) 2388–2403, arXiv:1011.3540 [hep-ph].
- [261] R. Gavin, Y. Li, F. Petriello, and S. Quackenbush, *W Physics at the LHC with FEWZ 2.1*, Comput.Phys.Commun. **184** (2013) 208–214, arXiv:1201.5896 [hep-ph].
- [262] U. Baur, S. Keller, and W. Sakumoto, *QED radiative corrections to Z boson production and the forward backward asymmetry at hadron colliders*, Phys.Rev. **D57** (1998) 199–215, arXiv:hep-ph/9707301 [hep-ph].
- [263] V. Zykunov, *Electroweak corrections to the observables of W boson production at RHIC*, Eur.Phys.J.direct **C3** (2001) 9, arXiv:hep-ph/0107059 [hep-ph].
- [264] U. Baur, O. Brein, W. Hollik, C. Schappacher, and D. Wackerroth, *Electroweak radiative corrections to neutral current Drell-Yan processes at hadron colliders*, Phys.Rev. **D65** (2002) 033007, arXiv:hep-ph/0108274 [hep-ph].
- [265] S. Dittmaier and M. Krämer, *Electroweak radiative corrections to W boson production at hadron colliders*, Phys.Rev. **D65** (2002) 073007, arXiv:hep-ph/0109062 [hep-ph].
- [266] U. Baur and D. Wackerroth, *Electroweak radiative corrections to $p\bar{p} \rightarrow W^\pm \rightarrow \ell^\pm \nu$ beyond the pole approximation*, Phys.Rev. **D70** (2004) 073015, arXiv:hep-ph/0405191 [hep-ph].
- [267] A. Arbuzov et al., *One-loop corrections to the Drell-Yan process in SANC. I. The Charged current case*, Eur.Phys.J. **C46** (2006) 407–412, arXiv:hep-ph/0506110 [hep-ph].
- [268] C. Carloni Calame, G. Montagna, O. Nicrosini, and A. Vicini, *Precision electroweak calculation of the charged current Drell-Yan process*, JHEP **0612** (2006) 016, arXiv:hep-ph/0609170 [hep-ph].
- [269] V. Zykunov, *Weak radiative corrections to Drell-Yan process for large invariant mass of di-lepton pair*, Phys.Rev. **D75** (2007) 073019, arXiv:hep-ph/0509315 [hep-ph].
- [270] C. Carloni Calame, G. Montagna, O. Nicrosini, and A. Vicini, *Precision electroweak calculation of the production of a high transverse-momentum lepton pair at hadron colliders*, JHEP **0710** (2007) 109, arXiv:0710.1722 [hep-ph].
- [271] A. Arbuzov et al., *One-loop corrections to the Drell-Yan process in SANC. (II). The Neutral current case*, Eur.Phys.J. **C54** (2008) 451–460, arXiv:0711.0625 [hep-ph].
- [272] S. Brensing, S. Dittmaier, M. Krämer, and A. Mück, *Radiative corrections to W^- boson hadroproduction: Higher-order electroweak and supersymmetric effects*, Phys.Rev. **D77** (2008) 073006, arXiv:0710.3309 [hep-ph].
- [273] S. Dittmaier and M. Huber, *Radiative corrections to the neutral-current Drell-Yan process in the Standard Model and its minimal supersymmetric extension*, JHEP **1001** (2010) 060, arXiv:0911.2329 [hep-ph].
- [274] S. Dittmaier, A. Huss, and C. Schwinn, *Mixed QCD-electroweak $\mathcal{O}(\alpha_s\alpha)$ corrections to Drell-Yan processes in the resonance region: pole approximation and non-factorizable corrections*, Nucl. Phys. **B885** (2014) 318–372, arXiv:1403.3216 [hep-ph].

- [275] T. Gleisberg, S. Höche, F. Krauss, M. Schönherr, S. Schumann, et al., *Event generation with SHERPA 1.1*, JHEP **0902** (2009) 007, arXiv:0811.4622 [hep-ph].
- [276] D. R. Yennie, S. C. Frautschi, and H. Suura, *The Infrared Divergence Phenomena and High-Energy Processes*, Ann. Phys. **13** (1961) 379–452.
<http://inspirehep.net/search?j=APNYA,13,379>.
- [277] M. Schönherr and F. Krauss, *Soft photon radiation in particle decays in Sherpa*, JHEP **12** (2008) 018, arXiv:0810.5071 [hep-ph].
<http://inspirehep.net/search?p=arXiv:0810.5071>.
- [278] T. Hahn and M. Perez-Victoria, *Automatized one loop calculations in four-dimensions and D-dimensions*, Comput.Phys.Commun. **118** (1999) 153–165, arXiv:hep-ph/9807565 [hep-ph].
- [279] K. Arnold et al., *VBFNLO: A Parton level Monte Carlo for processes with electroweak bosons*, Comput. Phys. Commun. **180** (2009) 1661–1670, arXiv:0811.4559 [hep-ph].
- [280] S. Becker, C. Reuschle, and S. Weinzierl, *Numerical NLO QCD calculations*, JHEP **12** (2010) 013, arXiv:1010.4187 [hep-ph].
- [281] S. Badger, B. Biedermann, and P. Uwer, *NGluon: A Package to Calculate One-loop Multi-gluon Amplitudes*, Comput.Phys.Commun. **182** (2011) 1674–1692, arXiv:1011.2900 [hep-ph].
- [282] V. Hirschi, R. Frederix, S. Frixione, M. V. Garzelli, F. Maltoni, et al., *Automation of one-loop QCD corrections*, JHEP **1105** (2011) 044, arXiv:1103.0621 [hep-ph].
- [283] G. Cullen, N. Greiner, G. Heinrich, G. Luisoni, P. Mastrolia, et al., *Automated One-Loop Calculations with GoSam*, Eur.Phys.J. **C72** (2012) 1889, arXiv:1111.2034 [hep-ph].
- [284] S. Actis, A. Denner, L. Hofer, A. Scharf, and S. Uccirati, *Recursive generation of one-loop amplitudes in the Standard Model*, JHEP **04** (2013) 037, arXiv:1211.6316 [hep-ph].
- [285] M. Chiesa, N. Greiner, and F. Tramontano, *Automation of electroweak corrections for LHC processes*, J. Phys. **G43** (2016) no. 1, 013002, arXiv:1507.08579 [hep-ph].
- [286] M. L. Mangano, M. Moretti, F. Piccinini, R. Pittau, and A. D. Polosa, *ALPGEN, a generator for hard multiparton processes in hadronic collisions*, JHEP **07** (2003) 001, hep-ph/0206293.
- [287] A. van Hameren, *Multi-gluon one-loop amplitudes using tensor integrals*, JHEP **0907** (2009) 088, arXiv:0905.1005 [hep-ph].
- [288] A. Denner, *Techniques for calculation of electroweak radiative corrections at the one loop level and results for W physics at LEP-200*, Fortsch.Phys. **41** (1993) 307–420, arXiv:0709.1075 [hep-ph].
- [289] M. V. Garzelli, I. Malamos, and R. Pittau, *Feynman rules for the rational part of the Electroweak 1-loop amplitudes*, JHEP **01** (2010) 040, arXiv:0910.3130 [hep-ph].
[Erratum: JHEP10,097(2010)].
- [290] A. Denner, S. Dittmaier, and L. Hofer, *Collier: a fortran-based Complex One-Loop Library in Extended Regularizations*, arXiv:1604.06792 [hep-ph].
- [291] A. Denner, S. Dittmaier, and L. Hofer, *COLLIER: a Complex One-Loop Library with Extended Regularizations*, <http://collier.hepforge.org>, 2016.
- [292] A. Denner, S. Dittmaier, M. Roth, and L. Wieders, *Electroweak corrections to charged-current $e^+e^- \rightarrow 4$ fermion processes: Technical details and further results*, Nucl.Phys. **B724** (2005) 247–294, arXiv:hep-ph/0505042 [hep-ph].
Erratum-ibid. **B854** (2012) 504–507.
- [293] S. Catani, S. Dittmaier, M. H. Seymour, and Z. Trocsanyi, *The Dipole formalism for next-to-leading order QCD calculations with massive partons*, Nucl. Phys. **B627** (2002)

- 189–265, [arXiv:hep-ph/0201036](#) [hep-ph].
- [294] F. Cascioli, J. Lindert, P. Maierhöfer, and S. Pozzorini, *OPENLOOPS one-loop generator*, <http://openloops.hepforge.org>, 2012.
- [295] A. Denner and S. Dittmaier, *Reduction of one-loop tensor 5-point integrals*, Nucl. Phys. **B658** (2003) 175–202, [arXiv:hep-ph/0212259](#).
- [296] A. Denner and S. Dittmaier, *Reduction schemes for one-loop tensor integrals*, Nucl. Phys. **B734** (2006) 62–115, [arXiv:hep-ph/0509141](#).
- [297] A. Denner and S. Dittmaier, *Scalar one-loop 4-point integrals*, Nucl.Phys. **B844** (2011) 199–242, [arXiv:1005.2076](#) [hep-ph].
- [298] G. Ossola, C. G. Papadopoulos, and R. Pittau, *CutTools: A Program implementing the OPP reduction method to compute one-loop amplitudes*, JHEP **0803** (2008) 042, [arXiv:0711.3596](#) [hep-ph].
- [299] A. van Hameren, *OneLOop: For the evaluation of one-loop scalar functions*, Comput.Phys.Commun. **182** (2011) 2427–2438, [arXiv:1007.4716](#) [hep-ph].
- [300] MUNICH is the abbreviation of “MULTI-chaNnel Integrator at Swiss (CH) precision”—an automated parton level NLO generator by S. Kallweit, in preparation.
- [301] T. Gleisberg and F. Krauss, *Automating dipole subtraction for QCD NLO calculations*, Eur. Phys. J. **C53** (2008) 501–523, [arXiv:0709.2881](#) [hep-ph].
- [302] T. Gleisberg and S. Höche, *Comix, a new matrix element generator*, JHEP **12** (2008) 039, [arXiv:0808.3674](#) [hep-ph].
- [303] S. Dittmaier, *A General approach to photon radiation off fermions*, Nucl. Phys. **B565** (2000) 69–122, [arXiv:hep-ph/9904440](#) [hep-ph].
- [304] S. Dittmaier, A. Kabelschacht, and T. Kasprzik, *Polarized QED splittings of massive fermions and dipole subtraction for non-collinear-safe observables*, Nucl. Phys. **B800** (2008) 146–189, [arXiv:0802.1405](#) [hep-ph].
- [305] R. Frederix, S. Frixione, F. Maltoni, and T. Stelzer, *Automation of next-to-leading order computations in QCD: The FKS subtraction*, JHEP **10** (2009) 003, [arXiv:0908.4272](#) [hep-ph].
- [306] C. Degrande, C. Duhr, B. Fuks, D. Grellscheid, O. Mattelaer, and T. Reiter, *UFO - The Universal FeynRules Output*, Comput. Phys. Commun. **183** (2012) 1201–1214, [arXiv:1108.2040](#) [hep-ph].
- [307] M. Cacciari, M. Greco, and P. Nason, *The $P(T)$ spectrum in heavy flavor hadroproduction*, JHEP **05** (1998) 007, [arXiv:hep-ph/9803400](#) [hep-ph].
- [308] A. Denner and S. Pozzorini, *One loop leading logarithms in electroweak radiative corrections. 1. Results*, Eur.Phys.J. **C18** (2001) 461–480, [arXiv:hep-ph/0010201](#) [hep-ph].
- [309] A. Denner and S. Pozzorini, *One loop leading logarithms in electroweak radiative corrections. 2. Factorization of collinear singularities*, Eur.Phys.J. **C21** (2001) 63–79, [arXiv:hep-ph/0104127](#) [hep-ph].
- [310] M. Chiesa, G. Montagna, L. Barze, M. Moretti, O. Nicrosini, et al., *Electroweak Sudakov Corrections to New Physics Searches at the LHC*, Phys.Rev.Lett. **111** (2013) no. 12, 121801, [arXiv:1305.6837](#) [hep-ph].
- [311] K. Mishra, T. Becher, L. Barze, M. Chiesa, S. Dittmaier, et al., *Electroweak Corrections at High Energies*, [arXiv:1308.1430](#) [hep-ph].
- [312] J. Campbell, K. Hatakeyama, J. Huston, F. Petriello, J. R. Andersen, et al., *Working Group Report: Quantum Chromodynamics*, [arXiv:1310.5189](#) [hep-ph].
- [313] J. Butterworth, G. Dissertori, S. Dittmaier, D. de Florian, N. Glover, et al., *Les Houches*

- 2013: *Physics at TeV Colliders: Standard Model Working Group Report*,
arXiv:1405.1067 [hep-ph].
- [314] F. Caravaglios and M. Moretti, *An algorithm to compute Born scattering amplitudes without Feynman graphs*, Phys.Lett. **B358** (1995) 332–338, arXiv:hep-ph/9507237 [hep-ph].
- [315] CMS Collaboration, V. Khachatryan et al., *Comparison of the $Z/\gamma^* + jets$ to $\gamma + jets$ cross sections in pp collisions at $\sqrt{s} = 8$ TeV*, JHEP **10** (2015) 128, arXiv:1505.06520 [hep-ex].
- [316] S. Ask, M. A. Parker, T. Sandoval, M. E. Shea, and W. J. Stirling, *Using $\gamma+jets$ Production to Calibrate the Standard Model $Z(nu\bar{\nu})+jets$ Background to New Physics Processes at the LHC*, JHEP **10** (2011) 058, arXiv:1107.2803 [hep-ph].
- [317] Z. Bern, G. Diana, L. J. Dixon, F. Febres Cordero, S. Höche, H. Ita, D. A. Kosower, D. Maître, and K. J. Ozeren, *Missing energy and jets for supersymmetry searches*, Phys. Rev. D **87** (2013) 034026, arXiv:1206.6064 [hep-ph].
- [318] J. Alwall, M. Herquet, F. Maltoni, O. Mattelaer, and T. Stelzer, *MadGraph 5 : Going Beyond*, JHEP **1106** (2011) 128, arXiv:1106.0522 [hep-ph].
- [319] T. Sjöstrand, S. Mrenna, and P. Z. Skands, *PYTHIA 6.4 Physics and Manual*, JHEP **05** (2006) 026, arXiv:hep-ph/0603175 [hep-ph].
- [320] J. Alwall, S. Höche, F. Krauss, N. Lavesson, L. Lönnblad, F. Maltoni, M. L. Mangano, M. Moretti, C. G. Papadopoulos, F. Piccinini, S. Schumann, M. Treccani, J. Winter, and M. Worek, *Comparative study of various algorithms for the merging of parton showers and matrix elements in hadronic collisions*, Eur. Phys. J. C **53** (2008) 473, arXiv:0706.2569 [hep-ph].
- [321] S. Frixione, *Isolated photons in perturbative QCD*, Phys. Lett. **B429** (1998) 369–374, arXiv:hep-ph/9801442 [hep-ph].
- [322] S. Kallweit, J. M. Lindert, S. Pozzorini, M. Schönherr, and P. Maierhöfer, *NLO QCD+EW automation and precise predictions for V +multijet production*, in *Proceedings, 50th Rencontres de Moriond, QCD and high energy interactions*, pp. 121–124. 2015. arXiv:1505.05704 [hep-ph].
<http://inspirehep.net/record/1372103/files/arXiv:1505.05704.pdf>.
- [323] CMS Collaboration, *Search for dark matter with jets and missing transverse energy at 13 TeV*, CMS-PAS-EXO-15-003, 2015.
- [324] NNPDF Collaboration, R. D. Ball, V. Bertone, S. Carrazza, L. Del Debbio, S. Forte, A. Guffanti, N. P. Hartland, and J. Rojo, *Parton distributions with QED corrections*, Nucl. Phys. **B877** (2013) 290–320, arXiv:1308.0598 [hep-ph].
- [325] SM MC Working Group, SM and NLO MULTILEG Working Group Collaboration, J. Alcaraz Maestre et al., *The SM and NLO Multileg and SM MC Working Groups: Summary Report*, in *Proceedings, 7th Les Houches Workshop on Physics at TeV Colliders*, pp. 1–220. 2012. arXiv:1203.6803 [hep-ph].
<http://inspirehep.net/record/1095506/files/arXiv:1203.6803.pdf>.
- [326] M. Cacciari, G. P. Salam, and G. Soyez, *The Anti- $k(t)$ jet clustering algorithm*, JHEP **04** (2008) 063, arXiv:0802.1189 [hep-ph].
- [327] A. Buckley, J. Butterworth, L. Lönnblad, D. Grellscheid, H. Hoeth, J. Monk, H. Schulz, and F. Siegert, *Rivet user manual*, Comput. Phys. Commun. **184** (2013) 2803–2819, arXiv:1003.0694 [hep-ph].
- [328] Setup, analysis, and results available from
<https://phystev.cnrs.fr/wiki/2015:groups:tools:hjets>.
- [329] H. van Deurzen, N. Greiner, G. Luisoni, P. Mastrolia, E. Mirabella, G. Ossola,

- T. Peraro, J. F. von Soden-Fraunhofen, and F. Tramontano, *NLO QCD corrections to the production of Higgs plus two jets at the LHC*, Phys. Lett. **B721** (2013) 74–81, [arXiv:1301.0493 \[hep-ph\]](#).
- [330] G. Cullen, H. van Deurzen, N. Greiner, G. Luisoni, P. Mastrolia, E. Mirabella, G. Ossola, T. Peraro, and F. Tramontano, *Next-to-Leading-Order QCD Corrections to Higgs Boson Production Plus Three Jets in Gluon Fusion*, Phys. Rev. Lett. **111** (2013) no. 13, 131801, [arXiv:1307.4737 \[hep-ph\]](#).
- [331] N. Greiner, S. Höche, G. Luisoni, M. Schönherr, J.-C. Winter, and V. Yundin, *Phenomenological analysis of Higgs boson production through gluon fusion in association with jets*, JHEP **01** (2016) 169, [arXiv:1506.01016 \[hep-ph\]](#).
- [332] T. Binoth et al., *A Proposal for a standard interface between Monte Carlo tools and one-loop programs*, Comput. Phys. Commun. **181** (2010) 1612–1622, [arXiv:1001.1307 \[hep-ph\]](#). [[1\(2010\)](#)].
- [333] S. Alioli et al., *Update of the Binoth Les Houches Accord for a standard interface between Monte Carlo tools and one-loop programs*, Comput. Phys. Commun. **185** (2014) 560–571, [arXiv:1308.3462 \[hep-ph\]](#).
- [334] P. Nogueira, *Automatic Feynman graph generation*, J. Comput. Phys. **105** (1993) 279–289.
- [335] J. A. M. Vermaseren, *New features of FORM*, [arXiv:math-ph/0010025 \[math-ph\]](#).
- [336] J. Kuipers, T. Ueda, J. A. M. Vermaseren, and J. Vollinga, *FORM version 4.0*, Comput. Phys. Commun. **184** (2013) 1453–1467, [arXiv:1203.6543 \[cs.SC\]](#).
- [337] G. Cullen, M. Koch-Janusz, and T. Reiter, *Spinney: A Form Library for Helicity Spinors*, Comput. Phys. Commun. **182** (2011) 2368–2387, [arXiv:1008.0803 \[hep-ph\]](#).
- [338] P. Mastrolia, E. Mirabella, and T. Peraro, *Integrand reduction of one-loop scattering amplitudes through Laurent series expansion*, JHEP **06** (2012) 095, [arXiv:1203.0291 \[hep-ph\]](#). [[Erratum: JHEP11,128\(2012\)](#)].
- [339] H. van Deurzen, G. Luisoni, P. Mastrolia, E. Mirabella, G. Ossola, and T. Peraro, *Multi-leg One-loop Massive Amplitudes from Integrand Reduction via Laurent Expansion*, JHEP **03** (2014) 115, [arXiv:1312.6678 \[hep-ph\]](#).
- [340] T. Peraro, *Ninja: Automated Integrand Reduction via Laurent Expansion for One-Loop Amplitudes*, Comput. Phys. Commun. **185** (2014) 2771–2797, [arXiv:1403.1229 \[hep-ph\]](#).
- [341] G. Heinrich, G. Ossola, T. Reiter, and F. Tramontano, *Tensorial Reconstruction at the Integrand Level*, JHEP **10** (2010) 105, [arXiv:1008.2441 \[hep-ph\]](#).
- [342] T. Binoth, J.-P. Guillet, G. Heinrich, E. Pilon, and T. Reiter, *Golem95: A Numerical program to calculate one-loop tensor integrals with up to six external legs*, Comput.Phys.Commun. **180** (2009) 2317–2330, [arXiv:0810.0992 \[hep-ph\]](#).
- [343] G. Cullen, J. P. Guillet, G. Heinrich, T. Kleinschmidt, E. Pilon, et al., *Golem95C: A library for one-loop integrals with complex masses*, Comput.Phys.Commun. **182** (2011) 2276–2284, [arXiv:1101.5595 \[hep-ph\]](#).
- [344] Bern, Z. and Dixon, L. J. and Febres Cordero, F. and Höche, S. and Ita, H. and Kosower, D. A. and Maitre, D., *Ntuples for NLO Events at Hadron Colliders*, Comput. Phys. Commun. **185** (2014) 1443–1460, [arXiv:1310.7439 \[hep-ph\]](#).
- [345] K. Hamilton, P. Nason, and G. Zanderighi, *MINLO: Multi-Scale Improved NLO*, JHEP **10** (2012) 155, [arXiv:1206.3572 \[hep-ph\]](#).
- [346] M. Rubin, G. P. Salam, and S. Sapeta, *Giant QCD K-factors beyond NLO*, JHEP **09** (2010) 084, [arXiv:1006.2144 \[hep-ph\]](#).

- [347] S. Höche, Y. Li, and S. Prestel, *Higgs-boson production through gluon fusion at NNLO QCD with parton showers*, Phys. Rev. **D90** (2014) no. 5, 054011, arXiv:1407.3773 [hep-ph].
- [348] G. Bozzi, S. Catani, D. de Florian, and M. Grazzini, *Transverse-momentum resummation and the spectrum of the Higgs boson at the LHC*, Nucl. Phys. **B737** (2006) 73–120, arXiv:hep-ph/0508068 [hep-ph].
- [349] D. de Florian, G. Ferrera, M. Grazzini, and D. Tommasini, *Transverse-momentum resummation: Higgs boson production at the Tevatron and the LHC*, JHEP **11** (2011) 064, arXiv:1109.2109 [hep-ph].
- [350] S. Catani, D. de Florian, and M. Grazzini, *Universality of nonleading logarithmic contributions in transverse momentum distributions*, Nucl. Phys. **B596** (2001) 299–312, arXiv:hep-ph/0008184 [hep-ph].
- [351] C. Balazs and C. P. Yuan, *Soft gluon effects on lepton pairs at hadron colliders*, Phys. Rev. **D56** (1997) 5558–5583, arXiv:hep-ph/9704258 [hep-ph].
- [352] J. C. Collins, D. E. Soper, and G. F. Sterman, *Transverse Momentum Distribution in Drell-Yan Pair and W and Z Boson Production*, Nucl. Phys. **B250** (1985) 199.
- [353] C. J. Glosser and C. R. Schmidt, *Next-to-leading corrections to the Higgs boson transverse momentum spectrum in gluon fusion*, JHEP **12** (2002) 016, arXiv:hep-ph/0209248 [hep-ph].
- [354] J. Wang, C. S. Li, Z. Li, C. P. Yuan, and H. T. Li, *Improved Resummation Prediction on Higgs Production at Hadron Colliders*, Phys. Rev. **D86** (2012) 094026, arXiv:1205.4311 [hep-ph].
- [355] J. Collins, *Foundations of perturbative QCD*. Cambridge University Press, 2013. <http://www.cambridge.org/de/knowledge/isbn/item5756723>.
- [356] P. Sun, J. Isaacson, C. P. Yuan, and F. Yuan, *Resummation of High Order Corrections in Higgs Boson Plus Jet Production at the LHC*, arXiv:1602.08133 [hep-ph].
- [357] J. M. Campbell and R. K. Ellis, *MCFM for the Tevatron and the LHC*, Nucl. Phys. Proc. Suppl. **205-206** (2010) 10–15, arXiv:1007.3492 [hep-ph].
- [358] I. W. Stewart, F. J. Tackmann, J. R. Walsh, and S. Zuberi, *Jet p_T resummation in Higgs production at NNLL' + NNLO*, Phys. Rev. **D89** (2014) no. 5, 054001, arXiv:1307.1808.
- [359] I. W. Stewart, F. J. Tackmann, and W. J. Waalewijn, *Factorization at the LHC: From PDFs to Initial State Jets*, Phys. Rev. **D81** (2010) 094035, arXiv:0910.0467 [hep-ph].
- [360] C. F. Berger, C. Marcantonini, I. W. Stewart, F. J. Tackmann, and W. J. Waalewijn, *Higgs Production with a Central Jet Veto at NNLL+NNLO*, JHEP **04** (2011) 092, arXiv:1012.4480 [hep-ph].
- [361] F. J. Tackmann, J. R. Walsh, and S. Zuberi, *Resummation Properties of Jet Vetoes at the LHC*, Phys. Rev. **D86** (2012) 053011, arXiv:1206.4312 [hep-ph].
- [362] Z. Ligeti, I. W. Stewart, and F. J. Tackmann, *Treating the b quark distribution function with reliable uncertainties*, Phys. Rev. D **78** (2008) 114014, arXiv:0807.1926 [hep-ph].
- [363] R. Abbate, M. Fickinger, A. H. Hoang, V. Mateu, and I. W. Stewart, *Thrust at N^3LL with Power Corrections and a Precision Global Fit for $\alpha_s(m_Z)$* , Phys. Rev. D **83** (2011) 074021, arXiv:1006.3080 [hep-ph].
- [364] I. W. Stewart and F. J. Tackmann, *Theory Uncertainties for Higgs and Other Searches Using Jet Bins*, Phys. Rev. **D85** (2012) 034011, arXiv:1107.2117 [hep-ph].
- [365] J. M. Campbell et al., *NLO Higgs Boson Production Plus One and Two Jets Using the POWHEG BOX, MadGraph4 and MCFM*, JHEP **1207** (2012) 092, arXiv:1202.5475

- [hep-ph].
- [366] M. Grazzini, *NNLO predictions for the Higgs boson signal in the $H \rightarrow WW \rightarrow \ell\nu\ell\nu$ and $H \rightarrow ZZ \rightarrow 4\ell$ decay channels*, JHEP **02** (2008) 043, arXiv:0801.3232 [hep-ph].
- [367] T. Sjöstrand, S. Ask, J. R. Christiansen, R. Corke, N. Desai, P. Ilten, S. Mrenna, S. Prestel, C. O. Rasmussen, and P. Z. Skands, *An Introduction to PYTHIA 8.2*, Comput. Phys. Commun. **191** (2015) 159–177, arXiv:1410.3012 [hep-ph].
- [368] *ATLAS Run 1 Pythia8 tunes*, Tech. Rep. ATL-PHYS-PUB-2014-021, CERN, Geneva, Nov, 2014. <https://cds.cern.ch/record/1966419>.
- [369] K. Hamilton, P. Nason, C. Oleari, and G. Zanderighi, *Merging $H/W/Z + 0$ and 1 jet at NLO with no merging scale: a path to parton shower + NNLO matching*, JHEP **05** (2013) 082, arXiv:1212.4504 [hep-ph].
- [370] L. Lönnblad and S. Prestel, *Merging Multi-leg NLO Matrix Elements with Parton Showers*, JHEP **03** (2013) 166, arXiv:1211.7278 [hep-ph].
- [371] L. Lönnblad and S. Prestel, *Unitarising Matrix Element + Parton Shower merging*, JHEP **02** (2013) 094, arXiv:1211.4827 [hep-ph].
- [372] J. Gao, C. S. Li, and H. X. Zhu, *Top Quark Decay at Next-to-Next-to Leading Order in QCD*, Phys. Rev. Lett. **110** (2013) no. 4, 042001, arXiv:1210.2808 [hep-ph].
- [373] S. Schumann and F. Krauss, *A Parton shower algorithm based on Catani-Seymour dipole factorisation*, JHEP **03** (2008) 038, arXiv:0709.1027 [hep-ph].
- [374] S. Höche, S. Schumann, and F. Siegert, *Hard photon production and matrix-element parton-shower merging*, Phys. Rev. **D81** (2010) 034026, arXiv:0912.3501 [hep-ph].
- [375] S. Höche, F. Krauss, M. Schönherr, and F. Siegert, *A critical appraisal of NLO+PS matching methods*, JHEP **09** (2012) 049, arXiv:1111.1220 [hep-ph].
- [376] S. Höche, F. Krauss, M. Schönherr, and F. Siegert, *$W + n$ -Jet predictions at the Large Hadron Collider at next-to-leading order matched with a parton shower*, Phys. Rev. Lett. **110** (2013) no. 5, 052001, arXiv:1201.5882 [hep-ph].
- [377] A. Alloul, N. D. Christensen, C. Degrande, C. Duhr, and B. Fuks, *FeynRules 2.0 - A complete toolbox for tree-level phenomenology*, Comput. Phys. Commun. **185** (2014) 2250–2300, arXiv:1310.1921 [hep-ph].
- [378] F. Demartin, F. Maltoni, K. Mawatari, B. Page, and M. Zaro, *Higgs characterisation at NLO in QCD: CP properties of the top-quark Yukawa interaction*, Eur.Phys.J. **C74** (2014) no. 9, 3065, arXiv:1407.5089 [hep-ph].
- [379] R. Frederix and S. Frixione, *Merging meets matching in MC@NLO*, JHEP **12** (2012) 061, arXiv:1209.6215 [hep-ph].
- [380] R. Frederix, S. Frixione, A. Papaefstathiou, S. Prestel, and P. Torrielli, *A study of multi-jet production in association with an electroweak vector boson*, arXiv:1511.00847 [hep-ph].
- [381] R. Frederix, S. Frixione, V. Hirschi, F. Maltoni, R. Pittau, et al., *Four-lepton production at hadron colliders: aMC@NLO predictions with theoretical uncertainties*, JHEP **1202** (2012) 099, arXiv:1110.4738 [hep-ph].
- [382] J. Bellm et al., *Herwig 7.0 / Herwig++ 3.0 Release Note*, arXiv:1512.01178 [hep-ph].
- [383] S. Plätzer and S. Gieseke, *Coherent Parton Showers with Local Recoils*, JHEP **01** (2011) 024, arXiv:0909.5593 [hep-ph].
- [384] S. Plätzer and S. Gieseke, *Dipole Showers and Automated NLO Matching in Herwig++*, Eur. Phys. J. **C72** (2012) 2187, arXiv:1109.6256 [hep-ph].
- [385] S. Plätzer, *Controlling inclusive cross sections in parton shower + matrix element merging*, JHEP **08** (2013) 114, arXiv:1211.5467 [hep-ph].

- [386] J. Bellm, *Higher order corrections to multi jet final states at colliders*, 2015. PhD Thesis, Karlsruhe Institute of Technology.
- [387] J. Bellm, S. Plätzer, and S. Gieseke, *Mutli-jet merging with the Herwig 7 dipole shower*, 2016. in preparation.
- [388] M. Sjö Dahl, *ColorFull – a C++ library for calculations in $SU(N_c)$ color space*, Eur. Phys. J. **C75** (2015) 236, [arXiv:1412.3967 \[hep-ph\]](#).
- [389] T. Gehrmann, S. Höche, F. Krauss, M. Schönherr, and F. Siegert, *NLO QCD matrix elements + parton showers in $e^+e^- \rightarrow \text{hadrons}$* , JHEP **01** (2013) 144, [arXiv:1207.5031 \[hep-ph\]](#).
- [390] S. Höche, F. Krauss, and M. Schönherr, *Uncertainties in MEPS@NLO calculations of h +jets*, Phys. Rev. **D90** (2014) no. 1, 014012, [arXiv:1401.7971 \[hep-ph\]](#).
- [391] S. Höche and M. Schönherr, *Uncertainties in next-to-leading order plus parton shower matched simulations of inclusive jet and dijet production*, Phys. Rev. **D86** (2012) 094042, [arXiv:1208.2815 \[hep-ph\]](#).
- [392] J. R. Andersen and J. M. Smillie, *Constructing All-Order Corrections to Multi-Jet Rates*, JHEP **01** (2010) 039, [arXiv:0908.2786 \[hep-ph\]](#).
- [393] J. R. Andersen and J. M. Smillie, *The Factorisation of the t -channel Pole in Quark-Gluon Scattering*, Phys. Rev. **D81** (2010) 114021, [arXiv:0910.5113 \[hep-ph\]](#).
- [394] J. R. Andersen and J. M. Smillie, *Multiple Jets at the LHC with High Energy Jets*, JHEP **06** (2011) 010, [arXiv:1101.5394 \[hep-ph\]](#).
- [395] J. R. Andersen and C. D. White, *A New Framework for Multijet Predictions and its application to Higgs Boson production at the LHC*, Phys. Rev. **D78** (2008) 051501, [arXiv:0802.2858 \[hep-ph\]](#).
- [396] J. R. Andersen, V. Del Duca, and C. D. White, *Higgs Boson Production in Association with Multiple Hard Jets*, JHEP **02** (2009) 015, [arXiv:0808.3696 \[hep-ph\]](#).
- [397] H.-L. Lai, M. Guzzi, J. Huston, Z. Li, P. M. Nadolsky, et al., *New parton distributions for collider physics*, Phys.Rev. **D82** (2010) 074024, [arXiv:1007.2241 \[hep-ph\]](#).
- [398] S. Catani and B. R. Webber, *Infrared safe but infinite: Soft gluon divergences inside the physical region*, JHEP **10** (1997) 005, [arXiv:hep-ph/9710333 \[hep-ph\]](#).
- [399] A. Banfi, P. F. Monni, G. P. Salam, and G. Zanderighi, *Higgs and Z-boson production with a jet veto*, Phys. Rev. Lett. **109** (2012) 202001, [arXiv:1206.4998 \[hep-ph\]](#).
- [400] G. A. et al. (ATLAS Collaboration), *Observation of a new particle in the search for the Standard Model Higgs boson with the ATLAS detector at the LHC*, Phys. Lett. **B716** (2013) 1, [arXiv:1207.7214 \[hep-ph\]](#).
- [401] T. Binoth, J. P. Guillet, E. Pilon, and M. Werlen, *A Full next-to-leading order study of direct photon pair production in hadronic collisions*, Eur. Phys. J. **C16** (2000) 311–330, [arXiv hep-ph/9911340](#).
- [402] L. Bourhis, M. Fontannaz, and J. Guillet, *Quarks and gluon fragmentation functions into photons*, Eur.Phys.J. **C2** (1998) 529–537, [arXiv hep-ph/9704447](#).
- [403] J. Owens, *Large Momentum Transfer Production of Direct Photons, Jets, and Particles*, Rev.Mod.Phys. **59** (1987) 465.
- [404] S. Catani, L. Cieri, D. de Florian, G. Ferrera, and M. Grazzini, *Diphoton production at hadron colliders: a fully-differential QCD calculation at NNLO*, Phys.Rev.Lett. **108** (2012) 072001, [arXiv:1110.2375 \[hep-ph\]](#).
- [405] P. Aurenche, M. Fontannaz, J.-P. Guillet, E. Pilon, and M. Werlen, *A New critical study of photon production in hadronic collisions*, Phys. Rev. **D73** (2006) 094007, [arXiv:hep-ph/0602133 \[hep-ph\]](#).

- [406] Z. Belghobsi, M. Fontannaz, J. P. Guillet, G. Heinrich, E. Pilon, and M. Werlen, *Photon - Jet Correlations and Constraints on Fragmentation Functions*, Phys. Rev. **D79** (2009) 114024, arXiv:0903.4834 [hep-ph].
- [407] *Search for resonances decaying to photon pairs in 3.2 fb⁻¹ of pp collisions at $\sqrt{s} = 13$ TeV with the ATLAS detector*, Tech. Rep. ATLAS-CONF-2015-081, CERN, Geneva, Dec, 2015. <http://cds.cern.ch/record/2114853>.
- [408] J. Gallicchio and M. D. Schwartz, *Quark and Gluon Tagging at the LHC*, Phys. Rev. Lett. **107** (2011) 172001, arXiv:1106.3076 [hep-ph].
- [409] J. Gallicchio and M. D. Schwartz, *Quark and Gluon Jet Substructure*, JHEP **04** (2013) 090, arXiv:1211.7038 [hep-ph].
- [410] D. Krohn, M. D. Schwartz, T. Lin, and W. J. Waalewijn, *Jet Charge at the LHC*, Phys. Rev. Lett. **110** (2013) no. 21, 212001, arXiv:1209.2421 [hep-ph].
- [411] F. Pandolfi and D. Del Re, *Search for the Standard Model Higgs Boson in the $H \rightarrow ZZ \rightarrow llqq$ Decay Channel at CMS*. PhD thesis, Zurich, ETH, 2012.
- [412] CMS Collaboration, S. Chatrchyan et al., *Search for a Higgs boson in the decay channel H to $ZZ(*)$ to $q \bar{q} \ell^- \ell^+$ in pp collisions at $\sqrt{s} = 7$ TeV*, JHEP **04** (2012) 036, arXiv:1202.1416 [hep-ex].
- [413] A. J. Larkoski, G. P. Salam, and J. Thaler, *Energy Correlation Functions for Jet Substructure*, JHEP **06** (2013) 108, arXiv:1305.0007 [hep-ph].
- [414] A. J. Larkoski, J. Thaler, and W. J. Waalewijn, *Gaining (Mutual) Information about Quark/Gluon Discrimination*, JHEP **11** (2014) 129, arXiv:1408.3122 [hep-ph].
- [415] B. Bhattacharjee, S. Mukhopadhyay, M. M. Nojiri, Y. Sakaki, and B. R. Webber, *Associated jet and subjet rates in light-quark and gluon jet discrimination*, JHEP **04** (2015) 131, arXiv:1501.04794 [hep-ph].
- [416] ATLAS Collaboration, G. Aad et al., *Light-quark and gluon jet discrimination in pp collisions at $\sqrt{s} = 7$ TeV with the ATLAS detector*, Eur. Phys. J. **C74** (2014) no. 8, 3023, arXiv:1405.6583 [hep-ex].
- [417] ATLAS Collaboration, G. Aad et al., *Jet energy measurement and its systematic uncertainty in proton-proton collisions at $\sqrt{s} = 7$ TeV with the ATLAS detector*, Eur. Phys. J. **C75** (2015) 17, arXiv:1406.0076 [hep-ex].
- [418] CMS Collaboration, V. Khachatryan et al., *Measurement of electroweak production of two jets in association with a Z boson in proton-proton collisions at $\sqrt{s} = 8$ TeV*, Eur. Phys. J. **C75** (2015) no. 2, 66, arXiv:1410.3153 [hep-ex].
- [419] ATLAS Collaboration, G. Aad et al., *Search for high-mass diboson resonances with boson-tagged jets in proton-proton collisions at $\sqrt{s} = 8$ TeV with the ATLAS detector*, JHEP **12** (2015) 055, arXiv:1506.00962 [hep-ex].
- [420] CMS Collaboration, V. Khachatryan et al., *Search for the standard model Higgs boson produced through vector boson fusion and decaying to $b\bar{b}$* , Phys. Rev. **D92** (2015) no. 3, 032008, arXiv:1506.01010 [hep-ex].
- [421] ATLAS Collaboration, G. Aad et al., *Measurement of the charged-particle multiplicity inside jets from $\sqrt{s} = 8$ TeV pp collisions with the ATLAS detector*, arXiv:1602.00988 [hep-ex].
- [422] H. P. Nilles and K. H. Streng, *Quark - Gluon Separation in Three Jet Events*, Phys. Rev. **D23** (1981) 1944.
- [423] L. M. Jones, *Tests for Determining the Parton Ancestor of a Hadron Jet*, Phys. Rev. **D39** (1989) 2550.
- [424] Z. Fodor, *How to See the Differences Between Quark and Gluon Jets*, Phys. Rev. **D41**

- (1990) 1726.
- [425] L. Jones, *TOWARDS A SYSTEMATIC JET CLASSIFICATION*, Phys. Rev. **D42** (1990) 811–814.
 - [426] L. Lönnblad, C. Peterson, and T. Rognvaldsson, *Using neural networks to identify jets*, Nucl. Phys. **B349** (1991) 675–702.
 - [427] J. Pumplin, *How to tell quark jets from gluon jets*, Phys. Rev. **D44** (1991) 2025–2032.
 - [428] C. F. Berger, T. Kucs, and G. F. Sterman, *Event shape / energy flow correlations*, Phys. Rev. **D68** (2003) 014012, arXiv:hep-ph/0303051 [hep-ph].
 - [429] L. G. Almeida, S. J. Lee, G. Perez, G. F. Sterman, I. Sung, and J. Virzi, *Substructure of high- p_T Jets at the LHC*, Phys. Rev. **D79** (2009) 074017, arXiv:0807.0234 [hep-ph].
 - [430] S. D. Ellis, C. K. Vermilion, J. R. Walsh, A. Hornig, and C. Lee, *Jet Shapes and Jet Algorithms in SCET*, JHEP **11** (2010) 101, arXiv:1001.0014 [hep-ph].
 - [431] A. J. Larkoski, D. Neill, and J. Thaler, *Jet Shapes with the Broadening Axis*, JHEP **04** (2014) 017, arXiv:1401.2158 [hep-ph].
 - [432] S. Catani, G. Turnock, and B. R. Webber, *Jet broadening measures in e^+e^- annihilation*, Phys. Lett. **B295** (1992) 269–276.
 - [433] P. E. L. Rakow and B. R. Webber, *Transverse Momentum Moments of Hadron Distributions in QCD Jets*, Nucl. Phys. **B191** (1981) 63.
 - [434] R. K. Ellis and B. R. Webber, *QCD Jet Broadening in Hadron Hadron Collisions*, Conf. Proc. **C860623** (1986) 74.
 - [435] E. Farhi, *A QCD Test for Jets*, Phys. Rev. Lett. **39** (1977) 1587–1588.
 - [436] A. Höcker, P. Speckmayer, J. Stelzer, J. Therhaag, E. von Toerne, H. Voss, M. Backes, T. Carli, O. Cohen, A. Christov, D. Dannheim, K. Danielowski, S. Henrot-Versille, M. Jachowski, K. Kraszewski, A. Krasznahorkay, Jr., M. Kruk, Y. Mahalalel, R. Ospanov, X. Prudent, A. Robert, D. Schouten, F. Tegenfeldt, A. Voigt, K. Voss, M. Wolter, and A. Zemla, *TMVA - Toolkit for Multivariate Data Analysis*, ArXiv Physics e-prints (Mar., 2007) , physics/0703039.
 - [437] M. Bähr, S. Gieseke, M. Gigg, D. Grellscheid, K. Hamilton, et al., *Herwig++ Physics and Manual*, Eur.Phys.J. **C58** (2008) 639–707, arXiv:0803.0883 [hep-ph].
 - [438] J. Bellm et al., *Herwig++ 2.7 Release Note*, arXiv:1310.6877 [hep-ph].
 - [439] W. T. Giele, L. Hartgring, D. A. Kosower, E. Laenen, A. J. Larkoski, J. J. Lopez-Villarejo, M. Ritzmann, and P. Skands, *The Vincia Parton Shower*, PoS **DIS2013** (2013) 165, arXiv:1307.1060.
 - [440] Z. Nagy and D. E. Soper, *A parton shower based on factorization of the quantum density matrix*, JHEP **06** (2014) 097, arXiv:1401.6364 [hep-ph].
 - [441] C. Flensburg, G. Gustafson, and L. Lönnblad, *Inclusive and Exclusive Observables from Dipoles in High Energy Collisions*, JHEP **08** (2011) 103, arXiv:1103.4321 [hep-ph].
 - [442] L. Lönnblad, *ARIADNE version 4: A Program for simulation of QCD cascades implementing the color dipole model*, Comput. Phys. Commun. **71** (1992) 15–31.
 - [443] S. Höche and S. Prestel, *The midpoint between dipole and parton showers*, Eur. Phys. J. **C75** (2015) no. 9, 461, arXiv:1506.05057 [hep-ph].
 - [444] ALEPH Collaboration, A. Heister et al., *Studies of QCD at e^+e^- centre-of-mass energies between 91-GeV and 209-GeV*, Eur. Phys. J. **C35** (2004) 457–486.
 - [445] DELPHI Collaboration, J. Abdallah et al., *A Study of the energy evolution of event shape distributions and their means with the DELPHI detector at LEP*, Eur. Phys. J. **C29** (2003) 285–312, arXiv:hep-ex/0307048 [hep-ex].
 - [446] L3 Collaboration, P. Achard et al., *Studies of hadronic event structure in e^+e^-*

- annihilation from 30-GeV to 209-GeV with the L3 detector*, Phys. Rept. **399** (2004) 71–174, [arXiv:hep-ex/0406049](#) [hep-ex].
- [447] OPAL Collaboration, G. Abbiendi et al., *Measurement of event shape distributions and moments in $e^+ e^- \rightarrow$ hadrons at 91-GeV - 209-GeV and a determination of $\alpha(s)$* , Eur. Phys. J. **C40** (2005) 287–316, [arXiv:hep-ex/0503051](#) [hep-ex].
- [448] A. Buckley and C. Pollard, *QCD-aware partonic jet clustering for truth-jet flavour labelling*, [arXiv:1507.00508](#) [hep-ph].
- [449] A. Banfi, G. P. Salam, and G. Zanderighi, *Infrared safe definition of jet flavor*, Eur. Phys. J. **C47** (2006) 113–124, [arXiv:hep-ph/0601139](#) [hep-ph].
- [450] J. Gallicchio and M. D. Schwartz, *Pure Samples of Quark and Gluon Jets at the LHC*, JHEP **10** (2011) 103, [arXiv:1104.1175](#) [hep-ph].
- [451] A. J. Larkoski and J. Thaler, *Unsafe but Calculable: Ratios of Angularities in Perturbative QCD*, JHEP **09** (2013) 137, [arXiv:1307.1699](#) [hep-ph].
- [452] A. J. Larkoski, I. Moult, and D. Neill, *Toward Multi-Differential Cross Sections: Measuring Two Angularities on a Single Jet*, JHEP **09** (2014) 046, [arXiv:1401.4458](#) [hep-ph].
- [453] M. Procura, W. J. Waalewijn, and L. Zeune, *Resummation of Double-Differential Cross Sections and Fully-Unintegrated Parton Distribution Functions*, JHEP **02** (2015) 117, [arXiv:1410.6483](#) [hep-ph].
- [454] A. Hornig, Y. Makris, and T. Mehen, *Dijet Event Shapes at the LHC in SCET*, [arXiv:1601.01319](#) [hep-ph].
- [455] W. J. Waalewijn, *Calculating the Charge of a Jet*, Phys. Rev. **D86** (2012) 094030, [arXiv:1209.3019](#) [hep-ph].
- [456] H.-M. Chang, M. Procura, J. Thaler, and W. J. Waalewijn, *Calculating Track-Based Observables for the LHC*, Phys. Rev. Lett. **111** (2013) 102002, [arXiv:1303.6637](#) [hep-ph].
- [457] H.-M. Chang, M. Procura, J. Thaler, and W. J. Waalewijn, *Calculating Track Thrust with Track Functions*, Phys. Rev. **D88** (2013) 034030, [arXiv:1306.6630](#) [hep-ph].
- [458] M. Cacciari, G. P. Salam, and G. Soyez, *FastJet User Manual*, Eur. Phys. J. **C72** (2012) 1896, [arXiv:1111.6097](#) [hep-ph].
- [459] D. Bertolini, T. Chan, and J. Thaler, *Jet Observables Without Jet Algorithms*, JHEP **04** (2014) 013, [arXiv:1310.7584](#) [hep-ph].
- [460] G. Salam, *E_t^∞ Scheme*, Unpublished.
- [461] G. C. Blazey, J. R. Dittmann, S. D. Ellis, V. D. Elvira, K. Frame, et al., *Run II jet physics*, [arXiv:hep-ex/0005012](#) [hep-ex].
- [462] Y. L. Dokshitzer, A. Lucenti, G. Marchesini, and G. P. Salam, *On the QCD analysis of jet broadening*, JHEP **01** (1998) 011, [arXiv:hep-ph/9801324](#) [hep-ph].
- [463] A. Banfi, G. P. Salam, and G. Zanderighi, *Principles of general final-state resummation and automated implementation*, JHEP **03** (2005) 073, [arXiv:hep-ph/0407286](#) [hep-ph].
- [464] M. Jankowiak and A. J. Larkoski, *Jet Substructure Without Trees*, JHEP **06** (2011) 057, [arXiv:1104.1646](#) [hep-ph].
- [465] J. Thaler and K. Van Tilburg, *Identifying Boosted Objects with N -subjettiness*, JHEP **03** (2011) 015, [arXiv:1011.2268](#) [hep-ph].
- [466] J. Thaler and K. Van Tilburg, *Maximizing Boosted Top Identification by Minimizing N -subjettiness*, JHEP **02** (2012) 093, [arXiv:1108.2701](#) [hep-ph].
- [467] A. V. Manohar and M. B. Wise, *Power suppressed corrections to hadronic event shapes*,

- Phys. Lett. **B344** (1995) 407–412, [arXiv:hep-ph/9406392](#) [hep-ph].
- [468] Y. L. Dokshitzer and B. R. Webber, *Calculation of power corrections to hadronic event shapes*, Phys. Lett. **B352** (1995) 451–455, [arXiv:hep-ph/9504219](#) [hep-ph].
- [469] G. P. Korchemsky and G. F. Sterman, *Power corrections to event shapes and factorization*, Nucl. Phys. **B555** (1999) 335–351, [arXiv:hep-ph/9902341](#) [hep-ph].
- [470] G. P. Korchemsky and S. Tafat, *On power corrections to the event shape distributions in QCD*, JHEP **10** (2000) 010, [arXiv:hep-ph/0007005](#) [hep-ph].
- [471] G. P. Salam and D. Wicke, *Hadron masses and power corrections to event shapes*, JHEP **05** (2001) 061, [arXiv:hep-ph/0102343](#) [hep-ph].
- [472] C. Lee and G. F. Sterman, *Momentum Flow Correlations from Event Shapes: Factorized Soft Gluons and Soft-Collinear Effective Theory*, Phys. Rev. **D75** (2007) 014022, [arXiv:hep-ph/0611061](#) [hep-ph].
- [473] V. Mateu, I. W. Stewart, and J. Thaler, *Power Corrections to Event Shapes with Mass-Dependent Operators*, Phys. Rev. **D87** (2013) no. 1, 014025, [arXiv:1209.3781](#) [hep-ph].
- [474] P. Skands, S. Carrazza, and J. Rojo, *Tuning PYTHIA 8.1: the Monash 2013 Tune*, Eur. Phys. J. **C74** (2014) no. 8, 3024, [arXiv:1404.5630](#) [hep-ph].
- [475] G. Miu and T. Sjöstrand, *W production in an improved parton shower approach*, Phys. Lett. **B449** (1999) 313–320, [arXiv:hep-ph/9812455](#) [hep-ph].
- [476] J. R. Christiansen and P. Z. Skands, *String Formation Beyond Leading Colour*, JHEP **08** (2015) 003, [arXiv:1505.01681](#) [hep-ph].
- [477] S. Gieseke, C. Rohr, and A. Siodmok, *Colour reconnections in Herwig++*, Eur. Phys. J. **C72** (2012) 2225, [arXiv:1206.0041](#) [hep-ph].
- [478] M. H. Seymour and A. Siodmok, *Constraining MPI models using σ_{eff} and recent Tevatron and LHC Underlying Event data*, JHEP **10** (2013) 113, [arXiv:1307.5015](#) [hep-ph].
- [479] M. Bähr, M. Myska, M. H. Seymour, and A. Siodmok, *Extracting $\sigma_{effective}$ from the CDF $\gamma+3jets$ measurement*, JHEP **03** (2013) 129, [arXiv:1302.4325](#) [hep-ph].
- [480] C. Bierlich, G. Gustafson, L. Lönnblad, and A. Tarasov, *Effects of Overlapping Strings in pp Collisions*, JHEP **03** (2015) 148, [arXiv:1412.6259](#) [hep-ph].
- [481] J. M. Butterworth, A. R. Davison, M. Rubin, and G. P. Salam, *Jet substructure as a new Higgs search channel at the LHC*, Phys. Rev. Lett. **100** (2008) 242001, [arXiv:0802.2470](#) [hep-ph].
- [482] S. D. Ellis, C. K. Vermilion, and J. R. Walsh, *Techniques for improved heavy particle searches with jet substructure*, Phys. Rev. **D80** (2009) 051501, [arXiv:0903.5081](#) [hep-ph].
- [483] S. D. Ellis, C. K. Vermilion, and J. R. Walsh, *Recombination Algorithms and Jet Substructure: Pruning as a Tool for Heavy Particle Searches*, Phys. Rev. **D81** (2010) 094023, [arXiv:0912.0033](#) [hep-ph].
- [484] D. Krohn, J. Thaler, and L.-T. Wang, *Jet Trimming*, JHEP **02** (2010) 084, [arXiv:0912.1342](#) [hep-ph].
- [485] M. Dasgupta, A. Fregoso, S. Marzani, and G. P. Salam, *Towards an understanding of jet substructure*, JHEP **09** (2013) 029, [arXiv:1307.0007](#) [hep-ph].
- [486] A. J. Larkoski, S. Marzani, G. Soyez, and J. Thaler, *Soft Drop*, JHEP **05** (2014) 146, [arXiv:1402.2657](#) [hep-ph].
- [487] ZEUS Collaboration, S. Chekanov et al., *Substructure dependence of jet cross sections at HERA and determination of $\alpha(s)$* , Nucl. Phys. **B700** (2004) 3–50, [hep-ex/0405065](#).

- [488] F. Maltoni, G. Ridolfi, and M. Ubiali, *b-initiated processes at the LHC: a reappraisal*, JHEP **07** (2012) 022, arXiv:1203.6393 [hep-ph]. [Erratum: JHEP04,095(2013)].
- [489] S. Frixione and B. R. Webber, *Matching NLO QCD computations and parton shower simulations*, JHEP **06** (2002) 029, arXiv:hep-ph/0204244 [hep-ph].
- [490] P. Nason, *A New method for combining NLO QCD with shower Monte Carlo algorithms*, JHEP **0411** (2004) 040, arXiv:hep-ph/0409146 [hep-ph].
- [491] ATLAS Collaboration, G. Aad et al., *Measurement of differential production cross-sections for a Z boson in association with b-jets in 7 TeV proton-proton collisions with the ATLAS detector*, JHEP **10** (2014) 141, arXiv:1407.3643 [hep-ex].
- [492] CMS Collaboration, S. Chatrchyan et al., *Measurement of the cross section and angular correlations for associated production of a Z boson with b hadrons in pp collisions at $\sqrt{s} = 7$ TeV*, JHEP **12** (2013) 039, arXiv:1310.1349 [hep-ex].
- [493] ATLAS Collaboration, G. Aad et al., *Measurement of the cross-section for W boson production in association with b-jets in pp collisions at $\sqrt{s} = 7$ TeV with the ATLAS detector*, JHEP **06** (2013) 084, arXiv:1302.2929 [hep-ex].
- [494] F. Cascioli, S. Höche, F. Krauss, P. Maierhöfer, S. Pozzorini, and F. Siegert, *Automatic one-loop calculations with Sherpa+OpenLoops*, J. Phys. Conf. Ser. **523** (2014) 012058.
- [495] S. Plätzer, *Summing Large-N Towers in Colour Flow Evolution*, Eur. Phys. J. **C74** (2014) no. 6, 2907, arXiv:1312.2448 [hep-ph].
- [496] S. Gieseke, P. Stephens, and B. Webber, *New Formalism for QCD Parton Showers*, JHEP **12** (2003) 045, hep-ph/0310083.
- [497] G. Luisoni, C. Oleari, and F. Tramontano, *Wbb̄j production at NLO with POWHEG+MiNLO*, JHEP **04** (2015) 161, arXiv:1502.01213 [hep-ph].
- [498] T. Stelzer and W. F. Long, *Automatic generation of tree level helicity amplitudes*, Comput. Phys. Commun. **81** (1994) 357–371, hep-ph/9401258.
- [499] J. Alwall, P. Demin, S. de Visscher, R. Frederix, M. Herquet, et al., *MadGraph/MadEvent v4: The New Web Generation*, JHEP **0709** (2007) 028, arXiv:arXiv:0706.2334 [hep-ph].
- [500] G. Luisoni, P. Nason, C. Oleari, and F. Tramontano, *HW[±]/HZ + 0 and 1 jet at NLO with the POWHEG BOX interfaced to GoSam and their merging within MiNLO*, JHEP **1310** (2013) 083, arXiv:1306.2542 [hep-ph].
- [501] J. C. Collins, F. Wilczek, and A. Zee, *Low-Energy Manifestations of Heavy Particles: Application to the Neutral Current*, Phys. Rev. **D18** (1978) 242.
- [502] J. M. Campbell, F. Caola, F. Febres Cordero, L. Reina, and D. Wackerroth, *NLO QCD predictions for W + 1 jet and W + 2 jet production with at least one b jet at the 7 TeV LHC*, Phys. Rev. **D86** (2012) 034021, arXiv:1107.3714 [hep-ph].
- [503] HEPDATA, IPPP <http://hepdata.cedar.ac.uk>, <http://hepdata.cedar.ac.uk/>.
- [504] G. C. Fox and S. Wolfram, *A Model for Parton Showers in QCD*, Nucl. Phys. **B168** (1980) 285.
- [505] P. Mazzanti and R. Odorico, *A Monte Carlo Program for QCD Event Simulation in e⁺e⁻ Annihilation at LEP Energies*, Z. Phys. **C7** (1980) 61.
- [506] R. D. Field and S. Wolfram, *A QCD Model for e⁺e⁻ Annihilation*, Nucl. Phys. **B213** (1983) 65.
- [507] T. D. Gottschalk, *A Realistic Model for e⁺e⁻ Annihilation Including Parton Bremsstrahlung Effects*, Nucl. Phys. **B214** (1983) 201.
- [508] G. Marchesini and B. R. Webber, *Simulation of QCD Jets Including Soft Gluon Interference*, Nucl. Phys. **B238** (1984) 1.

- [509] R. D. Field, G. C. Fox, and R. L. Kelly, *Gluon Bremsstrahlung Effects in Hadron - Hadron Collisions*, Phys. Lett. **B119** (1982) 439.
- [510] R. Odorico, *Cojets: A Monte Carlo Program Simulating QCD in Hadronic Production of Jets and Heavy Flavors with Inclusion of Initial QCD Bremsstrahlung*, Comput. Phys. Commun. **32** (1984) 139.
- [511] T. Sjöstrand, *A Model for Initial State Parton Showers*, Phys. Lett. **B157** (1985) 321.
- [512] R. K. Ellis, G. Marchesini, and B. R. Webber, *Soft Radiation in Parton Parton Scattering*, Nucl. Phys. **B286** (1987) 643. [Erratum: Nucl. Phys. B294,1180(1987)].
- [513] G. Marchesini and B. R. Webber, *Monte Carlo Simulation of General Hard Processes with Coherent QCD Radiation*, Nucl. Phys. **B310** (1988) 461.
- [514] S. Frixione, P. Nason, and C. Oleari, *Matching NLO QCD computations with Parton Shower simulations: the POWHEG method*, JHEP **0711** (2007) 070, [arXiv:0709.2092 \[hep-ph\]](#).
- [515] N. Lavesson and L. Lönnblad, *Extending CKKW-merging to One-Loop Matrix Elements*, JHEP **12** (2008) 070, [arXiv:0811.2912 \[hep-ph\]](#).
- [516] S. Alioli, C. W. Bauer, C. Berggren, F. J. Tackmann, J. R. Walsh, and S. Zuberi, *Matching Fully Differential NNLO Calculations and Parton Showers*, JHEP **06** (2014) 089, [arXiv:1311.0286 \[hep-ph\]](#).
- [517] W. T. Giele, D. A. Kosower, and P. Z. Skands, *A simple shower and matching algorithm*, Phys. Rev. **D78** (2008) 014026, [arXiv:0707.3652 \[hep-ph\]](#).
- [518] W. T. Giele, D. A. Kosower, and P. Z. Skands, *Higher-Order Corrections to Timelike Jets*, Phys. Rev. **D84** (2011) 054003, [arXiv:1102.2126 \[hep-ph\]](#).
- [519] Z. Nagy and D. E. Soper, *Parton distribution functions in the context of parton showers*, JHEP **06** (2014) 179, [arXiv:1401.6368 \[hep-ph\]](#).
- [520] Z. Nagy and D. E. Soper, *Ordering variable for parton showers*, JHEP **06** (2014) 178, [arXiv:1401.6366 \[hep-ph\]](#).
- [521] Z. Nagy and D. E. Soper, *Effects of subleading color in a parton shower*, JHEP **07** (2015) 119, [arXiv:1501.00778 \[hep-ph\]](#).
- [522] S. Catani, B. R. Webber, and G. Marchesini, *QCD coherent branching and semiinclusive processes at large x*, Nucl. Phys. **B349** (1991) 635–654.
- [523] T. Sjöstrand and P. Z. Skands, *Transverse-momentum-ordered showers and interleaved multiple interactions*, Eur. Phys. J. **C39** (2005) 129–154, [arXiv:hep-ph/0408302 \[hep-ph\]](#).
- [524] T. Sjöstrand, S. Mrenna, and P. Z. Skands, *A Brief Introduction to PYTHIA 8.1*, Comput. Phys. Commun. **178** (2008) 852–867, [arXiv:0710.3820 \[hep-ph\]](#).
- [525] J. R. Christiansen and T. Sjöstrand, *Weak Gauge Boson Radiation in Parton Showers*, JHEP **04** (2014) 115, [arXiv:1401.5238 \[hep-ph\]](#).
- [526] E. Norrbin and T. Sjöstrand, *QCD radiation off heavy particles*, Nucl. Phys. **B603** (2001) 297–342, [arXiv:hep-ph/0010012 \[hep-ph\]](#).
- [527] K. Zapp under development .
- [528] J.-C. Winter and F. Krauss, *Initial-state showering based on colour dipoles connected to incoming parton lines*, JHEP **07** (2008) 040, [arXiv:0712.3913 \[hep-ph\]](#).
- [529] E. Bothmann, M. Schönherr, and S. Schumann, *Fast evaluation of theoretical uncertainties with Sherpa and MCgrid*, PoS **DIS2015** (2015) 136, [arXiv:1507.03908 \[hep-ph\]](#).
- [530] L. Del Debbio, N. P. Hartland, and S. Schumann, *MCgrid: projecting cross section calculations on grids*, Comput. Phys. Commun. **185** (2014) 2115–2126,

- arXiv:1312.4460 [hep-ph].
- [531] A. Buckley, *Sensitivities to PDFs in parton shower MC generator reweighting and tuning*, arXiv:1601.04229 [hep-ph].
 - [532] S. Gieseke, *Uncertainties of Sudakov form-factors*, JHEP **01** (2005) 058, arXiv:hep-ph/0412342 [hep-ph].
 - [533] Z. Bern, G. Diana, L. J. Dixon, F. Febres Cordero, S. Höche, D. A. Kosower, H. Ita, D. Maitre, and K. Ozeren, *Four-Jet Production at the Large Hadron Collider at Next-to-Leading Order in QCD*, Phys. Rev. Lett. **109** (2012) 042001, arXiv:1112.3940 [hep-ph].
 - [534] Z. Bern, L. J. Dixon, F. Febres Cordero, S. Höche, H. Ita, D. A. Kosower, D. Maitre, and K. J. Ozeren, *Next-to-Leading Order $W + 5$ -Jet Production at the LHC*, Phys. Rev. **D88** (2013) no. 1, 014025, arXiv:1304.1253 [hep-ph].
 - [535] A. Gehrmann-De Ridder, T. Gehrmann, E. W. N. Glover, and G. Heinrich, *EERAD3: Event shapes and jet rates in electron-positron annihilation at order α_s^3* , Comput. Phys. Commun. **185** (2014) 3331, arXiv:1402.4140 [hep-ph].
 - [536] A. Gehrmann-De Ridder, T. Gehrmann, E. W. N. Glover, and G. Heinrich, *NNLO corrections to event shapes in e^+e^- annihilation*, JHEP **12** (2007) 094, arXiv:0711.4711 [hep-ph].
 - [537] A. Gehrmann-De Ridder, T. Gehrmann, E. W. N. Glover, and G. Heinrich, *Jet rates in electron-positron annihilation at $O(\alpha(s)^{**3})$ in QCD*, Phys. Rev. Lett. **100** (2008) 172001, arXiv:0802.0813 [hep-ph].
 - [538] K. G. Chetyrkin, J. H. Kühn, and A. Kwiatkowski, *QCD corrections to the e^+e^- cross-section and the Z boson decay rate: Concepts and results*, Phys. Rept. **277** (1996) 189–281.